Microstructure-Property Investigations Of Zinc Oxide Varistors

A thesis submitted for the degree of
Doctor of Philosophy
at the University of London



by

Ravji Dhanji Pindoria

Department of Materials
Imperial College of Science, Technology and Medicine
University of London
London SW7 2BP
England

September, 1994

BIBL.
LONDIN.
UNIV.

Abstract

Samples of ZnO were synthesised with different levels of doping and with different sintering conditions. The microstructure and the microscopic electrical behaviour of these ZnO ceramic varistors were studied using a number of analytical techniques; namely scanning electron microscopy (SEM), energy dispersive analysis by x-rays (EDAX), scanning transmission electron microscopy (STEM), electron beam induced current (EBIC), cathodoluminescence (CL), secondary ion mass spectrometry (SIMS) and impedance spectroscopy (IS). The bulk non-linear I-V characteristics of the ZnO varistors were interpreted in terms of their microstructure, compositional variations and microscopic electrical behaviour. A bi-crystal of ZnO was synthesised and a single GB interface was studied. This provided additional information about the properties of a well-defined grain boundary.

From SEM/STEM-EDAX, and x-ray diffraction (XRD) studies, complementary information about the presence of spinel SP ($Zn_7Sb_2O_{12}$) pyrochlore PY ($Zn_2Sb_3Bi_3O_{14}$) and Bi (Bi_2O_3) phases decorating the ZnO grain boundaries (GB) was found. The microscopic electrical behaviour was investigated by SEM-EBIC. The terrace EBIC pattern with the associated line scan profiling (LSP) enabled a direct observation (Schottky barrier) of the microscopic electrical behaviour at the GBs, which are mainly decorated by Bi and SP phases in a good varistor. Transitions occurring within the band gap of the ZnO material were studied by the CL technique.

From SIMS studies, complementary information at a very sensitive level, about the presence and distribution of dopants was found. The isotopic exchange / diffusion profiles (IEDP) [using ^{18}O as a tracer] with SIMS enabled the measurement of the oxygen self diffusion coefficient (D*) and the surface diffusion coefficients (k), in both doped and undoped samples of ZnO ceramic. The associated line-scan SIMS profiling (LSP) across the polished x-sections of the ceramic sample, extended the range of these measurable D* and k values.

The bulk and GB electrical response of ZnO ceramic with a varying number of dopants was studied by IS. Measurement of I-V characteristics of both the undoped and the doped (with a combination of a varying number of dopant additives) samples of ZnO ceramics were undertaken and their non-linear coefficient, α, evaluated.

Contents

Abstract..... 1

Contents 2
List of Figures..... 8
List of Tables..... 21
Acknowledgements..... 23

Chapter 1: Introduction..... 25

1.1. Background 25
1.2. Overview of ZnO based varistors 26
1.3. Aim Of This Project 30
1.3.1. Novel contribution to science..... 30

Chapter 2: Literature Survey 32

2.1. Discovery and development of the ZnO based Varistor..... 32
2.1.1. Overview 32
2.1.2. Discovery of ZnO varistor..... 32
2.1.3. Advances In Varistor Technology 36
2.1.4. Commercial Applications..... 37
2.1.5. Functional properties of the ZnO Varistor 38
2.1.5.1. The Pre-Breakdown Region 39
2.1.5.1.1. Leakage Current. 39
2.1.5.2. The Intermediate Non-linear Region..... 40
2.1.5.3. The high-Current Upturn Region..... 42

2.2. Properties Of Zinc Oxide..... 42
2.2.1. Zinc Oxide Preparation And Crystal Structure..... 42
2.2.2. Electrical Properties of ZnO 45

2.3. Properties of ZnO Varistor 48
2.3.1. Fabrication of ZnO Varistor 48
2.3.2. Microstructure 49
2.3.2.1. Summary of the microstructure of ZnO varistor..... 63

2.4. Theoretical Models 67
2.4.1. Introduction 67
2.4.2. Space Charge Limited Current (SCLC) 67
2.4.3. Models based on Tunnelling 69
2.4.3.1. "Tunnelling Through A Thin Layer At The Grain Boundary" 69
2.4.3.2. Tunnelling Through Schottky Barriers Caused By Interface States 71
2.4.3.3. Hole-assisted tunnelling through Schottky barriers. 75
2.4.3.4. Tunnelling through homojunctions 75
2.4.4. The Hole-induced breakdown model 76
2.4.5. Grain boundary defect model 77
2.4.6. Bypass effect at heterojunctions 79
2.4.7. Space-charge-induced current model 80

2.5. Summary of the Conduction Models 82
2.6. Aims and Objectives 85

Chapter 3: Characterisation Techniques 87

3.1. Scanning electron microscopy (SEM) 87
3.1.1. Basic overview of an SEM 87
3.1.2. SEM-EDAX 90
3.1.3. SEM-EBIC 91
3.1.3.1. Basic overview of an EBIC 91
3.1.3.2. Instrumentation (EBIC) 94
3.1.3.3. EBIC signal detection 95
3.1.4. SEM-CL 96
3.1.4.1. Basic overview 96
3.1.4.2. Instrumentation (CL) 97

3.2. TEM/STEM-EDAX 98
3.2.1. Basic overview 98

3.3. SIMS (Secondary Ion Mass Spectrometry) 100
3.3.1. Introduction 100
3.3.2. Basic principles of SIMS 100
3.3.3. Instrumentation (The Atomika 6500) 102
3.3.3.1. Overview of the System 102
3.3.3.1.1. Primary beam column 102
3.3.3.1.2. Scanning of primary beam 104

3.3.3.2. Main chamber 104
3.3.3.3. Secondary ion detection system 105
3.3.3.4. Data acquisition 105
3.3.3.5. Secondary Ion Gating 106
3.3.3.5.1. Normal Depth Profiling With Checkerboard Gating 106
3.3.4. Ion Imaging during SIMS profiling 107
3.3.5. Line scan SIMS profiling 107
3.3.6. Charge compensation 108
3.3.7. Calibration 112

3.4. IS (Impedance Spectroscopy) 113
3.4.1. Overview of (IS) 113
3.4.1.1. Brick layer model 119
3.4.2. Experimental Apparatus 120

3.5. X-ray diffraction (XRD) Method 122
3.5.1. Overview of (XRD) 122

3.6. I:V Measurements 123

Chapter 4: Experimental Procedure 124

4.1. Sample Preparation 124
4.1.1. Preparation of powders 124
4.1.2. Formation of varistor Pellets 126
4.1.3. Preparation of bi-crystal of ZnO 127
4.1.4. Deposition of Electrodes 128

4.2. Analysis of Samples 130
4.2.1. Microstructural and compositional analysis - SEM-EDAX 131
4.2.1.1. Qualitative SEM-EDAX analysis 131
4.2.2. Microscopic electrical analysis using SEM-EBIC 132
4.2.2.1. Experimental conditions 132
4.2.2.2. EBIC analysis at National Physical Laboratory (N.P.L) 133
4.2.2.3. Microprobe manipulator 133
4.2.2.4. I:V measurement in the SEM with microprobe manipulator 134
4.2.3. SEM-CL Analysis of some ZnO based ceramics 134
4.2.3.1. Experimental Conditions 134

4.2.4. Microscopic compositional variation of dopants using SIMS 135
4.2.4.1. Compositional variation of dopants 135
4.2.4.1.1. Experimental condition for analysis 136
4.2.4.1.2. Stages of measurements 137
4.2.4.2. The spatial distribution of oxygen in ZnO ceramic 138
4.2.4.2.1. Sample preparation for oxygen diffusion work..... 138
4.2.4.2.1.1. The $^{16}O/^{18}O$ exchange..... 138
4.2.4.2.1.2. X-section of a sample for line scan analysis..... 140
4.2.4.2.2. Oxygen diffusion analysis 140
4.2.3. IS analysis..... 140
4.2.4. TEM analysis 141
4.2.4.1. Sample preparation for TEM..... 141
4.2.4.2. TEM analysis 142
4.2.4.3. STEM-EDX work at NPL..... 142
4.2.5. I:V measurement..... 143
4.2.6. XRD measurement..... 143
4.2.6.1. Sample preparation for XRD..... 143
4.2.7. Summary of the Sample Preparations and analysis 143

Chapter 5 : Results and Discussion 145

5.1. SEM/STEM-EDAX and XRD Microstructural Compositional Analysis..... 145
5.1.1. Microstructural analysis of ZnO powders 147
5.1.2. Microstructural analysis of ZnO ceramics 147
5.1.2.1. Samples sintered at 800°C..... 147
5.1.2.2. ZnO ceramics sintered at 1250°C 153
5.1.2.3. TEM/STEM-EDAX analysis of ZnO ceramic..... 163
5.1.2 4. XRD 164
5.1.3. Discussion of the SEM/TEM-EDAX and XRD results 164
5.1.3.1. Starting powders..... 164
5.1.3.2. Discussion of the microstructural analysis (800°C) 165
5.1.3.3. Discussion of the microstructural analysis (1250°C)..... 166
5.1.6. Summary of the SEM/STEM-EDAX and XRD microstructural analysis..... 171

5.2. SEM-EBIC Analysis of ZnO ceramics..... 172

5.2.1. Preliminary EBIC work 172
5.2.2. EBIC work using micro-manipulator and line scan profiling (LSP) 180
5.2.2.1. ZnO ceramic sample with all dopants 180
5.2.2.2. EBIC of ZnO with single additive (Bi_2O_3) 185
5.2.2.3. EBIC analysis of a ZnO bi-crystal 189
5.2.3. EBIC experiments at NPL 191
5.2.4. SEM-EBIC Discussion 191
5.2.5. Summary of the EBIC results 195

5.3. SEM-CL Analysis of ZnO ceramic 196
5.3.1. CL results 196
5.3.2. Discussion 200
5.3.3. Summary of the CL work 203

5.4. SIMS Analysis of ZnO ceramic 204
5.4.1. Depth profiling and Ion imaging results 204
5.4.1.2. Discussion on the Depth profiling, Ion imaging results 209
5.4.2. $^{16}O/^{18}O$ exchange and SIMS line-scan profiling 211
5.4.2.1. $^{16}O/^{18}O$ exchange SIMS depth profiling results 213
5.4.2.2. Discussion on $^{16}O/^{18}O$ exchange SIMS depth profiling 216
5.4.2.3. $^{16}O/^{18}O$ exchange SIMS line-scan profiling results 216
5.4.2.4. Discussion on $^{16}O/^{18}O$ exchange SIMS line scan profiling 221
5.4.3. Summary of the SIMS analysis. 223

5.5. IS Analysis of ZnO ceramics 224
5.5.1. Electrical conductivity in materials. 226
5.5.2. Presentation of IS results 227
5.5.2.1. IS of Pure ZnO ceramic. 227
5.5.2.2. IS results of ZnO ceramic varistor. 229
5.5.2.3. Arrhenius plots 233
5.5.3. Discussion of the IS results 236
5.5.3.1. electronic conduction in ZnO ceramic 237

5.6. I:V Measurements of ZnO ceramic 242
5.6.1. Results 242
5.6.2. Discussion of I:V results 246

5.7. Discussion of Experimental results 249

Conclusions 253

Suggestions for future work 258

Appendix A: Kröger and Vink notations.....259

Appendix B: Theory for Impedance Spectroscopy 261

Appendix C: IS data for ZnO ceramics 262

Appendix D: The Dihedral angle 268

References..... 270

List of Figures

Chapter 1

Fig. 1.2.1. Typical application of ZnO varistor as a transient protective element [4]. A varistor with a rapid (10^{-9} second) response and much lower impedance can divert the transient before it reaches the load.

Fig. 1.2.2. (a) Current-Voltage behaviour of a commercial varistor material; (b) coefficient of non linearity, α=d ln I/d ln V [4].

Fig. 1.2.3. Applications of ZnO varistors [11].

Chapter 2

Fig. 2.1.1. Background for the development of varistors [8].

Fig. 2.1.2. (a) Transition of varistor voltage (b) Transition of withstanding-surge-current [14].

Fig. 2.1.3. I:V curve of anomalous sample [8].

Fig. 2.1.4. (a) Normal Sample with surface barrier effect. (b) Anomalous sample with "Grain Boundary" barrier effect [8].

Fig. 2.1.5. (a) Schematic of the microstructure of a ZnO varistor. Grains of conducting ZnO, average size d, with segregated cations at the grain boundaries. Electrodes are attached and current flows as indicated. (b) Block model of a ZnO varistor having grain size d(~10 μm) and intergranular depletion barrier thickness t (~100 nm) D = electrode separation (not to scale) [4].

Fig. 2.1.6. Simple equivalent circuit representing a metal oxide varistor as a capacitance in parallel with a voltage dependent resistor. C_p and R_p are the capacitance and resistance of the intergranular layer, respectively; R_g is the ZnO grain resistance. For low applied voltages, R_p behaves as an ohmic loss [4].

Fig. 2.1.7. Schematic of the varistor and capacitor in an electrically parallel arrangement. These two components form a monolithic device within the dashed line to give protection to an integrated circuit. Also shown on the side is the Schematic of the power-law relation of the applied voltage and the current flow in the varistor [13].

Fig. 2.1.8. I:V characteristics of the varistor and its relation to protective level (PL) and non-linear coefficient (α) [5].

Fig. 2.1.9. The wave form of the impulse current: 8 μs rise time and 20 μs decay time up to half the peak value [6].

Fig. 2.2.1. Crystal structure of ZnO (wurtzite structure) [5,19].

Fig. 2.2.2. The simple vacancy itself is known as a Schottky defect (A) and vacancy self-interstitial (B) is known as a Frenkel defect [29].

Fig. 2.2.3. Conductivity of ZnO as a function of oxygen pressure [19].

Fig. 2.2.4. Electronic energy band diagram for ZnO indicating possible energies associated with electronic defects [5,19,20,28]. For symbols, the reader is referred to KrÖger and Vink notations in Appendix A.

Fig. 2.2.5. Self-diffusion coefficient of zinc (on the left) and oxygen (on the right) in undoped ZnO ceramic [19,118]. Oxygen diffusion studies of both doped and undoped ZnO ceramic is presented in this work (section 5.4).

Fig. 2.3.1. Simplified flow diagram for the fabrication of ZnO varistors [5].

Fig. 2.3.2. Ratio of Bi to Zn (A) across precipitate-free boundary and (B) across small precipitate particle on boundary. For this analysis the grain boundary was aligned parallel to the incident electron beam [34].

Fig. 2.3.3. Solute profile across grain boundary oriented at high angle to the degrading electric field [36].

Fig. 2.3.4. Schematic of different intergranular phase morphologies in ZnO. For a dihedral angle of greater than 60^{o}, the intergranular phase takes the form of discontinuous particles at the multi-grain junction (A). For a non-zero dihedral angle of less than 60%, the intergranular phase is continuous along the multi-grain junctions forming three dimensional lacy network throughout the sample but does not wet the grain boundaries (B). For a dihedral angle of zero, the intergranular phase wets the grain boundaries as well (not shown) [42].

Fig. 2.3.5. Four main types of ZnO interfaces present in slowly cooled (50^{o}C/h) specimens (Not to scale). (a) Type A: a boundary between ZnO grains containing a thin(~2 nm) intergranular amorphous Bi-rich film. (b) Type B: a ZnO/ZnO interface without secondary phases but containing segregated Bi atoms. (c) Type C: an interface between ZnO and an intergranular mixture of Bi_2O_3 and spinel grains. (d) Type D: interface between ZnO and pyrochlore and spinel grains [32,46].

Fig. 2.3.6. Schematic showing the distribution of additives in the sintered sample of ZnO varistor.

Fig. 2.4.1. Simplified energy-band diagram for an injecting contact between an insulator and a metal. The contact is in thermal and electrical equilibrium. F is the thermodynamic Fermi level, Et a single, discrete trap level, and Ec the bottom level of the conduction band. Et and Ec are functions of the position *x*. The amount Γ of downward-bending of the bands at the contact is given by the difference of the work functions of the insulator and metal :$\Gamma = \phi I - \phi M$ [64].

Fig. 2.4.2. Log-log plot of limiting current density (J) versus voltage (V) characteristics for Space-Charge-Limited current in an insulator with traps [64].

Fig. 2.4.3. Idealised microstructure of a metal oxide varistor, having grain size d and intergranular barriers thickness t. D is the electrode separation (not to scale) [62].

Fig. 2.4.4. Schematic depiction of the escape of an electron from the ZnO conduction band into the conduction band of the intergranular material. Process (i) is Schottky emission. Process (ii) is tunnelling. Process (i) occurs at intermediate temperatures and moderate fields (pre-breakown region). Here, electron escape proceeds by thermal activation over a field-lowered barrier. At high fields [case (ii)] quantum-mechanical tunnelling occurs as shown. This is the mechanism giving rise to varistor action [62].

Fig. 2.4.5. Grain-boundary band diagram [a] for proposed model and [b] after Levine [60].

Fig. 2.4.6. SIS- type energy-band model for non-ohmic ZnO ceramics. (A) unbiased and (B) biased [56].

Fig. 2.4.7. Schematics of the depletion layers in the ZnO and the region of trap filling in the insulator; (a) without and (b) with an applied voltage V [59].

Fig. 2.4.8. Asymmetrical degradation of the I:V curve of non-Ohmic ZnO ceramic caused by dc biasing [56].

Fig. 2.4.9. Deformation of Schottky barriers due to the change of space charges. (a) Initial state of the Schottky barriers in the unseparated case. (b) Deformed Schottky barriers caused by dc biasing in the unseparated case. (c) Initial state of Schottky barrier in the separated case. (d) Deformed Schottky barriers caused by dc biasing in the separated case [56].

Fig. 2.4.10. The hole model. The holes are created on the forward side of the junction whenever the hole's chemical potential (μH) is below the valence band edge. The electron tunnelling from the interface is indicated by the arrow labelled J. (X_H is the maximum extent of the injected holes) [52].

Fig. 2.4.11. Experimental and calculated current - voltage characteristics of a single ZnO varistor grain junction. The observed decrease in non-linearity at high current densities is due to the series resistance of the ZnO grains. This has not been included in the calculation [4,52].

Fig. 2.4.12. (a) Band-band tunnelling in ZnO homojunction. Tunnel current Jt sets in when the bias voltage is approximately equal to the gap voltage, 3.2V Jh = hole current. (b) Enhancement effect on Jt by reduction of tunnel distance. Jr is the electron-hole recombination process [12].

Fig. 2.4.13. Energy band diagram proposed by Blatter and Greutter. Double Schottky barriers are formed by interface states and traps. The breakdown is caused by hole accumulation at the grain boundary. The holes are generated by impact ionisation in the depletion region [23,24].

Fig. 2.4.14. The proposed atomic defect model for Schottky barrier at the grain boundary. Analogy with band model is also shown [37].

Fig. 2.4.15. Bypass model for a variety of grain boundaries. A-A and B-B are the Schottky barriers corresponding to the Bypass and the Main current respectively. The conduction band in Bi_2O_3 - rich intergranular layer is not clear. In the equivalent circuit of the grain boundary structure, R's and C's correspond to the resistance and capacitance of the Schottky barrier, respectively. Ri and Ci corresponds to the resistance and the capacitance of the intergranular layer, respectively. Rg corresponds to the resistance of the ZnO grain [6].

Fig. 2.4.16. A schematic representation of a Bi_2O_3 single layer and a ZnO-Bi_2O_3 two layer specimen and the applied polarity [63].

Fig. 2.4.17. I:V characteristics of a ZnO single-layer (full curve), a Bi_2O_3 single-layer (broken curve) and a forward bias ZnO-Bi_2O_3 two-layer (chain curve) specimen [63].

Fig. 2.4.18. C-V characteristics of a ZnO-Bi_2O_3 two-layer sample [63].

Fig. 2.4.19. Band diagram for a ZnO-Bi_2O_3 two-layer specimen [63].

Chapter 3

Fig. 3.1.1. Schematic representation of the scanning electron microscope [72].

Fig. 3.1.2. The signals used in the six modes of scanning electron microscopy: (a) the five signals available with continuous bombardment and (b) the generation of decaying thermal waves and ultrasonic waves by beam chopped at a high frequency [70].

Fig. 3.1.3. Schematic diagram illustrating the limited spatial resolution attainable in bulk samples due to electron beam spreading within the specimen. A typical value of the minimum X-ray spatial resolution is ≈ 1μm at 30 kV irrespective of beam diameter [73].

Fig. 3.1.4. The process of carrier generation during electron bombardment of a semiconductor specimen [72].

Fig. 3.1.5. Schematic illustration of carrier generation during electron bombardment of a high resistivity material such as ZnO varistor. (a) Intergranular barrier without illumination. (b) With illumination barrier -lowering increases n(0) and thereby promotes recombination. Continuous distribution of interface states assumed.

Fig. 3.1.6. Schematic of the Grün range (Rg).

Fig. 3.1.7. (A) Conductive mode detection circuit for a high resistivity specimen (ZnO Varistor) where the beam and specimen act as a potentiometer (current divider). and (B) the form of signal variation for a line scan.

Fig. 3.1.8. Schematic diagram of (Matelect) ISM 5 control unit and head amplifier used during EBIC analysis.

Fig. 3.1.9. The energy transitions in direct (a) and indirect (b) gap semiconductors between initial states E_i and final states E_f. For indirect transitions (b) the participation of a phonon (E_{ph}) is required [70].

Fig. 3.1.10. Schematic diagram of a CL light collection system.

Fig. 3.1.11. The computer-controlled CL detection system.

Fig. 3.2.1. A schematic diagram showing the important components of the Electron Microscope [104,105].

Fig. 3.2.2. Schematic illustration of the use of a very thin specimen (less than the mean free path of the incident electrons). This reduces the extent of beam spreading. The spatial resolution in the X-ray microanalysis mode is than commensurate with the electron beam diameter [73].

Fig. 3.3.1. (a) Schematic of the sample ion beam interaction in SIMS [69].

Fig. 3.3.1. (b) Energy spectrum of secondary ions.

Fig. 3.3.2. Schematic diagram illustrating the principles of a quadrupole based SIMS instrument.

Fig. 3.3.3. Primary beam scanning.

Fig. 3.3.4. Checkerboard gating system.

Fig. 3.3.5. Schematic diagram of the ^{18}O isotopic exchange with line-scan SIMS profiling for ^{18}O isotopic concentration depth profile measurements in oxides of high diffusivity [101].

Fig. 3.3.6. Schematic diagram showing the decrease in the measured positive ion intensity as the energy distribution shifts during charging [95].

Fig. 3.4.1. (a) Complex impedance plot for the circuit shown in (b). The arrow indicates increasing frequency. (b) Circuit diagram of a so-called Voigt element comprising of a resistor and capacitor in parallel.

Fig. 3.4.2. (a) Schematic complex impedance plot of a Zirconia type solid electrolyte. (b) An equivalent circuit giving the response of (a) [92].

Fig. 3.4.3. Brick layer model for a two-phase ceramic: (a) Overall view, showing array of cubic grains, separated by flat boundaries. (b) Exploded view of a single cell, showing parallel electrical paths: 9i) through grains and grain boundaries, and (ii) along grain boundaries [71].

Fig. 3.4.4. Schematics of the experimental apparatus used to obtain the impedance spectra of ZnO ceramics at various temperatures.

Fig. 3.4.5. Schematic of the sample holder used in the furnace shown in figure 3.4.4.

Fig. 3.5.1. Diffraction of X-rays from a set of crystal planes.

Fig. 3.6.1. The schematic of an I:V measurement.

Chapter 4

Fig. 4.1.1. Flow diagram for the sample preparation of ZnO varistors.

Fig. 4.1.2. Schematic of the pellet die used for making ceramic samples.

Fig. 4.1.3. Heating and cooling ramp used during the sintering of ZnO varistors.

Fig. 4.1.4. Schematic of ZnO bi-crystal (not to scale).

Fig. 4.2.1. Schematic of an EBIC set-up using S-4000 SEM with BSE amplifier.

Fig. 4.2.2. **Energy spectrum of secondary ions.**

Fig. 4.2.3. Schematic of a rig used for $^{16}O/^{18}O$ isotopic exchange.

Fig. 4.2.4. Schematic of the polishing jig used for TEM sample preparation.

Chapter 5

Fig. 5.1.1. SEM micrographs showing the particle size and shape of the pure ZnO powders.

Fig. 5.1.2. ZnO powders, doped with additives: Bi_2O_3 ,Sb_2O_3 Co_3O_4, MnO_2 and Cr_2O_3 , and then calcined at 700^{o}C for about 5 hours.

Fig. 5.1.3. (a) SEM micrograph of the **undoped** ZnO ceramic sample sintered at 800^{o}C.

Fig. 5.1.3. (b) SEM micrograph of a ZnO ceramic sample **doped** (0.5mol.%) with the oxide of **Bi** and then sintered at 800^{o}C.

Fig. 5.1.3. (c) SEM micrograph of a ZnO ceramic sample **doped** (0.5 mol.%) with the oxides of **Bi** and **Co**, and then sintered at 800^{o}C.

Fig. 5.1.3. (d) SEM micrograph of a ZnO ceramic sample **doped** (0.5 mol.%) with the oxides of **Bi, Co** and **Mn**, and then sintered at 800^{o}C.

Fig. 5.1.3. (e) Back-scattered and secondary SEM micrograph of a ZnO ceramic sample **doped** (0.5 mol.%) with the oxides of **Bi, Sb, Co,** and **Mn** and then sintered at 800°C.

Fig. 5.1.3. (f) SEM micrograph of a ZnO ceramic sample **doped** (0.5 mol.%) with the oxides of **Bi, Sb, Co, Mn** and **Cr,** and then sintered at 800°C.

Fig. 5.1.3. (g) SEM micrograph of a ZnO ceramic sample **doped** (0.5 mol.%) with the oxides of **Bi,** and **Sb,** and then sintered at 800°C.

Fig. 5.1.3. (h) SEM-EDAX spectra of cluster (pyrochlore) regions in ZnO ceramic as shown in Fig. 5.1.3 (g), **doped** (0.5 mol.%) with the oxides of **Bi,** and **Sb,** and then sintered at 800°C.

Fig. 5.1.4. (a) SEM micrograph of the **undoped** ZnO ceramic sample, sintered at 1250°C.

Fig. 5.1.4. (b) SEM micrograph of a ZnO ceramic sample **doped** (0.5 mol. %) with **Bi** oxide, and then sintered at 1250°C.

Fig. 5.1.4. (c) SEM micrograph of a ZnO ceramic sample **doped** (0.5 mol.%) with the oxides of **Bi,** and **Co** and then sintered at 1250°C. The backscattered image on the right is X 2500 mag.

Fig. 5.1.4. (d) SEM micrograph of a ZnO ceramic sample **doped** (0.5 mol.%) with the oxides of **Bi, Co,** and **Mn** and then sintered at 1250°C .

Fig. 5.1.4. (e) SEM micrograph of a ZnO ceramic sample **doped** (0.5 mol.%) with the oxides of **Bi, Sb, Co, Mn** and **Cr,** and then sintered at 1250°C.

Fig. 5.1.4. (f) SEM micrograph of a ZnO ceramic sample, (fractured surface) **doped** (0.5 mol.%) with the oxides of **Bi, Sb, Co, Mn** and **Cr,** and then sintered at 1250°C.

Fig. 5.1.5. (a) **X-ray** mapping of **Bi** in a ZnO ceramic sample doped (0.5 mol.%) with the oxides of Bi, Sb, Co, Mn and Cr, and then sintered at 1250°C. The size of this image (110 μ m x 79μm) corresponds to that in Fig.5.1.4 (e). Due to instrumental effect, the image has reduced by ≈ 32% horizontally (10mm ≈14μm) and ≈18% vertically (10mm ≈ 12 μm).

Fig. 5.1.5. (b) **X-ray** mapping of **Sb** in a ZnO ceramic sample doped (0.5 mol.%) with the oxides of Bi, Sb, Co, Mn and Cr, and then sintered at 1250°C. The size of this image (110 μ m x 79μm) corresponds to that in Fig.5.1.4 (e). **Scale:** the image has reduced by ≈ 32% horizontally (10mm ≈14μm) and ≈18% vertically (10mm ≈ 12μm).

Fig. 5.1.5. (c) **X-ray** mapping of **Cr** in a ZnO ceramic sample doped (0.5mol%) with the oxides of Bi, Sb, Co, Mn and Cr, and then sintered at 1250°C. The size of this image (110 μ m x 79μm) corresponds to that in Fig.5.1.4 (e). **Scale:** the image has reduced by ≈ 32% horizontally (10mm ≈14μm) and ≈18% vertically (10mm ≈ 12μm).

Fig. 5.1.5. (d) **X-ray** mapping of **Mn** in a ZnO ceramic sample doped (0.5mol%) with the oxides of Bi, Sb, Co, Mn and Cr, and then sintered at 1250°C. The size of this image (110 μ m x 79μm) corresponds to that in Fig.5.1.4 (e). **Scale:** the image has reduced by ≈ 32% horizontally (10mm ≈14μm) and ≈18% vertically (10mm ≈ 12μm).

Fig. 5.1.5. (e) **X-ray** mapping of **Co** in a ZnO ceramic sample doped (0.5mol%) with the oxides of Bi, Sb, Co, Mn and **Cr. and then** sintered at 1250°C. The size of this image (110 μm x 79μm) corresponds to that in Fig.5.1.4 (e). **Scale:** the image has reduced by ≈ 32% horizontally (10mm ≈14μm) and ≈18% vertically (10mm ≈ 12μm).

Fig. 5.1.6. SEM micrograph of a ZnO ceramic sample **doped** (0.5mol%) with the oxides of **Bi, Sb, Co, Mn** and **Cr,** and then **sintered and rapidly cooled from** 1250°C.

Fig. 5.1.7. (a) SEM micrograph of an **etched residue** of a ZnO ceramic sample, **doped** (0.5mol%) with the oxides of **Bi, Sb, Co, Mn** and **Cr**, and then sintered at 1250°C. Analysis at points 1B, 2, 3 and 5 corresponds to spinel phase; point 1A and 4 corresponds to pyrochlore phase (fig. 5.1.7b).

Fig. 5.1.7. (b) EDAX spectra corresponding to phases in the etched sample of a ZnO varistor as shown in Fig. 5.1.7 (a).

Fig. 5.1.8. SEM micrograph of a ZnO **bi-crystal** sample with the Bi oxide sandwiched in between the polished single crystals and sintered at 1500°C for 10 hours.

Fig. 5.1.9. SEM micrograph of a commercial ZnO, **Bi** based varistor sample.

Fig. 5.1.10. SEM micrograph of a commercial ZnO, **Pr** based varistor sample.

Fig. 5.1.11. (a) STEM micrograph (10K mag.) taken at 200kV, showing the grain boundaries interface with triple point coinciding with the EDAX (1) analysis in Fig. 5.1.11 (b). Scale: 14mm = 1μm.

Fig. 5.1.11. (b) STEAM-EDAX analysis of the doped ZnO ceramic. This analysis was undertaken at various regions in the microstructure, marked with a X and labelled as EDAX 1-8 with the list of elements detected. Regions marked as EDAX (1) and (5) are spinel particles shown shaded in this figure. Regions marked as EDAX (2) and (3) are the Bi rich phases (cross sections of the lacy type of network as previously identified using SEM. Regions marked as EDAX (4) and (6) corresponds to the ZnO grain, while those marked as (7) and (8) are the points at the grain boundary.

Fig. 5.1.12. XRD spectra of the etched residue of the ZnO doped ceramic sample as shown in Fig. 5.1.7 (a). According to the JCPDS-ICDD 15-687, the 2 θ position and the relative intensity of these peaks corresponds to $Zn_7 Sb_2 O_{12}$ spinel compound.

Fig. 5.1.13. Model for the tetrapod-like particle of ZnO [107].

Fig. 5.1.14. Schematics of the microstructure of (A) Bi doped ZnO ceramic sample sintered at 800°C showing pools of Bi rich phase at triple points in the pore regions and (B) at higher temperatures sintering (1250°C) a lacy network is produced with empty pores shown here as shaded regions that may have been previously occupied by Bi rich phase.

Fig. 5.1.15. Schematics of the microstructure of (A) Bi doped ZnO ceramic sample sintered at 1200°C showing a lacy network with empty pores in place of the Bi phase. (B) ZnO with all dopants, sintered at (1250°C). Pores are replaced by the SP particles leaving a much finer lacy network in the varistor.

Fig. 5.2.1. (a) SEM-EBIC micrograph (200 x mag.) of a Bi based commercial ZnO ceramic sample (grain size: 35μm), **doped** with the oxides of **Bi, Sb, Co, Mn** and **Cr.** SEM beam parameters: **3keV,** 11nA. **Scale**: 17mm ≈ 100μm; (35μm ≈ 6mm).

Fig. 5.2.1. (b) SEM-EBIC micrograph (200 x mag.) of a Bi based commercial ZnO ceramic sample, **doped** with the oxides of **Bi, Sb, Co, Mn** and **Cr.** SEM beam parameters: **5keV,** 11nA. **Scale**: 17mm ≈ 100μm; (35μm ≈ 6mm).

Fig. 5.2.1. (c) SEM-EBIC micrograph (200 x mag.) of a Bi based commercial ZnO ceramic sample, **doped** with the oxides of **Bi, Sb, Co, Mn** and **Cr.** SEM beam parameters: **15keV,** 11nA. **Scale**: 17mm ≈ 100μm; (35μm ≈ 6mm).

Fig. 5.2.1. (d) SEM-EBIC micrograph (200 x mag.) of a Bi based commercial ZnO ceramic sample, **doped** with the oxides of **Bi, Sb, Co, Mn** and **Cr.** SEM beam parameters: **25keV,** 99nA. **Scale**: 17mm ≈ 100μm; (35μm ≈ 6mm).

Fig. 5.2.1. (e) SEM-EBIC micrograph (200 x mag.) of a Bi based commercial ZnO ceramic sample, **doped** with the oxides of **Bi, Sb, Co, Mn** and **Cr.** SEM beam parameters: **25keV,** 41nA. **Scale**: 17mm ≈ 100μm; (35μm ≈ 6mm).

Fig. 5.2.1. (f) SEM micrograph (200 x mag.) of a Bi based commercial ZnO ceramic sample, **doped** with the oxides of **Bi, Sb, Co, Mn** and **Cr.** SEM beam parameters: **25keV,** 41nA. **Scale**: 17mm ≈ 100μm; (35μm ≈ 6mm).

Fig. 5.2.2. (a) SEM-EBIC micrograph (1000 x Mag.) of a Bi based commercial ZnO ceramic sample (grain size ≈ 35μm), **doped** with the oxides of **Bi, Sb, Co, Mn** and **Cr.** SEM beam parameters: **5keV,** 11nA. **Scale**: 10mm ≈ 12μm; (35μm ≈ 29mm).

Fig. 5.2.2. (b) SEM-EBIC micrograph (1000 x Mag.) of a Bi based commercial ZnO ceramic sample, **doped** with the oxides of **Bi, Sb, Co, Mn** and **Cr.** SEM beam parameters: **25keV,** 11nA. **Scale**: 10mm ≈ 12μm; (35μm ≈ 29mm).

Fig. 5.2.2. (c) SEM micrograph (1000 x mag.) of a Bi based commercial ZnO ceramic sample, **doped** with the oxides of **Bi, Sb, Co, Mn** and **Cr.** SEM beam parameters: **25keV,** 82nA. **Scale**: 10mm ≈ 12μm; (35μm ≈ 29mm).

Fig. 5.2.2. (d) SEM-EBIC micrograph (300 x mag.) of a Bi based commercial ZnO ceramic sample (grain size 35μm) showing (in red) the strong and (in blue) the weak terraces. The corresponding BS image (e) show the regions giving rise to these EBIC terraces.

Fig. 5.2.3. Optical micrograph showing the evaporated Al contacts (0.1mm x 0.1mm) using an appropriate mask.

Fig. 5.2.4. (a) SEM-EBIC micrograph (1100 x mag.) of a Bi based commercial ZnO ceramic sample, **doped** with the oxides of **Bi, Sb, Co, Mn** and **Cr.** SEM beam parameters: 25keV, 82nA.

Fig. 5.2.4. (b) SEM micrograph (1100 x mag.) of a Bi based commercial ZnO ceramic sample, **doped with the oxides of Bi, Sb, Co, Mn** and **Cr. SEM beam parameters: 25keV, 82nA.**

Fig. 5.2.5. (a) SEM-EBIC and LSP micrograph (400 x mag.) of a Bi based ZnO ceramic sample, **doped** (0.5mol%) with the oxides of **Bi, Sb, Co, Mn** and **Cr.** SEM beam parameters: 25keV, 82nA. **The LSP at the bottom is due to topography while that on the top is due to EBIC.**

Fig. 5.2.5. (b) SEM micrograph (400 x mag.) of a Bi based ZnO ceramic (grain size 28μm) sample, **doped** (0.5mol%) with the oxides of **Bi, Sb, Co, Mn** and **Cr.** SEM beam parameters: 25keV, 82nA.

Fig. 5.2.5. (c) SEM-EBIC and LSP micrograph (1200 x mag.) of a Bi based ZnO ceramic sample, **doped** (0.5mol%) with the oxides of **Bi, Sb, Co, Mn** and **Cr. SEM beam parameters: 25keV, 82nA. Scale of the LSP: ≈ 8nA per division.**

Fig. 5.2.5. (d) SEM-EBIC micrograph (800 x mag.) of a Bi based ZnO ceramic sample, **doped** (0.5mol%) with the oxides of **Bi, Sb, Co, Mn** and **Cr.** SEM beam parameters: 25keV, 82nA. This micrograph show the probes used to make micro-contacts on the either side of the grain boundary.

Fig. 5.2.6. **(a)** SEM-EBIC micrograph (200 x mag.) of a ZnO ceramic sample, **doped** (0.5mol%) with an oxide of **Bi.** SEM beam parameters: 25keV, 82nA. The micrograph show black and white grain boundary contrast.

Fig. 5.2.6. **(b)** SEM micrograph (200 x mag.) of a ZnO ceramic sample, **doped** (0.5mol%) with an oxide of **Bi.** SEM beam parameters: 25keV, 82nA. The micrograph show one of the probes resting on the sample.

Fig. 5.2.6. **(c)** SEM-EBIC and LSP micrograph (500 x mag.) of a ZnO ceramic sample, **doped** (0.5mol%) with an oxide of **Bi.** SEM beam parameters: 25keV, 82nA. The LSP show the response of the black and white grain boundary contrast..

Fig. 5.2.6. **(d)** SEM-EBIC and LSP micrograph (550 x mag.) of a ZnO ceramic sample, **doped** (0.5mol%) with an oxide of **Bi.** SEM beam parameters: 25keV, 82nA. The micrograph show black and white grain boundary contrast..

Fig. 5.2.6. **(e)** SEM-EBIC and LSP micrograph (1000 x mag.) of a ZnO ceramic sample, **doped** (0.5mol%) with an oxide of **Bi.** SEM beam parameters: 25keV, 82nA. The micrograph show black and white grain boundary contrast.

Fig. 5.2.6. **(f)** SEM micrograph (1000 x mag.) of a ZnO ceramic sample, **doped** (0.5mol%) with an oxide of **Bi.** SEM beam parameters: 25keV, 82nA. The micrograph also show the voids present in this singly Bi doped sample.

Fig. 5.2.7. **(a)** and **(b)** show the SEM-EBIC and the SEI of a ZnO bi-crystal (230 x mag.) The interface has Bi in between the two single crystals of ZnO. The micrograph also show a number of voids due to high volatility of Bi during sintering (1500^{o}C for 10 hours). SEM beam parameters: 25keV, 82nA.

Fig. 5.2.7. **(c)** and **(d)** show the SEM-EBIC and the LSPs of a ZnO bi-crystal (600 x mag.) The interface has Bi in between the two single crystals of ZnO. The micrograph show the LSPs from the smooth and course regions of the sample. These coarser regions (1000 x mag.) are likely to be due to a number of voids created by the high volatility of Bi during sintering (1500^{o}C for 10 hours). SEM beam parameters: 25keV, 82nA.

Fig 5.2.8. SEM-EBIC image (acquired at NPL) of a Bi based commercial ZnO varistor of grain size of 35 μm.

Fig. 5.2.9. (A) SEM-EBIC detection circuit for a high resistivity grain boundary specimen (ZnO Varistor). (B) Bright and dark peaks at the grain boundary corresponds to the EBIC LSP on the SEM-EBIC micrograph shown in Fig. 5.2.5 (c). The beam and specimen act as a potentiometer (current divider).

Fig. 5.2.10. Schematic illustration of carrier generation during electron bombardment of a high resistivity material such as ZnO varistor. With illumination barrier-lowering increases n(0) and thereby promotes recombination. A continuous distribution of interface states assumed.

Fig. 5.2.11. Schematic illustration of carrier generation during electron bombardment of a ZnO material with Bi oxide as a single additive. 'Bright' and 'dark' signal intensities corresponds to the grain boundary contrast seen in Figs. 5.2.6 (a), (c), (d), and (e). With illumination, barrier -lowering increases n(0) and thereby promotes recombination. Continuous distribution of interface states assumed.

Fig. 5.3.1. (a) show panchromatic image of undoped ZnO ceramic sample, and (b) show the corresponding image of the microstructure.

Fig. 5.3.2. **Schematic** image showing CL contrast (shown as shaded) arising from the regions of the ceramic microstructure of doped ZnO with all the additives (not to scale).

Fig. 5.3.3. The CL spectra of (a) pure ZnO, polished, used S20 detector; (b) ZnO + all five dopants, polished, used Ge detector; (c) Single crystal of ZnO, used S20 detector; (d) ZnO + all + TiO2, polished, used S20 detector and (e), ZnO + all Sint. surface, used S20 detector.

Fig. 5.3.4. Schematic diagram of a radiative transitions between the conduction band (Ec) the valence band (Ev) and exciton (EE), donor (ED) and acceptor (EA) levels in a semiconductor [70].

Fig. 5.3.5. Flat band diagram for ZnO indicating possible energies associated with electronic defects. Processes associated with Co (1.8eV), $V_O^{\bullet\bullet}$(2.0eV), V"zn (2.8eV) and the band edge transistions(3.3eV) were seen in this work.

Fig. 5.4.1. (a) Raw SIMS data, showing the ion intensity vs time for ZnO varistor ceramic sample doped with the oxides of Co, Mn, Cr, Bi and Sb, all at 0.5 mol.% and then sintered at 1250^{o}C. The analysis was confined to a general area of 50μm x 50μm.

Fig. 5.4.1. (b) Ion images of the segregated elements corresponding to the analysis as shown in Fig. 5.4.1 (a). A primary beam energy of 10keV was used and for improved lateral resolution, the beam current was reduced to 0.1nA. Images are: 100μm x 100μm, at the top from left, are of Zn, Co and at the bottom from left are of Mn and Cr. Due to very low signal intensities of Bi and Sb, their ion imaging of these species was not possible.

Fig. 5.4.1. (c) Checkerboard patterns taken over :25μm x 25μm gated region, corresponding to the analysis in Fig. 5.4.1 (a). Relative brightness in the colour of these images corresponds to relatively higher concentration of the particular element it represents. In the intensity scale red is high and blue is low.

Fig. 5.4.2. Raw SIMS data, showing the ion intensity vs time for ZnO reference ceramic sample, doped with the oxides of Co, Mn, Cr, Bi and Sb, all at 0.5 mol.% and then sintered at 900^{o}C. The analysis was **confined to an area of** 48μm x 48μm).

Fig. 5.4.3. (a) Raw SIMS data, showing the ion intensity vs time for ZnO varistor ceramic sample doped with the oxides of Co, Mn, Cr, Bi and Sb, all at 0.5 mol.% and then sintered at 1300^{o}C. The analysis was **confined to a grain** region (16μm x 16μm).

Fig. 5.4.3. (b). SIMS ion image of a grain region corresponding to the profile in Fig. 5.4.1(a). Image is 50μm x 50μm, acquired using a very fine ion beam (10keV, 0.1nA).

Fig. 5.4.4. (a) Schematic diagram of the ^{18}O isotopic concentration depth profiles, Cx in a ceramic oxide solid, before and after anneal in an ^{18}O enriched atmosphere. The difference between Cg, and Cs arises from the gas/solid exchange coefficient. Cg, Cs and Cbg are respectively, the ^{18}O isotopic concentrations in the anneal gas ambient, the solid surface and throughout the solid initially [101].

Fig. 5.4.4. (b) The diagram shows the effect of fast and slow surface exchange on the isotopic profile in the solid. Note that the surface tracer conc. is equal to that of the gas [102].

Fig. 5.4.5. (a) SIMS depth profiling of ^{18}O, ^{16}O and Zn in the pure undoped doped ZnO ceramic sample (Sint. 1250^{o}C).

Fig. 5.4.5. (b) SIMS depth profiling of ^{18}O, ^{16}O and Zn in the doped ZnO ceramic sample (Sint. 1250^{o}C).

Fig. 5.4.6. (a) Raw SIMS data of isotopic ratioing (^{18}O/ ^{16}O + ^{18}O) for pure **undoped** ZnO ceramic sample (Sint. 1250^{o}C).

Fig. 5.4.6. (b) The raw SIMS data of isotopic ratioing ($^{18}O/ ^{16}O + ^{18}O$) for the **doped** ZnO ceramic sample (Sint. 1250°C).

Fig. 5.4.7. The ^{18}O depth profile for pure and doped samples of Zno ceramic (Sint. 1250°C). Depth measurement was made using Taylor Hobson, Talystep.

Fig. 5.4.8. (a) SIMS line-scan profiling for ^{18}O,^{16}O, and Zn, across the x-section of the $^{18}O/^{16}O$ exchanged sample of **undoped** ZnO ceramic sintered at 1250 °C.

Fig. 5.4.8. (b) SIMS line-scan profiling for ^{18}O,^{16}O, and Zn, across the x-section of the $^{18}O/^{16}O$ exchanged sample of **ZnO ceramic doped** with the oxides of Bi, Sb, Co, Mn, and Cr and then sintered at 1250 °C.

Fig.5.4.9. A map showing the spatial distribution of ^{18}O in the cross sectioned sample of ZnO varistor. Each pixel is 3 μm, 180 x 180 μm area.

Fig. 5.4.10. (a) Corrected Isotopic ratio [^{18}O / (^{18}O +^{16}O)] across the cross section of the doped and **undoped** ZnO ceramic as the line-scan profiling moves across the surface and into the bulk.. Unlike the doped sample, a rapid drop in the ^{18}O concentration, from Cs of 0.3 to Cbg (0.002) is observed for the undoped sample.

Fig. 5.4.10. (b) As the profiling reaches ≈ 50μm below the surface of **undoped** ZnO ceramic, the ^{18}O concentration drops from Cs of ≈ 0.35 to background (Cbg) level of 0.002. However, in the case of the doped sample of ZnO ceramic, the ^{18}O concentration remains an order of magnitude higher then the Cbg level, throughout the line scan.

Fig. 5.4.10. (c) **The** ^{18}O isotopic ratio line scan data and the fitted solution to the diffusion equation for the undoped ZnO ceramic. $D^*=1.19 \times 10^{-11}$ cm^2 s^{-1} and $K=5.77 \times 10^{-9}$ cm s^{-1} (1000°C) are the fitted parameters.

Fig. 5.4.10. (d)The ^{18}O isotopic ratio line scan data and the fitted solution to the diffusion equation for the doped ZnO ceramic. $D^*=2.08 \times 10^{-10}$ cm^2 s^{-1} and $K=4.37 \times 10^{-8}$ cm s^{-1} (1000°C) are the fitted parameters.

Fig. 5.4.11. **A modified model** (to the one presented by Fujitsu *et al.*, [113] **for the transport of oxygen in varistor.** (A) shows the schematic of different intergranular phase morphologies in doped ZnO ceramic. (B) shows that the lacy type of secondary phases acts as the major oxygen transport net-work, indicated by large arrows, while the oxygen transport through grain boundaries is indicated by smaller arrows.

Fig. 5.5 1. (a) Impedance spectra, acquired at 335°C, of a nominally undoped ZnO ceramic sample.

Fig. 5.5.2. (a) Impedance spectra of the ZnO ceramic (197°C) doped with additives (Bi, Sb, Mn, Co, and Cr) and then sintered at 1250°C.

Fig. 5.5.2. (b) IS spectra of ZnO ceramic varistor at 293°C.

Fig. 5.5.2. (c) IS spectra of ZnO ceramic varistor at 401°C.

Fig. 5.5.2. (d) IS spectra of ZnO ceramic varistor at 500°C.

Fig. 5.5.2. (e) IS spectra of ZnO varistor sample, acquired at 557°C. Points in the negative regions exerting a downward pull on the semi-circle are due to the lead inductance effect. Consequently the grain boundary capacitance value differs from analysis taken at lower temperatures, where the lead inductance is not dominant.

Fig. 5.5.3. (a) Conductivity as a function of temperature for ZnO ceramic doped with various additives (all at 0.5mole%) and then sintered at 1250^{o}C).

Fig. 5.5.3. (b) Conductivity as a function of temperature for ZnO ceramic doped with various additives (all at 0.5mole%) and then sintered at 1250^{o}C).

Fig. 5.5.4. (a) Arrhenius plots for some ZnO ceramics. Slopes are labelled as: (A), for the synthesised ZnO ceramic , doped with Bi, Sb, Mn, Co and Cr, (B), commercial Bi based varistor, (C), a commercial Pr based varistor and (D) corresponds to the undoped ZnO ceramic.

Fig. 5.5.4. (b) Arrhenius plot for ZnO ceramic doped with (E) single dopant Bi, and (F) double dopant Bi, Sb. Their respective Ea values are also shown on the diagram. For comparison, plots of nominally undoped ZnO ceramic (D) and the ZnO ceramic with varistor composition (A) are shown. Samples synthesised in the laboratory are labelled as (Lab).

Fig. 5.5.4. (c) Arrhenius plot for ZnO ceramic doped with (G) Bi, Co, Mn (H) Bi, Co and (I) Bi, Sb, Co, Mn. Their respective Ea values are also shown on the diagram. For comparison, plots of nominally undoped ZnO ceramic (D) and the ZnO ceramic with varistor composition (A) are shown. Samples synthesised in the laboratory are labelled as (Lab).

Fig. 5.5.4. (d) Arrhenius plots for ZnO ceramic doped with (J): Bi, Sb, Co, Mn Cr rapidly cooled, (K): Bi, Sb, Mn, Co, Cr slow cooled. Their respective Ea. values are shown in the diagram. For comparison, plots of nominally undoped ZnO ceramic (D) and the ZnO ceramic with varistor composition (A) are also shown. Samples synthesised in the laboratory are labelled as (Lab).

Fig. 5.5.4. (e) Summary of Arrhenius plots for ZnO ceramics with varying number of additives. Synergetic effect of the combination of various additives results in types of processes giving rise to their respective Ea values. As the number of additives in to ZnO increases, the processes corresponding to Ea ≈ (0.20eV - 0.35eV) are progressively depressed, and upon complete doping, only the processes prevailing at Ea of ≈ 0.9 - 1.1 eV remains dominant.

Fig. 5.6.1. I:V characteristics of pure ZnO ceramic sintered at 800^{o}C. The non-linear coefficient, $\alpha \approx 1.08$ is measured between and 1mA. I:V measurement on the undoped ZnO ceramic sintered at 1250^{o}C was not possible here due to its very small resistance.

Fig. 5.6.2. I:V characteristics of ZnO **bi-crystal** sample (with Bi at the interface) measured in both directions. The non-linear coefficient, $\alpha \approx 1.2$ measured between 0.5mA - 1mA. Threshold breakdown of about 1 V.

Fig. 5.6.3. (a) I:V characteristics of the ZnO ceramic doped (0.5mol%) with the oxide of **Bi** sintered at 1250^{o}C. The non-linear coefficient, $\alpha = 3.5$, **sample dimensions:** 2.15mm thickness x 10.5mm dia., giving a break down voltage of about 31V.

Fig. 5.6.3. (b) I:V characteristics of the ZnO ceramic doped (0.5mol%) with the oxides of **Bi and Sb,** sintered at 1250^{o}C. The sample was highly resistive and the non-linear coefficient, $\alpha = 2.9$. Sample dimensions: 2.05mm thickness x 10.05mm dia., giving a Breakdown voltage of 36V.

Fig. 5.6.3. (c) I:V characteristics of the ZnO ceramic doped (0.5mol%) with the oxides of **Bi and Co, sintered** at 1250^{o}C. The non-linear coefficient, $\alpha = 2.2$, sample dimensions: 2.35mm thickness x 10.6mm dia., giving a break down voltage of about 9V.

Fig. 5.6.3. (d) I:V characteristics of the ZnO ceramic doped (0.5mol%) with the oxides of **Bi, Co** and **Mn** sintered at 1250°C. The non-linear coefficient, α = **2.1, sample dimensions:** 1.5mm thickness x 10.5mm dia., giving a break down voltage of about 12 V.

Fig. 5.6.3. (e) I:V characteristics of the ZnO ceramic doped (0.5mol%) with the oxides of **Bi, Co, Mn** and Sb, sintered at 1250°C. The non-linear coefficient, α = **2.4, sample dimensions:** 1.7mm thickness x 10.5mm dia., giving a break down voltage of about 23 V.

Fig. 5.6.3. (f) I:V characteristics of the ZnO ceramic, doped (0.5mol%) with the oxides of Bi, Sb, Mn, Co and Cr, sample initially **rapidly cooled** from 1250°C sintering and then cured at 500°C for 3 hours. The non-linear coefficient, α = 9.1, **sample dimensions:** 1.6 mm thickness x 10.15 mm dia., giving a break down voltage of about 113 V.

Fig. 5.6.4. (a) I:V characteristics of **Pr** based ZnO ceramic, doped with the oxides of Pr, Co and La, sintered at 1340°C. The non-linear coefficient, α = **7.3, sample dimensions:** 1.45 mm thickness x 14.97 mm dia., giving a break down voltage of about 58 V.

Fig. 5.6.4. (b) I:V characteristics of **Pr** based ZnO ceramic, doped with the oxides of Pr at 0.5Mol%, Co at 1Mol% and La at 0.5Mol%, sintered at 1250°C for 30 min. The sample was highly resistive and the non-linear coefficient, α is usually measured at E0.5. In this case it is out of range but presumed to be over 50. Sample dimensions: 1.62mm thickness x 14.9 mm dia. The break down voltage is around about 200 V.

Fig. 5.6.5. (a) I:V characteristics of a commercial Bi based ZnO varistor (PD, good, degraded in oil, 1 dip of 4 sec.). The sample was highly resistive and the non-linear coefficient, α usually measured at $E_{0.5}$. In this case it is out of range. Manufacturer has quoted the following values for non-linear coefficients: at 0.1 - 1mA α=67, for 1mA - 10mA, α =56, for 1mA - 100mA, α=78. Sample dimensions: 3.6mm thickness x 16.2 mm dia. The break down voltage is around about 663V.

Fig. 5.6.5. (b) I:V characteristics of a commercial Bi based ZnO varistor (PD, 'bad', degraded in oil, 7 dips of 30 seconds each). The sample was highly resistive and the non-linear coefficient, α is usually measured at $E_{0.5}$. In this case it is out of range. Manufacturer has quoted the following values for non-linear coefficients: at 0.1 - 1mA α=1.7, for 1mA - 10mA, α=2.7, for 1mA - 100mA, α=9.3. Sample dimensions: 3.5mm thickness x 16.2 mm dia. The break down voltage is around about 288V.

Fig. AD1. Dihedral angle for solid-solid-liquid equilibrium [84].

Fig. AD2. Second-phase distribution for different values of the dihedral angle [84].

List of Tables

Table 2.3.1. Electrical properties and average grain size of ZnO ceramic with various combined additives [9].

Table 2.3.2. Roles of additives in ZnO varistors [6].

Table 2.3.3. Distribution of the additive components in the sintered ZnO ceramic doped with metal oxides of Bi, Sb, Co, Mn, and Cr [40,49].

Table 2.4.1. Models proposed to explain The Conductance Mechanism In ZnO Varistor.

Table 3.4.1. Magnitude of Capacitance vs Phenomenon responsible in IS.

Table 4.1.1. Calculated Mole % of compounds of additives.

Table 4.1.2. Experimental weight of compounds used to synthesise sample batches 1-6.

Table 4.1.3. Samples used in this project.

Table 4.2.1. Matrix of experiments undertaken.

Table 4.2.2. Experimental conditions used during the SIMS analysis.

Table 5.1.1. Samples Sintered at 800^{o}C

Table 5.1.2. Samples Sintered at 1250^{o}C

Table 5.2.1. Preliminary SEM-EBIC analysis of 60V ZnO varistor sample.

Table 5.3.1. CL information extracted from the CL spectra of the undoped samples of ZnO.

Table 5.3.2. CL information extracted from the CL spectra of the ZnO ceramic samples doped with Bi_2O_3, Sb_2O_3, MnO_2, Co_3O_4, Cr_2O_3 and then sintered at 1250^{o} - 1300^{o}C.

Table 5.3.3. CL information extracted from the CL spectra of the ZnO ceramic samples doped with Bi_2O_3, Sb_2O_3, MnO_2, Co_3O_4, Cr_2O_3 ,TiO_2 and then sintered at 1250^{o}.

Table 5.4.1. Signal intensity ratios and the calculated % concentration in the standard ref. to the single grain of ZnO in the varistor sample.

Table 5.5.1. Capacitance values and their possible interpretation.

Table 5.5.2. Typical values of electrical conductivity.

Table 5.5.3. IS data for Pure ZnO ceramic sample coated with Al electrodes.

Table 5.5.4. IS Data for ZnO varistor synthesised in the laboratory, Al electrodes

Table 5.5.5. Summary of the IS data taken from the Appendix (ApndxTables 1- 13).

Table 5.5.6. Defect ionisation energies near room temperature has been estimated [28] from data in the literature.

The following (**ApndxTables 1- 13**) are presented in Appendix C

ApndxTable 1. IS Data for ZnO varistor synthesised in the laboratory, Ag electrodes.

ApndxTable 2. IS Data for Bi based ZnO varistor (Commercial sample)

ApndxTable 3. IS Data for Bi based ZnO varistor (Commercial sample).

ApndxTable 4. IS Data for Pr based ZnO varistor (Commercial sample).

ApndxTable 5. IS Data for ZnO ceramic doped with Bi.

ApndxTable 6. IS Data for ZnO ceramic doped with Bi, Co.

ApndxTable 7. IS Data for ZnO ceramic doped with Bi, Sb.

ApndxTable 8. IS Data for ZnO ceramic doped with Bi, Sb , Bias 35V.

ApndxTable 9. IS Data for ZnO ceramic doped with Bi, Co, Mn

ApndxTable 10. IS Data for ZnO ceramic doped with Bi, Sb, Mn, Co

ApndxTable 11. IS Data for ZnO ceramic doped with Bi, Sb, Mn, Co, Cr. Rapidly cooled.

ApndxTable 12. IS Data for ZnO ceramic commercial varistor, sample 13.3mm Ø x 1.6mm.

ApndxTable 13. IS Data for ZnO ceramic commercial varistor (35V bias), sample 13.3mm Ø x 1.6mm)

Table 5.6.1. Summary of I:V results.

Acknowledgements

I would like to thank my Project supervisors: Dr. D. S. McPhail and Professor B. C. H. Steele, for their invaluable guidance and support through this work.

Thanks are given to my industrial supervisors: Drs. M. Stewart, M. Gee and R. Morrell for their invaluable guidance and support in this work at the National Physical Laboratory, Teddington.

Thanks to Professor D. B. Holt, Professor J. A. Kilner, Dr. Rainer Waser and Mr. R.J. Chater for many helpful discussions during the course of my Ph.D., from which I have greatly benefited.

Mr. P. Manning, Mr. R. J. Chater and Mr. V. K. M. Sharma are all thanked for proof reading various parts of this thesis. Thanks to Dr. S. B. Patel who made many useful suggestions towards the write-up of this thesis and also for trying out my cold showers, even in winter! Thanks to Mr. G. Brias and Dr. X. Zhang for their invaluable guidance in TEM sample preparation. Thanks to Dr. H. Middleton and Mr. D. Waters for discussing with me some aspect of the IS results.

I would like to thank all my colleagues in the SIMS group for the kindness they have shown during the course of my Ph.D.

I would like to thank NPL and SERC for funding this project.

Power Development L.T.D. are thanked for providing some industrial samples with their I:V characteristics.

And finally, I would like to thank my wife Ratan, and my parents for their invaluable support during the course of this project.

To My Family

Chapter 1

Introduction

1.1. Background

Advances in science are often discussed in terms of the three main dominant technologies: Bio-technology, electronic technology and advanced materials technology. Today advanced ceramics are regarded as one very important aspect of advanced materials technology [1]. Ceramics represent one of the oldest materials used by the human race. The traditional ceramic, as it is called from its early usage, finds applications in refractories, sanitary ware, sheet glass, building materials, etc. The high strength of the chemical bond (a combination of ionic and covalent bonds) is responsible for the generally high melting point of ceramics, their brittle nature, good corrosion resistance, low thermal conductivity and high compressive strength. In general these materials are formed from powders and are hard, brittle, electrical and thermal insulators, and require high-temperature processing.

The sharp distinction between the traditional and advanced ceramic is made in terms of the starting material, processing, properties and applications. Traditional ceramics require little or no processing. Natural minerals, for example clay and sand, are used. Advanced ceramics require high purity starting materials and good control over the sintering process, considered very important as the final stage of fabrication. Processing is critical to ensure reproducibility and homogeneous distribution of intentionally added impurities [2]. Without such processing control the fired ceramic can possess a broad range of grain sizes, porosity and uncontrolled grain boundary phases. These can degrade the physical properties and increase the environmental sensitivity of the ceramic component. Variability in properties and environmental degradation must be minimised because advanced ceramics are often selected for high performance applications over organic based electronic components, due to greater stability and reliability. Therefore, it is essential that processing controls be sufficient to produce uniform and reliable microstructures. The first step in controlling reliability is understanding the relationship between chemical composition, crystal structure and microstructure and the electronic properties of electronic ceramics [2]. Some of the desirable properties of the advanced ceramics are: High resistivity, high dielectric constants, low dielectric loss factor and controllable magnetic properties.

1.2. Overview of ZnO based varistors

Ceramic materials with the ability to perform in both sensing and actuating functions are classed as "Smart" electroceramics [3]. The highly non-linear electrical characteristics of the ZnO ceramic varistor with its very fast (10^{-9} s) response time, make it a "smart-passive" electroceramic. This "smart" nature of the ZnO varistor is used as a protection phenomenon for components in electronics technology. Modern electronic systems, for example, data processing computers, communications systems, and power transmission systems, are often subjected to severe voltage transients, such as lightning, switching and electrostatic discharges due to charge accumulated on the human body. This can seriously affect the integrity of the sensitive components. To overcome these drawbacks, the system designers can either over-specify or incorporate protection. The economical criterion generally favours protection, as it enables the reduction of component costs by specifying moderate rating. A suitable device to combat these high voltage surges needs to be highly sensitive, yet resilient to high power stresses and sufficiently compact to suit the intricate architecture of the advanced electronic systems [4,5].

A varistor, also known as voltage dependent resistor (VDR), is a polycrystalline ceramic solid state device with the characteristics of an electrical insulator at low voltages (the stand by mode) and of a good conductor in the protective mode in a high voltage transient situation [4]. This dual performance is attributed to its non-linearity region, where there is an increase in current up to over 5 orders of magnitude with a small increase in voltage above threshold (turn on voltage). This phenomenon, coupled with a 10^{-9} second response time enables currents from as little as 10^{-3} A to as large as 10^{3} A to be passed through the low impedance path provided by a varistor and offers protection to sensitive components from high voltage transients Fig.1.2.1.

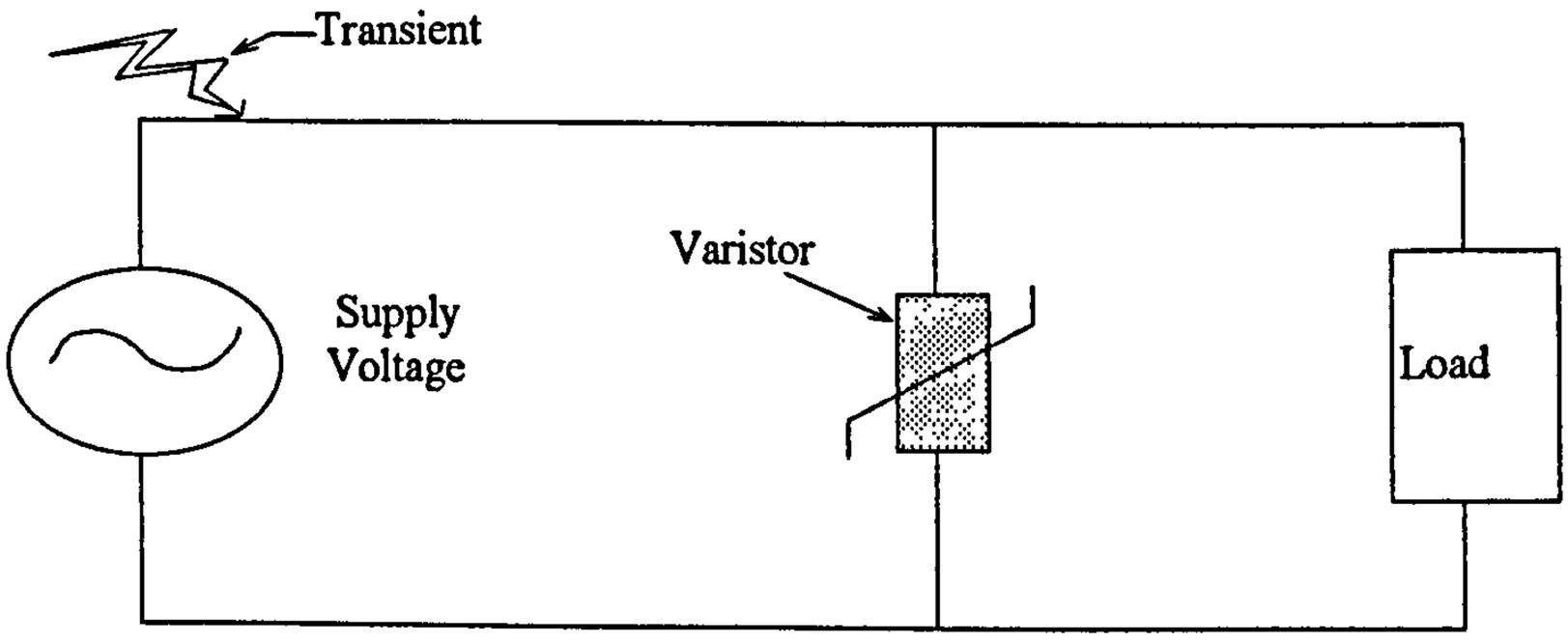


Fig. 1.2.1. Typical application of ZnO varistor as a transient protective element [4]. A varistor with a rapid (10^{-9} second) response and much lower impedance can divert the transient before it reaches the load.

Functionally, the varistor acts as a near insulator (resistor) prior to reaching a voltage known as the breakdown or threshold voltage, and it acts as a conductor thereafter. As illustrated in Fig.1.2.2, these functional properties of the ZnO varistor device are discussed in terms of the three main regions in the I:V characteristics (the Pre-Breakdown Region, the Intermediate Non-linear Region and the High-Current Upturn Region) and the non-linear coefficient α.

The **Pre-Breakdown Region** exhibits ohmic (i.e. low current linear region) I:V characteristics with a very small leakage current in this region ($<10^{-4}$ A/cm^2). The ohmic property in this region known as the pre-threshold voltage, is strongly temperature dependent [6]. Below the breakdown voltage ZnO varistors are highly capacitive. The dielectric constant of pure ZnO ceramic is 8.5, whereas an apparent dielectric constant of a ZnO varistor is typically 1000. These increased dielectric properties are mainly caused by thin depletion layers (1000 Å) at the grain boundaries giving rise to very high resistivity ($\rho_{gb} \approx 10^{10}$ - 10^{12} Ω cm) [5].

The **Intermediate Non-linear Region** is at the heart of the operation of a ZnO varistor. In this region the varistor device conducts an increasingly large amount of current for a small increase in voltage. The extent of increased conductivity within this region is attributed to (a) negligible resistance due to grain boundaries as the voltage sensitive electrical barriers (discussed in section 2.4) are surmounted and (b) to a very low resistivity ($\rho_g \approx 1$ - 10 Ω cm) of the ZnO grains [5]. The non-linear region may extend to 6 to 7 orders of magnitude of current. The characteristic non-linear voltage ($E_{0.5}$) is measured at 0.5 mA/cm^2.

In the **High-Current Upturn Region** ($>10^3$ A/cm^2), the I:V characteristic becomes linear, with the voltage rising faster with current than in the non-linear region. This region is mainly controlled by the impedance of the grains in the ZnO microstructure. Further details of these functional characteristics of ZnO varistor are presented in section 2.1.5. The varistor phenomenon is attributed to the microstructural properties of the doped ZnO ceramic (discussed in section 2.3.2). The pure undoped ZnO ceramic does not exhibit any useful varistor effect [7].

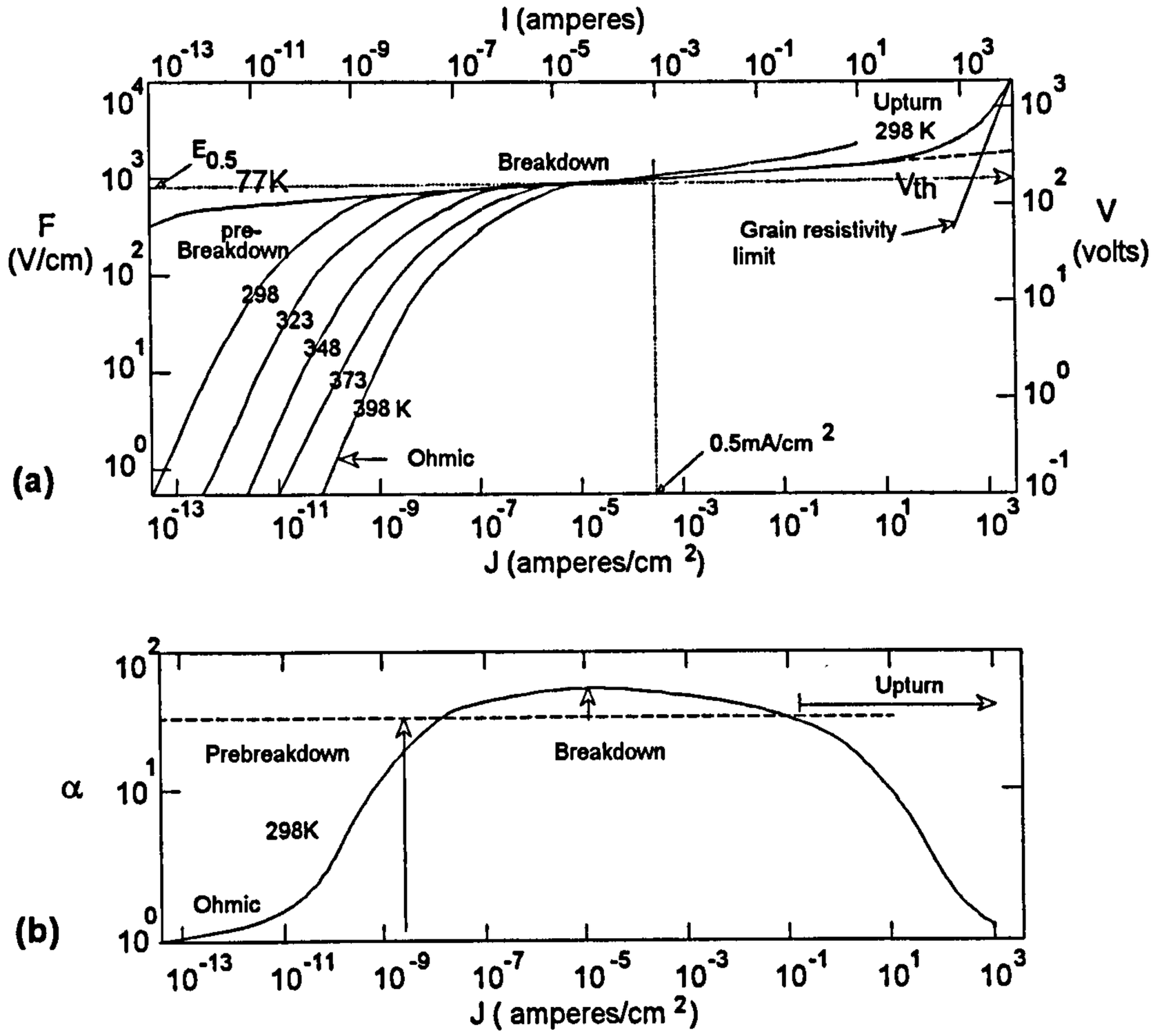


Fig. 1.2.2. **(a)** Current-Voltage behaviour of a commercial varistor material; **(b)** coefficient of non linearity, α=d ln I/d ln V [4].

Perhaps the most important parameter of the ZnO varistor is the **non-linear coefficient** α, is taken as *dlnI/dlnV* from the I:V curve (Fig. 1.2.2). The importance of the non-linear region is discussed in section 2.1.5.2, and is defined by the equations (2.1-3, 2.1-4 and 2.1-5). The greater the value of α, the better the device. As the current increases, the α values are progressively changed as shown in Fig.1.2.2(b). The α value increases in the pre-breakdown region, reaches a maximum value in the breakdown region, and then diminishes in the upturn region [5]. This is illustrated in Fig. 1.2.2(b). If α=1, we would have an ohmic device, i.e. the current is proportional to the applied voltage. As $\alpha \Rightarrow \infty$, resulting in a perfect varistor, i.e. the current varies infinitely for small changes in the applied field. The importance of ZnO varistors results from the fact that they outrank other varistors in α values.

Varistors based on selenium rectifiers ($\alpha \approx 8$) were perhaps the oldest types used in early telephone systems and other surge suppressing applications [5]. With the advent of new technology, these rectifiers have been largely replaced by a Zener diode ($\alpha \approx 35$) based on single-crystal silicon for low voltage applications and varistors based on SiC ($\alpha \approx 5$) or ZnO ($\alpha \approx 35$ to 100) polycrystalline ceramics for high voltage-high power applications

[6]. SiC based varistors were used before the advent of zinc oxide varistors [5,8]. Vast improvements in performance mean that ZnO varistor devices have replaced SiC devices in most areas of power applications. Additionally, as a result of size reductions, the ZnO based devices have also been extended to low voltage applications [4].

Today, ZnO based varistors offer unequivocally superior properties over SiC, with the ability to perform at nano-second response times and in high power applications [9,4]. Commercial applications of varistors include the absorption of switching transients, as a lightning arrestor in the national power grid system, computers and many other microelectronics systems (Fig.1.2.3). Special varistor devices are of considerable interest for military applications. One example of a military application is in zinc oxide military modules (ZOMM), which are intended to protect military communications and control electronics from nuclear electromagnetic pulses in the event of nuclear explosions [10]. These are just few examples; there are many other applications that have stimulated growth in this area of technology.

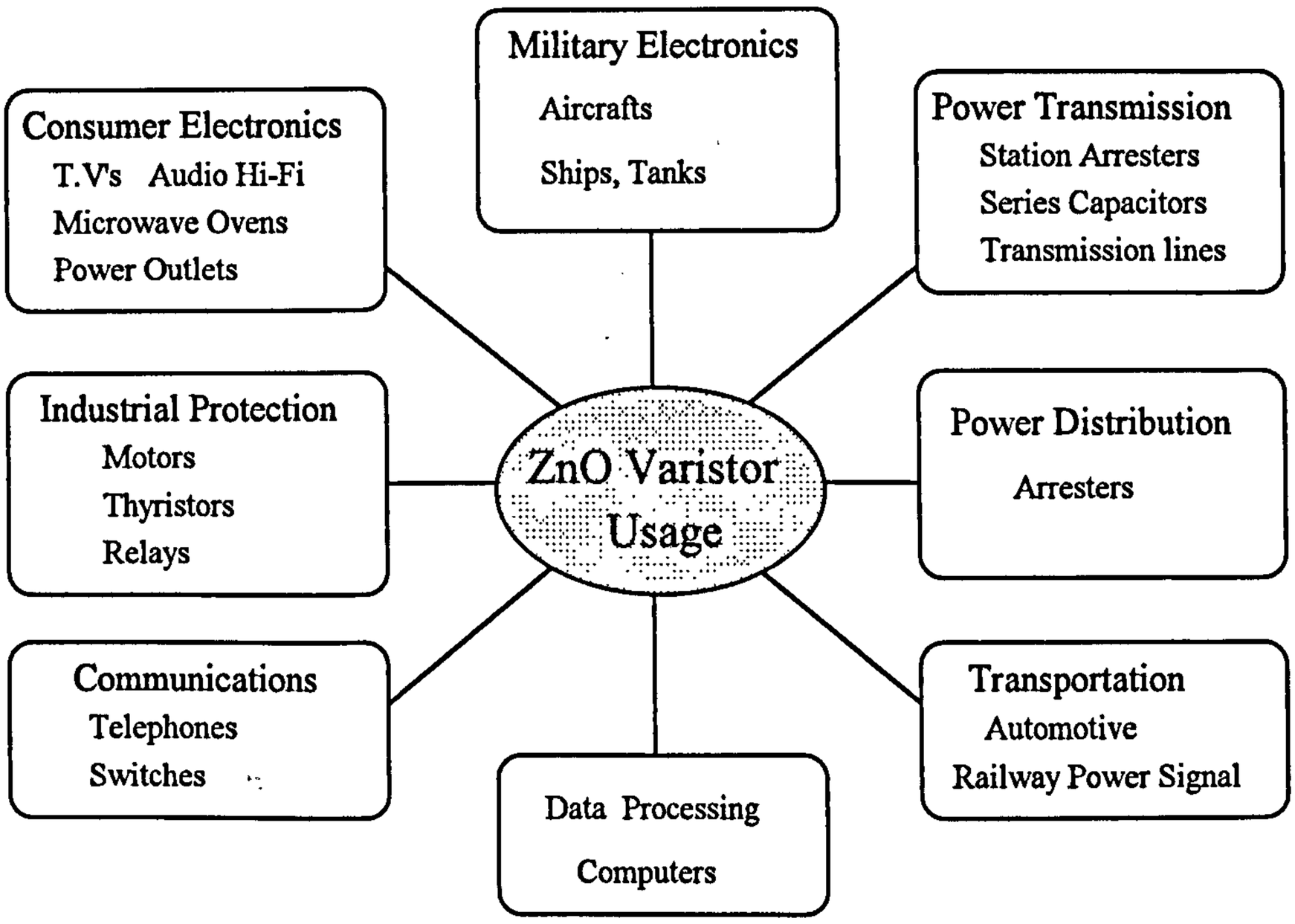


Fig. 1.2.3. Applications of ZnO varistors [11].

1.3. Aim Of This Project

The theme of this Ph.D. project has been to synthesise ZnO based varistors containing selected additives, with different sintering conditions and then to study their properties using a group of powerful analytical techniques. The principle aim has been to study and relate the bulk non-linear I:V characteristics to the microscopic properties such as the electrical behaviour, morphology and compositional variations in the microstructure using a number of analytical techniques: SEM/STEM-EDAX, XRD, SEM-EBIC, SEM-CL, SIMS, IS and I:V measurements.

1.3.1. Novel contribution to science

The main theme of this work has been to study ZnO ceramics with single, double and multiple dopant compositions, using a combination of both traditional and relatively novel analytical techniques. Some examples of the approaches used are given below:

1. One particular aspect of the new work in this project has been the use of SIMS to study the compositional variation of additives in ZnO based varistors. The use of SIMS ion imaging and line scanning in conjunction with the oxygen isotope exchange-diffusion work was explored, to study the distribution of dopants and oxygen at, and near the grain boundaries, as well as within the bulk of the ceramic.

2. From the SEM-EBIC work, electrically active terraces corresponding to the grain boundaries and the associated line-scan profiling, enabled a direct observation of the Schottky barriers in the varistor. A sample of ZnO ceramic, singly doped with Bi, exhibited different type of terraces than the one doped with a complete varistor composition (Bi, Sb, Co, Mn and Cr). Information about the properties of a well defined grain boundary was further assisted by investigating a bi-crystal of ZnO.

3. IS analysis of ZnO based varistor samples prepared with different compositions and sintering conditions has been yet another field of study featuring some very new and interesting results.

4. Studies based on SEM-EDAX analysis with X-ray dot mapping undertaken on a group of ZnO based varistor samples of different compositions and sintering

conditions has shown an important relationship between the variation of grain size and porosity as a function of sintering conditions and the presence of single, double or multiple combinations of additives. Additionally the use of SEM analysis, using its traditional modes, back scattered imaging BSI and secondary electron imaging SEI provided valuable complimentary information to the SIMS and X-ray imaging. The distribution of traditionally well known phases such as Bi-rich, spinel and pyrochlore were also observed using this technique.

5. Results of the I:V measurement of samples doped with additives at single and multi compositions, showed the varying effect of additives to the non-linear coefficient (α) of the ZnO ceramic device. This includes an I:V measurement of the ZnO bi-crystal sample, using micro-manipulator probes attached to the SEM.

Chapter 2

Literature Survey

2.1. Discovery and development of the ZnO based Varistor

2.1.1. Overview

Following the discovery of ZnO based varistors in the late sixties, their development over the last two decades has resulted in many published papers. These include some very instructive review papers [4,5,6,8,9,11,12] summarising the progress and development in this area of technology. This chapter reviews the research activities over this period, identifying the various findings on the varistor mechanism, in relation to the bulk and microscopic properties. The microstructure of ZnO, the morphology of the ZnO/ZnO grain boundaries, the crystal structure of the Bi rich phases and the local compositional variations all significantly affect the microscopic electrical behaviour of the varistor.

2.1.2. Discovery of ZnO varistor

ZnO varistors were first developed by **Matsuoka** et al., at Matsushita Electronic Components Co., Ltd. (Japan) in 1968 [6,8]. This development followed a discovery that took place in July 1967.

The search for a new material with varistor properties had started around 1965, following a major change of key devices [8] in electronic circuits from vacuum tubes to semiconductors (Fig. 2.1.1). As these changes began to extend to electrical equipment systems, it led to a reduction in the operating voltages of the electronic circuits. The first commercially available ZnO varistors were built by Matsushita to serve for 120 V and higher range of applications. Subsequent improvements in production resulted in ZnO varistors with a successively wider range of application voltages (Fig.2.1.2).

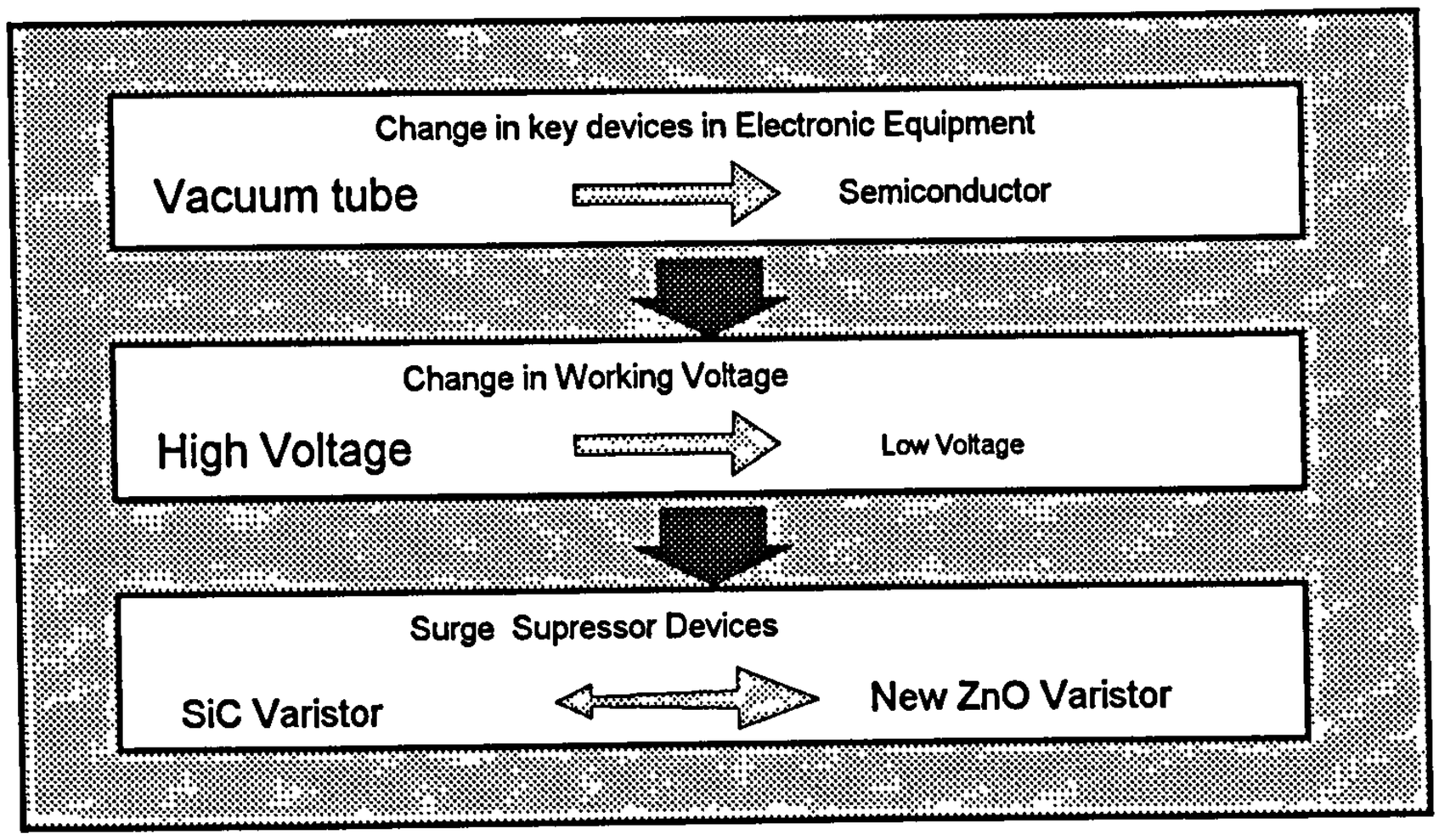


Fig. 2.1.1. Background for the development of varistors [8].

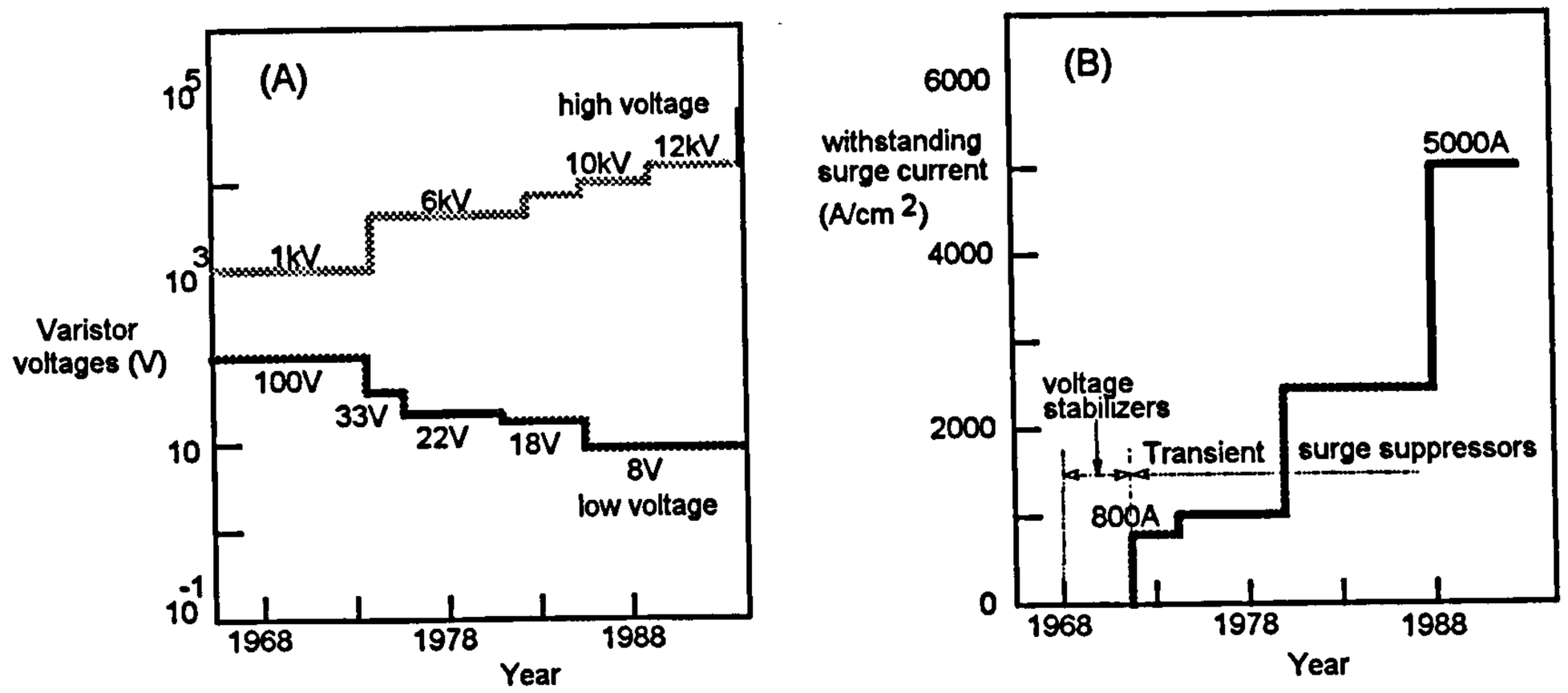


Fig. 2.1.2. (a) Transition of varistor voltage (b) Transition of withstanding-surge-current [14].

Inevitably, a very sensitive level of protection from a wide range of voltage transients was required. SiC varistors, considered to be the best surge suppression devices at the time, offered reasonable protection in high voltage-high power situations, but their limited value of non-linear coefficient ($\alpha \approx 5$) in highly sensitive applications at very low voltages, necessitated the development of a new varistor [5,8].

The basic principle of operation required of the new varistor was the non-ohmic properties of the contact interface between a semiconductor and a metal electrode. Further investigation was focused on the selection of the material for the new varistor. From the view point of the cost and ease of production, ceramic oxides were preferred

to single crystals. Moreover, the oxide can be sintered in air, which gives it an added advantage in mass production. From the many types of oxides, ZnO was finally selected due to its ease of sintering and its favourable electrical properties [6]. This preliminary stage of the development of varistors based on the surface barrier property was completed in 1967. Fig. 2.1.3 includes the I:V characteristics of the surface barrier type of device illustrated in Fig. 2.1.4 (a). The observed non-linear properties were still limited to the non-ohmic contact between the surface of the ZnO and metal electrodes [8]. The resultant breakdown voltage of this device was very small (<10V) since only two surface barriers were involved at the electrode interfaces. The next stage of development was to extend this range and it was in the process of the subsequent set of experiments that a very interesting and unusual phenomenon was observed. A much higher threshold voltage (~ 200V) was observed in a group of ZnO samples that had been unintentionally over heated during electrode formation. This unintentional high temperature sintering of the ZnO ceramic, with Bi and Mn compounds present as impurities in the Ag paste electrodes, resulted in a several fold increase in its threshold voltage. The increased threshold voltage (Fig. 2.1.3) in these anomalous samples (Fig.2.1.4 (b)) was found to be inversely proportional to the grain size of the ZnO ceramic.

The high threshold and improved non linearity in the ZnO ceramic were presumed to be due to the grain boundaries being decorated with an intergranular layer of diffused impurities such as the Bi and Mn [9]. This discovery, which can be described as planned serendipity, led to a vast improvement in performance of the Zinc Oxide varistor. Subsequent investigations showed that the zinc oxide varistor material did not rectify and had a high threshold voltage (Vth) which varied according to the thickness of the sintered body, rather then a single barrier as previously observed. The sintered body had pronounced discoloration [6] (Fig. 2.1.4 (b).

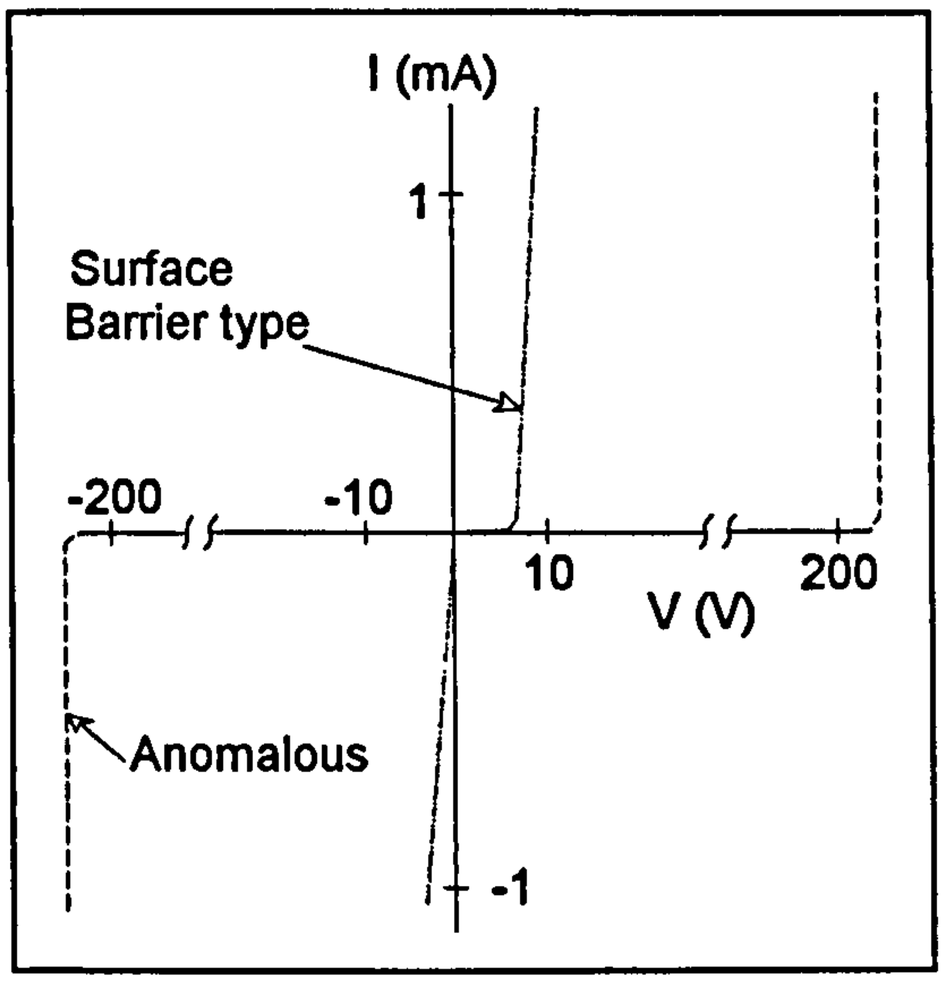


Fig. 2.1.3. I:V curve of anomalous sample [8]

It was clear that the varistor action was arising from the sintered material itself. One obvious explanation was that each grain boundary presents an electrical barrier of a few volts and an associated depletion region [4]. Thus the observed threshold voltage was the sum of the breakdown voltages at each grain boundary, Vg, i.e.

$$Vth = (ng\ Vg) = (D/d)Vg \qquad (2.1\text{-}1)$$

Where (Vth) is break down voltage, (ng) is number of grains, (Vg) is breakdown voltage per intergranular barrier, (D) is electrode spacing and (d) is the ZnO grain size as shown in Figs. 2.1.5 (a) and (b). Typical varistor values for protection of equipment on 120V ac power lines are Vth = 200V, d = 20μm, D = 1.6 mm, and n = 80, implying a breakdown voltage of 2.5 volts per barrier.

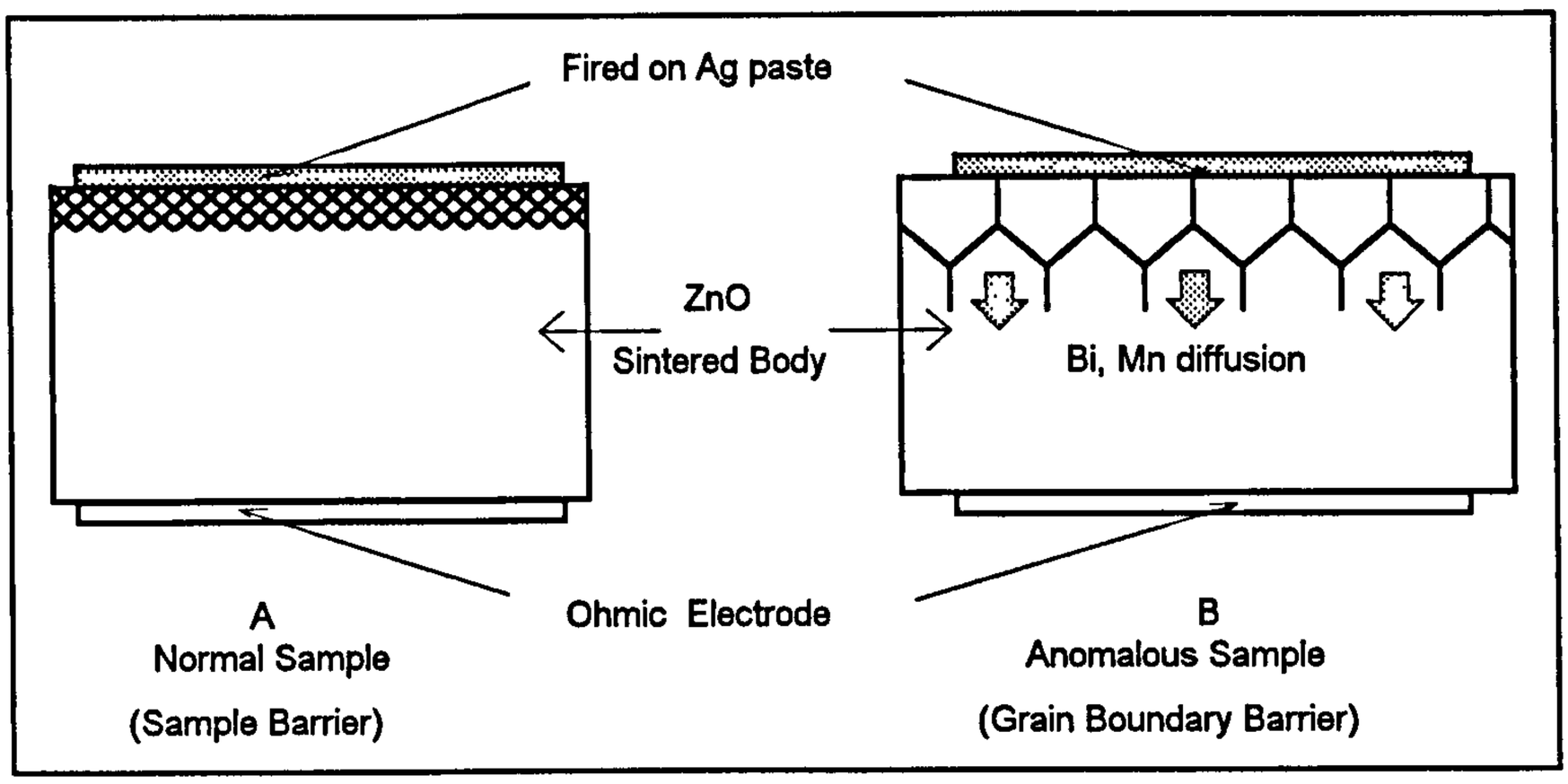


Fig. 2.1.4. (a) Normal Sample with surface barrier effect. **(b)** Anomalous sample with "Grain Boundary" barrier effect [8].

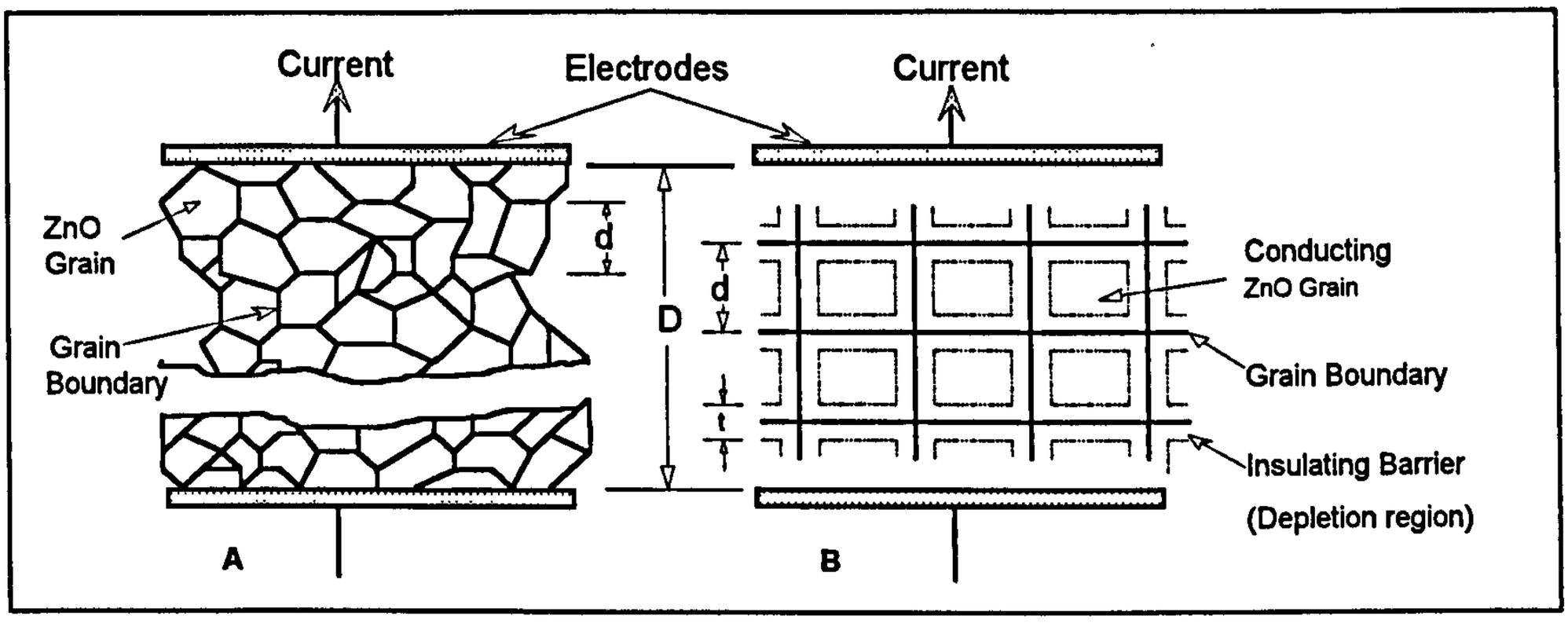


Fig. 2.1.5. **(a)** Schematic of the microstructure of a ZnO varistor. Grains of conducting ZnO, average size d, with segregated cations at the grain boundaries. Electrodes are attached and current flows as indicated. **(b)** Block model of a ZnO varistor having grain size d(~10 μm) and intergranular depletion barrier thickness t (~100 nm) D = electrode separation (not to scale) [4].

Dielectric measurement suggested that at the grain boundaries the dielectric constant was higher implying the presence of a depletion layer. The thickness t, of the depletion layers at the ZnO grain boundaries have been estimated [4] from measurements of the dielectric constant, ε, of ZnO varistor, which has a typical value of ε = 1000. Pure ZnO has the dielectric constant of ε_g = about 10. Looking at the varistor model in Fig. 2.1.5, d is much greater than t and it is clear that the volume between the varistor electrodes is largely occupied by conducting ZnO grain material. The thickness of insulating dielectric lying between the sample electrodes is not D but Dt/d. Hence, if ε_g is the dielectric constant of the ZnO in the depletion layers, the varistor capacitance, C, is given by:

$$C = \varepsilon_g \varepsilon_o A/(Dt/d) = (d/t)\varepsilon_g \varepsilon_o A/D \qquad (2.1\text{-}2)$$

i.e. the effective dielectric constant is increased by a factor of d/t. Since the measured values of the effective dielectric constant are 1000, this implies d/t = 100, since ε_g=10 for ZnO. Taking d=10μm, t is estimated to be 100 nm [4]. In practice it has been difficult to measure this thickness accurately due to the limited lateral resolution of the analytical techniques used. The depletion layer largely controls the varistor low-voltage capacitance. The varistor intergranular barriers are described by a parallel capacitor (C_p) resistor (R_p) pair (Fig. 2.1.6), when R_p, is voltage dependent. Both R_p and C_p vary with frequency and temperature [4].

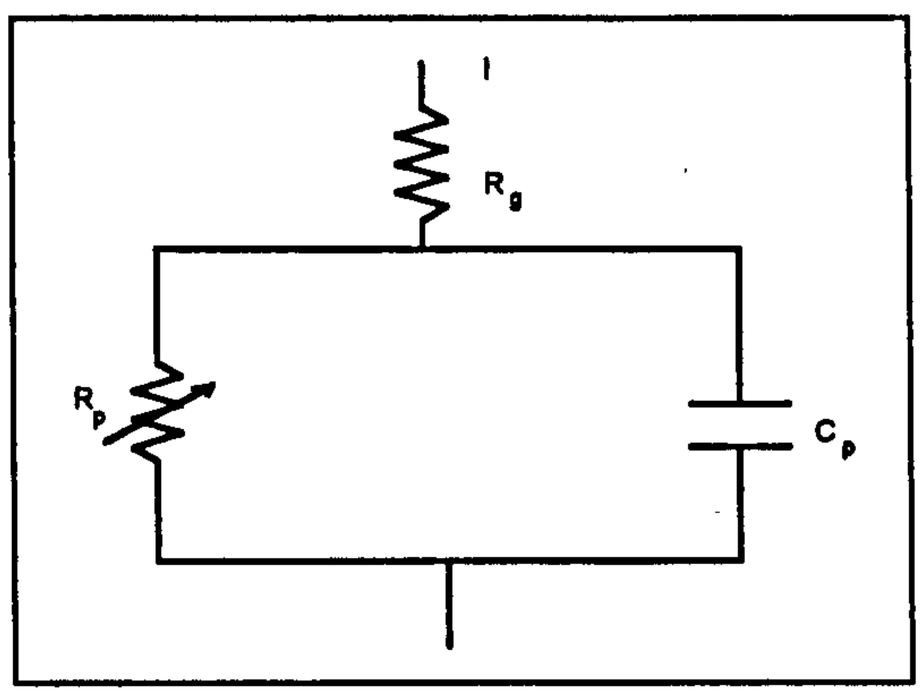


Fig. 2.1.6. Simple equivalent circuit representing a metal oxide varistor as a capacitance in parallel with a voltage dependent resistor. C_p and R_p are the capacitance and resistance of the intergranular layer, respectively; R_g is the ZnO grain resistance. For low applied voltages, R_p behaves as an ohmic loss [4].

2.1.3. Advances In Varistor Technology

The development of ZnO ceramic varistors over the last two decades have resulted in many published papers. This includes some very instructive review papers [4,5,6,8,9,11,12] summarising the progress and development in this area of technology.

Zinc oxide Varistor technology has enjoyed over twenty years of history. The first international conference, in Tokyo in 1978, marked its tenth anniversary [11]. The main topics covered at the meeting were novel fabrication methods for the devices and scientific studies of how they work. The second conference on ZnO ceramic varistors

was held at the General Electric Corporation Research and Development Centre, New York, in 1988. This marked the twentieth anniversary in the growth, development and application of the ZnO based varistors [11]. Over fifty proceedings were presented at the second international conference [8] and the technology was then seen as dominant in a large portion of the surge protection market. This included a number of applications for ZnO varistors to solve the problems of circuit or system damage, caused by the abnormal voltages arising from lightning, electrostatic discharge, switching, and electromagnetic transients [14]. The range of applications has extended year by year as a result of improvement to the threshold voltage region, the non-ohmic exponent, the surge withstand capability and the long term reliability [8].

In 1968 the voltage range of the ZnO varistor was very narrow and limited, for example, from 100V to 1kV. This range has been extended to higher voltages for lightning arrester applications and to lower voltages for IC circuit protection. Presently it ranges from 8V to 12 kV per disk. The extension of this voltage range has been attributed to the development of new techniques to control the ZnO grain size (which determines the varistor voltage), new additives, improved fabrication processes and research on the varistor formation mechanism. In 1972, the rating of the surge-current capacity of the ZnO based varistor was specified as 800 A/cm^2. Development of new additives and homogeneous fabrication techniques has increased this range to 5 kA/cm^2 and have made transient surge suppressers smaller and more reliable. The energy handling capacity per disk has been increased by the enlargement of disk size and volume. A single disc can handle 20 kJ and disks can be connected in parallel or in series to obtain a much higher energy-handling capability. The sintered body volume can range from 0.005 to 150 cm^3 to absorb a wide range of abnormal voltages.

2.1.4. Commercial Applications

At present, ZnO varistors are extensively used in modern technology [4,5,6]. They are a simple and cost-effective way to protect electrical systems from transient voltage surges and this has stimulated a dramatic growth in their production. There are over one billion devices thought to be in use.

ZnO varistors vary in size from units less then $1mm^3$ to high-energy blocks weighing a few Kilogram and capable of withstanding currents well in excess of 100,000A and energies of hundreds of kilo joules [4]. A number of useful features related to the ceramic nature of the material makes the ZnO varistor very suitable for certain specific applications. For example some useful device parameters such as energy absorption capability, maximum surge current, fast response to voltage transient and ability to form into a particular device to conform to system constraints are related to the material

properties of the ZnO varistors [4]. Its polycrystalline properties enable energy absorption, essentially at the grain boundaries, which can be distributed throughout the volume of the material. This inherent power absorbing facility of multi junction ZnO varistors enables them to absorb more energy than a single-junction protective device, such as a Zener diode. Energy absorption capability in 100's of J/cm^3 are now routinely available in ZnO based varistors [8].

One example of a novel application [13] of ZnO based technology, is a monolithic device incorporating both the functions of a capacitor and a varistor (Fig. 2.1.7).

This device operates with a dual function as a varistor and as a capacitor, to offer protection against low amplitude and high-frequency transients, which could cause errors in signal processing or in the stored signals. A capacitor and a Zener diode in parallel would normally be suitable for this type of application, but they are often bulkier than the circuit they are protecting. A monolithic device, incorporating both a varistor and a ceramic capacitor, is thus a solution offered by multi-layer ceramic capacitor technology. Recently, surface mountable devices (SMDs) with very low self-inductance have also become available [12]. Multi layer ceramic chip varistors [11] and fabrication of varistors based on (Sr, Ca) TiO_3 are amongst the other novel applications. The successful usage of the ZnO lighting arrester in power stations has significantly simplified and increased the reliability of electrical power system protection against transient surges [4]. There is also a dramatic reduction in component size compared with the earlier varistor technology based on SiC. The typical life of a Varistor is estimated to be more than 50 years when installed to protect electric power lines [6].

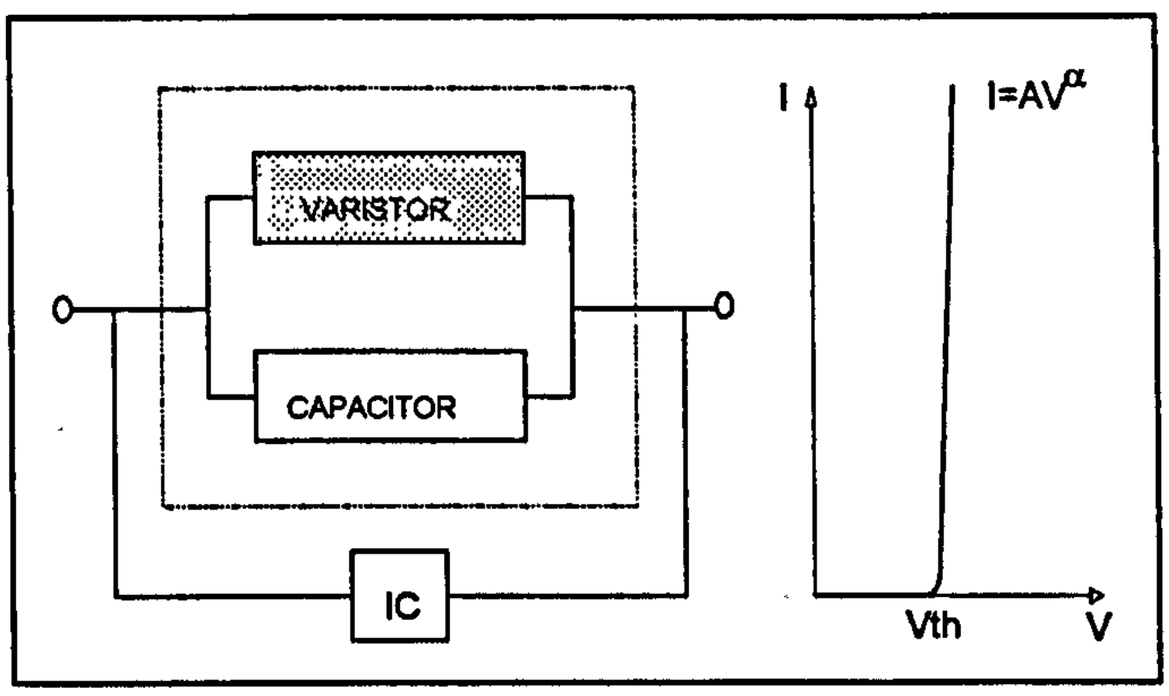


Fig. 2.1.7. Schematic of the varistor and capacitor in an electrically parallel arrangement. These two components form a monolithic device within the dashed line to give protection to an integrated circuit. Also shown on the side is the Schematic of the power-law relation of the applied voltage and the current flow in the varistor [13].

2.1.5. Functional properties of the ZnO Varistor

Zinc oxide varistors [4,6] are highly non-ohmic resistors with a non-linear coefficient value α, of 35 - 100. They are also known as Voltage Dependent Resistors (VDR) and find application mainly in the field of circuit over-voltage protection. The primary

function of a varistor is to sense and limit transient voltage surges repeatedly without being destroyed. Although the I:V characteristic is non-linear, (similar to a Zener diode), the varistor can limit over-voltages equally in both polarities, giving I:V characteristics analogous to two back-to-back diodes.

The highly non-ohmic characteristics of ZnO varistors, with energy absorption capacity of 100's of J/cm^3 associated with a response time in the order of few nano seconds and an extended non-linear region of 6 to 7 orders of magnitude of current have strongly favoured the use of these devices in place of the SiC varistors.

In this section the functional properties of the ZnO varistors are discussed in terms of the three main regions of the I:V curve as shown in Chapter 1 (Fig. 1.2.2).

2.1.5.1. The Pre-Breakdown Region

The Pre-Breakdown Region is a low-current linear region. The I:V characteristic is ohmic in this region (<10^{-4} A/cm^2). The ohmic property in this region known as the pre-threshold voltage, is known to be strongly temperature dependent [6]. The ac current is about 2 orders of magnitude higher than the dc current for a given operating voltage. The difference is presumed to be due to the contribution of the dielectric loss upon application of an ac voltage [5]. The total ac current is composed of a capacitor current (Ic) and a resistive current (I_R) and is determined by the impedance of the ZnO grain boundaries [5]. Below the breakdown voltage ZnO varistors are highly capacitive. The dielectric constant of pure undoped ZnO ceramic is 8.5, whereas an apparent dielectric constant of a ZnO varistor is typically 1000. These increased dielectric properties are mainly caused by thin depletion layers (1000 Å) at the grain boundaries giving rise to very high resistivity ($\rho_{gb} \approx 10^{10}$ - 10^{12} Ω cm) [5]. These barriers are presumed to derive from trap states at the grain-boundaries caused by the presence of segregating additives such as Bi_2O_3 [4]. The pure undoped ZnO ceramic does not exhibit any useful varistor effect [7].

2.1.5.1.1. Leakage Current

Leakage currents in ZnO varistors are important for two reasons. Firstly, they determine the amount of watt loss that a varistor is expected to generate upon application of a steady-state operating voltage. This is illustrated in Fig.2.1.8 with the voltage V_1 causing a leakage I_L, which appears as I^2_L R heat. Secondly, the amount of leakage current determines the magnitude of the steady state operating voltage V_1 that the device can accept without generating an excessive amount of heat, for example, V_1 must be lowered to reduce the values I_L. The need to balance the values of V_1 and I_L results, on

the one hand, from a desire to set the operating voltage as close to the onset of non linearity, i.e., $E_{0.5}$, as possible (to maximise the protective level) and, on the other hand, to keep the device from thermal runaway due to excessive heating. For most power applications, the steady-state operating voltage is set between 70% to 80% of $E_{0.5}$. For an ac application, the total leakage current (I_L) in the breakdown region is composed of a resistive current (I_R) and a capacitive current (I_C) corresponding to the grain-boundary resistor and capacitor. Although the magnitudes of these currents may vary from varistor to varistor, by and large, the total leakage current is comprised primarily of capacitive current whose magnitude is several times greater than that of the resistive current. In this region , the varistors thus act as "lossy" (not perfect) capacitors. In the non-linear region, the current is mostly resistive.

2.1.5.2. The Intermediate Non-linear Region

The Intermediate Non-linear Region is at the heart of operation of the ZnO varistor. In this region the varistor device conducts an increasingly large amount of current for a small increase in voltage. In this region, the extent of increased conductivity is attributed to (a) negligible resistance due to grain boundary barrier and (b) to a very low resistivity ($\rho_g \approx 1$ - 10 Ω cm) of the ZnO grain [5]. The non-linear region may extend to 6 to 7 orders of magnitude of current. The characteristic non-linear voltage $E_{0.5}$ is measured at 0.5 mA/cm^2. This large non linearity region over a wide range of current densities is in fact the unique property of the ZnO varistors and makes the device distinctly different from any other non-linear resistor.

The quality of the device is discussed in terms of the **non-linear coefficient** α. The non-linear coefficient α, is the most important parameter of the ZnO varistor. The degree of non linearity is determined by the flatness of the non-linear region in the I:V curve (Fig.1.2.2). The flatter the I:V curve in this region, the better the device. This is measured by taking the reciprocal of the non-linear slope (Reciprocal slope = α). In the non-linear region this is defined by equation (2.1-3) as shown below:

$$\alpha = \frac{d \ln I}{d \ln V} \qquad (2.1\text{-}3)$$

The greater the value of α, the better the device. However, as the current increases, the α values are progressively changed as illustrated in, Fig.1.2.2 (b) in Chapter 1. The α values increases in the pre-breakdown region, reaches a maximum value in the breakdown region, and then diminishes in the upturn region. Because of this change in the α value with current, it is important to determine the value of α with reference to the magnitude of currents over which the application is desired.

Hence, in practice, the α value is estimated between two desired magnitudes of current and corresponding voltages by :

$$\alpha = \frac{\log I2 - \log I1}{\log V2 - \log V1} \qquad (2.1\text{-}4)$$

Where V1 and V2 are the voltages at current I1 and I2 (I2>I1). Because of the above definition (Eqn. 2.1-4), the current ranges over which the α values cited are between current ranges of 0.1 to 1mA., 1 to 10mA, and, at best, to 100mA. For high-current applications, e.g., 1kA, the designer must be careful in choosing the α values from the literature.

The non-linear portion of the I:V curve has been empirically defined by the equation:

$$I = \left(\frac{V}{C}\right)^{\alpha} = KV^{\alpha} \qquad (2.1\text{-}5)$$

where C and K are material constants and $K = (1/C)^{\alpha}$. The practical implication of Eqn. (2.1-5) is that, for a given discharge current, the voltage rise is lowered with increasing values of α [5]. This is the basis of protection of associated electrical equipment from transient surges. An example of the protective characteristic of the ZnO varistor is described with reference to Fig.2.1.8.

The protective characteristic is defined as the ratio of the voltage V2 at a given discharge current Id to the continuous steady operating voltage V1 at the given leakage current IL (discussed in section 2.1.5.1.1). This ratio is known as the protective level (PL=V2/V1) and is a measure of the clamping efficiency of the device. Fig.2.1.8 illustrates that, by comparing the two curves, curve 2 has a better clamping efficiency than that of curve 1, because the voltage rise is less with curve 2 (V3/V1 <V2/V1), which also has a higher value of α ($\alpha_2 > \alpha_1$). Using the equation in Fig. 2.1.8 a relationship between α and the protective level can be obtained for a given application.

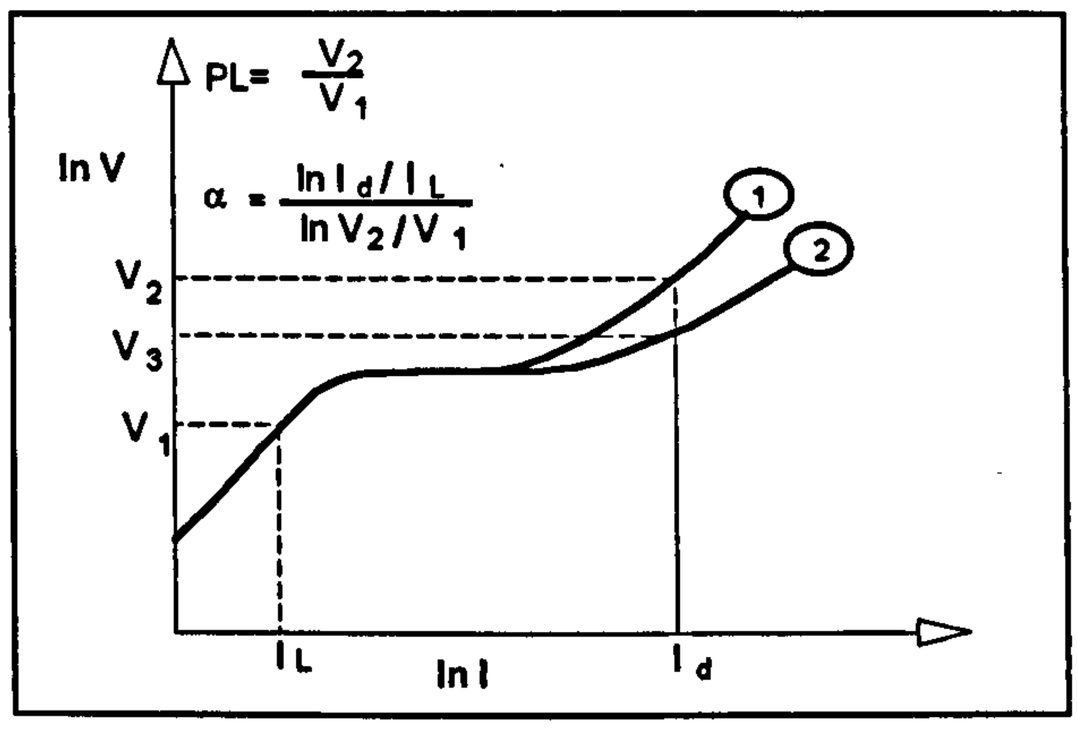


Fig. 2.1.8. I:V characteristics of the varistor and its relation to protective level (PL) and non-linear coefficient (α) [5].

The non-linear coefficient α of ZnO varistors is typically 25 to 50 and ranges up to 100 [4, 12]. The controlling parameters for this important region are only qualitatively understood [5] The addition of Bi_2O_3 has been found to be essential for forming non-ohmic behaviour. The addition of transition oxides such as Co_3O_4, and MnO_2 enhances non-linearity. Similarly, multiple dopants such as a combination of Bi_2O_3, Sb_2O_3, MnO_2, SiO_2, Co_3O_4, Cr_2O_3 etc., have produced greater non-linearity than that by a single dopant. The pure undoped ZnO ceramic does not exhibit any useful varistor effect [7]. The significance of these additives to the ZnO microstructure and their role in altering the electronic properties of the varistor device are discussed in section 2.3.

2.1.5.3. The high-Current Upturn Region

(C) The high-Current Upturn Region: In this region (>10^3 A/cm^2), the I:V characteristic becomes linear, with the voltage rising faster with current than in the non-linear region. This region is mainly controlled by the impedance of the grain in the ZnO microstructure. Zinc oxide varistors are characterised by the size of the α values and the width of the range where the highly non-ohmic property is displayed. The I:V characteristics below 100 mA/cm^2 are usually measured using a dc electric source, whereas those above 1 A/cm^2 are measured by an impulse current source to avoid heat generation and thermal breakdown. The wave form of the impulse current is an 8μs rise time and 20 μs decay time up to one-half the peak value as shown in Fig. 2.1.9. This wave form is used as a standard impulse current to test lightning arresters [5,6].

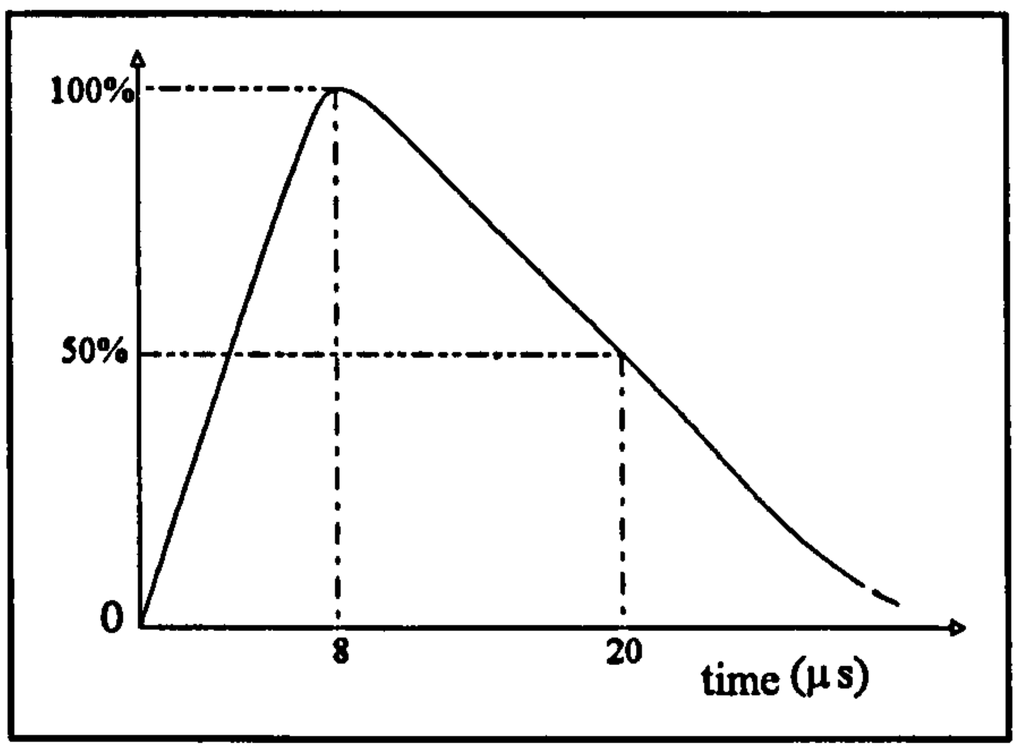


Fig. 2.1.9. The wave form of the impulse current: 8 μs rise time and 20 μs decay time up to half the peak value [6].

2.2. Properties Of Zinc Oxide

2.2.1. Zinc Oxide Preparation And Crystal Structure

Zinc oxide is commercially the most important compound of zinc and is used considerably in the rubber, ceramic, paint and other industries [15]. Compound zinc

oxide is amphoteric. It is a white powder (yellow when hot) made industrially by vapour-phase oxidation of Zn vapour. The following chemical reaction is proposed [16].

$$2Zn + O_2 \text{ -----> } 2(Zn^{2+} O^{2-}) \qquad (2.2\text{-}1)$$

Zinc oxide can be made in the laboratory by dissolving zinc metal in dilute nitric acid, followed by evaporating the resultant zinc nitrate solution to dryness and finally heating the residue.

$$3Zn + 8HNO_3 \text{ --->} 3Zn(NO_3)_2 + 4H_2O + 2NO \qquad (2.2\text{-}2)$$

$$2Zn(NO_3)_2 \text{ ------->} 2ZnO + 4NO_2 + O_2 \qquad (2.2\text{-}3)$$

The theoretical density of pure ZnO is 5.61 g cm^{-3} [25] and the melting point is 1970°C [26]. ZnO contains 4.21 x 10^{22} units (ZnO) per cm^3. Zinc Oxide crystallises with the hexagonal wurtzite structure (hcp) (a_o = 3.249 Å, c_o=5.205Å) at ordinary temperatures and under atmospheric pressure. ZnO under high pressure, has another crystal structure, zinc blend type (cubic), [17]. In the more common, wurtzite structure the oxygen atoms are arranged in a hexagonal close-packed type of lattice with zinc atoms occupying half the tetrahedral sites. In this structure, the Zn and O atoms are tetrahedrally co-ordinated to each other and are therefore, equivalent in position. The Zn-O bonding is not uniform and although mainly ionic, covalent bonding occurs along the c axis, so that the tetrahedral structure composing the lattice is not entirely symmetrical [15]. The effective charge of each ion is estimated as about one electron charge [18]. Each cation (Zn^+) is surrounded by four anions (O^-) situated at the corner of a nearly regular tetrahedron and each anion is similarly surrounded by four cations (Fig. 2.2.1).

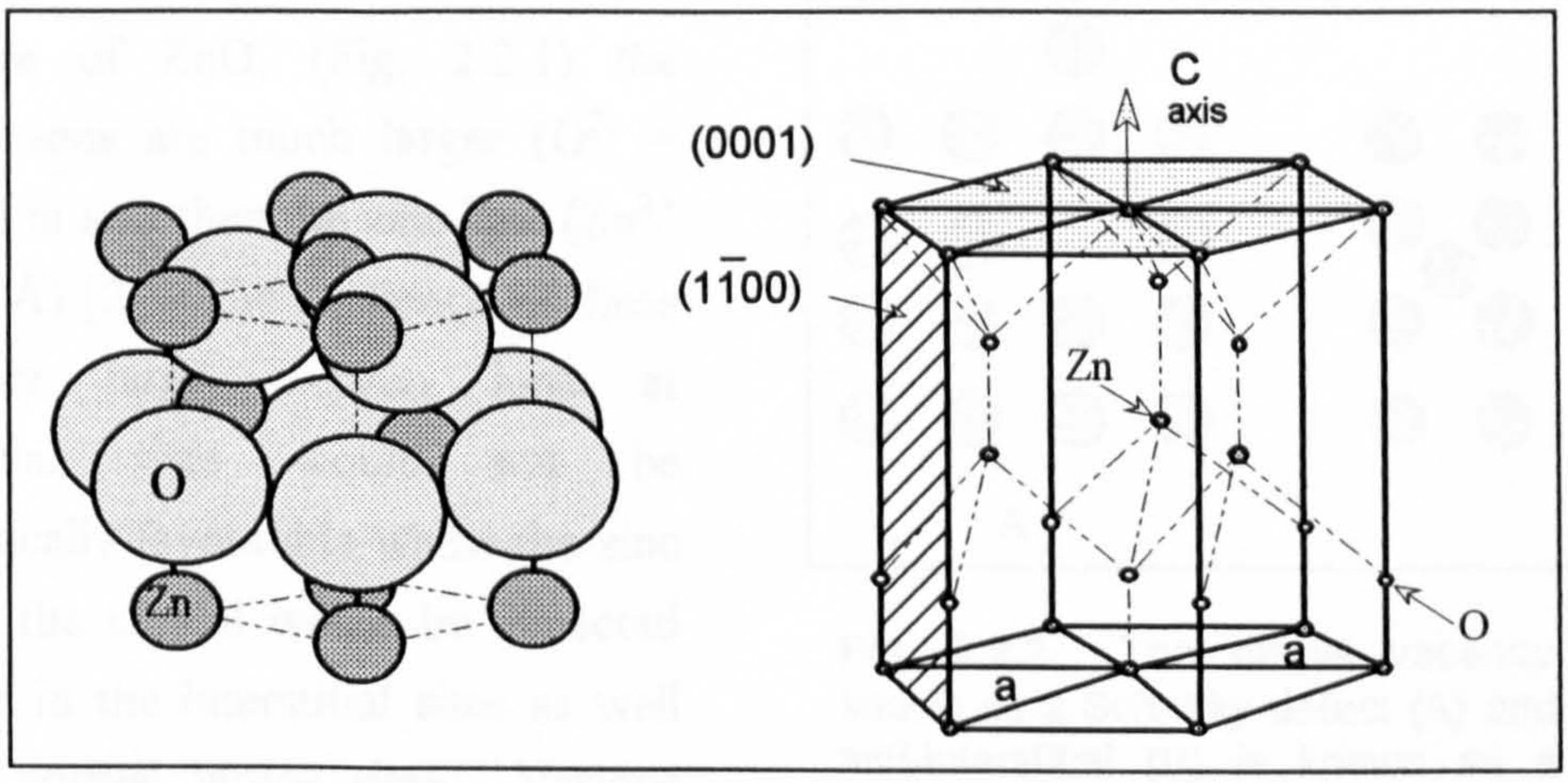


Fig. 2.2.1. Crystal structure of ZnO (wurtzite structure) [5,19].

The structure can also be described as a series of atomic double layers stacked normal to the c-axis. The series terminates on both sides with two different [0001] surfaces, one composed of zinc ions, the other of oxygen ions. The two different surfaces can be distinguished by suitable etching procedures (30% solution of HCl or HNO_3 or H_3PO_4). The prism surfaces (parallel to the c-axis) contain an equal number of cations and anions [18]. Another feature of the lattice is that it is relatively open, since the zinc and oxygen ions can be considered to occupy only 44% of the volume (with all the octahedral and half the tetrahedral sites empty), leaving a relatively large space. As a result other metal atoms can enter the lattice at elevated temperatures and introduce marked changes in properties [15]. It is, therefore, relatively easy to incorporate external dopants into the ZnO lattice as is observed in a varistor. Many crystalline compounds and metals exhibit twinning consisting of two lattices growing from a common junction, ZnO is the only inorganic compound which forms four acicular spines united at a common base. By suitable growth and doping procedures, ZnO crystals can be made either insulating (10^{10} ohm-cm) or n-type semiconducting (typically 1-100 ohm-cm) [18]. So far, no p-type samples have been reported. In pure samples the room-temperature electron mobility ranges between 100 and 300 cm^2/V sec [18]. Hole mobilites of 180 cm^2/V sec at 300 K., have been quoted by **Sze** [27]. By suitable heat treatment, in a reducing atmosphere at 900°C, the Zn/O ratio can be increased leaving excess zinc atoms which migrate to interstitial sites [15]. These carry two positive charges, having released two electrons which cause the increase in conductivity. ZnO also exhibits photoconductive properties. By heating in hydrogen to produce excess zinc in the lattice, a photoconductive peak effect with white light at 420 nm can be produced, and this effect is utilised in photocopying [15].

Looking once again at the crystal structure of ZnO, (Fig. 2.2.1) the oxygen ions are much larger (O^{2-} = 1.39 Å) in size then the zinc ions (Zn^{2+} = 0.77 Å) [2]. The existence of these relatively large oxygen ions at interstitial sites would not be energetically favourable whilst the zinc ions in the crystal would be expected to exist in the interstitial sites as well as the normal lattice sites. Various experimental data suggests that Frenkel disorder predominates at lower temperatures, with Schottky disorder becoming increasingly more important at higher temperatures (Fig. 2.2.2). Over the conditions of

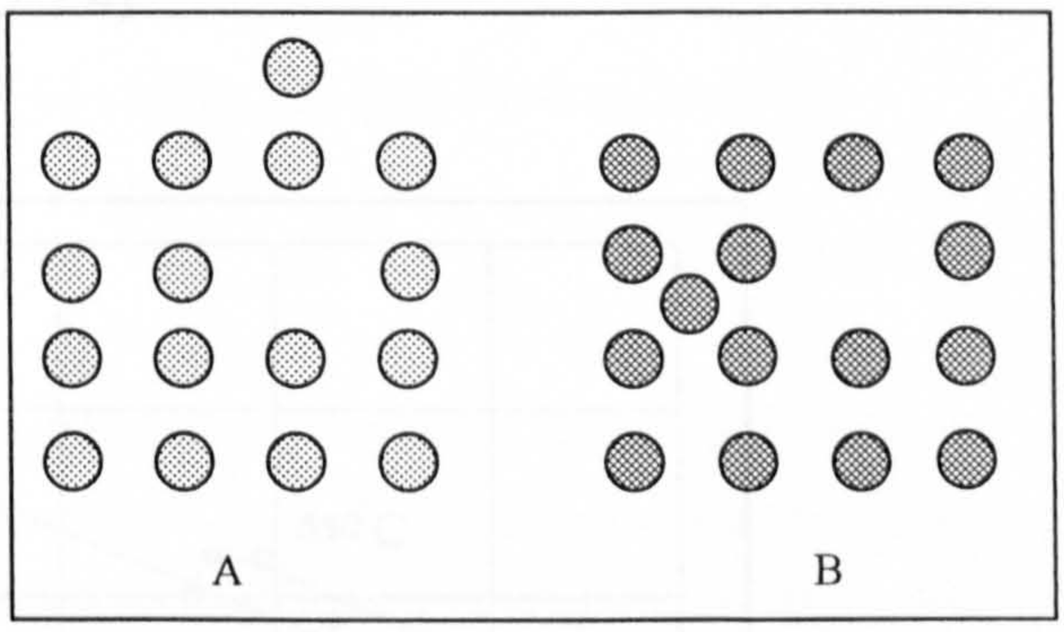


Fig. 2.2.2. The simple vacancy itself is known as a Schottky defect (A) and vacancy self-interstitial (B) is known as a Frenkel defect [29].

fabrication and operation (low to intermediate temperatures), Frenkel disorder predominates over Schottky disorder in ZnO [19,28].

2.2.2. Electrical Properties of ZnO

Conductivity studies of ZnO as a function of oxygen pressure [19] have shown that the conductivity, and hence the concentration of electrons in the conduction band, decreases as the partial pressure is increased as shown in Fig. 2.2.3.

$$\sigma \sim [\grave{e}] \sim Po_2^{-1/4} \qquad (2.2\text{-}5)$$

The chemical analysis of zinc oxide crystals indicate that zinc oxide is non stoichiometric ($Zn_{1+x}O$) with [Zn]/[O] > 1, indicating an excess of zinc. The n-type semiconducting property of zinc oxide is associated with the presence of excess Zn [19]. When ZnO is heated in zinc vapour, the number of zinc interstitials goes up and the conductivity will be proportional to the zinc vapour pressure, following the equation:

$$\sigma \propto P_{Zn}^{1/2} \qquad (2.2\text{-}6)$$

Gupta *et al.*, [37] attributes the instability of the varistor to these mobile positively charged metastable zinc interstitials (Discussed in section 2.4.5).

The band gap of zinc oxide [19] has been determined from optical studies to be 3.3 eV. Hall measurements have confirmed that the donor level (zinc interstitial as the native donors) lies 0.05 eV below the conduction band and that the donors are completely ionised at room temperature and above (Fig. 2.2.4).

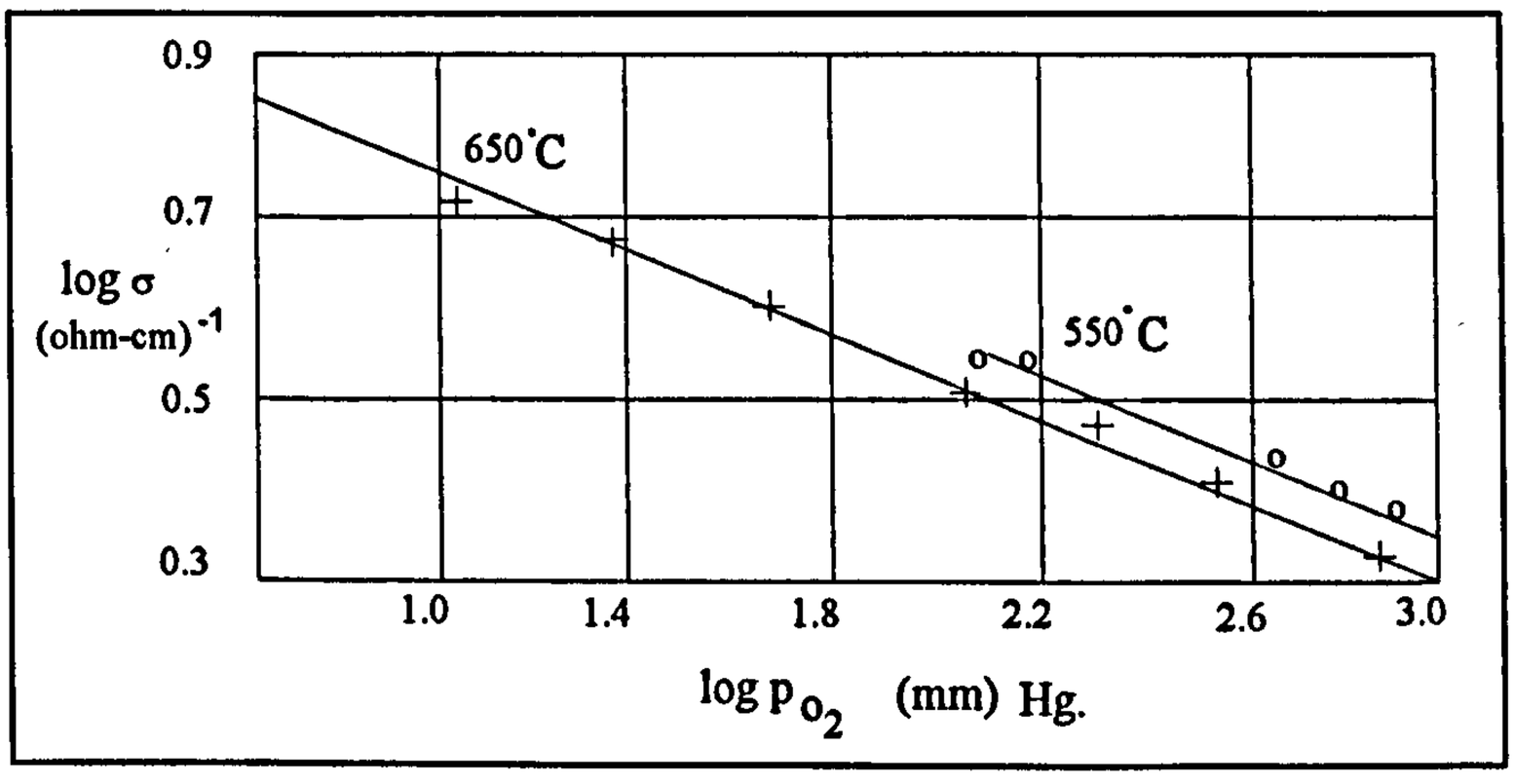


Fig. 2.2.3. Conductivity of ZnO as a function of oxygen pressure [19].

Two possible mechanisms are proposed to explain this type of behaviour:

(a) Formation of anion vacancies with complete ionisation of anion vacancy donors according to the following reaction:-

$$Oo = 1/2O_2(g) + Vo^{o} + \grave{e} \qquad (2.2\text{-}6)$$

An anion vacancy acts as a donor and contributes an electron to the conduction band.

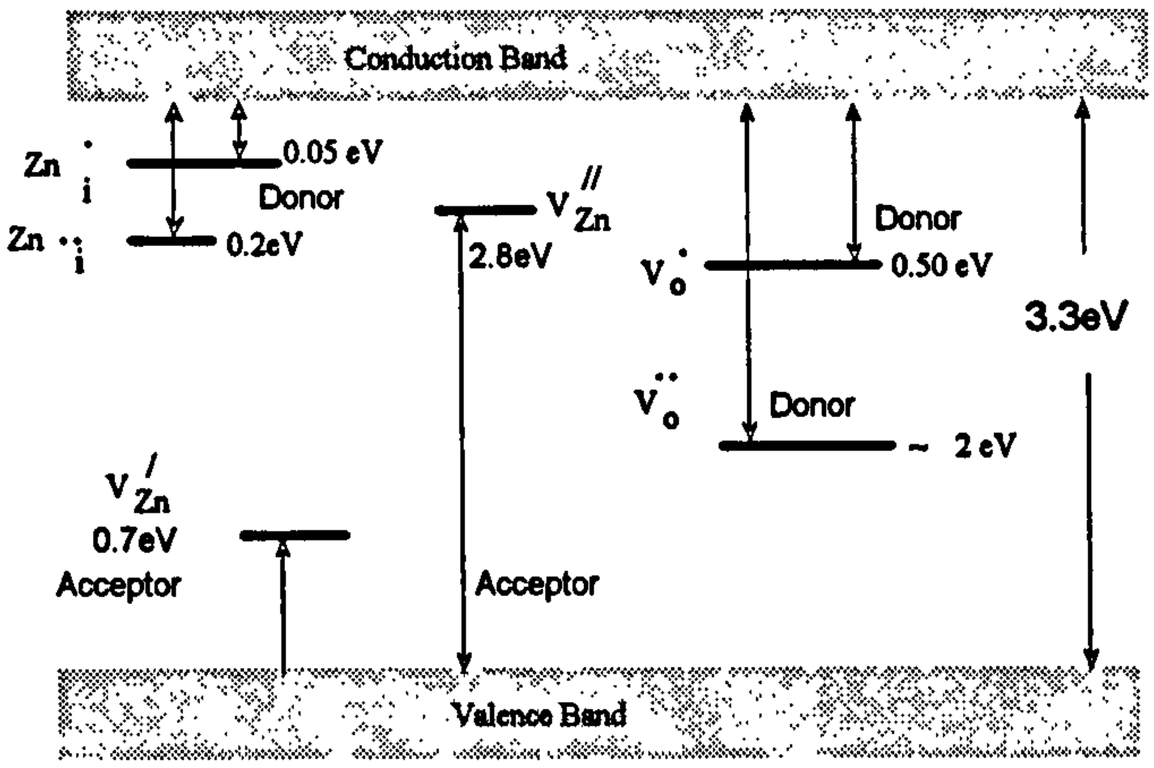


Fig. 2.2.4. Electronic energy band diagram for ZnO indicating possible energies associated with electronic defects [5,19,20,28]. For symbols, the reader is referred to Kröger and Vink notations in Appendix A.

Symbols:- $Zn_i^{\cdot}$ -donor defect, $Zn_i^{\cdot\cdot}$ -donor defect, $V_{zn}^{''}$ -acceptor defect, $V_{zn}^{'}$ -acceptor defect, $V_O^{\cdot}$ -donor defect, $V_O^{\cdot\cdot}$ -donor defect , Oo -oxygen at oxygen site, è - excess charge imparted to crystal by the introduction of the defect, in this case vacancy at oxygen site Vo^{o} .For **Kröger** *and* **Vink** [21] notations the reader is referred to Appendix A.

(b) Formation of an ionised cation interstitial, according to the following reaction:-

$$Zn(g) = Zn_i^{o} + \grave{e} \qquad (2.2\text{-}7)$$

Physically, this corresponds to transferring a neutral zinc atom from the vapour phase to an interstitial position. The interstitial cation tends to act as a donor and since the donor lies so close to the conduction band, the interstitial would be completely ionised. The second ionisation step could proceed by the following reaction:-

$$Zn_i^{o} = Zn_i^{oo} + \grave{e} \qquad (2.2\text{-}8)$$

The equilibrium constants for processes (a) and (b) are

$$K_a = Po_2^{1/2}[Vo^{o}][\grave{e}] \qquad (2.2\text{-}9)$$

$$K_b = [Zn_i^{o}][\grave{e}]\, PZn^{-1} \qquad (2.2\text{-}10)$$

The quantities Pzn and Po_2 are not independent of each other, since for the formation of ZnO,

$$Zn(s) + 1/2O_2(g) = ZnO(s) \qquad (2.2\text{-}11)$$

there is an equilibrium constant,

$$K = PZn.Po_2^{1/2} \qquad (2.2\text{-}12)$$

Substitution of eqn. (2.3-12) into (2.3-10) yields

$$KK_b = [Zn_i^{o}][\grave{e}]Po_2^{1/2} \qquad (2.2\text{-}13)$$

Comparing the equations (2.2-9) and (2.2-13) with the data in Fig.2.2.3, shows that a decrease in the oxygen partial pressure, Po_2, leads to an increase in [è] and therefore the conductivity, σ. Fig. 2.2.5, shows data for the self-diffusion of zinc in ZnO [19], where the diffusion coefficient D is given by:

$$D = 5.3 \text{ X } 10^{-4} \exp(-0.55/kT). \qquad (2.2\text{-}14)$$

The activation energy of the order of 0.55 eV., for the diffusion of zinc in zinc oxide is considered to be too low for diffusion by a vacancy mechanism [19]. Thus the only way to explain the fast diffusion is to postulate the existence of interstitial Zn, thereby giving support to alternative (b) above. According to the reaction (2.2-8), interstitial Zinc ions are produced in concentration equal to the electron concentration [è].

Thus $[Zn_i^{o}] = [\grave{e}]$ (Neutrality condition)

Substitution of this relation into (2.2-13) gives,

$KK_b = [\grave{e}]\,[\grave{e}]\, Po_2^{1/2}$

$KK_b\, Po_2^{-1/2} = [\grave{e}]^2$

$[\grave{e}] = \sqrt{KK_b}\; Po_2^{-1/4}$

$\sigma \sim [\grave{e}] \sim Po_2^{-1/4}$

$\sigma = ne\mu, \quad \sigma \alpha\, n = [\grave{e}]$

$\sigma \alpha\, [\grave{e}] \alpha\, Po_2^{-1/4}$

Symbols: σ -is the conductivity, n -is the free carrier density, [è] -is the electron concentration and Po_2 -is the partial pressure.

(μ - mobility assumed to be constant, e- and n-)

Hence the fast diffusion is attributed to the existence of interstitial Zn.

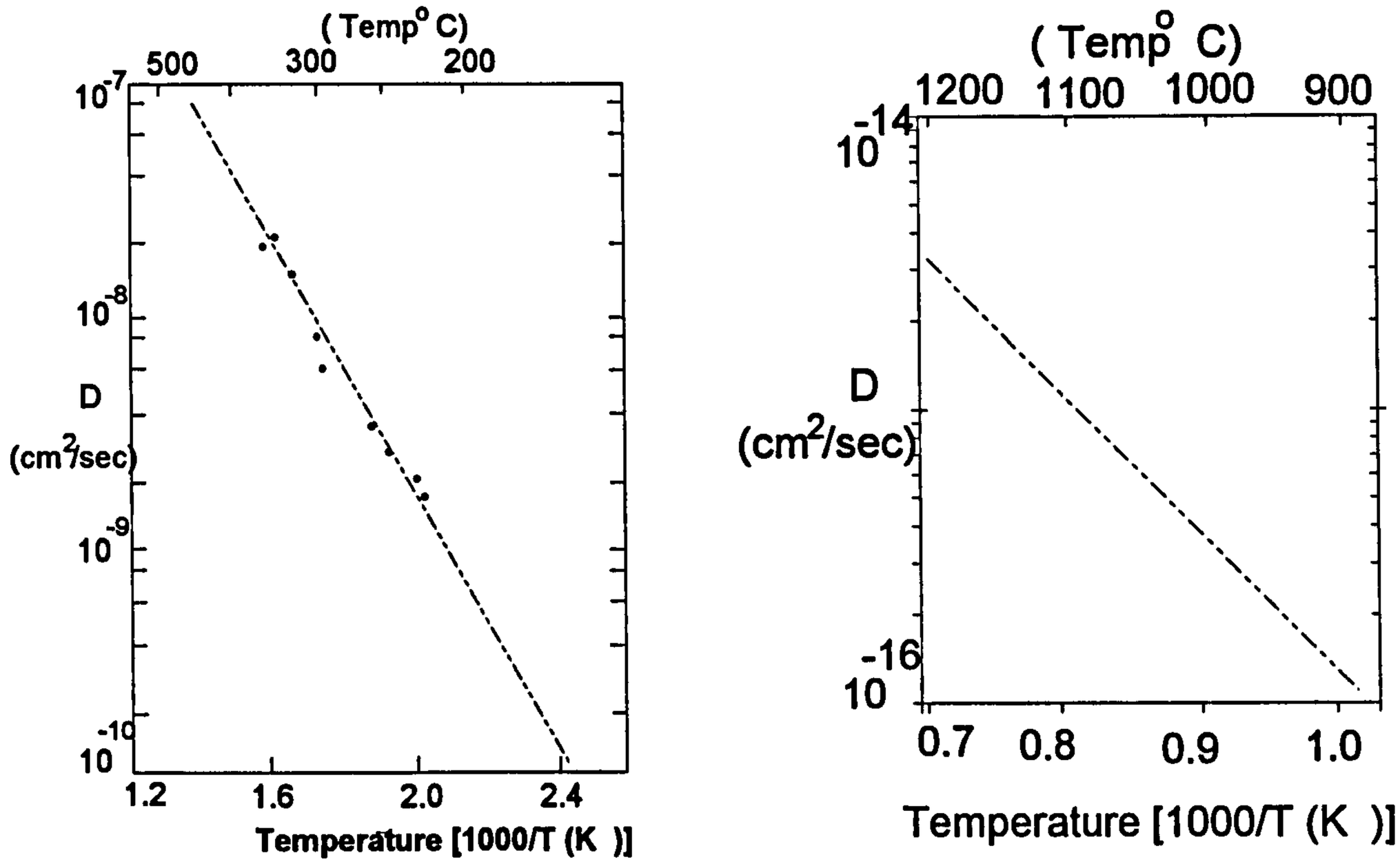


Fig. 2.2.5. Self-diffusion coefficient of zinc (on the left) and oxygen (on the right) in undoped ZnO ceramic [19,118]. Oxygen diffusion studies of both doped and undoped ZnO ceramic is presented in this work (section 5.4).

2.3. Properties of ZnO Varistor

2.3.1. Fabrication of ZnO Varistor

ZnO varistors are made by accurately weighing out the required amount of powder constituents followed by milling, calcining and finally consolidating the pressed powders by sintering at temperatures, usually above 1200°C (Fig. 2.3.1).

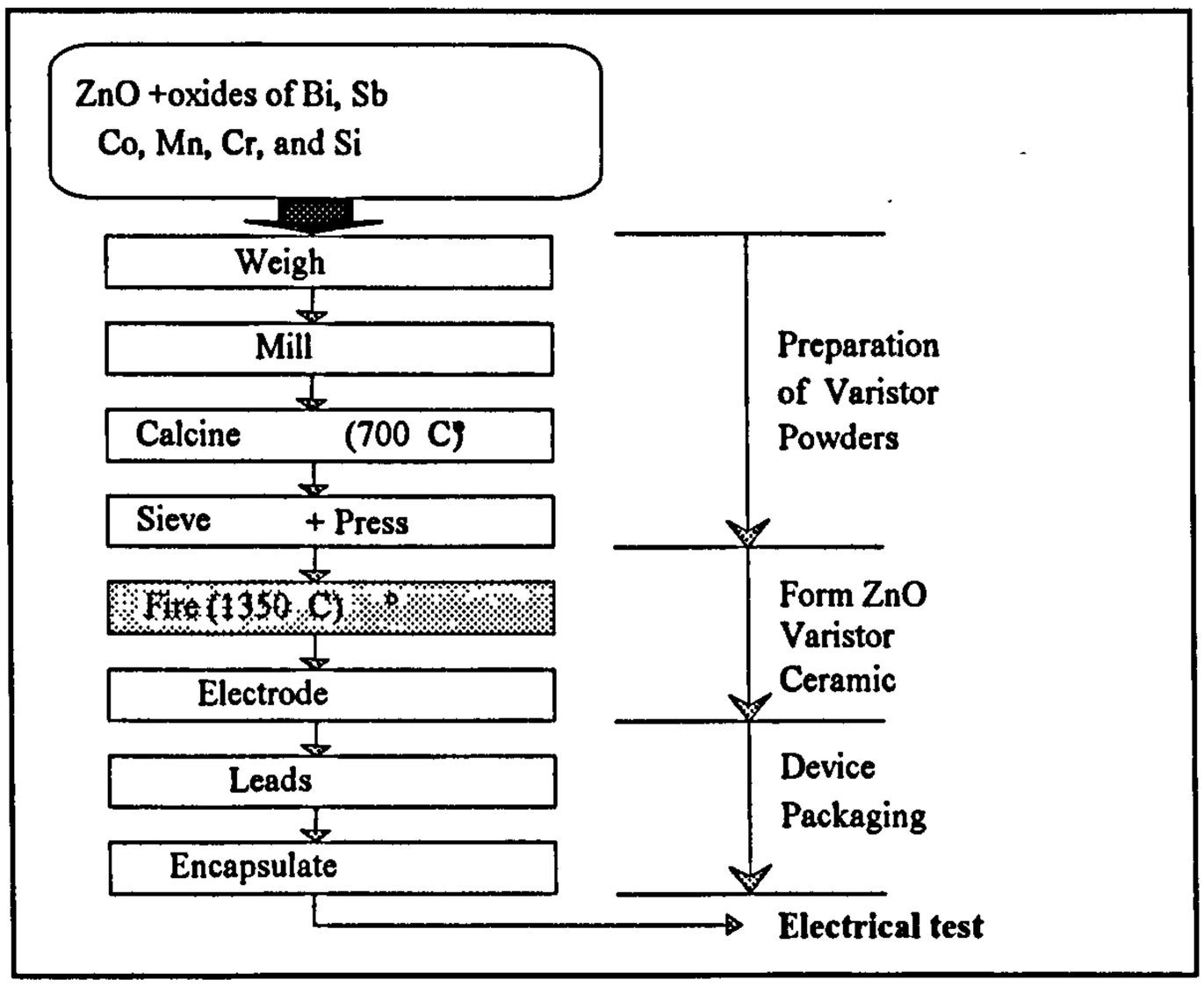


Fig. 2.3.1. Simplified flow diagram for the fabrication of ZnO varistors [5].

2.3.2. Microstructure

A chronological review of the findings on microstructure, since the discovery of the ZnO varistor phenomenon are presented below.

Initially **Matsuoka** *et al.*,[7] in 1969 discovered that sintered ZnO without any additives did not exhibit any varistor behaviour and had α=1 (ohmic behaviour). Moreover, the addition of oxides with ionic radius smaller (BeO, MgO) than that of Zn, also failed to produce any non-linear behaviour. However, the addition of oxides with ionic radius larger (CaO, SrO, BaO) than that of Zn exhibited varistor behaviour (α>1). Solubility of these additives and their favourable segregation to form secondary phases at the grain boundaries was presumed to be responsible for the non-linear behaviour.

Interrelated effects of additives in ZnO based varistors were subsequently investigated by **Matsuoka** [9] in 1970. A ZnO varistor system doped (at 0.5 mol.%, except Sb_2O_3 at 1.0 mol. %) with Bi_2O_3, CoO, MnO, Cr_2O_3 and Sb_2O_3 was studied. The influence of single and combined additives in relation to the sintering temperature, additive content, and the effect of temperature on the non-linear characteristics of the sample were investigated using SEM-EDAX, I:V and the capacitance measurement techniques. The effects of single addition of Bi_2O_3, or Sb_2O_3, produced a low value (3 to 4) of the non-linearity coefficient α. The double additions, such as Bi_2O_3 + CoO or Bi_2O_3 + MnO, led to an increase in α, up to 18. Further addition of up to five oxides, produced higher values of α up to 50 (Table 2.3.1).

BIBL. LONDIN.

Additives	(mol. %)	Sintering Temp. (^{o}C)	Grain size (μm)	α
O	O	1150	20	1
Bi_2O_3	0.5 each	1150	20	4
Sb_2O_3	0.5 each	1150	3	3
Bi_2O_3 + CoO	0.5 each	1250	25	13
Bi_2O_3 + MnO	0.5 each	1350	30	18
Bi_2O_3+ CoO+ MnO	0.5 each	1350	30	22
Bi_2O_3+CoO+MnO+Cr_2O_3	0.5 each	1250	20	21
Bi_2O_3+CoO+MnO+Cr_2O_3 +1 mol.%(Sb_2O_3)	0.5 each	1350	10	50

Table 2.3.1. Electrical properties and average grain size of ZnO ceramic with various combined additives [9].

Matsuoka [9] also discovered that the ceramic compositions with multiple additives were progressively more stable at high temperatures than the ones with a single addition. For example, a double addition of Bi_2O_3 + CoO or Bi_2O_3 + MnO formed a compound which prevented the evaporation of Bi_2O_3 at 1250°C to 1350°C. The single addition of Bi_2O_3 additive resulted in evaporation of Bi_2O_3 at much lower temperatures. The grain boundary interface layer of approximately 1μm was presumed to be coating the ZnO grains and responsible for the non-ohmic properties. Matsuoka's study on the effect of sintering temperature showed that the α-value increased with the sintering temperature up to 1350°C and exhibited the highest value of α = 50 at this temperature. Above 1350°C the α-value declined steeply with increasing temperature to just 1 at 1450°C. Moreover the increase in sintering temperature from 950°C to 1450°C resulted in a corresponding grain growth from 1μm to 15μm with a concomitant increase in capacitance of the entire sample from 0.20nF to 2.75 nF respectively. The α-value increased steeply with an increase in the additive content above 0.1 mol. % and showed a maximum of α=50 at 3.0 mol. %. Further increases in additive content led to a sharp decline of α = 4 at 30 mol. %. A mixture composed solely of the five oxides (100 mol. % of additive) did not produce nonohmic properties. The non-linear resistance did not show any maximum but increased with the additive content. The nonohmic region becomes narrow in the current range as the temperature rises with a total extinction at 900°C. The estimated electrical resistivity and dielectric constant of the segregation layers were reported to be 10^3 ohm-cm and 170 respectively. A model (as will be

discussed in a section on the conduction models), based on the space-charge-limited-current (SCLC), was proposed to explain the non-ohmic I:V characteristics.

In this initial analysis by **Matsuoka** [9], interpretation of the varistor phenomenon in ZnO ceramic was based exclusively on the segregated layer at the grain boundaries. Subsequent studies [32,33,34,38,46] including more recent ones by the present author have questioned this requirement for a 1μm intergranular layer. It is presumed that since phases such as the pyrochlore **PY** ($Zn_2Sb_3Bi_3O_{14}$) and spinel **SP** ($Zn_7Sb_2O_{12}$) were not then identified by Matsuoka, that their presence could have been mistaken for the proposed 1μm intergranular layer. Moreover the appearance of such intergranular phases surrounding the grains on the surface does not necessarily coat the majority of the grains within the bulk ceramic. This rather deceptive 1μm intergranular layer has also been described by **Gambino** *et al* [42] as a three-dimensional lacy network and appears exclusively at the surface. More details of its formation will be discussed later.

Morris [22] in 1973, reported studies of the microstructural electrical properties of ZnO-Bi_2O_3 ceramics. His investigations included ZnO ceramics containing 0.5 mol.% Bi_2O_3 and some studies of evaporated thin films of Bi_2O_3 on ZnO substrates. The electrical properties were related to the microstructure using measurements of capacitance and resistance and their variation with frequency, voltage, and temperature. For the intergranular phase a thickness of about 60 nm was estimated on the basis of structural examination (SEM-EDAX) of the Bi doped ZnO sample (with 0.5 Mol. % addition of Bi_2O_3) etched in NH_4Cl solution for several hours. Morris proposed conductive ZnO grains separated by a continuous amorphous Bi_2O_3 to be pertinent to gain desirable electrical properties in the ZnO based varistor.

These studies were limited to this two component system previously studied by **Matsuoka** [9] giving a maximum non-linear value of, α to be around 2-8. It was observed that ZnO with a grain size of 10 μm can absorb a maximum of 1 mol.% Bi_2O_3 ; any excess flows out during sintering. Although the non-linear conduction was presumed to be originating in the intergranular layer of this two phase microstructure, the instability of the varistor with just a single additive had not been considered. A conduction mechanism based on a combination of hopping and tunnelling in the amorphous phase was presumed by **Morris**. The limited resolution of the SEM-EDAX (as explained in the chapter on experimental techniques) makes it difficult to investigate the thickness of intergranular layers of such small dimensions (60 nm).

Wong in 1974 [25] studied the microstructure and phase transformation in ZnO based varistors, working with a ZnO based ceramic similar to that used by **Matsuoka** [9]. However, he substituted Cr_2O_3 with tin oxide, and used sintering conditions: of 1100°C

to 1400°C. Morphologies of the as-sintered and polished interior surfaces, and thin sections (50 - 100μm thick) were studied using SEM and optical microscopy techniques. Phases were studied using an X-ray-powder method and additionally, absorption spectra of thin sections (about 100μm.) were obtained, using a Cary 14 spectrophotometer. The results implied substitutional doping of Co ions in the ZnO lattice, giving the green coloration to the sintered compact. Pyrochlore PY (Zn_2 $Sb_3Bi_3O_{14}$) was observed as a liquid phase at high temperatures in samples sintered at 1300°C. The SP phases was presumed not to play any significant role in the non-linear characteristics. Samples sintered beyond 1450°C exhibited a loss in varistor properties.

According to **Wong** [25] the loss in varistor behaviour is accompanied by a corresponding reduction in PY phase at high temperatures. The pyrochlore phase is regarded as a favourable intergranular phase in the varistor system [25]. However this description of the varistor microstructure as a three-dimensional series-parallel network of ZnO-PY junctions is controversial and inconsistent with many subsequent studies [30,32,46]. **Wong** [25] also presumed the PY ⇒ **SP** phase transformation at much higher temperatures (1450°C). The general [30,46,49] consensus is that unless a very low rate of cooling is used during the sintering procedure, the PY phase should not remain as a predominant phase in the microstructure. The PY phase formation in ZnO varistors is usually accompanied by a very low rate (50°C/h) of cooling. **Inada** [32] found that PY ⇒ SP transformation takes place at much lower temperatures (850 ~ 950°C). Moreover, PY is not at all favoured in the ZnO microstructure, since it can give rise to leakage currents at voltages well below threshold [30,46,49].

In 1974, **Wong** and **Morris** [31] studied the non-ohmic properties in a binary ZnO-Bi_2O_3 system as a function of composition range and sintering temperature. The varistor behaviour was observed up to at least 20 mol.% Bi_2O_3 when sintered at 1000°C. The degree of non linearity (α) was found to increase with Bi_2O_3 content and with the rate of cooling, but it decreased at higher sintering temperatures. The value of α in these binary ceramics ranged from 2 to 8. The overall structure of the varistor was described as a three-dimensional series parallel network of ZnO-Bi_2O_3 junctions. The crystal structure of a pure Bi_2O_3 sample was identified to be α-Bi_2O_3. This phase was observed to be highly insulating with its crystal structure (monoclinic) dependant on the rate of cooling 200°C/h in this case.

Inada [32] in 1977, used a range of analytical techniques, (such as an SEM with back scatter x-ray imaging facilities, Electron microscopy with etched surfaces using the replica method, and optical microscopy) and studied ZnO based varistors with a mixture of 97.0 ZnO, 0.5 Bi_2O_3, 1.0 Sb_2O_3, 0.5 Co_2O_3, 0.5 MnO_2 and 0.5 Cr_2O_3 (Mol. %). The varistor ceramic was found to consist of ZnO phase dissolving Co and Mn, spinel of

$Zn_7Sb_2O_{12}$ dissolving Co, Mn and Cr, and mixed phases of ß-and δ-Bi_2O_3. The ZnO phase was found to correspond to the main constituent grains, which were of 10-20 μm in size with a twinning structure and randomly oriented. The spinel phase exists as grains of a few microns in size, situated discontinuously in regions where three or more grains meet. The width of the intergranular layers as observed by the electron microscope were presumed to be less than 500 Å. These findings are consistent with many subsequent studies including those by the present author. The abundance of pyrochlore PY phase occurring in the manner as previously reported by **Wong** [25] has not been found in this case.

Clarke [33], in 1977, investigated commercial ZnO based varistors using high-resolution electron-microscopy techniques of bright-field imaging and lattice-fringe imaging to look at the distribution and location of intergranular phases. Clarke found that the majority of the ZnO-ZnO grains were not surrounded by intergranular oxide layers as previously assumed [9, 32, 22, 25, 31]. The Bi rich phases were found to be located principally at three and four ZnO grain junctions and exhibited non-zero contact angles with the ZnO grains. However, due to finite dihedral angles those few grain boundaries that did contain intergranular phases were regarded as "special" boundaries. These are formed by the basal plane of one of the adjacent ZnO grains resulting in a straight boundary and an intergranular phase of constant width over several microns.

Similar observations were made by **Kingery** [34] *et al*, in 1979, using high spatial resolution scanning transmission electron microscopy (STEM), with imaging and energy dispersive X-ray microanalysis capabilities. A point-to-point composition analysis, was accomplished with a minimum spacing of 25 Å, as shown in Fig. 2.3.2. The results showed the precipitate particles to have a high Bi content relative to the matrix and additionally, as previously reported [33], that due to the finite dihedral angle there were in fact only a few grain boundaries containing intergranular phases.

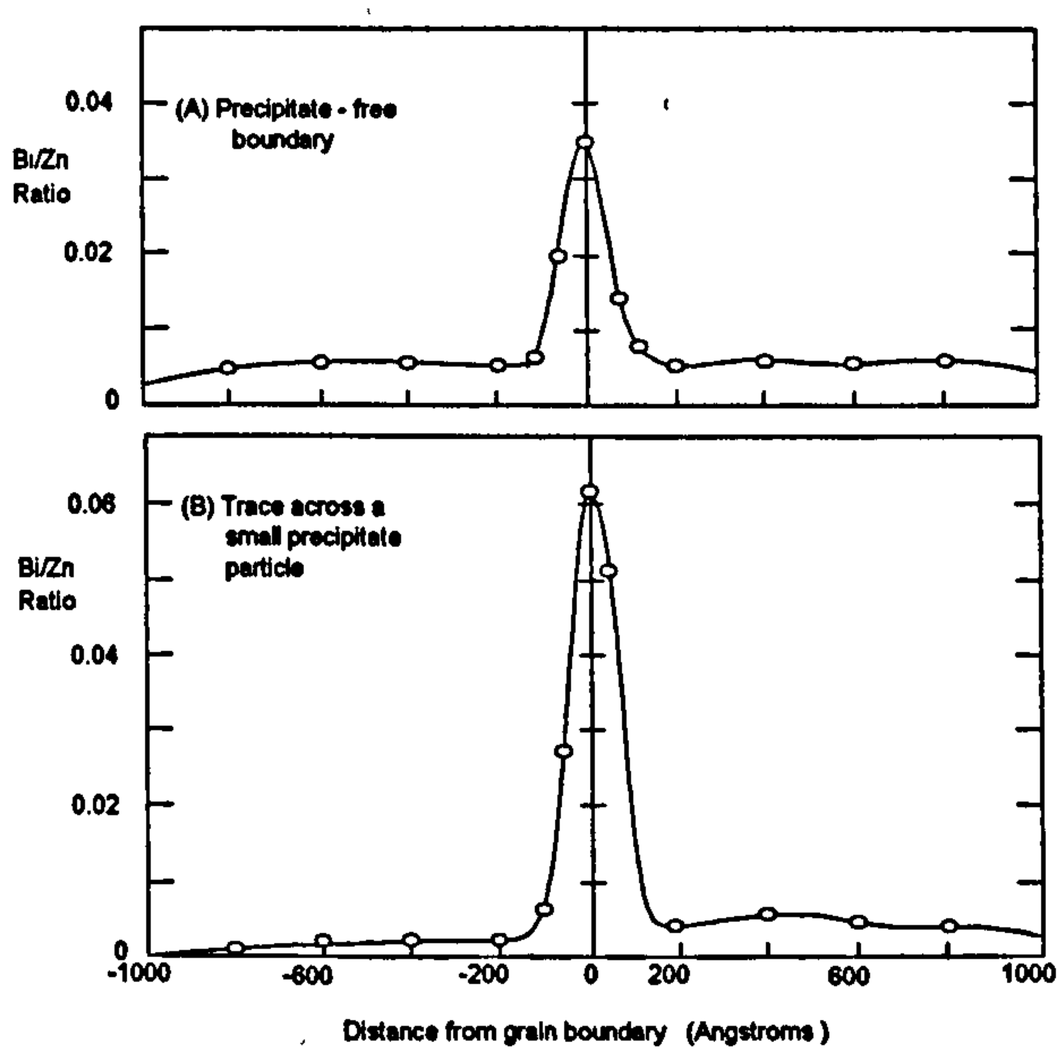


Fig. 2.3.2. Ratio of Bi to Zn **(A)** across precipitate-free boundary and **(B)** across small precipitate particle on boundary. For this analysis the grain boundary was aligned parallel to the incident electron beam [34].

Subsequent studies (1978) by **Inada** [35] included investigation of ZnO based varistors containing ZnO, Bi_2O_3, Sb_2O_3, Co_2O_3, MnO_2, and Cr_2O_3. He studied the effect of heat-

treatment on the crystal phases, microstructure, and nonohmic properties of ZnO ceramics consisting of ZnO grains with dissolved Co and Mn, spinel SP ($Zn_7Sb_2O_{12}$) containing dissolved Co, Mn and Cr, and β-Bi_2O_3, δ-Bi_2O_3 phases containing dissolved Zn and Sb. He used differential thermal analysis DTA to study the thermal change of the nonohmic ZnO, X-ray diffraction analysis to look at crystal phases and SEM to look at the microstructure. The samples as previously studied [32] were sintered at 1350°C for 1 hour in an air furnace then cooled to room temperature. His findings show that the α-value decreases at around 600°C to 700°C, and becomes lowest at 800°C, then changes abruptly and almost recovers at 900°C to 1100°C. These changes were presumed to be associated with the corresponding changes in crystal phases and microstructure. The crystal structure and the microstructure of the SP, PY and the Bi-rich phases would normally be affected by sintering conditions, particularly the rate of cooling during the heat treatment [30,32]. The Bi_2O_3 phase can exhibit a number of different crystal structures as denoted by α, β, δ and γ phases. **Inada** [35] observed that the crystal phase β-and δ-Bi_2O_3 begins to change into γ-Bi_2O_3 at about 600-700°C. This phase transformation resulted in coarsening of the intergranular layer and a decrease in the α-value. At 900°C the γ-Bi_2O_3 phase disappears into a δ-Bi_2O_3 solid solution containing dissolved Zn, Sb, and Cr. Corresponding to this phase change, a dense intergranular layer was observed to form from the liquid phase produced by the melting of the γ-Bi_2O_3. The recovery of the α-value at 900 to 1100°C was presumed to be affected by the reduction of Cr in δ-Bi_2O_3 solid solution and the decrease in lattice constant of δ-Bi_2O_3 in solid solution. At 1100°C the phases, microstructure and α-value recovered completely. The pyrochlore PY ($Zn_2Bi_3Sb_3O_{14}$) phase disappears by reaction with the ZnO to produce SP and the Bi_2O_3-rich liquid. The Cr moves out from Bi_2O_3 into the SP phase. **Inada** has explained these findings in terms of the following reactions that occur in the sintering process:

$$Zn_2Bi_3Sb_3O_{14}\ (Co, Mn, Cr)\ [PY] + [ZnO] \Rightarrow (850°C\text{-}950°C)$$

$$\Rightarrow\Rightarrow [Zn_7Sb_2O_{12}\ (Co, Mn, Cr)\ [SP]] + [Bi_2O_3\ (Cr)\ [liq.]], \quad 2.3\text{-}1$$

$$[Bi_2O_3\ (Cr)\ [liq.]] \Rightarrow (950°C\text{-}1300°C) \Rightarrow\Rightarrow [Bi_2O_3\ (Zn,Sb,Cr)\ [liq.]] \quad 2.3\text{-}2$$

dissolution of spinel **SP** ($Zn_7Sb_2O_{12}$), ZnO and absorption of chromium **Cr** by **SP**.

$$[Bi_2O_3\ (Zn,Sb,Cr)\ [liq.]] \Rightarrow (\cong 1300°C) \Rightarrow\Rightarrow [Bi_2O_3\ (Zn,Sb)\ [liq.]] \quad 2.3\text{-}3$$

absorption of **Cr** by **SP**

Here, the brackets show the phases and the parentheses the dissolved components; and SP, PY and liq. means spinel, pyrochlore and liquid. After the $Zn_2Bi_3Sb_3O_{14}$ pyrochlore phase containing dissolved Co, Mn, and Cr is first formed at temperatures of about 750°

to 850°C, the reaction of formulas 2.3-1, 2.3-2, and 2.3-3 occurs at temperatures above 850°C. The Cr-content in the liquid phase containing dissolved Zn, Sb, and Cr gradually decreases with the absorption of Cr by the spinel phase, and finally becomes extinct above 1300°C. The gradual decrease and final extinction of Cr in the liquid phase, when quenched, results in a decrease of the lattice constant of δ-Bi_2O_3 solid solution containing dissolved Zn, Sb, and Cr, and the formation of β-and δ-Bi_2O_3 containing dissolved Zn and Sb, respectively. Although the Zn_7 Sb_2 O_{12} spinel phase containing dissolved Co, Mn, and Cr is stable against the Bi_2O_3 -rich liquid phase, the reaction occurs only slightly on slow cooling. The degree of this reaction becomes smaller with the rise of sintering temperature [35].

$$[Zn_7Sb_2O_{12}\ (Co,Mn,Cr)\ [SP]] + [Bi_2O_3\ (Zn,Sb,Cr)\ [liq.]], \Rightarrow$$

Slow cooling

$$\Rightarrow \qquad \Rightarrow [Zn_2Bi_3Sb_3O_{14}\ (Co,Mn,Cr)\ [PY]] + [ZnO\ (Co,Mn)] \qquad 2.3\text{-}4$$

(partially)

Yet-Ming *et al.*, [36] in 1981, were perhaps the first to report the direct observation of electric field-induced movement of ionic charge in the ZnO varistor at grain-boundary region (Fig. 2.3.3).

With an aid of STEM, they had investigated the distribution of segregant at the grain boundaries in a heavily degraded sample of ZnO doped with 0.5 mol.% Bi_2O_3 and 0.5 mol.% Co_2O_3. This composition exhibited high non-linearity ($\alpha \approx 50$). The sample was sintered at 1150°C for 90 min, and cooled at a rate of 150 °C/h. The resulting grain size was in the range 10-50μm with considerable porosity. Samples were degraded by passage of a dc current density of 20mA/cm^2 for several hours with temperature maintained at 140 ± 10°C. Samples for electron microscopy were cut from beneath the electrode regions of degraded samples, mechanically polished to a thickness of about 40 μm and ion thinned to perforation. A point by point composition profile was obtained across suitable grain boundaries in a thinned specimen using a fixed finely focused electron beam of about 1nm (FWHM). The effective spatial resolution of the instrument was about 5 nm for metal oxides. A marked asymmetry in the distribution of Bi and Co with respect to the physical location of the boundary was observed. This was

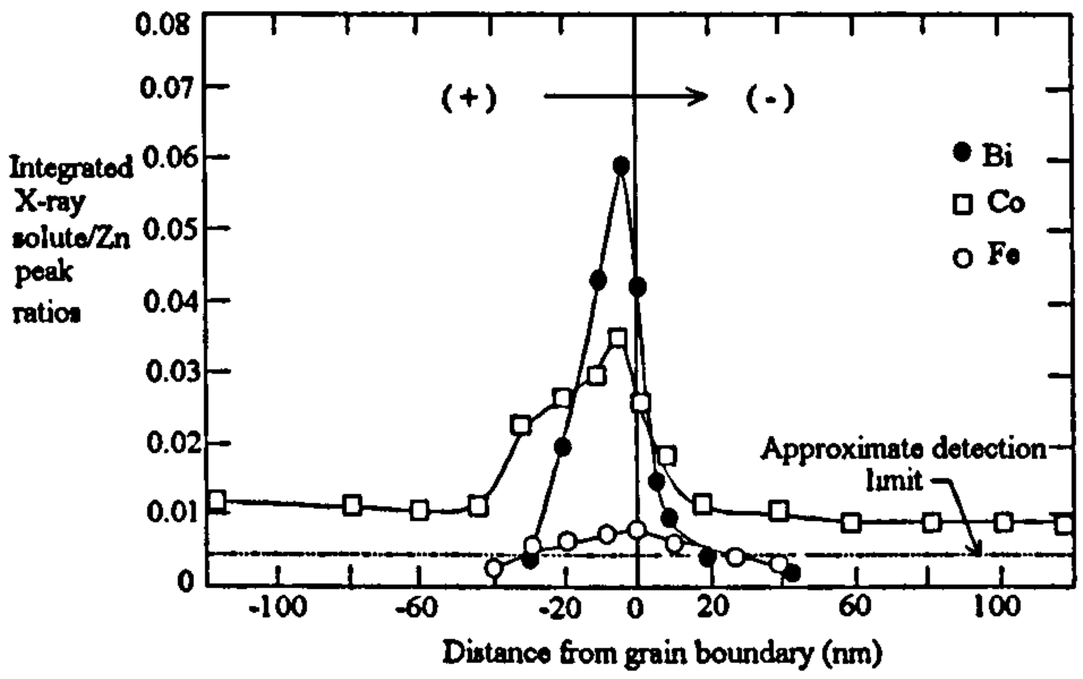


Fig. 2.3.3. Solute profile across grain boundary oriented at high angle to the degrading electric field [36].

consistent with the accumulation of mobile cations on one side of the boundary under the influence of a dc electric field (Fig. 2.3.3). It is to be noted that the data in this report reflected the accumulation of solute ions adjacent to the boundary rather then any necessary altered ion distributions at the boundary. The correlation between the two is presumed but inference drawn on this basis would be speculative. More spatially precise chemical data are necessary for correlation with electrical data. The overall conclusion drawn from this work was that the grain boundaries in a degraded ZnO varistor containing Bi and Co show a marked asymmetry in solute distribution. During degradation an accumulation of any Zn interstitial ions that are present should also occur. Such a redistribution would not be observed since the relative increase in Zn concentration would be minor compared to that of Co or Bi. However, the accumulation of Zn in absolute numbers of ions may be significant. **Gupta** *et al.*, [37] in their recent work, have interpreted the ac degradation of ZnO varistors, to be attributed to the diffusion of metastable Zn interstitial migrating to the grain-boundary region.

Experimental work based on micro-contact measurements on the adjacent grains were undertaken by **Einzinger,** [38] in 1982. He showed that the heterogeneous segregation layers between ZnO grains are not essential for the varistor effect. The varistor effect was presumed to be located in the vicinity of the interfacial regions of directly touching ZnO grains and attributed exclusively to the property of doped zinc oxide. Directly touching ZnO grains were found to exhibit varistor I:V curve with a breakdown voltage near 3.5 eV, slightly above the ZnO band gap of 3.3 eV. He also demonstrated that the presence of the massive intergranular oxide layers, of the order of 1μm thickness, are not required, as in some of his own investigations [12], such layers were not found.

Moreover, in his subsequent investigations **Einzinger** found that the Bi_2O_3 rich intergranular layers in fact prevented the varistor action, by electrically insulating the adjacent ZnO grains, up to voltages 10-20 times higher than 3.4 - 4 V. He concludes that intergranular layers are extremely rare and in any case they are not favoured in the varistor system. Likewise in his proposed conduction model as will be discussed later he has not allowed for the possible fine intergranular layers. This obviously contradicts some of the previous assumptions on varistor based on active heterolayers [9, 22, 25]. According to **Einzinger,** only those ZnO grains which lie in direct mechanical contact would exhibit good varistor behaviour!

In 1985, **Olsson** *et al.*,[39] investigated the microstructure of a ZnO varistor using a combination of x-ray diffractometry and analytical electron microscopy techniques (SEM, TEM, STEM, EDAX). The varistor sample contained 90 mol.% ZnO together with additions of oxides of Bi, Sb, Mn, Co, Ni, and Cr. The powders were cold pressed and sintered at 1200°C. All the usual phases (SP, PY) were observed. Additionally this

sample contained intergranular film on a majority proportion of ZnO-ZnO interfaces. In this case there were only a small proportion of such interfaces without any intergranular films and these were presumed to have instead a trace of Bi segregated at the interfacial layers. The main difference between this finding and the previous ones [34,33,38] lies in the morphology of the ZnO-ZnO grain boundaries. In this present case, three types of Bi-rich phases have been reported in the intergranular regions of the microstructure. These are: (1). an amorphous phase, (2). α-Bi_2O_3 and (3) pyrochlore, $Zn_2Bi_3Sb_3O_{14}$. The vast majority of the grain boundaries between ZnO grains contained thin continuous and presumably amorphous second phase film of a thickness often less than 10nm [39]. Clark has stated that the majority of the boundaries in his investigation were free of second phase films [33], while the opposite can be said of this case. This anomaly is presumed to be due to the intergranular microstructure which is largely a result of processes which occur during liquid phase sintering and are a function of the subsequent rate of cooling to room temperature.

A similar group of analytical techniques (to those used by **Olsson** *et al.*), [39] were employed by **Cerva** *et al.*,[40] to study the microstructure and crystal structure of Bi_2O_3 phases of as-sintered and additionally heat-treated ZnO based varistors. Samples were prepared by conventional mixed oxide technology. ZnO was doped with 1 mol.% Bi_2O_3, 1 mol.% Sb_2O_3, 0.5 mol.% Co_2O_3, 1 mol.% MnO_2, and 0.5 mol.% Cr_2O_3. Samples were sintered at 1200°C for a few hours and then furnace cooled. A batch of samples were cut into two parts and one part was additionally heat-treated at about 600°C for a few hours in air with the intention of improving the electrical ageing behaviour. The analysis was carried out before and after an additional heat treatment of the sample. In the heat treated sample, most of the β-Bi_2O_3 and all of the α-Bi_2O_3 had changed to the γ -Bi_2O_3 phase. These metastable Bi_2O_3 phases were thought to affect the ZnO-ZnO homojunction, which can be electrically bypassed, and affect the ideal varistor characteristics. **Eda** [6] and **Olsson** *et al.*,[46] had reported similar findings, where the resultant leakage current enhances the power consumption of the system [41]. The crystal structure of these phases were estimated as follows: The α-Bi_2O_3 is monoclinic, with lattice parameters: a = 5.848 Å, b = 8.166 Å and c = 7.51 Å. The tetragonal ß-Bi_2O_3 phase is metastable (can change to a stable phase) at room temperature; with lattice parameters: a = 7.742 Å, c = 5.631 Å (JCPDS FILE CARD 27-0050) [40].

Temperature dependent grain boundary wetting by Bi-rich intergranular phase in ZnO varistor was studied by **Gambino** *et al*, in 1986 [42]. The effect of heat treatments on the wetting behaviour of Bi-rich intergranular phase were investigated. It was found that the grain-boundary wetting by a Bi-rich intergranular phase increases with temperature. The average equilibrium dihedral angle for the Bi-rich phase at a grain boundary was found to be O^o at 1140°C and 55^o at 610°C. During sintering the Bi-rich liquid phase

coats all ZnO grains. If the varistor was rapidly cooled from the sintering temperature, the Bi-rich phase was found to be frozen at the grain boundaries. However, if the varistor was slowly cooled, the liquid phase was found to leave the grain boundaries and was replaced by ZnO-ZnO junctions [42]. The distribution of Bi-rich intergranular phase observed for different heat treatments has been classified by **Gambino** *et al* [42], in three categories:

1 The first category corresponds to a dihedral angle of zero as was observed for the sample quenched from 1140°C. ZnO grains are completely wetted by the liquid phase and are thus separated by the Bi-rich phase in 88% of the cases. The Bi-rich grain-boundary phase acts as a low-resistance path which can shunt the grain-boundary barriers. On this basis, as the fraction of the grain boundary area occupied by a Bi-rich phase increases, the pre-breakdown resistivity and the degree of non-linearity, α, should decrease. So merely coating the ZnO grain with Bi-rich phase is not sufficient to produce good varistor electrical properties, and may even be detrimental [40,42,].

2. The second category corresponds to a dihedral angle of less than 60°, (please see **Appendix D**) observed for the slowly cooled, as-sintered sample quenched from 780°C. Only 25-30% of boundaries were in direct contact. At the same time, the Bi-rich phase remains stable at the multi-grain junctions and forms a continuous three-dimensional lacy network throughout the sample (Fig.2.3.4).

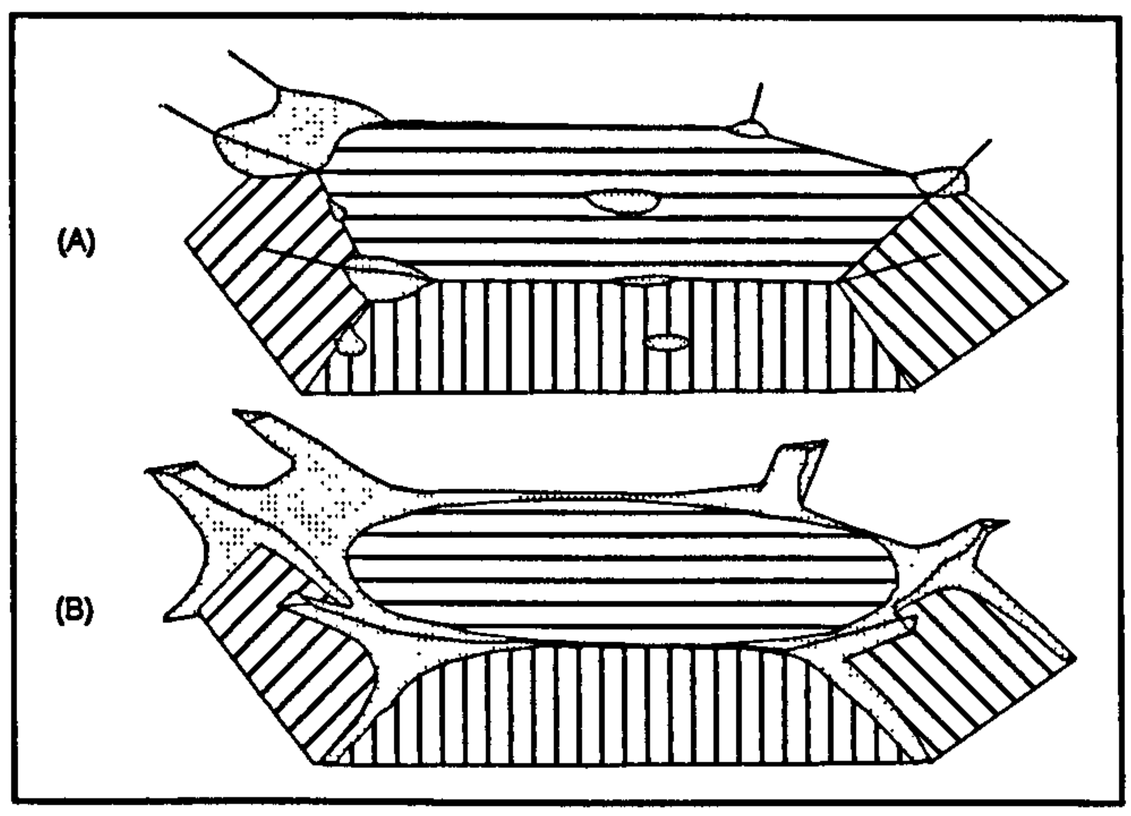


Fig. 2.3.4. Schematic of different intergranular phase morphologies in ZnO. For a dihedral angle of greater than 60°, the intergranular phase takes the form of discontinuous particles at the multi-grain junction (A). For a non-zero dihedral angle of less than 60%, the intergranular phase is continuous along the multi-grain junctions forming three dimensional lacy network throughout the sample but does not wet the grain boundaries (B). For a dihedral angle of zero, the intergranular phase wets the grain boundaries as well (not shown) [42].

3. The third category corresponds to a dihedral angle of more than 60°, as was observed for the sample annealed at 610°C. Again the ZnO grains are in direct contact. However, the Bi-rich phase in this case remains discontinuous and does not form a lacy network throughout the sample (Fig.2.3.4). Although the treatment described in the third category above would produce the best varistor action, it is to be noted that very slow cooling (15 to 50°C/h) can also encourage formation of PY phase which is unfavourable to the stability of the varistor [30,49]. Moreover at a very slow

cooling rates, Bi_2O_3 can transfer in to a metastable phase [40] which is electrically unstable. Cooling rates of 150 - 200° C/h are presumed favourable to impart good overall varistor characteristics.

Asokan *et al.*, and **Iyenger** [43, 44] in 1987 investigated the grain growth and density of sintered ZnO-based systems containing one or more additives of the type 0.1% Nb_2O_5, 6% Bi_2O_3, 3.5% Sb_2O_3, 0.55% CoO, 0.9% Cr_2O_3, 0.7% MnO_2, 0.9% NiO and 0.025% Al_2O_3. The effective role of the Sb_2O_3 as grain growth inhibitor was investigated. The presence of Bi_2O_3 was found to enhance grain growth, while the addition of CoO or MnO_2 was presumed to prevent the evaporation of Bi_2O_3 at higher sintering temperatures. A small addition of Cr_2O_3 and NiO was thought to control grain size while addition of Al_2O_3 in small quantities reduced the pore volume of the ceramic.

Asokan *et al.*, had found a significant improvement in the useful characteristics of the ZnO based varistor as a result of (1) incorporating 0.2 wt % of Nb_2O_5 in to the system, (2) by slightly modifying the preparation parameters such as calcination of powders at higher temperature (1200°C) and (3) extended ball milling for 30 hours, sintering at 1250°C for 2h, followed by post-sintering at 1100°C for 10 h. A considerable improvement was observed in these preparations, with respect to the energy handling capability (>325J/cm^3), combined with a high non-linearity index ($\alpha > 50$) with the life of the device estimated to be in the range 160 to 200 years [43]. They attributed these superior properties to the addition of an appropriate amount of Nb_2O_5 leading to the formation of $Zn_3\ Nb_2\ O_8$ spinel phase, calcining at higher temperatures and ball milling for longer duration to reduce the initial particle size. They had found 0.2 wt.% of Nb_2O_5 dopant to be the optimum level of concentration to impart these favourable properties.

Kim *et al.*,[45] in 1989, studied the sintering behaviour and phase change in the ZnO-Bi_2O_3-Sb_2O_3 system. The densification behaviour was found to be related to the formation of the liquid phases and the pyrochlore. The forming temperature of the liquid phase was found to depend on the Sb/Bi ratio: about 750°C for Sb/Bi<1 by the eutectic melting in the system ZnO-Bi_2O_3, and about 1000°C for Sb/Bi>1 by the reaction of the pyrochlore phase with ZnO. The densification rate was retarded with high Sb content and in any case found to depend on the Sb/Bi ratio and not by the total amount of additives.

Olsson *et al.*, [46] in (1989) studied individual interfacial barriers in a ZnO based varistor. They used a special electrode configuration to allow both the I:V characterisation of an individual interfacial junction, and to allow TEM studies of the same specimens. Their sample preparation was the same as in their previous studies [39]. Four main types of ZnO interfaces were observed, in slowly cooled (50°C/h)

samples, as shown in Fig. 2.3.5. The formation of a barrier to electrical conduction was presumed to have taken place during cooling of the ZnO ceramic from the sintering temperature. The details of the interfaces are as follows: The ZnO/ZnO interface of type A, with a thin (10nm) intergranular amorphous Bi-rich film, exhibited symmetrical current-voltage characteristics with a break down of 3.6 V. The ZnO/ZnO interfaces of type B, did not reveal any second intergranular phase but had thin (0.2nm) Bi atomic monolayers due segregated Bi atoms (the grains were observed to be in direct physical contact and no distinct intergranular layer was seen by SEM or TEM).

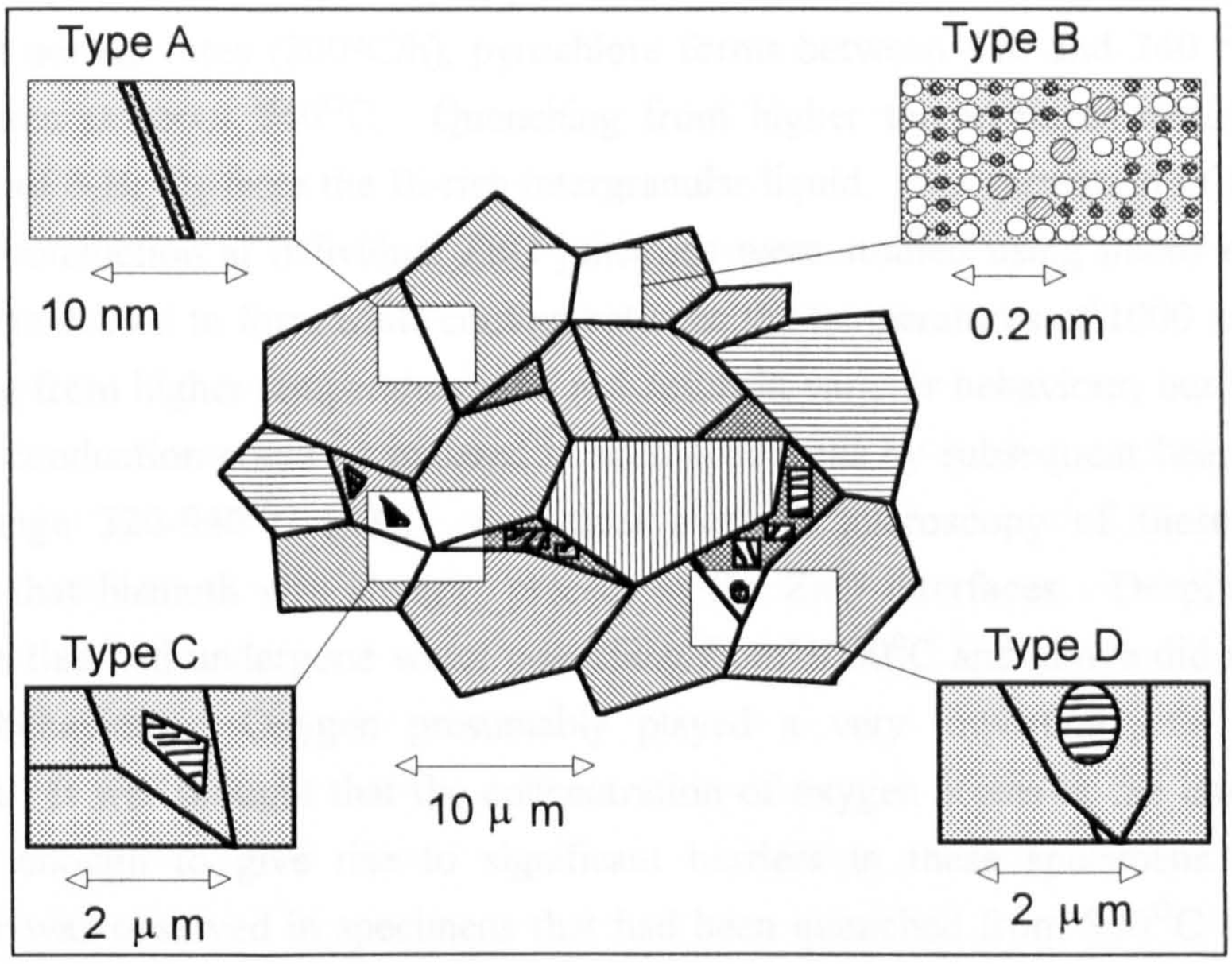


Fig. 2.3.5. Four main types of ZnO interfaces present in slowly cooled (50^{o}C/h) specimens (Not to scale). **(a)** Type A: a boundary between ZnO grains containing a thin(~2 nm) intergranular amorphous Bi-rich film. **(b)** Type B: a ZnO/ZnO interface without secondary phases but containing segregated Bi atoms. **(c)** Type C: an interface between ZnO and an intergranular mixture of Bi_2O_3 and spinel grains. **(d)** Type D: interface between ZnO and pyrochlore and spinel grains [32,46].

Type B boundaries exhibited symmetrical current-voltage characteristic but with a break down of 3.2 V. The heterojunction ZnO/ZnO interface of type C (2μm), with ZnO grains separated by a thick intergranular region containing Bi_2O_3 and grains of spinels, exhibited asymmetrical I:V characteristics between ZnO and intergranular α-Bi_2O_3 and δ -Bi_2O_3 phases. Electrons travelling from ZnO grains to the intergranular region experienced a barrier with a breakdown field of 3.2 V, while in the opposite direction, a barrier breakdown potential of 0.4 and 0.9 V was encountered. The barrier breakdown at 0.4 V and 0.9 V corresponded to junctions between α-Bi_2O_3 and δ-Bi_2O_3 to ZnO respectively [47]. In their subsequent investigations [48], a barrier breakdown at 0.6 V was encountered, which corresponds to heterojunctions between τ-Bi_2O_3 and ZnO. The

type D structure, consisting of ZnO grains separated by a (2μm) thick layer of pyrochlore with grains of spinel, did not exhibit distinct varistor properties [6,46,47]. The volume fraction of pyrochlore decreased with increasing sintering temperature and thus the fraction of inactive ZnO junctions reduced were at higher sintering temperatures.

In their subsequent works (1989), **Olsson** *et al.*, [48] investigated the effect of sintering sequences, where the specimens were water quenched from sintering temperatures of between 1000 and 1200^{o}C. The pyrochlore has been reported to be the first Bi rich phase to crystallise from the liquid-phase sintering medium during cooling. When cooling at normal rates (200^{o}C/h), pyrochlore forms between 940 and 740 ^{o}C, and τ-Bi_2O_3 forms at about 740^{o}C. Quenching from higher temperatures resulted in the formation of δ-Bi_2O_3 from the Bi-rich intergranular liquid. The formation of barriers to electrical conduction at individual ZnO junctions were studied using micro electrodes. The barriers started to form while cooling between the temperatures of 1000 and 800^{o}C. Quenching from higher temperatures did not result in varistor behaviour, but barriers to electrical conduction could be initiated in such specimens by subsequent heat treatment in the range 320-940^{o}C [48]. Analytical electron microscopy of these materials indicated that bismuth was always present at the ZnO interfaces. Despite this, the specimens that had undergone water quenching from 1000^{o}C and above did not exhibit varistor behaviour. Oxygen presumably played a very important role in barrier formation. It was thought that the concentration of oxygen atoms at the interface was not high enough to give rise to significant barriers in these specimens. Varistor behaviour was observed in specimens that had been quenched from 800^{o}C and below, suggesting that oxygen atoms had then accumulated at the interfaces. It was presumed by **Mahan** *et al* [51] that as the equilibrium concentration of oxygen vacancies decreases with decreasing temperature, the concentration of Zn vacancies increases. At temperatures below 900^{o}C concentration of Zn vacancies exceeds that of oxygen vacancies. This can provide an explanation for the absence of barriers in specimens that had been quenched from 1000^{o}C and above, and the presence of barriers below 800^{o}C. The temperature at which the equilibrium concentration of Zn vacancies exceeds that of oxygen vacancies lies somewhere in range of 940-1000^{o}C. Extrinsic defects such as Co are thought to change the temperature at which the concentration of oxygen vacancies equals that for Zn vacancies [48]. Moreover, the heat treatment presumably allows oxygen to accumulate at the ZnO interfaces by diffusion, since post-sintering heat treatments gave rise to varistor behaviour in specimens that had been previously quenched from the sintering temperature. Heat treatment at 230^{o}C for 1 h was found to be insufficient to obtain the necessary accumulation of oxygen, but heat treatment for 1 h. at 320^{o}C was sufficient [48].

Gee, and **Stewart**, [65], in 1990, studied commercial ZnO varistors, heat treated at 1200°C for different times up to 192 hours. Changes in the microstructure and the corresponding electrical behaviour were observed. Samples were examined by optical microscopy, scanning electron microscopy and transmission electron microscopy. Energy dispersive x-ray analysis was used for compositional analysis in both the SEM and TEM. Some samples were etched in perchloric acid prior to examining by X-ray powder diffraction XRD. The electrical measurements were made by clamping samples between copper plates, and measuring the current flow through the specimen as a known voltage (0-200V) was applied. The non-linear coefficient α was taken as the reciprocal of the slope of the curve of log V against log I, above the breakdown voltage. The untreated sample was porous with grain size of about 10μm., with two intergranular phases namely antimony oxide Sb_6O_{13} with high Bi content and the spinel $Zn_7Sb_2O_{12}$, containing Cr, Mn and Co. The grain size increased with the treatment time and was measured as 20μm after 192 hours of heat treatment. Samples heat-treated for 8.5 hours still displayed two phases but the antimony oxide had now been replaced by bismuth oxide containing some zinc. The non-linear coefficient α, was found to be in the range 7 to 15 for samples undergone heat treatment for less than 20 hours. After longer heat treatments the non-linear behaviour was essentially lost. For samples heat-treated for more than over 20 hours, bismuth was entirely removed by evaporation, leaving a structure of ZnO with rounded spinel particles. After 51 hours heat treatment the sample structure was of rounded spinel particles in ZnO matrix. From their studies of the grain boundaries of a sample treated for 5 hours, they observed spinel precipitates at triple points separated from each other by bismuth oxide. For the samples treated for 192 hours there was no sign of bismuth oxide and only rounded spinel particles were present, mostly at triple points. This study [65] confirmed that the electrical properties of the varistors are dependent on the structure and composition of the grain boundaries. The presence of bismuth at or near the grain boundaries seems to be essential to the electronic properties of the varistor. Thus the non-linear electrical properties, attributed to the formation of double Schottky barriers at the grain boundaries, disappears when bismuth is removed from the structure i.e., by prolonged heat-treatment.

Peigney *et al* [50] in 1992 studied Bi (1%)-Ti (0.4, 0.6, 0.8 and 1.0%)-doped ZnO, made of spherical grains (diameter between 1 and 10μm) prepared by a co-precipitation method. They had used dilatometry and scanning electron microscopy techniques to study the shrinkage and showed a correlation between the shape of the shrinkage curve and the microstructure of the ceramics. They found that a liquid phase sintering (LPS) process prevailed at all levels of Ti dopant but the marked effect of maximum shrinkage was observed only at 0.6% level of Ti and produced a maximum increase in grain size (100μm on average).

2.3.2.1. Summary of the microstructure of ZnO varistor

Following the discovery of ZnO based varistor in 1968, there has been much controversy over the interpretation of the microstructure, microscopic electrical behaviour, morphology and compositional variations of the grain boundaries. In this brief summary on studies of the microstructure and the morphology of grain boundaries, it is intended to draw some form of consensus.

Matsuoka *et al.*, in 1969 [7], attributed the non-linear I:V characteristics of ZnO based varistors to the presence of Bi and Mn at the grain boundary interface. This was realised at the time of the discovery of ZnO based varistor, when these elements supposedly diffused from the glass frit of an Ag paste electrodes into the ZnO ceramic [8]. It was found that the sintered ZnO without any additives did not exhibit any varistor behaviour and had α=1 (ohmic behaviour). Moreover, an addition of oxides of ionic radius smaller (BeO, MgO) than that of Zn also failed to produce any non-linear characteristics. From these initial solubility studies [7], addition of oxides of ionic radius larger (CaO, SrO, BaO) than that of Zn, resulted in segregation, forming a physical inter granular layer at the grain boundaries. Formation of an inter granular layer in this manner was presumed responsible for the observed non-linear behaviour (α>1). Contemporary experiments (1970) [9] studied the role of the additive oxides (Bi_2O_3, Sb_2O_3, Co_3O_4, Cr_2O_3, and MnO). Microstructural examination showed that the doping elements such as Bi, Sb and Cr segregates and presumably formed an intergranular layer of 1μm at the grain boundaries [9]. However, high resolution electron-microscopy studies by **Clark** [33] (1977), **Kingery** [34] (1979) and **Einzinger** [12] (1987), indicated that the majority of these ZnO-ZnO interfaces were found to be devoid of any intergranular layers. These findings not only questioned the proposed 1μm intergranular layer, they are also inconsistent with the work by **Morris** and **Wong** (1974) [25, 31], who described the over-all varistor microstructure as a three-dimensional series-parallel network of ZnO-PY junctions; pyrochlore (PY) phase was considered essential to give rise to the observed non-linear characteristics. More recent studies by **Olsson** *et al*, between 1985 and 1989 [30,39,46,49], **Inada**, [32] (1978) and the present author [75] indicate that the PY phase proposed by **Morris** and **Wong** does not usually dominate the microstructure, unless very slow cooling rates are used. In any case the PY phase is unfavourable as it gives rise to leakage currents at voltages well below threshold [30,39,46,49].

Although **Clark**, **Kingery** and **Einzinger** [12,38], (1982) identified that the majority of ZnO grains are not covered with 1μm intergranular layers, they also presumed ZnO GBs to be completely devoid of any physical intergranular layers. However, it has been shown that there are in fact very thin, perhaps less than 10nm, amorphous intergranular layers surrounding the majority of the ZnO grains [30,39,46,49] and that under specific

sintering conditions followed by subsequent heat treatment, a majority of the grain boundaries can in fact have a distinct amorphous phase (Bi rich) of around 10nm. **Gee** [65] *et al* showed that the non-linear electrical properties disappear when bismuth is removed from the structure i.e., by prolonged heat-treatment. The presence of bismuth at or near the grain boundaries seems to be essential to the electronic properties of the varistor. **Gambino** [42] *et al* (1986) showed that 1μm intergranular layers can in fact be a part of a lacy 3-D network which does not coat the entire grain. The extent of very thin (10nm) coating has been associated with the temperature dependent dihedral angles between the grains presumed responsible for the formation of such intergranular layers.

Microstructural analysis by **Inada**, [30,32] (1978) found that the doping additives such as Bi, Pr, and Sb segregate to the grain boundary region, forming compounds such as spinel **SP** ($Zn_7Sb_2O_{12}$) pyrochlore **PY** ($Zn_2\,Bi_3\,Sb_3O_{14}$) and bismuth oxide Bi_2O_3 **BI** (α, β, γ, δ). From these studies of the morphology of the grain boundaries and the phases, it was found that the formation of these phases largely depends on the sintering procedures. For example the rate of cooling from 1250°C sintering temperatures largely influences the SP/PY ratio, the crystal structure of the BI compounds and possible formation of PY types of phases [25,30,34,37,41,44].

Amidst this controversy over the microstructural morphology of the intergranular layers at the ZnO/ZnO grain boundaries, the following consensus is drawn:

1. Pure ZnO is a non-stoichiometric n-type semiconductor with a linear I:V behaviour [5,7]. To make it non-linear, additive oxides are incorporated in the ZnO. The main oxide being Bi_2O_3 (an alternative is Pr_2O_3 which will not be discussed here) which can be considered as a varistor former, without which it is difficult to make a varistor. Incorporation of these oxides causes atomic defects to form at the grain boundaries, with donor or donor-like defects dominating the depletion layer and acceptor and acceptor-like defects dominating the grain boundary states.

2. In the ZnO based varistor, grain boundaries are responsible for non-linear I:V characteristics. where the threshold voltage:

$$V_{th} \propto \frac{1}{grain\,size} \qquad (2.3\text{-}5)$$

3. The role of the additives in ZnO ceramics are as summarised in table 2.3.2 below.

Table 2.3-2 Roles of additives in ZnO varistors [6].

Role	Additives
Isolation among ZnO grains and supplying required elements to grain boundaries (O_2,Co,Mn,Zn, etc.)	Bi > Pr > Ba, Sr, Pb, U
Improvement of non-ohmic exponent -formation of interface states	Co, Mn > (Sb)
Improvement of stability	Sb, glass frit, Ag, B > Ni, Cr
Improvement of non-ohmic exponent in a high current region-formation of donors in ZnO	Al, Ga > F, Cr
Grain growth inhibition	Sb, Si
Grain growth promoter	Be > Ti > Sn

4. The basic compounds formed in the microstructure are ZnO, spinel ($Zn_7Sb_2O_{12}$) SP, pyrochlore (Zn_2, Bi_3 Sb_3O_{14}) PY, and several bismuth oxide (Bi_2O_3) Bi rich phases. The oxides (Bi_2O_3, Sb_2O_3, Co_3O_4, Cr_2O_3, MnO) are added in a concentration of 0.5 mol.% The location of the compounds are indicated in the Fig. 2.3.6 and Table 2.3.3 below. The highly non-linear electrical properties of the ZnO varistor depend upon the unique properties of the grain boundaries which are influenced by the crystal structure of the Bi phases (α,β,δ,γ) and the thermal stability of these phases in the microstructure [5].

5. Typical grain sizes in commercial varistors are between 10 and 20μm. The spinel and pyrochlore phases are known to exert a restraining influence on grain growth. During the sintering process various chemical elements are distributed in such a way in the microstructure that the near-grain boundary region becomes highly resistive ($\rho gb \approx 10^{12}$ Ω cm), and the grain interior becomes highly conductive ($\rho g \approx 1$ to 100 Ω cm) with a donor density of about 10^{17}-10^{19} cm^{-3} [52]. A sharp drop in resistivity from grain boundary to grain occurs within a distance of 50 to 100 nm, known as the depletion layer.

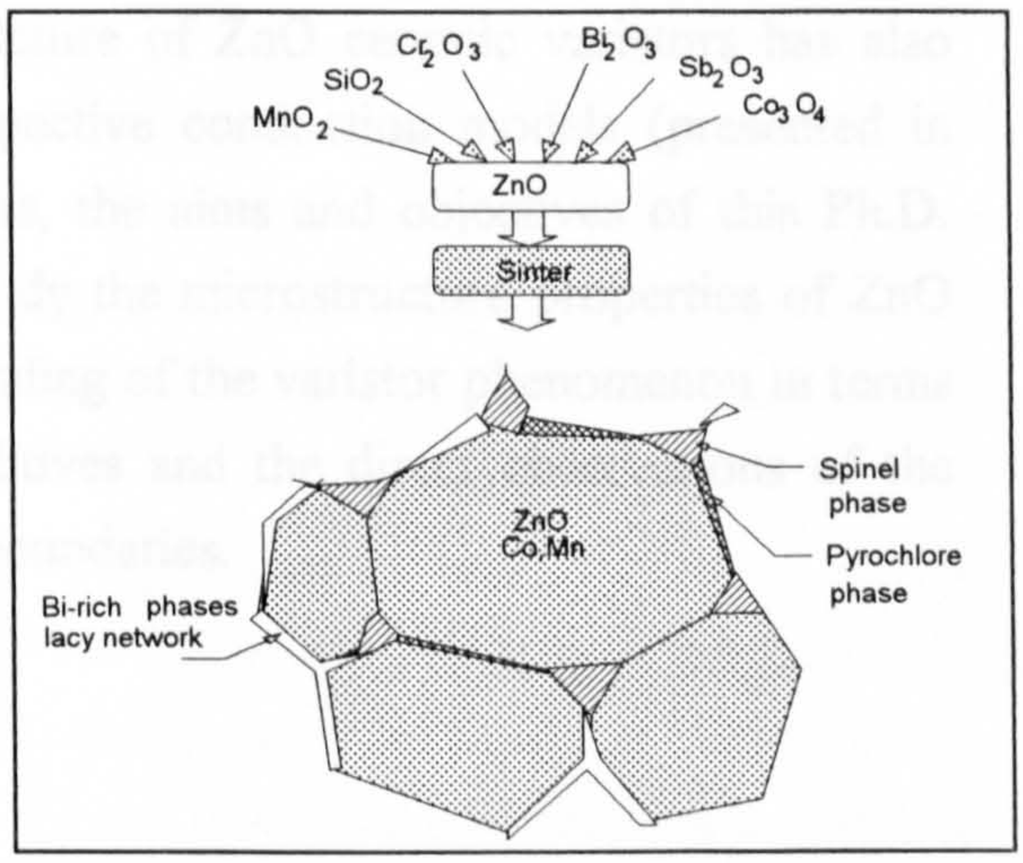


Fig. 2.3.6. Schematic showing the distribution of additives in the sintered sample of ZnO varistor.

Thus at each grain boundary, there exists a depletion layer on both sides of the grain boundary extending into the adjacent grains. The varistor action arises as a result of the presence of this depletion layer within the grains. It is a bulk property of the ceramic. The presence of two depletion layers on both sides of the grain boundary makes the ZnO varistor insensitive to polarity changes [5].

Table 2.3.3. Distribution of the additive components in the sintered ZnO ceramic doped with metal oxides of Bi, Sb, Co, Mn, and Cr [40,49].

Sintering Temp.^{o}C	Cooling rate ^{o}C/hour	Compound present	Location in microstructure
1250	200	ZnO	Grains
740-940	normal(200)	Zn_2, Bi_3 Sb_3O_{14}	Intergranular layer
1200-1300	normal (200)	$Zn_7Sb_2O_{12}$	Triple points
1200-1300		α-Bi_2O_3 [monoclnic]	Lacy network
1200-1300		β-Bi_2O_3 [Tetragonal_fcc]	Lacy network
1200-1300	Quench	Bi-rich phases δ-Bi_2O_3 [cubic fcc]	Lacy network
740	100-200	Bi-rich phases τ-Bi_2O_3 [bcc]	Lacy network
1200-1300	slow (15)	PY ⇑	Intergranular layer

The preceding interpretation of the microstructure of ZnO ceramic varistors has also resulted in a degree of anomalies in the respective conduction models (presented in section 2.4) as discussed in section 2.5. Thus, the aims and objectives of this Ph.D. project (as discussed in section 2.6) are to study the microstructure properties of ZnO ceramic varistors and to improve the understanding of the varistor phenomenon in terms of the compositional variation of dopant additives and the direct observations of the microscopic electrical behaviours at the grain boundaries.

2.4. Theoretical Models

2.4.1. Introduction

In ZnO based varistors, grain boundaries are responsible for the varistor effect. Theoretical models for the electronic ceramics need to address the unique properties of the grain boundaries. This includes the structure of the grain boundaries, segregation effects, depletion space charge layers at the grain boundaries, high-field transport across the grain boundary and transport along the grain boundaries. **Waser** [74] 1993, has given a review of the role of the grain boundaries in electronic ceramics. In this section a review of the conduction models are presented. Since the discovery of non-ohmic properties of ZnO ceramics, there have been many papers on the nonohmic conduction mechanisms [4,6,9,12,23,24,37,55,56,59,60,62,63]. An ideal varistor model would allow us to correlate the total input of all the results acquired from different analytical techniques and yield a unified understanding of the varistor mechanism. The model for the varistor should explain the nonohmic I:V curve, its temperature dependence, the effect of additives, dielectric properties, bias voltage dependence of capacitance, transient conduction phenomena and degradation of the I:V curve [56]. The model should also be consistent with the physical and chemical properties of the ZnO varistor [5]. A complete theory of the varistor phenomenon can be a useful guide for quality control from the production point of view and the theoretical understanding can also be applied to predict the behaviour of many advanced ceramic materials. A summary of the progress of the varistor conduction mechanism is given in table 2.4.1

2.4.2. Space Charge Limited Current (SCLC)

A conduction model proposed by **Matsuoka** [9] in 1971 was perhaps the very first model for the ZnO based varistors. The theme of this model is a Space-Charge-Limited-Current (SCLC) process associated with deep traps situated at an intergranular layer of the ZnO ceramic (1μm wide Bi_2O_3-rich layer).

The **SCLC** results from carriers injected into the insulator, where there is no charge compensation present and the current is considerably affected by carrier mobility. An intergranular layer of about 1μm in this case, is analogous to an insulator. When a high electric field is applied to this region in contact with two adjacent conducting grains, it is possible to inject electrons into the conduction band of the material and generate a current (Fig 2.4.1).

The crystal is then said to be supporting current flow as a "conducting insulator", quite analogous to the vacuum in an electron tube which freely allows electrons to pass through it. The extreme non-linearity of the varistor I:V characteristic curve is

represented by Child's law for solids ($J \alpha V^2$) and a traps-filled-limit curve (Fig.2.4.2) which has a voltage threshold and an enormously steep current rise [64]. Varistor characteristics have been explained in terms of traps originated from the supposed (1μm) segregation layer.

The trap density Nt and density of the trapped electrons nt are the important parameters considered [64]. For example, when the segregation layer has a trap density, Nt, the density of trapped electrons nt can be expressed as follows:

$$nt = Nt/(1+1/g \exp (Et-Fn/kT)) \quad (2.4\text{-}1)$$

where Et is trap level; Fn, Fermi level; and g, a degeneration factor for traps which is nearly 2 [64].

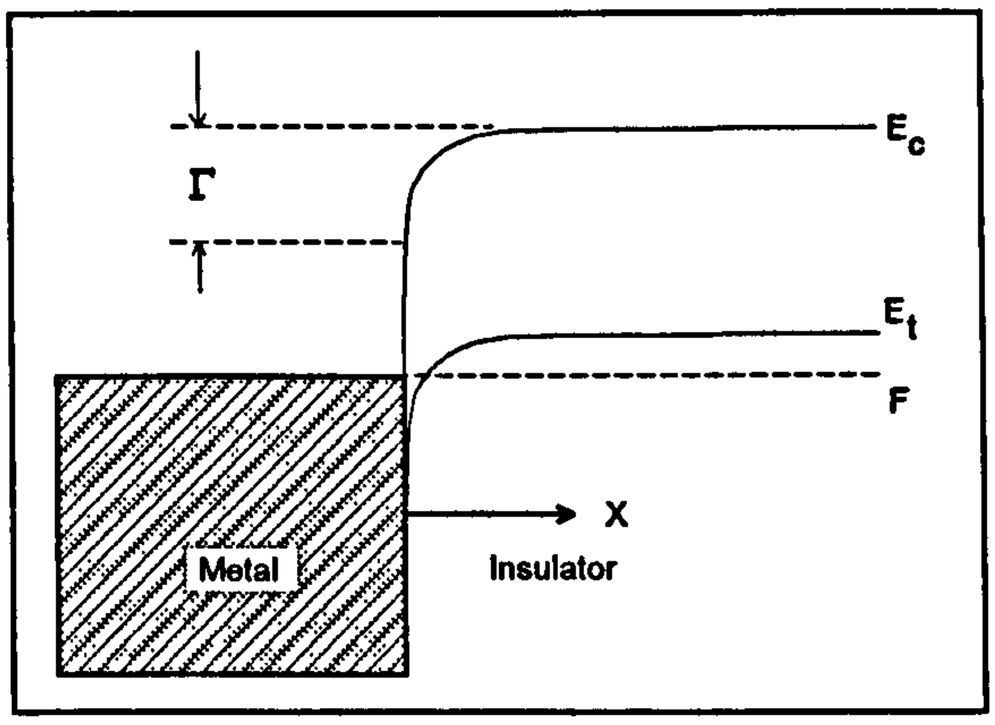


Fig. 2.4.1. Simplified energy-band diagram for an injecting contact between an insulator and a metal. The contact is in thermal and electrical equilibrium. F is the thermodynamic Fermi level, Et a single, discrete trap level, and Ec the bottom level of the conduction band. Et and Ec are functions of the position *x*. The amount Γ of downward-bending of the bands at the contact is given by the difference of the work functions of the insulator and metal :$\Gamma = \phi I - \phi M$ [64].

Acceptors and traps are presumed to influence SCLC by decreasing the electron mobility. On this basis the resultant, abrupt decrease of electron mobility at breakdown voltage (Vb) in the varistor causes a steep decrease in the grain boundary resistance and gives rise to the varistor behaviour.

On the basis of SCLC theory of this model, Matsuoka presumed the conduction mechanism to be attributed to the electron mobility with a break down field of 10^4 V/cm, rather than the potential barrier heights as proposed in many subsequent models based on double schottky barriers (DSB).

Although large values of α can be achieved at the trap-filled-limit voltage, V_{TFL}, this voltage is proportional to the trap density in the intergranular material. Hence V_{TFL} would be expected to be highly variable upon altering varistor composition or processing. However this analogy is inconsistent with experimental observation, where it is found that these variables do not extensively influence the I:V characteristics. Moreover this model fails to explain other experimental results, such as the small temperature dependence of the I:V curve in the highly non-linear region. Also the obvious lack of massive intergranular non-zinc oxide layers as varistor active zones, makes this model unreliable [51].

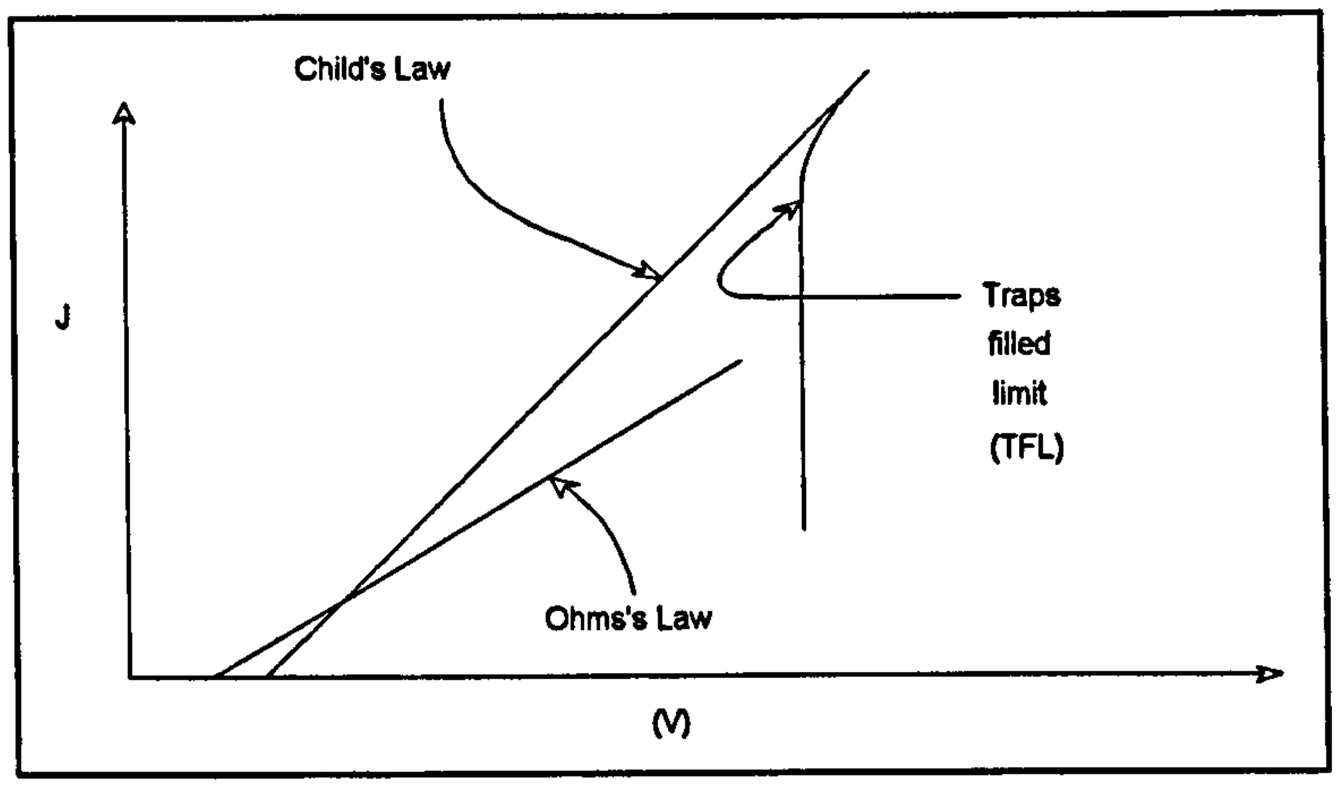


Fig. 2.4.2. Log-log plot of limiting current density (J) versus voltage (V) characteristics for Space-Charge-Limited current in an insulator with traps [64].

2.4.3. Models based on Tunnelling

2.4.3.1. "Tunnelling Through A Thin Layer At The Grain Boundary"

The second model was proposed by **Levinson** and **Philipp** [62] in 1975. This model is based upon tunnelling through a thin layer (~100 Å) at the grain boundaries of the ZnO ceramic. An idealised microstructure (Fig. 2.4.3) was presumed, with an average grain size, d, of conducting ZnO, completely surrounded by an insulating oxide of thickness t. This model is derived from experimental results associated with the I:V curve and its temperature dependence. The varistor studied here had a mean grain size of ≈ 25μ m, and a breakdown voltage Vg = 2.5 V per barrier, estimated from the breakdown field of about 1000 V/cm, with a high non-linearity α of 30 - 50. Current-Voltage characteristics at different temperatures were measured. Measurements of the dielectric properties as a function of frequency were undertaken. I:V measurements were made using a pulse technique to avoid heating at high current levels. Varistor characteristics in the breakdown region were found to be temperature insensitive, whilst temperature dependent behaviour was observed in the pre-breakdown region. Intergranular layers of

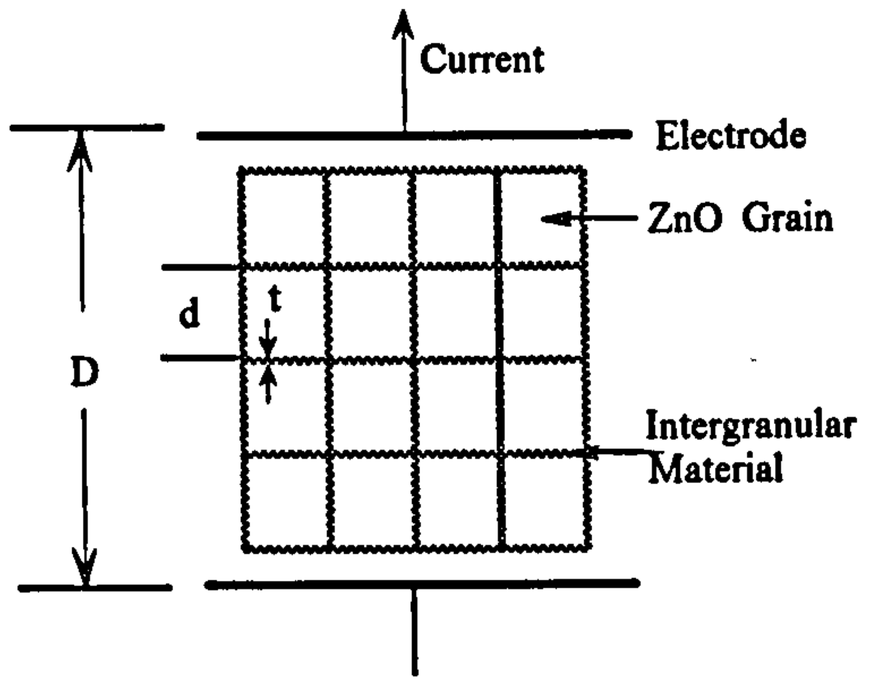


Fig. 2.4.3. Idealised microstructure of a metal oxide varistor, having grain size d and intergranular barriers thickness t. D is the electrode separation (not to scale) [62].

the order of ~100 Å in thickness were estimated from the capacitance data and the dielectric properties of the grains and insulating layers. Based on these observations and the above microstructure, with the intergranular layer of ~100 Å, a grain - to - grain field of F~10^6 V/cm had been estimated. In this model the conduction mechanism dominant in the pre-breakdown or linear region of the I:V characteristics has been explained in terms of thermionic emission over the field-lowered potential barrier (Fig.2.4.4). In this case the applicable relation between the current density J and field F is:

$$J = J1 \exp [-(Ei - ß \sqrt{F})/kT] \qquad (2.4.2)$$

Where ß depends upon the true dielectric constant of the intergranular layer material. J1 is constant, and F is the field in the intergranular layer.

The conduction mechanism at the breakdown region (the non-linear I:V characteristics) has been explained in terms of the tunnelling process obeying a current - density - vs - field relation given by:

$$J \propto \exp (- \tau/F), \text{ where } \tau \text{ is a constant.} \qquad (2.4.3)$$

At the breakdown region, this process is dominant where the field F, is so high that electrons can tunnel through the narrowed potential hill into the conduction band. The model energy-level diagrams (Fig.2.4.4) show the schematic depiction of the escape of an electron from the ZnO conduction band into the conduction band of the intergranular material.

Hence, process (I) Schottky (Poole-Frenkel) emission and process (II) tunnelling are the proposed mechanisms to represent the ohmic and nonohmic regions of the I:V characteristics respectively.
This model based on tunnelling [27] accounts for the general insensitivity of the varistor breakdown characteristic to varistor composition and processing, and gives the correct negative temperature coefficient of varistor breakdown voltage.

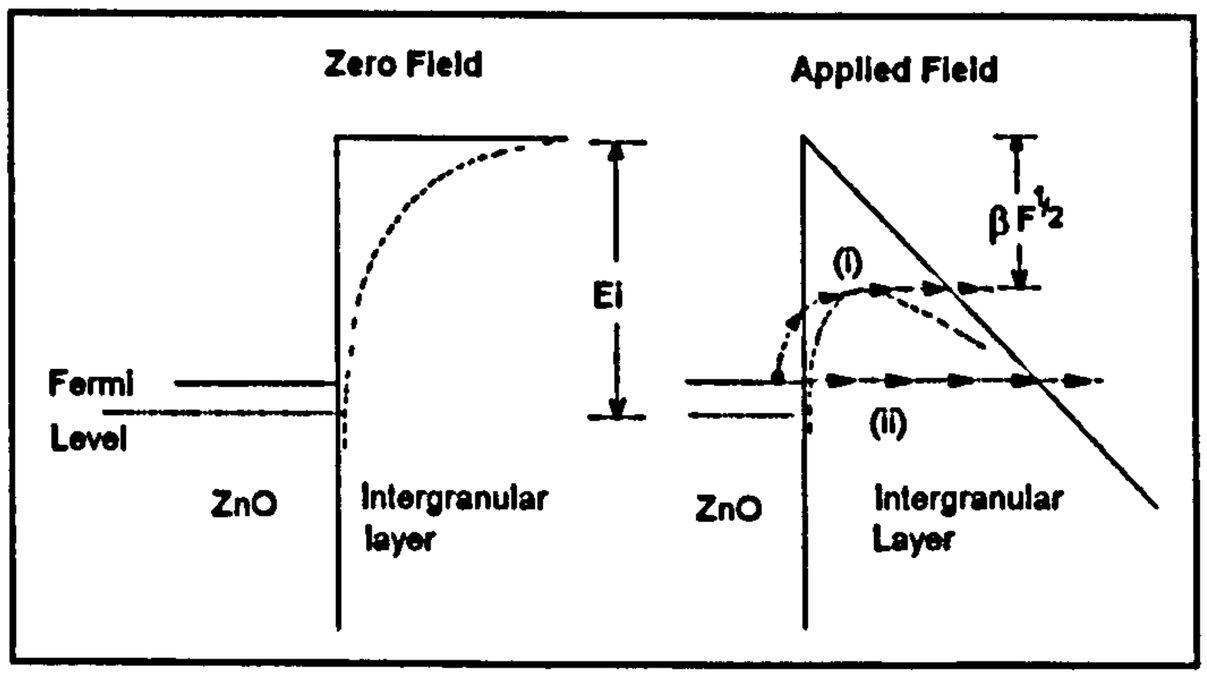


Fig. 2.4.4. Schematic depiction of the escape of an electron from the ZnO conduction band into the conduction band of the intergranular material. Process (i) is Schottky emission. Process (ii) is tunnelling. Process (i) occurs at intermediate temperatures and moderate fields (pre-breakdown region). Here, electron escape proceeds by thermal activation over a field-lowered barrier. At high fields [case (ii)] quantum-mechanical tunnelling occurs as shown. This is the mechanism giving rise to varistor action [62].

However this simple tunnelling model remains inadequate to explain α values in the 50-100 range. This model based on tunnelling through a thin intergranular layer region leads to maximum values of $\alpha \sim 30$ at a current density of 10^{-3} A/cm^2 [51]. Moreover, the theme of this model remains incomplete in its explanation of certain experimental results, such as the effect of additives and the asymmetrical degradation of the I:V curve.

2.4.3.2. Tunnelling Through Schottky Barriers Caused By Interface States

In this third case there are *two* types of models proposed. In the *first* instance, models proposed by **Levine** [76] (1975) and **Morris** [77] (1976), did not take into consideration the heterojunctions composed of ZnO and the Bi_2O_3 -rich intergranular layer. **Hower-Gupta** [60] (1979) presented a modified version of Levine's model, with the major difference being the inclusion of a thin ($\cong$ 10 Å) disordered layer which separates the single-crystal ZnO grains (Fig.2.4.5). They had assumed type **B** structure [46] (ZnO/ZnO without any physical intergranular layers) to be essential in order to exhibit high non-ohmic properties in the varistor. In the *second* instance, models proposed by **Emtage** [59] (1977) and **Eda** [56] (1978), gave due consideration to heterojunctions present in the ceramic microstructure.

Levine [76] (1975) in his model presumed that the addition of additives lead to formation of double Schottky barriers (DSB) at the grain boundaries in ZnO, and gives rise to the non-linear I:V behaviour [66]. Moreover, he speculated that the double-sided depletion layer at the grain boundary, and behaviour in the "breakdown" region was analogous to the reverse I:V characteristics of metal-semiconductor diodes, where the increase in current would be due to a decrease in the barrier height ϕ_B resulting from a finite density of surface states.

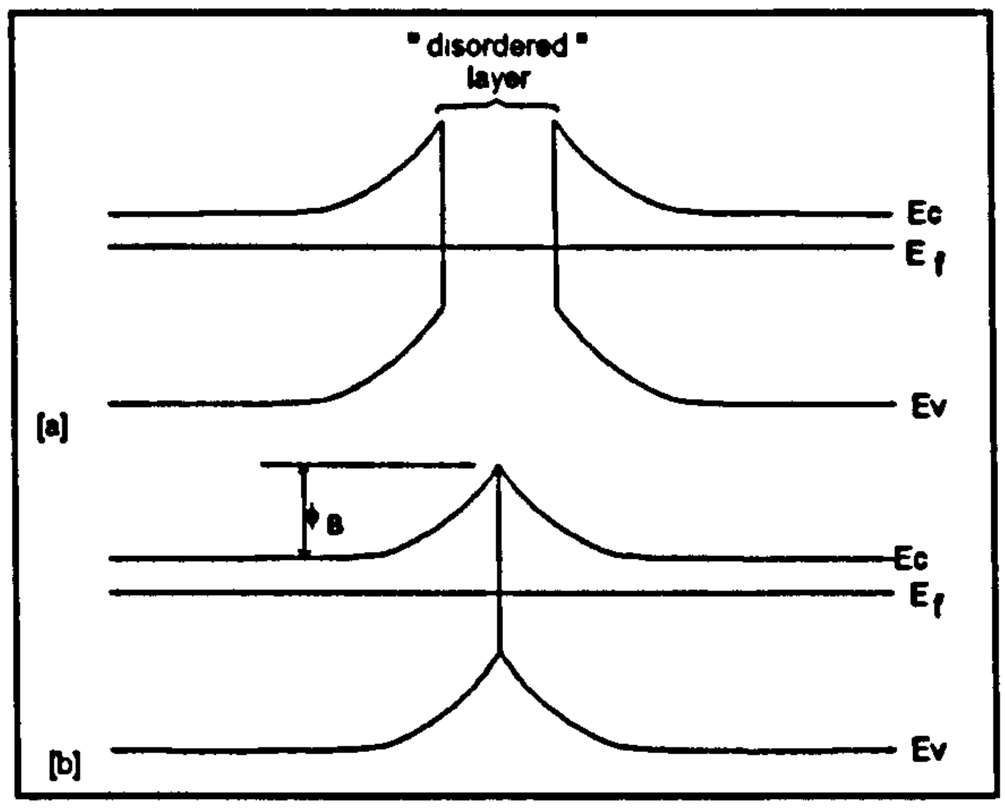


Fig. 2.4.5. Grain-boundary band diagram [a] for proposed model and [b] after Levine [60].

Bernasconi *et al.*, [79] (1977) and **Ematage** [59] noted that the barrier model of Levine couldn't explain the varistors non-linear exponent α values greater then 25, in the breakdown region.

The work by **Hower** and **Gupta** [60] was based on the calculation of I:V characteristics for different surface-state density $N_S(E)$ profiles. They had extracted the surface-state density $N_S(E)$ and doping profiles from C-V and I-V data.

The theme of this modified version of the Levine's model explains the maximum α being approximately proportional to the grain voltage. These models are suitable for the explanation of the nonohmic I:V curve, its temperature dependence, and effect of additives. The proposed model was consistent with electrical and microstructural observations and account for α's in excess of 60. However the other limitations still remained.

The *second* type of model in this case, "Tunnelling Through Schottky Barriers Caused By Interface States", as proposed by **Emtage** [59] in 1977 and **Eda** [56] (1978), took into consideration the heterojunctions. **Eda** [56] estimated the thickness of an intergranular layer (insulator) to be less then 500 Å (Fig. 2.4.6).

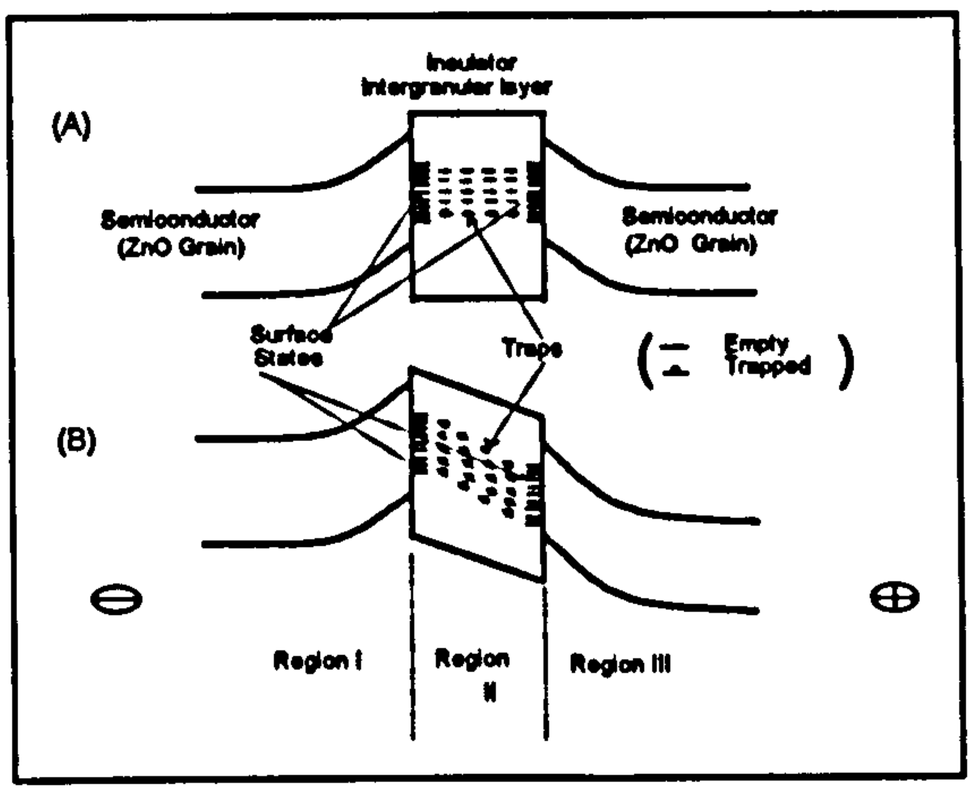


Fig. 2.4.6. SIS- type energy-band model for non-ohmic ZnO ceramics. (A) unbiased and (B) biased [56].

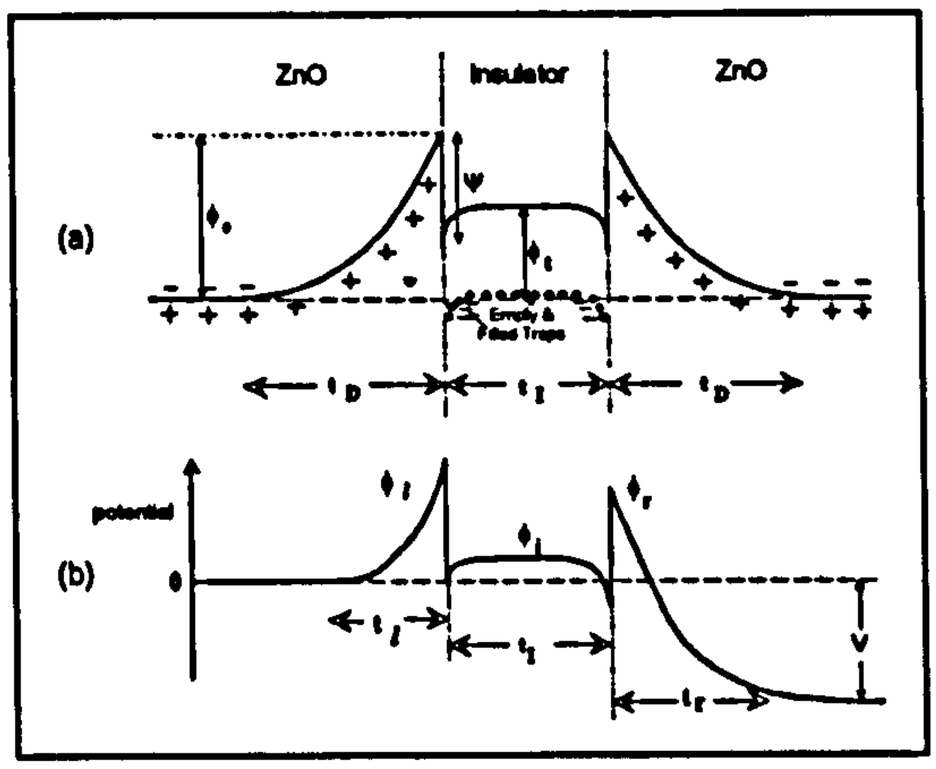


Fig. 2.4.7. Schematics of the depletion layers in the ZnO and the region of trap filling in the insulator; (a) without and (b) with an applied voltage V [59].

Emtage [59] in his work, considered 900 Å as a mean insulator thickness and 400 Å at the thinnest regions of the intergranular layers (Fig. 2.4.7). A thin intergranular layer with traps, sandwiched between Schottky barriers formed opposite each other has been proposed (Figs.2.4.6 and 2.4.7).

The microstructure was composed of 10 to 30 μm grains. I:V characteristics were measured using dc power supply in a current range up to 100 mA. The frequency dependence of capacitance and dielectric loss (tanδ), were measured using a capacitance bridge. Thermally stimulated current and the Varistor I:V characteristics were also observed. The ZnO varistor sample contained the oxides of Bi, Sb, Mn, Cr, and Co.

An energy-band model was considered, for each of the experimental results mentioned above. From the bias-voltage dependence of capacitance, the interface barriers were deduced to be Schottky type barriers. The asymmetrical degradation of the I:V curve (Fig.2.4.8) [56] caused by dc biasing, indicated that there were two rectifying barriers faced opposite one another. These were presumed to be Schottky barriers at each side of the intergranular layer.

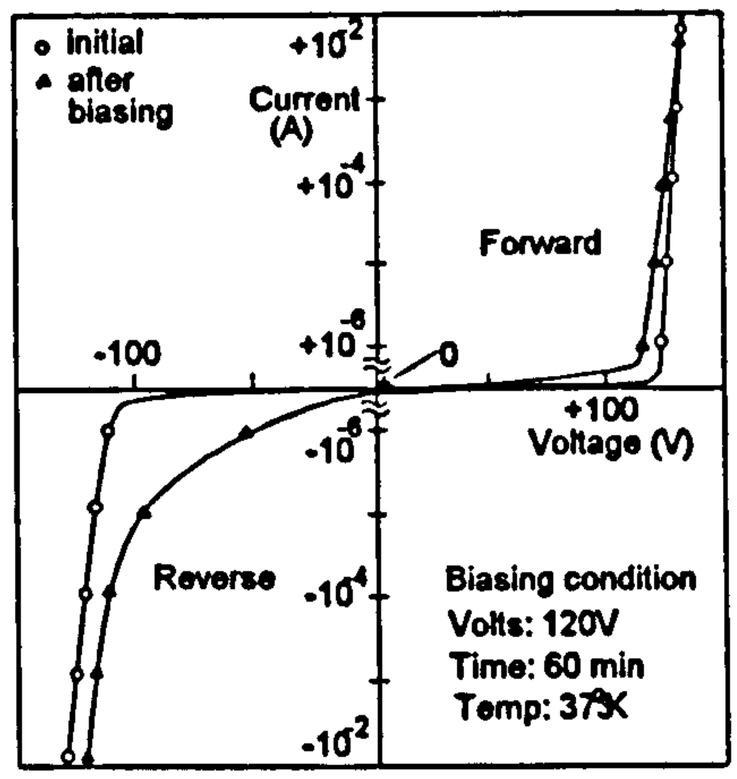


Fig. 2.4.8. Asymmetrical degradation of the I:V curve of non-Ohmic ZnO ceramic caused by dc biasing [56].

From these results, a structure composed of semiconductor insulator-semiconductor (SIS) was presumed (Fig.2.4.6). This structure (less then 500 Å) was presumably composed of an intergranular layer sandwiched between the Schottky barriers formed at the surface of n-type ZnO grains. From the experimental results of the thermally stimulated current, the presence of traps in the insulator was speculated. Moreover it was presumed that the Schottky barriers are attributed to the surface states caused by the additives, hence accounting for the effect of additives that influence the non-ohmic properties of ZnO ceramics. The resistivity of the ZnO grains and the donor concentration was estimated to be 0.2-0.5 Ω cm and (1.35-3.5) $X10^{17}$ cm^{-3} respectively. The threshold voltage Vth per grain boundary was estimated to be about 2.3 V.

From these considerations, a conduction mechanism as shown in Fig.2.4.6 (b), based on the forward-biased Schottky barrier was proposed. This was based on thermionic emission from the conduction band of a semiconductor to a conduction band of an insulator. In the region (I), the presence of surface states at the interface between the semiconductor and the insulator, raised possibility for the electrons to tunnel from the conduction band of the semiconductor to the surface states at the interface by a process such as the thermally assisted field emission or the field emission as discussed for a metal-semiconductor contact. For region II, mechanisms such as Frenkel-Poole emission, (ii) tunnelling, (iii) thermally activated hopping, and (iv) SCLC were proposed.

In this study [56] the samples doped with varied concentrations of MnO showed a strong influence on the non-Ohmic properties of a varistor. Addition of MnO led to an increase in the Schottky-barrier height and the non-Ohmic properties. From these observation it was presumed that the Schottky barriers played a dominant role in the conduction phenomena. MnO was presumed to form surface states or traps at the grain boundaries leading to an increase in the height of the Schottky

barrier increased due to the trapping of electrons in this manner. The varistor degradation was explained on the basis of the asymmetrical degradation of the I:V curve as a result of dc biasing. This also resulted in an increase of current in the reverse direction for bias voltage. The degradation phenomenon has been further explained in terms of a possible damage, by dc biasing, to one of the rectifying barriers facing opposite each other. The bias-voltage dependence of the capacitance was also affected by dc biasing. These results suggested that the degradation of the I:V curve is caused by the change of the Shottky - barrier height (Fig.2.4.9).

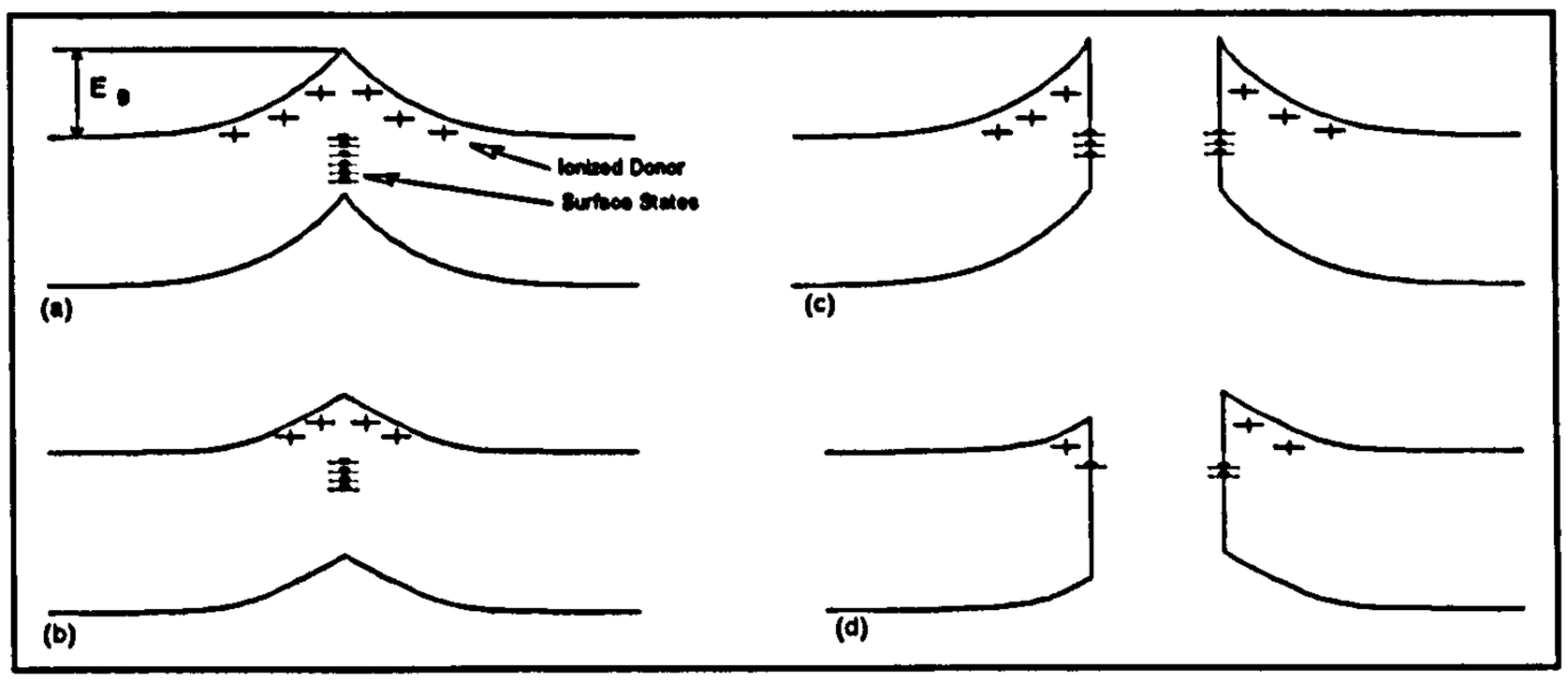


Fig. 2.4.9. Deformation of Schottky barriers due to the change of space charges. (a) Initial state of the Schottky barriers in the unseparated case. (b) Deformed Schottky barriers caused by dc biasing in the unseparated case. (c) Initial state of Schottky barrier in the separated case. (d) Deformed Schottky barriers caused by dc biasing in the separated case [56].

A thermally stimulated current (TSC) was observed for samples degraded by dc biasing. A close connection between the observed TSC and the degree of degradation was obtained. The origin of the deformation of the Schottky barriers was attributed to the non-uniform distribution of the space charges. The asymmetrical deformation of the Schottky barriers would require these barriers to be separated by an intergranular layer of finite distance. If the size of an intergranular layer is infinitely thin or zero, both of the Schottky barriers opposite one another change to the same degree, due to the change of the space charges at the grain boundary (Fig. 2.4.9). A large asymmetrical deformation was observed in the case of the Schottky barriers separated by thick intergranular regions.

This model [56,59] appears to explain many aspects of the experimental parameters of the ZnO varistor. This includes, the nonohmic I:V curve, its temperature dependence, dielectric properties, bias-voltage dependence of capacitance, microstructure, and asymmetrical degradation of the I:V curve.

2.4.3.3. Hole-assisted tunnelling through Schottky barriers.

The fourth model was proposed in 1979, by **Mahan, Levinson,** and **Phillip** [52]. The model was based on "tunnelling through Schottky barriers with hole creations" [51]. This model demonstrates the importance of minority carriers (holes) at the grain boundaries. The ceramic microstructure includes an interface layer of an oxide other than ZnO, of an uncertain thickness of between 10 and 100Å (Fig.2.4.10) .

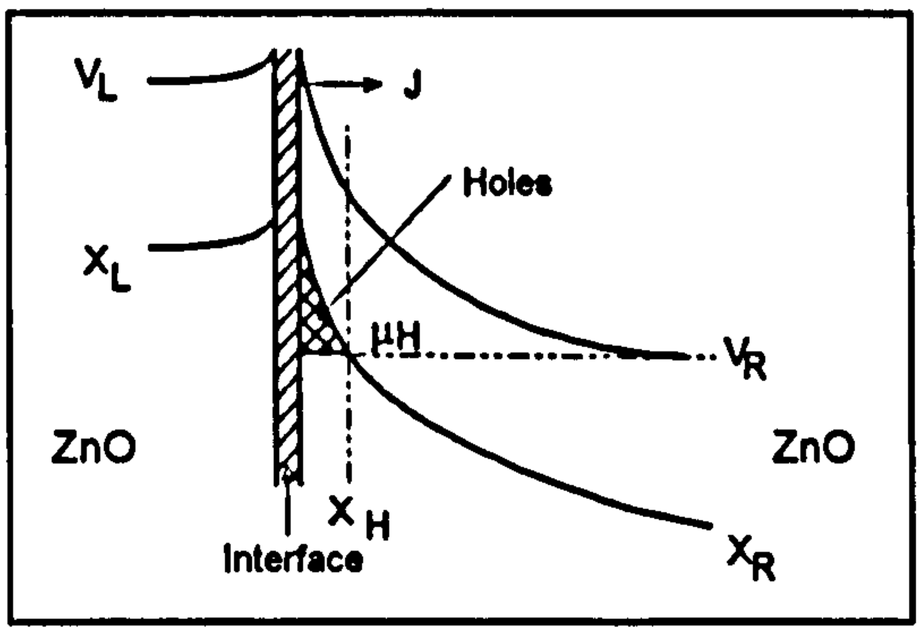


Fig. 2.4.10. The hole model. The holes are created on the forward side of the junction whenever the hole's chemical potential (μH) is below the valence band edge. The electron tunnelling from the interface is indicated by the arrow labelled J. (X_H is the maximum extent of the injected holes) [52].

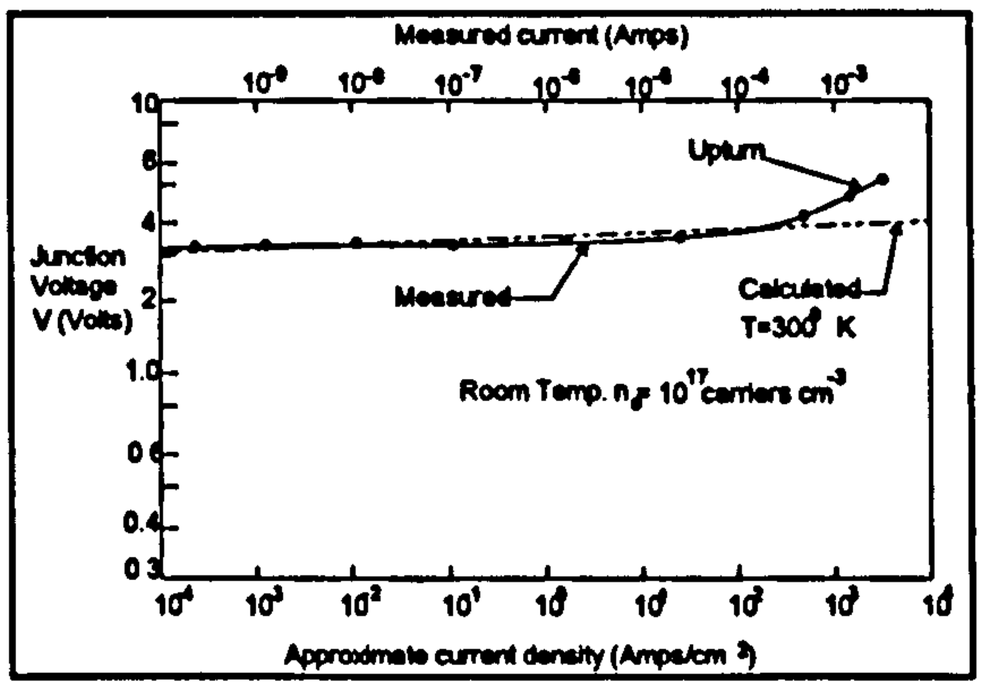


Fig. 2.4.11. Experimental and calculated current - voltage characteristics of a single ZnO varistor grain junction. The observed decrease in non-linearity at high current densities is due to the series resistance of the ZnO grains. This has not been included in the calculation [4,52].

The interface is negatively charged by electrons, which can reach the conduction bands by tunnelling. At an applied voltage that equals or exceeds the ZnO band gap of 3.2 eV, holes are created by interband excitation. The hole population assembles next to the interface and its recombination rate is presumed to be small. The crucial effect is that the additional positive charge of the holes squeezes the potential barrier making it steeper, which shortens the tunnelling distance for electrons in the interface layer. The enhanced tunnelling probability diminishes the negative interface charge, thus the barrier itself vanishes and current flow starts.

The theory of this model was comparable with the experimental findings [4], as shown in Fig. 2.4.11. However it is to be noted that this model has limited predictive value in that it does not consider (much less clarify) the role of the individual chemical additives.

2.4.3.4. Tunnelling through homojunctions

The fifth model based on "tunnelling through homojunctions of ZnO" was proposed by **Einzinger** [12] in 1978. This model is based on band-band tunnelling in ZnO homojunction with the introduction of an α value enhancement effect. The band diagram is shown in Fig. 2.4.12. The shape of the potential barrier is different from any of the models discussed up to this point and additionally in this case, there are no dominant interface states .

The band bending is caused by a drop of the ionised donor concentration towards the boundary as expected for a n-i semiconductor diode and a series connection of two such diodes. High α values are presumed to be caused by an applied voltage-dependent shortening of the tunnel distance. This is shown in Fig. 2.4.12 (a), in which the hole conductivity generated by the tunnel effect is shown to lower the resistivity in a part of the barrier zone, thus concentrating the electric field in a thinned region of pronounced tunnel current flow. The arrow labelled Jr in Fig. 2.4.12 (b), indicates an electron-hole recombination process. The model highlights the importance of the thermal equilibrium of defects formed during cooling at the grain boundaries. A value of the coefficient of non-linearity (α) up to 60, have been reported for this model.

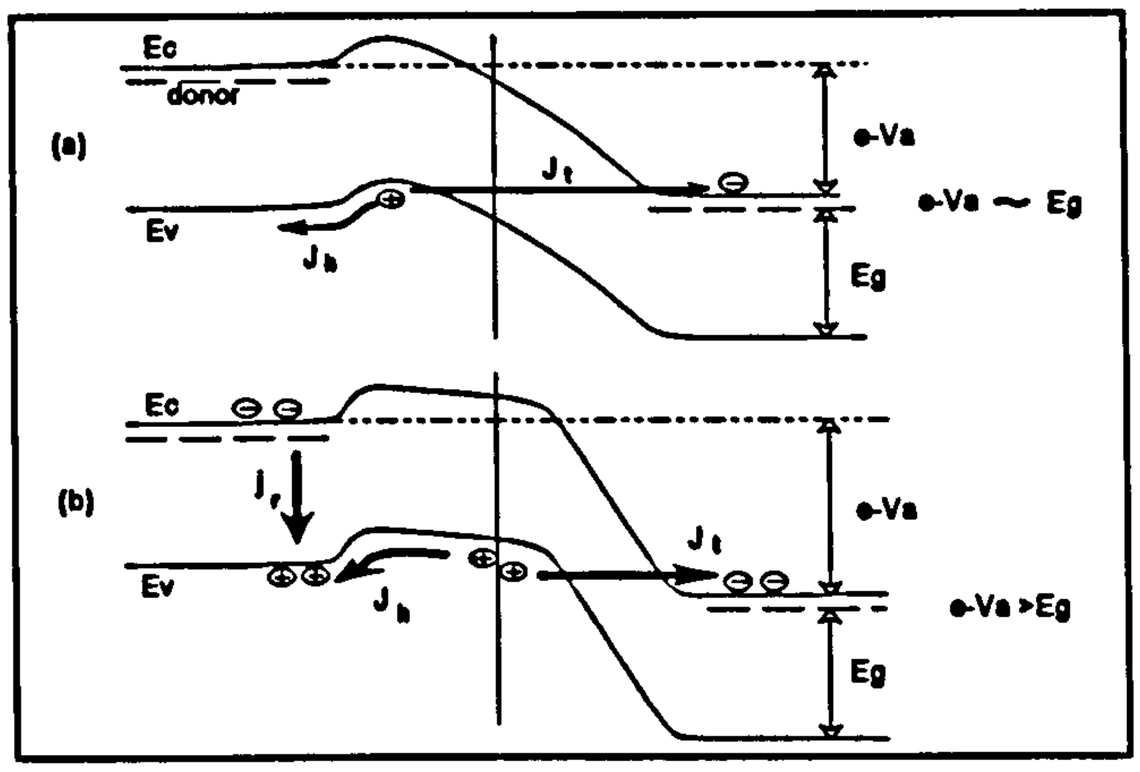


Fig. 2.4.12. (a) Band-band tunnelling in ZnO homojunction. Tunnel current Jt sets in when the bias voltage is approximately equal to the gap voltage, 3.2V Jh = hole current. (b) Enhancement effect on Jt by reduction of tunnel distance. Jr is the electron-hole recombination process [12].

2.4.4. The Hole-induced breakdown model

The sixth model "The Hole-induced breakdown model", was initially proposed by **Pike** *et al.*, [55,61] in 1984, and subsequently updated by **Blatter** and **Greuter** in 1986 [23,24]. The model is based upon the formation of Double Schottky Barriers at the grain boundary interface. The energy band diagram proposed by **Blatter** and **Greuter** is shown in Fig. 2.4.13. These Double Schottky Barrier (DSB) barriers are presumed to derive from traps and states at the grain-boundaries induced by additive elements such as Bi, Co, Pr, Mn, etc., [4] and are situated at the region of the boundaries of essentially zero width [53]. At this interfaces, electronic states are negatively charged, free electrons are depleted in a certain range on both sides of the interface, thus uncovering

the positive charges of the immobile, ionised donors. As a negative charge ϕI, is trapped at this interface, the bands of the n-type semiconductor ZnO bend upwards and form a potential barrier ϕB, which controls the current flow through the material. As a theme of this model, the high non-ohmic property is caused by lowering of the potential barrier at the grain boundaries due to hole accumulation.

The potential barriers depend both on the interface states and on the bulk traps. The holes are created by accelerated electrons in the depletion region. **Mahan** *et al.*, [52,14] proposed that the extreme current non-linearity in the breakdown region results from minority carrier creation in the Schottky barrier region of the ZnO semiconductor. They proposed that the holes are formed as a result of impact ionisation and creation of electron hole pairs by energetic electrons surmounting these barriers. This requires band gap radiation to be emitted.

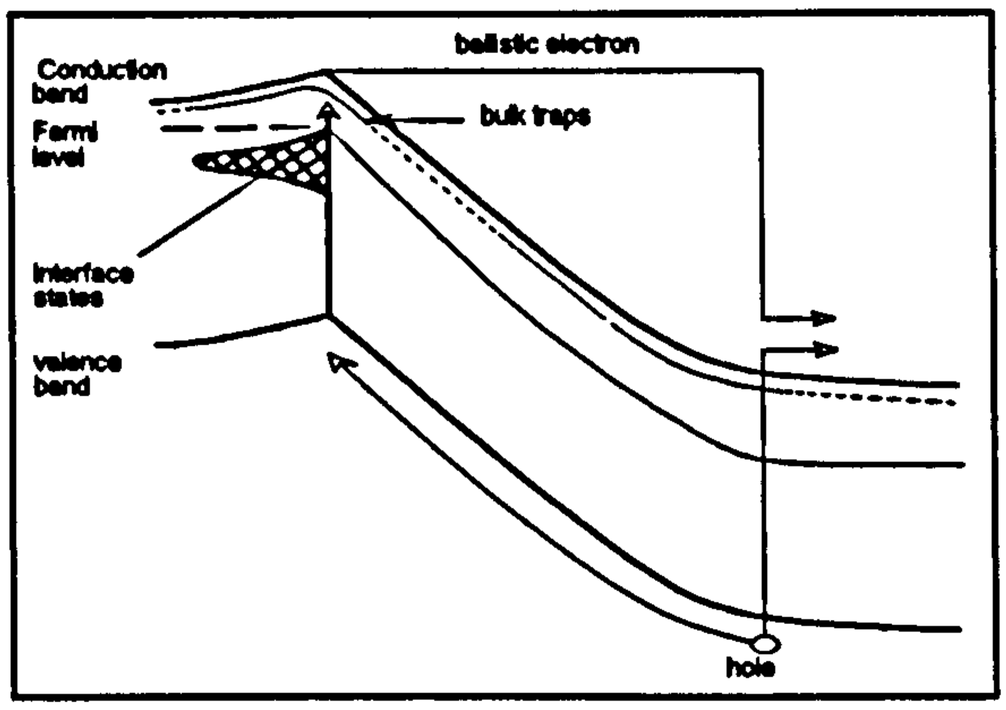


Fig. 2.4.13. Energy band diagram proposed by Blatter and Greutter. Double Schottky barriers are formed by interface states and traps. The breakdown is caused by hole accumulation at the grain boundary. The holes are generated by impact ionisation in the depletion region [23,24].

This hypothesis of hole creation as the origin of the highly non-linear conduction in ZnO varistors was subsequently verified by **Pike** *et al.*, [55] (1985) who have observed electroluminescence ~ 3.3 eV band gap. This luminescent intensity increased with the non-linearity of the varistor and was found to be proportional to the square of the varistor current, which is consistent with a model of hole creation by impact ionisation near ZnO grain boundaries [4].

Recently **Blatter** and **Greuter** [23,24] used, Deep Level Transient Spectroscopy (DLTS) and admittance spectroscopy to study this model. Various parameters such as the conductance (G) and the capacitance (C) were studied as a function of frequency (w), voltage (V) and temperature (T). These measurements provided information on the density of interface states, their trapping cross section, and the relaxation time. The Hole Induced Breakdown Model has been consistent with the highly non-ohmic (I:V) property, the high α values, the interface state and the bulk trap effects.

2.4.5. Grain boundary defect model

This seventh model is the grain boundary defect model proposed by **Gupta** *et al.*, [37] in 1985. The model was intended to explain the phenomena of voltage instability / stability of the ZnO varistor. The key element of this model are the zinc interstitial present in the

depletion layer as excess zinc arising from the non-stoichiometric nature of ZnO, that arises during the fabrication of the varistor. Both instability and stability of the varistor has been described in terms of field assisted diffusion of these interstitial in the depletion layer, followed by chemical interaction with defects at the grain boundary interface (Fig. 2.4.14).

The basic concept of this model was that the depletion layer comprising the barrier consists of two components: a stable component of spatially fixed positively charged ions and a metastable component consisting of mobile positively charged zinc interstitial. In the stable component, ions are trivalent substitutional ions, the donor ions, $D^{\bullet}_{Zn}$ (D = Bi, Sb, etc.) and the native oxygen vacancies $V_O^{\bullet}$ $V_{O2}^{\bullet\bullet}$.

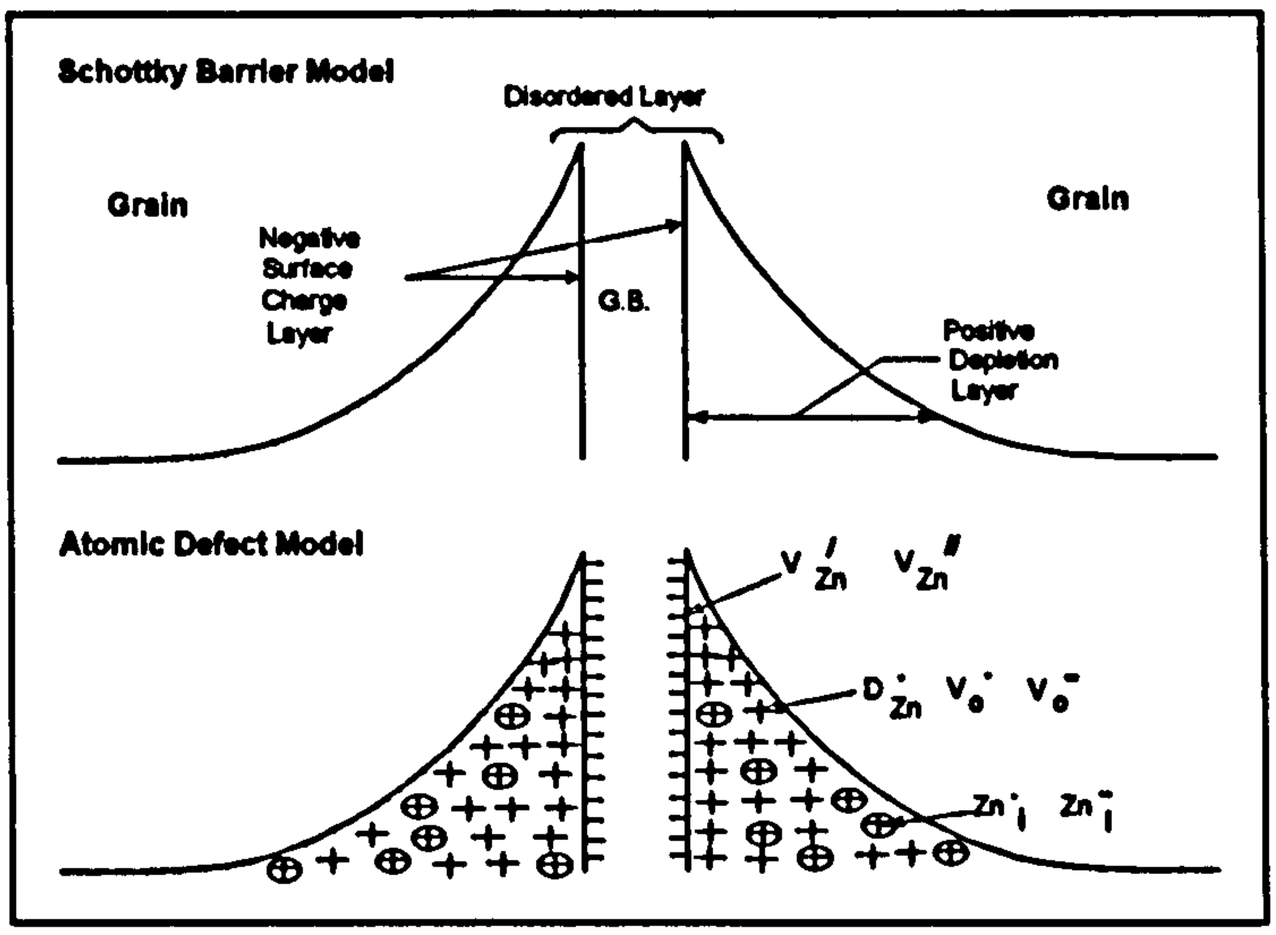


Fig. 2.4.14. The proposed atomic defect model for Schottky barrier at the grain boundary. Analogy with band model is also shown [37].

In the metastable component
ions are the singly and doubly charged native zinc interstitial $Zn_i^{\bullet}$, $Zn_i^{\bullet\bullet}$. Previous studies [28] by **Sukkar** and **Tuller** have assigned $V_O^{\bullet}$ and $V_{O2}^{\bullet\bullet}$donor levels at 0.5 and ~ 2eV below the conduction band and $Zn_i^{\bullet}$, and $Zn_i^{\bullet\bullet}$donor levels at 0.05 and 0.2eV below the conduction band edge. These positively charged ions extend from both sides of the grain boundary into the adjacent grains and are compensated by a layer of negatively charged ions at the grain-boundary interface, comprised primarily of native zinc vacancies, V'_{Zn} and V''_{Zn} whose acceptor levels have been assigned [28] at 0.7 and ~ 2.8 eV respectively, above the valence band edge.

Gupta *et al.*, [37] from their studies of the electrical stressing of ZnO based varistors, presumed that both the electric field and the elevated test temperature provide the necessary driving force for the interstitial migration in the depletion layer. This consequently has a significant effect on the stability of the barrier height and barrier voltage.

The model predicts that in an unstable device the barrier height should decrease continuously with time upon stressing. Moreover if the zinc interstitial in the depletion layer comprising the metastable component of the barrier are responsible for the instability of the device, then the removal of the metastable component should restore

stability. Stability of the device can be restored by heating in an oxidising atmosphere, at 600 to 800 °C for several hours. Such devices when stressed showed little or no change in barrier voltage or leakage current with time. In the literature [32,40,46] this was presumed to be due to a change in the Bi_2O_3 crystal phase. It was concluded that the zinc interstitial are removed by heat treatment. In a more recent study [5] **Gupta** *et al.*, suggested chemical induced stability as an alternative procedure to enhance varistor stability. The strategy was to incorporate amphoteric dopants, such as Na or K in the ZnO lattice. These dopant, have the ability to occupy both the lattice and the interstitial sites. By occupying interstitial sites, the dopants will first block the formation of zinc interstitial in the available sites, and secondly, they will prevent the migration of zinc interstitial via available sites. In this situation Na doping (280 ppm Na) was particularly favoured as it acts as an acceptor on the interstitial site and as a donor on the lattice site. This scheme reduces the density of the interstitial, thus enhancing the stability.

Other forms of degradation have been described by **Fagan** *et al* [86] (1993), in their study of positive temperature coefficient (PTC) thermistor devices exposed to oil vapours. They had found that oils begin to oxidise at moderate temperatures (120-200 °C), with C=C double bonds adsorbing chemisorbed grain-boundary oxygen in the ceramic. Therefore, degradation occurs at moderate temperatures if the oil vapour can diffuse into the grain boundary regions. This form of degradation can also occur in the ZnO based varistor device as experienced by the present author (R. D. Pindoria) during his visit to a manufacturing company making ZnO based varistors. The grain boundary glassy layers, and/or fluorinating of the grain boundaries is presumed to decrease the degradation in these devices. Chemisorbed fluorine creates the necessary boundary-acceptor states and is believed to form a stronger bond than oxygen [86].

2.4.6. Bypass effect at heterojunctions

The eighth model was based on the " bypass effect" at heterojunctions. This model was initially proposed by **Eda,** [56] in 1982 and then **Levingson** and **Philip** in 1986 [4]. The model describes the important role of the Bi_2O_3 rich intergranular layers in the linear region. In this model the important role of the Bi_2O_3 rich intergranular layer in the small current region is represented by the "bypass effect". The parallel current paths through the heterojunctions and the Bi_2O_3- rich intergranular layers are considered. Fig. 2.4.15, illustrates the typical grain-boundary structures [46] and the schematic conduction band diagram and the equivalent circuit are also shown [6]. This model is consistent with the electrical properties in the small current (linear) region, the effect of Bi_2O_3-rich intergranular layer on degradation, the observed varistor actions both in the ZnO ceramics with a large amount of Bi_2O_3, and the thin-film ZnO-Bi_2O_3 heterojunction [6].

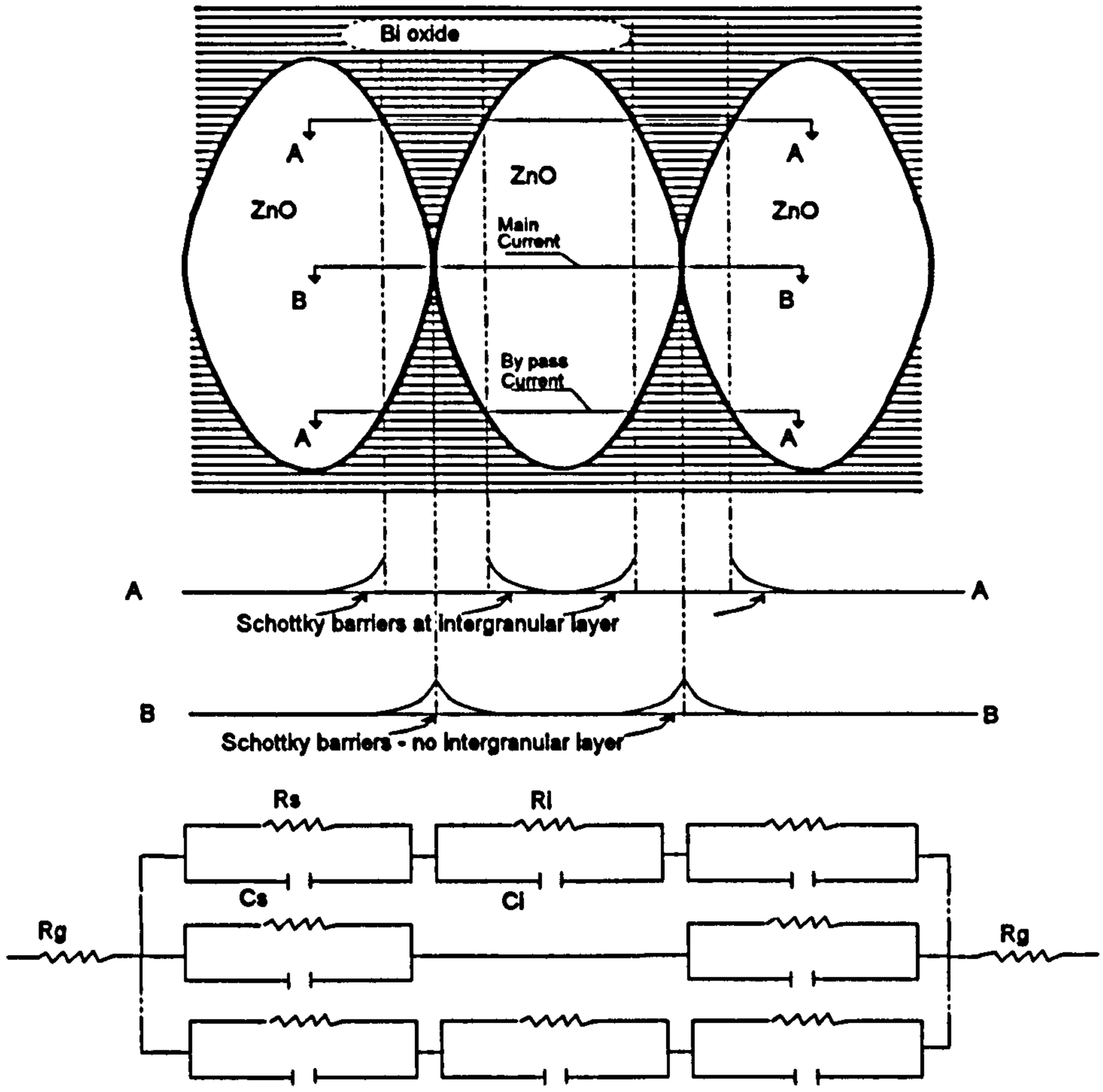


Fig. 2.4.15. Bypass model for a variety of grain boundaries. A-A and B-B are the Schottky barriers corresponding to the Bypass and the Main current respectively. The conduction band in Bi_2O_3 - rich intergranular layer is not clear. In the equivalent circuit of the grain boundary structure, R's and C's correspond to the resistance and capacitance of the Schottky barrier, respectively. Rl and Cl corresponds to the resistance and the capacitance of the intergranular layer, respectively. Rg corresponds to the resistance of the ZnO grain [6].

2.4.7. Space-charge-induced current model

The ninth model "induced space-charge current at the heterojunction", was proposed by **Suzuoki** *et al.*, [63] in 1987. This model has been derived experimentally. The experimental sample used in this investigation was composed of thin films of ZnO and Bi_2O_3. A ZnO-Bi_2O_3 two-layer composite was prepared by RF sputtering the compound oxides on to a clean glass substrate with pre-evaporated gold electrodes (Fig.2.4.16).

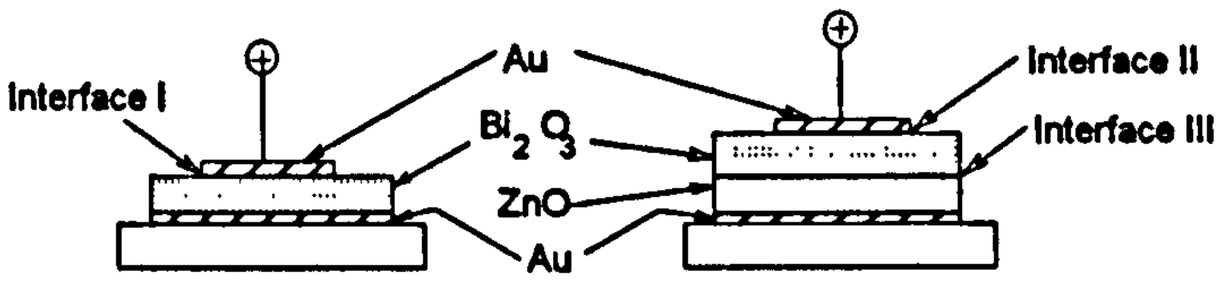


Fig. 2.4.16. A schematic representation of a Bi_2O_3 single layer and a ZnO-Bi_2O_3 two layer specimen and the applied polarity [63].

The ZnO layers were deposited in Ar gas using a ZnO target (gas pressure, 34 Pa; input voltage, 1.5 kV; sputtering time, 1.5h). The Bi_2O_3 layer was deposited in O_2 gas using a Bi_2O_3 target (gas pressure, 20 Pa; input voltage, 1.2 kV; sputtering time, 5 min).

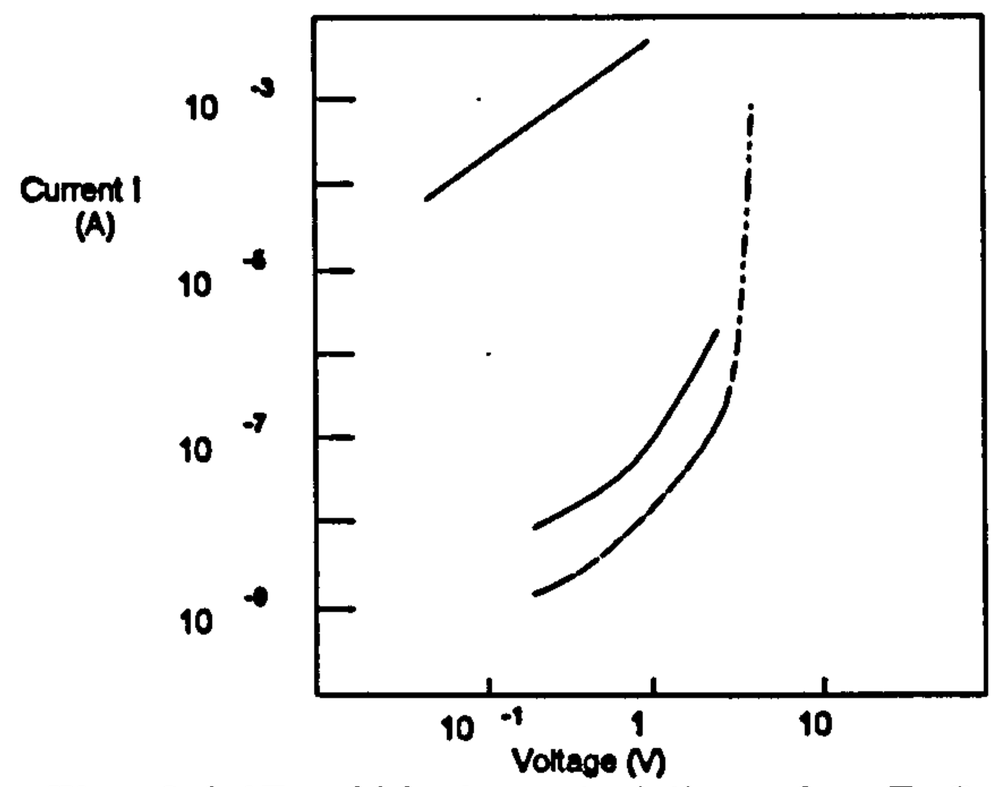


Fig. 2.4.17. I:V characteristics of a ZnO single-layer (full curve), a Bi_2O_3 single-layer (broken curve) and a forward bias ZnO-Bi_2O_3 two-layer (chain curve) specimen [63].

The films formed under these conditions were approximately 1μm and 0.3 μm thick, respectively. Investigations using the reflection-high-energy electron diffraction (RHEED) pattern of the deposited layers suggested the deposited ZnO to be crystalline whilst the Bi_2O_3 layer was found to be amorphous. The conduction and degradation mechanism in this model are discussed in the light of the I:V and C-V (capacitance-voltage) characteristics of the thin-film model system (Fig. 2.4.17 and 2.4.18).

The corresponding band diagrams for a ZnO-Bi_2O_3 two-layer specimen is shown in Fig. 2.4.19. The steep current increase under forward bias condition was presumed to be due to the disappearance of the interfacial potential barriers in the ZnO layer. Explanations of the characteristics of this system are presented in terms of three well known regions (I, II, and III) of the varistor characteristics. The specimens showed a decrease in resistance after voltage application which was thought to correspond to the degradation of ZnO varistors. A negative charge associated with the potential barrier at the ZnO-Bi_2O_3 interface was presumed to control the non-linear I:V characteristics. The extreme high non-linearity under reverse-bias was attributed to electrons tunnelling through the barrier at the reverse-bias ZnO-Bi_2O_3 interface. Theoretical values of the coefficient of non-linearity (α) of up to 60-90, have been reported for this model.

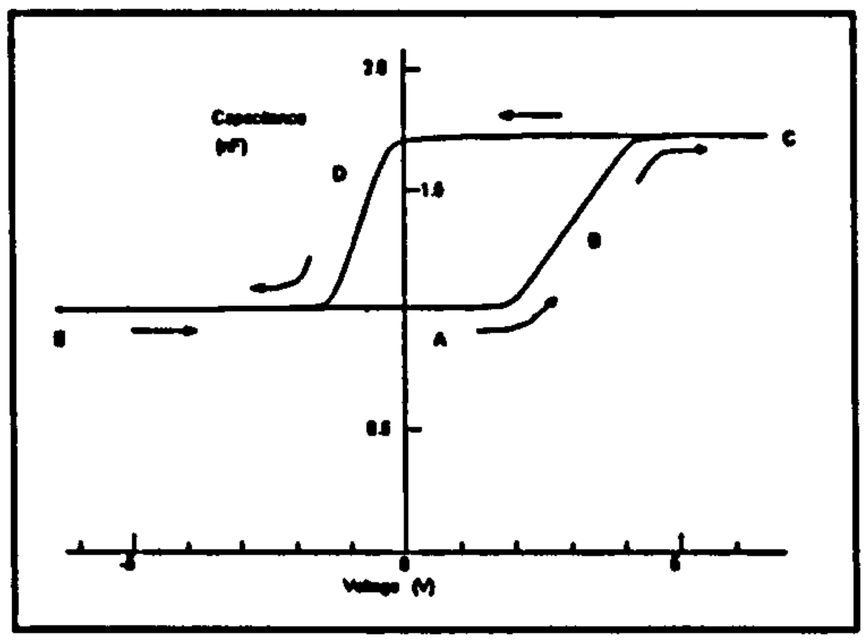


Fig. 2.4.18. C-V characteristics of a ZnO-Bi_2O_3 two-layer sample [63].

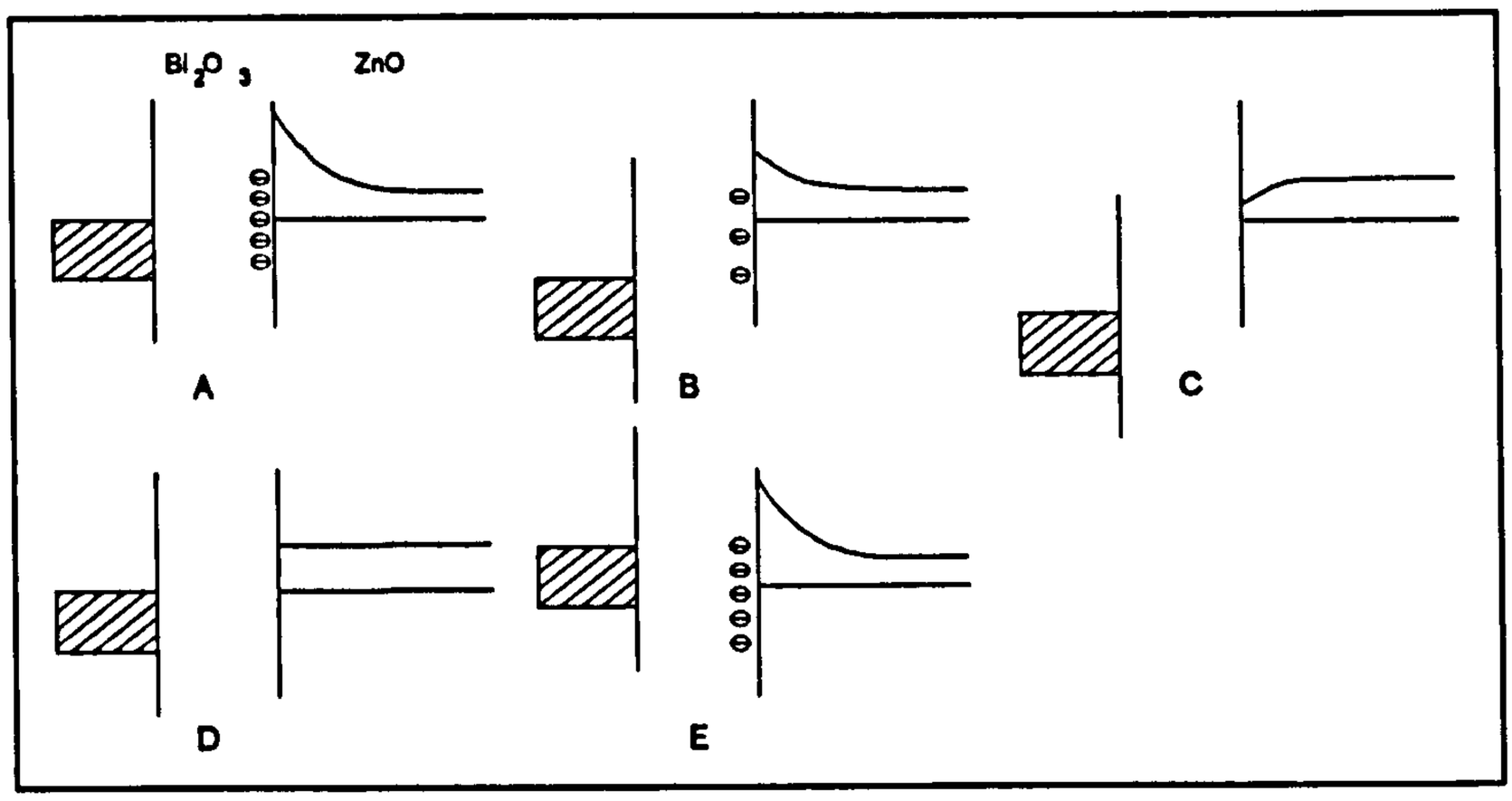


Fig. 2.4.19. Band diagram for a ZnO-Bi_2O_3 two-layer specimen [63].

2.5. Summary of the Conduction Models

The first explanation of the nonohmic conduction in the ZnO varistor was based on a space-charge-limited-current (SCLC) process in the intergranular layer with deep traps [9]. This theory explained the effect of additives on nonohmic properties. However, the theory was insufficient to explain other experimental results, such as the small temperature dependence of the I-V curve in the highly nonohmic region, the asymmetrical degradability phenomenon, and the lack of massive (1μm) intergranular non-zinc oxide layers at the grain boundary interface. In the second model a theory by **Levingson** and **Philipp** [62] (1975) proposed that the highly nonohmic properties observed in the voltage region above threshold voltage in the I:V curve are consistent with a tunnelling process in the intergranular layer (100Å). This model was derived from experimental results associated with the I:V curve and its temperature dependence. This theory could not explain certain experimental results, such as the effect of additives and the asymmetrical degradation of the I:V curve. In the third model, **Morris** [77] (1976) and **Hower-Gupta** [60] (1979) proposed a model based on the Schottky barrier formed at the interface (10Å) between ZnO grains and the intergranular layer. These models were suitable for the explanation of the nonohmic I:V curve, its temperature dependence, and the effect of additives but failed to explain the asymmetrical degradation. **Eda** and **Ematage** [56,59] (1977-1978) derived a barrier model taking into account the thin intergranular layer (500 and 900Å) sandwiched between Schottky barriers formed opposite each other. According to the tunnelling process in this model, the nonohmic I:V curve, its temperature dependence, the effect of additives, dielectric properties, bias voltage dependence of capacitance, transient conduction phenomena and asymmetrical

degradation of the I:V curve can be adequately explained. The fourth model by **Mahan Levinson** and **Philipp** [51] (1979), was based on tunnelling through Schottky barriers with hole creation. This model demonstrated the importance of minor carriers (holes) at the grain boundaries interface (10-100Å). The fifth model by **Einzinger** [12] (1979) was based on tunnelling through homojunctions (zero intergranular layer) of ZnO, which pointed out the importance of the thermal equilibrium of defects formed during cooling at the grain boundaries. The sixth model by **Pike** *et al* [55,61] (1984) was based on the hole induced breakdown at the grain boundary of essentially zero width. According to the theory subsequently (1986) presented by **Blatter** and **Greuter** [23,24], the highly non-ohmic property is caused by lowering of the potential barriers at the grain boundaries due to hole accumulation. The holes are created by accelerated electrons in the depletion region. The potential barriers depend both on the interface states and on the bulk traps. The seventh model was the grain boundary defect model proposed by **Gupta** *et al.*, [37] (1985). This model explains the phenomena of voltage instability / stability of the ZnO varistor. The key elements of this model is the presence of zinc interstitial in the depletion layer as excess zinc, arising from the non-stoichiometric nature of ZnO which are formed during the fabrication of the varistor. Both the instability and stability of the varistor has been described in terms of field assisted diffusion of these interstitials in the depletion layer, followed by chemical interaction with defects at the grain boundary interface. The eighth model was the bypass effect [6] which represented the important role of the Bi_2O_3 rich intergranular layer in the small current region and supposed that parallel current paths through the heterojunctions and the Bi_2O_3 -rich intergranular layers should be considered. The ninth model by **Suzuoki** *et al* [63] (1987) was based on induced space-charge current at the heterojunction, composed of thin films of ZnO and Bi_2O_3. The experimental non linear coefficient α, has been reported to be unexpectedly high as 60-90. This is presumed to be attributed to the quality of the 0.3μm Bi_2O_3 amorphous film grown in a controlled sputtering process; as it has been found that certain crystalline phases of Bi_2O_3 are not favourable. Moreover a varistor based exclusively on this type of thin film of single Bi_2O_3 layer would also be susceptible to degradation and hence not commercially viable. Looking back at the initial studies by **Matsuoka** *et al* [9] the non-linearity coefficient of ZnO doped with just Bi_2O_3 oxide was only α=4. Table 2.4.1 gives a summary of the conduction models discussed.

Table 2.4.1. Models proposed to explain The Conductance Mechanism In ZnO Varistor

1968	Invention of Zno varistor (**Matsuoka** *et al*) [7]
1968	Discovery of the effect of various kinds of additives (**Matsuoka** *et al*) [9]
1971	Space-charge-limited current (**Matsuoka**) [9]
1975	Tunnelling through a thin layer (**Levinson** and **Philip**)[62]
1975	Tunnelling through Schottky barriers (**Levine**) [76]
1976	Tunnelling through Schottky barriers (**Morris, Bernasconi** *et al*) [77]
1977	Tunnelling through Schottky barriers with heterojunctions (**Emtage**) [59]
1978	Tunnelling through Schottky barriers with heterojunctions (**Eda**) [56]
1978	Tunnelling through homojunctions (**Einzinger**) [12]
1979	Tunnelling through schottky barriers (**Hower** and **Gupta**) [60]
1979	Hole-assisted tunnelling through Schottky barriers (**Mahan, Levingson,** and **Philip**) [51]
1982	Bypass effect at heterojunctions (**Eda**) [56]
1984	Hole-induced breakdown (**Pike**) [55,61]
1985	Grain boundary defect model (**Gupta**) [37]
1986	Bypass effect at heterojunctions (**Levingson** and **Philip**) [4]
1986	Hole-induced breakdown (**Blatter** and **Greuter**) [23,24]
1987	Space-charge-induced current (**Suzoki** *et al*) (Tunnelling) [63]

All the proposed models (Table 2.4.1) agree on the importance of the grain boundaries as the functional feature of the ZnO varistor ceramics. Anomalies arise in the interpretation of the structure and hence the transport properties across the grain boundaries which is at the heart of the electronic ceramics such as ZnO varistors. Some consensus can be drawn from the preceding literature survey:

(a) The varistor effect is attributed to the dopant decorated grain boundaries in the ZnO ceramic and it is hence a bulk phenomenon.

(b) There is a varied interpretation of the structure of the grain boundaries and hence the mechanisms of charge transport across the grain boundaries. For example, apart from the first model based on 1μm intergranular layers, all of the other models consider much thinner (10-1000Å) intergranular layers with associated space charge layers on either side of the grain boundary. This large variation in thickness presumably depends on the processing parameters and the method used in measuring these small dimensions.

(c) The role of oxygen in the Bi rich amorphous intergranular layer of around 5-10Å thickness is at the heart of the functional characteristic of a varistor.

(d) The stability of a varistor is improved by additional additives (Sb_2O_3, MnO_2. Co_3O_4 and Cr_2O_3) besides Bi_2O_3 . The addition of Bi_2O_3 has been found to be essential for forming nonohmic behaviour. Addition of transition oxides such as Co_3O_4 and MnO_2 also enhance non-linearity. Similarly, multiple dopants such as a combination of Bi_2O_3, Sb_2O_3, MnO_2, Co_3O_4, Cr_2O_3 etc., have produced greater non-linearity than that by a single dopant. The synergistic effect of various dopants has not been established yet.

2.6. Aims and Objectives

The preceding literature survey has brought to light several aspects of the microstructural properties and the conduction mechanisms of ZnO based varistors. There is however a lack of general consensus in the literature. Further investigations using a group of novel analytical techniques would be beneficial to elucidate the relationship between the bulk non-linear I:V characteristics of ZnO based varistor material to its microstructure, compositional variations and microscopic electrical behaviour. For example:

(1) To undertake extensive SEM-EDAX, and some STEM analysis to investigate (a) the microstructure of the ZnO ceramic whilst varying the numbers of additives, and (b) the formation and distribution of phases and the spatial distribution of additives in samples prepared under different sintering conditions.

(2) To use the high sensitivity of the SIMS technique to undertake $^{18}O/^{16}O$ isotopic exchange / diffusion profiles (IEDP) and line-scan SIMS profiling (LSP) [using ^{18}O as a tracer] to elucidate the oxygen diffusion coefficient and its path in both doped and undoped ZnO ceramics. Also to use the ion imaging mode of this technique to gain information about the compositional distribution of additives.

(3) To investigate the microscopic electrical behaviour using SEM-EBIC to enable direct observation of the electrically active grain boundaries and double Schottky barriers (DSB). Also to undertake local electrical measurement across single junctions or a few grain boundaries using micro-probe manipulator equipment attached to an SEM.

(4) To study the synergetic behaviour of additives in ZnO ceramic by synthesising samples with a combination of different additives and measuring their I:V properties.

(5) To investigate samples synthesised with a combination of different additives, using Impedance spectroscopy IS, in order to investigate the bulk grain boundary properties such as capacitance and resistance. Thus to deduce an equivalent circuit for the electrical properties of the bulk device.

(6) To synthesise a bi-crystal and study the properties of a well-defined grain boundary.

(7) To conduct some XRD analysis to identify and hence verify the dominant phases in etched samples.

A combined use of the above analytical techniques (as discussed in section1.3.1), particularly the SIMS and SEM-EBIC has produced a significant novel contribution in this work and have consequently improved the understanding of varistor phenomenon.

Chapter 3

Characterisation Techniques

The characterisation of electronic ceramics requires information on the microstructure, the compositional variation of dopants, the morphology of the grain boundaries (intergranular layers) and the associated electrical properties giving rise to non-linear I:V characteristics. In order to obtain this variety of information, a combined use of several analytical techniques is desired. This requires a high spatial resolution and high sensitivity to detect chemically, elementally and electronically the multi phase, polycrystalline nature of the ceramic microstructure and in particular the unique properties of the grain boundaries which are responsible for the varistor effect. Experimental techniques such as the SEM-EDAX, SEM-EBIC, SEM-CL, TEM, SIMS, IS, and XRD were used in this project to investigate ZnO based ceramic varistors. Some I:V measurements were undertaken at the National Physical Laboratory, Teddington. The procedure for synthesising samples and the matrix of experiments using the above group of techniques are presented in chapter 4. This chapter gives a brief introduction to each of the analytical techniques used in this work.

3.1. Scanning electron microscopy (SEM)

3.1.1. Basic overview of an SEM

Microscopy-based techniques enable visual observation during analysis, so that any microstructural heterogeneity and analysis induced artefacts can be identified. The scanning electron microscope (SEM) is a very useful instrument and simple in principle [72]. It consists essentially of two cathode ray tubes (CRT) as shown schematically in Fig. 3.1.1.

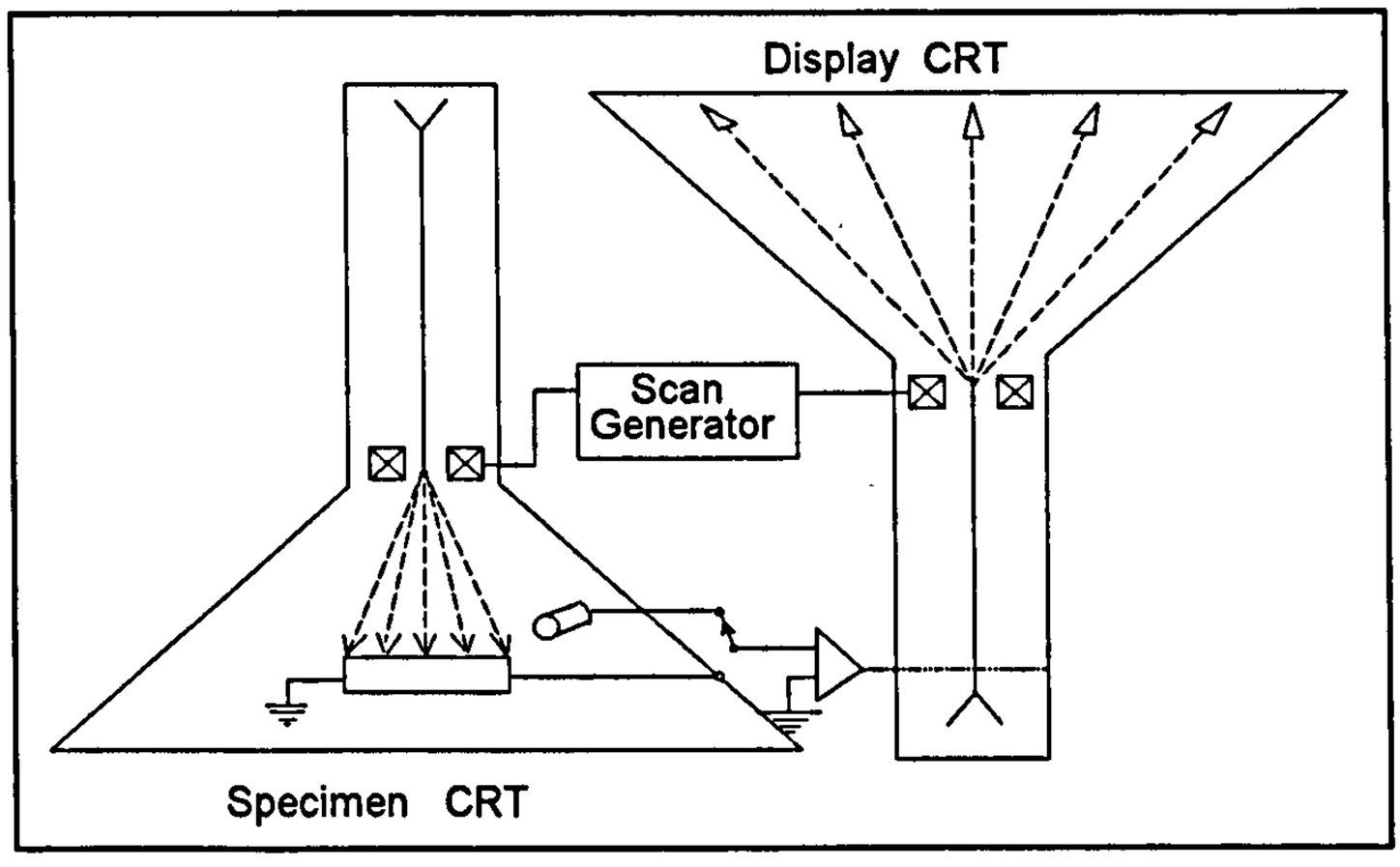


Fig. 3.1.1. Schematic representation of the scanning electron microscope [72].

In one of these the object to be examined is subjected to bombardment by a focused beam of electrons. The effects of this bombardment is sensed by a suitable detector and a proportional voltage signal is fed to the grid of the second or display CRT. Because both CRT's are scanned in synchrony, an image of the specimen is built up, point by point, on the display CRT. A great advantage of this point-by-point method of image formation is that detectors of different types may be fitted to the SEM and operated simultaneously to yield a multiplicity of "images", each of which depends upon the specimen-electron beam interaction in a different way (Figs. 3.1.2a and 3.1.2b).

There are six types of resultant energy that may be detected [70]. These are (1) X-rays, (2) emitted electrons, (3) charge collection (CC) or conductive mode signals, (4) cathodoluminescence (CL) light, (5) transmitted electrons and (6) acoustic (ultrasonic) waves. The most commonly used are: the secondary and backscattered electrons, and the X-rays for SEM-EDAX analysis. The SEM technique is thus suitable for microcharaterisation of solids and in particular electronic materials, since it provides high spatial resolution, depth of field and simultaneous availability of a variety of SEM-modes and contrast Figs. 3.1.2 *and* 3.1.3.

Scanning electron microscope manufacturers guarantee resolutions of 100-200Å. Compared to conventional electron or light microscopes, SEM pictures exhibit remarkable three-dimensional effects due to the extraordinary depth of field made possible by the wavelength and apertures involved. Depth of field is 1cm at 100x and 1μm at 10,000x. Sample preparation is easy compared to the transmission electron microscope. Specimen of nearly any size can be examined since it is unnecessary to thin

specimens. Finally, the ease of operation and the correspondence of the image to normal vision put this instrument into a unique class.

In this project, secondary and back scattered electron imaging were used to observe the microstructures of ZnO ceramic specimens prepared under different conditions.

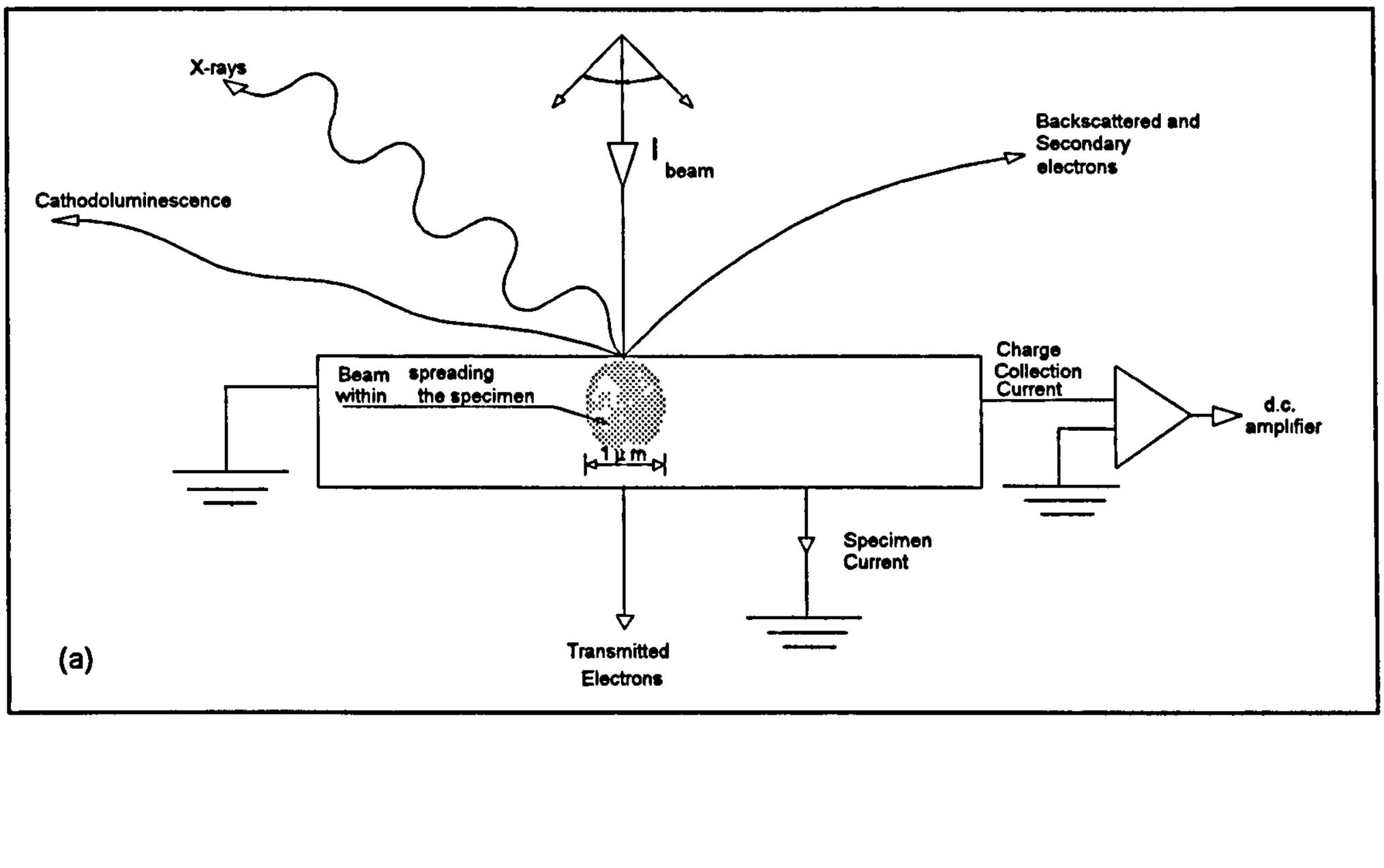


Fig. 3.1.2. The signals used in the six modes of scanning electron microscopy: (a) the five signals available with continuous bombardment and (b) the generation of decaying thermal waves and ultrasonic waves by beam chopped at a high frequency [70].

3.1.2. SEM-EDAX

One of the most significant effects of the incident electron beam is the formation of X-rays (Fig. 3.1.3). Two kinds of X-ray signals can be distinguished [73].

The first is the continuum or bremsstrahlung (from the German "braking radiation"). This arises because the incident electrons are decelerated by the field from the positive charges on the cores of the atoms. The intensity extends from zero energy up to the incident beam energy and at some energy E, the intensity I(E) has the form:

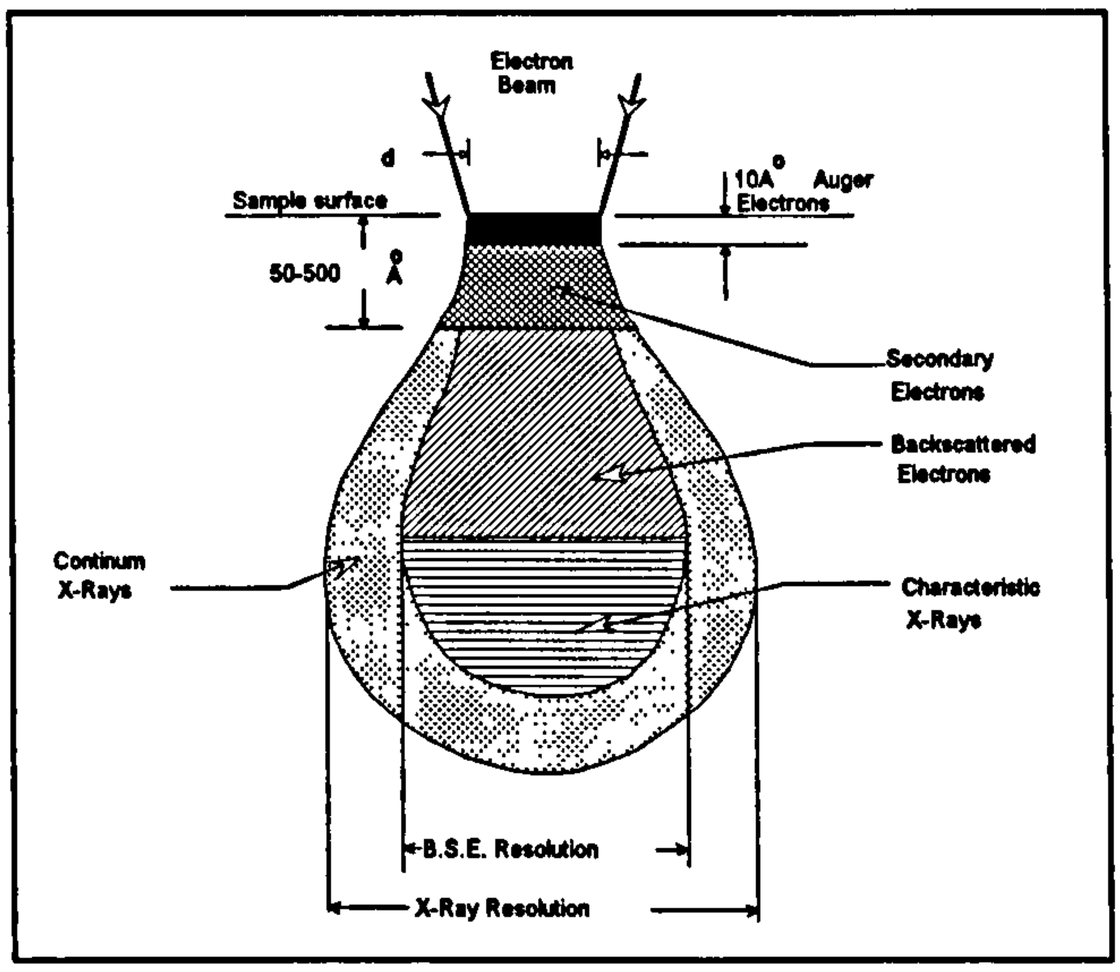


Fig. 3.1.3. Schematic diagram illustrating the limited spatial resolution attainable in bulk samples due to electron beam spreading within the specimen. A typical value of the minimum X-ray spatial resolution is ≈ 1μm at 30 kV irrespective of beam diameter [73].

$$I(E) = iZ_m (E_o - E)/E \qquad (3.1\text{-}1)$$

where I(E) is the bremsstrahlung intensity at the electron energy E, *i* is the electron current, Z_m is the mean atomic number of the target and E_o is the incident beam energy. The generated continuum intensity rises rapidly as the energy falls. Also the intensity is proportional to the mean atomic number of the sample so the continuum signal does not contain any specific chemical information. Secondly, the interaction of an incident electron with an inner-shell electron can result in an ionisation event in which the bound electron is ejected leaving a vacancy. Subsequently, the atom de-excites by an electron dropping from an outer shell and emits its excess energy either as an Auger electron or as an X-ray. The energy of the X-ray is equal to the difference in energy between the inner and outer shells involved in the transition. The energy of the X-ray is characteristic of the inner shell ionisation that occurs in an atomic species energised by the primary electron beam. These X-rays emitted are called "characteristic" X-rays because their energies (or wavelengths λ) are unique to the particular element that was ionised to produce them. The energies of the shells vary with atomic number and the energy difference between shells changes significantly even for atoms with adjacent atomic numbers. This fact was first discovered by **Moseley** [70] (1913, 1914) who showed that

$$\lambda = B/(Z-C)^2 \qquad (3.1\text{-}2)$$

where B and C are constants for each family of X-ray lines, i.e. L_α K_β, etc. If the energy, or wavelength λ, of the emitted X-rays can be measured, then the elemental composition of the sample region irradiated by the beam can be determined. The characteristic X-ray signal is collected by the detector, amplified and presented in a form of an intensity vs energy spectrum showing peaks corresponding to the specific elements that are present locally.

The scanning electron microscope energy dispersive analysis by X-ray (SEM-EDAX), thus enabled the local elemental analysis of phases in the microstructure. SEM-EDAX was used to investigate the elemental variations of dopants in the microstructure of the ZnO-based varistors. Compositional variation images were obtained by the technique of X-ray mapping; they are more time consuming to obtain but when superimposed on to SEI or BSI images provide useful complementary information. Samples were mounted on to a specimen holder (usually earthed). Typical instrumental parameters when undertaking an X-ray analysis were: a beam voltage of 25 keV and a beam current Ib, of several nano Amperes.

3.1.3. SEM-EBIC

3.1.3.1. Basic overview of an EBIC

EBIC (electron beam induced current) is one of the most important types of signal in the charge collection (CC) mode in the SEM. One of its major applications is to identify electrically active defects in semiconductor materials and devices [72]. Charge carriers are generated by the collision of an energetic primary electron with valence electrons in the material which "ionise" the atoms to produce electrons in the conduction band and holes in the valence band (Fig. 3.1.4). The charge carriers generated are collected by an electric field within the material and are sensed as a current in an external circuit (Fig. 3.1.5).

The mode of image formation is assisted by the specimen itself acting as the detector or "collector" of the electronic charge that makes up the video signal. If the specimen is non-metallic and therefore capable of supporting an internal electric field, mobile charge carriers generated by the impinging beam within the sample move in response to the field to produce a measurable signal [72]. It is not possible for an electron beam to excite significant signal in metals because (i) the charge carrier density is too large to be significantly altered by injection

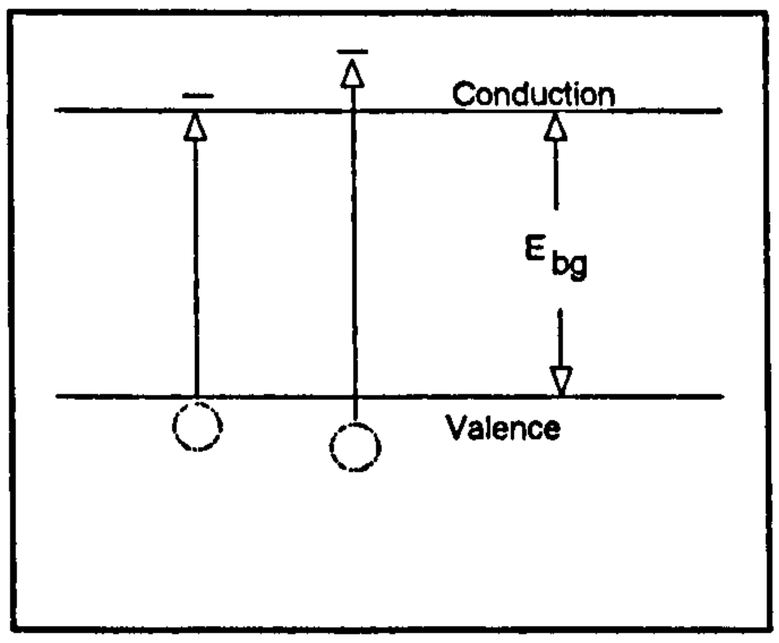


Fig. 3.1.4. The process of carrier generation during electron bombardment of a semiconductor specimen [72].

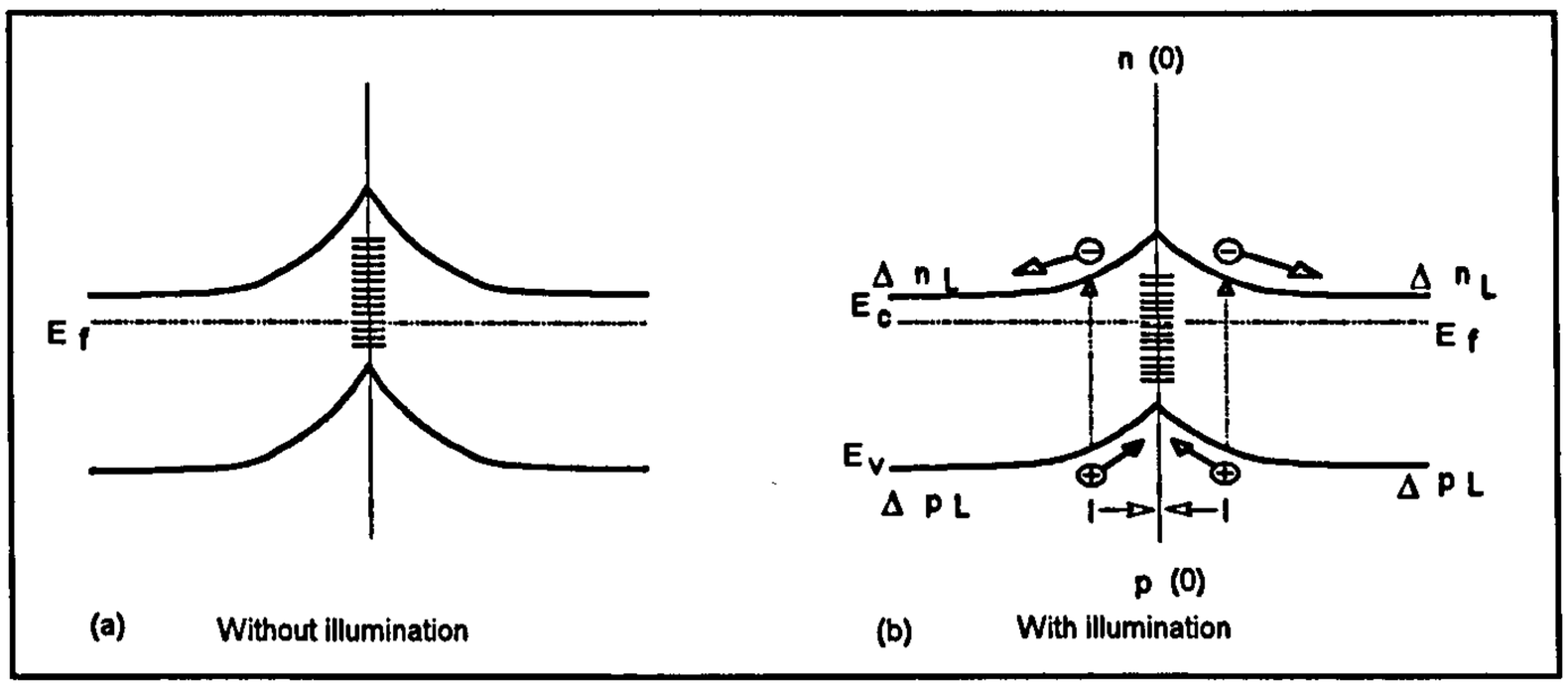


Fig. 3.1.5. Schematic illustration of carrier generation during electron bombardment of a high resistivity material such as ZnO varistor. (a) Intergranular barrier without illumination. (b) With illumination barrier - lowering increases n(0) and thereby promotes recombination. Continuous distribution of interface states assumed.

from the incident beam, (ii) electron - hole pairs cannot be generated by the incident electrons and (iii) the carrier electrons screen any locally induced potentials.

The incident electron beam I_b generates a number of hole-electron pairs per second ΔN given by [70] :

$$\Delta N = G\, I_b / q \qquad (3.1\text{-}3)$$

where the generation factor (G) is defined as the number of hole-electron pairs generated per incident electron. It is given by:

$$G = (1-f)\, E_b / e_i \qquad (3.1\text{-}4)$$

f is the average fraction of the energy of the incident beam electrons lost by back scattering, q is the charge on the electron, E_b is the energy of the incident beam electrons (in eV), and e_i is the "ionisation" energy, i.e. the effective average energy required to generate a hole-electron pair. e_i is about 3 times E.g., the bandgap energy, due to other forms of energy loss of carriers by immediate recombination (i.e. carriers that recombine immediately do not contribute to the EBIC signal). A linear relationship between this formation ("ionisation") energy e_i and the bandgap energy E.g. was noted by **Klein** (1968) [87] and extended by **Ehrenberg** and **Gibbons** (1981) [88]. They found that

$$e_i = 2.1\, E_g + 1.3 \qquad (3.1\text{-}5)$$

where all terms are in eV.

Hence only a fraction of the incident beam energy (few eV) generates the secondary electrons used for imaging. The vast majority of the electron beam energy (usually tens

of keV) is absorbed by the creation of electron/hole pairs within the material. When Eb is tens of kiloelectronvolts, G is of the order 10^3-10^4 so CC currents are often much larger than the specimen or beam current. Since about 9.6 eV is required to generate an electron/hole pair in ZnO, a 1keV electron beam can produce about a hundred such pairs [70]. The hole-electron pairs are produced in a generation or energy dissipation volume. This volume acts as a probe, determining the spatial resolution of the CC mode.

The carriers generated by the incident electron beam diffuse randomly, become trapped, and annihilate one another until all excess carriers are eliminated. The application of an electric field will cause these carriers to depart from purely random motion to a more ordered movement creating a current, which can be detected in an external circuit, hence the name "electron beam induced current." The charge collection (e-h pair separation) effects will occur provided that (i) there are built-in field regions in the sample and (ii) λ, the carrier drift length, is not negligible relative to the separation of the contacts. The required electric field can be externally applied (bias voltage) or it can be internally generated (i.e. built in) in the vicinity of a Schottky barrier. The induced current can be collected at the contacts on either side of the sample or the specimen stage of the microscope. This current can be used to create an image of a specimen or to modulate a normal secondary electron image[70,72].

The distribution of the carriers is also important. The depth of electron beam penetration, in the incident beam direction, at which the primary electrons have been slowed to thermal equilibrium with the lattice is the range R (Fig. 3.1.6). This value R is slightly greater than the usual empirical measure used, the Grün range (R_G). The full details of the work of Grün are presented by **Holt** [70]. The depth-dose, lateral-dose and other dose distributions can also be readily extracted from Monte Carlo simulations [70]. R_G can be estimated by knowing the electron beam interaction as a function of the beam parameter according to the equation:

$$R_G = [\,(3.98 \times 10^{-2})/\rho\,]\, E_o^{1.75} \qquad (3.1\text{-}6)$$

where

Rg is the Grün range (R, the "electron range", is usually taken to be R_G) = generation range

E_o = Acceleration voltage (kV)

ρ = Density in g/cm^3

(for pure ZnO ceramic $\rho = 5.61 g\ cm^{-3}$).

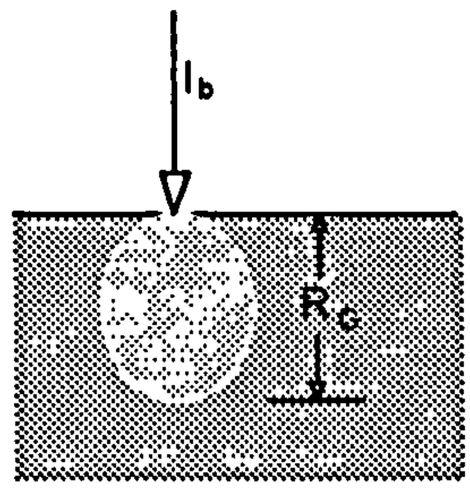


Fig. 3.1.6. Schematic of the Grün range (Rg).

This equation (3.1-6) gives the range in μm if E_o is in kV [70].

3.1.3.2. Instrumentation (EBIC)

In the experimental situation shown in Fig. 3.1.7, the specimen (ZnO varistor) is of non-uniform high resistivity, containing electrical (charge collecting) barriers; it has no bias applied.

The beam and specimen act as a potentiometer (current divider). Beam bombardment produces a negative potential, V, at the impact point. Consequently a specimen (absorbed electron) current, flows to earth. This is given by:

$$Is = Ib - Ie \qquad (3.1\text{-}7)$$

where Ib and Ie are the beam current and the total emitted current respectively. It is assumed that Ie does not vary as the beam scans along the specimen so Is, is constant. Let the resistance in the path from the impact point directly to earth be Rd and in the path via the amplifier be Ra. Then

$$V = Ia\,Ra = Id\,Rd \qquad (3.1\text{-}8)$$

and

$$Is = Id + Ia \qquad (3.1\text{-}9)$$

As the beam scans from left to right over the specimen, Rd undergoes a linear increase and Ra a linear decrease with distance. Thus the current passing through the amplifier (the signal), varies linearly from Ia = 0 when the beam is incident on the direct-to-earth contact at x = 0 to Ia = Is when it is incident on the amplifier contact at x = D, where D is the length of the specimen. This ohmic variation as shown in figure 3.1.7b is the base line (solid straight line) for all conductive mode observations on high resistivity, wide gap materials [70]. All other electrical effects (e.g. stepped profile) are superimposed on it and result in local signal variations i.e. contrast. The slope of the line is proportional to the resistivity and in low resistivity materials an approximately horizontal line of little interest is obtained.

The SEM-EBIC mode was used to study ZnO based varistors. A line scan analysis of a single grain boundary was undertaken with the aid of a micro-manipulator apparatus. I:V measurements across a single grain boundary in ZnO ceramic as well as in the bi-crystal sample of ZnO were facilitated.

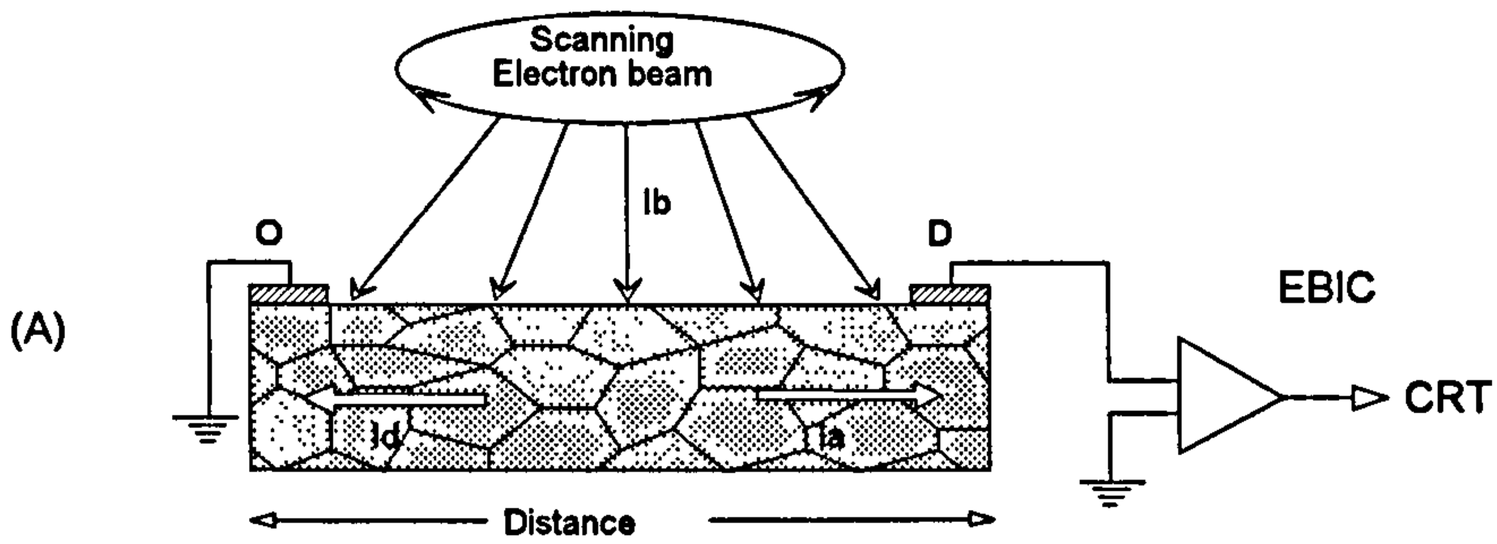


Fig. 3.1.7. (A) Conductive mode detection circuit for a high resistivity specimen (ZnO Varistor) where the beam and specimen act as a potentiometer (current divider). and (B) the form of signal variation for a line scan.

3.1.3.3. EBIC signal detection

The EBIC signal detection and processing is facilitated by the Matelect ISM 5 monitor. This instrument is designed to detect and process induced current and voltage signals which are produced in the sample undergoing observations in a scanning electron microscope. The instrument consists of a head amplifier, which is attached to the microscope, and a control unit to which the head amplifier is connected by a multi-core cable (Fig. 3.1.8).

Two outputs are provided on the control unit: the RECORDER output and the ANALOG output. The RECORDER output provides a buffered output of the signal from the head amplifier for a chart recorder. The ANALOG output is connected to the CRT of a scanning electron microscope to produce micrographs.

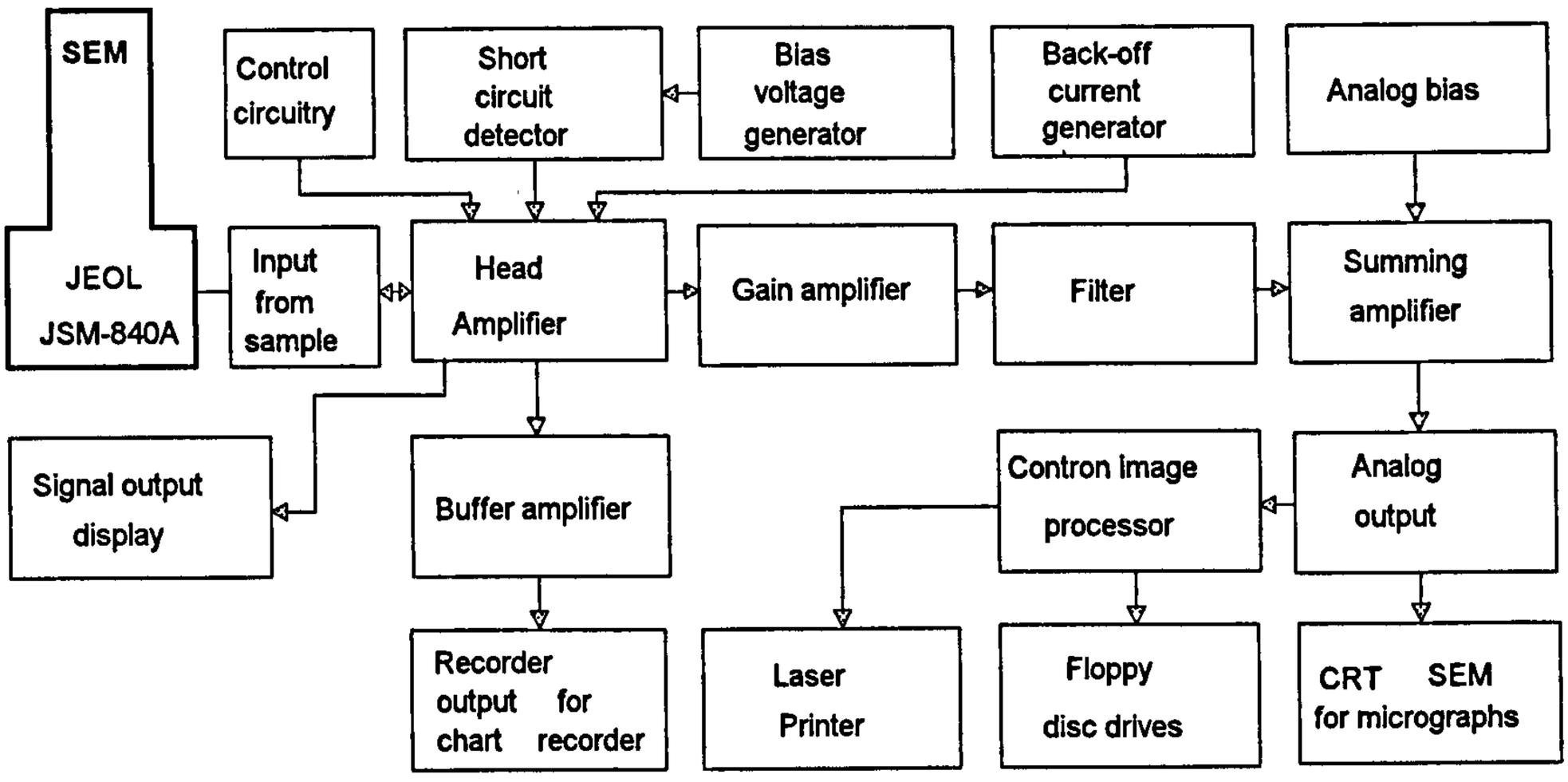


Fig. 3.1.8. Schematic diagram of (Matelect) ISM 5 control unit and head amplifier used during EBIC analysis.

3.1.4. SEM-CL

3.1.4.1. Basic overview

Cathodoluminescence (CL) is a name given to light emitted from the surface of the material irradiated by (primary source of energy) an electron beam [70]. These light photons (CL signal) are emitted as a result of electronic transitions between the conduction and valence band and levels lying in the band gap of the material (Fig. 3.1.9). The commonest radiative transition in lightly doped semiconductors at room temperature is band-to-band. Bandgap information of the material can be obtained

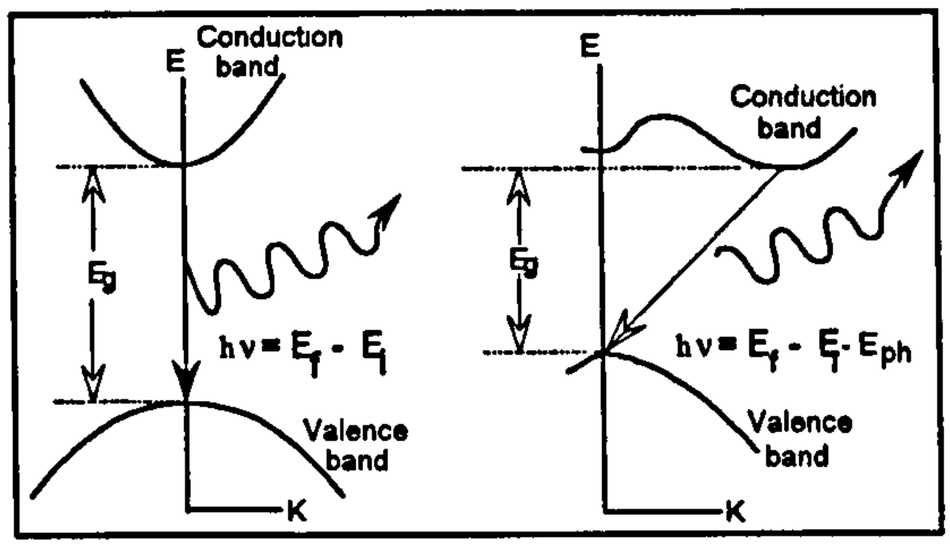


Fig. 3.1.9. The energy transitions in direct **(a)** and indirect **(b)** gap semiconductors between initial states E_i and final states E_f. For indirect transitions **(b)** the participation of a phonon (E_{ph}) is required [70].

if the electron beam of an SEM provides the
excitation (1 to 40keV) and a spectroscopic system collects and detect the CL.
Mechanisms leading to emission of light in a solid are similar for different forms of the excitation energy. Based on this principle the CL technique is non-destructive with high spectral resolution for microcharacterisation of luminescent materials. The CL method is non-destructive provided the material being irradiated can sustain repeated bombardment by electrons. The electron irradiation may ionise or create defects and so alter the electronic properties of the material temporarily or permanently. Depth resolution is possible by varying the range of the electron penetration, which is dependent on the

electron beam energy. The essential requirements for the CL detection system design are a high efficiency of light collection, transmission and detection.

Two types of signal from the photomultiplier can be extracted to produce micrographs or spectra. CL micrographs can be obtained by a constant monochromator setting and a secondary electron beam condition. Spectral information for a point analysis can be derived when the monochromator is stepped through the wavelength range of interest, and the electron beam set to scan a small area or remain stationary. From the measured value of the λ, energy of the radiative recombination can be calculated using eqn. 3.1-10.

$$E = \frac{\hbar c}{\lambda} \qquad (3.1\text{-}10)$$

where E is energy, $\hbar$ is the Plank's constant: 6.63×10^{-34} Js, C is the speed of light: 2.99792458×10^{8} ms^{-1} and the eV is electron -volt energy: 1.6×10^{-19} J

3.1.4.2. Instrumentation (CL)

An Oxford Instruments CL301 specially designed semiellipsoidal mirror-cryostat assembly mounted on a side port of a JEOL 840A SEM was used for light collection inside the microscope. The collecting mirror directs collected light to a periscope attached to a monochromator fitted with a photomultiplier and a liquid nitrogen cooled Germanium detector. The schematic of the light collection and transmission of the CL signal is illustrated in Fig. 3.1.10.

The mirror is designed with a small orifice for the incident electron beam. The CL signal is first focused by this semi-ellipsoidal mirror, which concentrates the emitted light through the second focus of the mirror where it is collimated by a lens and guided into the entrance slit of the monochromator. The complete system is computer controlled, allowing it to operate in either spectroscopic or imaging mode.

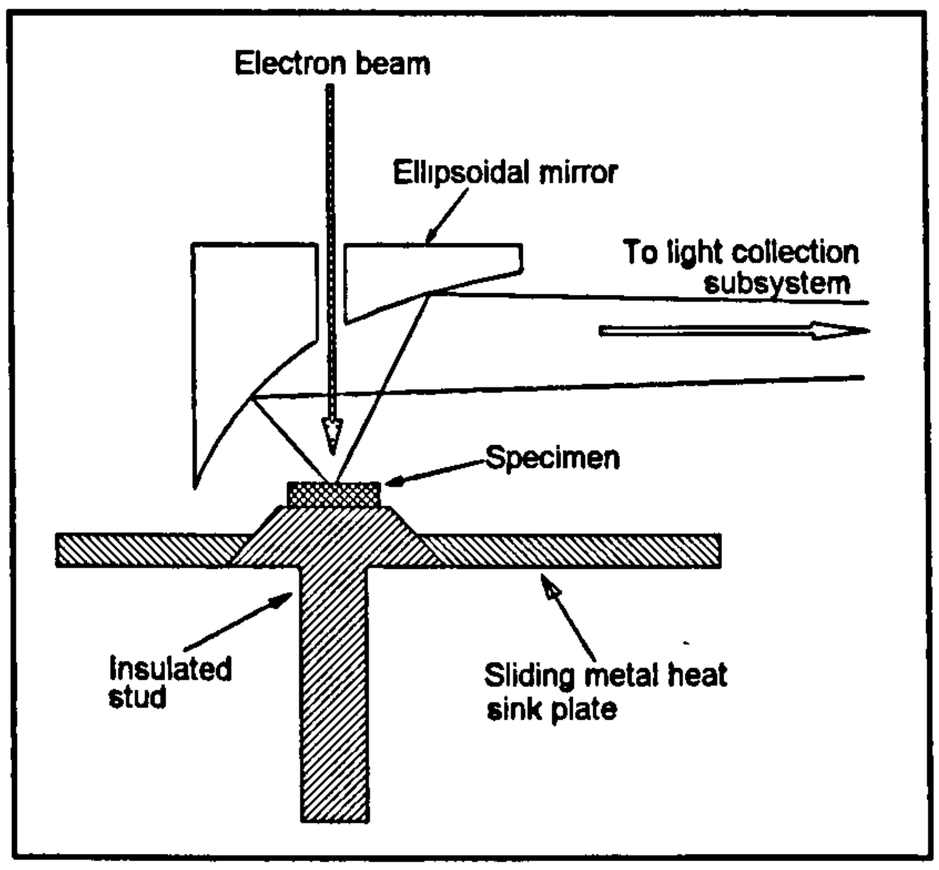


Fig.3.1.10. Schematic diagram of a CL light collection system.

Light with a narrow range of wavelengths then falls on the photomultiplier. The output is a train of pulses which corresponds to the incident photons. This output signal is then filtered to reject noise and amplified and fed through a video amplifier to a cathode-ray-oscilloscope display to produce CL images, or alternatively, sent to a computer for data analysis [70].

A schematic of the CL system is shown in Fig. 3.1.11. A light collector takes the CL emitted by the specimen and delivers it to the entry slit of the Bentham Instruments M300 monochromator (which contains an order-sorting filter mounted on a wheel). The software program can automatically insert order sorting filters (at 0.4 and 0.7μm wavelength) during spectrum acquisition, for removal of higher order diffraction peaks. After passing through the monochromator, photons of a narrow wavelength range fall on the cooled and magnetically focused photomultiplier tube (PMT). This produces a train of pulses which are detected by a photon counter in the form of a discriminator / amplifier and pulse shaper. This discriminates against certain forms of noise by thresholding. The output of the photon counter is recorded by a microcomputer which contains a counter board. The computer also operates the monochromator stepper motor drive via an IEEE 488 interface board. SEM-CL was used to study pure and doped specimens of ZnO ceramic.

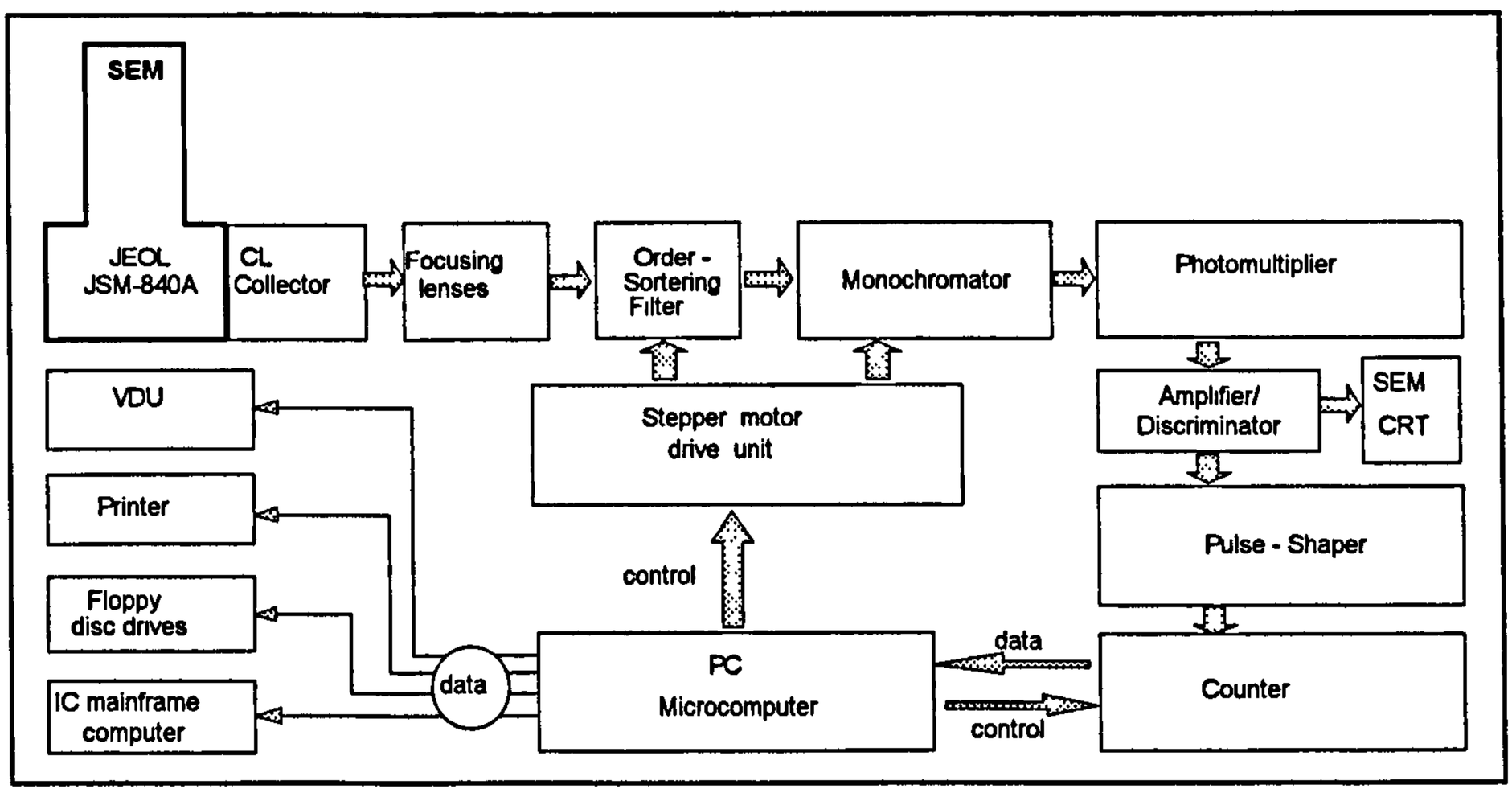


Fig. 3.1.11. The computer-controlled CL detection system

3.2. Scanning transmission electron microscope TEM/STEM-EDAX

3.2.1. Basic overview

Fig. 3.2.1 shows a schematic diagram showing the important component of the TEM. X-ray microanalysis in the transmission electron microscope is analogous to the SEM-EDAX. It has the intrinsic advantage over SEM of the use of very thin samples. When

the sample is thin (less then the mean free path of the incident electron) the extent of beam spreading is reduced and the spatial resolution is commensurate with the electron beam diameter (Fig. 3.2.2). Any limitation to resolution is due to beam spreading as a result of the type of specimen, and defects in lenses.

STEM-EDAX was used to study the details at the grain boundaries and secondary phases. The sample preparation is discussed in Chapter 4 section 4.2.4. For a detailed discussion of TEM the reader is referred to some excellent reviews by **Edington** [104,105].

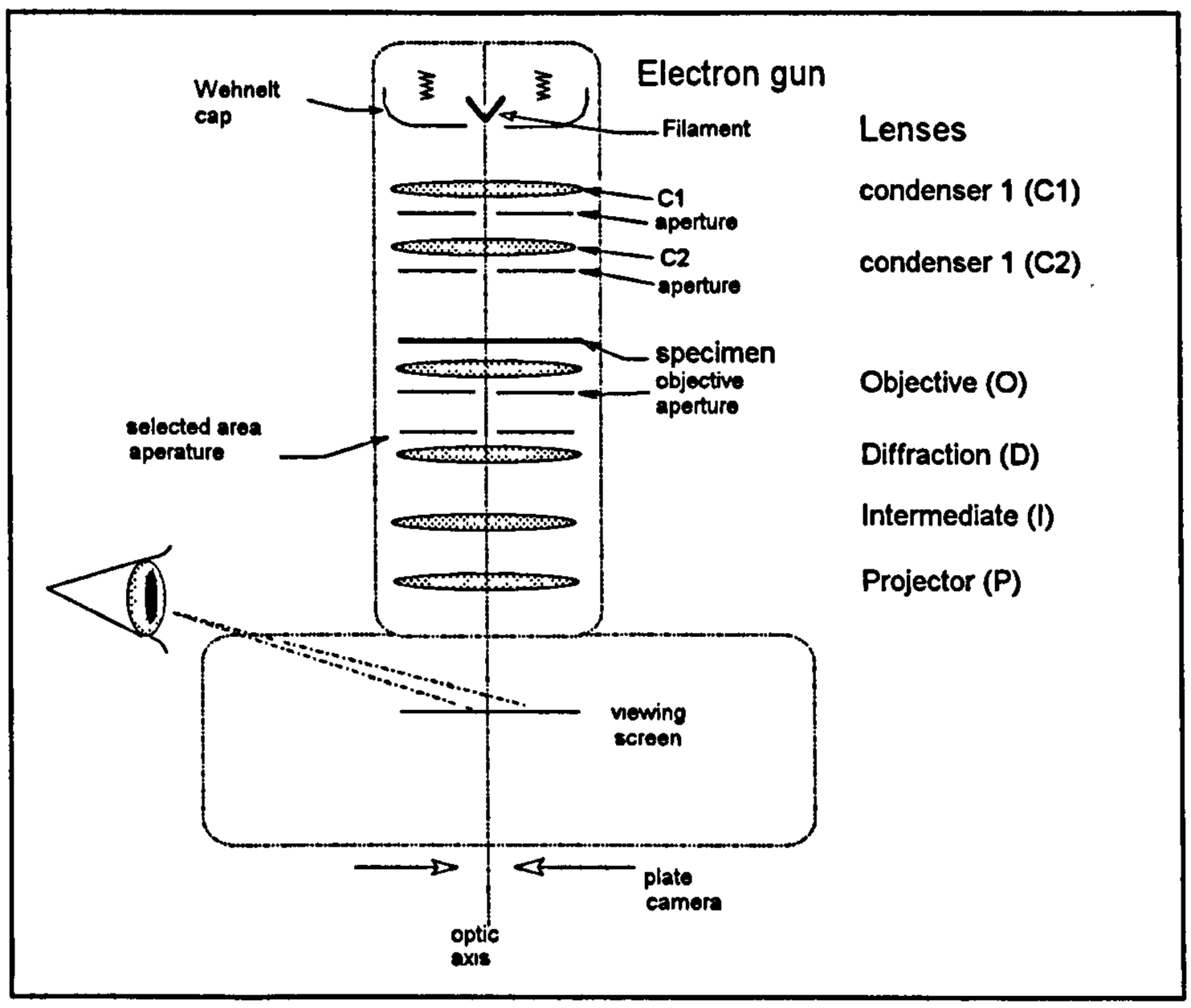


Fig. 3.2.1 A schematic diagram showing the important components of the Electron Microscope [104,105].

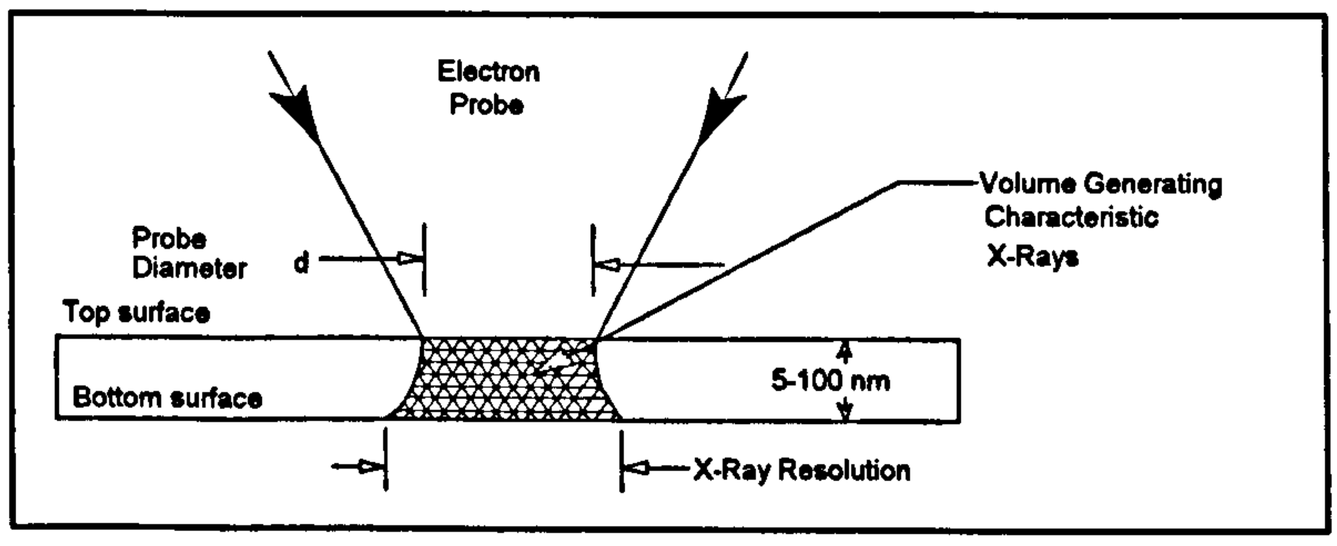


Fig.3.2.2. Schematic illustration of the use of a very thin specimen (less than the mean free path of the incident electrons). This reduces the extent of beam spreading. The spatial resolution in the X-ray microanalysis mode is then commensurate with the electron beam diameter [73].

3.3. SIMS (Secondary Ion Mass Spectrometry)

3.3.1. Introduction

The high sensitivity of SIMS was used to study the compositional variation of dopants in ZnO based varistors. In this section a brief introduction is given to explain the basic principles of SIMS and an overview of the system used in this work.

3.3.2. Basic principles of SIMS

Secondary Ion Mass Spectrometry (SIMS) is a surface analysis technique that involves mass analysing secondary ions that are ejected from the sample surface by primary ion bombardment. As material is removed (sputtered) from the sample surface the secondary ions successively originate from deeper depths, allowing the concentration of various elements to be determined as a function of depth. The basic SIMS equation ($I_S = I_P\ S\ \gamma\ c(V)\ f$) relates the secondary ions current (I_S) the primary ion beam current (I_P), the secondary ion yield (S), ionisation probability (γ) fractional concentration of impurity c(V) in the matrix and the instrumental transmission factor (f). This relationship is derived in section 3.3.7. During analysis the secondary ion intensity (of the selected species) is recorded as a function of analysis time. The conversion of the secondary ion intensity to concentration is based on the assumption that the ion intensity is directly proportional to the concentration of the element ($Is \propto c(V)$).

Thus, SIMS in its depth profiling mode is a technique capable of determining the elemental concentration of dopant and impurity atoms within a material as a function of depth. The technique is popular for its high sensitivity, with detection limit of atom concentrations of less than one part per million atomic (ppma) for almost all elements, and 10 ppba (10^{13}-10^{20} atoms cm^{-3}) for some elements, together with the good depth resolution, usually between a few nanometres and a few tens of nanometres [69] and lateral resolution of a few μm. The technique as illustrated schematically in Figs. 3.3.1(a) and 3.3.1(b) can be employed to characterise the surface and near surface (~30 μm) region of solids and the surface of some liquids [69].

The technique has been applied to a wide variety of vacuum compatible materials, including semiconductor materials, ceramics, polymers, composites and biological materials amongst others. SIMS uses a focused energetic ion beam (typically 1-15 keV) to erode (sputter) atoms from a selected sample region, producing ionised secondary

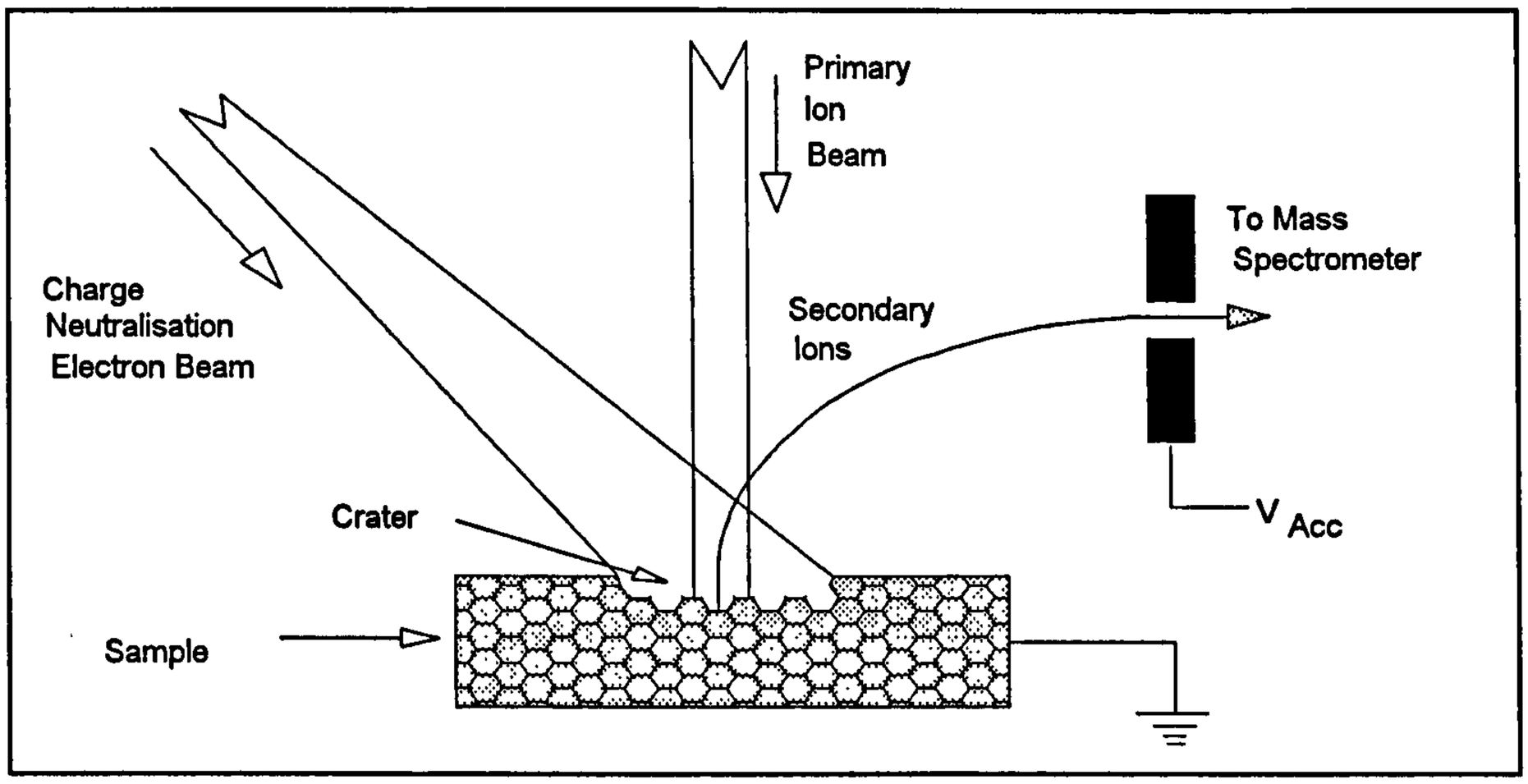


Fig. 3.3.1 (a). Schematic of the sample ion beam interaction in SIMS [69]

particles that are collected, mass analysed and counted. While most of the sputtered atoms are neutral, a small fraction are ejected as positive or negative ions. These secondary ions carry information about the sample composition at the location of the primary ion bombardment. The sputtering process is not just limited to the surface layer but it involves the implantation of the primary species into the sample and the removal of surface atoms by the energy loss of the primary species in the form of a collision cascade. Each primary ion that penetrates the sample generates an intense but short-lived collision cascade which involves the breaking of bonds and the displacement of many target atoms from their lattice sites. Some of these displaced atoms are ejected from the sample as low-energy secondary species and the surface of the sample gradually erodes. Amongst the species that are formed by the interaction of the beam with the sample only the positive and negative secondary ions are of interest for SIMS; the secondary ions are extracted by electric fields and are then energy and mass analysed.

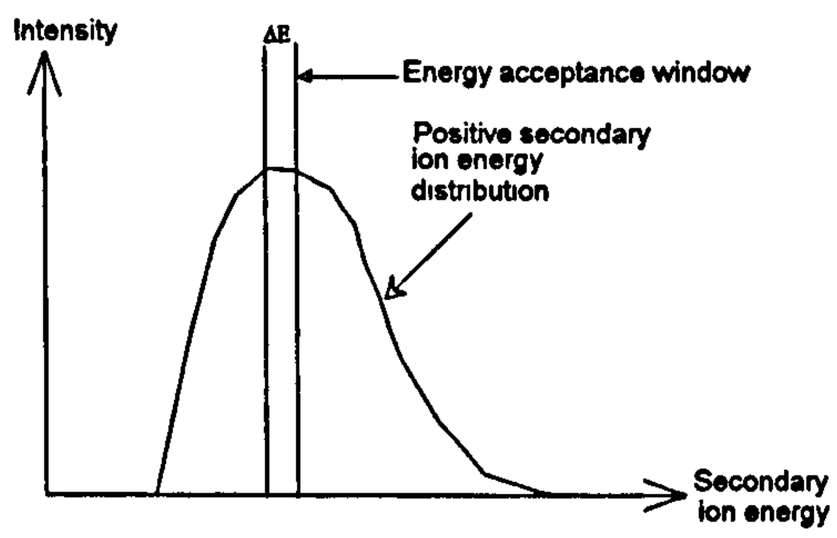


Fig. 3.3.1(b). Energy spectrum of secondary ions.

Detection is by an electron multiplier, Faraday cup, or ion sensitive image amplifier for imaging. The analysis is carried out in a vacuum compartment. Since the sample is being eroded continuously, it is possible to build up chemical information as a function of depth. The lateral distribution of impurities is obtained by scanning the ion beam across the sample surface and detecting the secondary species in synchronism with the scan. However a well focused beam is required for good lateral resolution. The mass

spectrometric analysis of the secondary ions results in a capability to detect not only chemical elements but also to differentiate between the individual isotopes of those elements. The relative sensitive factor (RSF) vary enormously in SIMS. The appropriate primary beam is important in order to detect positive or negative secondary ions. Chemical compounds can be identified and measured by examining the peaks in the mass spectrum of the material under examination associated with molecular ions.

3.3.3. Instrumentation (The Atomika 6500)

The instrument used in this project was an Atomika 6500 ion microprobe, schematically shown in Fig. 3.3.2. This SIMS instrument consists of two primary ion beam columns (one to generate gas ions and a separate one to produce metal ions), a main chamber and a secondary ion detection system. The Atomika 6500 is a quadrupole based SIMS instrument as opposed to magnetic sector type. A comprehensive discussion of the differences between these two types of instrument is discussed elsewhere [95]. For more detailed information on features that are specific to the Atomika 6500 instrument the reader is referred to **Frenzel** *et al* [96].

3.3.3.1. Overview of the System

3.3.3.1.1. Primary beam column

The two types of ion source that are on the instrument are the gas ion source and the cesium ion source. These ion sources have separate beam lines and independent controls. The gas source is mounted vertically and the Cs source horizontally, Fig.3.3.2. Although the ion generation mechanisms in the two sources are different, they are, however, operated in a similar manner.

The ion beam can be one of many species, typically O_2^+,Cs^+,Ar^+ and Xe^+ or any of a number of other species that have been used successfully for various applications [80]. Apart from Ga^+ and O^-, all the species as mentioned above are presently available on the Atomika 6500. The selection of primary species depends on many factors: secondary ion yield, detection limit, depth resolution, lateral resolution, charge neutralisation, availability and sputter rate. Xe^+ and Ar^+ are inert and frequently used, whereas, O_2^+ are used to increase the positive secondary ion yield. Cs^+ primaries are used to enhance the negative ion yield.

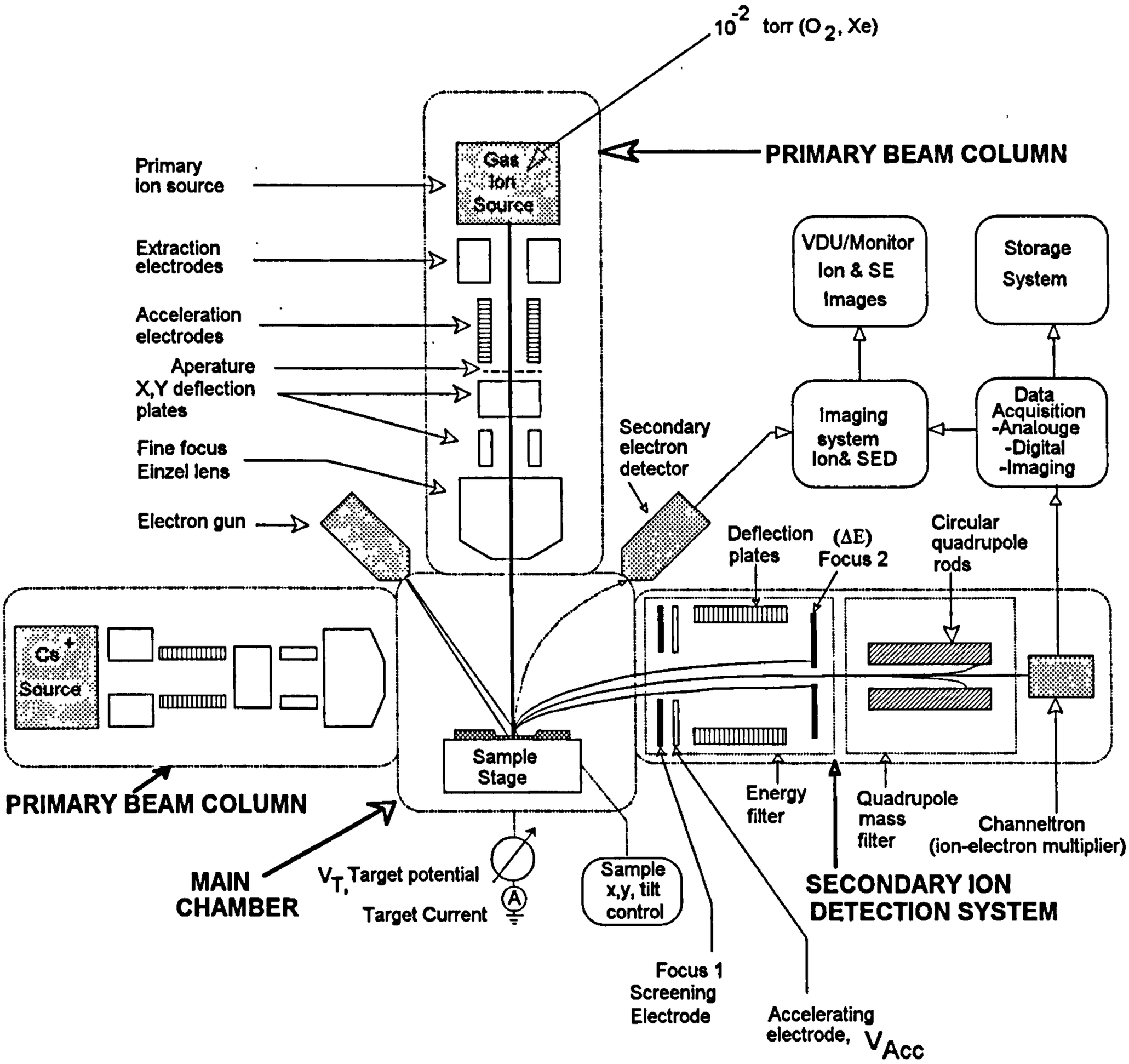


Fig. 3.3.2. Schematic diagram illustrating the principles of a quadrupole based SIMS instrument.

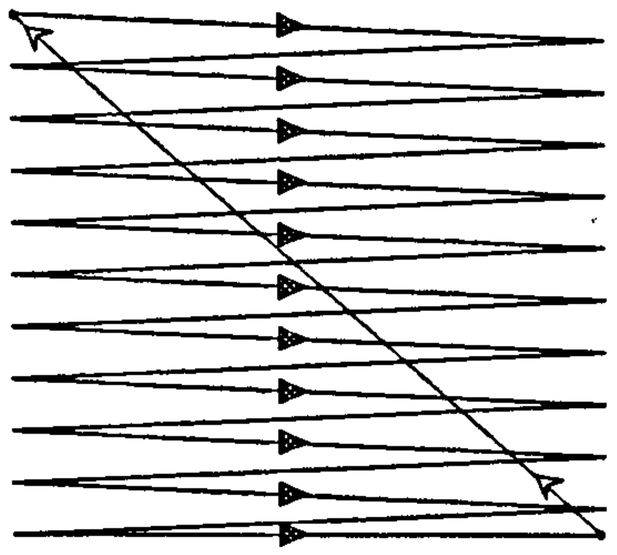
The primary beam columns (gas and / or caesium ion sources), operate at pressures in the range 10^{-7} - 10^{-6} torr. The primary ions are extracted from the source, and accelerated towards the sample. The energy of the beam can be varied from 1keV up to a maximum of 15 keV while the beam current ranges from 1nA to 1000 nA. The pressure in the gas source is typically 1.2×10^{-6} Torr, while the beam is running.

Before entering the target chamber, the primary beam is mass analysed by passing it through a velocity filter and then through an adjustable aperture. Only ions with the correct velocity pass through the filter into the target chamber. Before the primary beam reaches the aperture it is made to bend by about 2°. This process helps to remove any neutral species which travels vertically downward.

3.3.3.1.2. Scanning of primary beam

Once inside the target chamber, the ion beam passes through X and Y scanning plates, followed by an einzel lens which focuses the beam before it strikes the sample. The beam diameter may be varied from 1μm to several mm.

The primary beam current will not be uniform across the beam spot and will tend to vary, with a maximum current at the centre of the spot. If the beam was stationary on the sample the depth resolution would be poor. To eliminate this effect, the primary beam is scanned on the surface of the sample in order to obtain a flat-bottomed crater. The focused beam is scanned across the area under investigation creating a square crater of size typically 400-1000 μm across. Using electronic gating, secondary ions originating from the centre of the sputtered area are collected so as to suppress edge effects from the crater walls as this can influence the depth resolution of the profile. There are two scanning modes that are available on the Atomika 6500 instrument: raster and spiral scan. In the *raster* mode (Fig.3.3.3), the beam like that used in TV set, sweeps across slowly and then flies back at a lower position and then sweeps across again. This continues until the beam reaches the bottom, after which the beam flies-back to the top left position. In this mode, the beam spends a finite time flying-back.



RASTER SCAN

Fig. 3.3.3. Primary beam scanning.

3.3.3.2. Main chamber

During analysis the main chamber is at a pressure of about 10^{-8} - 10^{-9} torr. The chamber walls can be heated (baked) to evaporate any adsorbed gases, notably H_2O. This helps to achieve a base pressure of ~ 10^{-10} Torr. Such low pressure is favoured to reduce the effect of beam-divergence, ionisation of residual gas molecules, and adsorption of impurity gas atoms onto the sample surface. The sample is transferred into the main chamber without breaking the vacuum via a transfer chamber, which is pumped down to about 10^{-7} torr before transfer. The sample is mounted on a carousel that can be rotated and tilted. An electron gun is used to produce an electron beam (E≤5 keV) for charge compensation (discussed in section 3.3.6) during the analysis of poorly conducting samples. During imaging, the electron beam is scanned over the desired area, while for charge compensation, the beam is co-bombarded at the analysed area during analysis.

3.3.3.3. Secondary ion detection system

The sample is intercepted by the primary beam at different angles of incidence, with a typical range from normal to 60^{o} degrees from normal. These ions sputter the uppermost surface of the sample. The ejected material consists of a great number of different species including neutral atoms. Secondary ions of either negative or positive charge are accelerated through an aperture and into the energy filter by accelerating electrodes at a potential Vacc. The focusing potential, (screening electrode) Focus 1, in front of the accelerating electrodes serve as an additional potential to collect secondary ions from all angles of emission. In the energy filter, the secondary ions are deflected by the deflection plates, at a potential $V_{\Delta E.}$ Apertures before and after the deflection plates (not shown in Fig. 3.3.2), together with the potential $V_{\Delta E,}$ defines the energy window (energy band pass). Since the apertures are fixed, the energy window is adjusted by varying $V_{\Delta E}$, while the central energy is determined by the target potential V_{target}, that is applied to the sample via the sample carousel. The secondary ions that pass through the energy filter are decelerated and focused into the quadrupole mass filter by the Focus 2 electrodes. The ions have to be decelerated because optimum separation between the mass peaks is only achieved when the ions have a few eV of energy.

The emitted secondary ions are thus passed through a series of electrodes the secondary ion optics), which collect a fraction of the secondary ions and guides them towards the quadruple mass filter. The quadrupole mass filter consists of four rods to which a DC voltage with an RF component is applied. Only those ions with the selected charge-to-mass ratio are transmitted through this filter. The transmitted ions are then strongly accelerated and detected by a channeltron multiplier.

On the Atomika 6500 instrument, the channeltron operates in a pulse counting mode. In this mode, each electron pulse, corresponding to an individual ion arriving at the channeltron, is amplified and counted by a high-speed electronic counter (up to 3MHz).

3.3.3.4. Data acquisition

The total number of electron pulses counted for each complete scan of the crater (frame), is recorded as the secondary ion intensity for that frame. The frame number or the analysis time to scan each frame, is also recorded. Therefore, the measured secondary ion intensity can be given in counts per second or in counts per frame.

The secondary ion detection system can only measure either positive or negative secondary ions of a specific energy and mass. Therefore, in order to measure different secondary ions during analysis, various potentials (in the energy filter, mass filter and the target potential) are required to be simultaneously adjusted at

the start of each frame, so that secondary ions of different mass, energy or polarity, are sequentially measured within a cycle. Different modes of analysis that are available on the SIMS system include:

1. The ability to measure the intensity of different secondary ions as a function of time. The process is mass spectrometer based, and consequently can discriminate between individual isotopes. This aspect of the SIMS technique can be useful to measure the isotopic exchange / diffusion profile (IEDP) to provide data about the surface exchange coefficient (k) and the oxygen self diffusion coefficient (D^*). This is discussed in Chapter 5 section 5.4.3.

2. The ability to measure the mass spectrum of the emitted secondary ions. This is done by measuring the secondary ion intensity while the mass filter scans the specific mass range.

3. The ability to perform line-scans across the sample (discussed in section 3.3.5).

4. The ability to ion image (discussed in section 3.3.4).

3.3.3.5. Secondary Ion Gating

As the primary beam scans the sample surface, overlapping of the beam spot occurs as the distance between adjacent scan lines is smaller than the diameter of the beam spot thus forming a flat-bottomed crater with sloping edges. During analysis, the secondary ions will be measured from the flat-bottomed region and the sloping edges, resulting in poor depth resolution. This problem is known as the crater edge effect. To eliminate this effect, a technique called gating is employed, in which only the secondary ions leaving the centre (gated area) of the crater are counted. The gated area is adjusted and is usually set between 10% and 25% of the scanned area and can also be optimised after the measurement.

3.3.3.5.1. Normal Depth Profiling With Checkerboard Gating

The Checkerboard gating option available on the Atomika 6500 is a very powerful method of data acquisition that allows retrospective secondary ion gating and data manipulation. This method also helps to overcome the crater-edge effects and uneven sputtering errors introduced during depth profiling. The "checkerboard" name originates from the very first matrix gate which was an array of 8x8 sub-gates. For the checkerboard gating mode, the raster scan is selected. The checkerboard gating divides

the central 25% of the rastered area into a square array of 16x16 sub-gates (Fig. 3.3.4), (each sub-gate contains 64 pixels). A size of 16x16 is used because it is thought to be a good compromise between data load (signal intensity per gate) and sufficient lateral data points. During an analysis the primary beam is rastered across a square grid of 256x256 pixels, and the secondary ions collected for each of the raster positions. The secondary ion counts coming from each of the 256 sub-gates are stored as a data point so that data is stored as a 16x16xN (XYN) three dimensional array, where N is the number of scans. This array can then be manipulated retrospectively to produce profiles, any permutation of columns from the 256 available can be selected and summed to produce a plot of counts versus time or depth. In addition a map of secondary ion intensity across the 256 sub-gates can be reviewed as the profile reaches any abrupt changes in the concentration of any particular species in the microstructure. The increased flexibility of this mode allows the topography of the crater base to be taken into consideration and the largest flat area selected. One of the disadvantages of gating is that the intensity of the signal is reduced. Hence the signal-to-noise ratio (SNR) is reduced.

3.3.4. Ion Imaging during SIMS profiling

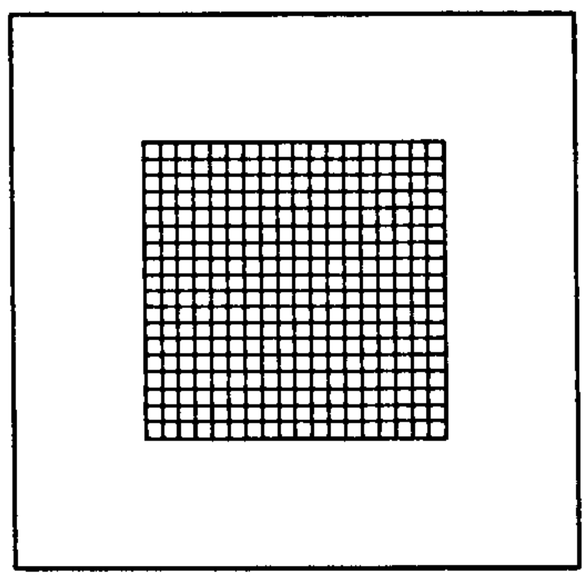


Fig.3.3.4. Checkerboard gating system.

Chemical images can be generated by raster scanning the beam across a sample area where the secondary ions emanating from each point are collected and their relative signal intensity assessed and electronically processed to display bright and dark dots on to the CRT screen of the imaging system. Information at every point and in phase with the primary beam can be recorded on a micrograph as real-time ion images. The ion images present complementary information to checker-board images. The information is presented in a form of square arrays of 16x16 sub gates, collected for a set time interval (5 seconds over each frame) corresponding to the selected mass window of a particular element. The data is stored numerically and the relative brightness of each pixel on the sub-gate represents the localised signal intensity in the scanned area (of 25μm x 25μm in this study).

3.3.5. Line scan SIMS profiling

Line scan profiling (LSP) is usually performed to study the depth of penetration of diffusive elements such as ^{18}O following an $^{16}O/^{18}O$ exchange using cross-sectioned samples. Details of this technique have been published by **Chater** *et al* [101], where the LSP technique was used to determine the oxygen self-diffusion coefficient (D*) and surface exchange coefficient (k), in $YBa_2Cu_3O_7$-δ single crystals. The sample is mounted with the prepared section normal to the SIMS primary ion beam and angled so

that a well-focused beam can be traversed perpendicular to the original polished surface. This is illustrated schematically in Fig.3.3.5. The region of the intended beam path is first raster cleaned for steady state sputtering conditions. The ^{16}O and ^{18}O secondary ion intensities are recorded at regular and known intervals along a line path from the original polished surface as illustrated in Fig.3.3.5. The $^{18}O/(^{16}O/^{18}O)$ isotopic ratio depth profile is calculated from the raw data and fitted to the diffusion equation solution for the parameters D* and k. This is further discussed in Chapter 5, section 5.4.3.

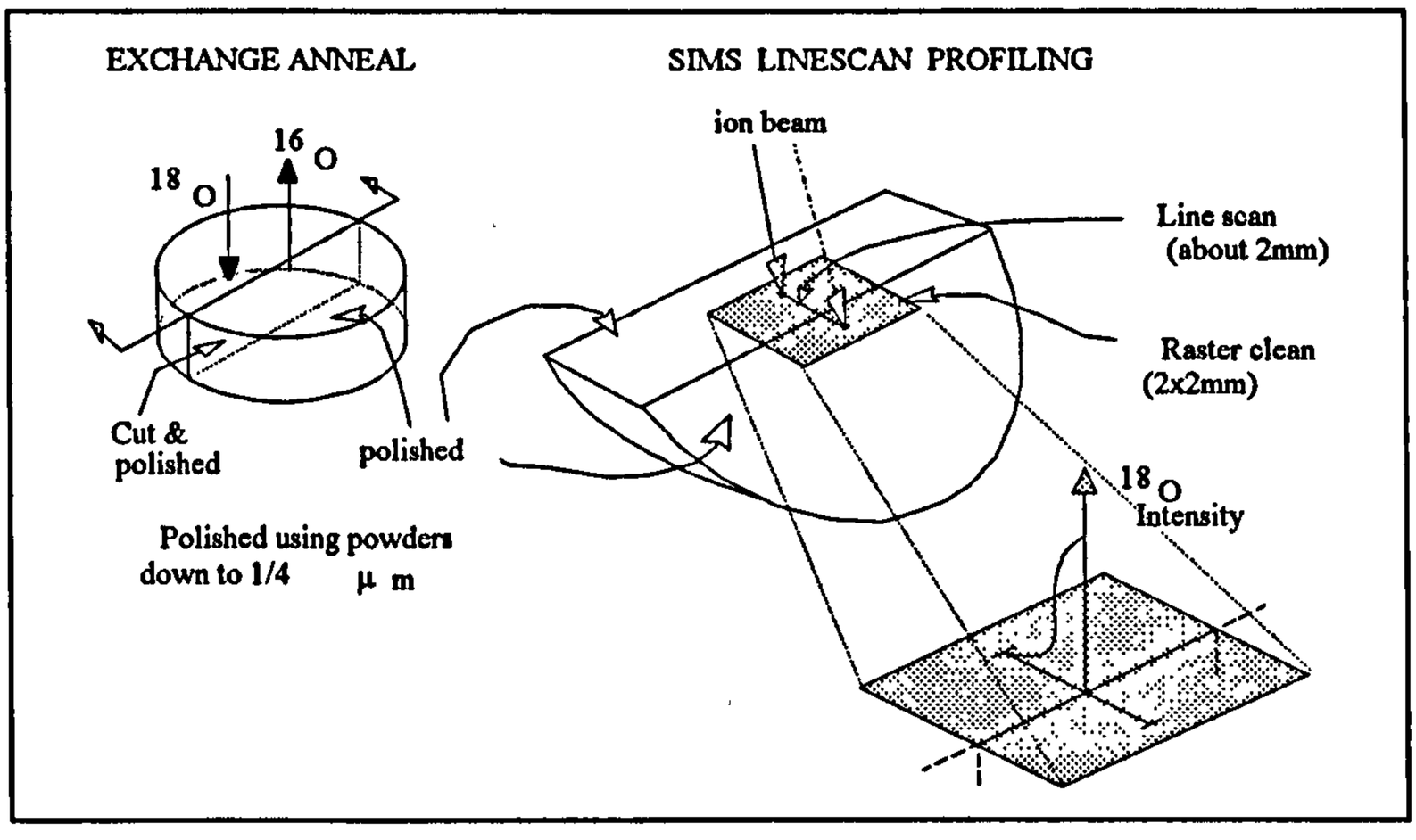


Fig.3.3.5. Schematic diagram of the ^{18}O isotopic exchange with line-scan SIMS profiling for ^{18}O isotopic concentration depth profile measurements in oxides of high diffusivity [101].

3.3.6. Charge compensation

Sample charging during SIMS analysis is a very serious and complex problem associated with poorly conducting samples. The charging effect can cause the measured secondary ion intensities to decrease dramatically, and for that reason the effect is undesirable. One of the symptoms of sample charging is the associated shift of the energy distribution of the secondary ions towards higher energies. Since the position of the energy window (quadruple machines have an energy window of about 10 eV) remains fixed, a shift in the energy distribution will cause a drop in the measured intensity. This effect is shown schematically in Fig.3.3.6.

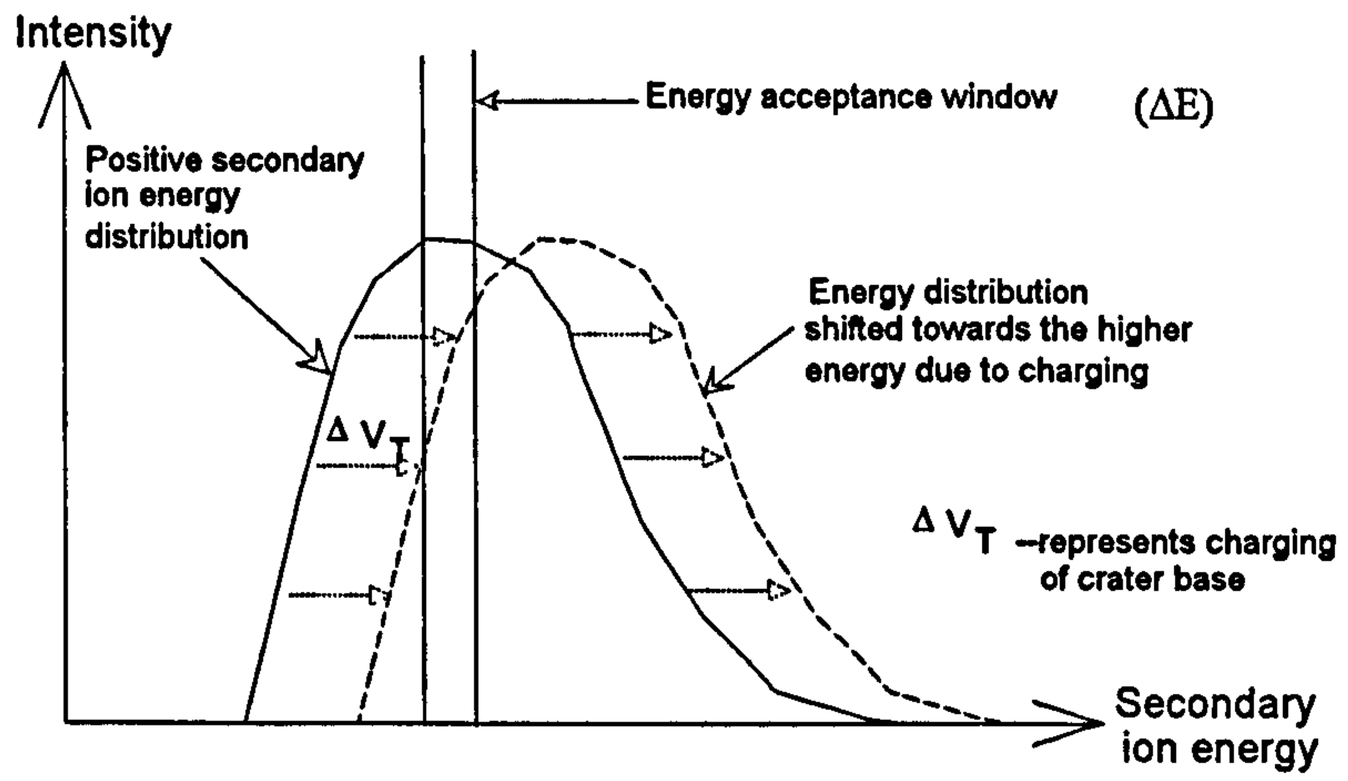


Fig. 3.3.6. Schematic diagram showing the decrease in the measured positive ion intensity as the energy distribution shifts during charging [95].

Various techniques have been used in an attempt to overcome these charging effects. An electron bombardment method (Fig. 3.3.1(a)) as demonstrated by **Wittmaack** in 1979 [97] is perhaps the most commonly used for charge compensation. However, the experimental condition for optimum compensation is usually achieved by trial and error. Moreover, as shown by **Littlewood** *et al* [98] this method of charge compensation is usually more difficult to achieve when analysing negative secondary ions than for positive ions. In addition, molecular ions are generally more sensitive to charging than the atomic ions. In some cases, as reported by **McPhail** *et al* [99,100], charge compensation using an electron beam is inappropriate and providing a thin gold coating on the sample surface is an alternative very effective method to counter charging effects. Ratioing an impurity signal with a matrix signal can also eliminate a large proportion of signal distortion that arises due to charging. Ratioing can be applied to energy spectra of the same shape for M^+ or M^- secondary ions. A detailed account on charge compensation on the Atomika 6500 has been recently reported by **Patel** [95].

3.3.7. Basic SIMS relationship

During primary ion bombardment many different secondary ion species are simultaneously sputtered from the sample surface. Consequently, the total number of species sputtered per incident primary ion is defined by the *sputter yield*, **S**. Hence , from definition S can be expressed as,

$$S = \frac{I_s^T}{I_p} \qquad (3.3.1)$$

Where I_s^T is the total current of all the secondary ions and neutral species that are sputtered and I_p is the primary ion current.

The measurement of a particular element in a matrix is in practice carried out by detecting either atomic or molecular secondary ions of either positive or negative charge. In this section it is assumed that an impurity **V** in a matrix **W**, is analysed by detecting V^+ and W^+ secondary ions for the impurity and matrix respectively. The secondary ion intensities will be in counts per second.

The secondary ion yield, **S'**, is defined as the number of secondary ions sputtered per incident primary ion, for a particular secondary ion species. The secondary ion yield, for V^+, can be given as,

$$S'(V^+) = \frac{I_s(V^+)}{I_p} \tag{3.3.2}$$

where $I_s(V^+)$ is the secondary ion intensity of V^+.

The ionisation probability, γ, is defined as the number of secondary ions emitted per sputtered particle of that species. Therefore, the ionisation probability of V^+,$\gamma(V^+)$, can be expressed as ,

$$\gamma(V^+) = \frac{I_s(V^+)}{I_s^T . c(V)} \tag{3.3.3}$$

where c(V) is the fractional concentration of V in the matrix W.

Combining equations 3.3.1 and 3.3.3 gives,

$$I_s(V^+) = I_p \cdot S \cdot \gamma(V^+) \cdot c(V) \tag{3.3.4}$$

Eqn. 3.3.4 relates the secondary ion intensity of V^+ to the fractional concentration of V. However, $I_s(V^+)$ is not the actual intensity measured because many V^+ ions that are sputtered will not be detected due to several factors: some ions will not enter the secondary ion detection system and will be lost somewhere in the main chamber, while some of the ions that enter the secondary ion detection system will not reach the channeltron. The instrumental transmission factor, *f*, accounts for this loss in the number of secondary ions that are detected. The instrumental transmission factor for V^+,$f(V^+)$, can be defined as the ratio of the number of V^+ ions detected to number of V^+ ions sputtered from the detected area. Thus, the measured secondary intensity, $I_s^m(V^+)$, can be given as,

$$I_s^m\ (V^+) = I_p \cdot S \cdot \gamma\ (V^+) \cdot c(V) \cdot f(V^+) \qquad (3.3.5)$$

Eqn. 3.3.5., relates the measured secondary ion intensity of V^+ to the fractional concentration of V. This equation is sometimes referred to as the basic SIMS equation.

The number of V atoms removed per second from the material, n'(V) (atoms. s^{-1}), can be given as,

$$n'(V) = S.\ c(V)\ .\ I_p \qquad (3.3.6)$$

now n'(V) is simply the product of the number density of V, C^v (atoms. cm^{-3}), and the volume removed per second, v' (cm^3. s^{-1}), therefore,

$$C^v\ .\ v' = S.c(V)\ I_p. \qquad (3.3.7)$$

v' can now be replaced by the scanned area, A, and the depth sputtered per second (sputter rate), z' (cm s^{-1}), thus,

$$C^v\ A \cdot z' = S.c(V)\ I_p. \qquad (3.3.8)$$

substituting equation 3.3.8. in to 3.3.5. gives,

$$I_s^m(V^+) = C^v \cdot A \cdot z' \cdot \gamma(V^+) \cdot f(V^+) \qquad (3.3.9)$$

During SIMS analysis, all parameters on the right hand side of equation 3.3.9, except C^v, are assumed to remain constant, so that the measured secondary ion intensity, $I_s^m\ (V^+)$, is quantifiable on the assumption that it varies linearly with the concentration of V, C^v. In practice, however, some of the other parameters can also vary, thus complicating the quantification.

The useful ion yield , Y, is an important quantity that is commonly used. Y is defined as the ratio of the number of secondary ions detected to the number of particles sputtered from the detected area, for a particular species. Therefore, the useful yield of V^+, Y (V^+), can be expressed as,

$$Y(V^+) = \frac{I_s^m(V^+)}{I_s^T \cdot c(V)} \qquad (3.3.10)$$

combining equations 3.3.1, 3.3.5, and 3.3.10 gives,

$$Y(V^+) = \gamma\,(V^+)\, f\,(V^+) \qquad (3.3.11)$$

Thus, the useful yield is simply a product of the ionisation probability and the instrumental transmission factor of the secondary ion. The useful yield has no dimension.

3.3.7. Calibration

Direct calibration of the depth scale is usually done by measuring the depth of the crater after the analysis and calculating the depth scale on the assumption that the sputter rate is constant during analysis. Stylus techniques are generally used to determine the crater depth after removing the sample from the main chamber. An indirect method is to measure sputter rate, used in a case where crater is too small to find.

Due to the concentration variability of ion yields, absolute quantification is made rather difficult in SIMS analysis. The intensity of a secondary ion signal for a given measured species I_s^m, is given by the general expression in equation 3.3.5.

$$I_s^m\,(V^+) = I_p \cdot S \cdot \gamma\,(V^+) \cdot c(V) \cdot f(V^+)$$

where I_p is the SIMS primary ion current, S is the sputter yield, γ is the ionisation yield, c(V) is the fractional concentration of V in the matrix, *f* an instrumental factor and V is the concentration of the species of interest. This makes quantification dependent upon species, matrix and the type of primary ion beam used. For example the yield of positive secondary ions is enhanced by the use of oxygen primary beams and that for negative secondary ions by ceasium primary beams [102]. Consequently, at present, the majority of quantitative analysis is achieved by the use of standard samples. These are ideally produced by implanting known species at some desirable depth.

Further difficulties arises when examining polycrystalline samples such as the ZnO varistors with segregated secondary phases. Under these circumstances, ratioing the signals from the matrix (ZnO) with the element additive (Co, Mn,) of a reference (without any segregation) sample to the sample under analysis can provide a valid first approximation (discussed in Chapter 5 section 5.4.2).

3.4. IS (Impedance Spectroscopy)

3.4.1. Overview of (IS)

The impedance spectroscopy (IS) technique can be used to investigate the dynamics of the bound or mobile charge in the bulk or interfacial regions of any kind of solid or liquid material: ionic, semiconducting, mixed electronic-ionic, and even insulators (dielectric) [71].

The measurement of bulk and grain boundary resistance in electro-ceramics can not be determined by simply using either: the two probe d.c., four probe d.c., or even fixed frequency a.c., analysis techniques. The problem with the two probe d.c. technique is that the measured resistance is due to the sample as well as the electrode materials. Although this problem can be resolved by four probe d.c. methods, it will only work for single crystals. For polycrystalline ceramic samples, however, the measured value is the sum of the bulk and the grain boundary resistances, such that:

$$Rdc = Rb + Rgb \qquad (3.4\text{-}1)$$

In equation (3.4-1) the symbols Rdc, Rb and Rgb, represent the measured d.c., the bulk and the grain boundary resistances, respectively. The grain boundary resistance is very sensitive to parameters such as impurity content and heat treatment of the ceramics and may vary considerably between materials of the same composition. The fixed frequency a.c., analysis technique is often used to overcome electrode effects and may also give correct values of the d.c. resistance, as defined by equation (3.4-1), but only for a certain temperature range [90]. At lower temperatures, however, the fixed frequency a.c. measurement diverges significantly from the true d.c. value. This was realised by **Schouler** *et al* in 1973 [92].

Bauerle [82], in 1969, noted the limitation of these three measurement techniques to produce satisfactory conductivity data for polycrystalline solid electrolytes and investigated the possibility of using complex impedance measurements instead. By experimenting with pure and impure polycrystalline materials, with a variety of different electrodes this method of analysis was found to be suitable to study separately the bulk, grain boundary and electrode effects. Since then the development of this technique has extended its applications in many other fields [71].

The principle of the IS method is to apply an electrical stimulus (a known a.c voltage or current) across a sample and to observe the response (the resulting current or voltage);

and the phase difference between the current and the voltage can be worked out by an instrument known as the frequency response analyser (FRA).

When a sinusoidal voltage, V(t), is applied across the specimen it causes a sinusoidal current, I(t), to flow. For a linear system, V(t) and I(t) are given by:

$$V(t) = V_o \text{ Sin } \omega t \qquad (3.4\text{-}2)$$

$$I(t) = I_o \text{ Sin } (\omega t+\phi) \qquad (3.4\text{-}3)$$

Where V(t) and I(t) are the voltage and current at time t, V_o and I_o are the maximum voltage and current values, ω is the angular frequency of the signal, given by $\omega = 2\pi f$, where f is the frequency, and ϕ is the phase angle by which the current leads the voltage.

The two phasors can be defined in terms of the complex numbers V and I, such that:

$$V = V_o \text{ Cos}\omega t + jV_o \text{ Sin } \omega t$$

$$V = V_o \, e^{j\omega t} \qquad (3.4\text{-}4)$$

$$I = I_o \text{ Cos } (\omega t+\phi) + jI_o \text{ Sin } (\omega t+\phi)$$

$$I = I_o \, e^{j(\omega t+\phi)} \qquad (3.4\text{-}5)$$

The complex impedance is defined as the ratio V/I, so that :

$$Z = (V_o \, e^{j\omega t})/I_o \, e^{j(\omega t+\phi)} \qquad (3.4\text{-}6)$$

$$Z = |Z| \, e^{-j\phi} \qquad (3.4\text{-}7)$$

where $|Z| = V_o/I_o$.

Hence it is seen that the impedance depends only upon the relative magnitude of the maximum voltage and current and the phase angle between them.

It has been shown [90,94] that a complex plane plot of impedance (Z) will describe a semicircle (Fig. 3.4.1). At the apex of the semi-circle, $|Z'| = |Z''|$ and we thus have:

$$\omega_c = (RC)^{-1} \qquad (3.4\text{-}8)$$

Where ω_c = the frequency at the apex of the semi-circle and is known as the time constant of the circuit. Impedance usually has both resistive and reactive (capacitive/inductive) components, both of which must be determined. One of the ways of achieving this is to apply an alternating voltage across a sample and a standard resistor which are in series. The in-and out-of-phase components of the voltage across the sample are then measured. Dividing these components by the magnitude of the current gives the resistive and reactive components of the impedance. These measurements are repeated as a step-wise function of frequency. Different regions of a ceramic are characterised by a resistance and a capacitance, usually placed in parallel.

The characteristic relaxation time or time constant, τ, of each "parallel RC element" is given by the product of R and C [68].

$$\tau = R\,C \qquad (3.4\text{-}9)$$

$$\omega_{max}\,C\,R = 1 \qquad (3.4\text{-}10)$$

The inter-relationship between equivalent circuits and sample microstructure can be provided by first outlining the main features of the response of a simple circuit to an A.C. signal. This relationship is presented in Appendix B.

In the frequency domain, RC elements are separable due to the relation shown in Equation (3.4-9) which holds at the frequency of maximum loss ω (max) in the impedance spectrum. From the impedance spectrum, it is therefore usually possible to identify different RC elements and assign them to appropriate regions of the sample.

When the impedance, Z, is measured over a range of frequencies, it is found to describe a locus in the complex plane, which is characteristic of the particular region (bulk grain, grain boundary, electrode interface) of the sample under investigation. Detailed information can be obtained from this locus, if it can be modelled by an electrical circuit giving a similar response in the complex plane. This is then known as the equivalent circuit as shown in Fig. 3.4.1 (b).

The general form of a complex impedance plot for a ceramic solid electrolyte is shown in Fig. 3.4.2. The high frequency arc is attributed to the bulk response of the sample which is governed by the permittivity and resistivity of the material and the overall sample dimensions. The low frequency arc corresponds to the electrodes on the sample. Between the high and the low frequency arcs is the grain boundary semi-circle which is characterised by its own resistivity. It is possible to distinguish between these arcs by observing how they react to changes in other parameters. For example, the electrode

characteristics will be very sensitive to the amplitude of the applied voltage. The bulk properties will be sensitive to the sample geometry whilst the grain boundaries will be sensitive to factors such as the grain size. By identifying the individual semi-circles in this way it is thus possible to find the electrical resistance of each region from the real axis intercepts [91,92]. It is important to note that an impedance spectrum of the circuit in Fig. 3.4.2 (b), will only unveil three distinct semi-circles if the time constants of the individual Voigt elements are sufficiently separated.

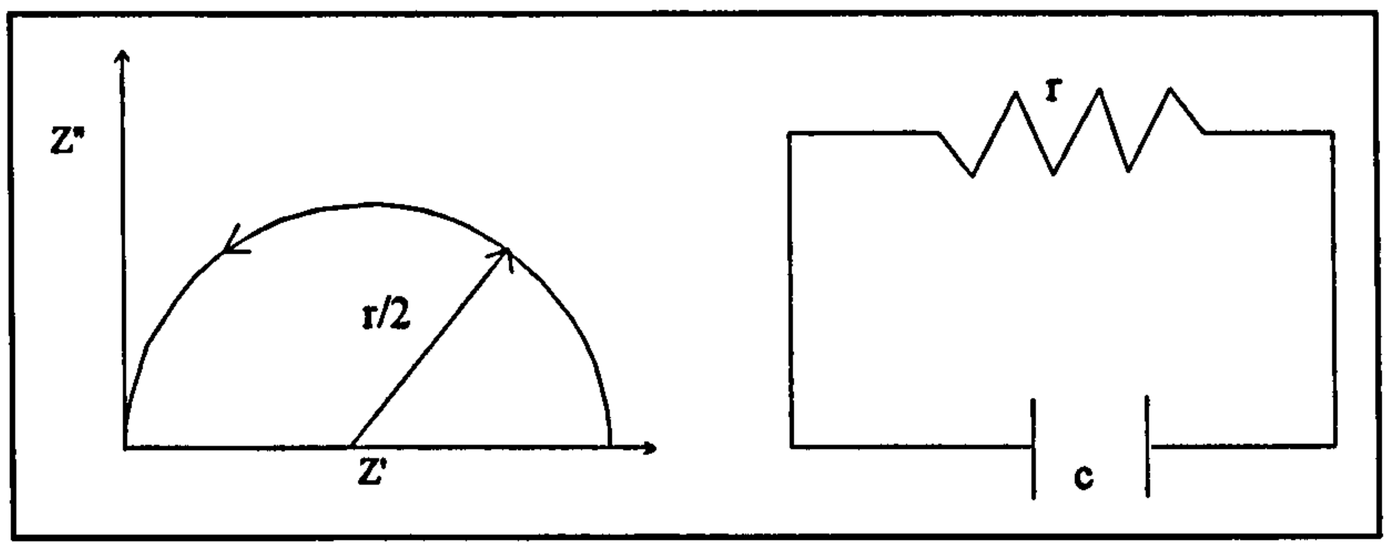


Fig. 3.4.1. (a) Complex impedance plot for the circuit shown in (b). The arrow indicates increasing frequency. (b) Circuit diagram of a so-called Voigt element comprising of a resistor and capacitor in parallel.

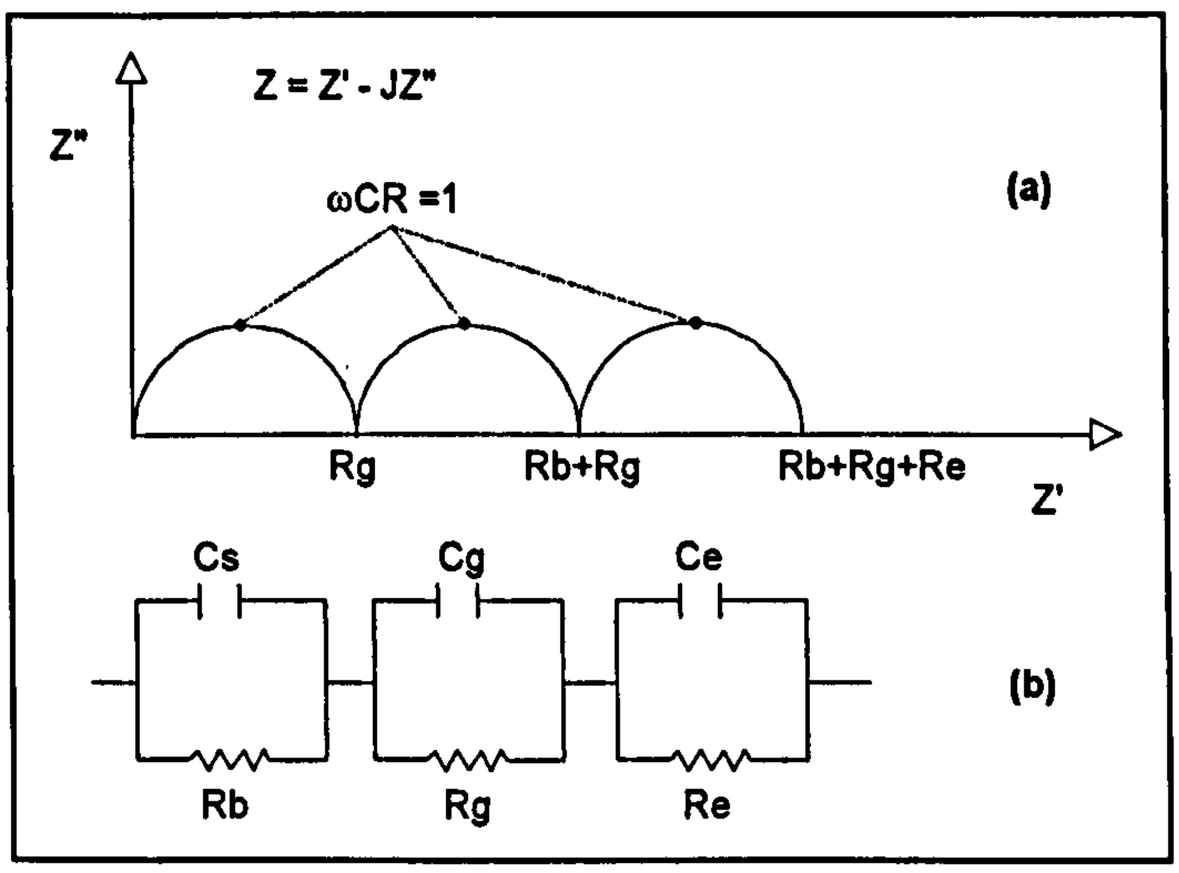


Fig. 3.4.2. (a) Schematic complex impedance plot of a Zirconia type solid electrolyte. (b) An equivalent circuit giving the response of (a) [92].

Identification of semi-circles is helped by applying two rules of thumb [90]:

(1) As the temperature of the measurement is increased, the "observable range" shifts from the left to the right of the complete impedance plot. Thus, the bulk

properties are more easily observed at low temperatures and electrode characteristics at high temperatures.

(2) The associated capacitance with the three semi-circles are, of the order of pico-nano-and-micro Farads ($\approx 10^{-12}$ F, $\approx 10^{-9}$ F and $\approx 10^{-6}$ F), for the bulk, grain boundary and electrode semi-circle respectively. Further range of these values are presented in table 3.4.1.

Alternatively, the impedance of a series of samples of different thicknesses and varying electrode areas may be measured [82].

The impedance Z, of the sample is measured as a function of frequency at different temperatures. The properties of the electrode-material system are assumed to be time-invariant. Modern instrumentation allows the measurement of the impedance over a wide range of the frequency spectrum (10^{-2} to 10^{7} Hz.) and the data acquired at different frequencies can be plotted in an Argand diagram also known as "complex impedance plot" (CIP). The form of such a plot is then modelled using an equivalent circuit, usually comprised of a combination of resistors and capacitors in parallel [71] (Fig. 3.4.2b).

Impedance data are presented in the form of imaginary, Z" (capacitive) against real, Z' (resistive) impedance. Each parallel RC element gives rise to a semicircle from which the components R and C values may be extracted. R values are obtained, from the intercepts on the Z' axis, C values are obtained by applying Equation (3.4-10) to the frequency at the maximum of each semicircle. These values for the capacitance and the corresponding resistances can be assigned to regions of the sample. The assignment is based on the magnitudes of the capacitance (Table 3.4.1). Identification of semi-circles is not always straightforward. In a given measurement system with a limited frequency range, the three semi-circles are not usually present in the same impedance plot. Sometimes it becomes difficult to determine which response has given rise to an observed semi-circle.

For a parallel plate capacitance with area A, separation l between the plates and a medium of permittivity ε' between the plates, the capacitance is given by:

$$C = \varepsilon' \varepsilon_o A/l \qquad (3.4\text{-}11)$$

Where ε_o is the permittivity of free space, 8.854×10^{-14} F cm^{-1}. .For a material with unit cell constant (i.e. $l/A = 1\ cm^{-1}$) and a typical permittivity of ~ 10, a capacitance value of ~1×10^{-12} F is expected. Thus, this is a typical value for the bulk capacitance of a sample. These interpretations can provide useful information about the ceramic samples:

(a) To indicate whether the overall resistance of a material is dominated by bulk or grain boundary components.

(b) To assess the quality and electrical homogeneity of an electroceramic, since there is generally a link between sintering/microstructure and AC response.

(c) To measure the values of the component resistances and capacitance.

The temperature dependence of resistance is usually plotted in Arrhenius format [$\log_{10}\sigma$ (T) vs 1000/T]. By analysis of the specimen at several temperatures the activation energy and conductivity at higher temperatures can be found, using the relationship:

$\sigma(T) = \sigma_o \exp(-E_a/kT)$
T = absolute temperature
σ_o = pre-exponential factor
E_a = activation energy (eV)
k = Boltzmann's constant (8.61735×10^{-5} eV)

Taking natural logarithms gives the linear equation:

$$\ln \sigma(T) = \ln(\sigma_o) - E_a/kT \qquad (3.4\text{-}12)$$

Therefore, plotting $\ln \sigma$ (T) vs 1/T gives a straight line of slope E_a/k and intercept on the Y axis = σ_o

Table 3.4.1. Magnitude of Capacitance vs Phenomenon responsible in IS.

Capacitance [F]	Phenomenon Responsible
$\approx10^{-12}$	bulk
$\approx10^{-11}$	minor, second phase
$\approx10^{-11}$ to 10^{-8}	grain boundary
$\approx10^{-10}$ to 10^{-9}	bulk ferroelectric
$\approx10^{-9}$ to 10^{-7}	surface layer
$\approx10^{-7}$ to 10^{-5}	sample-electrode interface
$\approx10^{-4}$	electrochemical reactions

3.4.1.1. Brick layer model

The brick layer model [71, 91] is perhaps the simplest representation of the microstructure of a ceramic. This is illustrated in Fig. 3.4.3, where the cubes represent the grains of the ceramic separated by flat grain boundaries. Assuming no curvature of the current paths, current will either flow along the grain boundaries only, or through grains and across grain boundaries. Accordingly, there are two limiting cases for the description of the current flow which are:

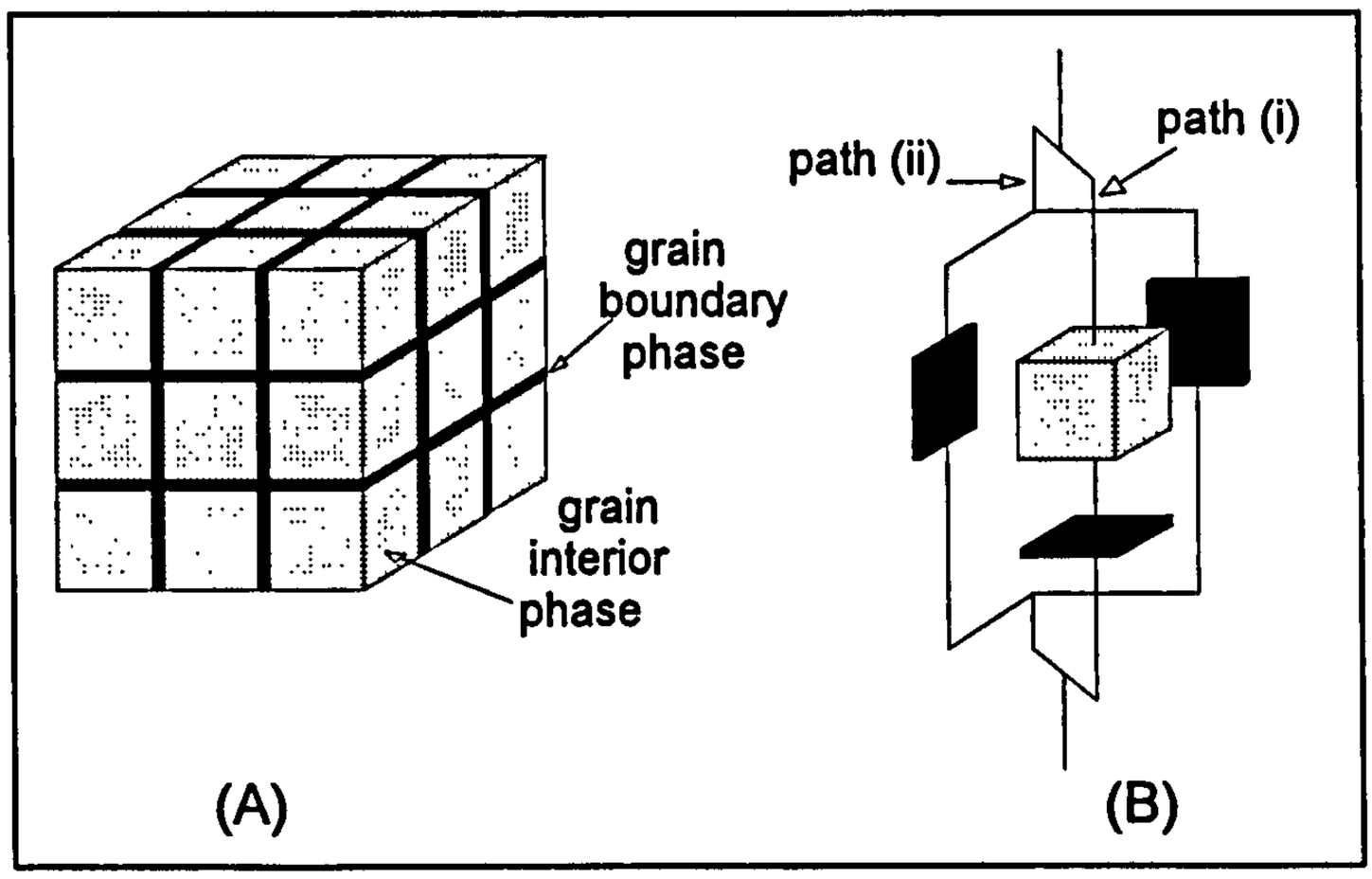


Fig.3.4.3. Brick layer model for a two-phase ceramic: (a) Overall view, showing array of cubic grains, separated by flat boundaries. (b) Exploded view of a single cell, showing parallel electrical paths: (i) through grains and grain boundaries, and (ii) along grain boundaries [71].

(a) $\sigma_g >> \sigma_{gb.}$ In this case the grain and grain boundary regions are best represented as a series combination of Voigt elements, leading to a semi-circle for both the grain and grain boundaries in the complex impedance plot (CIP).

(b) $\sigma_{gb} >> \sigma_{g.}$ In this case the grain boundary and grain regions are best represented as a a parallel combination of Voigt elements and only one semi-circle will show up in the CIP. It is thus possible on the basis of (a) and (b) to distinguish highly conducting, from poorly conducting grain boundaries using IS.

Further correlation between microstructure and IS analysis can be seen by virtue of the fact that the capacitance of the grain arc will be determined by the overall geometry of the sample and its dielectric properties. Hence, for the sample with dimension length =

L, and cross section area = A, the bulk arc will be characterised by a capacitance of the form:

$$C=\epsilon A/l \qquad (3.4\text{-}13)$$

Where ϵ is the permittivity of the material. In terms of the brick layer model, the grain boundary capacitance is given by,

$$C_{gb} = (\epsilon_{gb}A/L)(d_g/d_{gb}) \qquad (3.4\text{-}14)$$

Where ϵ is the permittivity of the grain boundaries, and d_g , d_{gb} are the thicknesses of the grain and grain boundary regions respectively. From equations (3.4.13) and (3.4.14) it is possible to relate IS measurement with the microstructural properties of the grain and intergrain regions in a ceramic.

The IS technique is suitable for characterisation of heterogeneous materials such as ceramics with many phases, and in particular the inherent electrical properties attributed to the elemental segregation at the grain boundaries. The bulk ceramic with its various microscopic regions such as the grain boundary interface, electrode interface, etc., can be investigated by their response to the particular frequency corresponding to their relaxation processes. Individual contributions of these features can be determined by virtue of their different relaxation time constants. **Irvine**. *et al.*,[68] (1990) have used Impedance Spectroscopy for the characterisation of Electroceramics. They have confirmed that AC impedance measurements can be made over a wide range of frequencies and the different regions of the material are characterised according to their electrical relaxation times or time constants. **Smith** et al [89] (1989) used IS to study the effect of MgO addition on a ZnO varistor composition. MgO is a grain growth inhibitor which in the case of ZnO based varistors, significantly increases the breakdown voltage per unit length. It was found that in a very highly resistive ($R> 10^{14}\ \Omega$) sample, the impedance spectra only have the beginning of an arc of a circle. At low frequency the current does not flow in a straight line from one electrode to the other. It has to go through tortuous and constricted paths to avoid locally any regions of high resistivity. At high frequency the impedance of the sample, approximately equals to $1/C\omega$, and is small. Hence, routes that are too resistive at low frequencies are short circuited by the associated capacitance. The alternating current then flows evenly through the entire ceramic at high frequency.

3.4.2. Experimental Apparatus

The IS technique was used here to study the bulk grain boundary properties of the pure and doped ZnO ceramics prepared under a variety of different conditions. The frequency response analyser was of the type: HP. 4192A LF (5Hz to 13 MHz), interfaced with a Hewlett Packard (HP) 9153C, 9000, computer and a Carbolite furnace (Temp. range up to 1200°C). The range and number of data points is controlled by the computer which also controls the temperature of the sample in the furnace to within +/- one Kelvin. The function of this system is based on the Auto-Balance bridge, which performs the vector-voltage-current ratio measurements. The experimental apparatus is illustrated in Fig. 3.4.4.

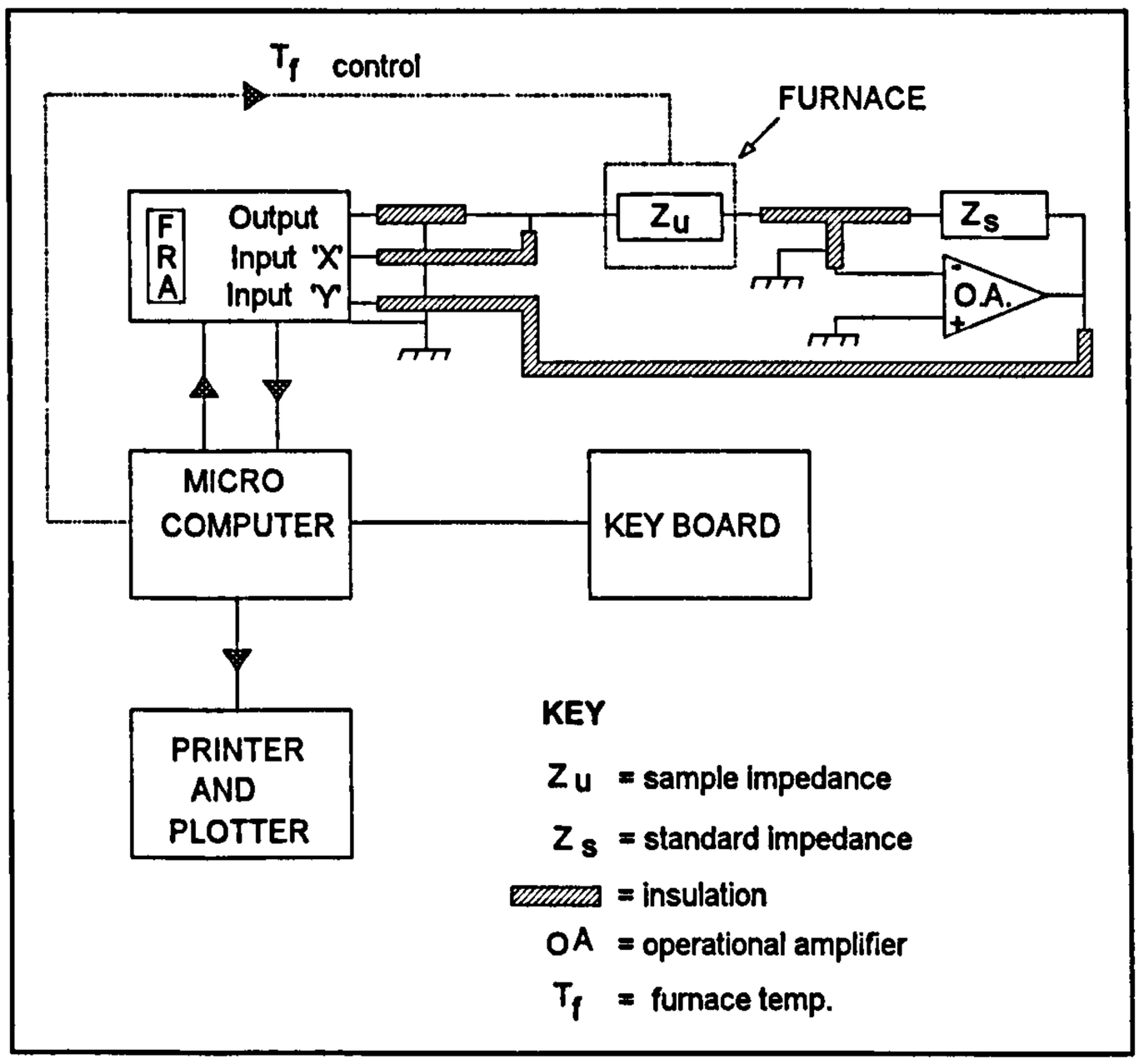


Fig.3.4.4. Schematics of the experimental apparatus used to obtain the impedance spectra of ZnO ceramics at various temperatures.

The FRA measures the in phase and 90° out of phase components of the voltage applied to the terminals "X" and "Y" which, together with the measurement frequency, are fed to the computer as complex numbers. The impedance of the sample is then given by,

$$Z_u = -(V_x/V_y)Z_s$$

Z_u, Z_s are the sample and standard impedance respectively, and V_x , V_y, are the voltages measured at terminals "X" and "Y". The samples are in the form of cylindrical sintered pellets, with painted silver electrodes on the circular faces. The sample is placed in the

furnace in the holder illustrated in Fig. 3.4.5, where it is held firmly between two platinum contacts pressed against the electrodes.

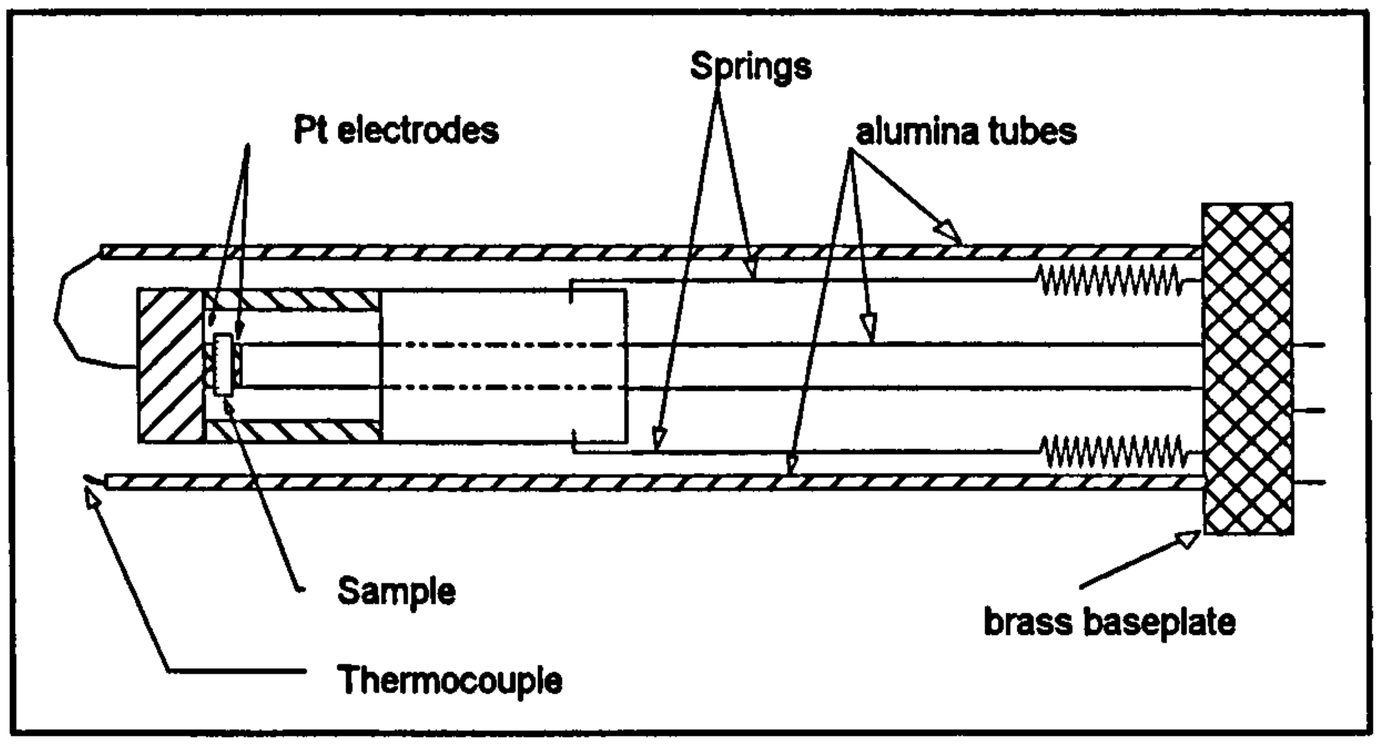


Fig.3.4.5. Schematic of the sample holder used in the furnace shown in figure 3.4.4.

3.5. X-ray diffraction (XRD) Method

3.5.1. Overview of (XRD)

XRD is a traditional method and only a brief introduction is presented here.

The principle of the X-ray diffraction technique is based upon the relationship between the wavelength (λ) of the X-ray beam, the angle of diffraction (θ) and the distance between each set of atomic planes of the crystal lattice, d. This is given by the Bragg condition:

$$n\lambda = 2d \sin\theta \qquad (3.5.1)$$

where n represents the order of the diffraction.

The geometric relations are shown in Fig. 3.5.1. For the ray reflected by the second plane of the crystal, the distance CBD represents the increased path length travelled by that ray compared to one reflected from the surface. Angle CAB and BAD are both equal to θ.

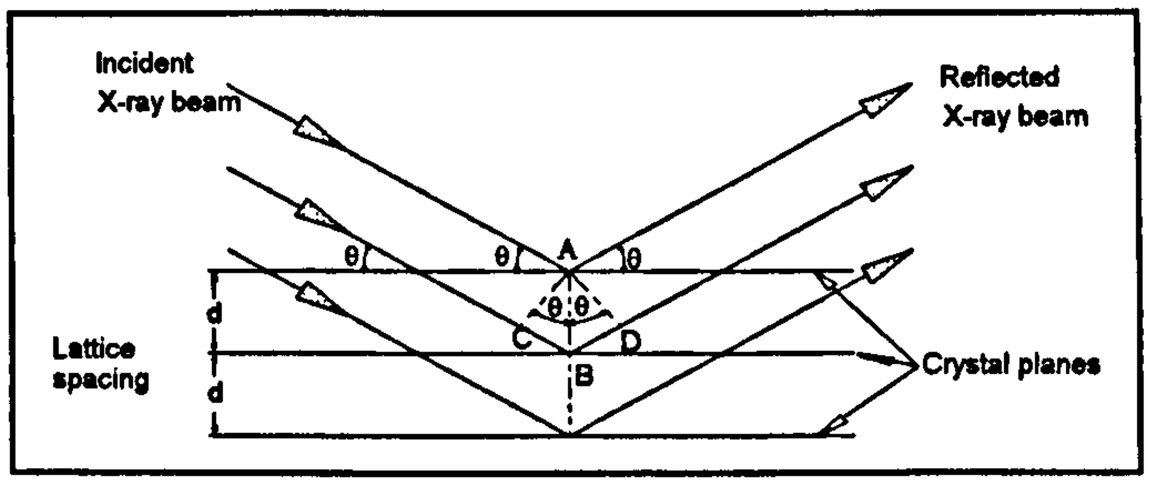


Fig. 3.5.1. Diffraction of X-rays from a set of crystal planes.

Hence :

$$CB = BD = AB \sin\theta. \qquad (3.5.2)$$

The XRD technique was used to study the crystal structure of the etched residue of the ZnO varistor. Analysis was undertaken on Siemens instrument at The National Physical Laboratory (NPL) Teddington. A piece of 30 mm diameter and 5mm thick ZnO varistor (Sintered at 1300°C) was dissolved in perchloric acid ($HClO_3$). The residue was filtered, dried in a dessicator and then extracted for analysis. The resultant sample (powder like) was mounted on to a single crystal Si holder using alcohol as a wetting medium.

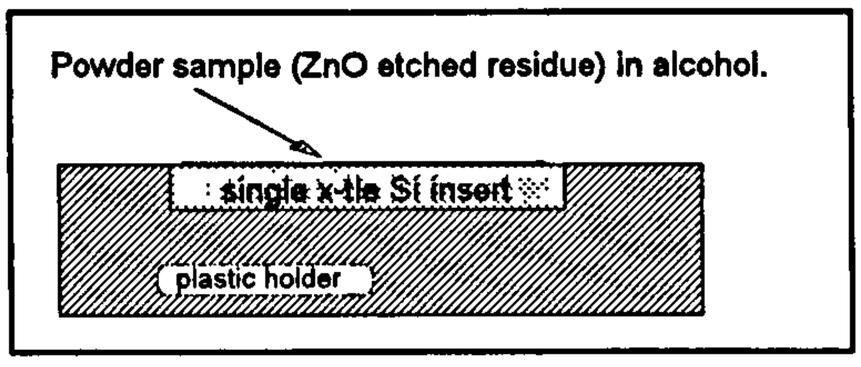


Fig. 3.5.2. The schematic of an XRD sample holder

The reader is refereed to a review by **Merritt** *et al.*[106], for detailed information on the instrumentation of XRD technique.

3.6. I:V Measurements

The schematic for the I:V measurements is shown in Fig. 3.6.1 A Hewlet Packard power source (Hp 6030A) was used to apply a DC load (0-200V and 0.17A) with Voltage Current sensing meters. The measurement was facilitated by a PC micro computer, programmed to apply a suitable voltage to the sample in increments of 5 volts every 2 seconds and measure the output of the resultant I:V characteristics. The resultant current readings were stored on computer for subsequent analysis.

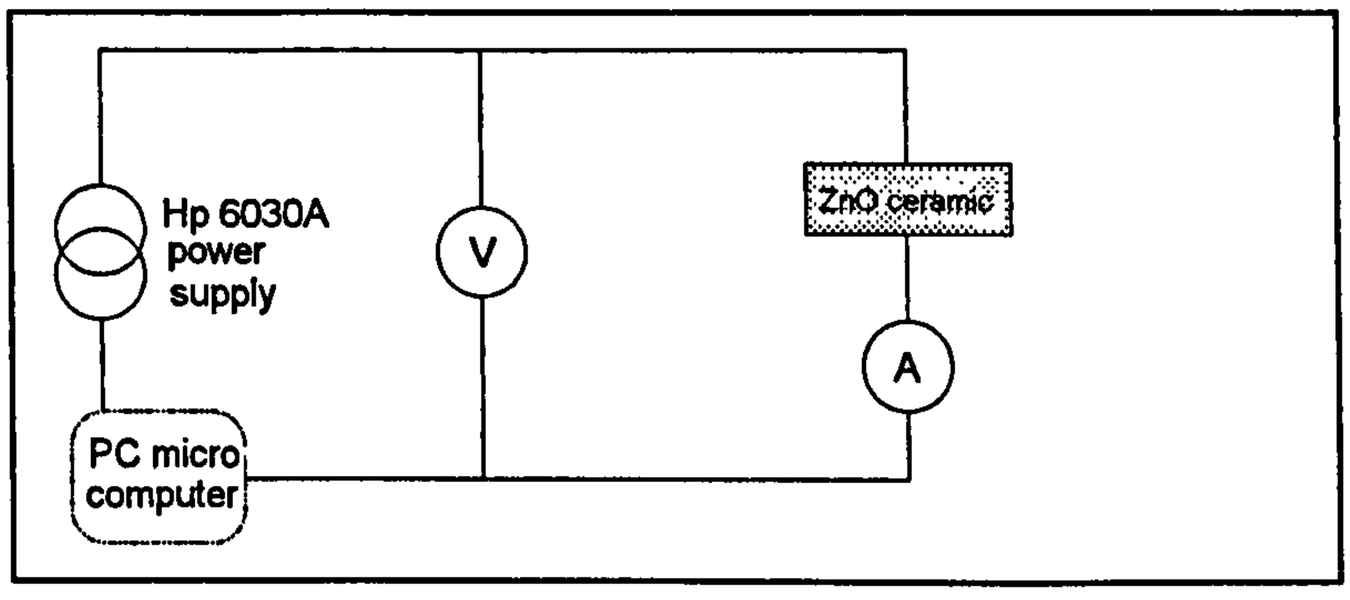


Fig. 3.6.1. The schematic of an I:V measurement.

Chapter 4

Experimental Procedure

This chapter describes the preparation of ZnO varistor samples and the procedures for their analyses using experimental techniques described in Chapter 3.

4.1. Sample Preparation

4.1.1. Preparation of powders

The materials used in this study were made by solid state reaction from their constituent oxides. Fig.4.1.1 shows the schematic of the procedure used each time a batch of samples was synthesised. Varistor compositions based on ZnO containing a number of additives (at a level of approximately 0.5 Mol.%) were synthesised. The oxides: Bi_2O_3, Sb_2O_3, MnO_2, Co_3O_4, and Cr_2O_3 were used as additives into ZnO powders (all obtained from Aldrich chemical company Ltd., as 99.999% pure). Hence a number of batches of compositions were prepared with single, double and up to an addition of five metal oxides, as shown below (mol.% given).

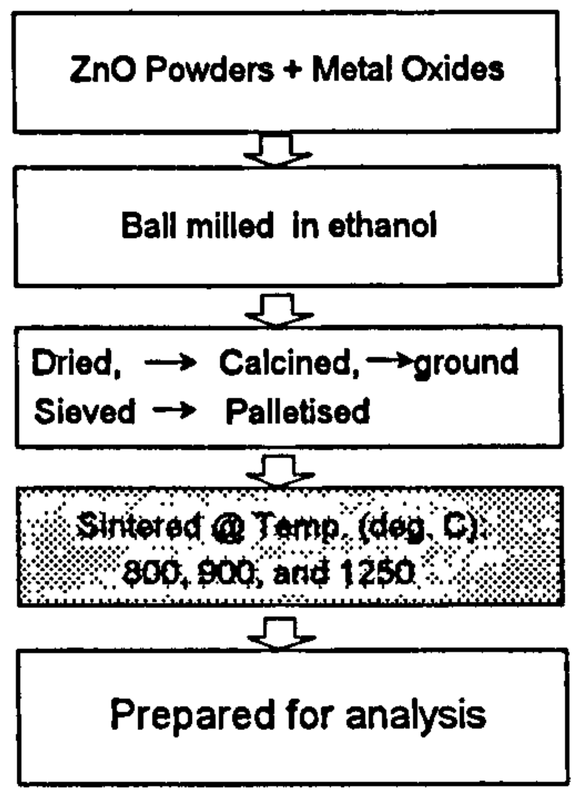


Fig. 4.1.1. Flow diagram for the sample preparation of ZnO varistors.

1. 100 ZnO
2. 99.5 ZnO + 0.5 Bi_2O_3
3. 99.0 ZnO + 0.5 Bi_2O_3 + 0.5 Co_3O_4
4. 98.5 ZnO + 0.5 Bi_2O_3 + 0.5 Co_3O_4 + 0.5 MnO_2
5. 98.0 ZnO + 0.5 Bi_2O_3 + 0.5 Co_3O_4 + 0.5 MnO_2 + 0.5 Sb_2O_3
6. 97.5 ZnO + 0.5 Bi_2O_3 + 0.5 Co_3O_4 + 0.5 MnO_2 + 0.5 Sb_2O_3 + 0.5 Cr_2O_3
7. 99.0 ZnO + 0.5 Bi_2O_3 + 0.5 Sb_2O_3

Below is an example of the calculations required to make a 30g batch of powder mixture:-

One mole of ZnO = 81.37g. Hence 30g of ZnO = 0.36860 mole.

e.g. for 0.5 mol.% of Bi_2O_3 additive in batch 2 above, requires:-

$$\frac{0.36860 \text{ (mole of ZnO)} \times 0.5 \text{ (required mol.\% of Bi)} \times 465.96 \text{ (M.W of } Bi_2O_3)}{100}$$

$$\Rightarrow 0.85895\text{g } (Bi_2O_3).$$

Calculations for other compounds were expediently performed on this basis. Table 4.1.1 shows the theoretical amount of ZnO and additives required to synthesise batches 2-7. Table 4.1.2 shows the experimental amounts of ZnO and additives as weighed out when synthesising sample batches 2-7. The calculated figures in Table 4.1.2 corresponds very closely (within ± 0.03%) to the experimental ones in Table 4.1.1.

Table 4.1.1 Calculated Mole % of compounds of additives

ZnO mole (%)	ZnO mole used	ZnO Wt. (g)	Compounds	M.W (g)	colour	wt of 1.843e-3 mole (g)
100.0000	0.3686	30.0000	ZnO	81.3700	White	
99.5000	0.3668	29.8500	Bi_2O_3	465.9600	Yellow	0.8589
99.0000	0.3650	29.7000	Co_3O_4	240.8000	Black	0.4439
98.5000	0.3631	29.5500	MnO_2	86.94000	Black	0.1603
98.0000	0.3613	29.4000	Sb_2O_3	291.4970	White	0.5373
97.5000	0.3595	29.2500	Cr_2O_3	151.9900	Green	0.2802

Table 4.1.2 Experimental weight of compounds used to synthesise sample batches 1-6

Sample batch	ZnO Wt (g)	Bi_2O_3	Co_3O_4	MnO_2	Sb_2O_3,	Cr_2O_3	Sintered Colour
1	30						Cream
2	29.8493	0.8584					Yellow
3	29.8500	0.8589	0.4438				Green
4	29.5503	0.8590	0.4438	0.1606			Black
5	29.4005	0.8587	0.4439	0.1601	0.5376		Black
6	29.2496	0.8590	0.4437	0.1598	0.5375	0.2802	Black
7	29.6995	0.8589			0.5371		Yellow

Additional batches (8-10 in Table 1.4.3) were prepared in a similar manner. Preparation of the ZnO bi-crystal is discussed in section 4.1.3.

4.1.2. Formation of varistor Pellets

The constituent powders were weighed out accurately (with a possible error of less then ±0.05%), using an analytical balance (Tables 4.1.1 and 4.1.2). Powders were then introduced in to a cylindrical plastic sample container (a bottle of 0.5 litre capacity). To this, yttria stabilised zirconia (YSZ) grinding medium (ball size 0.5 inches in diameter) was introduced with about 150 ml. ethanol. The container was then sealed and assembled on to the rotating rollers for the intended milling (for about 5 h). The resultant mixed slurry was dried at about 100°C and calcined at 700°C for 5h. At this stage of the preparation, the powdered sample was of a light creamy coloration, presumably due to the additive Bi_2O_3.

The mixed powders were ground using agate mortar and pestle, sieved (106μm sieve) and pelletised into a cylindrical pellets in a 13 mm diameter hardened steel die under a uni-axial pressure of about 75 MPa., for about 30 seconds (Fig. 4.1.2).

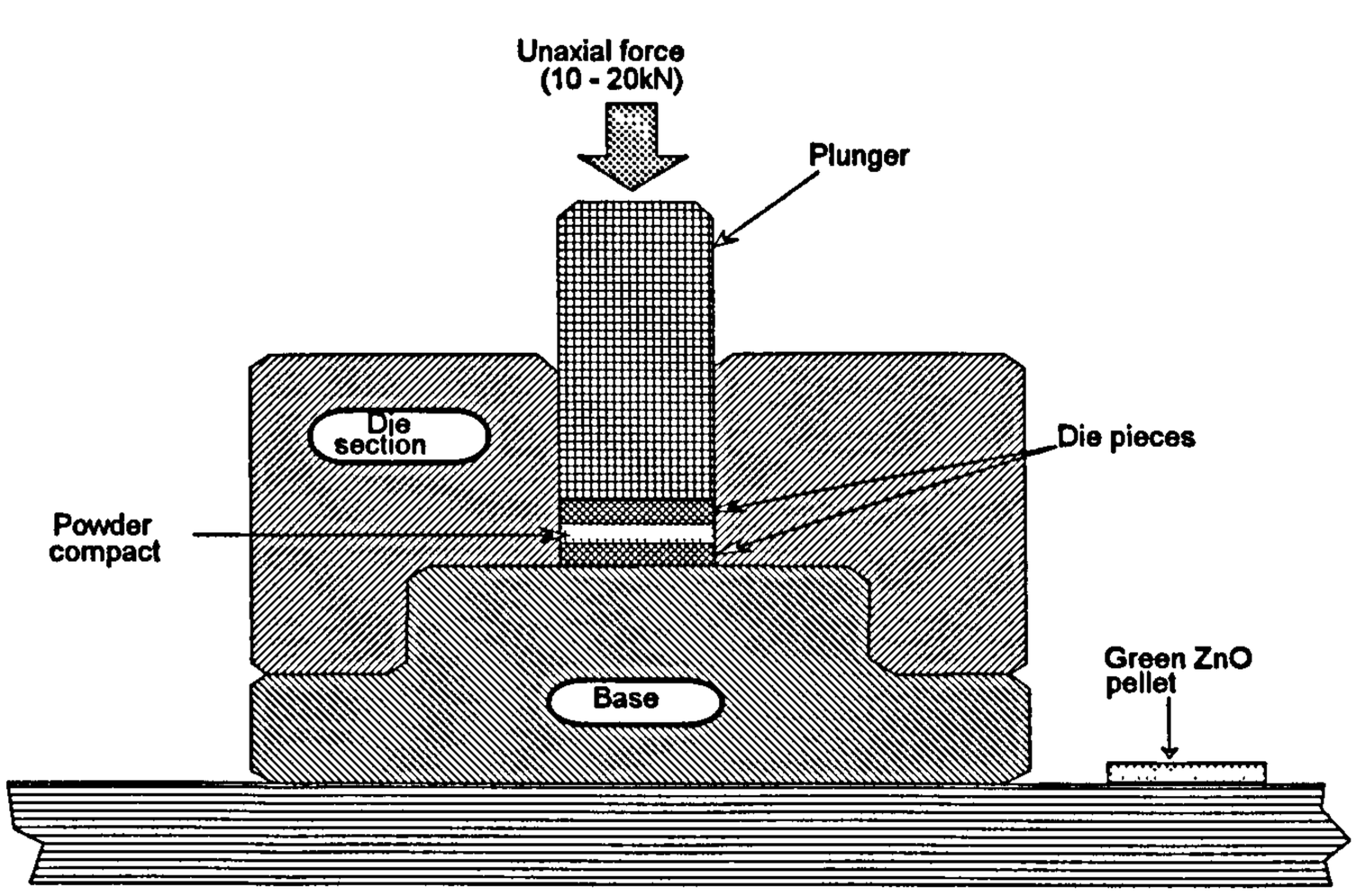


Fig. 4.1.2. Schematic of the pellet die used for making ceramic samples.

The sample pellet thus produced had a thickness of about 1.5 mm., green density of 3.0 g/cm^3, and was sintered at 1250°C, for 3h, in a furnace programmed to a heating and cooling ramp of 4°C/min (Fig.4.1.3). The sintered pellet had a diameter of 10.6 mm, with a density of 5.0 to 5.2 g/cm^3 and was of a darker greenish coloration. From each

batch (1-7), 12 pellets were made. From these 12 pellets, 4 pellets of each sample were sintered at 800°C, 1250°C and rapidly cooled from 1250°C. The densities of the sintered pellets were calculated from their weight and dimensions. In all cases the densities were calculated from the measurement made on four samples of the same type and an average value was taken. Ceramic compacts were in the range 89 to 96%. of the theoretical density [25] of pure ZnO (5.61 g. cm^{-3}). For a given batch, variation in the density from sample to sample was found to be within ± 3%.

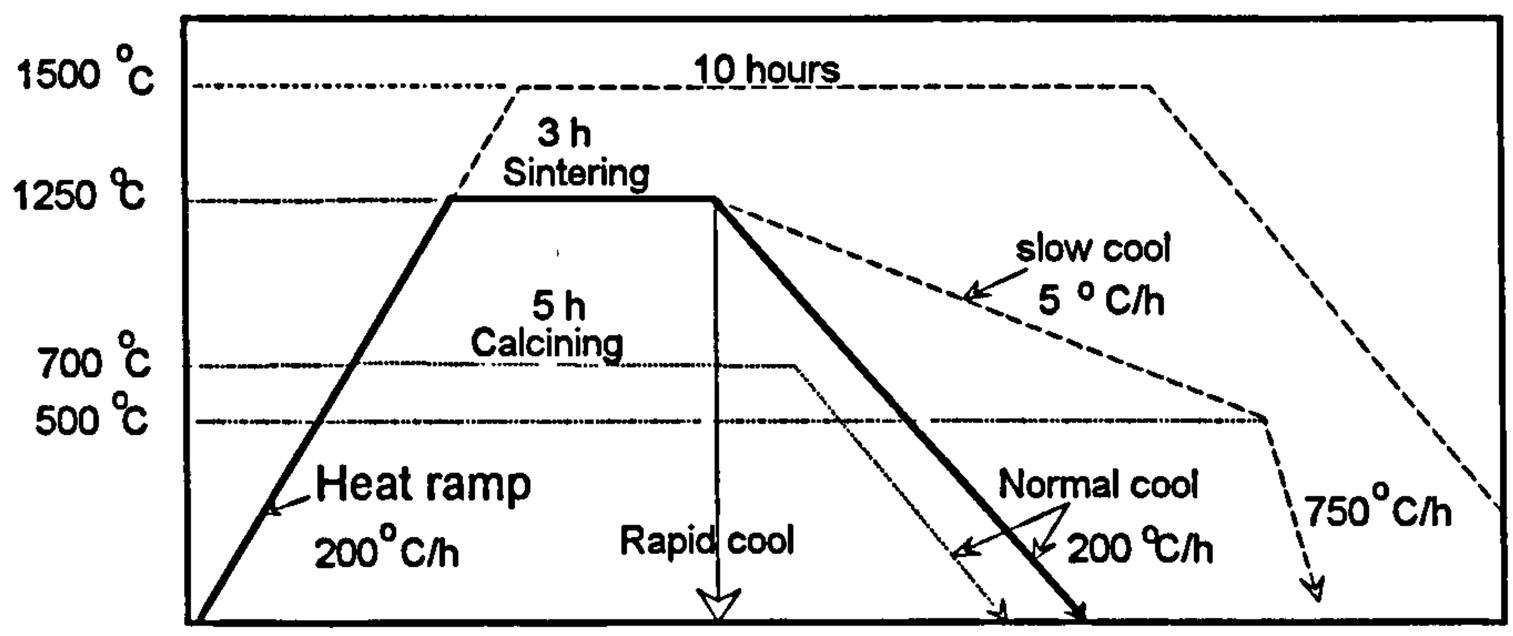


Fig. 4.1.3. Heating and cooling ramp used during the sintering of ZnO varistors.

Many different compositions were synthesised (as shown in Tables 4.1.2 and Table 4.1.3) with varied sintering temperatures (800°C, 900°C. 1250°C and 1300°C) to study the interrelated effect of dopants and sintering temperatures on the microstructure and the I:V electrical characteristics. In one of the above preparations the samples were rapidly cooled (batch No 8, Table 4.1.3) from 1200°C, by quenching in water. In this case, samples were taken out of the furnace and dropped into cold water. A varistor sample was slowly cooled (5°C/h) from 1200°C to promote the pyrochlore (**PY**) phase in the microstructure (batch No.9, Table 4.1.3). A sample was also etched in perchloric acid in order to reveal phases at the triple points (batch No.11, Table 4.1.3). This was intended to complement initial observations of the surface analysis. Additional samples from commercial source (batches 13-16) were obtained for comparative analysis.

4.1.3. Preparation of bi-crystal of ZnO

A bi-crystal of ZnO was synthesised by joining two single crystals of ZnO. The single crystals were hexagonal needles with a diameter of ≈ 3 mm and length of 10 mm and were obtained from Dr. J. T. Czernuszka of the Department of Materials, University of Oxford, as vapour-phase grown hexagonal prisms. Initial preparation included polishing

down a prism face along the c-axis (Fig.4.1.4 A), using a silicon carbide abrasive of 1200 mesh going to finer powders down to 1/4 μm diamond spray.

A coat of Bi_2O_3 mixed in ethanol was applied on to the polished surfaces of the single crystal prior to their joining (Fig.4.1.4 B). Pure ZnO powders were used to cover around the sample to prevent evaporation of Bi_2O_3 at high temperatures. The sintering of the bi-crystal was assisted by placing a small mass (0.5kg) on to the sandwich (ZnO-Bi_2O_3 -ZnO) situated in to a pre-machined slot (3.5 mm wide x 3 mm deep) on a flat piece of alumina. This was followed by sintering at 1500°C for 10h. Finally a number of bi-crystal samples were produced by cutting a joined crystal perpendicular to its c-axis with a wire saw (Fig.4.1.4 C).

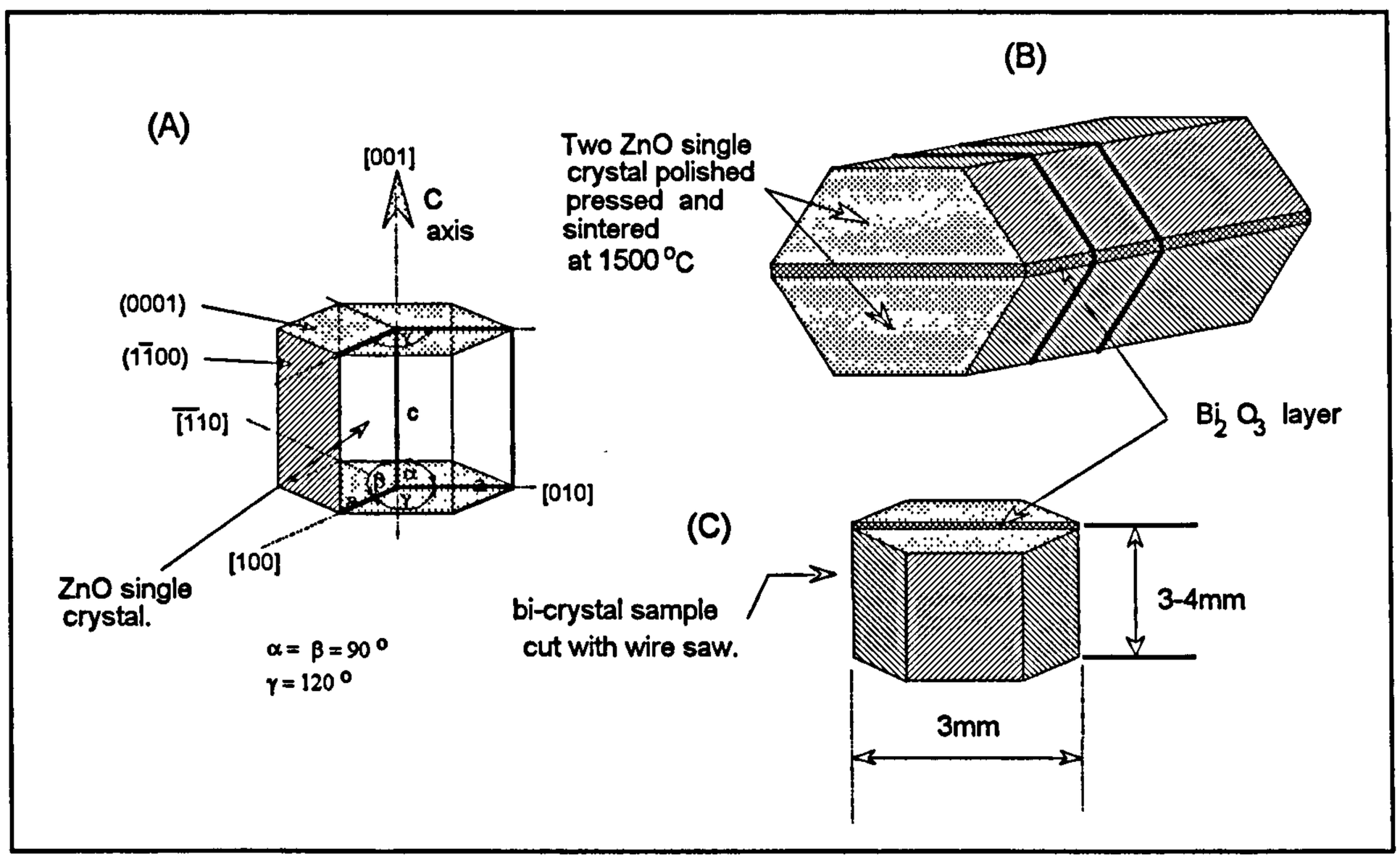


Fig.4.1.4. Schematic of ZnO bi-crystal (not to scale).

4.1.4. Deposition of Electrodes

Electrodes were formed to enable electrical measurements. The faces of the pellets were first ground on SiC paper (grit nos. 600, 800 and 1200) to make them parallel to one another. A thin layer of silver paste was applied on both faces. These electrodes were fired at 800°C for 5 min. On some samples electrodes were formed by evaporating aluminium. Masked electrodes were also prepared on some samples, to facilitate grain

boundary electrical measurements using the micro-probe manipulator during the SEM-EBIC analysis.

Table 4.1.3 Samples used in this project.

Sample No	Type of Sample	Additive oxides	Sintering Temp. (^{o}C)
1.(Lab)	Undoped ZnO	None	800, 1250, 1300
2 (Lab)	Bi, based ZnO ceramic	Bi	800, 1250
3 (Lab)	Bi, based ZnO ceramic	Bi, Co	800, 1250
4 (Lab)	Bi, based ZnO ceramic	Bi, Co, Mn	1250
5.(Lab)	Bi, based ZnO ceramic	Bi, Sb, Co, Mn	800, 1250
6 (Lab)	Bi, based ZnO ceramic	Bi, Sb, Mn, Co and Cr	800, 900, 1250, 1300
7.(Lab)	Bi, based ZnO ceramic	Bi, Sb	800, 1250
8 (Lab)	Bi-based ZnO ceramic rapidly cooled (1250^{o}C)	Bi, Sb, Mn, Co and Cr	1250
9. (Lab)	Slow cooled 5^{o}C/h	Bi, Sb, Mn, Co and Cr	1250
10.(Lab)	Bi, based ZnO ceramic	Bi, Sb, Mn, Co, Cr and Ti (1mol.%)	1250
11 (Lab)	Etched residue of ZnO ceramic	Bi, Sb, Mn, Co and Cr	1300
12 (Lab)	Pure ZnO bi-crystal	Bi	1500
13 (Com)	Bi, based ZnO varistor	Bi, Sb, Mn, Co, and Cr	1200 -1300
14 (Com)	Pr, based ZnO varistor	Pr, La and Co	1200-1300
15 (Com)	Bi, based ZnO, degraded varistor P.D.,	Bi, Sb, Mn, Co, B	1200-1300
16 (Com)	$BaTiO_3$ PTCR Thermistor	Ca, Mn Y	Not known

4.2. Analysis of Samples

Samples listed in Table 4.1.3 were prepared for a matrix of experiments as shown here marked with a tick, in Table 4.2.1 below. Samples marked as Com., were commercially obtained and those marked as Lab., were prepared in the laboratory.

Table 4.2.1 Matrix of expereiments undertaken

Sample No	Sample	SEM EDAX	SEM EBIC	SEM-CL	SIMS	IS	IV	XRD	TEM
1.(Lab)	Undoped ZnO	√	√	√	√	√	√	√	
2 (Lab)	ZnO + Bi ceramic	√				√	√		
3 (Lab)	ZnO + Bi + Co	√				√	√		
4 (Lab)	ZnO + Bi + Co + Mn, ceramic	√				√	√		
5.(Lab)	ZnO + Bi + Sb + Co + Mn ceramic	√				√	√		
6 (Lab)	ZnO + Bi + Sb + Mn + Co + Cr, ceramic	√	√	√	√	√	√	√	√
7.(Lab)	ZnO + Bi + Sb ceramic	√				√	√		
8 (Lab)	As in 6 above but **rapidly cooled** from 1250^{o}C	√				√	√	√	
9. (Lab)	As in 6 above but Slow cooled (5^{o}C/h)	√							
10.(Lab)	ZnO + Bi + Sb + Mn + Co + Cr and Ti (1mol.%) ceramic	√	√						
11 (Lab)	**As in 6 above, etched residue** of the ceramic	√				√	√	√	
12 (Lab)	Pure ZnO bi-crystal	√	√			√	√		
13 (Com)	Bi, based ZnO varistor	√	√	√	√	√	√		
14 (Com)	Pr, based ZnO varistor	√	√		√	√	√		
15 (Com)	Bi, based ZnO, **degraded varistor** P.D.,	√	√			√	√		
16 (Com)	$BaTiO_3$ Thermistor	√	√	√	√	√			√

4.2.1. Microstructural and compositional analysis using SEM-EDAX

The imaging mode of an SEM with the energy dispersive analysis by x-rays **(EDAX),** were used to study the microstructural properties of ZnO varistor. The majority of these analysis were undertaken using S-4000 SEM at the National Physical Laboratory, Teddington. The electron gun of this SEM had a field induced emission source (LaB_6). For all EDAX work the electron beam energy of 25kV was used.

Initially the size, shape and distribution of the starting powders with and without the additives were studied. The microstructure of sintered compacts fired at 700, 900, 1250, 1300°C and that of the rapidly cooled and slow cooled samples (Table 4.1.3) were studied to elucidate the effects of additives and sintering temperatures on the grain size and the inherent distribution of phases. In order to observe bulk and surface morphology, sample preparation prior to analysis were as polished, fractured and sintered. Some samples (including powders and those sintered at 900°C and below) were coated by sputtering a thin film of gold to stop the sample from charging up under the electron beam. Almost all the samples (batches 1 - 16) were studied using this technique.

4.2.1.1. Qualitative SEM-EDAX analysis

X-ray mapping associated with EDAX, was undertaken to complement the SEM images showing the elemental distribution of dopants corresponding to the phases present in the microstructure. For more detailed observations of the phases within the ceramic a sample (batch 11) of about 30 mm. diameter and of about 5 mm. thickness, ZnO varistor (sintered at 1300°C) was completely dissolved in diluted (1:3 in water) perchloric acid. The residue was filtered, dried and then sampled for analysis. These investigations based on the elemental, imaging aspect of the SEM-EDAX analysis, were intended to complement the SIMS ion imaging (discussed in section 4.2.4.1).

4.2.1.2. Quantitative SEM-EDAX analysis

The concentration of the metallic elements in the sample were determined by SEM-EDAX using the LINK system on JSM 35CF scanning electron microscope (JEOL Ltd.). ZnO ceramic doped with the metal oxides (Bi, Sb, Co, Mn, and Cr) was analysed. Analysis was facilitated with Links analytical software (ZAF4). This software and the analysis conditions were configured to perform quantitative analysis. SEM beam energy of, 25keV and 2.08×10^{-9} A, current was set using Co standard. Initially the electron beam was focused onto the Co standard and the x-ray spectra of Co was collected for 100 seconds. Spectra of a sample was then collected for the same period of time, but over a general area of 50μm x 50μm. Subsequently a spectra was collected as a point

analysis on grain region. The accuracy of this analysis technique is quoted as ± 1%, but might be lower for these particular samples because of their porosity.

4.2.2. Microscopic electrical analysis using SEM-EBIC

The electron beam induced current analysis (EBIC) technique was used to study the microscopic electrical behaviour of ZnO varistors. A sample of $BaTiO_3$ PTCR thermistor (130°C switch on point) was also studied. This experiment was intended to enable (a) a direct observation of the electrically active grain boundaries in the ZnO ceramic varistor, (b) to perform line scan profiling (using micro-manipulator as discussed in section 4.2.2.3) across a single grain boundary interface in both ZnO ceramic varistor and the ZnO bi-crystal sample and to elucidate the Schottky barriers, presumed responsible for the varistor phenomenon. The instrumental aspects of this technique have been described in Chapter 3, section 3.1.3.

Samples of varying compositions and sintering conditions, as shown in Table 4.1.3 and 4.1.4, were studied using the EBIC technique. An EBIC terrace pattern with line scan profiling (LSP) and the corresponding BSI were obtained for a number of samples that had undergone different condition of preparation. This includes analysis of several commercial sample of ZnO varistors and a sample of $BaTiO_3$ thermistor investigated to observe any grain boundary specific EBIC contrast.

4.2.2.1. Experimental conditions

Samples investigated by the EBIC technique were polished using powders down to (0.25μm) diameter. Electrode contacts were made using gold wire with silver dag. Samples were mounted on to an SEM (Jeol, JSM-840A) sample holder with a provision made for appropriate electrical connections to the EBIC pre-amplifier. A Metalec amplifier ISM5 (shown schematically in Chapter 3.3, Fig.3.1.8) was used to monitor and re-modulate the EBIC signal on to the SEM.

Initially the beam parameter was varied, with acceleration voltage from 1 to 25kV and the beam current from 5nA to around 1μA. This enabled an optimum condition (82nA with 25kV) for analysis yielding a strong EBIC signal. Such a high beam energy is necessary to yield a good EBIC signal. Depth information can also be gained as the beam penetration depends on the acceleration voltage (discussed in Chapter 3, section 3.1.3.1, Fig. 3.1.6). Some samples were subjected to a bias voltage by means of a power source available on ISM5 metalec device (discussed in Chapter 3, Section 3.1.3.2). The computer imaging system (Kontron) was used to process the EBIC line scan profiling

(LSP) and the electron beam induced current (EBIC) images. Micrographs of EBIC images with line scan profiling were taken using a camera arrangement attached directly to the SEM, independent of the Kontron imaging system.

An EBIC analysis was also successfully performed at the National Physical Laboratory using S-4000 SEM with a back scatter electron amplifier used to process the EBIC signal (discussed in section 4.2.2.2 below).

4.2.2.2. EBIC analysis at National Physical Laboratory (N.P.L)

This work was undertaken at the National Physical Laboratory, Teddington. It was intended to investigate whether or not an EBIC analysis can be facilitated by using a basic amplifier system such as the one normally used for signal processing in the SEM. These experiments were successfully undertaken using S-4000 SEM with an amplifier usually dedicated to collect back scattered electrons (BSE). Looking at the schematic of a sample arrangement shown in Fig. 4.2.1., it is shown that EBIC imaging capability can be arranged inexpensively on any SEM. Some interesting EBIC images were obtained as discussed in Chapter 5.

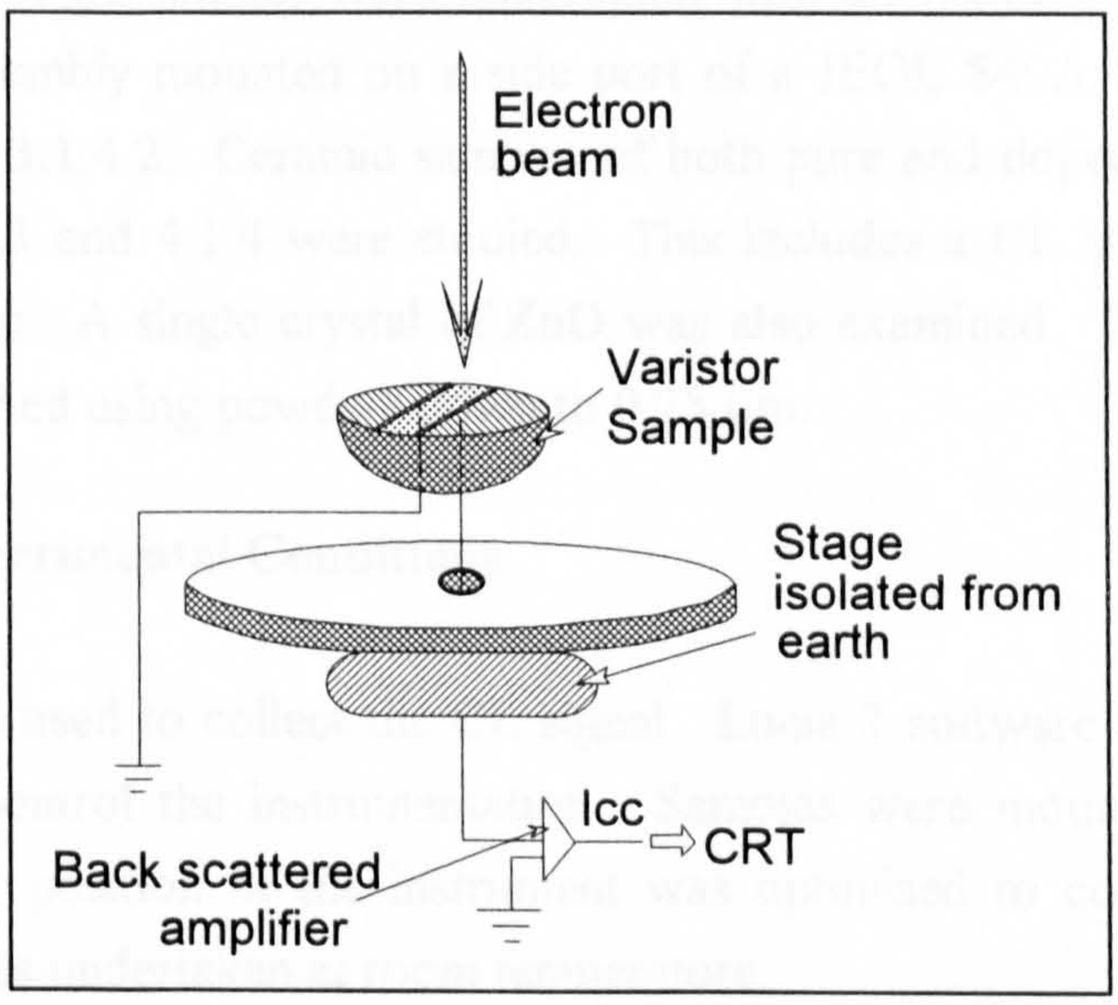


Fig. 4.2.1. Schematic of an EBIC set-up using S-4000 SEM with BSE amplifier.

4.2.2.3. Microprobe manipulator

The micro probe manipulator attached to the (Jeol, JSM-840A) SEM facilitated the EBIC line scan profiling (LSP) and I:V measurements across a single and multiple grain

boundary (GB) junctions. Initially measurements were performed with tungsten wire (40 μm) probes directly in contact with the polished surface of the sample. Concern about the quality of the ohmic contact at the tip prompted a development of a masking technique. A copper grid (normally used to support TEM samples) was used as a mask when evaporating aluminium contacts on the ceramic samples. This method created a matrix of small point contacts of evaporated aluminium or sputtered gold on to the sample. During analysis the probes can be manipulated to reach a pair of such contacts on either side of the grain boundary.

4.2.2.4. I:V measurement in the SEM using microprobe manipulator

Microscopic I:V measurements on the ZnO ceramic based varistor and the bi-crystal sample were acquired using micro-electrodes attached to an SEM. The bulk I:V measurements were undertaken using a different set of apparatus (discussed in section 4.2.7).

4.2.3. SEM-CL (Cathodoluminescent) Analysis of some ZnO based ceramics

SEM-CL measurements were intended to study the band gap related information. This mode of an SEM was applied to investigate some doped and pure ZnO based ceramics (Table 4.2.1). SEM-CL studies were undertaken with an Oxford Instruments CL301 mirror-cryostat assembly mounted on a side port of a JEOL 840A SEM (discussed in Chapter 3, section 3.1.4.2. Ceramic samples of both pure and doped ZnO materials as listed in Table 4.1.3 and 4.1.4 were studied. This includes a CL study of a pure and doped ZnO ceramic. A single crystal of ZnO was also examined. Prior to analysis all samples were polished using powders down to 0.25 μm.

4.2.3.1. Experimental Conditions

A Ge detector was used to collect the CL signal. Lucia 2 software was installed on to the computer to control the instrumentation. Samples were mounted on a insulated stage. The mirror position of the instrument was optimised to collect the maximum signal. Analysis was undertaken at room temperature.

It is crucially important that a strict procedure is followed prior to mounting the CL mirror system. Improper handling can result in a mirror touching the various components, including the sample, inside the SEM chamber. This can lead to permanent damage to the mirror assembly. Hence the sample work distance, W.D. = 48, i.e. the lowest stage position usually selected and then raised to W.D.= 25.

It is very important to obtain a good strong CL signal. Initially beam conditions of 35kV with 25nA were selected with W.D. = 18mm. The sample was further raised to a W.D.= 15mm. A signal intensity of I ≈ 5082 cps was observed at 1200 magnification. Further optimisation with the beam current of Ib=31nA resulted in improved signal intensity (I≈ 8000 cps).

Initial observation of CL processes in a sample, giving rise to any peaks and their location within the spectrum, can be assisted by setting the following collection parameters:

Starting $\lambda = 1000$
Stop $\lambda = 4500$
Incremental $\lambda = 50$Å
Dwell time = 1000 sec

For example when looking at ZnO with all the dopants, a peak at 3450 eV, with an intensity of 7567 cps was observed. Further optimisation of the beam parameters, magnifications and increase in dwell time enabled an observation of other neighbouring CL peaks (discussed in Chapter 5, section 5.3).

4.2.4. Microscopic compositional variation of dopants using SIMS

Analytical options such as the normal depth profiling with checkerboard gating, ion imaging, and line scan were used on the SIMS instrument (Atomika 6500 ion microprobe). Experiments using these options were intended to:-

1. Investigate the compositional variation of dopants (Bi, Sb, Co, Mn and Cr) in the ZnO ceramic, using ion imaging and depth profiling options.

2. Investigate the spatial distribution of oxygen using a combination of imaging and line scan options.

4.2.4.1. Compositional variation of dopants

The ion imaging, using a fine focus oxygen primary beam was used to investigate the elemental segregation of dopants in ZnO ceramic sintered at 1300^{o}C. The instrument was carefully tuned to optimise the imaging conditions and set to profile at 5 second intervals for each mass channel selected, corresponding to the masses of Zn, Co, Bi, Sb, Cr, and Mn. The scan area was 50μm x 50μm. This experiment was useful to investigate the compositional variation of dopants in the varistor material. The checkerboard option was used to compare the signal intensities of the reference sample

to a single point on the varistor sample. Samples used in this experiment were ZnO ceramic doped with oxides of Bi, Sb, Mn, Co, and Cr. (0.5 mol.% each). Two samples of this composition were prepared, with the only difference being in their sintering temperatures (one was sintered at 1300^{o}C and the other one at 900^{o}C). The sample sintered at 900^{o}C was used as a reference. For the ion imaging mode a very good lateral resolution is required. The SIMS instrument was carefully tuned to optimise these imaging conditions by adjusting the parameters as noted below.

4.2.4.1.1. Experimental condition for analysis

Table 4.2.2 Experimental conditions used during the SIMS analysis.

	O_2^+beam (Positive secondary ions)	Xe^+ beam (Negative and Positive secondary ions)	Xe^+ beam (Negative and Positive secondary ions)
Samples	ZnO Var. (900^{o}C) ZnO Var. (1300^{o}C)	ZnO pure (1250^{o}C), ZnO + all (1250^{o}C).	ZnO pure (1250^{o}C), ZnO + all (1250^{o}C).
Batch No ⇒	6, 13 (table 4.1.3)	1, 6 (table 4.1.3)	1, 6 (table 4.1.3)
Primary beam			
Primary beam energy (keV)	10	10	10
Primary beam current (nA)	5 profile. 0.1 for imaging	6, for ^{18}O depth profile, 0.6 for ion imaging.	12 for line scan and 1 for imaging
Primary beam angle (deg)	0	0	0
Primary beam scan mode	Raster, for Depth profiling, and imaging.	Raster, for Depth profiling, and imaging.	Raster, for line scanning and imaging.
Crater size (μm)	50 profile., 16 grain, 100 imaging.	32 profiling. 64 imaging.	1500, 512, 256
Charge compensation			
Electron beam energy (keV)	3	3	3
Electron beam current (μ A)	4, 5	2.7	2.6
SECONDARY IONS			
Secondary ion species measured	^{64}Zn,^{59}Co,^{55}Mn, ^{52}Cr, ^{209}Bi, and ^{121}Sb (all +)	^{18}O,(-) ^{16}O,(-) ^{64}Zn,(+), ^{52}Cr (+)	^{18}O,^{16}O,^{64}Zn, ^{9}Co,^{55}Mn, ^{52}Cr
Energy Distributions			
Energy offset (eV)	-12.79	10.5 except for Zn and Cr (-10.5)	2.4 for ^{18}O, and ^{16}O, for Zn (-9.5)

An oxygen primary beam of energy of 10kV and 5nA was selected for this analysis. To overcome the charging problems a 3kV beam of electrons of 4 - 5μA was used. The instrument was set to profile at 5 second intervals for every window selected corresponding to the mass of Zn, Bi, Sb, Co, Mn and Cr.

The beam energy 10kV was maintained throughout the analysis. The beam current was required to be varied from, initially 24nA, 5nA, 1nA and finally to 0.1nA. This procedure was taken to obtain, initially a more intense signal for the detection of the various dopants in the ZnO sample. Once the detection of all the dopants was established the beam current was reduced to finally 0.1nA in order to optimise the focusing and lateral resolution. Smaller apertures were selected for 1 and 0.1nA beam currents. The mass detection conditions were adjusted to improve the secondary ion detection until the signal intensity reaches its maximum in every mass window selected (Fig. 4.2.2). To avoid any beam drift the instrument was left to stabilise for about 30 minutes prior taking any measurements.

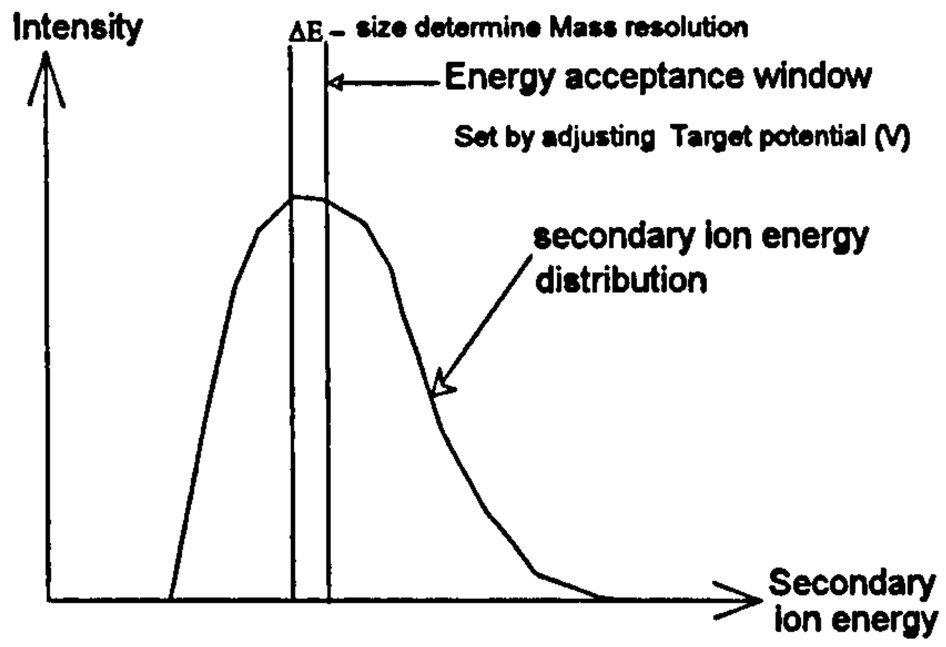


Fig. 4.2.2. Energy spectrum of secondary ions.

4.2.4.1.2. Stages of measurements

The imaging and depth profiling experiment was undertaken over three stages:

(1) Initially the ZnO varistor sample (1300^{o}C) was analysed using the ion imaging mode. The analysis was confined to the scan area of 50μm x 50μm. The images corresponding to the distribution of elements (Zn, Sb, Co, Mn, and Cr were observed and recorded on micrographs. Secondary signal due to Bi was very weak and did not produce any image

(2) Secondly the above analysis was confined to the single grain (ZnO) on the sample. Here secondary electron images were useful to identify the grain region.

(3) Finally the sample sintered at 900^{o}C was analysed as a reference, ie. homogeneous distribution of dopants was assumed, with respect to grain size/ lateral resulation of the primary beam. The checkerboard map profile showing the distribution of the dopants was acquired from the analysis.

4.2.4.2. The spatial distribution of oxygen in ZnO ceramic

This experiment was designed to investigate the oxygen diffusion profiles in both pure and doped ZnO ceramic. Samples used were pure and doped (Bi, Sb, Co, Mn, and Cr) ZnO ceramics. A small piece of single crystal of Si was also included with the above samples. This is oxygen exchanged to discover percentage of ^{18}O. This experiment was intended to investigate the high oxygen concentration along the grain boundary interface decorated by secondary phases in the doped ceramic, presumed responsible for good varistor phenomenon [47, 113]. Use of both the ion imaging and the line scan options on the SIMS were explored to investigate the spatial distribution of oxygen and to deduce some numerical values for surface exchange coefficient (k) of the oxygen and its self diffusion coefficient (D*) in both of these ceramic samples.

4.2.4.2.1. Sample preparation for oxygen diffusion work

Samples of both pure and doped ZnO (Bi, Sb, Co, Mn, and Cr at 0.5 mol.%) ceramic were initially polished (diamond spray) using powders down to 0.25μm followed by heating to 1000^{o}C for 16 h. in an ^{16}O environment (940 m Bar), and then an ^{18}O exchange for similar exposure times, temperatures and pressures. As an initial equilibrating procedure ^{16}O anneal is initially done at the temperature (1000^{o}C) desired for the final $^{18}O/^{16}O$ exchange.

4.2.4.2.1.1. The $^{16}O/^{18}O$ exchange

The ^{18}O isotope of oxygen has a low natural abundance (0.2%) and it is used as a tracer to study the diffusion of oxygen.

Samples are initially annealed in the natural oxygen and finally annealed in oxygen of a constant and known enrichment of ^{18}O. The enriched oxygen is held in a reservoir (Fig. 4.2.2) and can be pumped into and out of the main experimental chamber by the use of a small molecular sieve sorption pump. The anneal is performed by initially evacuating the sample chamber to high vacuum ($\approx 10^{-5}$ Torr) and then introducing pure (unlabelled) oxygen [103].

The $^{16}O/^{18}O$ isotopic exchange was facilitated in a suitable rig. Fig.4.2.3 shows a very simplified schematic of this rig. The samples are accommodated in a silica tube which can be inserted into a programmable tube furnace. Initially the samples were given an anneal in ^{16}O atmosphere at 1000^{o}C. The samples are then allowed to cool down prior to $^{16}O/^{18}O$ exchange. The base pressure in the rig is lowered to $\leq 10^{-6}$ torr. This is achieved by the turbo molecular pump. It is important that the water vapour in the rig is at its minimum. This can be typically 1 - 2ppm and will need to go down to 1ppm

(indicated by water vapour meter, before any exchange is to take place. The rig can be baked to achieve this.

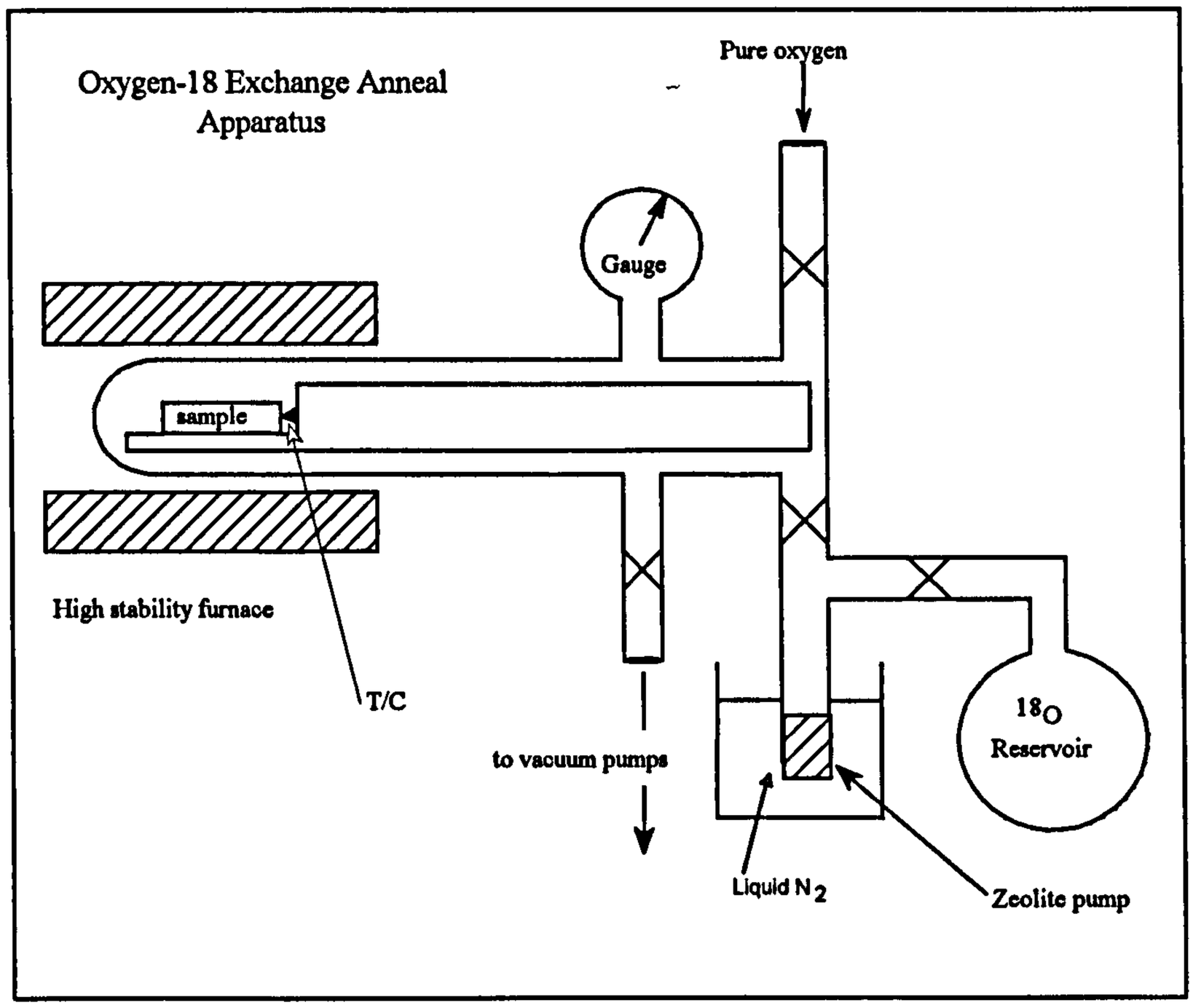


Fig. 4.2.3 Schematic representation of the apparatus used for the oxygen exchange experiment [103].

The ^{18}O is initially drawn from the reservoir into the Zeolite pump connected much nearer to the orifice of the silica tube and is liquid nitrogen cooled. The change in the resultant pressures draws ^{18}O in to the spare sieve as soon as the inter connecting valve to the reservoir is opened.

Once the ^{18}O was drawn from the reservoir in to the Zeolite pump it was introduced in to a part of the rig where the sample is located. All the other valves are shut, confining the ^{18}O to the sample chamber. The pressure readings on the gauge rises as the ^{18}O is gradually introduced in to the sample chamber. Further heating of the Zeolite pump introduces more ^{18}O and the pressure rises eventually going up to near atmospheric pressure. The tube furnace at 1000^{o}C was rolled in position housing the sample contained in the silica tube. All the valves to and from the Zeolite pump were shut off. As the temperature raised, the pressure also raised and stabilised at 943 mbar and was monitored throughout the run (24hours) with a chart recorder. At the end of the run the ^{18}O was retrieved back into the molecular sieve by cooling it with liquid nitrogen. Once

the majority of the ^{18}O is retrieved the pressure of the system should go down to its initial zero point reading (-0.09mbar).

4.2.4.2.1.2. Cross-section of a sample for line scan analysis

Samples of pure and doped ZnO ceramics were cut perpendicular to the initially polished face after undergoing $^{16}O/^{18}O$ exchange as discussed in section 4.2.4.2.1.1. The samples were sandwiched between two dummy samples of ZnO ceramic and were glued with Epoxy Resin (Araldite Rapid Adhesive) on to a brass polishing block. The cross sectioned plane were thus polished using powders down to 0.25μm (diamond polish) and ultrasonically cleaned in solvent. Further details about the line scan are discussed in Chapter 3, section 3.3.5.

4.2.4.2.2. Oxygen diffusion analysis

Samples were mounted on to a carousel and introduced into the loading port of the SIMS instrument and later transferred to the sample chamber. The samples were analysed using a 10keV Xe^+ primary ion beam to profile for ^{16}O, ^{18}O and Zn. Initially the ion beam (12nA) was located by sputtering on the fluorescence spot on the carousel.

4.2.3. IS analysis

As discussed in Chapter 3, section 3.4.1, the measurement of bulk and grain boundary resistance in electro-ceramic cannot be determined by simply using either: the two probe dc., four probe dc., or even fixed frequency ac., analysis techniques. For polycrystalline ceramic samples, the measured value is the sum of the bulk and the grain boundary resistance. The grain boundary resistance is very sensitive to parameters such as impurity content and heat treatment of the ceramics and thus, may vary considerably between materials of the same composition. Complex impedance measurements were thus employed to study the bulk and grain boundary resistance in the ZnO based ceramic.

Both pure, doped, and some commercial ZnO based varistor samples were investigated. Amongst the samples studied, were some degraded samples, commercially obtained. The sample was initially polished and the contacts of Al were formed by evaporation. Subsequent samples had painted contacts of Ag subsequently fired at 800°C for 5min. The sample was mounted in a spring loaded holder (discussed in Chapter 3 section 3.4.2) and the whole assembly was placed in the tube furnace dedicated to the IS system. Measurements were taken from 20 °C up to 600°C at 50°C intervals.

4.2.4. TEM analysis

TEM analysis was undertaken to enable much closer observations of the grain boundaries and the secondary phases. Both dark and bright field imaging modes of the TEM were explored and electron diffraction patterns obtained. Some STEM-EDAX work (discussed in section 4.2.4.3, was undertaken at the National Physical Laboratory, Teddington. Sample preparation for TEM was rather tricky and difficult. After much perseverance and numerous attempts to produce thin and round samples the following procedure was established.

4.2.4.1. Sample preparation for TEM

Samples for TEM analysis were required to be 3 mm in diameter with the thickness varying from about 100 μm towards the circumference to nothing in the central region. Ceramic samples with a grain size of 15-20μm are very fragile as the grains are only supported by a few grain boundaries. Faced with this challenge, a method of preparation was finally established as presented here:

1. Initially the sample was mounted on to a small brass block (30 mm dia.) with the aid of heat sensitive resin. It was then thinned down to about 500μm, by lightly rubbing it on SiC papers (grit No 1200) followed by polishing both sides using powders down to 1/4 μm (diamond spray) in diameter.

2. After polishing the sample was transferred on to a student drilling machine where a pre-machined cylindrical brass tool with a bore size of 3 mm, was used for producing the required diameter of the sample. The brass tool rotating at about 300 revolution per minutes was charged with fine (30-50 μm) SiC abrasive with paraffin and then gradually lowered down on to the polished surface of the sample. The cutting action was provided by the impregnated SiC on to a soft surface of brass. The tip of the tool was constantly recharged with the slurry of SiC and a number of 3 mm., circles were thus inscribed. The inscribed disks were then carefully separated using a sharp tool. The tiny 3 mm

diameter specimens were then thinned to about 100μm, using a metal jig (Fig.4.2.4) as a form of support whilst polishing.

3. The samples were then dimpled in the centre to about 50 μm, using a dimpling tool. During dimpling, an arm speed of 30-40 rev/min. with a loading weight of 30g was used. The dimpling solution had 3μm polishing aggregates. It took about 25-35 minutes to dimple ZnO based samples and around 18 minutes for the $BaTiO_3$ sample. The thickness of the sample at this stage was estimated by focusing at the top and the bottom plane of the surface on an optical microscope.

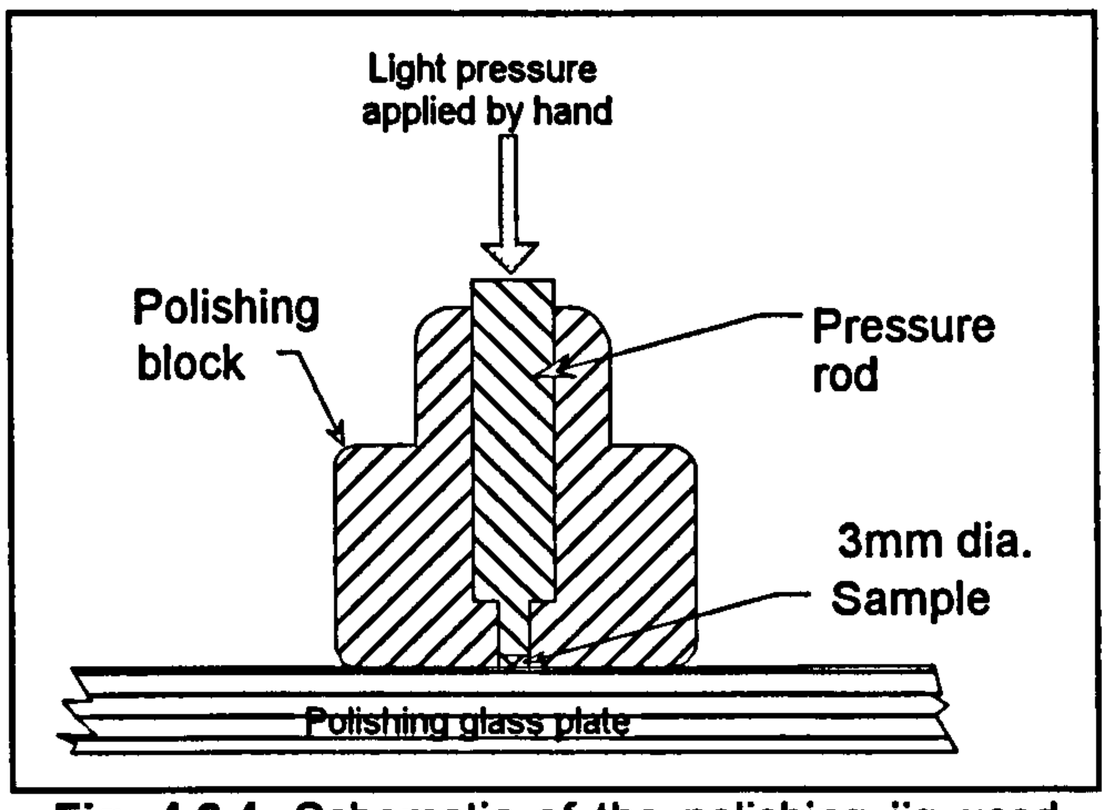


Fig. 4.2.4. Schematic of the polishing jig used for TEM sample preparation.

4. A copper ring was secured on to the sample (using rapid drying epoxy adhesive) to give it some support, and then the final thinning was completed onto the ion beam milling machine (Gaton Dual Ion Mill model 600). The initial angle of milling was set to 15^{o} and the gun voltage to 6-7kV, with a current of 4 milli Amperes. The angle of milling was set to a much lower settings (10^{o} and voltage to 3kV) at the final stage of the process. Finally the Ion beam thinning was completed after about 12 hours of milling, when light was seen passing through the middle of the sample.

Samples of pure, doped and commercial ZnO based varistors were prepared for TEM analysis.

4.2.4.2. TEM analysis

TEM micrographs at different magnifications, and electron diffraction patterns of the phases and grain boundaries were obtained.

4.2.4.3. STEM-EDX work at NPL

ZnO varistor sample (No 5, Table 3.1.2, sintered at 1300°C) was prepared in accordance with the procedures discussed in section 4.2.4.1 and was loaded in the JEOL STEM 2000FX. The EDAX system had a window-less detector and was thus sensitive to low

atomic number elements such as oxygen. The grain boundaries and the phases of the ZnO varistor sample were studied.

4.2.5. I:V measurement

The sample was held in a suitable jig with spring loaded contacts on either sides. The voltage in the range 0 to 200V was gradually applied across the ZnO varistor in small increments and the corresponding increase in the current was monitored. The resultant I:V curves of a group of samples prepared with different doping and sintering parameters were thus obtained.

4.2.6. XRD measurement

4.2.6.1. Sample preparation for XRD

The analysis was undertaken on a Siemens instrument at the National Physical Laboratory (NPL) Teddington. A piece of about 30 mm diameter by about 5 mm thickness of ZnO varistor (sample No 5, Table 3.1.2, sintered at 1300°C) was dissolved in perchloric acid ($HCLO_3$). The residue was filtered, dried in a desiccator and then extracted for XRD analysis. The extracted residue was mounted on to a single crystal Si sample holder (discussed in Chapter 3 section 3.5.1) using alcohol as a wetting medium.

4.2.7. Summary of the Sample Preparations and analysis

All the samples used in this work are listed in Table 4.1.3. Samples marked from 1-12, in Table 4.1.3, were synthesised in the laboratory, and those marked from 13-16 were commercially obtained .

ZnO samples of many different compositions batches (1-7) were synthesised with varied sintering temperatures (800°C, 900°C. 1250°C and 1300°C) to study the interrelated effect of dopants and sintering temperatures on the microstructure and the I:V electrical characteristics. Different sintering conditions (rapid and slow cooling from 1250°C) were applied to a batch of samples to study the effect of sintering conditions on the microscopic properties. In addition to the five metal oxides (Bi, Sb, Co, Mn, and Cr), in one preparation TiO_2 oxide at 1mol% was added. The sample (10) synthesised in this manner was intended to promote the grain growth and to enable the study of grain boundaries.

ZnO ceramic doped with the oxides of Bi, Sb, Co, Mn, and Cr was etched in perchloric acid to dissolve away the ZnO grains leaving just the secondary phases for SEM-EDAX and XRD analysis.

A bi-crystal of ZnO was synthesised to produce a single interface for analysis.

Batches (13-15) of commercial ZnO varistor samples including (16) a sample $BaTiO_3$ positive temperature coefficient of resistance (PTCR) thermistor were obtained from commercial sources for comparative analysis.

The SIMS work was intended to study the compositional variation of the dopants and to study the oxygen diffusion properties in both the doped and undoped ZnO based ceramic.

Impedance analysis technique was used to take complex impedance measurements to study the bulk and grain boundary resistance in the ZnO based ceramic.

Whilst SEM-CL was intended to explore band gap related properties in both pure and doped ZnO based ceramic, the SEM-EBIC undertaken to study the microscopic electrical properties and to explore the EBIC contrast at the grain boundaries.

Chapter 5

Results and Discussion

A number of analytical techniques were used to provide in-depth information about the microstructural property of the ZnO ceramic varistor. Results arising from a group of traditional techniques such as the **SEM-TEM -XRD** highlight information about the segregation of insoluble additives such as Bi, Sb, and Cr in ZnO ceramic microstructure. The associated SEM/TEM micrographs taken as topographical images, the back-scattered electron images, and SEM- x-ray dot mapping, show microscopic details about the associated secondary phases, grain size variations, and the thickness of the intergranular layer at the grain boundary interface. In the first instance, these results complement many of the previous studies of ZnO varistors and are useful to compare and contrast the varistor information in the literature as discussed in section 2.3.2.1. Amongst the significant novel contributions, results from **SEM-EBIC** analysis in section 5.2 presents resistive contrast imaging **(RCI)** and line-scan-profiling **(LSP)** as direct evidence of the electrically active grain boundaries in ZnO ceramic. Additionally, section 5.4 presents novel results from **SIMS** ion imaging and line-scan profiling studies of the oxygen diffusion using a tracer isotope (^{18}O). These results on the segregation of insoluble additives and in particular the oxygen percolation along the lacy network and at the grain boundary interface are invaluable to explain the theory of the double Schottky barrier models discussed in section 2.4. Due to its sensitivity the **SEM-CL** (section 5.3) technique availed information about the dopant induced defect states that are present in the ZnO ceramic. Impedance spectroscopy **(IS)** showed the interrelated influence of the dopant additives to the electrical properties (section 5.5), while **IV** measurements (section 5.6) showed the non-linear I-V characteristics of some of the ZnO ceramics samples. Sample preparation (as discussed in section 4.7.) was varied according to the techniques used.

Results are presented in a form of: SEM-EBIC/TEM micrographs, XRD, EDAX IS spectra, SIMS ion imaging depth profiling, checkerboard pattern and IV curves. A modified version of the oxygen diffusion model is proposed to show the oxygen diffusion in ZnO ceramic. Clearly the unique aspect of this work is attributed to the acquisition of a wealth of information on the microscopic properties such as the morphology, compositional variation of dopant additives and a microscopic electrical behaviour in ZnO ceramic varistors, acquired by a combined use of these traditional and novel analytical techniques.

5.1 SEM/TEM-EDAX and XRD Microstructural-Compositional Analysis

Analysis of the distribution of the elemental additives in the microstructure of the ZnO ceramic was undertaken using analytical instruments such as the SEM using back scattered electron imaging (BSE) mode. As the primary beam is incident onto the sample, the back-scatter yield increases with atomic number, implying that regions of a sample having a higher average atomic number will appear brighter than those of a lower average atomic number. This would provide phase related contrast. SEM-EDAX, and STEM-EDAX were used for the identification of the elements present in the microstructure and particularly in these secondary phases.

Microstructural-Compositional Analysis using SEM was thus intended to provide a detailed study of the microstructure of, (a) the starting ZnO powders, (b) the calcined powders with additives and (c), secondary phases in sintered ZnO ceramic samples (with and without any additives) synthesised at 800°C and 1250°C sintering conditions. Secondary electron (SE) imaging, back scattered electron (BSE) imaging and energy dispersive analysis by X-rays (EDAX) modes of the SEM were used to study the microstructure of the powders and the doped ZnO ceramic samples. SE imaging provided topographical imaging while BSE imaging related atomic number-phase-related contrast and was used to provide a detailed visual image of the microstructure with its phases. SEM/STEM-EDAX with associated X-ray mapping was used to positively identify these elemental distributions within the microstructure.

The surfaces analysed were as sintered, polished (using powders down to 0.25μm) or fractured to reveal the internal morphology. To complement the individual phase analysis of the polished ceramic sample, studies of an etched residue of a ZnO varistor sample was intended by SEM-EDAX and XRD. Analysis of the ZnO ceramic sample containing all 5 additives, but rapidly cooled from 1250°C sintering temperature to room temperature (by quenching in cold water), was undertaken. This was to freeze the prevailing microstructure at this temperature in order to study the phases present.

Grain sizes were measured by the linear intercept technique described by **Mendelson** (1969) [109] and **Dey** *et al* [108], to calculate the average grain size of ZnO ceramics. The average grain size, G, was found to be :

$$G = 1.56\bar{L} \qquad (5.1\text{-}1)$$

Where $\bar{L}$ in equation 5.1-1 is the average grain-boundary intercept length of a series of random lines on the photomicrographs and the value 1.56 is the proportionality constant which relates the average grain size with shape (truncated octahedral) to the average intercept size [109]. This method described by **Mendelson** can be used to determine the average grain size of a sintered powder compact composed of non textured grains which shows no discontinuous grain growth [109].

5.1.1 Microstructural analysis of ZnO powders

Micrographs of the starting powders of pure and doped-calcined (700°C) ZnO materials are presented in Figs. 5.1.1 and 5.1.2. The figure shows the particle size and shape of the starting materials used to make the ceramic samples used in this project. The starting ZnO powders are elongated with a particle size of sub-micron. After the dopant additives have been introduced, followed by grinding and calcining the powders are less angular and the particle size has not been significantly altered.

5.1.2 Microstructural analysis of ZnO ceramics

5.1.2.1 Samples sintered at 800°C

Microstructural analysis (using SEM) of the ZnO based ceramics sintered at 800°C shows, at an early stage of the sintering process, the effective role of additives in altering the morphology of the ZnO ceramic. Conditions of samples prior to analysis were as fractured. Figs. 5.1.3 (a), (b), (c), (d), (e), (f), and (g), show the fractured microstructure of ZnO based ceramics doped with oxides of single double and multiple dopants, all sintered at 800°C. As a summary, Table 5.1.1 shows several samples of different composition. The grain size measurement has a relative mean deviation of around 6%.

Table 5.1.1 Samples Sintered at 800°C

	ZnO ceramic samples	Grain size(μm) RMD ≈ 6%
5.1.3 (a)	Undoped ZnO ceramic	1.2
5.1.3 (b)	ZnO + Bi ceramic	2.1
5.1.3 (c)	ZnO + Bi + Co ceramic	2.2
5.1.3 (d)	ZnO + Bi + Co + Mn, ceramic	3.2
5.1.3 (e)	ZnO + Bi + Sb + Co + Mn ceramic	0.5
5.1.3 (f)	ZnO + Bi + Sb + Mn + Co + Cr, ceramic	0.7
5.1.3 (g)	ZnO + Bi + Sb ceramic	0.3
5.1.3 (h)	SEM-EDAX spectra of ZnO + Bi + Sb ceramic	0.3

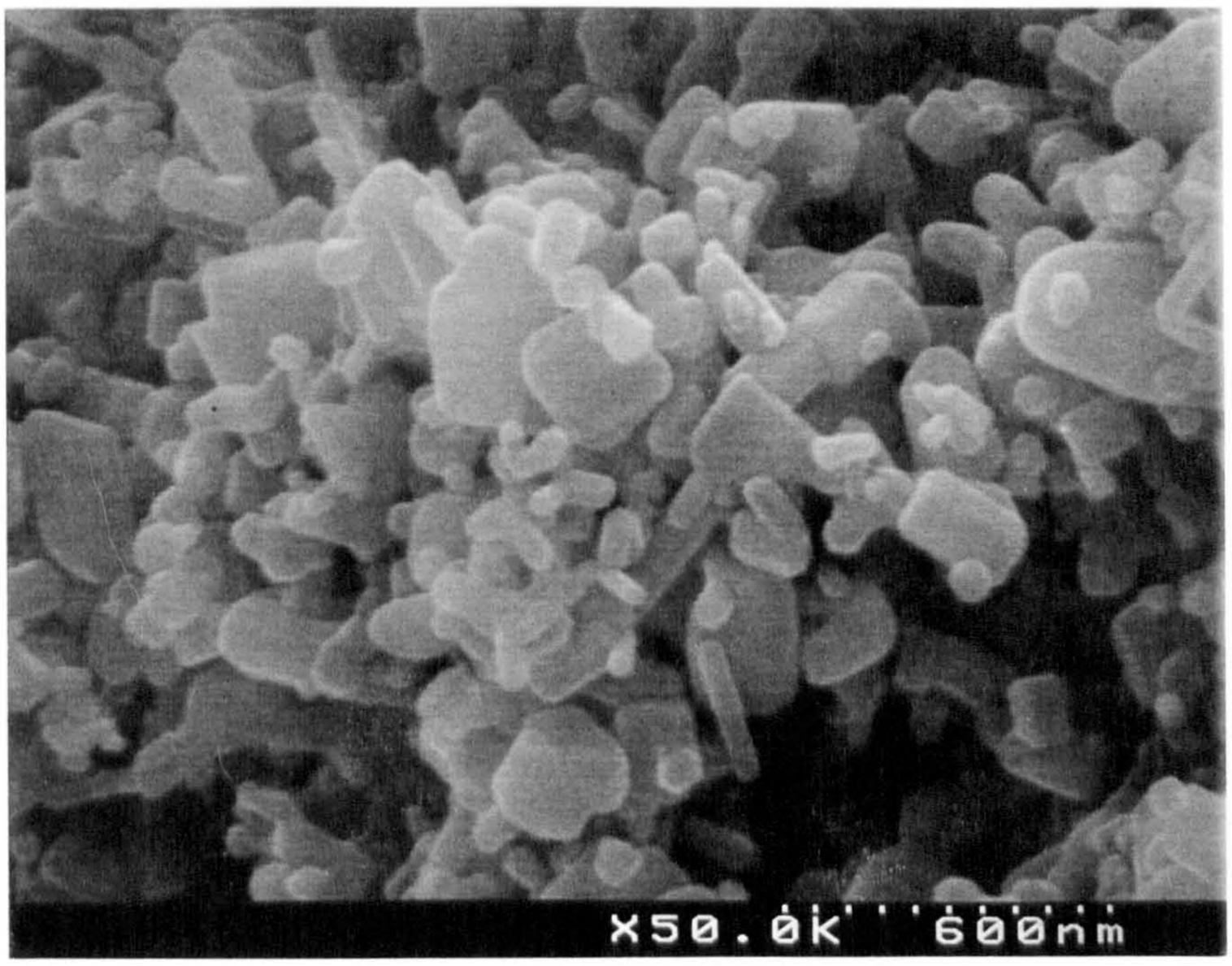


Fig. 5.1.1. SEM micrographs showing the particle size and shape of the pure ZnO powders.

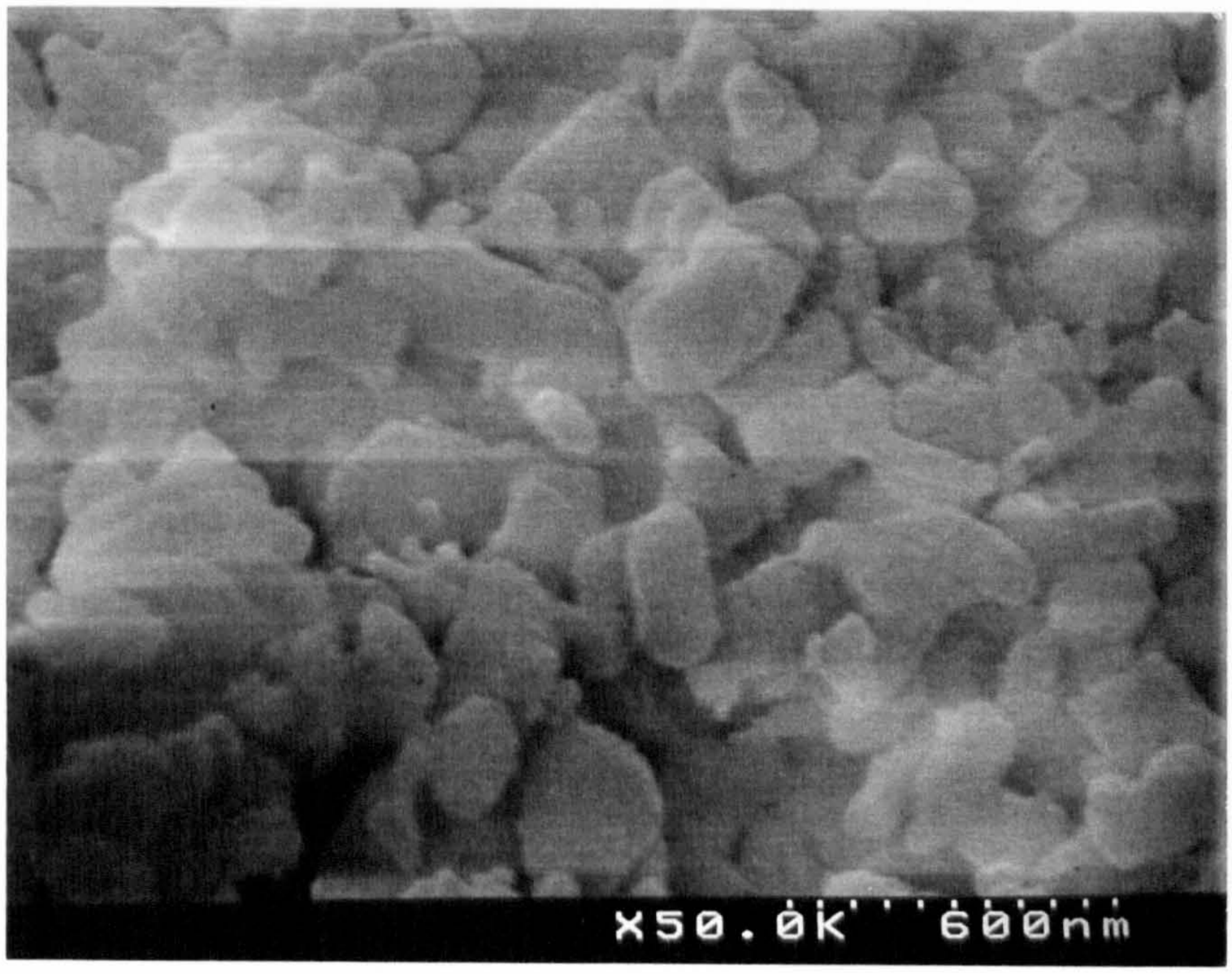


Fig. 5.1.2. ZnO powders, doped with additives: Bi_2O_3 ,Sb_2O_3 Co_3O_4, MnO_2 and Cr_2O_3 , and then calcined at 700^oC for about 5 hours.

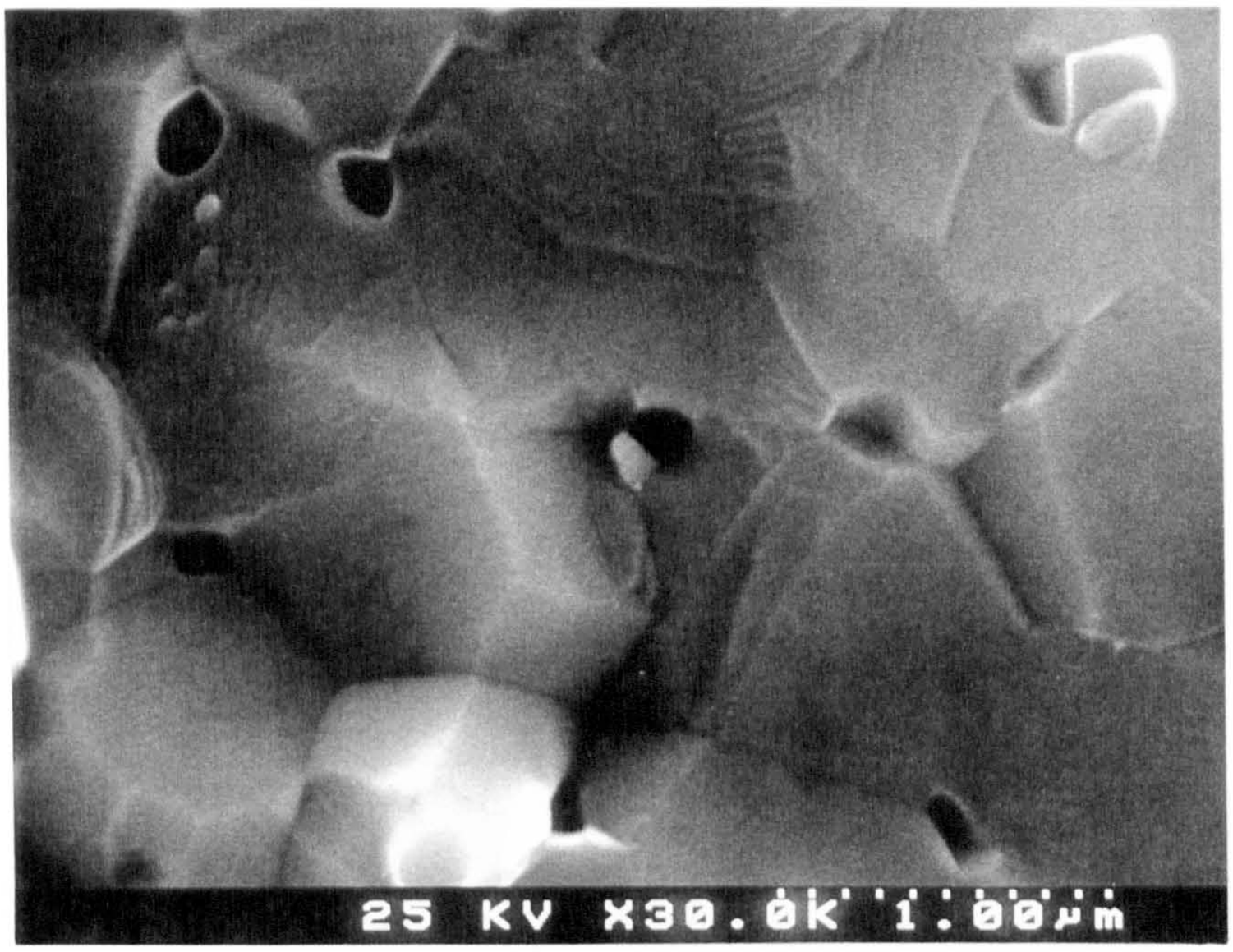


Fig. 5.1.3 (a). SEM micrograph of the **undoped** ZnO ceramic sample sintered at 800°C.

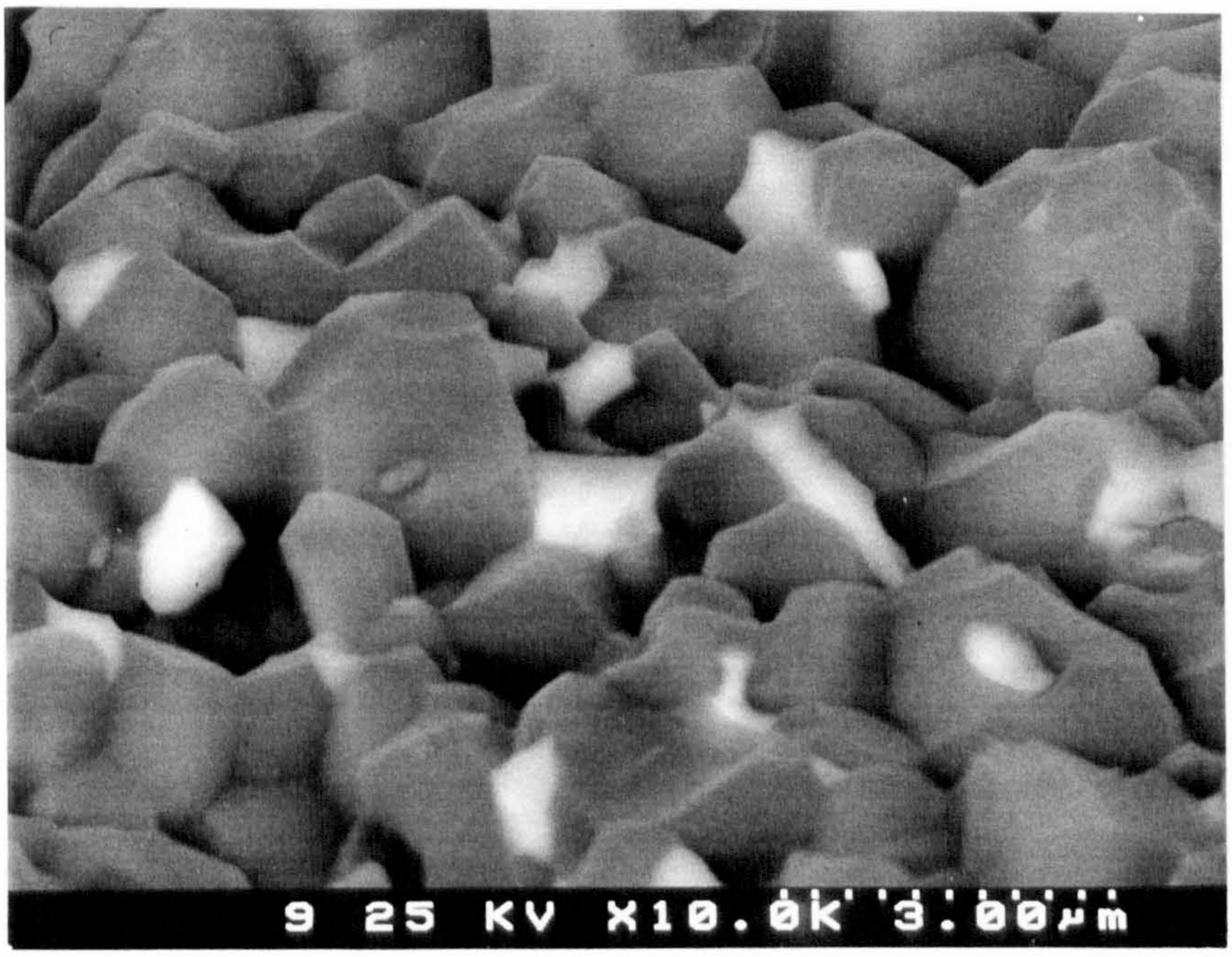


Fig. 5.1.3 (b) SEM micrograph of a ZnO ceramic sample **doped** (0.5 mol.%) with the oxide of **Bi** and then sintered at 800°C.

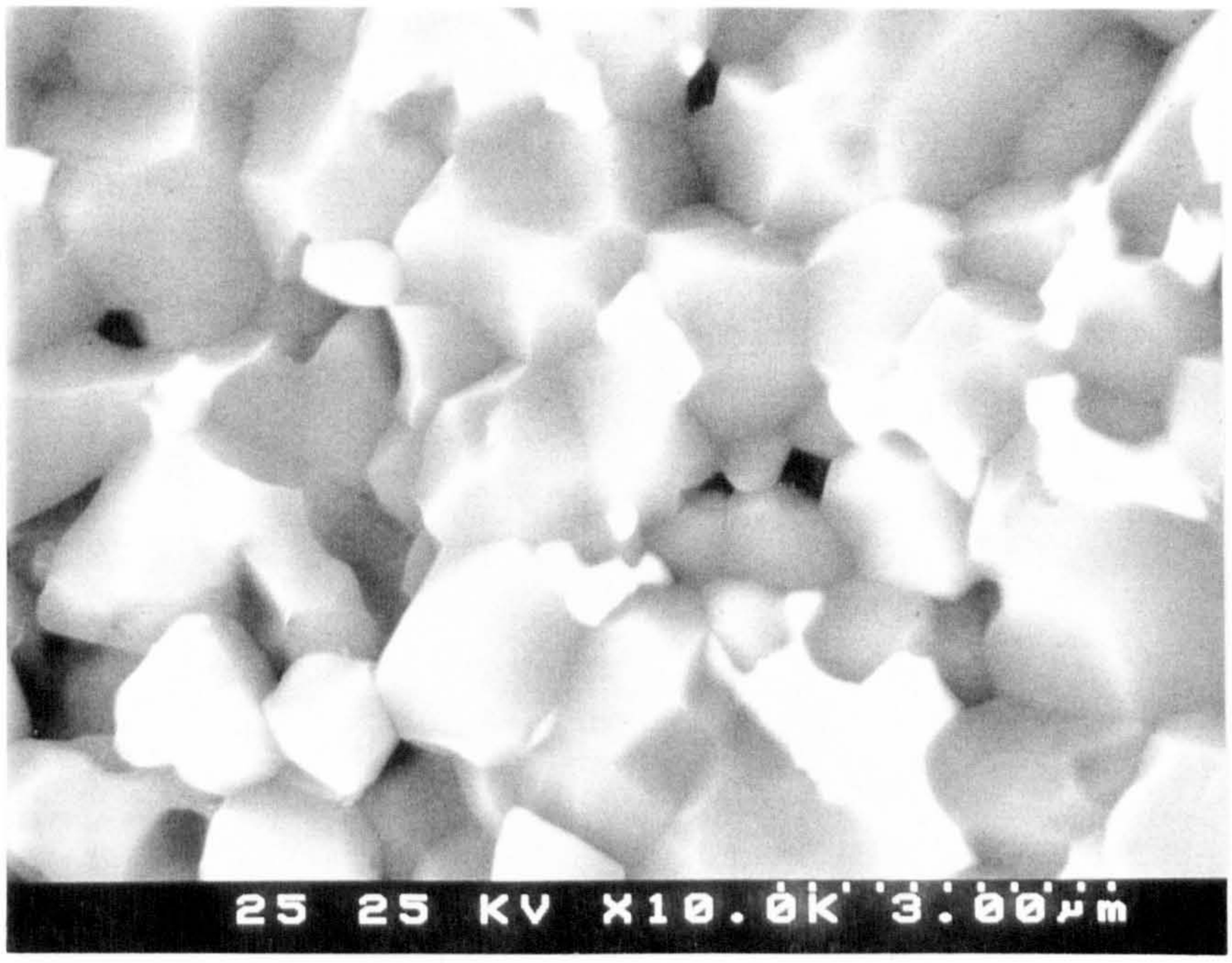


Fig. 5.1.3 (c) SEM micrograph of a ZnO ceramic sample **doped** (0.5 mol.%) with the oxides of **Bi** and **Co**, and then sintered **at** 800°C.

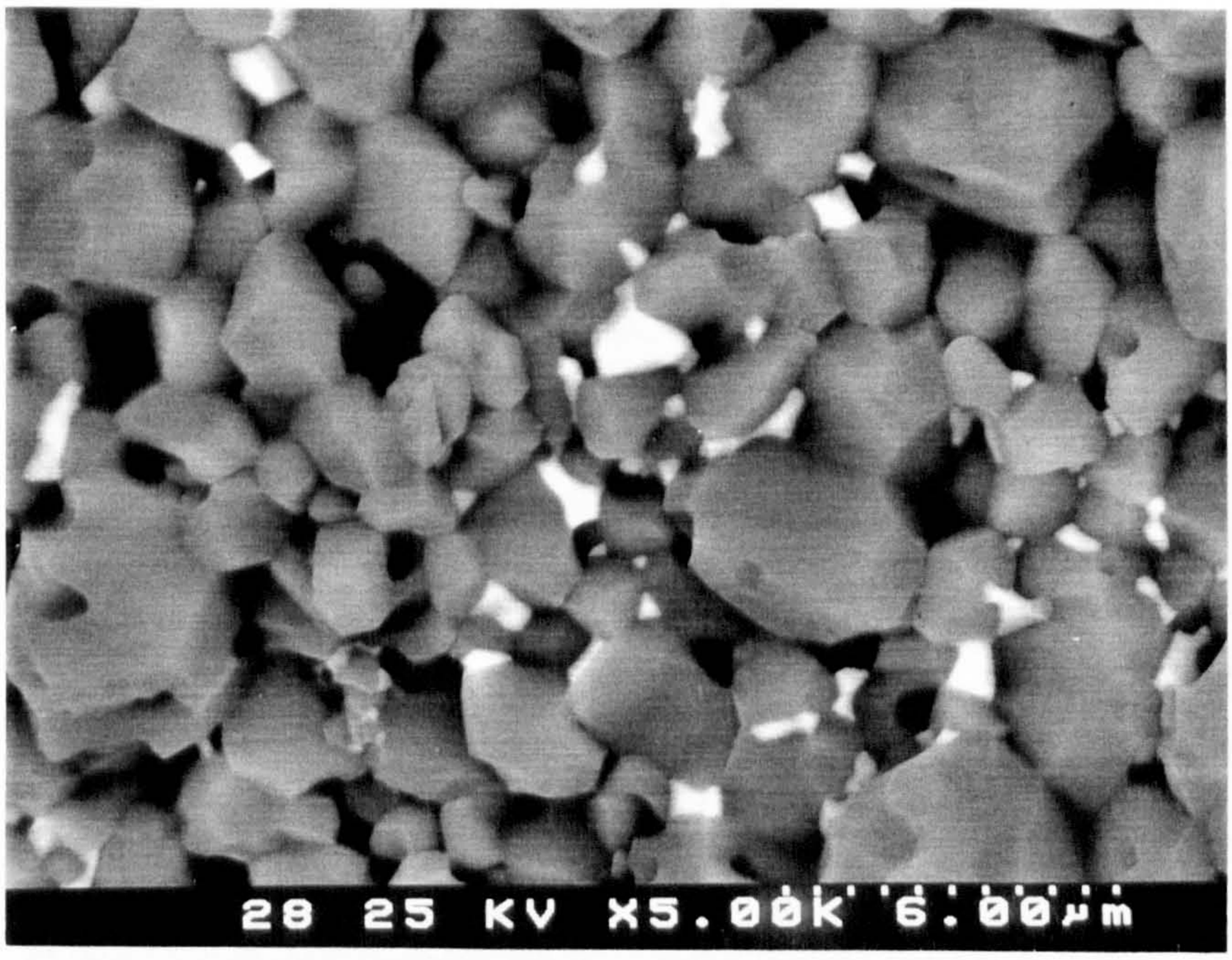


Fig. 5.1.3 (d) SEM micrograph of a ZnO ceramic sample **doped** (0.5 mol.%) with the oxides of **Bi, Co** and **Mn,** and then sintered at 800°C.

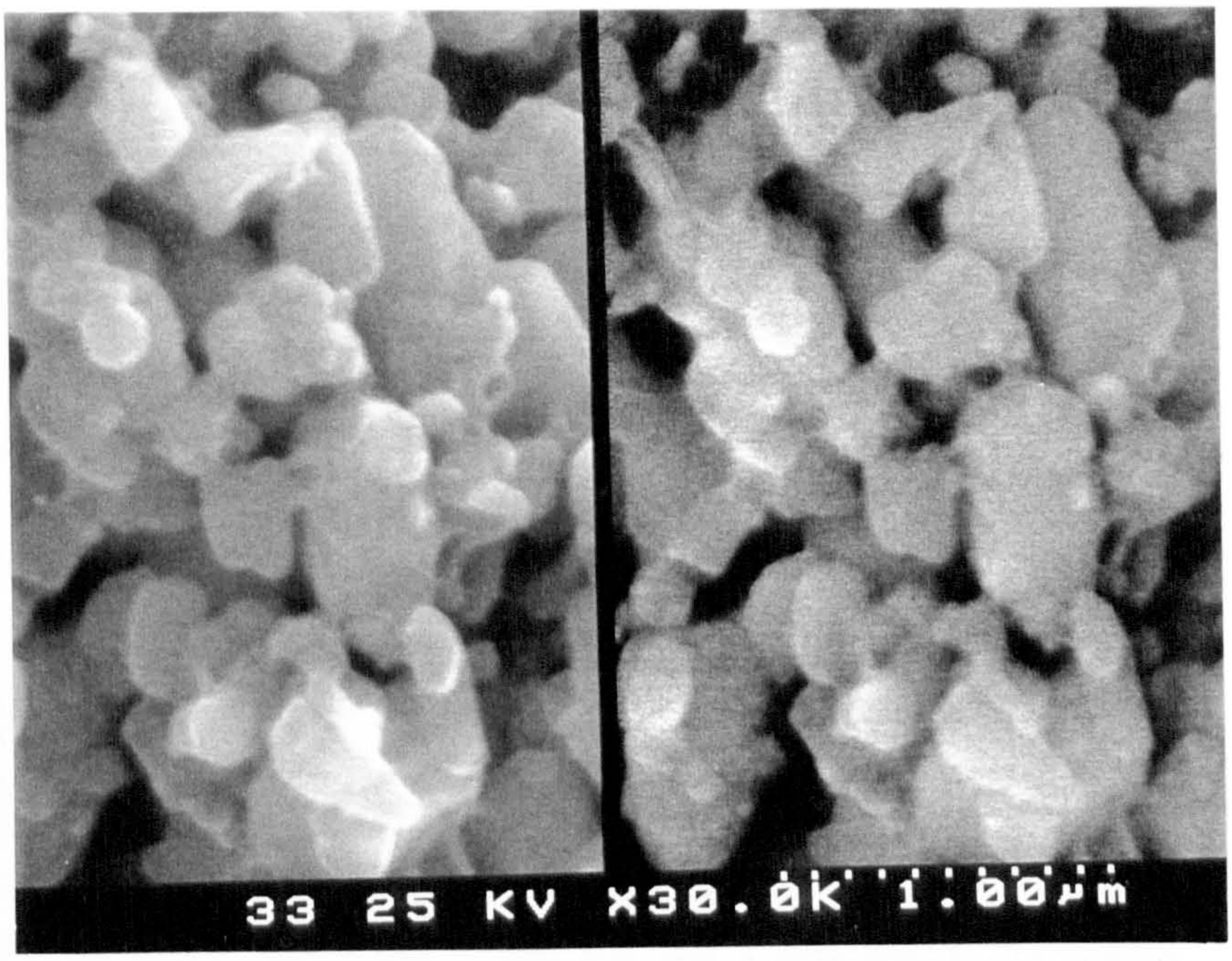


Fig. 5.1.3 (e) Secondary and backscattered electron images of ZnO ceramic sample **doped** (0.5 mol.%) with the oxides of **Bi**, **Sb**, **Co**, and **Mn** and then sintered at 800°C.

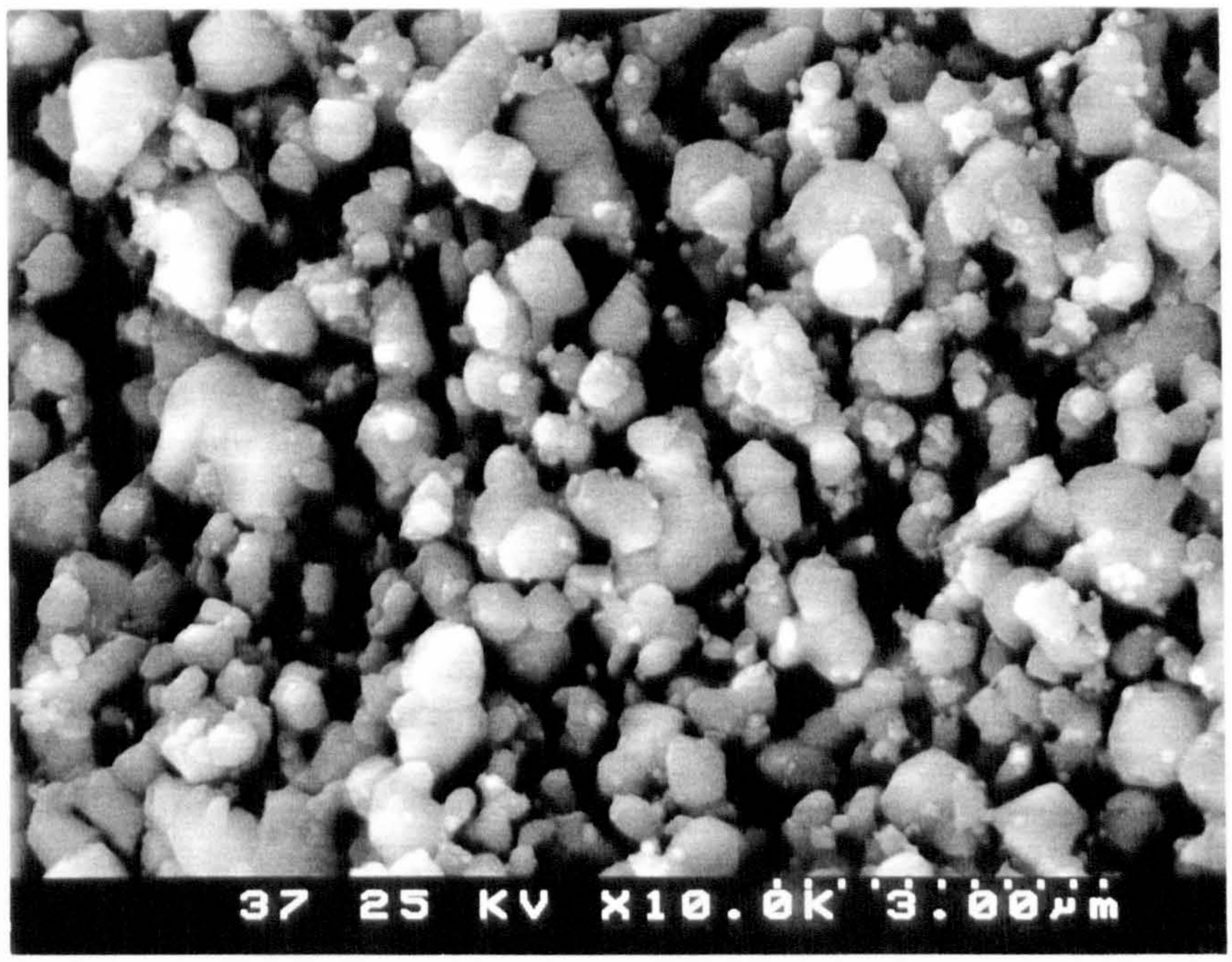


Fig. 5.1.3 (f) SEM micrograph of a ZnO ceramic sample **doped** (0.5 mol.%) with the oxides of **Bi**, **Sb, Co**, **Mn** and **Cr**, and then sintered at 800°C.

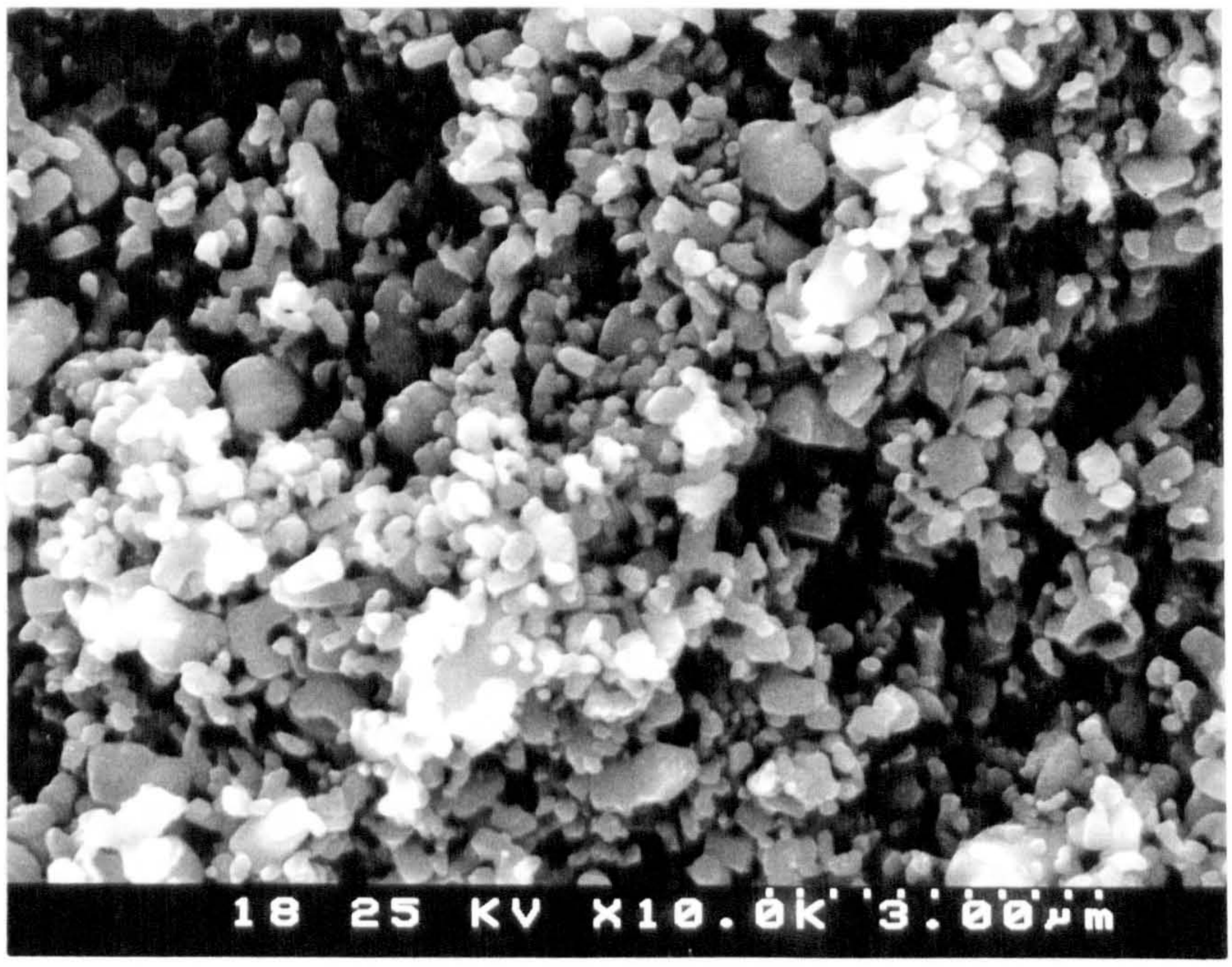


Fig. 5.1.3 (g) SEM micrograph of a ZnO ceramic sample **doped** (0.5 mol.%) with the oxides of **Bi**, and **Sb,** and then sintered at 800^{O}C.

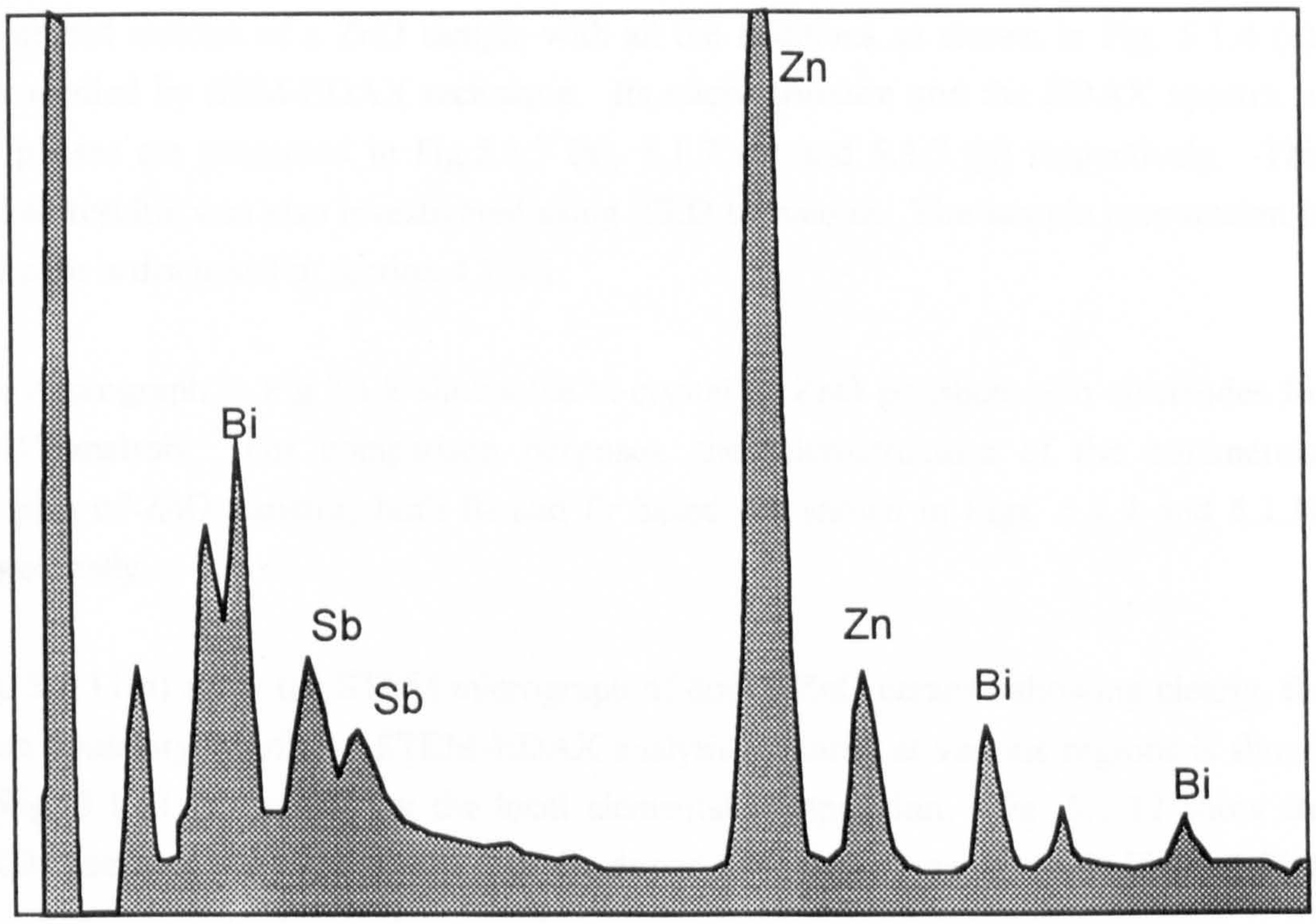


Fig. 5.1.3 (h) SEM-EDAX spectra of cluster (pyrochlore) regions in ZnO ceramic as shown in Fig. 5.1.3 (g), **doped** (0.5 mol.%) with the oxides of **Bi**, and **Sb**, and then sintered at 800^{O}C.

5.1.2.2 ZnO ceramics sintered at 1250°C

In section 5.2.1.1, results of the samples sintered at 800°C were intended to show the interrelated effects of dopant additives on grain growth and phase formations such as pyrochlore at this temperature. ZnO ceramic varistors are usually sintered at 1250°C. At these temperatures, the ZnO powders and additives are expected to have reacted and the resultant ceramic compact to have transformed into a particular type of microstructure, exhibiting varistor characteristics. Samples of different compositions have been studied to elucidate the interrelated effect of dopants on the microstructure. The resultant electrical behaviour (I:V) are discussed in sections 5.7.

Fig. 5.1.4 (a), (b), (c), (d), and (e) shows microstructure of ZnO based ceramic doped with oxides of single double and multiple dopants. Figs. 5.1.5 (a), (b), (c), (d), and (e), shows the X-ray mapping of the elements distributed in a ZnO ceramic sample doped with the oxides of Bi, Sb, Co, Mn and Cr, and then sintered at 1250°C. This was intended to characterise and show the distribution of additive elements in the microstructure. The X-ray mapping analyses complement the individual EDAX microprobe analyses. Fig. 5.1.6 shows the microstructure of the sample that was rapidly cooled from 1250°C. This preparation was intended to study the phases such as the SP or PY, present at this temperature.

An etched residue of a ZnO sample with all the additives as shown in Fig. 5.1.4 (e), was studied by SEM-EDAX technique. Its microstructure and the EDAX spectra of the phases are presented in Fig.5.1.7 (a), 5.1.7 (b) and 5.1.7 (c) respectively. This etched residue was also investigated using XRD technique. The sample preparation in this case is discussed in section 4.2.6.1.

The micrograph in Fig.5.1.8 shows the bi-crystal of ZnO polished with electrodes for EBIC analysis. For comparison purposes, the microstructure of the commercial samples of ZnO varistor, both Bi and Pr based are shown in Figs. 5.1.9 and 5.1.10 respectively.

Fig. 5.1.11(a) show the STEM micrograph of doped ZnO ceramic showing clearly, the grain boundary interface. STEM-EDAX analysis acquired at various regions is shown in Fig. 5.1.11 (b), indicating the local elemental composition. Fig. 5.1.12 show the XRD spectra of the etched residue of the doped ZnO ceramic as shown in Fig. 5.1.7(a).

As a summary, table 5.1.2 show several samples of different composition all sintered at 1250°C.

Table 5.1.2. Samples Sintered at 1250^{o}C

Fig. No	Sample composition	Grain size (μm) RMD ≈ 6%
5.1.4 (a)	Undoped ZnO ceramic	36
5.1.4 (b)	ZnO + Bi ceramic	51
5.1.4 (c)	ZnO + Bi + Co ceramic	41
5.1.4 (d)	ZnO + Bi + Co + Mn, ceramic	32
5.1.4.(e)	ZnO + Bi + Sb + Mn + Co + Cr, **ceramic**	28
5.1.4 (f)	Fractured microstructure of 5.1.**4 (e)**	28
5.1.5 (a,b,c,d, e)	x-ray mapping of microstructure in Fig. 5.1.4 (e)	28
5.1.6	As in Fig 5.1.4e above but **rapidly cooled** from 1250^{o}C	19
5.1.7 (a),	**Etched residue** of the ZnO ceramic **in Fig. 5.1.4 (e).**	**28**
5.1.7 (b) and (c)	x-ray analysis of the etched residue of ZnO varistor	/
5.1.8	Pure ZnO bi-crystal	2-3mm
5.1.9	Microstructure of a Commercial ZnO varistor (Bi, based)	35
5.1.10	Microstructure of a Commercial ZnO varistor (Pr, based)	52
5.1.11 (a)	STEM micrograph of the sample in Fig. 5.1.4 (e)	28
5.1.11 (b)	Schematic showing the region of STEM-EDAX analysis	
5.1.12	XRD of the etched residue of the sample in Fig. 5.1.7 (a)	

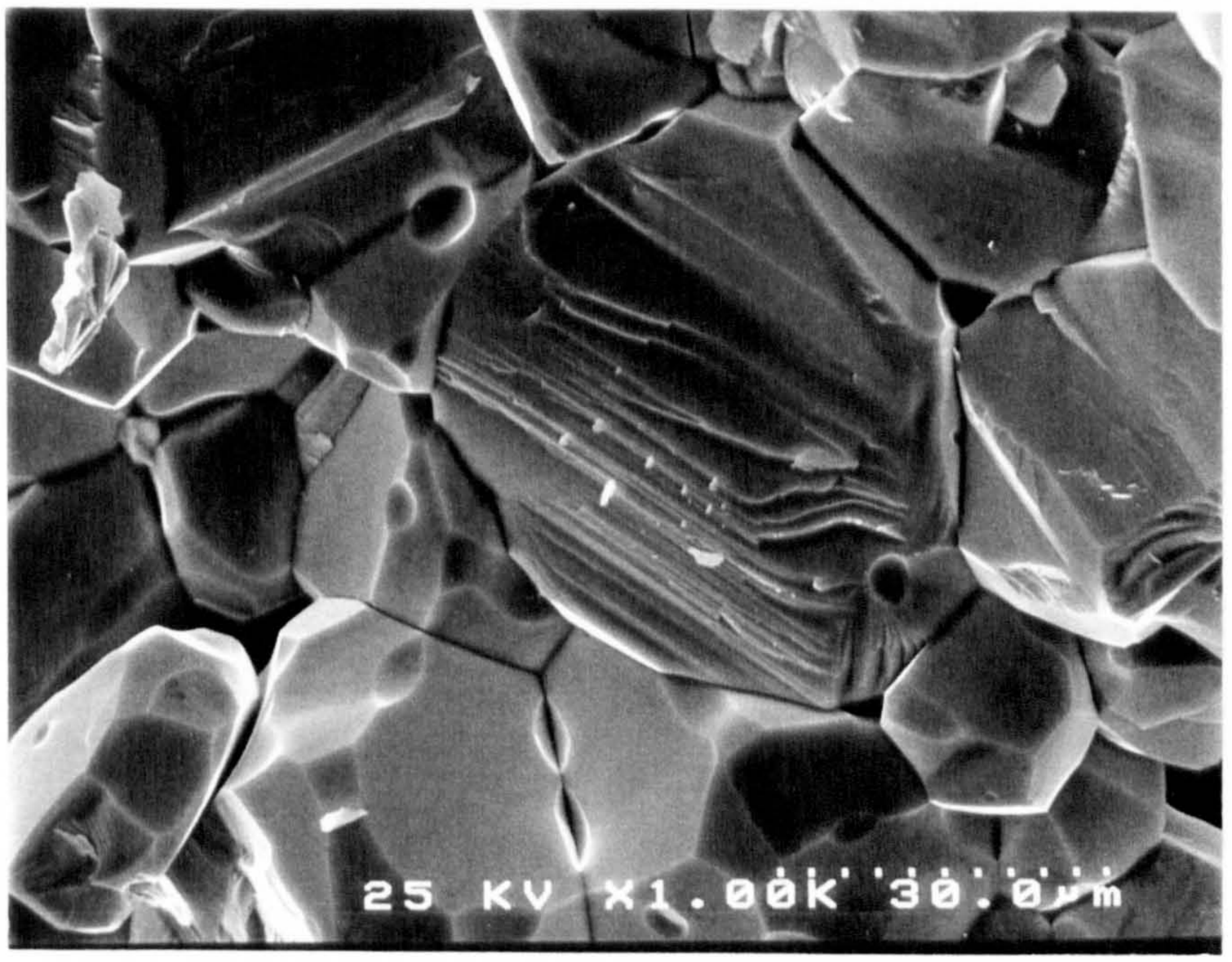


Fig. 5.1.4 (a) SEM micrograph of the **undoped** ZnO ceramic **sample, sintered** at 1250^{o}C.

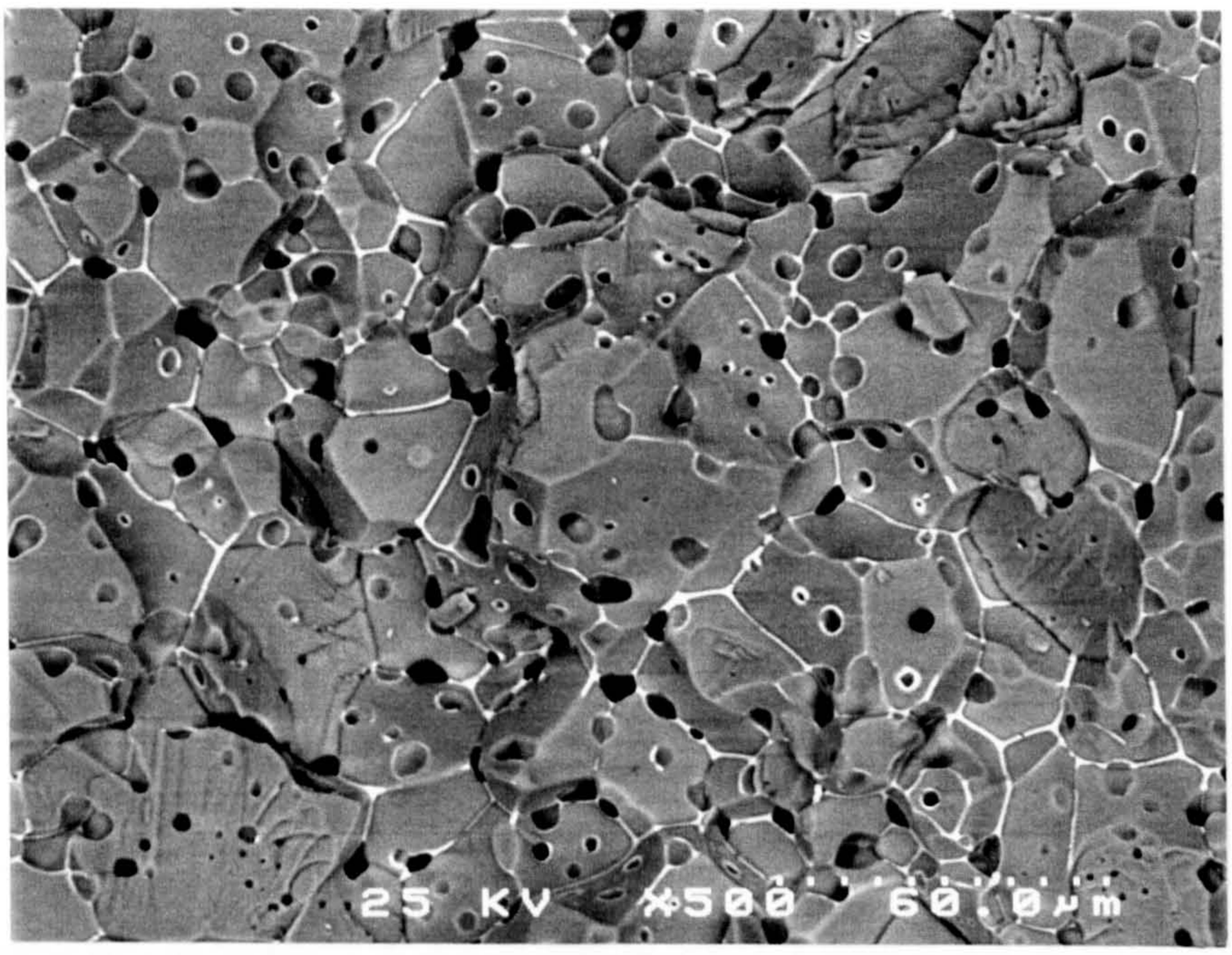


Fig. 5.1.4 (b) SEM micrograph of a ZnO ceramic sample **doped** (0.5mol%) with **Bi** oxide, and then sintered at 1250°C.

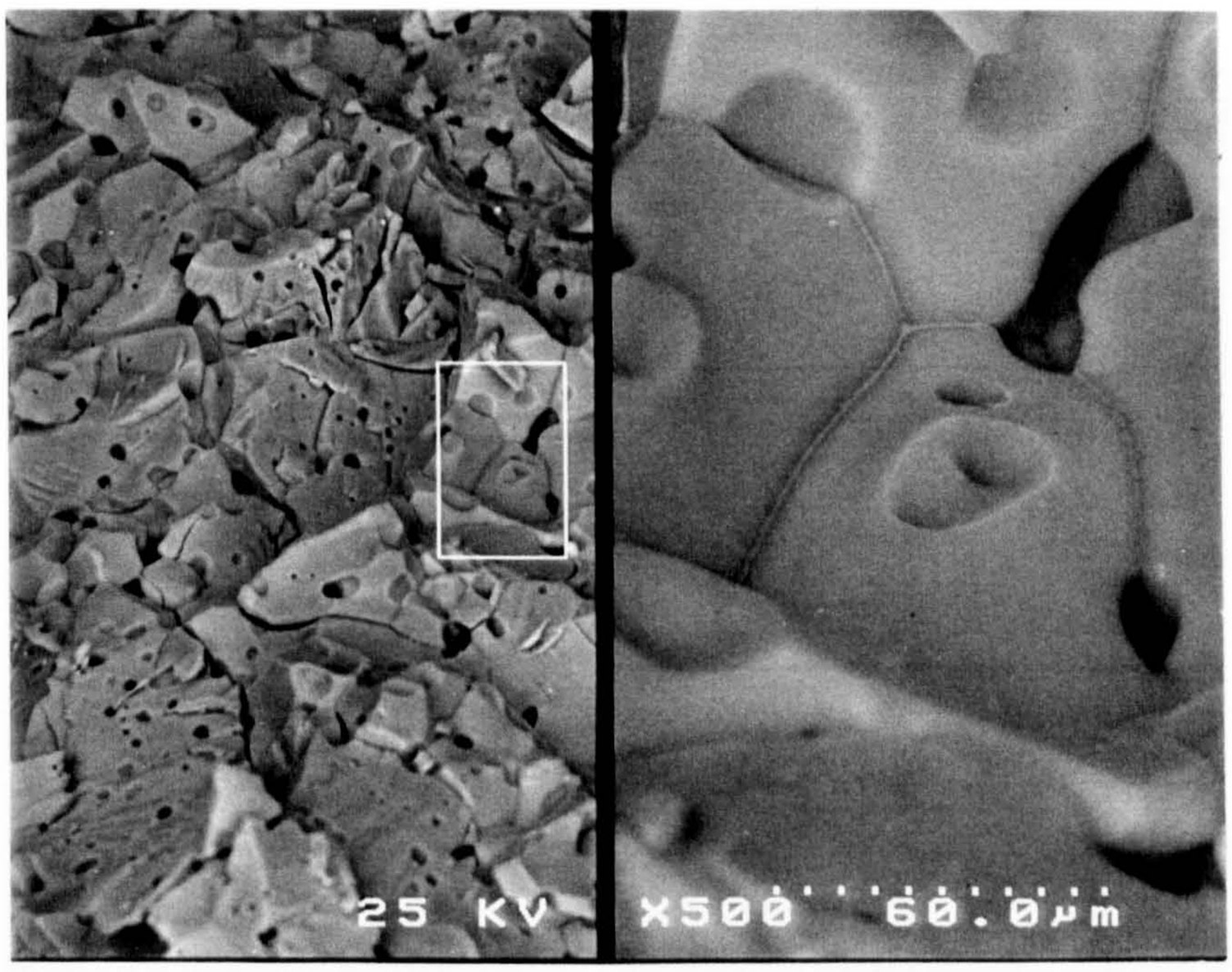


Fig. 5.1.4 (c) SEM micrograph of a ZnO ceramic sample **doped** (0.5mol%) with the oxides of **Bi**, and **Co** and then sintered at 1250°C. The backscattered image on the right is X 2500 mag.

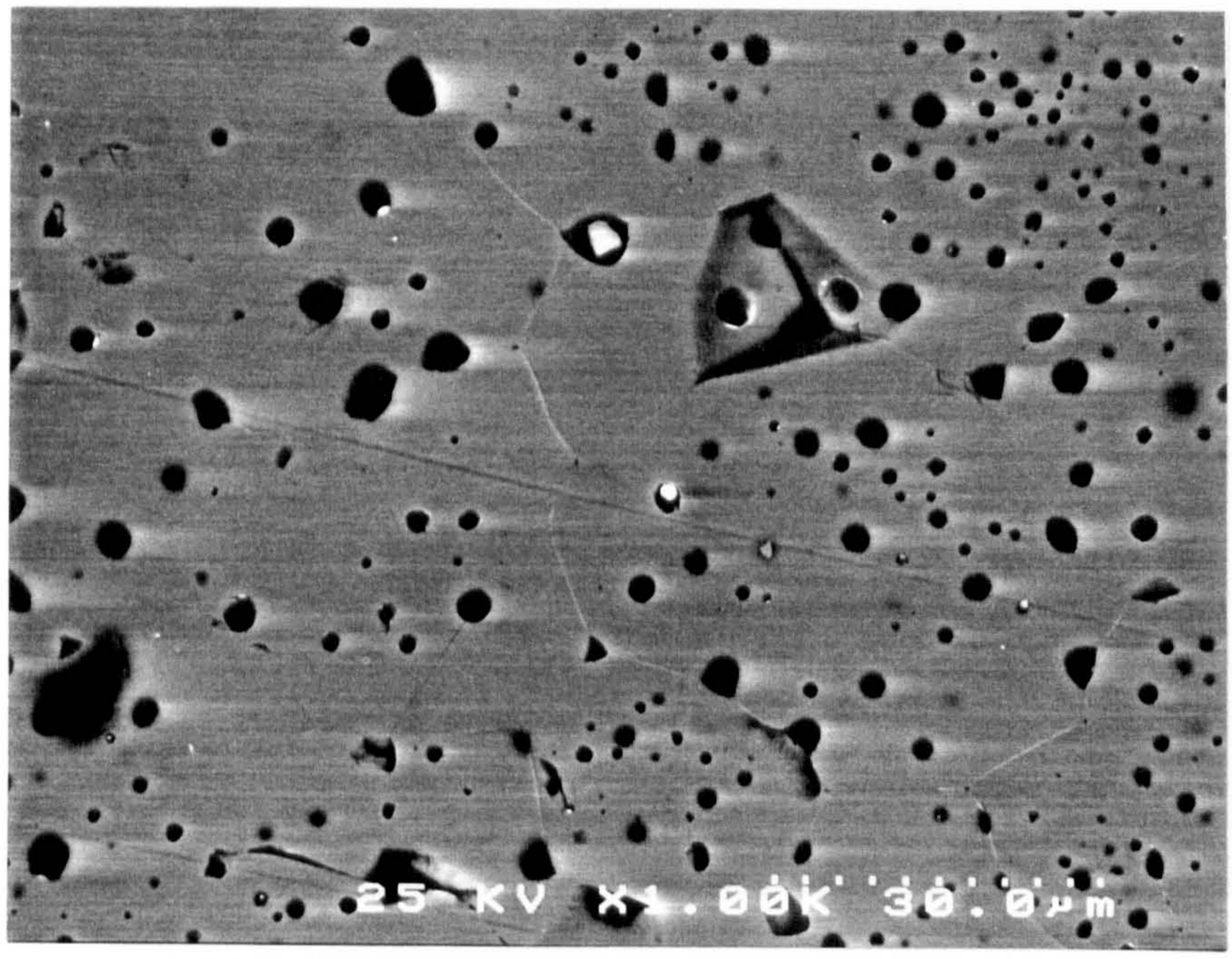


Fig. 5.1.4 (d) SEM micrograph of a ZnO ceramic sample **doped** (0.5mol%) with the oxides of **Bi**, **Co**, and **Mn** and then sintered at 1250^{o}C .

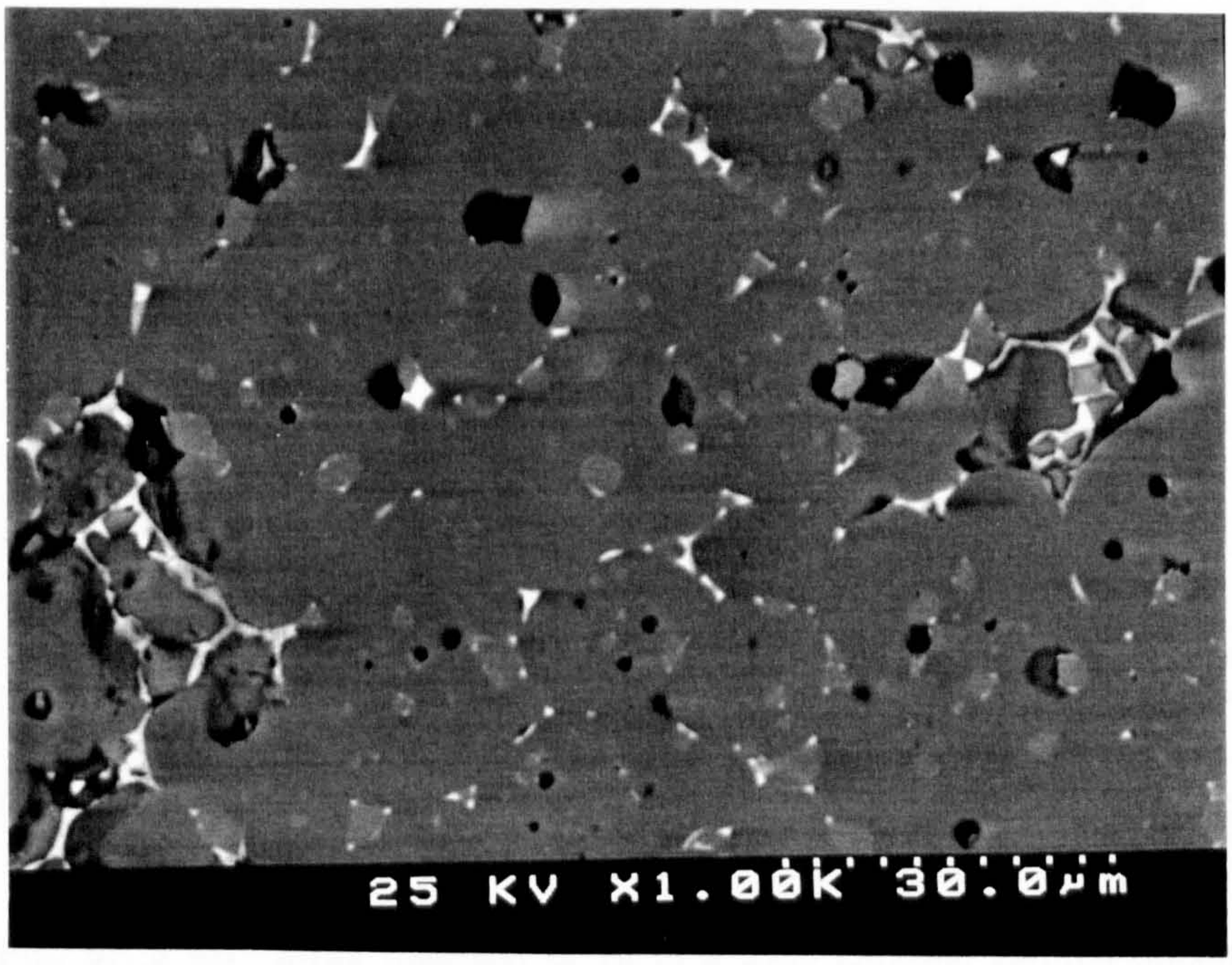


Fig. 5.1.4 (e) SEM micrograph of a ZnO ceramic sample **doped** (0.5mol%) with the oxides of **Bi, Sb**, **Co**, **Mn** and **Cr**, and then sintered at 1250^{o}C.

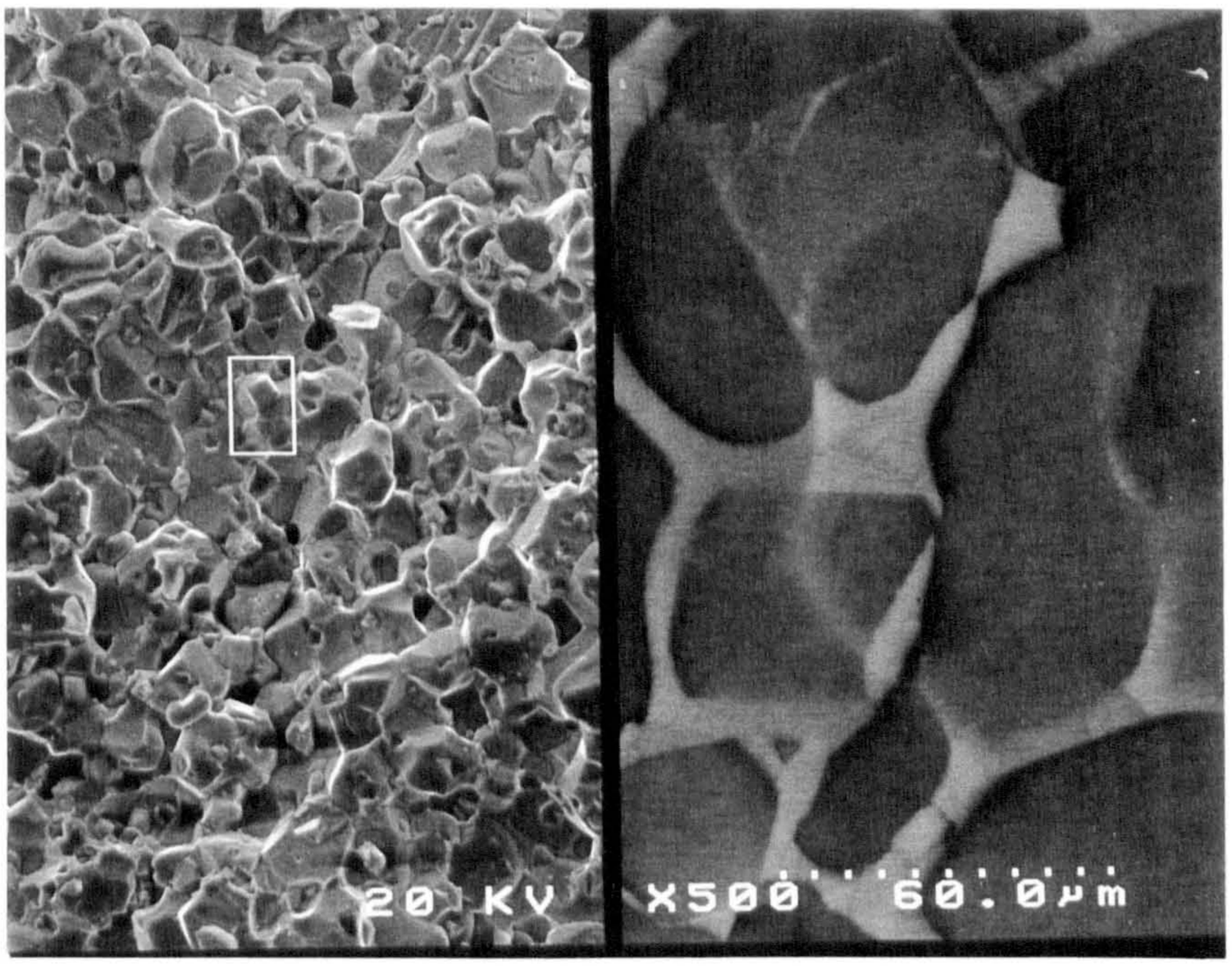


Fig. 5.1.4 (f) SEM micrograph of a ZnO ceramic sample, (fractured surface) **doped** (0.5mol%) with the oxides of **Bi, Sb**, **Co**, **Mn** and **Cr**, and then sintered at 1250°C.

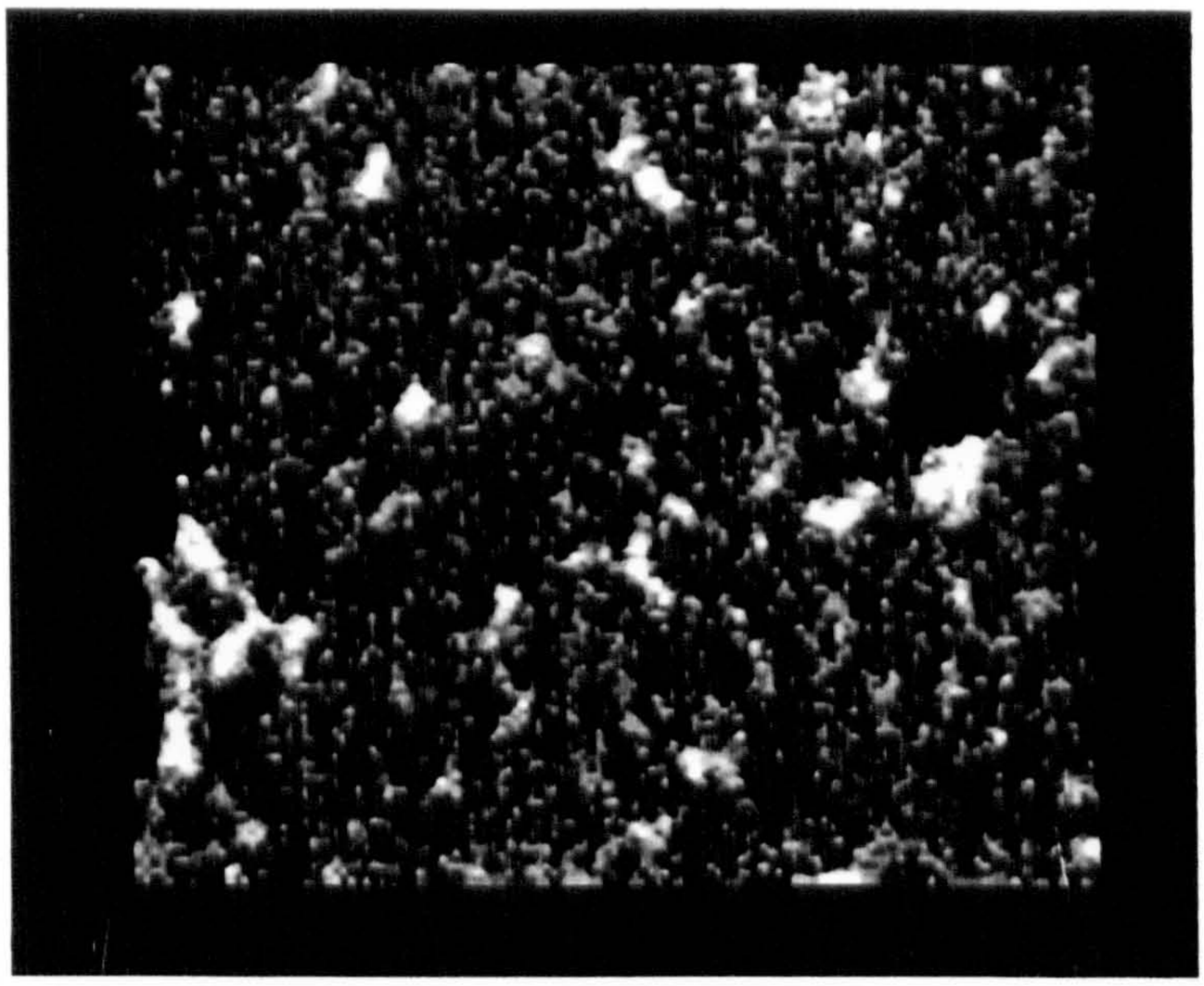


Fig. 5.1.5 (a) **X-ray** mapping of **Bi** in a ZnO ceramic sample doped (0.5mol%) with the oxides of Bi, Sb, Co, Mn and Cr, and then sintered at 1250°C. The size of this image (110 μm x 79μm) corresponds to that in Fig.5.1.4 (e). **Scale**: the image has reduced by ≈ 32% horizontally (10mm ≈14μm) and ≈18% vertically (10mm ≈ 12μm).

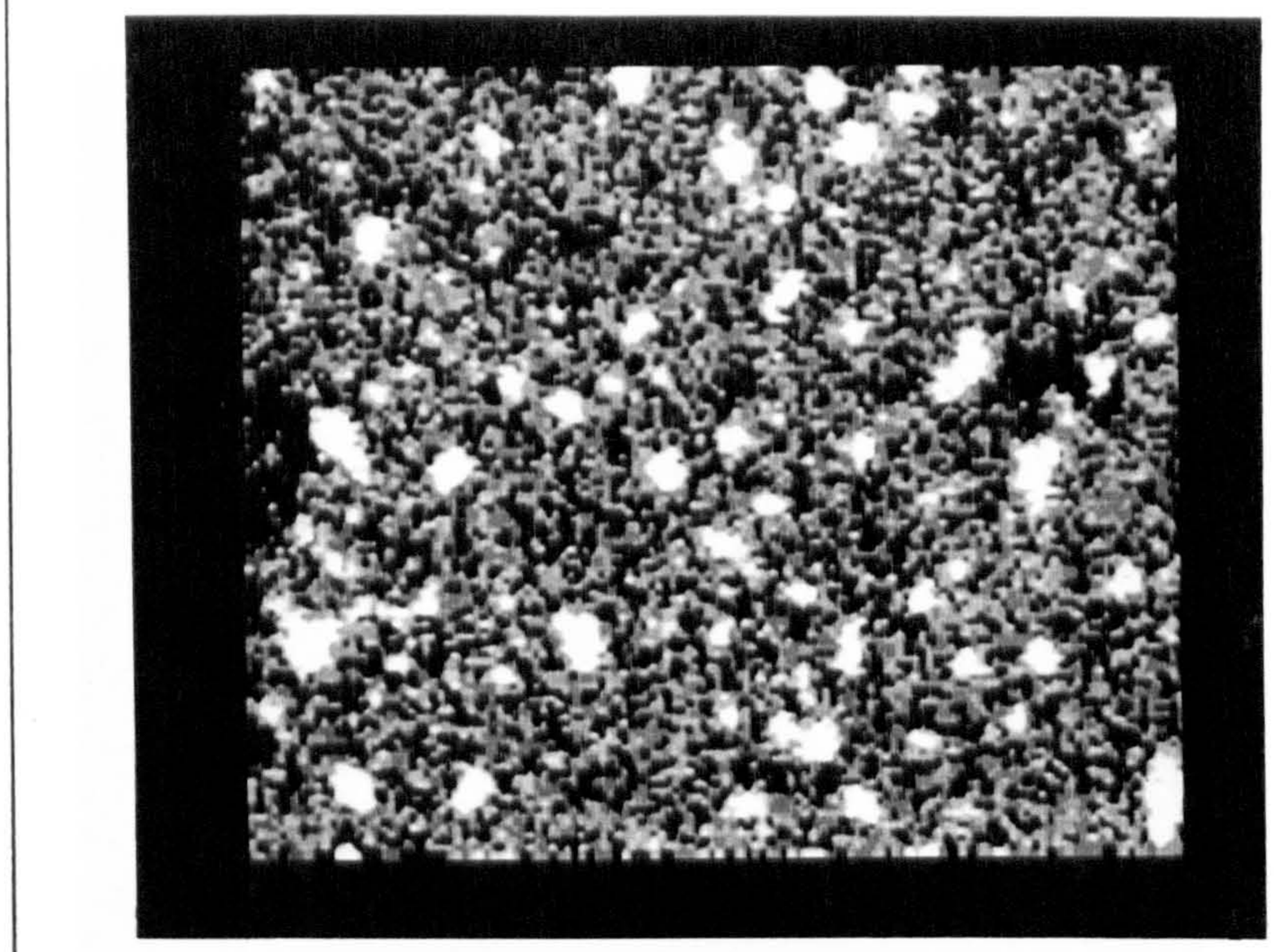


Fig. 5.1.5 (b) X-ray mapping of **Sb** in a ZnO ceramic sample doped (0.5 mol.%) with the oxides of Bi, Sb, Co, Mn and Cr, and then sintered at 1250°C. The size of this image (110 μm x 79μm) corresponds to that in Fig.5.1.4 (e). **Scale**: the image has reduced by ≈ 32% horizontally (10mm ≈14μm) and ≈18% vertically (10mm ≈ 12μm).

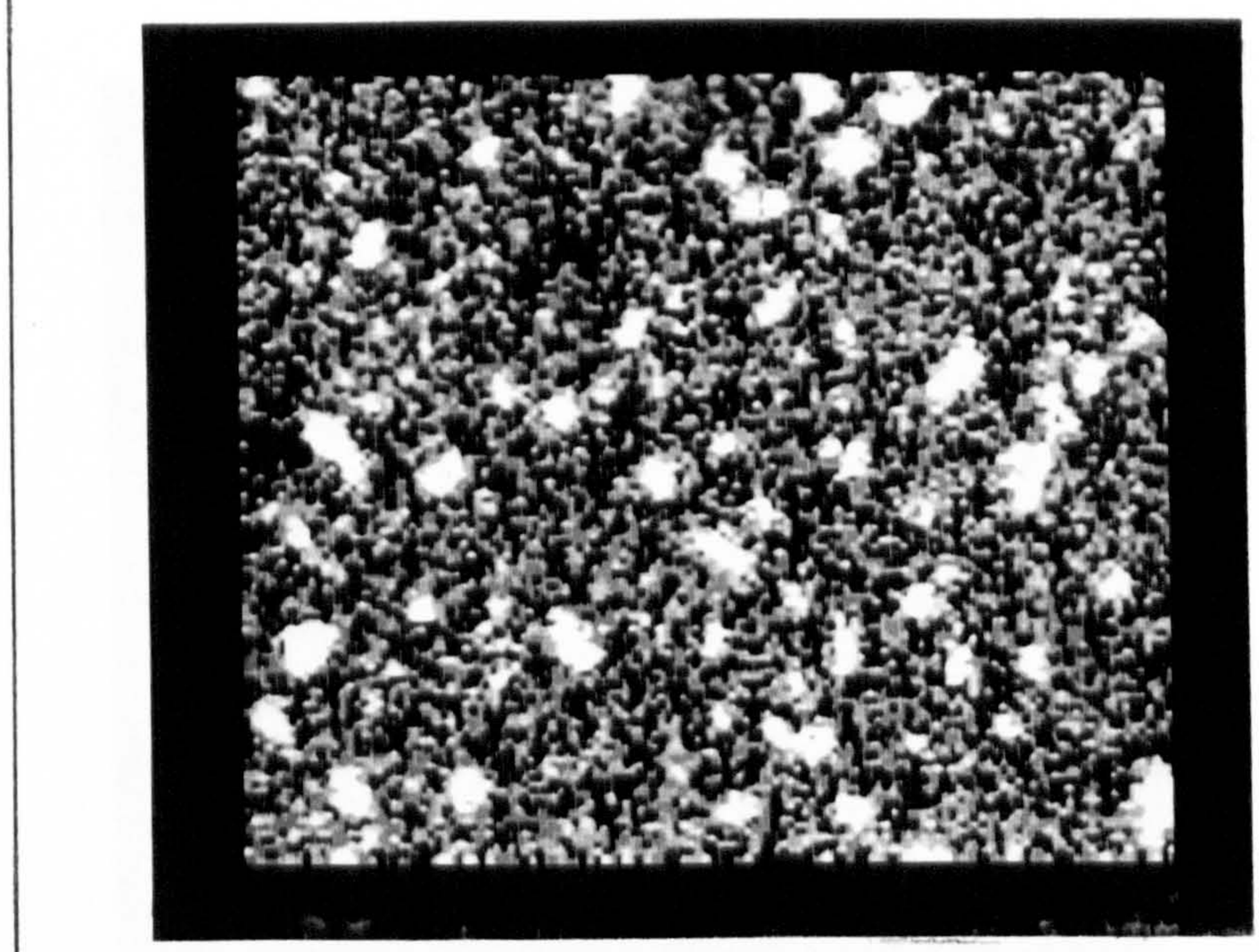


Fig. 5.1.5 (c) X-ray mapping of **Cr** in a ZnO ceramic sample doped (0.5 mol.%) with the oxides of Bi, Sb, Co, Mn and Cr, and then sintered at 1250°C. The size of this image (110 μm x 79μm) corresponds to that in Fig.5.1.4 (e). **Scale**: the image has reduced by ≈ 32% horizontally (10mm ≈14μm) and ≈18% vertically (10mm ≈ 12μm).

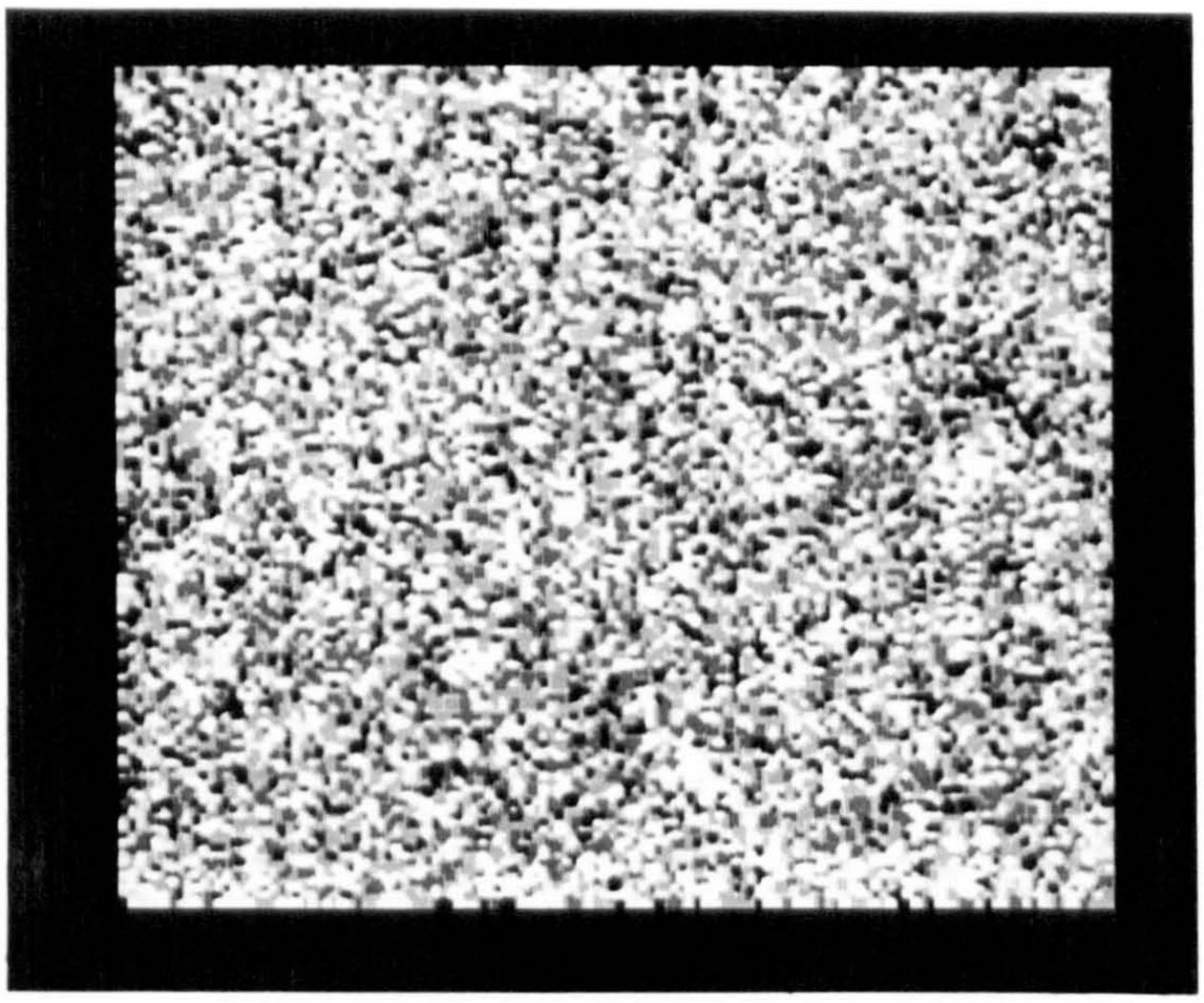


Fig. 5.1.5 (d) X-ray mapping of **Mn** in a ZnO ceramic sample doped (0.5 mol.%) with the oxides of Bi, Sb, Co, Mn and Cr, and then sintered at 1250^{o}C. The size of this image (110 μm x 79μm) corresponds to that in Fig.5.1.4 (e). **Scale**: the image has reduced by ≈ 32% horizontally (10mm ≈14μm) and ≈18% vertically (10mm ≈ 12μm).

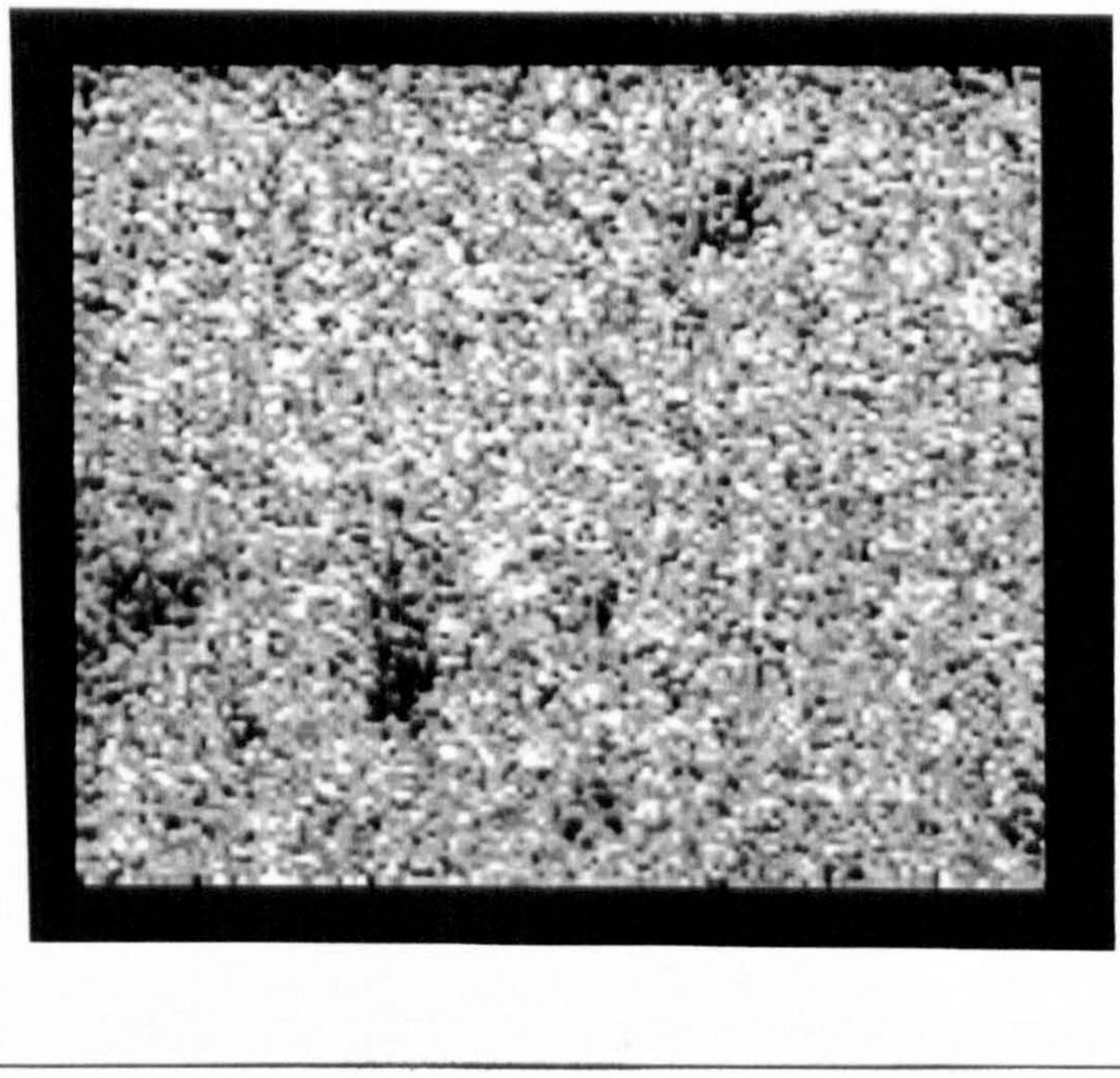


Fig. 5.1.5 (e) X-ray mapping of Co in a ZnO ceramic sample doped (0.5 mol.%) with the oxides **of Bi**, Sb, Co, Mn and Cr. **and then** sintered at 1250^{o}C. The size of this image (110 μm x 79μm) corresponds to that in Fig.5.1.4 (e). **Scale**: the image has reduced by ≈ 32% horizontally (10mm ≈14μm) and ≈18% vertically (10mm ≈ 12μm).

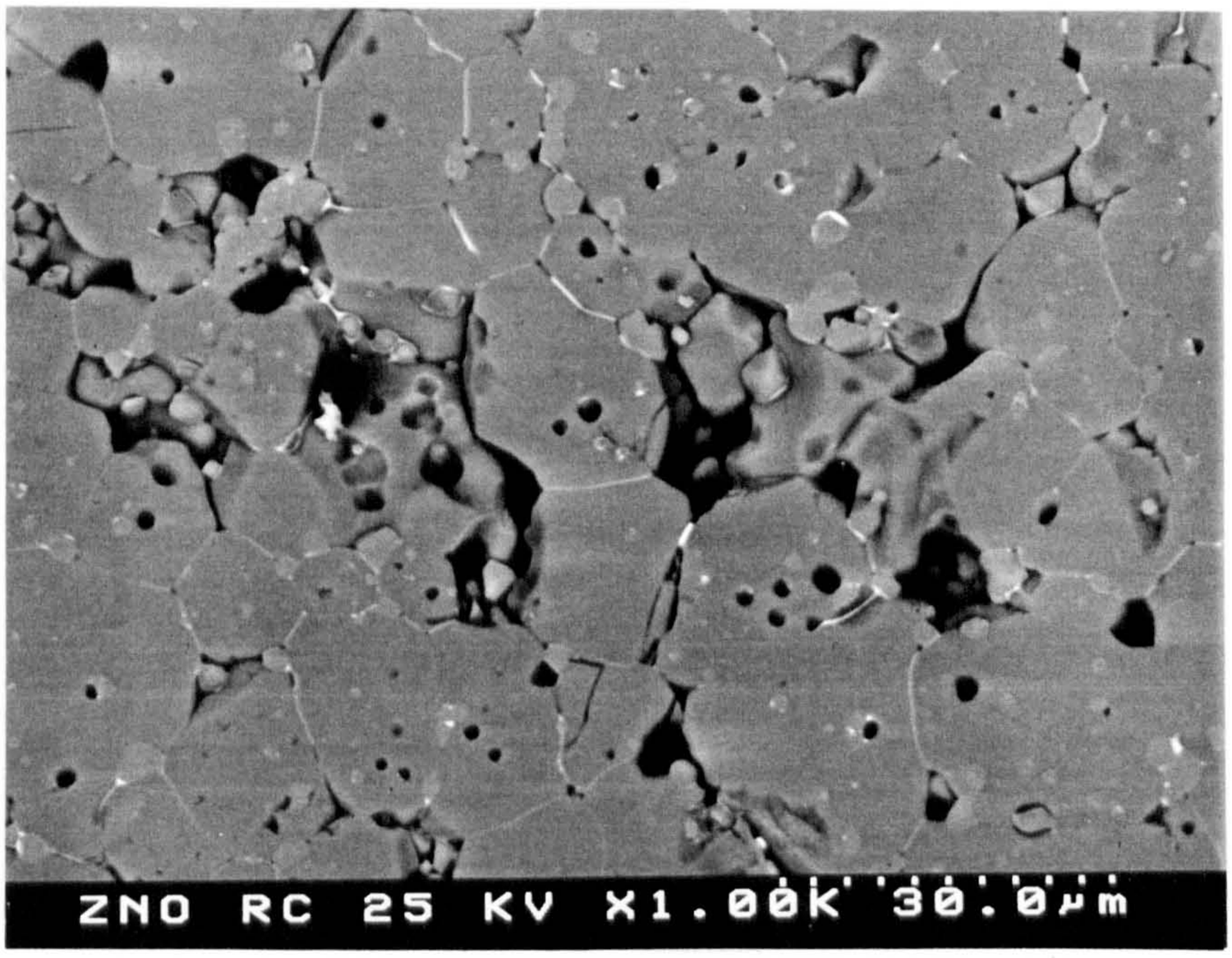


Fig. 5.1.6 SEM micrograph of a ZnO ceramic sample **doped** (0.5 mol.%) with the oxides of **Bi**, **Sb**, **Co**, **Mn** and **Cr**, and then **sintered and rapidly cooled from** 1250°C.

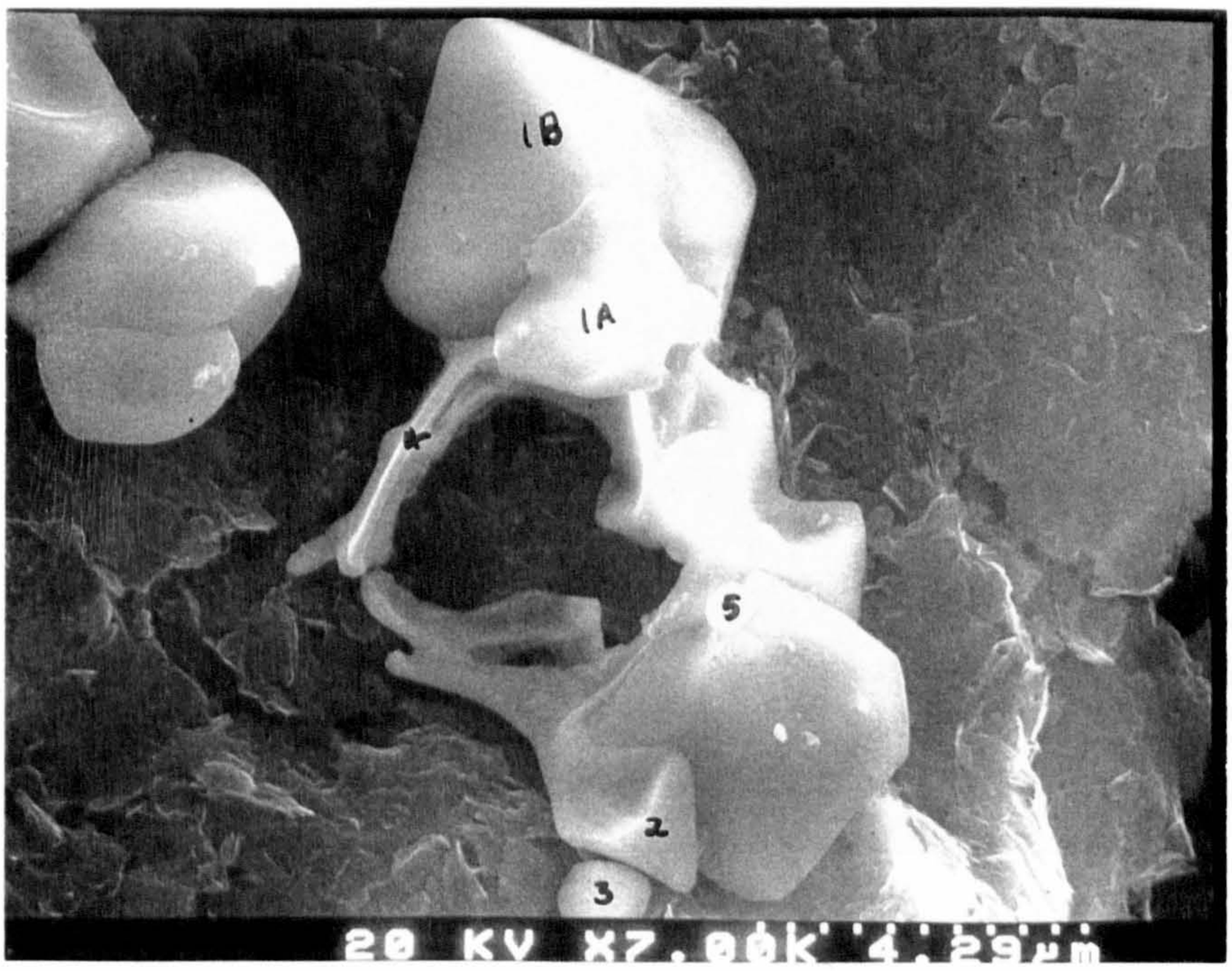


Fig. 5.1.7 (a) SEM micrograph of an **etched residue** of a ZnO ceramic sample, **doped** (0.5 mol.%) with the oxides of **Bi**, **Sb, Co**, **Mn** and **Cr**, and then sintered at 1250°C.

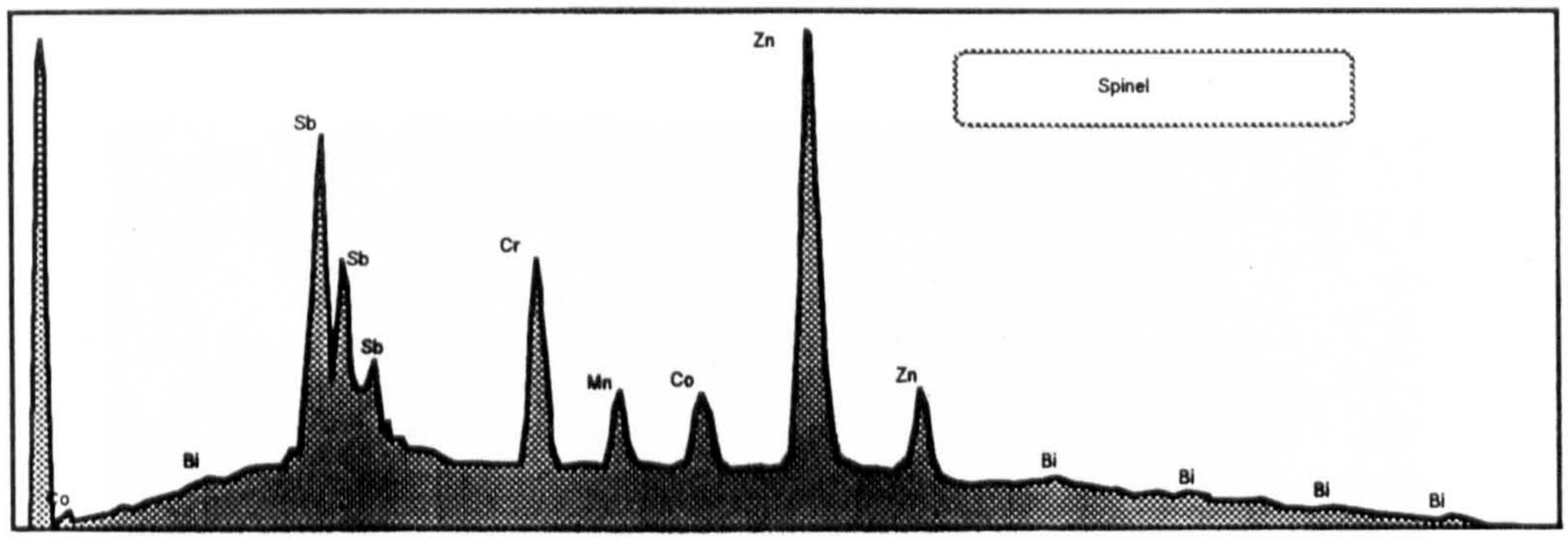


Fig. 5.1.7 (b) SEM-EDAX spectra (A) and (B) respectively corresponds to phases marked (1B) and (1A) in the etched sample of the ZnO varistor as shown in Fig. 5.1.7 (a).

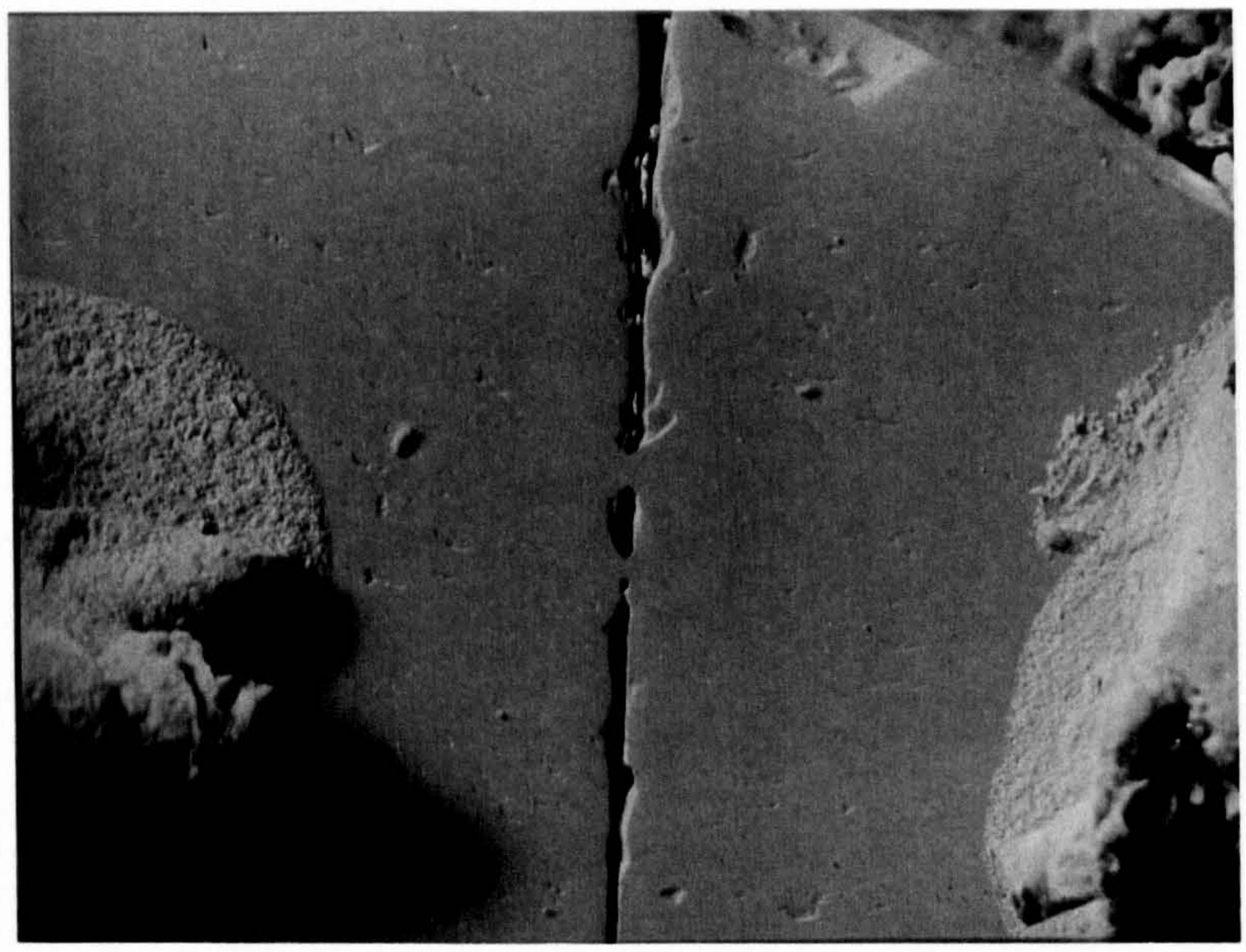


Fig. 5.1.8 SEM micrograph of a ZnO bi-crystal sample with the Bi oxide sandwiched in between the polished single crystals and sintered at 1500°C for 10 hours.

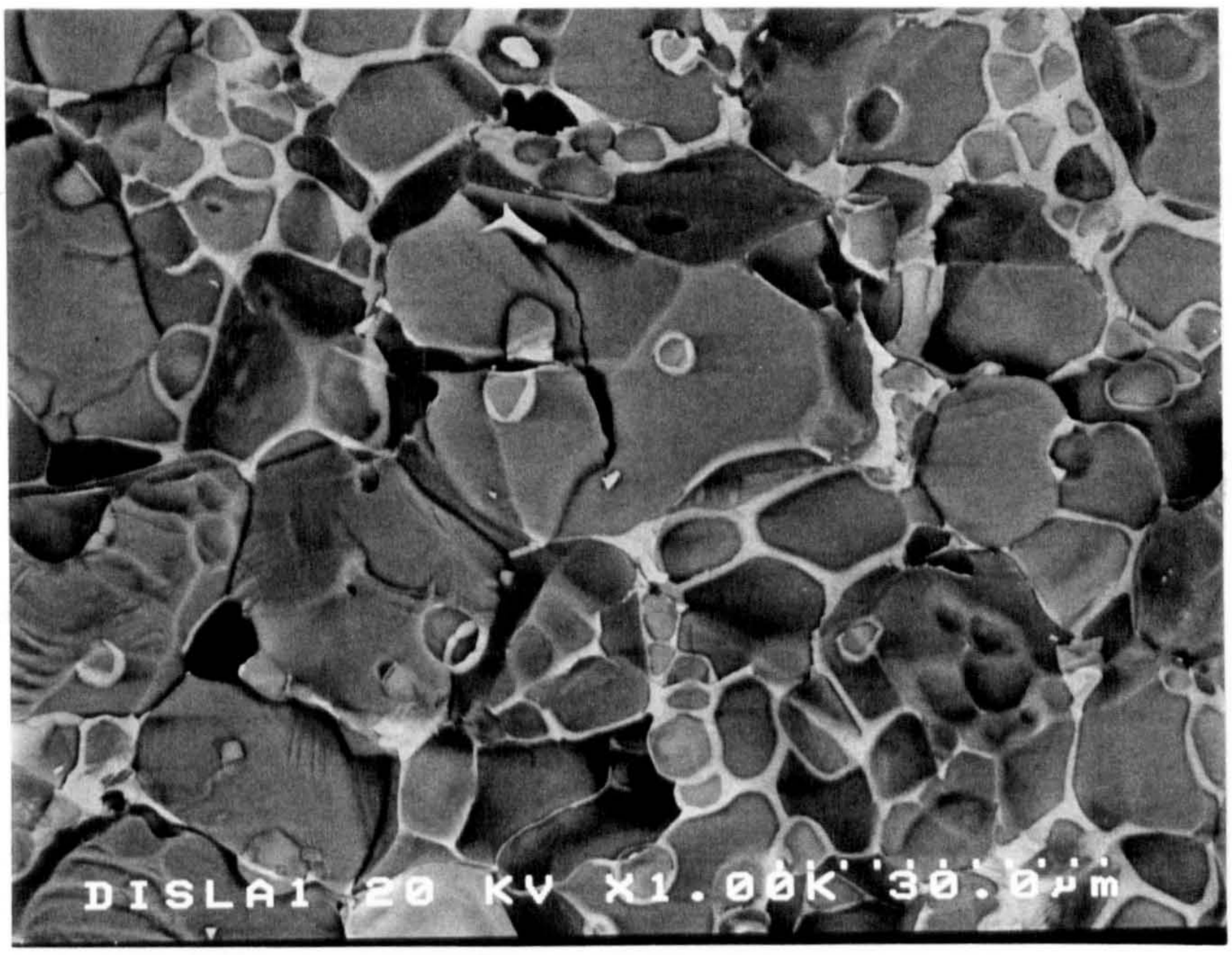


Fig. 5.1.9 SEM micrograph of a commercial ZnO, **Bi** based varistor sample.

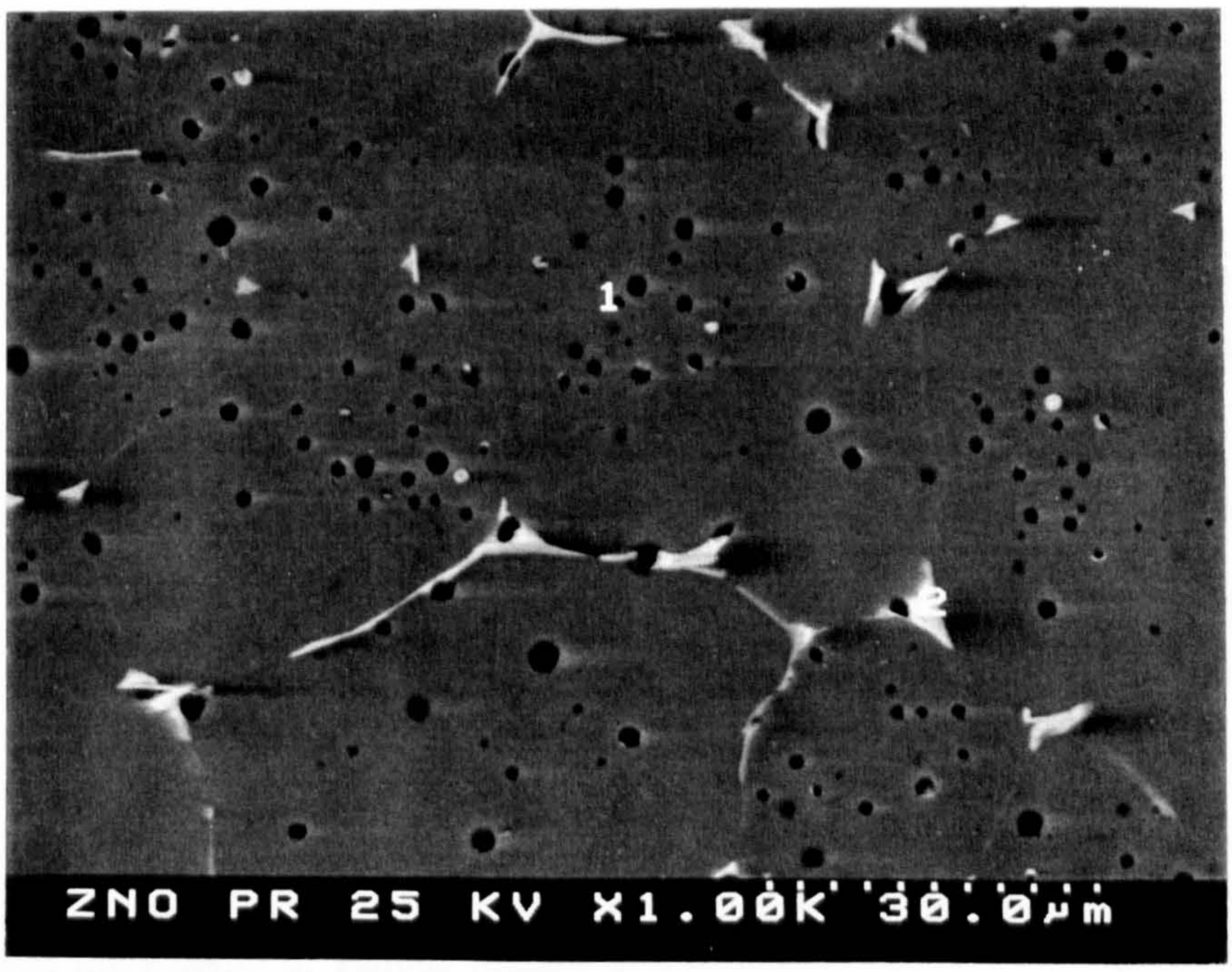


Fig. 5.1.10 SEM micrograph of a commercial ZnO, **Pr** based varistor sample.

5.1.2.3. TEM/STEM-EDAX analysis of ZnO ceramic

Sample preparation for TEM analysis has been discussed in Chapter 4, section 4.2.4. Fig. 5.1.11 (a) shows a STEM micrograph showing grain boundary interface and phases at the triple points. Fig. 5.1.11 (b) show various regions identified by STEM-EDAX analysis.

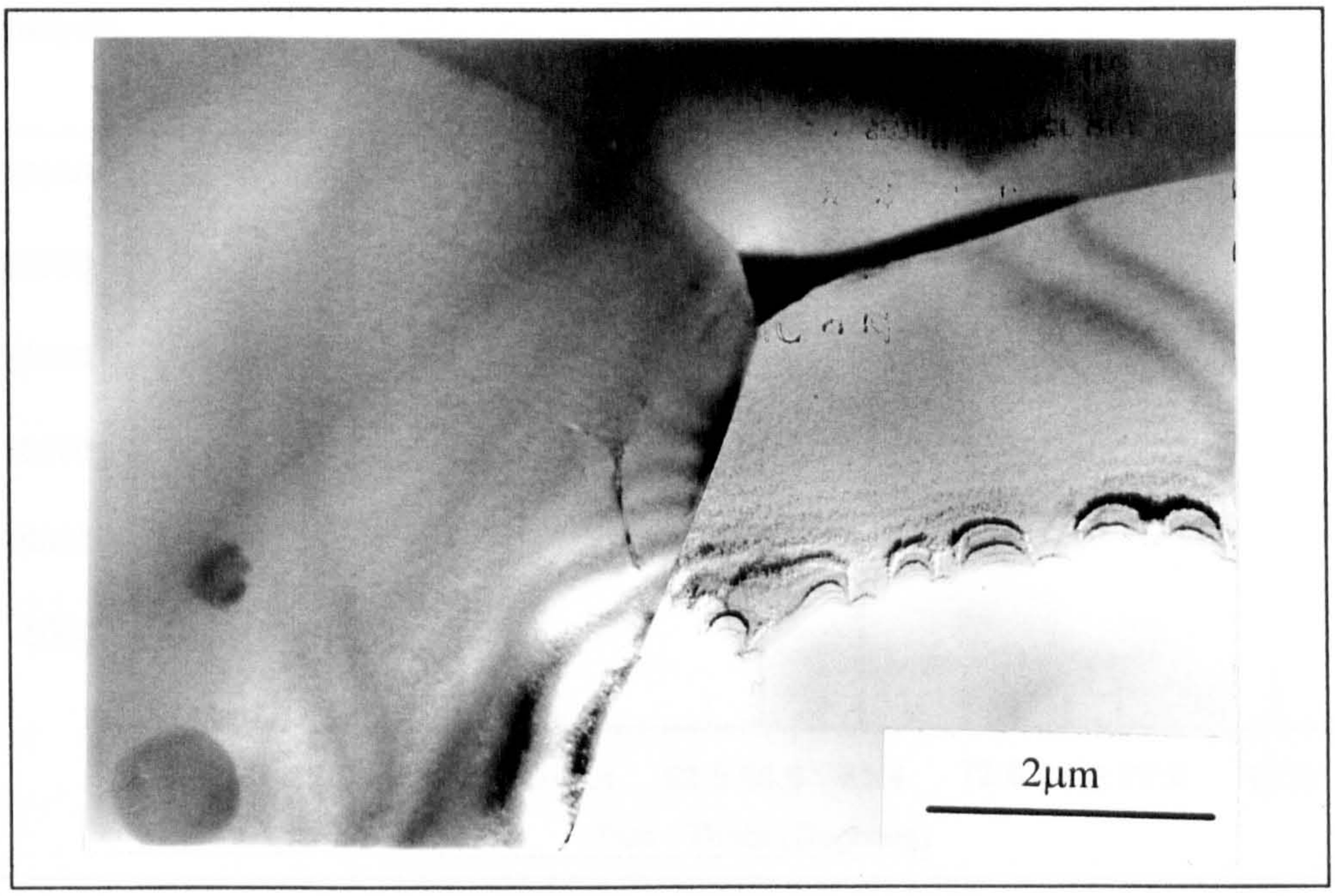


Fig.5.1.11. (a) STEM micrograph (10K mag.) taken at 200kV, showing the grain boundaries interface with triple point coinciding with the EDAX (1) analysis in Fig. 5.1.11 (b). Scale: 14mm = 1μm.

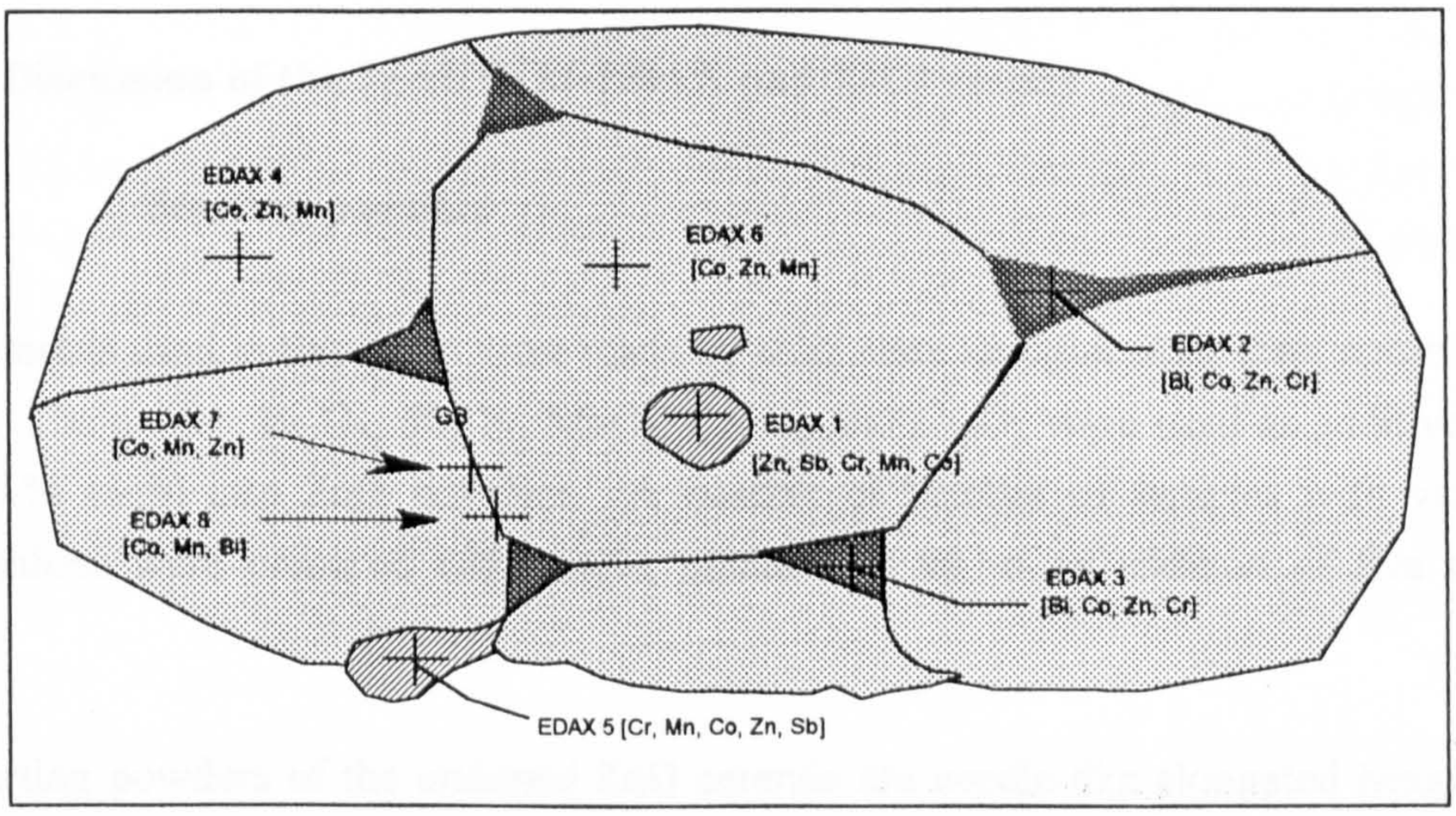


Fig.5.1.11 (b) STEAM-EDAX analysis of the doped ZnO ceramic. Analysis was undertaken at various regions in the microstructure as in fig.5.1.11 (a), marked with a X and labelled as EDAX 1-8 with the list of elements detected. Regions marked as EDAX (1) and (5) are spinel particles shown shaded in this figure. EDAX (2) and (3) are the Bi rich phases (cross sections of the lacy type of network as previously identified using SEM. Regions marked as EDAX (4) and (6) corresponds to the ZnO grain, while those marked as (7) and (8) are the points at the grain boundary.

5.1.2 4 XRD

Fig. 5.1.12 show an XRD analysis of etched residue of doped ZnO ceramic. This residue consists of mainly spinel phase with a trace of pyrochlore phase. An SEM micrograph of this residue is shown in Fig. 5.1.7 (a). A trace of pyrochlore phase was detected by SEM-EDAX but the spinel ($Zn_{2.33}$ $Sb_{0.67}$ O_4) phase is dominant as confirmed here by XRD analysis.

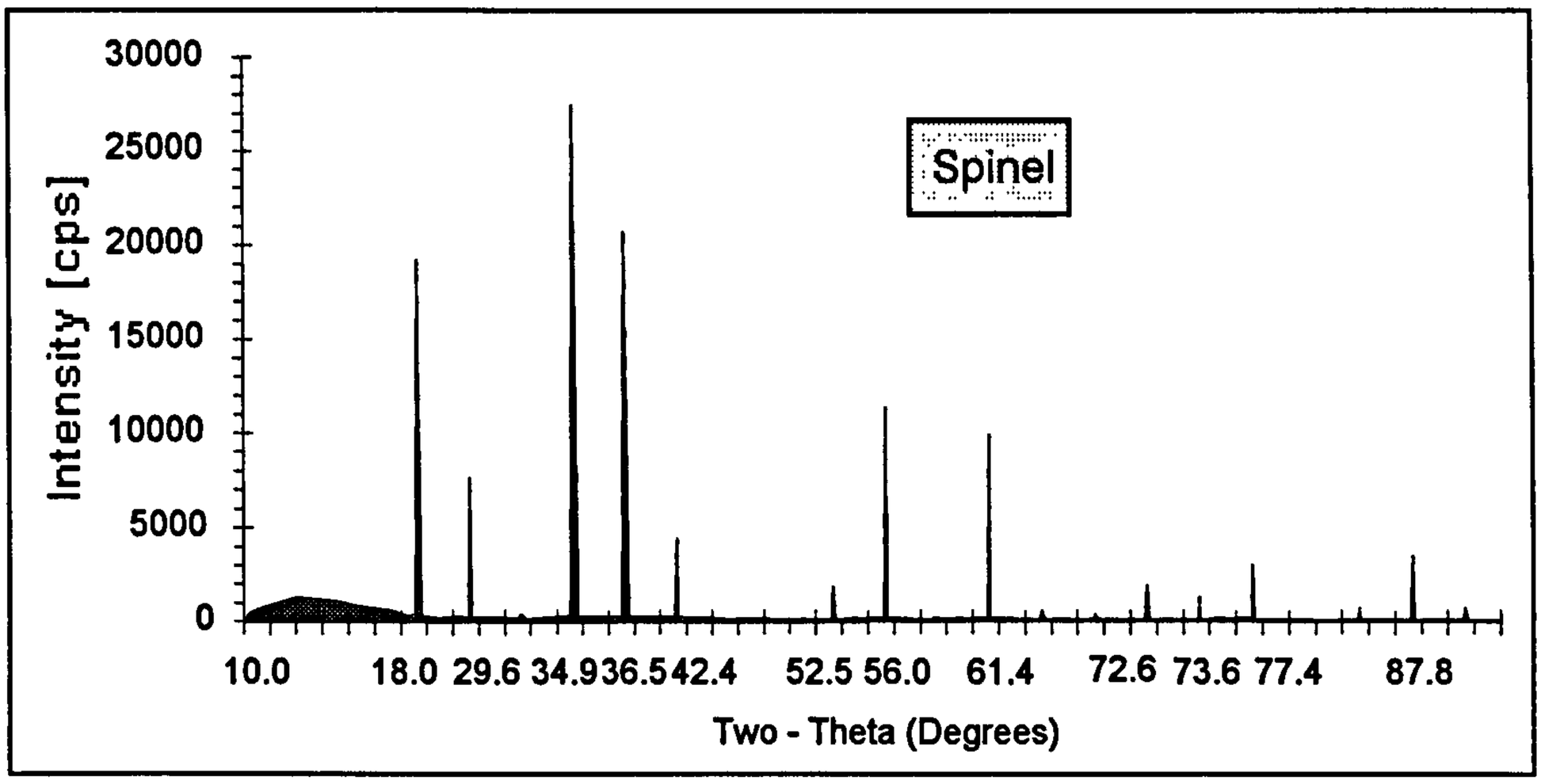


Fig. 5.1.12. XRD spectra of the etched residue of the ZnO doped ceramic sample as shown in Fig. 5.1.7 (a). According to the JCPDS-ICDD 15-687, the 2 - θ position and the relative intensity of these peaks corresponds to Zn_7 Sb_2 O_{12} spinel compound.

5.1.3 Discussion of the SEM/TEM-EDAX and XRD results

5.1.3.1. Starting powders

The materials used in this study were made by solid state reaction from their constituent oxides. The oxides: Bi_2O_3, Sb_2O_3, MnO_2, Co_3O_4 and Cr_2O_3 were used as additives (at 0.5 mol.% each) into ZnO powders. A number of batches of samples with varying compositions were prepared with single, double and up to an addition of five metal oxides.

The starting powders of the undoped ZnO ceramic are needle-like elongated hexagonal prisms. In Fig. 5.1.1, it can be seen that in the pure ZnO powders, amongst the small needle like particles, some of the particles are joined as 4 hexagonal prisms meeting at a point presumably oriented at 109° to each other. This is analogous to the tetrapod-like structures (Fig. 5.1.13) observed by **Suyama** [107]. Once the ZnO powders are mixed with additives and calcined at 700°C, the particle size appears slightly coarser due to agglomeration.

5.1.3.2. Discussion of the microstructural analysis (800°C).

The microstructure of pure and doped (ZnO + Bi_2O_3) ceramic samples sintered at 800°C, as shown in Figs. 5.1.3 (a) and 5.1.3 (b) suggest that the consolidation of powders of pure ZnO must occur below 800°C with grain growth from ≈ 0.3μm, as in the starting powders to ≈ 1.2μm. (Fig. 5.1.1). At this low temperature of sintering, the consolidation is likely to be solely due to the solid-state diffusion of the Zn^{2+} cations as there is no liquid phase present.

The addition of Bi oxide lead to the formation of some liquid phase [32,33,45,56] and is compounded by further consolidation, with increase in grain size (≈ 2.1μm) as compared to the undoped case (≈ 1.2μm). The microstructure as shown in Fig. 5.1.3 (a), has many voids due to pore formation at the triple points. The bright phases in the back scattered imaging micrograph in Fig. 5.1.3 (b), suggest that the voids are occupied by Bi phases. In addition, there appears to be no continuous network of the Bi phases.

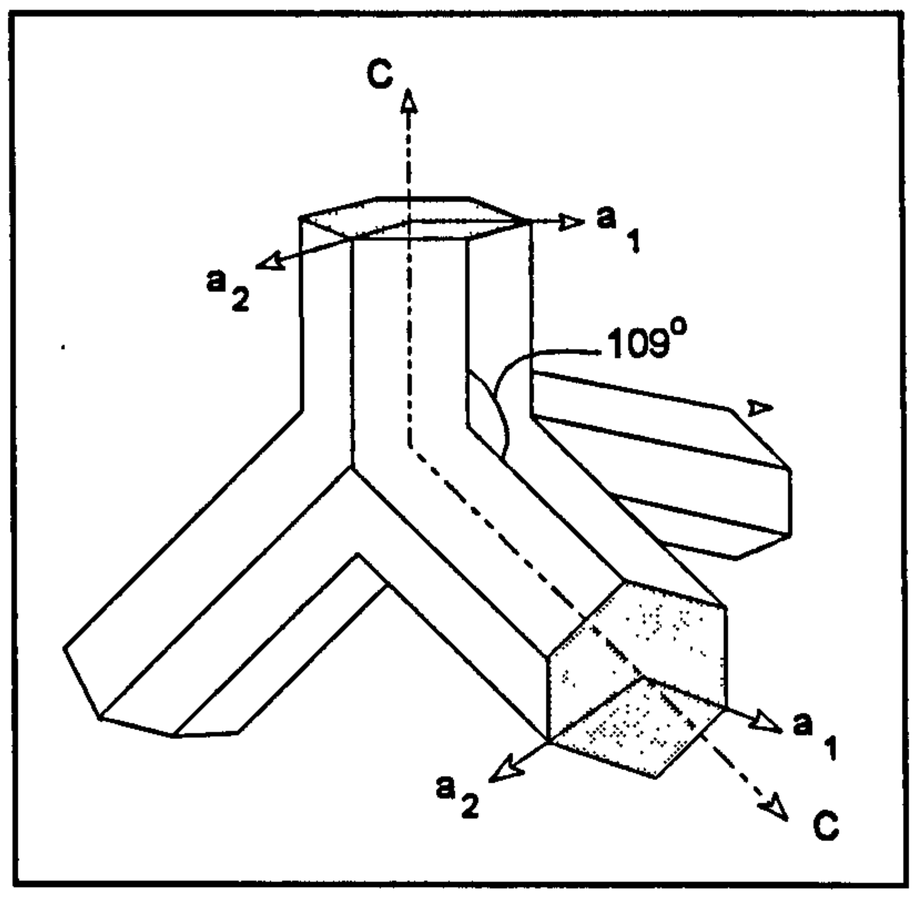


Fig 5.1.13 Model for the tetrapod-like particle of ZnO [107].

Addition of Co_3O_4 to this binary composition:
ZnO + Bi_2O_3, results in perhaps a slight increase in the grain size to about 2.2μm, as shown in Fig. 5.1.3 (c). Apart from this it does not appear to have any marked effect on the microstructure at this temperatures (800°C). This is not surprising as Co, due to its increased solubility in ZnO, does not segregate out and is thought to have an insignificant effect on the microstructure.

Addition of Mn to the composition: ZnO + Bi_2O_3 + Co_3O_4 resulted in a noticeable increase in the grain size to ≈ 3.2μm (Fig. 5.1.2 (d)). Mn is also known to be soluble [32, 75] in the ZnO ceramic and there is no other major change in the microstructure.

Fig. 5.1.3 (e) shows that a marked change has occurred to the microstructure upon the addition of Sb_2O_3 to this composition: ZnO + Bi_2O_3 + Co_3O_4 + MnO_2. There is a big reduction in the grain size (0.5μm) particularly noticeable in this low temperature (800°C) sintered sample. The reason for this would be that [32] the Sb_2O_3 reacts with Bi_2O_3 and ZnO and coats the grains thereby hampering the solid-state diffusion and liquid phase reactions by consuming the Bi oxide to form phases such as pyrochlores

$Zn_2Sb_3Bi_3O_{14}$ (PY). The following reactions may be occurring according to **Einzinger** [12] and **Inada** [32]:

$$ZnO + Bi_2O_3 + Sb_2O_3\ (ZBS) + Co_3O_4 + MnO_2. + Cr_2O_3 \Rightarrow (\text{above } 650^oC)$$

$$\Rightarrow\Rightarrow \quad Zn_2Sb_3Bi_3O_{14.}\ (PY)\ (Co, Mn, Cr) + ZnO$$

Hence in the pure ZBS (Zn, Bi, and Sb) system a pyrochlore phase $Zn_2Sb_3Bi_3O_{14.}$ (PY) forms above 650°C and melts at higher temperatures by reacting with ZnO to produce spinel $Zn_7Sb_2O_{12}$ (SP) and Bi_2O_3.-rich liquid [32,33,45,56] (discussed further in section 5.1.3.3.).

The addition of Sb_2O_3 effectively reduces the grain size and its effects are greater in the absence of other additives (Co_3O_4, MnO_2, Cr_2O_3). This is shown in Fig.5.1.3 (g), where the average grain size of the ZnO sample with just Bi_2O_3 and Sb_2O_3 additives, is ≈ 0.3μ m. In the presence of all the additives: $Bi_2O_3 + Sb_2O_3 + Co_3O_4 + MnO_2. + Cr_2O_3$, the average grain size in the sample sintered at (800°C), is ≈ 0.7μm as shown in Fig. 5.1.3 (f). Moreover, Figs. 5.1.3 (e) and 5.1.3 (f) show that the presence of Cr_2O_3 also lessens the severity of Sb_2O_3, in reducing the grain size of ZnO ceramic.

Antimony oxide (Sb_2O_3) disperses into the powders of ZnO and other additives in the early stage of sintering, and finally gathers again as particles of spinel at higher sintering temperatures (discussed in section 5.1.3.3 for samples sintered at 1250°C).

Fig. 5.1.3 (g) shows that the distribution of Sb coincides with small particles and it is similar to the distribution of Bi. This has been confirmed by SEM-EDAX spectra shown in Fig. 5.1.3 (h) of a ZnO ceramic sample doped with Bi_2O_3 and Sb_2O_3 additives and then sintered at 800°C. The SEM-EDAX analysis of these cluster regions in Fig. 5.1.3 (f) and 5.1.3 (g), indicates phases rich in Bi, Sb and Zn. This cluster may corresponds to a pyrochlore PY phase made up of: $Zn_2Sb_3Bi_3\ O_{14}$. This is known to be the first phase to form at around these temperatures [32]. The densification behaviour has been found to be related to the formation of the liquid phase and the pyrochlore. The liquid phase promotes and PY phase retards the densification [45].

5.1.3.3. Discussion of the microstructural analysis (1250°C)

High temperature sintering (1250°C) of undoped ZnO ceramic leads to a reduction in the voids initially observed in the samples sintered at 800°C. This is accompanied by further grain growth (≈ 20μm) as shown in Fig. 5.1.4 (a).

Dey *et al* [108] studied the grain growth of ZnO during the liquid-phase sintering of the ZnO-Bi_2O_3 ceramics with Bi_2O_3 contents from 0.54 to 2.33 mol.% and sintering temperatures from 900°C to 1400°C. Their samples were fired at four different temperatures and at each temperature, a series of specimens was fired for four different times (1, 2, 4, and 8h). The grain size of the samples were measured using equation 5.1-1. They found that the activation energy for ZnO grain growth initially decreases from the 'pure' ZnO value with the initial introduction of Bi_2O_3. With further increases of the Bi_2O_3 content, the activation energy for ZnO grain growth remained nearly constant at 178 ± 16 kJ/mol., up to about 1mol.% Bi_2O_3 and then gradually increased. This latter increase in the activation energy is accompanied by a decrease in the ZnO grain size with increasing Bi_2O_3 content [108].

Dey *et al* [108] found that the rate of grain growth in undoped ZnO ceramic depends on solid-state diffusion of Zn^{++} cations within the ZnO lattice, with associated activation energy of 225kJ/mol. Their study of the grain-growth kinetics for pure and doped ZnO ceramic showed that introduction of Bi_2O_3 into ZnO @ 0.5mol%, resulted in an initial decrease in the activation energy (from 225kL/mol to 178kJ/mol). This decrease in the activation energy has been attributed to a change in the mechanism for grain growth from one of the solid-state diffusion in the undoped case, to that of solution of the ZnO in the Bi_2O_3 - rich liquid followed by precipitation on the larger ZnO grains. However, further increase in Bi_2O_3 content resulted in increase in activation energy (from 178 to 274kJ/mol). This has been explained in terms of the rate controlling mechanism: diffusion through the liquid phase from the smaller grains to the larger grains. The activation energies corresponding to the amount of Bi_2O_3 dopant (mol%) are :

178 ± 16 kJ/mol for 0.54 mol.%, 232 ± 34 kJ/mol for 1.1 mol.%, 269 ± 37 kJ/mol for 1.7 mol.%, and 274 ± 44 kJ/mol for 2.33 mol.% [108].

Hence this variatioin in activation energy is due to the change in rate-controlling mechanisms. For ZnO with Bi_2O_3 additions (@ 0.5mol%), a liquid phase occurs during sintering, so that grain growth during sintering occurs in the presence of a liquid phase. When the liquid phase wets the solid grains and the solid grains have significant solubility in the liquid phase, the smaller solid grains (thermodynamically unstable) dissolve into the liquid phase and subsequently precipitate on the larger grains. Consequently the activation energy is lower. The rate of growth of the ZnO grains can be controlled either by the solid-liquid phase-boundary reaction or (in higher Bi_2O_3 content regime) by diffusion through the liquid phase from the smaller grains to the larger grains.

Hence, according to grain growth studies by **Dey** *et al* [108] the introduction of Bi to ZnO results in a formation of a liquid phase which reacts with ZnO and leads to an initial

reduction in activation energy (178 ± 16 kJ/mol) as compared to the pure ZnO and results in a further increase in grain growth to about 28μm (Fig.5.1.4 (b)). The Bi phase then exists as a continuous lacy type of network presumably due to the change in the dihedral angle between the grains as observed by **Gambino** [42] (discussed in Chapter 2, section 2.3).

The pores in the microstructure may be attributed to the possibility of a higher level of volatility of the Bi_2O_3 at higher temperatures. Fig.5.1.14 show schematics drawn from the micrographs of Figs 5.1.3 (b) and 5.1.4 (b), to illustrate the transformation of the microstructure of a ZnO ceramic sample doped with Bi_2O_3 and then sintered at 800°C and at 1250°C respectively.

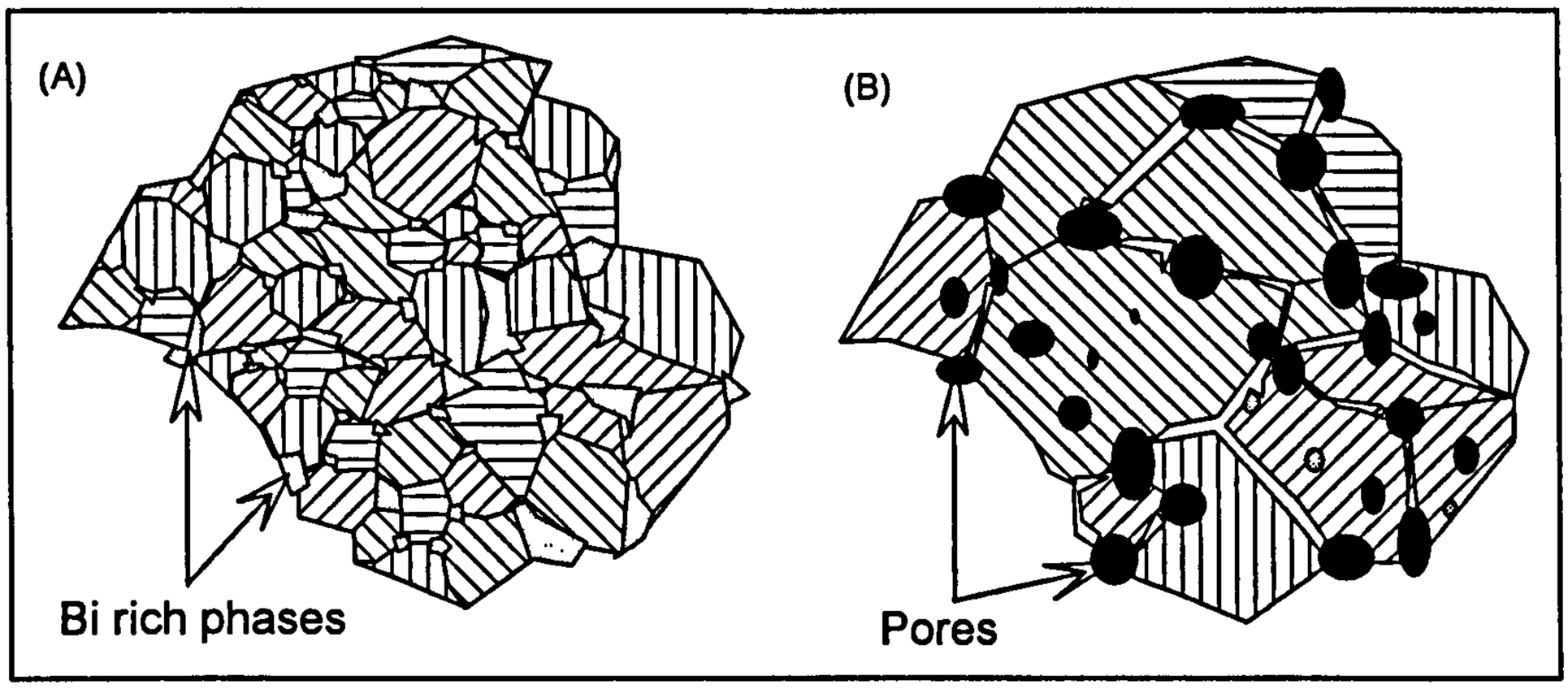


Fig.5.1.14 Schematics of the microstructure of (A) Bi doped ZnO ceramic sample sintered at 800°C showing pools of Bi rich phase at triple points in the pore regions and (B) at higher temperatures sintering (1250°C) a lacy network is produced with empty pores shown here as shaded regions that may have been previously occupied by Bi rich phase.

Addition of Co_3O_4 to this binary composition (ZnO + Bi_2O_3) does not show any marked change in the microstructure at 800°C but in a sample sintered at 1250°C, it influences the lacy network of Bi phase by reducing its thickness and presumably improves the distribution of Bi rich materials as shown in Fig 5.1.4 (c). Further addition of Mn to this composition (ZnO + Bi_2O_3 + Co_3O_4) sintered at 1250°C does not show any additional changes in the microstructure except that the Bi phase is perhaps less prominent in the sample without the Co and Mn oxides. Hence, the addition of Co and Mn in ZnO ceramic, sintered at 1250°C leads to a reduced thickness of the Bi rich lacy network and an improved distribution of Bi at the grain boundary interface as shown by Figs. 5.1.4 (c) and 5.1.4 (d). A noticeable change was observed at 800°C, upon the addition of Sb_2O_3 to this composition :ZnO + Bi_2O_3 + Co_3O_4 + MnO_2. A relative change in the

microstructure doped with and without the Sb_2O_3 is observed in Figs 5.1.3 (d) and 5.1.3 (g) and is discussed in section 5.1.3.2.

The microstructure of the ZnO ceramic sample with all the dopants (Bi_2O_3 + Sb_2O_3 + Co_3O_4 + MnO_2. + Cr_2O_3), sintered at 1250°C is shown in Fig.5.1.4 (e). The bright phases in Fig. 5.1.4 (e) are Bi rich with Zn and some trace of Co. A clear example of the lacy type of network is seen here in the fractured microstructure shown in Fig. 5.1.4 (f). Other phases were identified by EDAX. Their compositions are confirmed by the corresponding x-ray imaging as shown in Figs. 5.1.5 (a), (b), (c), (d), and (e). The voids initially observed in the sample (Figs. 5.1.4 (b) and 5.1.14) with Bi_2O_3 additives were present in all the subsequent compositions except in the case of this sample (Fig. 5.1.4 (e)) with all the dopants. The voids in this case appear to be occupied by grains of spinel $Zn_7Sb_2O_{12}$ (SP) containing Cr, Mn, and Co dissolved within (Fig. 5.1.15). This has been confirmed by EDAX analysis.

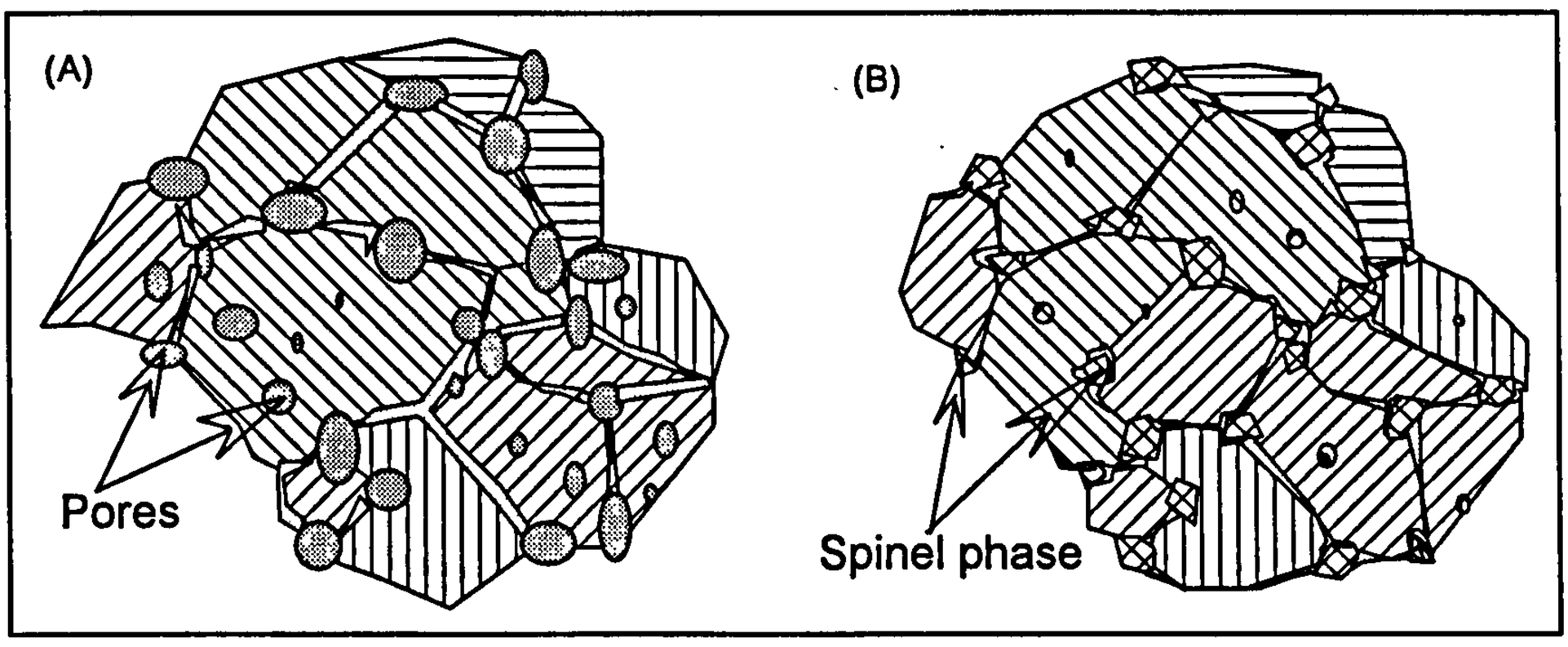


Fig.5.1.15 Schematics of the microstructure of (A) Bi doped ZnO ceramic sintered at 1250°C showing a lacy network with empty pores in place of the Bi phase. (B) ZnO with all dopants sintered at (1250°C). Pores are replaced by the SP particles leaving a much finer lacy network in the varistor.

After influencing the reactions at an earlier stage of sintering the final role of Sb_2O_3 appears to remain as a SP phase occupying the voids created by the volatility of the Bi oxide. This can be seen by comparing the microstructure of ZnO doped with Bi_2O_3 (Fig. 5.1.3(b)) to the fractured surface of the ZnO ceramic doped with all the additives (Fig.5.1.3(f)).

In the ZnO ceramic, Bi also evaporates during higher temperature sintering [65]. In the case of such a sample, when one looks at the ceramic surface as-sintered, the presence of Bi is not obvious. However, when looking at the fractured surface of the same sample Bi rich regions can be clearly seen. Hence a combination of polished and fractured surfaces of the ceramic samples enabled a more representative analysis.

The average grain size of ZnO ceramics in this preparation is about 20μm for pure ZnO, 28μm for ZnO with Bi oxide, 30μm for ZnO with the oxides of Bi, CO, and Mn, and about 18μm for ZnO with all five dopants (Bi + Sb + Mn + Co + and Cr) sintered at 1250°C.

At higher temperatures (1250°C) sintering the ZnO with all the additives, the increase in the liquid phase increases the formation of spinel phase SP ($Zn_7\ Sb_2\ O_{14}$) grains which are formed by the reaction between the PY phase and ZnO. The inter-grain particles meet with them, resulting in the microstructure composed of ZnO grains and intergranular layers of the liquid phase and SP particles. According to **Inada** [32] the following reactions may be occurring to explain the the PY phase transforming to the SP phase,

$$ZnO + Bi_2O_3 + Sb_2O_3\ (ZBS) + Co_3O_4 + MnO_2. + Cr_2O_3 \Rightarrow (\text{above } 650^oC) \quad (5.1\text{-}1)$$

$$\Rightarrow\Rightarrow \quad Zn_2Sb_3Bi_3O_{14.}\ (PY)\ (Co, Mn, Cr) + ZnO$$

$$Zn_2Sb_3Bi_3O_{14.}\ (PY)\ (Co, Mn, Cr) + ZnO \Rightarrow (850^oC\text{-}\ 950^oC) \quad (5.1\text{-}2)$$

$$\Rightarrow \Rightarrow [Zn_7Sb_2O_{12}\ (Co, Mn, Cr)\ [SP]] + [Bi_2O_3\ (Cr)\ [liq.]],$$

$$[Bi_2O_3\ (Cr)\ [liq.]] \Rightarrow (950^oC\text{ -}1300^oC) \Rightarrow \Rightarrow [Bi_2O_3\ (Zn, Sb, Cr)\ [liq.]] \quad (5.1\text{-}3)$$

dissolution of SP, ZnO and absorption of Cr by SP

$$[Bi_2O_3\ (Zn, Sb, Cr)\ [liq.]] \Rightarrow (\cong 1300^oC) \Rightarrow \Rightarrow [Bi_2O_3\ (Zn, Sb)\ [liq.]] \quad (5.1\text{-}4)$$

absorption of Cr by SP

The idea of a rapidly cooled ZnO sample (cooled from 1250°C) was to study the state of the microstructure with all the phases frozen at this temperature. In this case the microstructure has more porosity then the normally prepared sample. The lacy network of Bi-rich phase is similar to the normally treated sample with perhaps a slightly smaller grain size (≈14μm). SEM-EDAX studies revealed regions of a Bi rich network with some cluster of spinel phase ($Zn_7\ Sb_2\ O_{12}$) decorating the microstructure. X-ray dot mapping revealed a similar composition pattern to that observed for the normally prepared ZnO sample. There was no trace of any pyrochlore phase ($Zn_2\ Sb_3\ Bi_3\ O_{14}$) in this sample treated at this temperature. This unequivocally refutes **Wong's** [25] theory proposing PY phases at high temperatures, and their requirements for the varistor effect, as discussed in section 2.3.

An etched specimen of the Bi based ZnO varistor (Fig. 5.1.7(a)) revealed the phases which were identified using SEM-EDAX (Fig.5.1.7 (a) and 5.1.7 (b)). The

microstructural analysis revealed details of the skeleton of the intergranular phases. The SEM-EDAX, analysis (Fig. 5.1.7) was undertaken at various sites as marked on the micrographs in Fig.5.1.7(a). This confirms the presence of spinel phase (containing Sb, Cr, Co Mn and Zn) and Bi-rich phases marked as 1B and 2 respectively. A trace of pyrochlore (containing Bi, Sb, Zn, Cr, Mn and Co) phase was also detected, marked as region 4. The Mn peak overlaps with Cr-Kβ and remains hidden when looking at the EDAX spectra.

SEM-EDAX analysis of the microstructure of a Bi based commercial ZnO varistor shown in Fig. 5.1.9, confirmed that SP type phases mainly occupy the voids with a lacy type of network of Bi-rich phases as described for the sample synthesised in the laboratory (Fig.5.1.4(e)). The microstructure of Pr based commercial ZnO varistors is shown in Fig. 5.1.10. EDAX analysis showed the presence of La, Pr Co and some Zn in the bright phase. The grain region predominantly contains Zn with a trace of Co. The microstructure is less complex then the Bi, Sb based system. The bright phase at the triple points in this Pr based ZnO ceramic are analogous to the lacy type of network as observed in the Bi based varistors.

STEM-EDAX ánalysis

Looking at Figs. 5.1.11 (a) and (b) our TEM results show that round particles of spinels mainly occupy the pores created by the volatility of Bi, within the ZnO grains. Majority of the grain boundaries are devoid of any secondary phase at the interface. These observations agree with those of **Clarke** [32] and **Cerva** *et al.*, [40]. Cross section of the lacy type of network of Bi rich phases appears as triangles at the triple points. The STEM-EDAX analysis also complements the SEM-EDAX results discussed earlier.

XRD analysis of an etched residue as shown in Fig. 5.1.12 confirms that in the sintered (1250°C) doped ZnO ceramic, the majority of the etched residue has a spinel ($Zn_7Sb_2O_{12}$) type of structure.

5.1.6 Summary of the SEM/STEM-EDAX and XRD microstructural analysis

1 Pure ZnO ceramic powder starts to consolidate below 800°C. Addition of additives such as Bi_2O_3, MnO_2, Co_3O_4 and Cr_2O_3 to the ZnO ceramic, does not have a marked effect at this temperature. However, Sb_2O_3 additive reacts with ZnO and Bi_2O_3 at an early stage of the sintering process (800°C), resulting in a 2 fold reduction in grain size and the formation of PY ($Zn_2Sb_3Bi_3O_{14}$,) phase in the microstructure.

2 Volatile reaction between Bi_2O_3 additive and ZnO ceramic at high sintering temperatures (1250°C), results in the formation of many pores on the surface of the ZnO grains. Bi oxide provides liquid phase during sintering and at about 0.5 mol.% it lowers the activation energy and promotes grain growth. In the sintered compact Bi_2O_3 segregates at the grain boundary interfaces and forms a lacy type of network.

3 MnO_2 and Co_3O_4 additives are soluble in ZnO ceramic. Their distribution is homogeneous.

4 At higher sintering temperatures (1250°C) the PY ($Zn_2Sb_3Bi_3O_{14}$,) phase transforms to SP ($Zn_7Sb_2O_{12}$,) phase and remains present in the ceramic microstructure as round particles at the triple points and largely in the intragrain pores created by Bi_2O_3 liquid phase [120].

5 SEM and TEM results from this work complements studies by **Clarke** *et al,* [33] and **Cerva** *et al,* [40] to show that there is no evidence of a 1μm intergranular layer of Bi rich phase as previously reported by **Matsuoka** [9]. The microstructure of the varistor sample is largely decorated by SP phases surrounded by Bi rich lacy network. The scarcity of PY phase in the microstructure, questions its importance to the varistor phenomenon. This is in contrast to a previous report by **Wong** [25] who described the over-all varistor microstructure as a three-dimensional series-parallel network of ZnO-PY junctions; pyrochlore phase was considered essential to give rise to the observed non-linear characteristics.

5.2 SEM-EBIC analysis of ZnO ceramic

Overview

The varistor phenomenon is a bulk phenomenon involving the sintered material, exhibiting strong non-linear electrical characteristics with fast response time ($\approx 10^{-9}$s) (discussed in chapter 2, section 2.2.1). One obvious explanation as proposed by **Levinson** *et al* [4], is that each grain boundary presents an electrical barrier of a few volts and an associated depletion region [56, 61, 23]. The I:V characteristic of the varistor is non-linear, (similar to a Zener diode) analogous to two back-to-back diodes. A group of symmetrical back to back Schottky barriers are modelled to represent the

microscopic electrical behaviour of the ideal varistor. Models based on the Schottky barrier have been proposed to explain the varistor phenomenon. **Eda** [56] (1978) and **Einzinger** [38] (1982), suggested that the quality of the varistor depends on the quality of these barriers corresponding to the grain/grain boundary interface. **Bernds** *et al.*, [110] (1984) reported using SEM-EBIC to investigate ZnO varistor ceramic. They used a lock-in-amplifier and electron beam chopping facility to separate the electron beam induced current (EBIC) from the dc bias current and found that the EBIC signal showed a strong variation with bias voltage. In this work, SEM-EBIC analysis was intended to study the microscopic electrical behaviour of a number of ZnO ceramic samples and in particular to observe the contrast arising due to the grain boundary specific electrical barriers.

5.2.1. Preliminary EBIC work

The SEM-EBIC measurements were initially undertaken using a commercial varistor sample, cross sectioned, polished and surface ultrasonically cleaned in solvent to get rid of any polishing debris. The procedure for sample connection to the SEM EBIC apparatus is discussed in Chapter 4, section 4.2.2. Once this procedure to acquire good SEM-EBIC signal was established, analysis of doped samples as synthesised in this work was undertaken.

Table 5.2.1. Preliminary SEM-EBIC analysis of 60V ZnO varistor sample.

EBIC Analysis	Beam Voltage (keV)	Beam Current I (nA)	Depth range RG μm
1	2	5.5	0.02
2 [Fig. 5.2.1 (a)]	3	11	0.04
3 [Fig. 5.2.1 (b)]	5	11	0.1
4	5	24	0.1
5	10	11	0.4
6 [Fig. 5.2.1 (c)]	15	11	0.8
7. [Fig. 5.2.1 (d)]	25 (Comp. 200x)	41	2
7	25	11	2
8	25	24	2
9 [Fig. 5.2.1 (e)]	25	41	2
10	25	53	2
11	25	82	2
12 [Fig. 5.2.1 (f)]	25	99	2
13 [Fig. 5.2.2 (a)]	5	11	0.1
14 [Fig. 5.2.2 (b)]	25	11	2
15 [Fig. 5.2.2 (c)]	25 (Comp. 1000x))	82	2

Initially it was intended to acquire a possible EBIC response using a sample of commercial ZnO varistor. The sample was mounted onto a special holder facilitating two pin contacts (to Earth and Current input of the pre-amplifier) to be made and insulated from any other mechanical parts of the SEM stage. The EBIC amplifier (METALEC) was connected to an SEM and the system was optimised to enable a clear noise free picture so that even a faint EBIC image could be viewed. The electron beam parameters (beam voltage and current) were varied to optimise the EBIC response. Initially the observation was carried out using a 60V commercial varistor, with the SEM beam parameters as summarised in Table 5.2.1.

Figs 5.2.1 (a), (b), (c), (d) and (e), show the SEM-EBIC terraces (200x magnifications) acquired at different beam conditions. Fig 5.2.1 (f) show the corresponding microstructure at 200 x magnifications. The EBIC terraces corresponds to the grain boundaries, and the EBIC contrast acquired from the sample region appears to be greatly influenced by the SEM beam voltage. The electron penetration range was varied by varying the SEM beam accelerating voltage (2 - 25keV). Table 5.2.1 show the range of depth penetration corresponding the accelerating voltage, calculated using equation (3.2.6), (discussed in Chapter 3 section 3.2.3). Figs. 5.2.2 (a) and (b) show EBIC response arising from the phase regions at triple points in the ceramic microstructure (1000x magnifications). Fig 5.2.2 (c) shows the corresponding microstructure at 1000 x magnification. It is seen here that the EBIC contrast highlights more clearly the triple point phase regions at low (5keV) beam voltages.

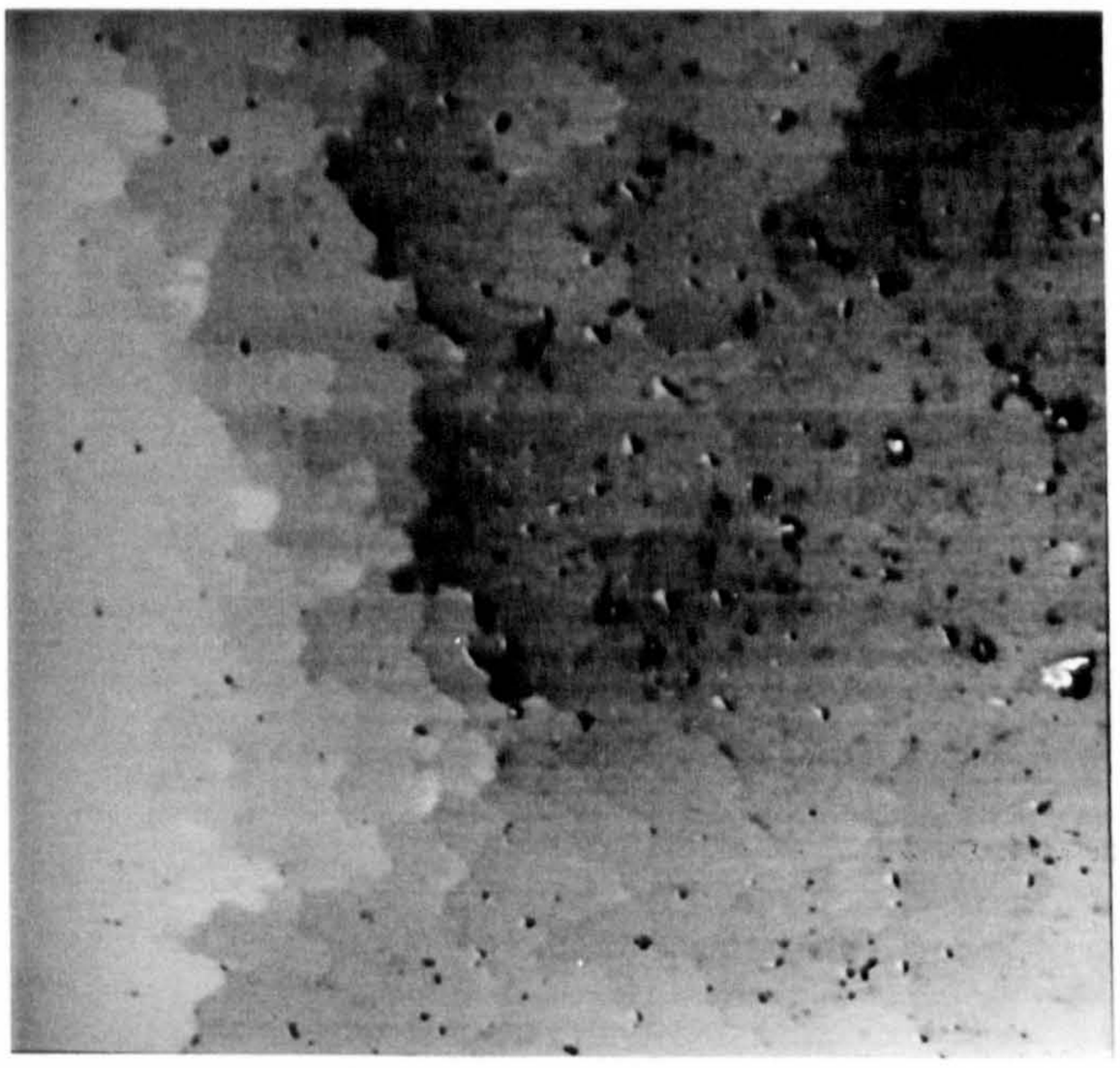


Fig. 5.2.1 (a) SEM-EBIC micrograph (200 x mag.) of a Bi based commercial ZnO ceramic sample (grain size: 35μm), **doped** with the oxides of **Bi**, **Sb, Co**, **Mn** and **Cr.** SEM beam parameters: **3keV**, 11nA. **Scale**: 17mm ≈ 100μm; (35μm ≈ 6mm).

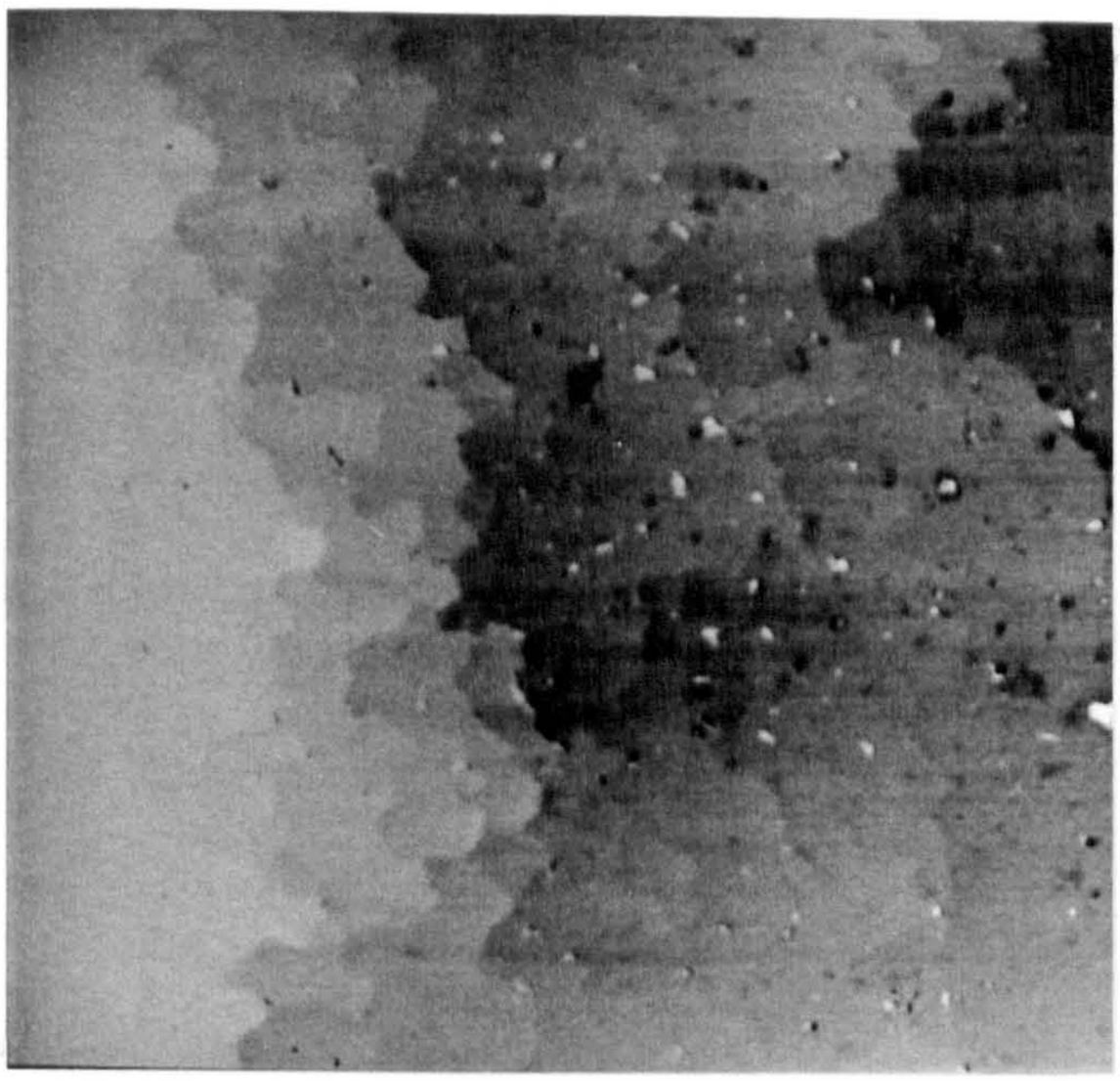


Fig. 5.2.1 (b) SEM-EBIC micrograph (**200 x mag.**) of a Bi based commercial ZnO ceramic sample, **doped** with the oxides of **Bi, Sb, Co**, **Mn** and **Cr.** SEM beam parameters: **5keV**, 11nA. **Scale**: 17mm ≈ **100**μm; (35μm ≈ 6mm).

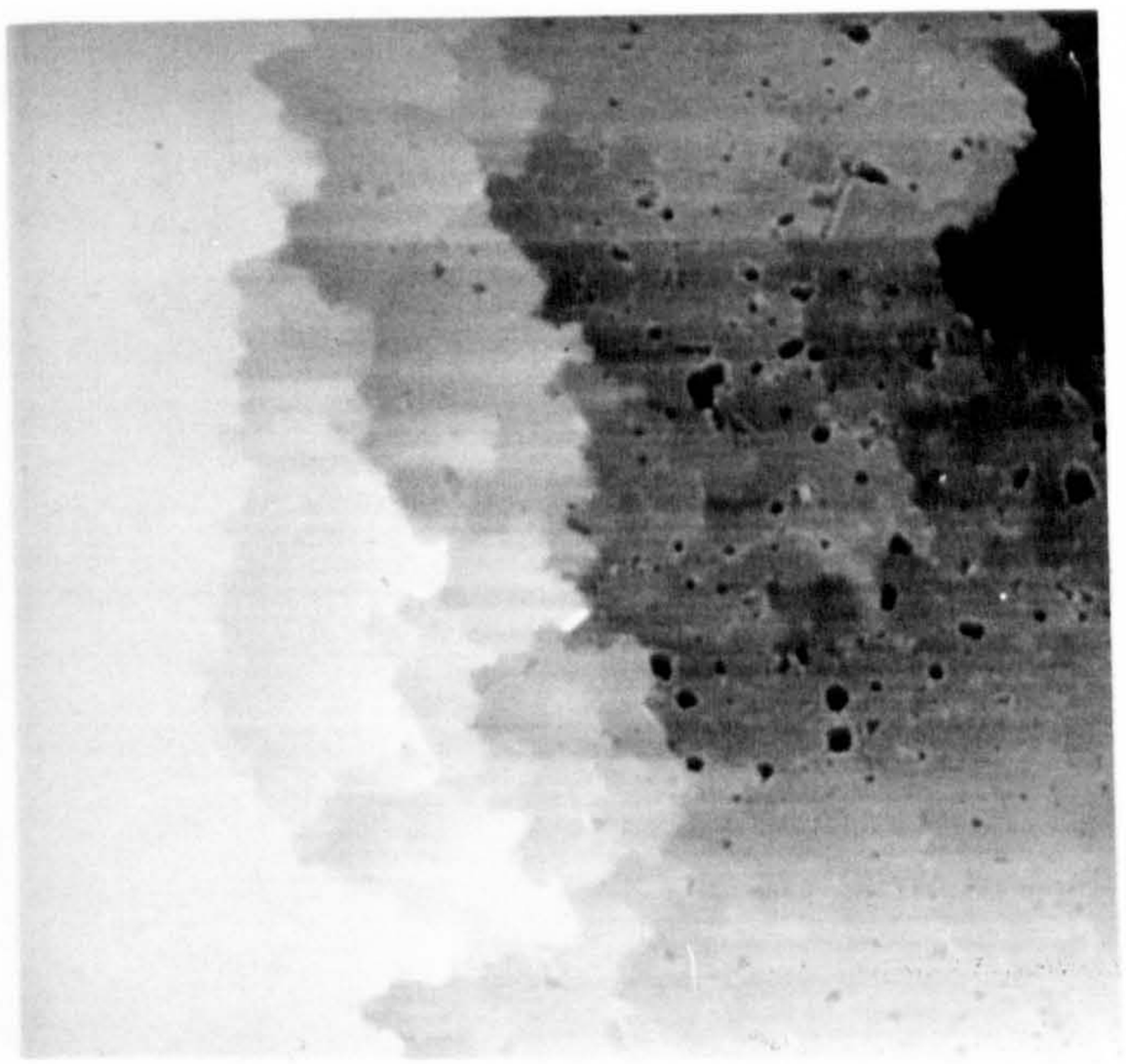


Fig. 5.2.1 (c) SEM-EBIC micrograph (200 x mag.) of a Bi based commercial ZnO ceramic sample, **doped** with the oxides of **Bi**, **Sb, Co**, **Mn** and **Cr.** SEM beam parameters: **15keV**, 11nA. **Scale**: 17mm ≈ 100μm; (35μm ≈ 6mm).

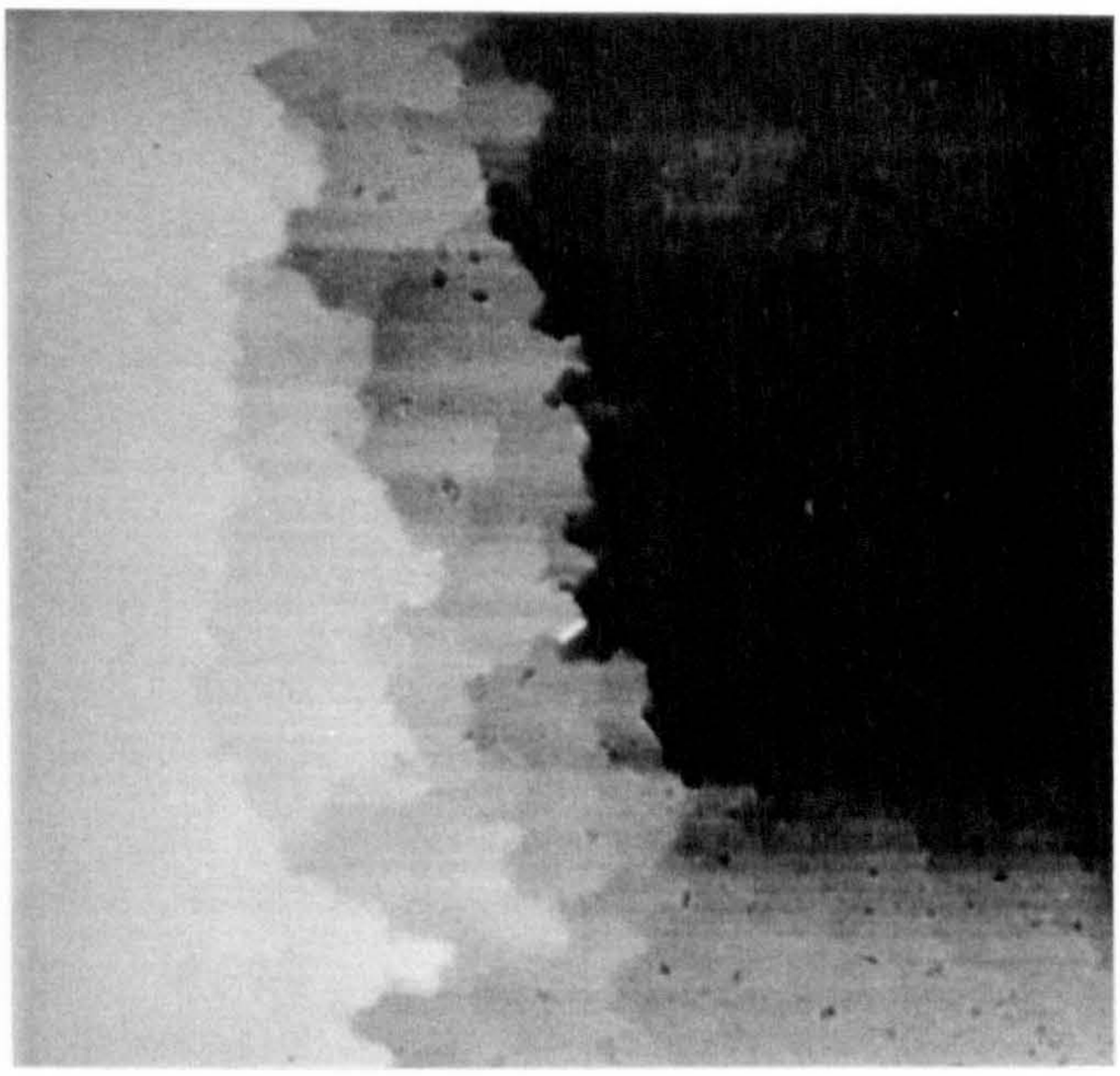


Fig. 5.2.1 (d) SEM-EBIC micrograph **(200 x** mag.) of a Bi based commercial ZnO ceramic sample, **doped with the oxides of Bi, Sb, Co, Mn** and **Cr.** SEM beam parameters: **25keV**, 99nA. **Scale**: 17mm ≈ 100μm; (35μm ≈ 6mm).

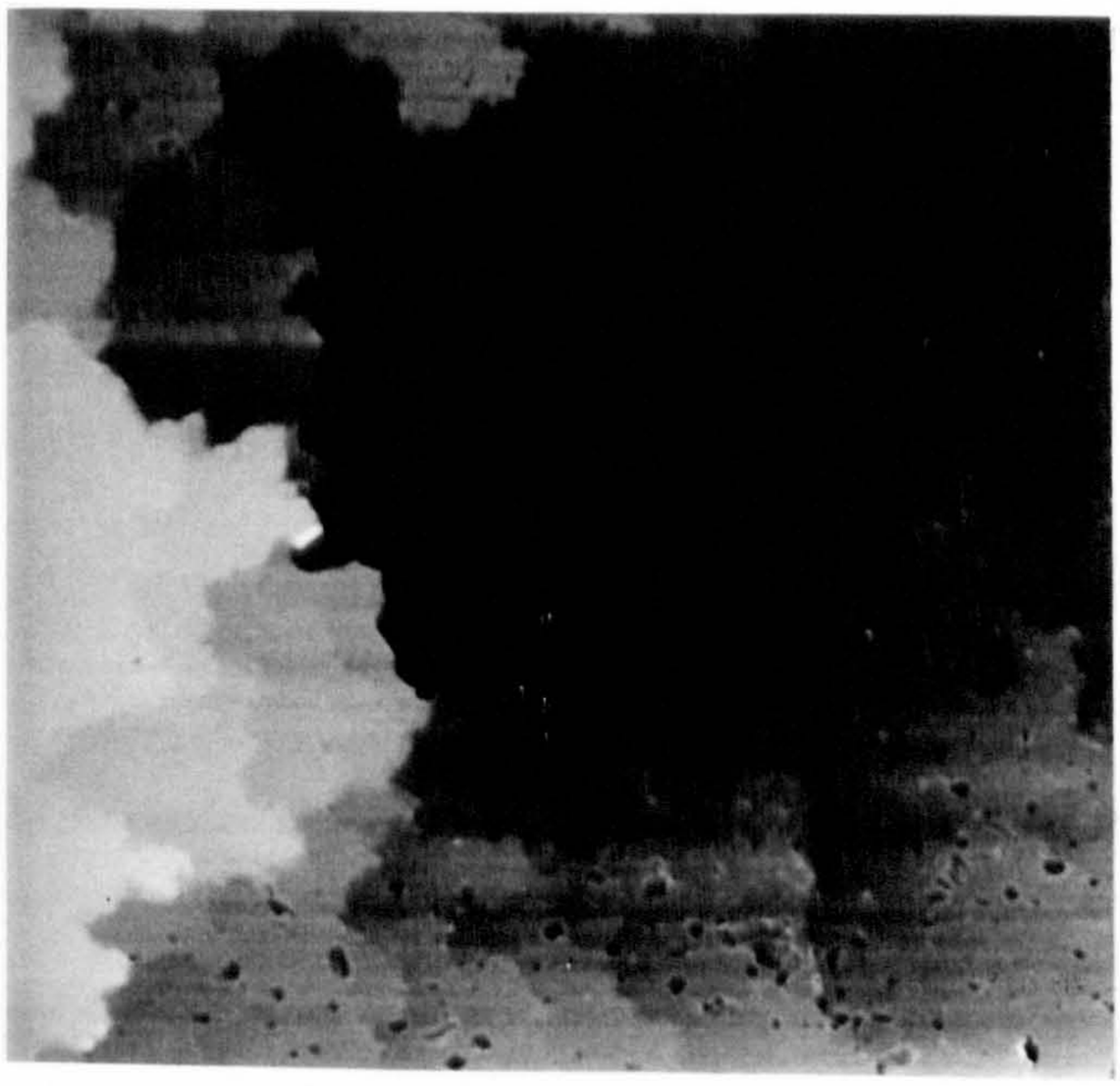


Fig. 5.2.1 (e) SEM-EBIC micrograph (200 x mag.) **of a Bi** based commercial ZnO ceramic sample, **doped with** the oxides of **Bi, Sb, Co, Mn** and **Cr.** SEM beam parameters: **25keV, 41nA. Scale**: 17mm ≈ 100μm; (35μm ≈ 6mm).

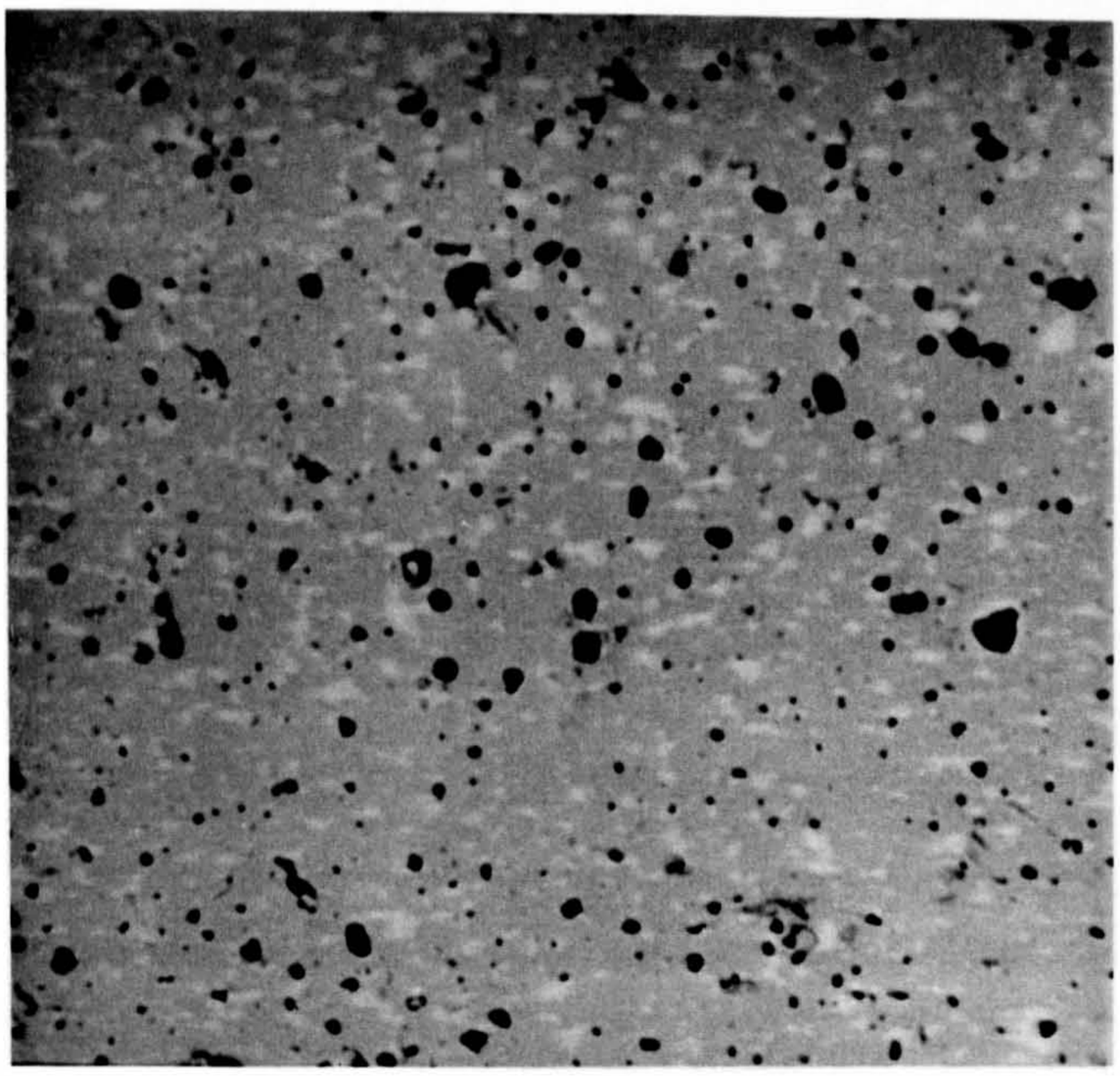


Fig. 5.2.1 (f) SEM micrograph (200 x mag.) of a Bi based commercial ZnO ceramic sample, **doped** with the oxides of **Bi**, **Sb, Co**, **Mn** and **Cr.** SEM beam parameters: **25keV, 41nA. Scale**: 17mm ≈ 100μm; (35μm ≈ 6mm).

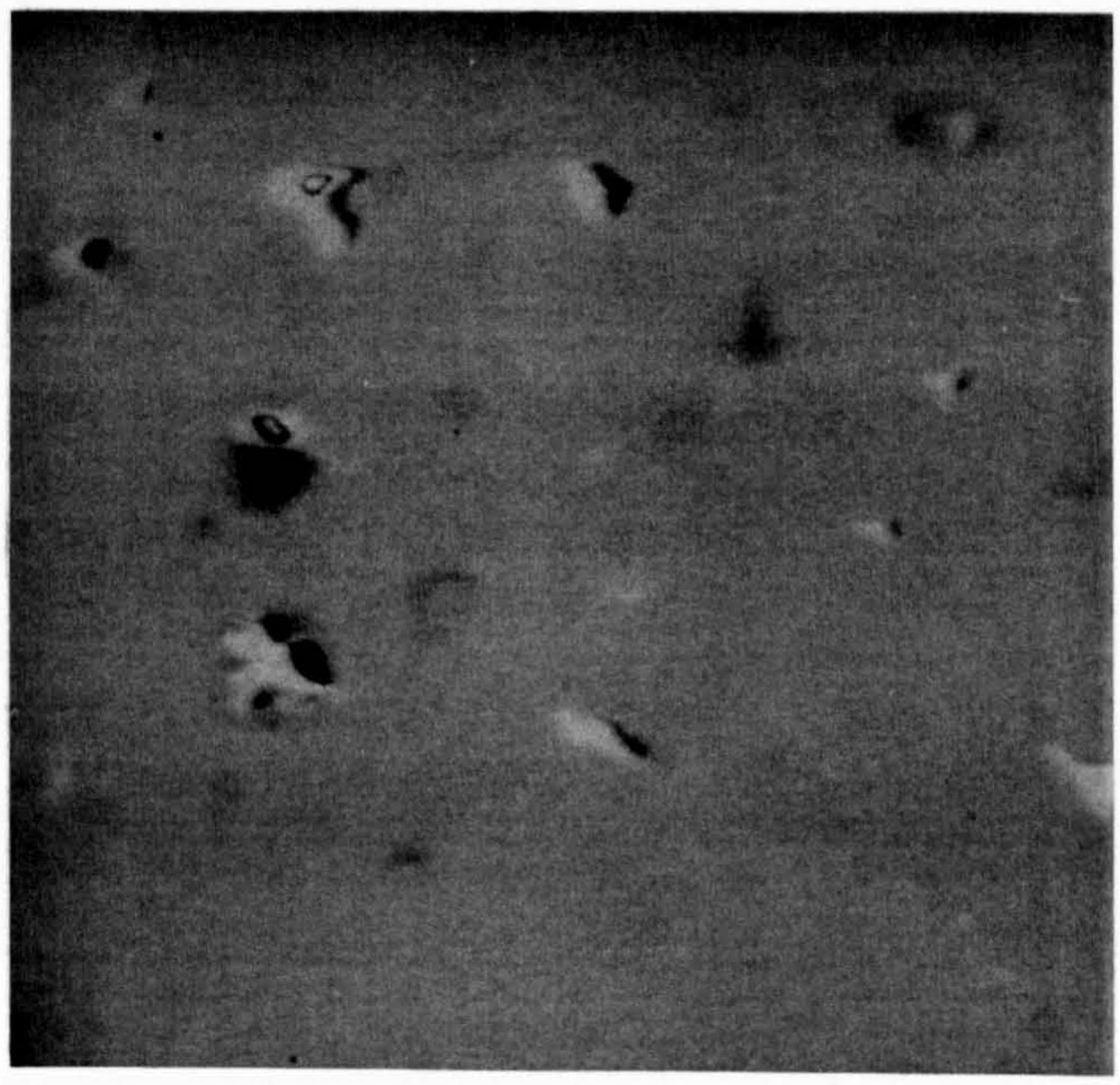


Fig. 5.2.2. (a) SEM-EBIC micrograph (1000 x Mag.) of a Bi based commercial ZnO ceramic sample (grain size ≈ 35μm), **doped** with the oxides of **Bi**, **Sb, Co**, **Mn** and **Cr.** SEM beam parameters: **5keV**, 11nA. **Scale**: 10mm ≈ 12μm; (35μm ≈ 29mm).

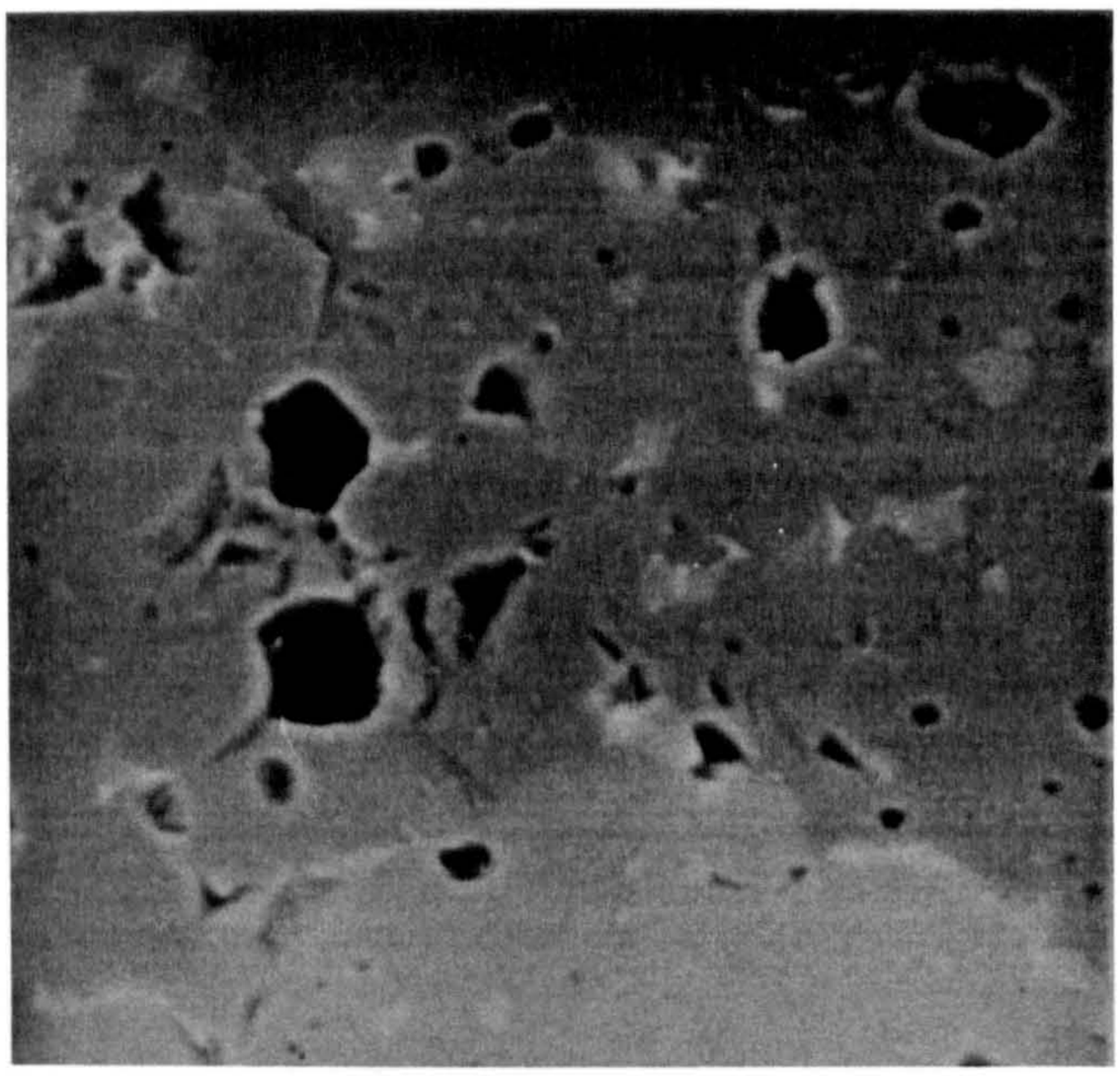


Fig. 5.2.2 (b) SEM-EBIC micrograph (1000 x Mag.) of a Bi based commercial ZnO ceramic sample, **doped** with the oxides of **Bi**, **Sb, Co**, **Mn** and **Cr.** SEM beam parameters: **25keV**, 11nA. **Scale**: 10mm ≈ 12μm; (35μm ≈ 29mm).

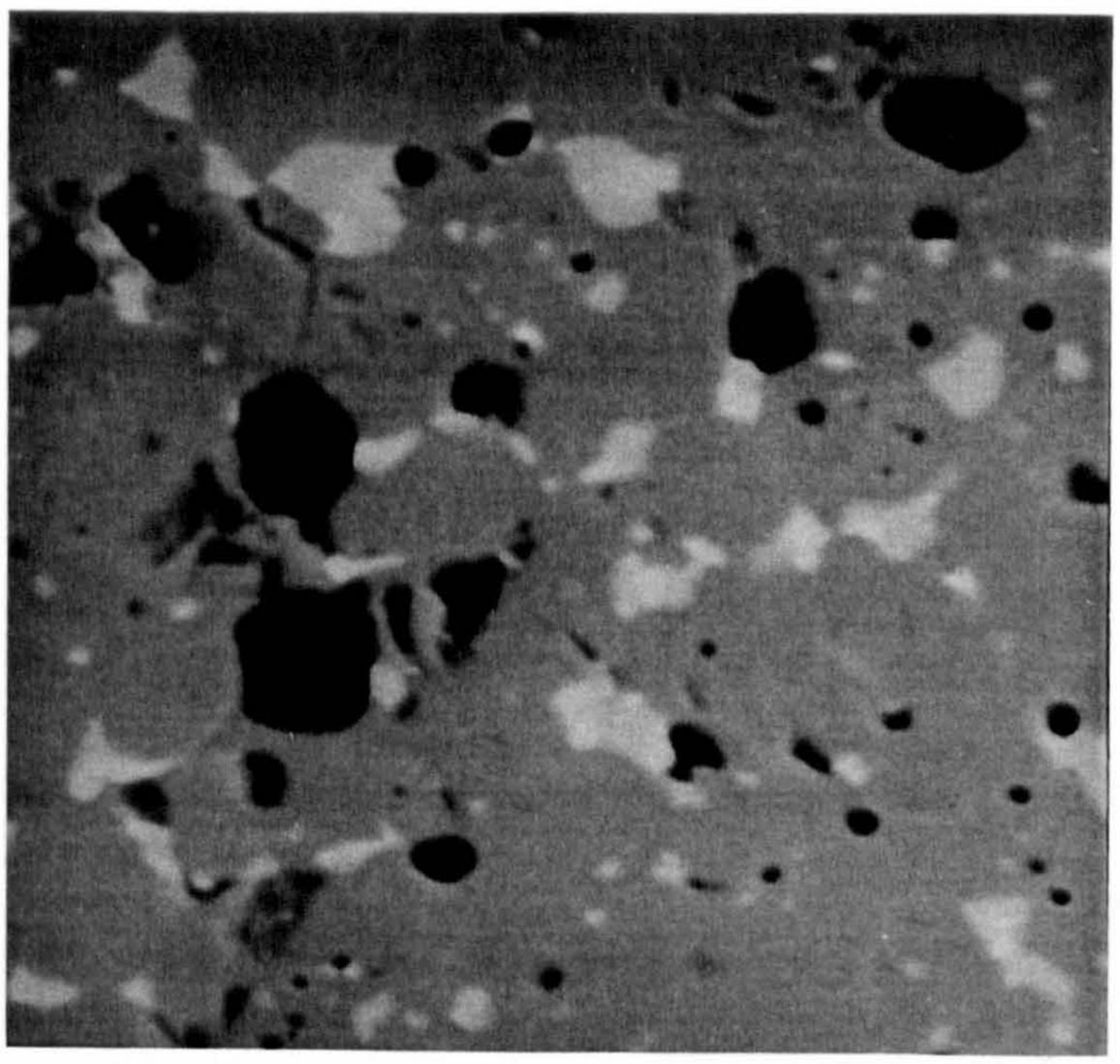


Fig. 5.2.2 (c) SEM micrograph (1000 x mag.) of a Bi based commercial ZnO ceramic sample, **doped** with the oxides of **Bi**, **Sb, Co**, **Mn** and **Cr.** SEM beam parameters: **25keV**, 82nA. **Scale**: 10mm ≈ 12μm; (35μm ≈ 29mm).

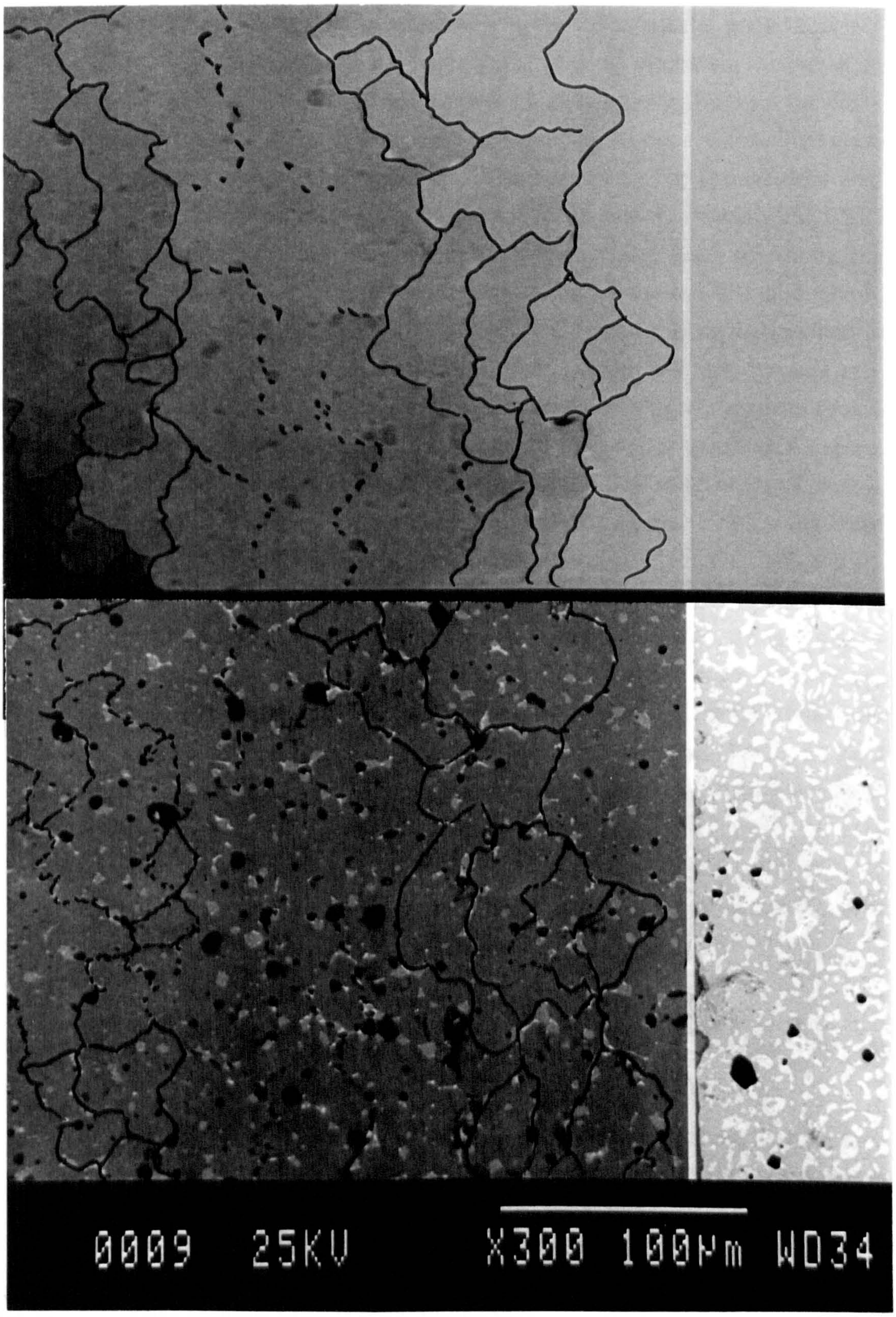


Fig. 5.2.2 (d) SEM-EBIC micrograph (300 x mag.) of a Bi based commercial ZnO ceramic sample (grain size 35µm) showing (in red) the strong and (in blue) the weak terraces. The corresponding BS image below, show the regions giving rise to these EBIC terraces.

The EBIC contrast was interpreted as series of terraces following the grain boundary contours. This is interpreted as an example of an array of electrically active grain boundaries in the ZnO varistor. The back scattered imaging mode (BSI) on the SEM provided a useful heavy/light elemental contrast arising along the dopant decorated grain boundaries. This was useful to correlate the EBIC terraces to the dopant decorated grain boundaries in ZnO ceramic. An attempt was made to closely correlate the EBIC terraces to the grain boundaries giving rise to this pattern. Fig. 5.2.2 (d) shows the highlighted EBIC terraces corresponding to the grain boundaries in the BSI micrograph. Close examination show that the contrast from the EBIC terraces, is strong (marked in red) in some areas and faint (marked in blue) in others. Strong and faint terraces may correspond to regions consisting of perhaps, (a) electrically active grain boundaries and (b) some electrically inactive boundaries. The quality of the varistor would then depend on the ratio of these active/inactive grain boundaries. SEM-EBIC of an undoped sample of ZnO ceramic and $BaTiO_3$ PTCR did not show any EBIC response. Following these initial observation of the EBIC terraces, it was intended to:-

1. Undertake closer observations of the individual grain boundaries, using a micro-probe-manipulator apparatus, in order to make contacts on either sides of the grain boundary. This was to enable a close study of the individual grain boundary and to perform line scan profiling (LSP) (as discussed in section 5.2.3), on ZnO ceramic samples. To apply this procedures to undertake SEM-EBIC analysis of ZnO ceramic doped with the oxides of Bi, Sb, Mn, Co, Cr and Ti.

2. Undertake SEM-EBIC including the LSP analysis of ZnO ceramic sample with just a single dopant ($ZnO + Bi_2O_3$);

3. Undertake the LSP analysis using a bi-crystal of ZnO, providing a single interface for investigation.

4. Set up the basic SEM-EBIC capability at the National Physical Laboratory (NPL), Teddington (discussed in section 5.2.2).

5.2.2. EBIC work using micro-manipulator and line scan profiling (LSP)

5.2.2.1. ZnO ceramic sample with all dopants

Once a clear EBIC image was attainable and correlated with the microstructure, as shown in Figs 5.2.4 (a) and (b), attempts were made to study a single grain boundary interface using micro-probes associated with the micro-manipulator apparatus attached to the SEM. This was to enable a control over the separation between the micro-probes,

thus making it possible to look at a single grain boundary interface. For good electrical contacts a series of dots of silver dag, were made. Photolithography was considered but was not undertaken due to time involved in preparing appropriate masks. Instead, evaporated Al contacts through copper masks were tried (Fig.5.2.3).

In a number of ZnO ceramic varistor samples, the SEM-EBIC response across the grain boundaries was studied, using the line scanning profiling (LSP) technique. A micro manipulator was used to obtain the line scanning profile (LSP) across some individual GBs. Figs. 5.2.5 (a) show EBIC terraces and LSP of a ZnO sample with the additive oxides: Bi, Sb, Mn, Co, Cr and Ti. The corresponding image of the microstructure is shown in Fig 5.2.5 (b). Fig. 5.2.5 (c) presents the above at 1200 x magnification, showing the LSP across the single grain boundary of a ceramic sample. Fig 5.2.5 (d) show the manipulator probes (at 800x magnification), used to acquire these EBIC terrace patterns.

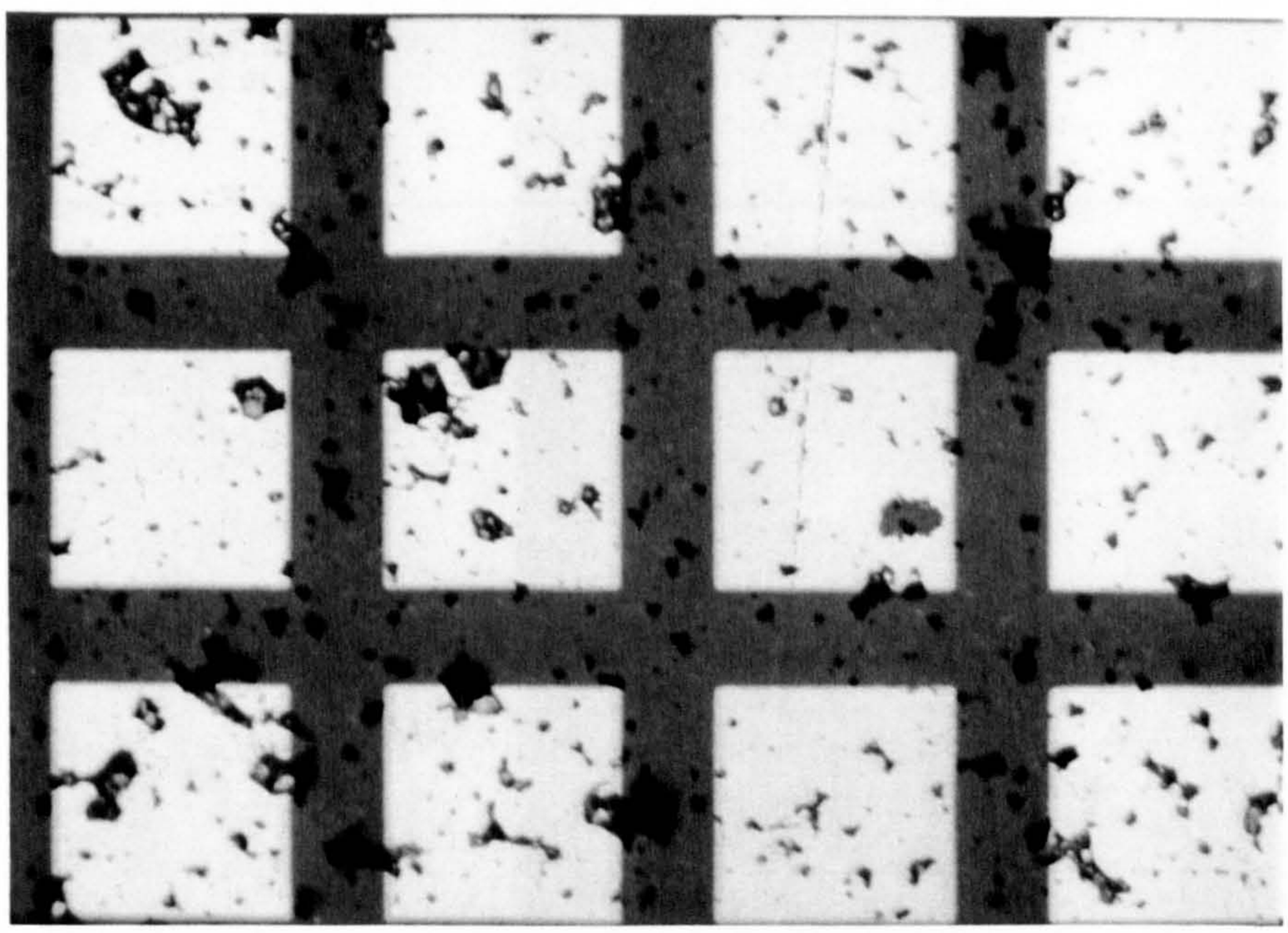


Fig. 5.2.3 Optical micrograph showing the evaporated Al contacts (0.1mm x 0.1mm) using an appropriate mask.

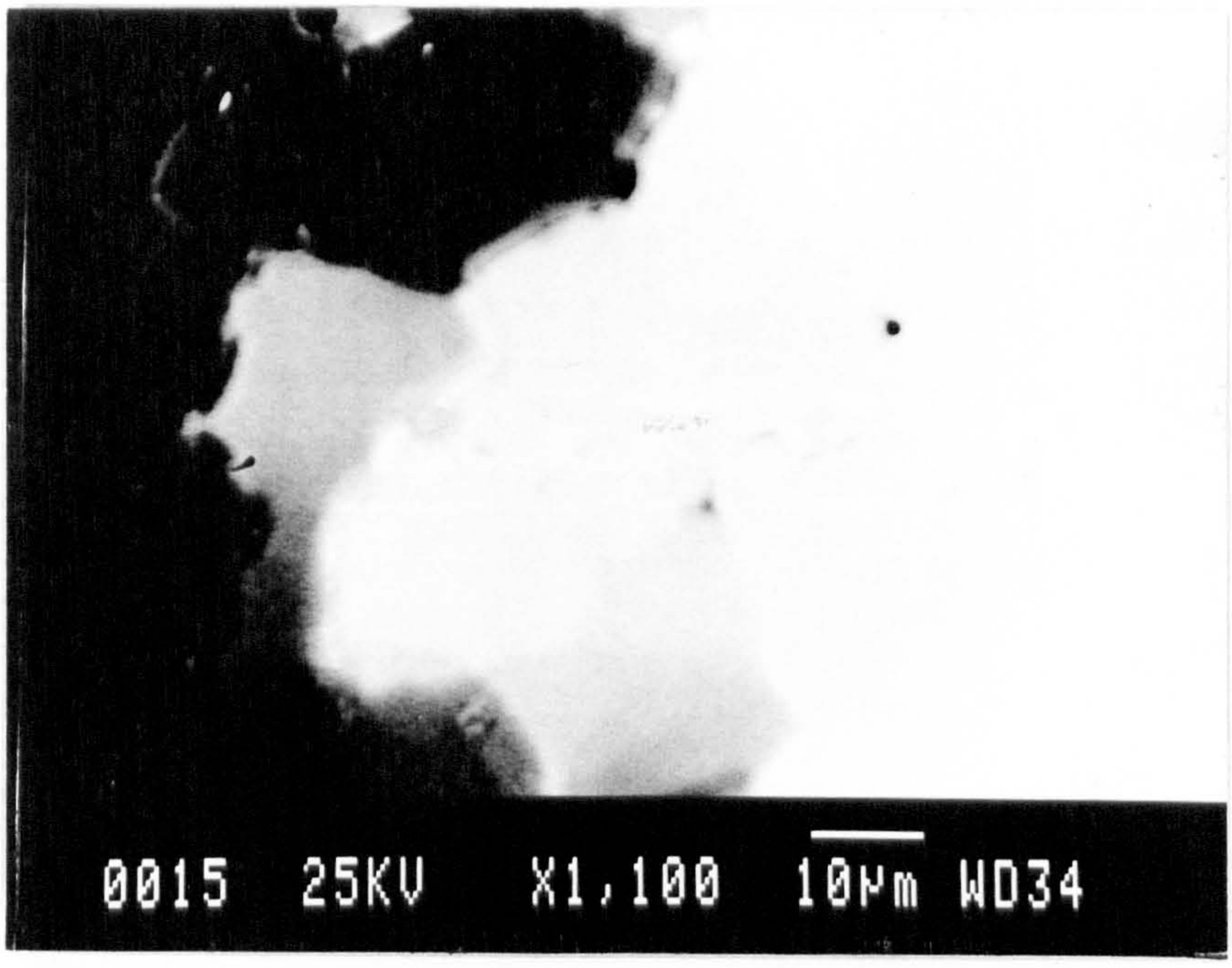


Fig. 5.2.4 (a) SEM-EBIC micrograph (1100 x mag.) of a Bi based commercial ZnO ceramic sample, **doped with the** oxides of **Bi**, **Sb, Co**, **Mn** and **Cr.** SEM beam parameters: 25keV, 82nA.

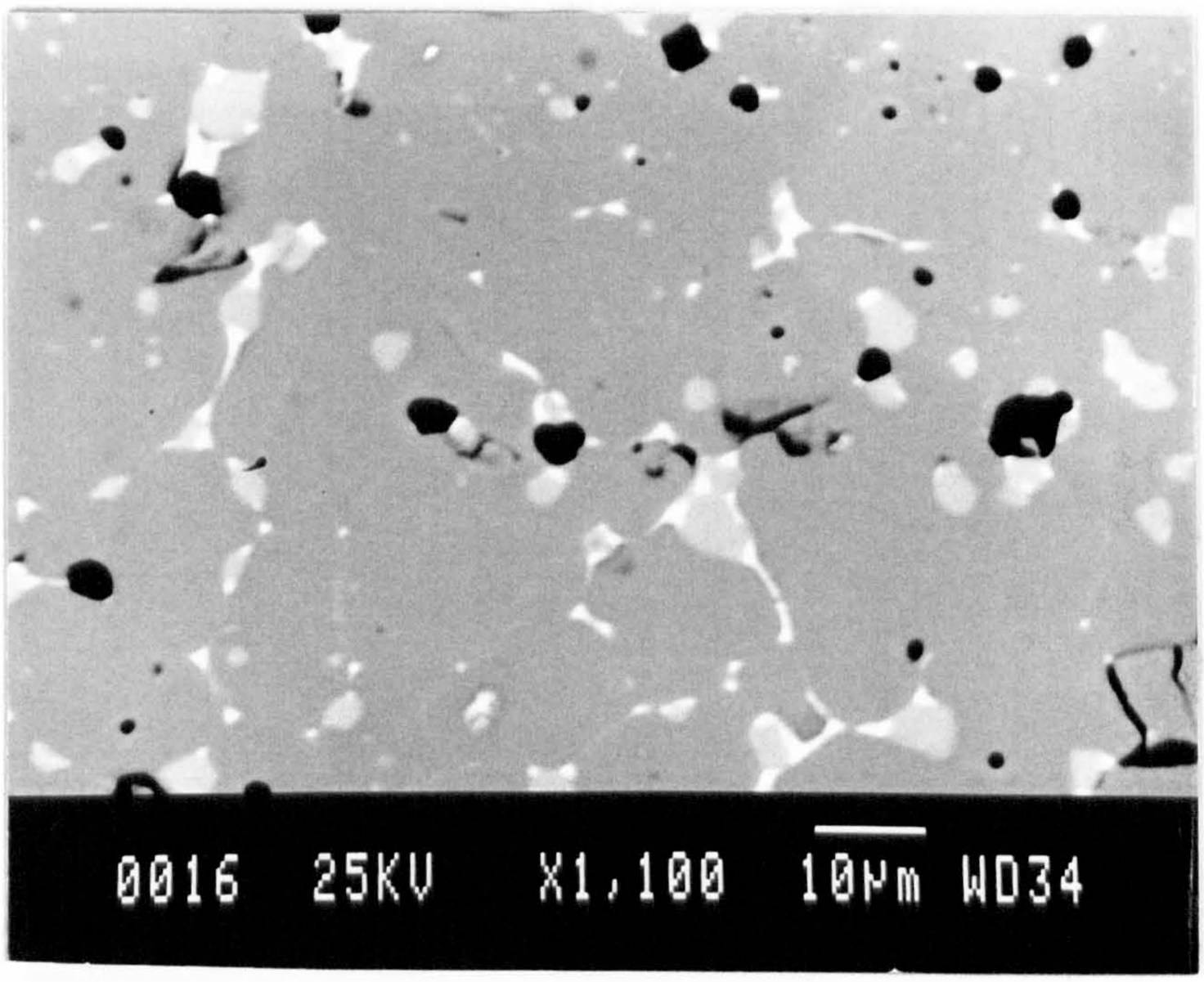


Fig. 5.2.4 (b) SEM micrograph (1100 x mag.) of a Bi based commercial ZnO ceramic sample, **doped** with the oxides of **Bi**, **Sb, Co**, **Mn** and **Cr. SEM beam parameters: 25keV, 82nA.**

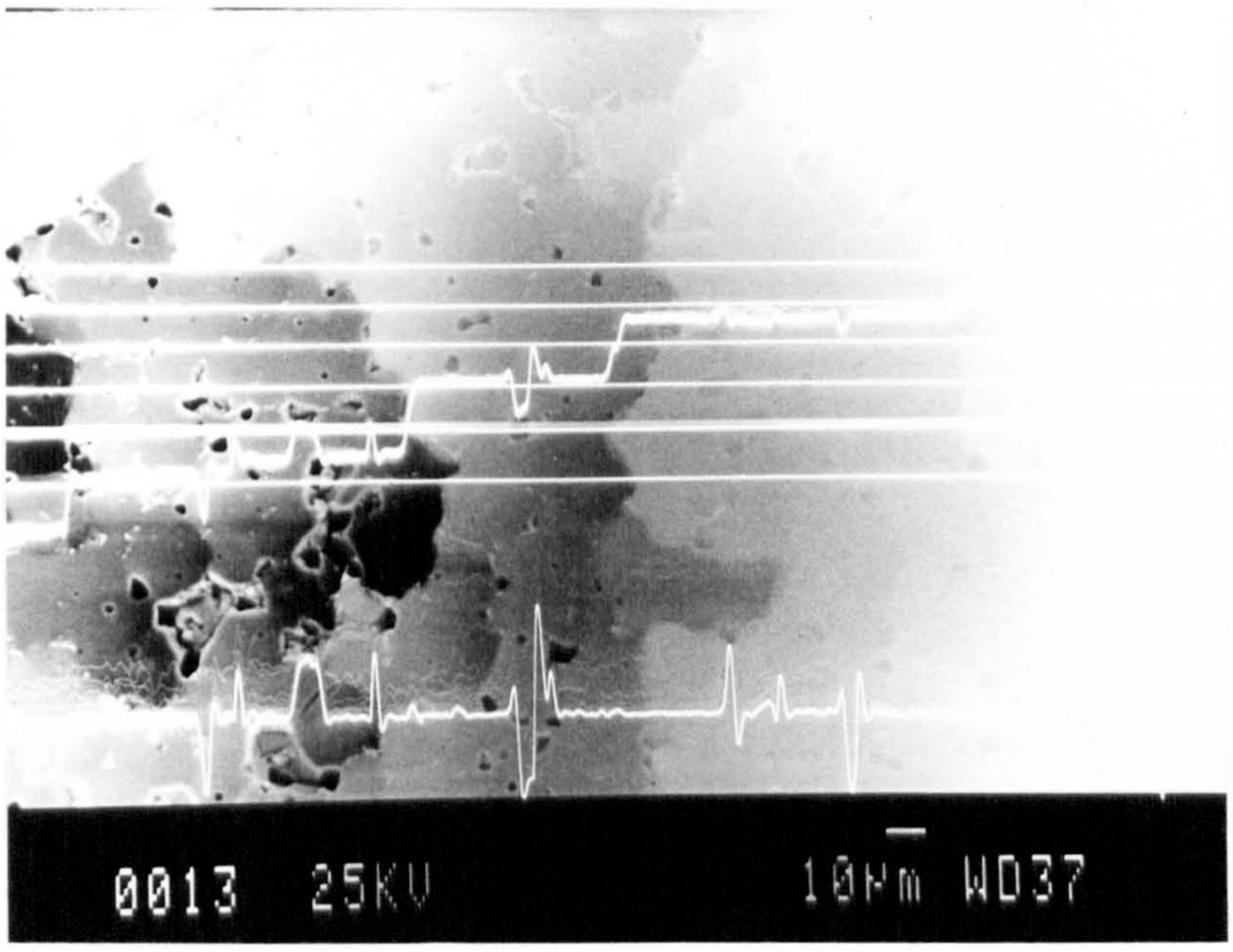


Fig. 5.2.5 (a) SEM-EBIC and LSP micrograph (400 x mag.) of a Bi based ZnO ceramic sample, **doped** (0.5 mol.%) with the oxides of **Bi**, **Sb, Co**, **Mn** and **Cr.** SEM beam parameters: 25keV, 82nA. **The LSP at the bottom is due to topography while that on the top is due to EBIC.**

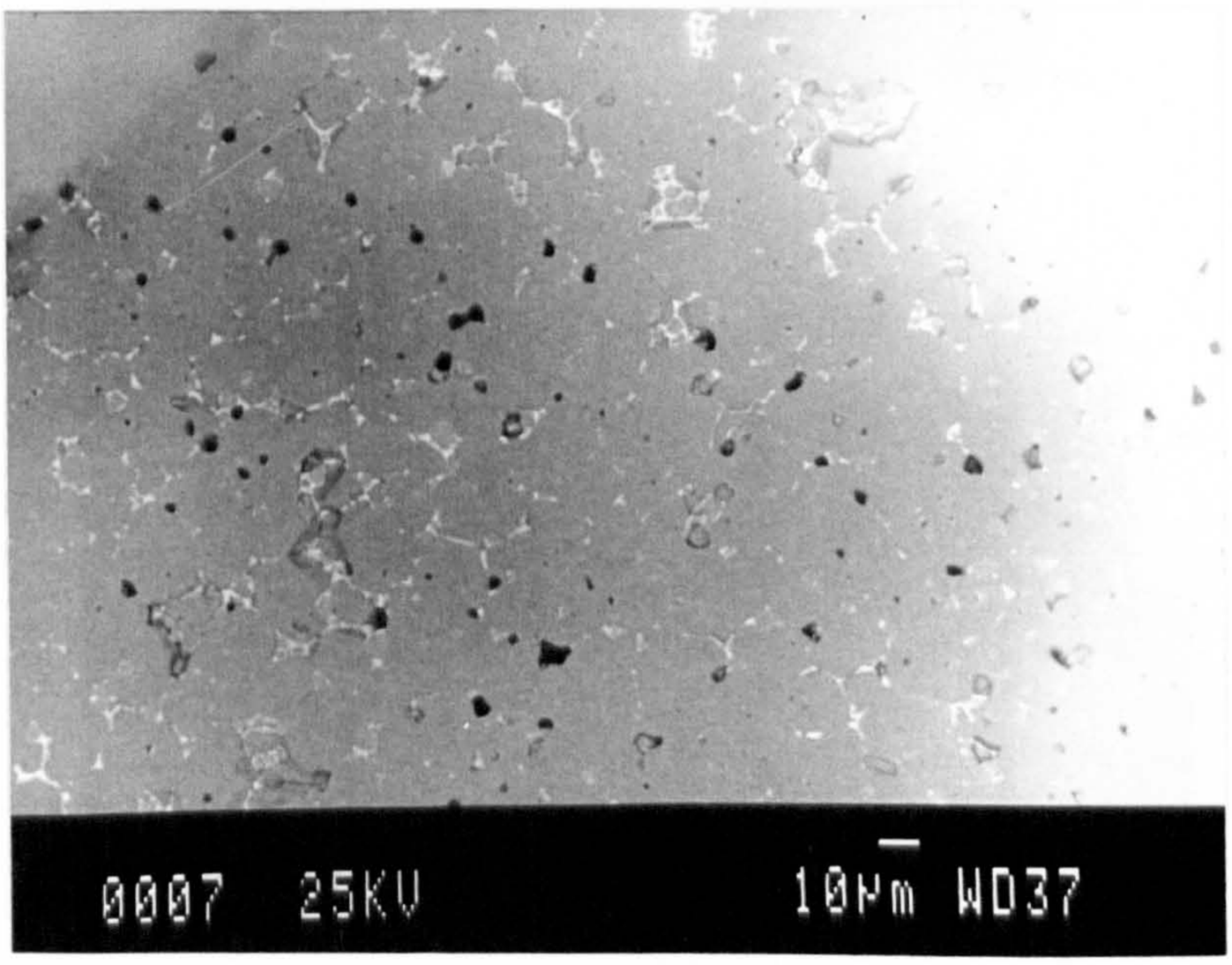


Fig. 5.2.5 (b) SEM micrograph (400 x mag.) of a Bi based ZnO ceramic (grain size 28 μm) sample, **doped** (0.5 mol.%) with the oxides of **Bi**, **Sb, Co**, **Mn** and **Cr.** SEM beam parameters: 25keV, 82nA.

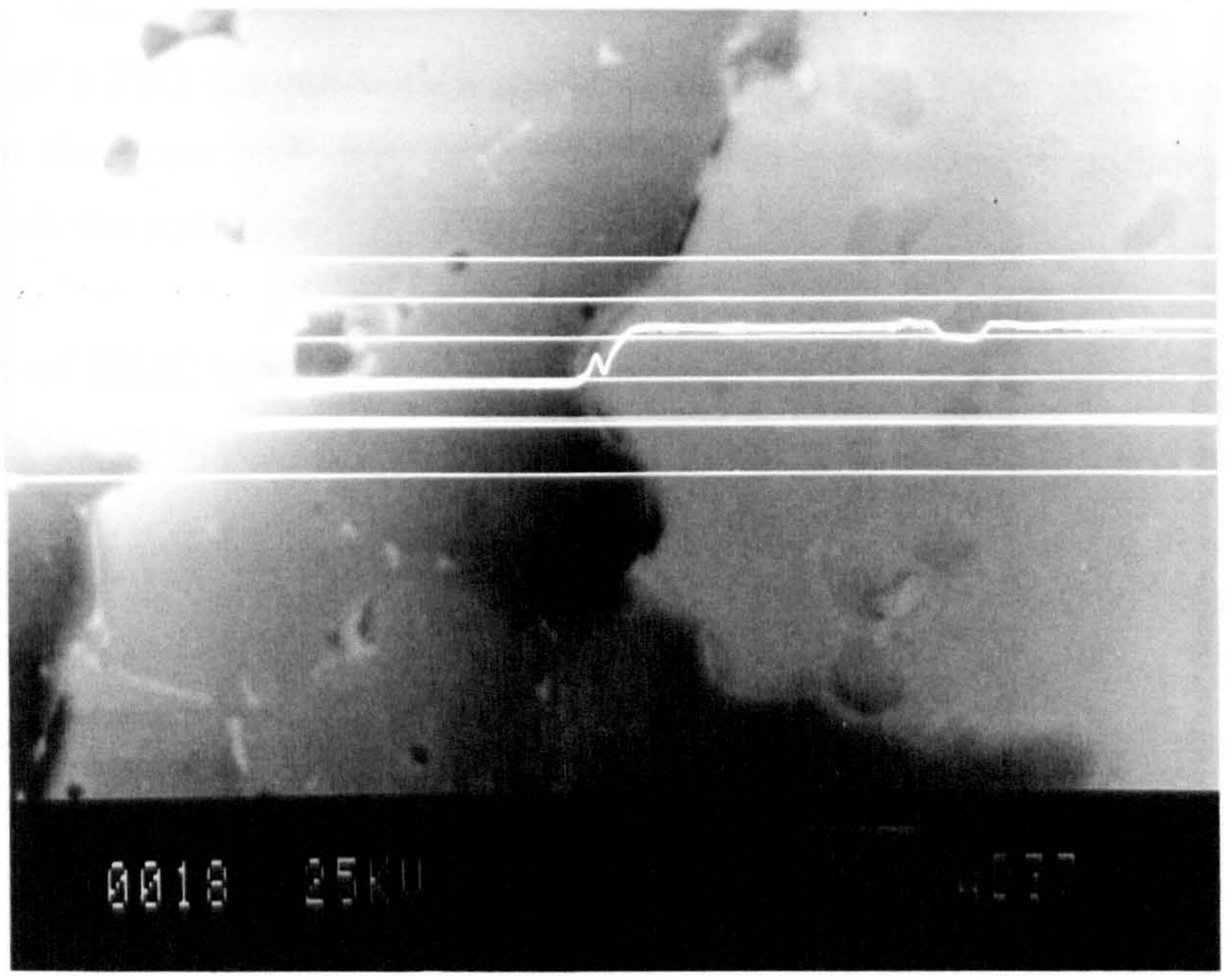


Fig. 5.2.5 (c) SEM-EBIC and LSP micrograph (1200 x mag.) of a Bi based ZnO ceramic sample, **doped** (0.5 mol.%) with the oxides of **Bi**, **Sb, Co**, **Mn** and **Cr. SEM beam parameters: 25keV, 82nA. Scale of the LSP: ≈ 8nA per division.**

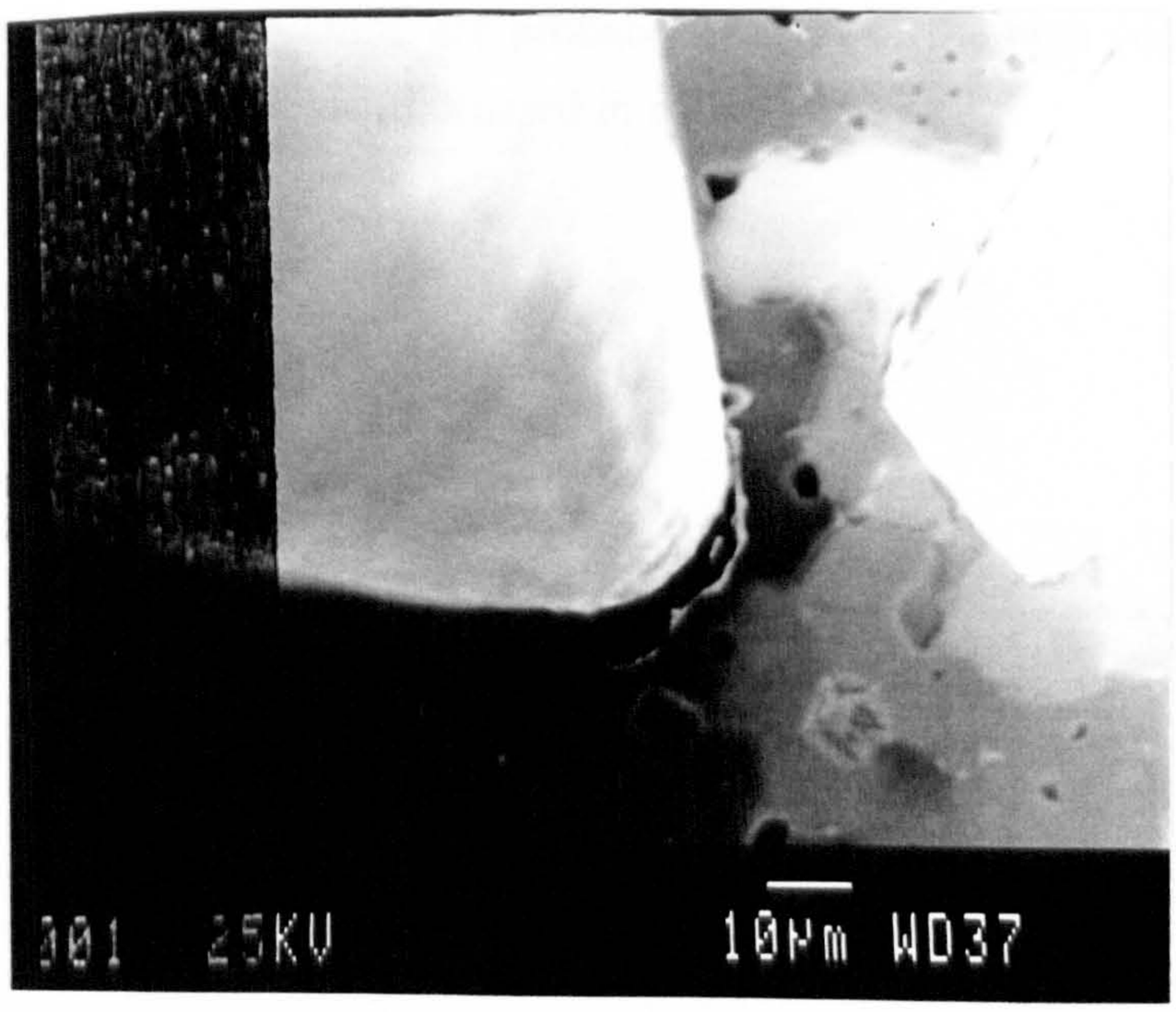


Fig. 5.2.5 (d) SEM-EBIC micrograph (800 x mag.) of a Bi based ZnO ceramic sample, **doped** (0.5 mol.%) with the oxides of **Bi**, **Sb, Co**, **Mn** and **Cr.** SEM beam parameters: 25keV, 82nA. This micrograph show the probes used to make micro-contacts on the either side of the grain boundary.

5.2.2.2. EBIC of ZnO with single additive (Bi_2O_3)

SEM-EBIC of a ZnO sample with a single additive (Bi_2O_3) was undertaken to explore and compare the grain boundary properties of ZnO with a single additive oxide to the sample with all the additives.

Micrographs of EBIC terraces and line scan profiling (LSP) corresponding to the grain boundaries of the Bi based ZnO ceramic with a single additive Bi_2O_3, were obtained.

Fig.5.2.6(a) and 5.2.6(b) show micrographs (200x magnification) of the SEM-EBIC terrace pattern and the corresponding microstructure of the Bi-based ZnO varistor sample. The dark point like feature of about 100μm, is an image of the micro-probe used to make contacts on the sample.

A close up view (500 x magnification) of the above is shown in Figs. 5.2.6(c). Also shown in this figure is the LSP across a grain boundary exhibiting a dark contrast. Figs.5.2.6(d) show EBIC terrace (550 x mag.) with a LSP across some grain boundaries giving rise to a bright EBIC contrast. Fig.5.2.6(e) show yet another example (1000x mag.) of an EBIC terrace and the LSP across a grain boundary exhibiting dark contrast. Finally the corresponding image of the microstructure, giving rise to the above EBIC terraces is shown in Fig. 5.2.6 (f) taken at 1000 x magnifications. The dark voids seen here decorating the microstructure, are probably created by the high volatility of Bi with ZnO during the sintering process (discussed in section 5.1).

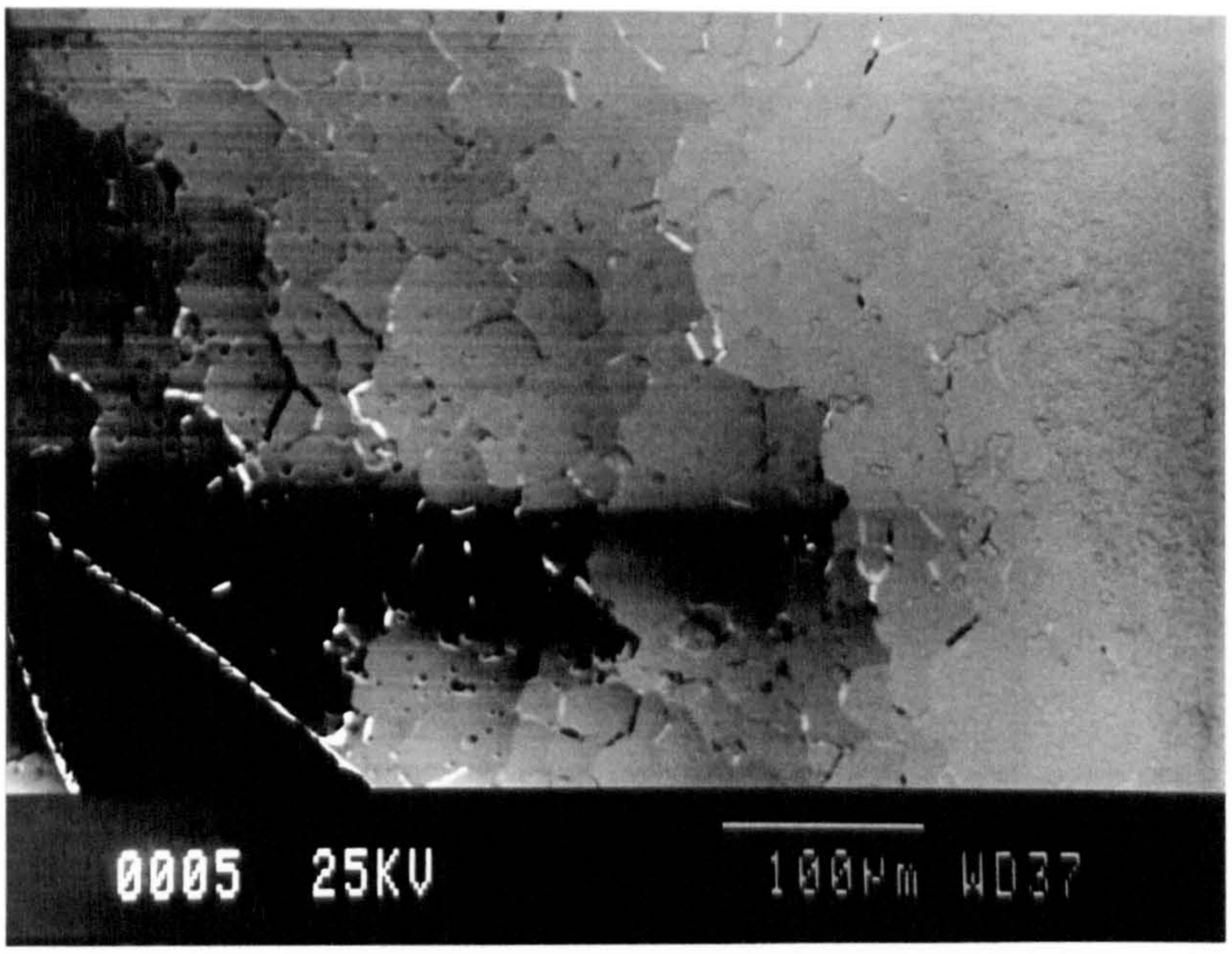


Fig. 5.2.6 (a) SEM-EBIC micrograph (200 x mag.) of a ZnO ceramic **sample, doped** (0.5 mol.%) with an oxide of **Bi.** SEM beam parameters: 25keV, 82nA. The micrograph show black and white grain boundary contrast.

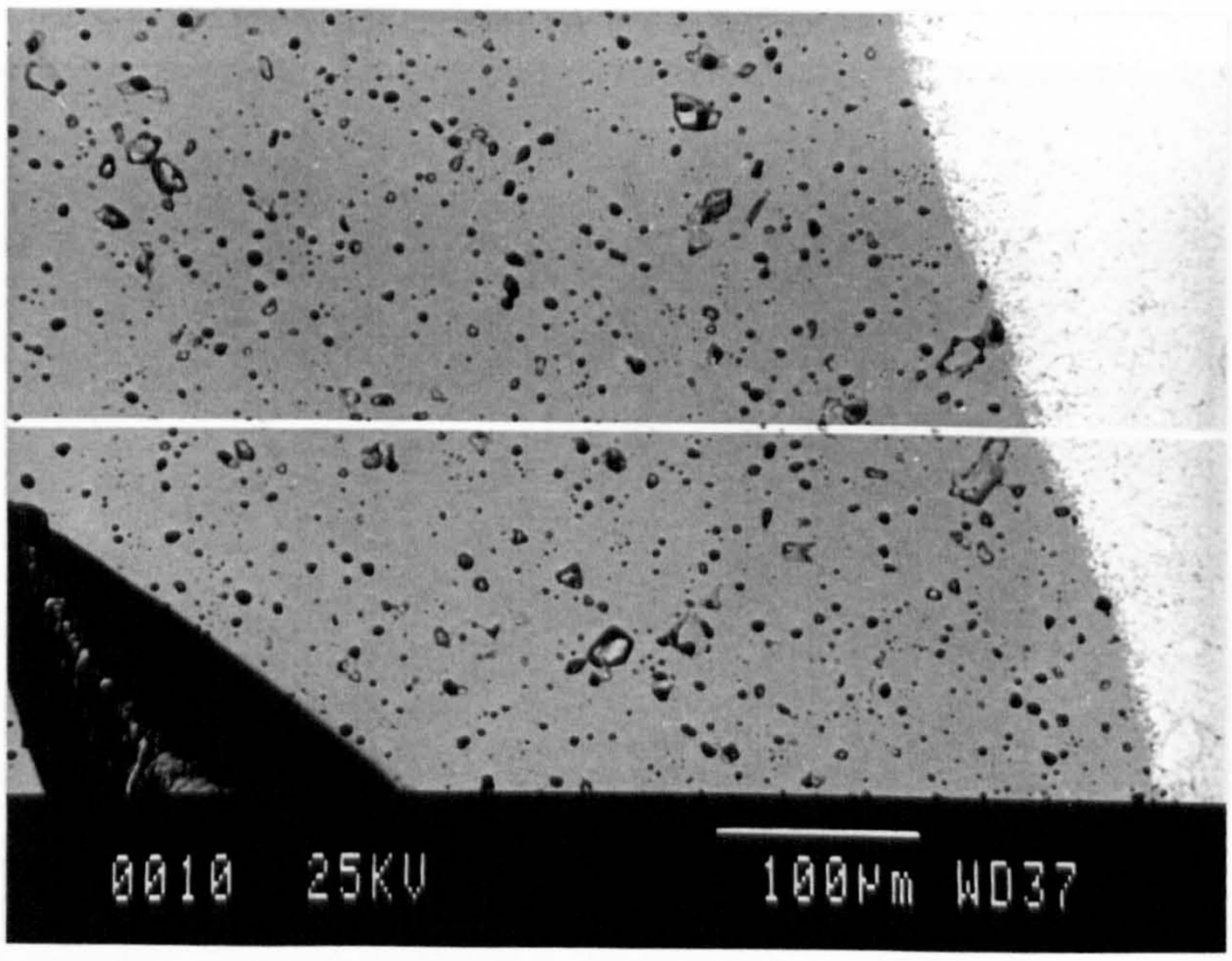


Fig. 5.2.6 (b) SEM micrograph (200 x mag.) of a ZnO ceramic sample, **doped** (0.5 mol.%) with an oxide of **Bi.** SEM beam parameters: 25keV, 82nA. The micrograph show one of the probes resting on the sample.

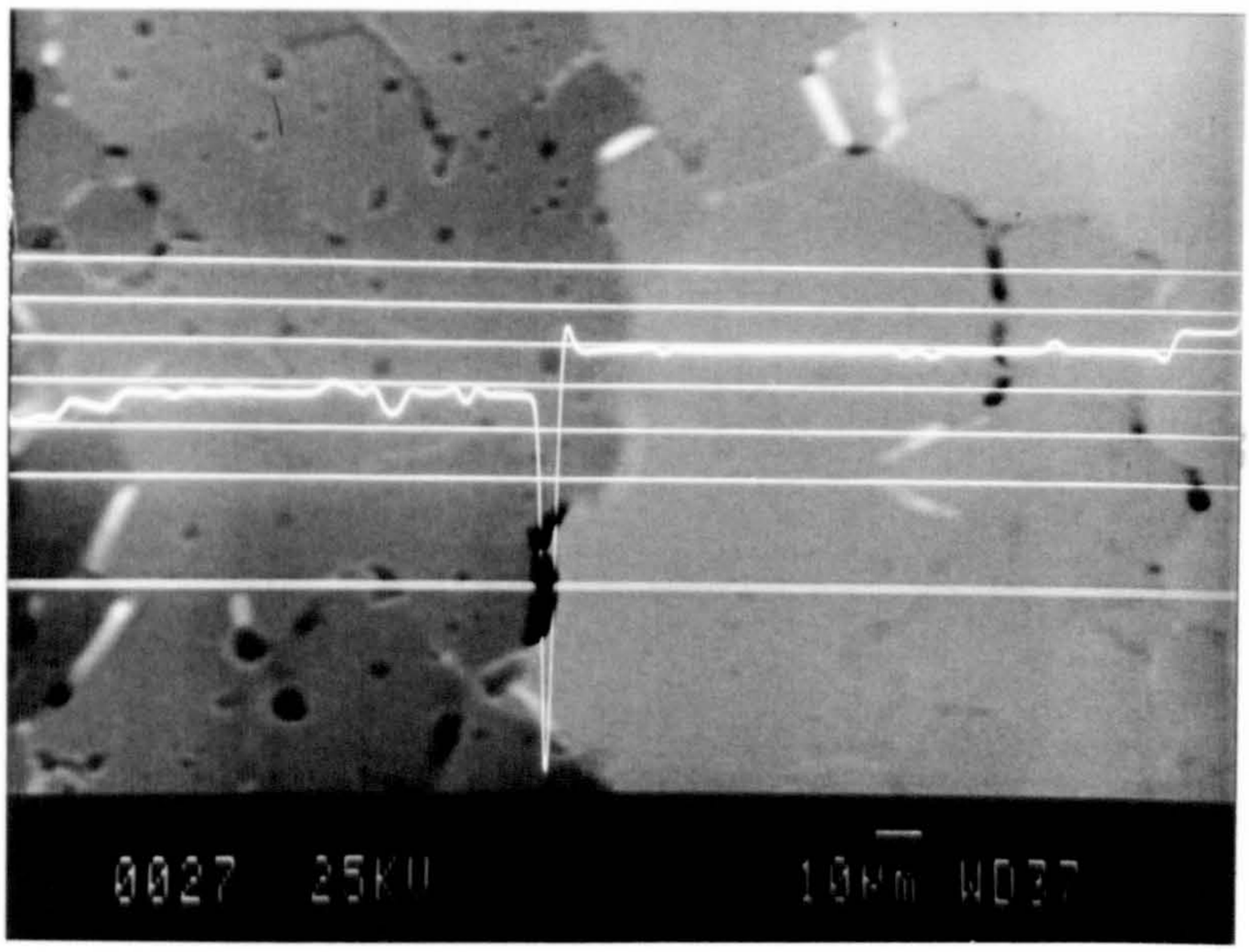


Fig. 5.2.6 (c) SEM-EBIC and LSP micrograph (500 x mag.) of a ZnO ceramic sample, **doped** (0.5 mol.%) with an oxide of **Bi.** SEM beam parameters: 25keV, 82nA. The LSP show the response of the black and white grain boundary contrast..

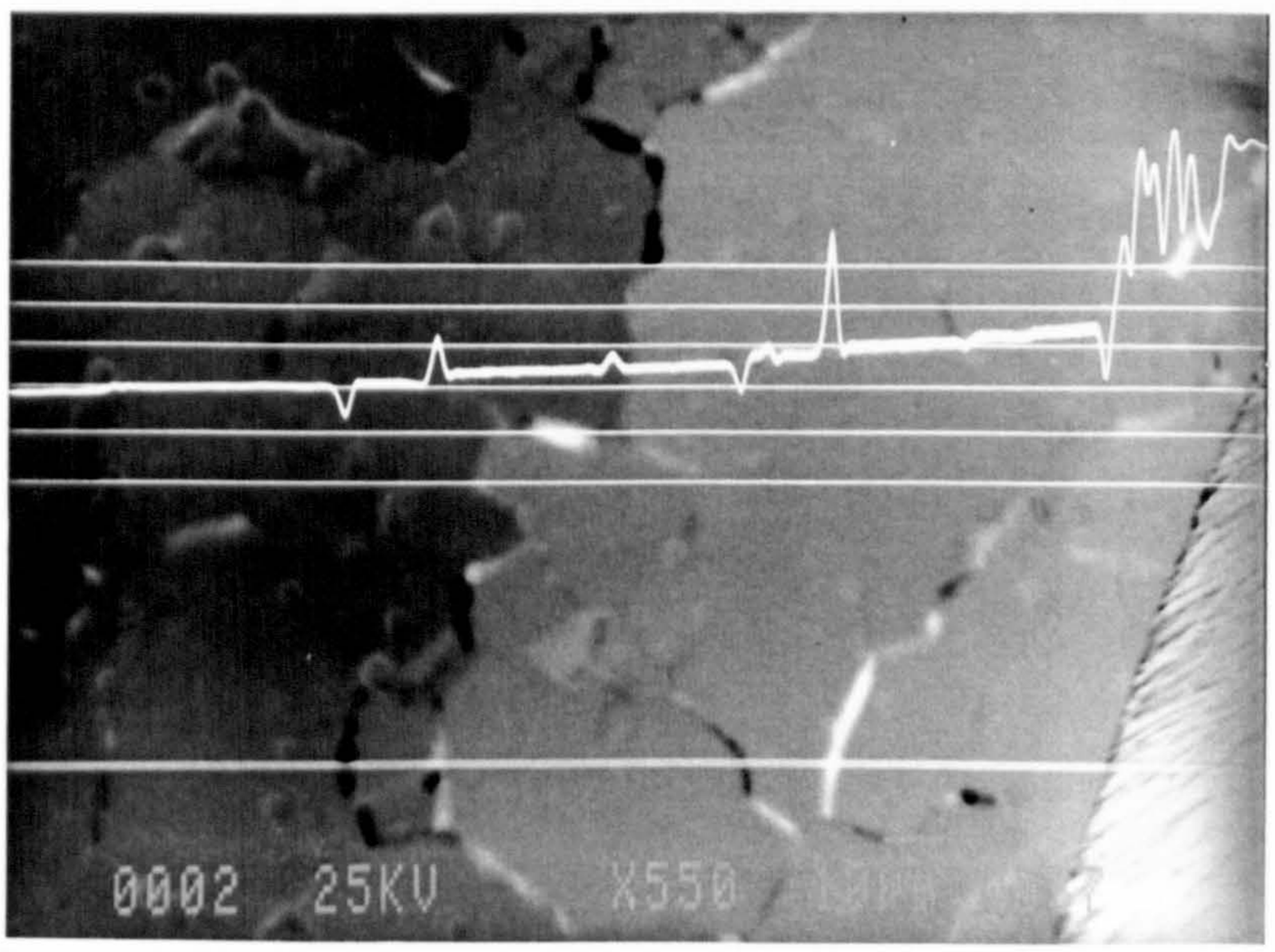


Fig. 5.2.6 (d) SEM-EBIC and LSP micrograph (550 x mag.) of a ZnO ceramic sample, **doped** (0.5 mol.%) with an oxide of **Bi.** SEM beam parameters: 25keV, 82nA. The micrograph show black and white grain boundary contrast..

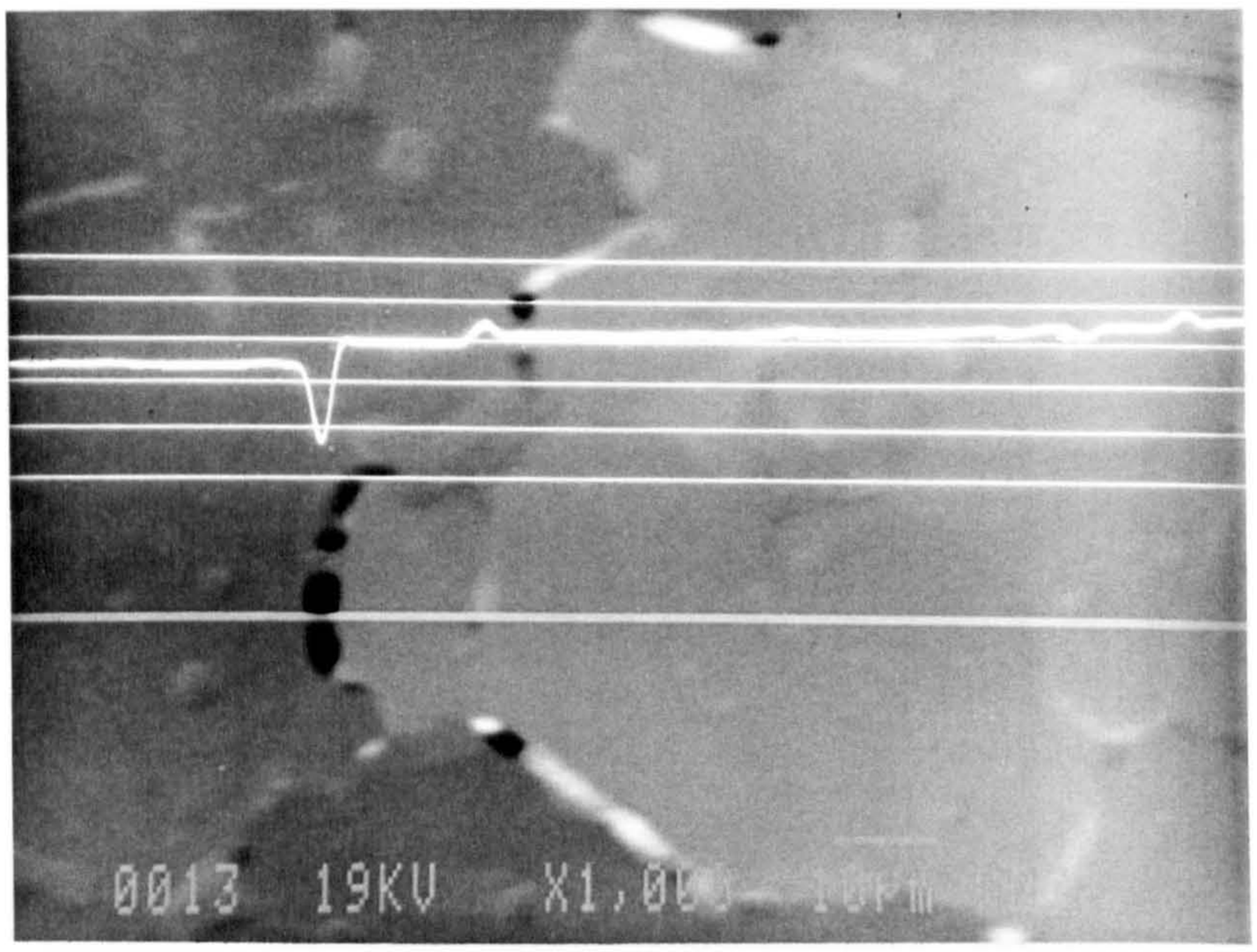


Fig. 5.2.6 (e) SEM-EBIC and LSP micrograph (1000 x mag.) of a ZnO ceramic sample, **doped** (0.5 mol.%) with an oxide of **Bi.** SEM beam parameters: 25keV, 82nA. The micrograph show black and white grain boundary contrast.

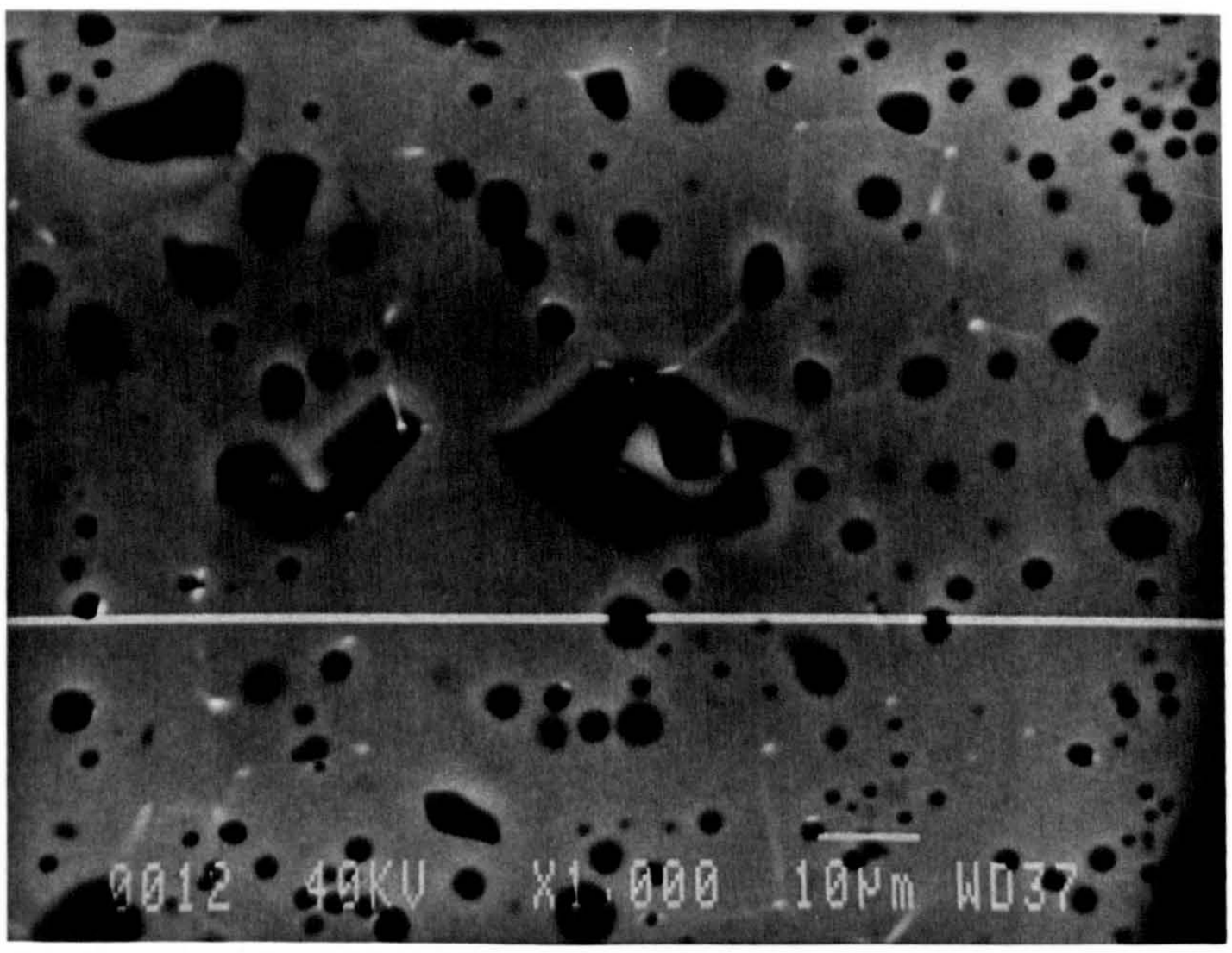


Fig. 5.2.6 (f) SEM micrograph (1000 x mag.) of a ZnO ceramic sample, **doped** (0.5 mol.%) with an oxide of **Bi.** SEM beam parameters: 25keV, 82nA. The micrograph also show the voids present in this singly Bi doped sample. This image corresponds to figs 5.2.6 (a-e).

5.2.2.3. EBIC analysis of a ZnO bi-crystal

Figs. 5.2.7 (a) and (b) show the SEM-EBIC and the corresponding image of the microstructure of the bi-crystal. Figs 5.2.7 (c) and 5.2.7 (d) show the LSP across the bi-crystal interface.

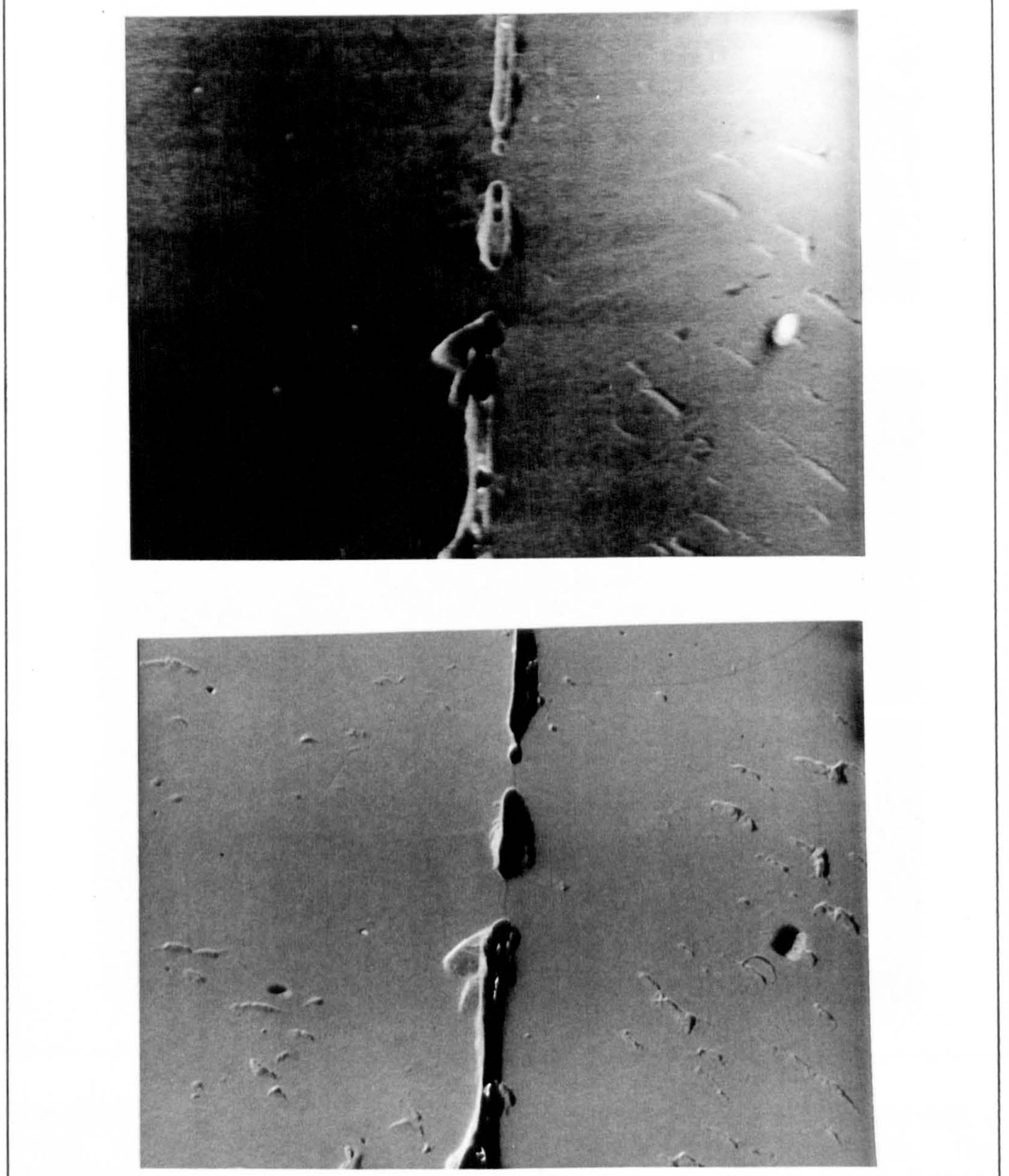


Fig. 5.2.7 (a) and **(b)** show the SEM-EBIC and the SEI of a ZnO bi-crystal (230 x mag.) The interface has Bi in between the two single crystals of ZnO. The micrograph also show a number of voids due to high volatility of Bi during sintering (1500^{o}C for 10 hours). SEM beam parameters: 25keV, 82nA.

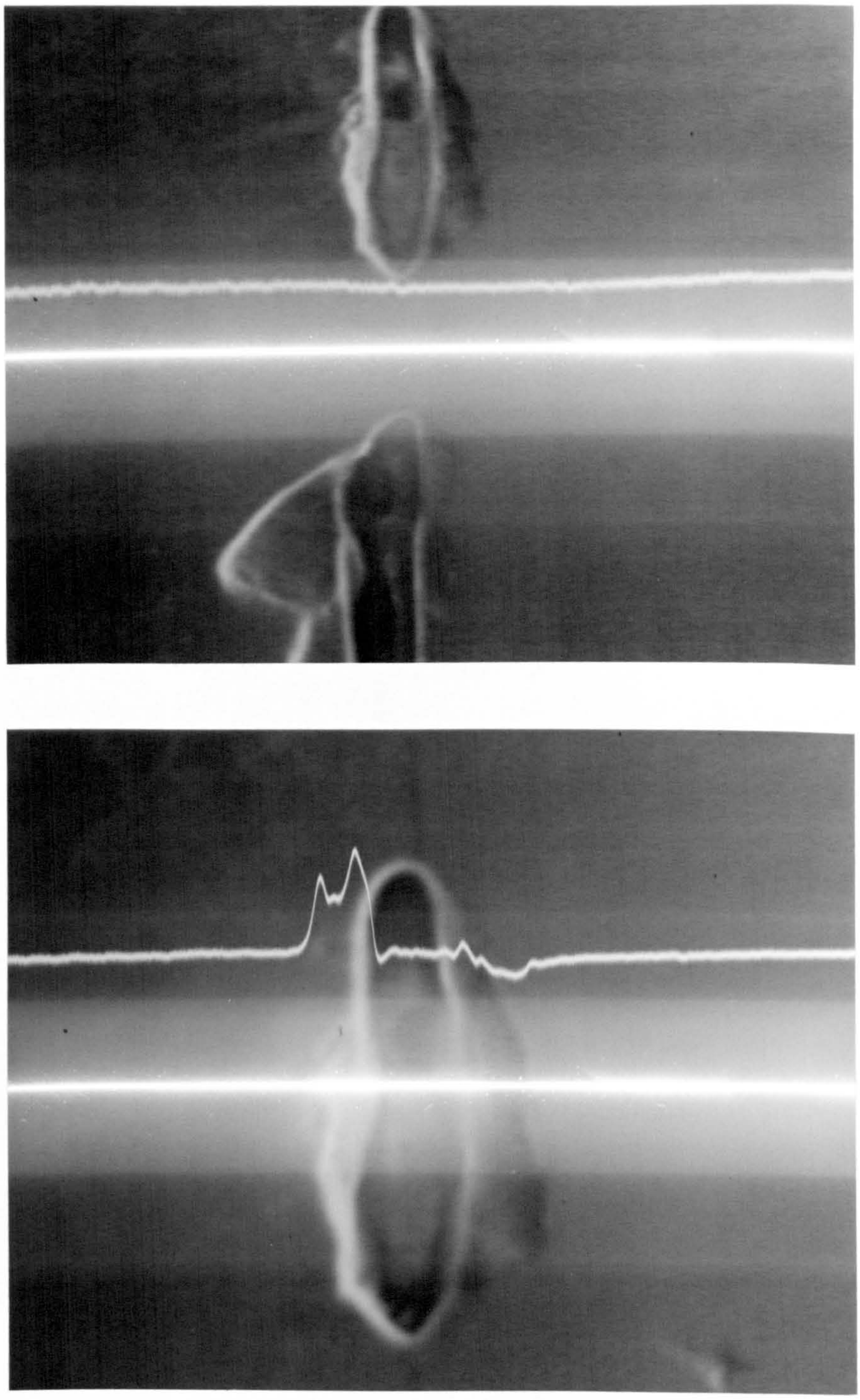


Fig. 5.2.7 (c) and **(d)** show the SEM-EBIC and the LSPs of a ZnO bi-crystal (600 x mag.) The interface has Bi in between the two single crystals of ZnO. The micrograph show the LSPs from the smooth and course regions of the sample. These coarser regions (1000 x mag.) are likely to be due to a number of voids created by the high volatility of Bi during sintering (1500^{o}C for 10 hours). SEM beam parameters: 25keV, 82nA.

5.2.3. EBIC experiments at NPL

It was intended to set up a basic SEM-EBIC procedure using the SEM equipment at the National Physical Laboratory (NPL), Teddington. An SEM of the type S-4000, with an amplifier usually dedicated to collect back scattered electrons (BSE) was used to amplify and re-modulate the EBIC signal, collected from the polished cross section of the ZnO ceramic varistor. The experimental set-up is discussed in Chapter 4 section 4.2.2.2. This experiment enabled an observation of EBIC terraces (Fig.5.2.8) similar to that obtained in the laboratory at Imperial College. Through this experiment it was shown that even a relatively simple experimental set up such as this can be used to observe EBIC response of ZnO varistors.

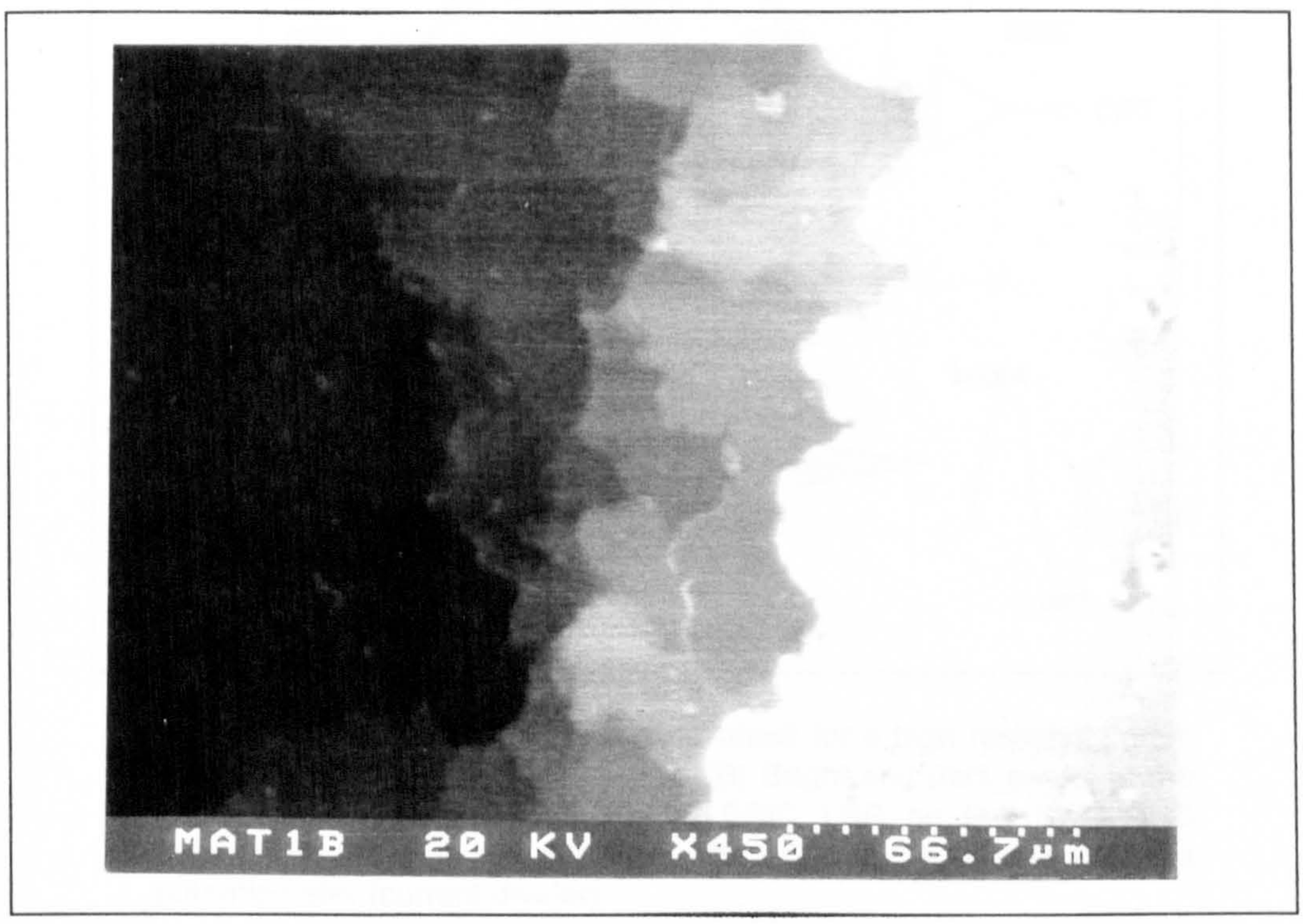


Fig 5.2.8 SEM-EBIC image (acquired at **NPL) of a Bi** based commercial ZnO varistor of grain size of 35 µm.

5.2.4. SEM-EBIC Discussion

Looking at the over view of the SEM-EBIC technique (discussed in Chapter 3, section 3.2.3), as the electron beam is incident on the sample, two components of signals are produced. One part of the signal is constituted from that part of the absorbed primary electrons which flows to the ground via the current amplifier (Fig 5.2.9). The other part of the absorbed electrons flow to ground from the earth contact 'O', and are not detected.

The magnitude of these two components is given by the ratio of the resistance values for the current path from the e-beam position to the 'O' and 'D' contacts respectively. This ratio changes only when the e-beam moves across a grain boundary (GB) since the resistance is exclusively controlled by the GB's. Thus the signal is different from grain to grain and drops stepwise at each GB. Charge carriers (ΔnL) generated by the incident electron beam (Fig. 5.2.9) are detected as the EBIC signal. Inside the grains the effect of carrier generation is negligible [110], since there is a large concentration of free electrons ($10^{17}cm^{-3}$). At the GB's, however, there is a depletion of free carriers due to the acceptor-like, negatively charged interface states [23,56, 61,].

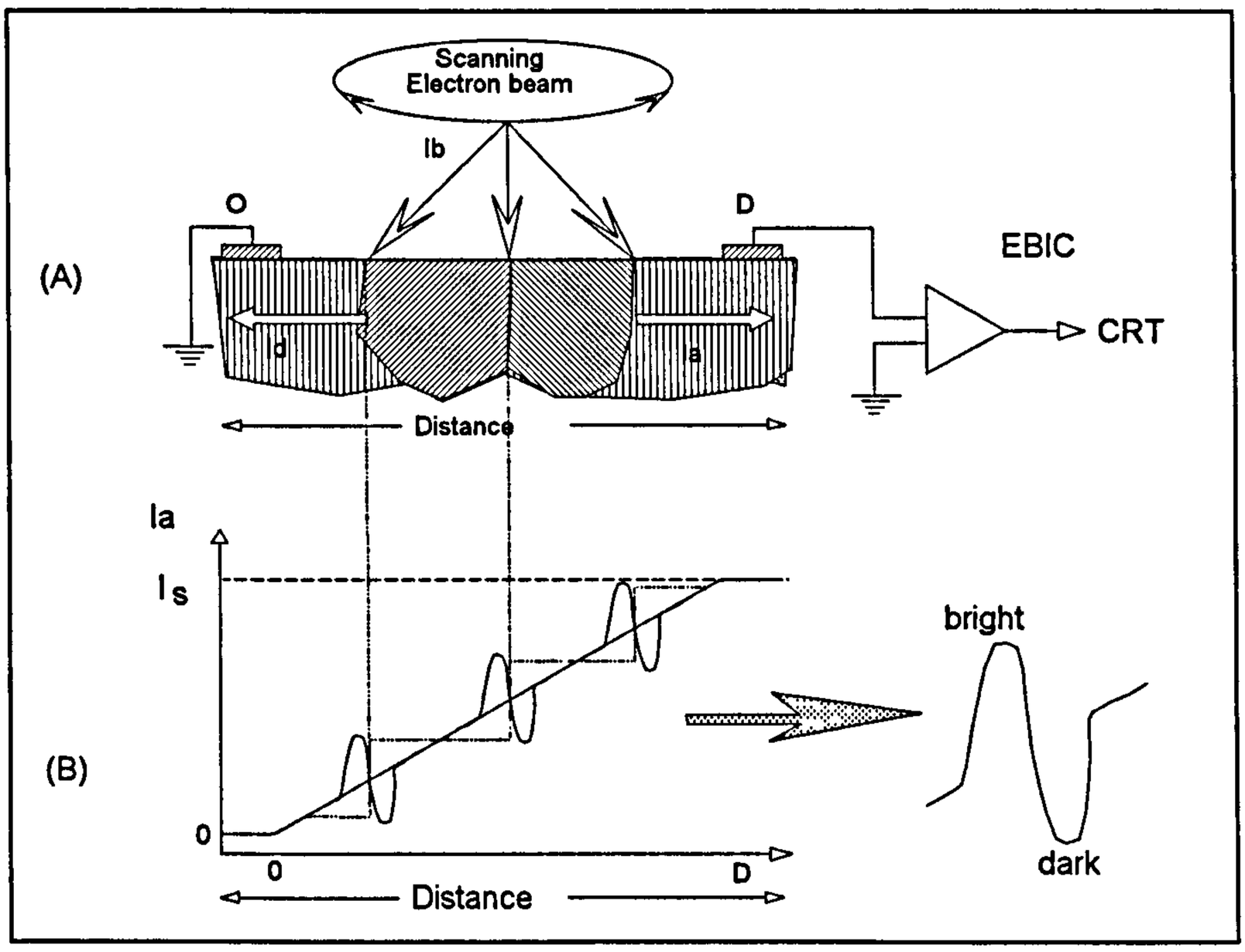


Fig. 5.2.9. (A) SEM-EBIC detection circuit for a high resistivity grain boundary specimen (ZnO Varistor). (B) Bright and dark peaks at the grain boundary corresponds to the EBIC LSP on the SEM-EBIC micrograph shown in Fig. 5.2.5 (C). The beam and specimen act as a potentiometer (current divider).

Figs. 5.2.1 (a) - (e) show re-modulated images of the stepwise drop in EBIC signal. These images show the EBIC terraces corresponding to the grain boundaries (Fig. 5.2.1 (f)). At certain beam parameters (2keV-5keV) phases at the triple points appear as bright clusters, as seen in the EBIC images (Figs. 5.2.1 (a) (b) and Fig. 5.2.2 (a). At higher beam voltages (15keV- 25keV) however, these same phases appear as dark clusters as shown in Figs. 5.2.1 (c), (d) (e) and Fig. 5.2.2 (b).

Close examination of the EBIC terraces, as shown in Figs. 5.2.4 (a) and (b), reveals bright and dark contrast along the electrically active grain boundaries. Further details are

gained by looking at the LSP across the electrically active boundaries as shown in Figs. 5.2.5 (a) and (c). This type of LSP response can be modelled (Fig.5.2.9) as two back to back Schottky barriers, symmetrically oriented (Fig.5.2.10). When the electron beam is incident directly upon the grain boundary, the holes thus generated can be captured into the negative surface states, resulting in a reduction of the interface charge density Q and the associated electrical barrier V_B. The electron transition from the Vb to Cb results in generation of charge carriers (ΔnL) which produces current going in the opposite direction as shown in Fig. 5.2.10. The grain boundaries, in this situation, cause the collected signal (I_{CC}) to proceed in the opposite direction resulting in dark and bright contrast along the grain boundaries. The EBIC current across a grain boundary was measured to be about 8.5nA. Recently, **Russell** *et al* [116], did a similar analysis and his results are found to be consistant with these interpretations.

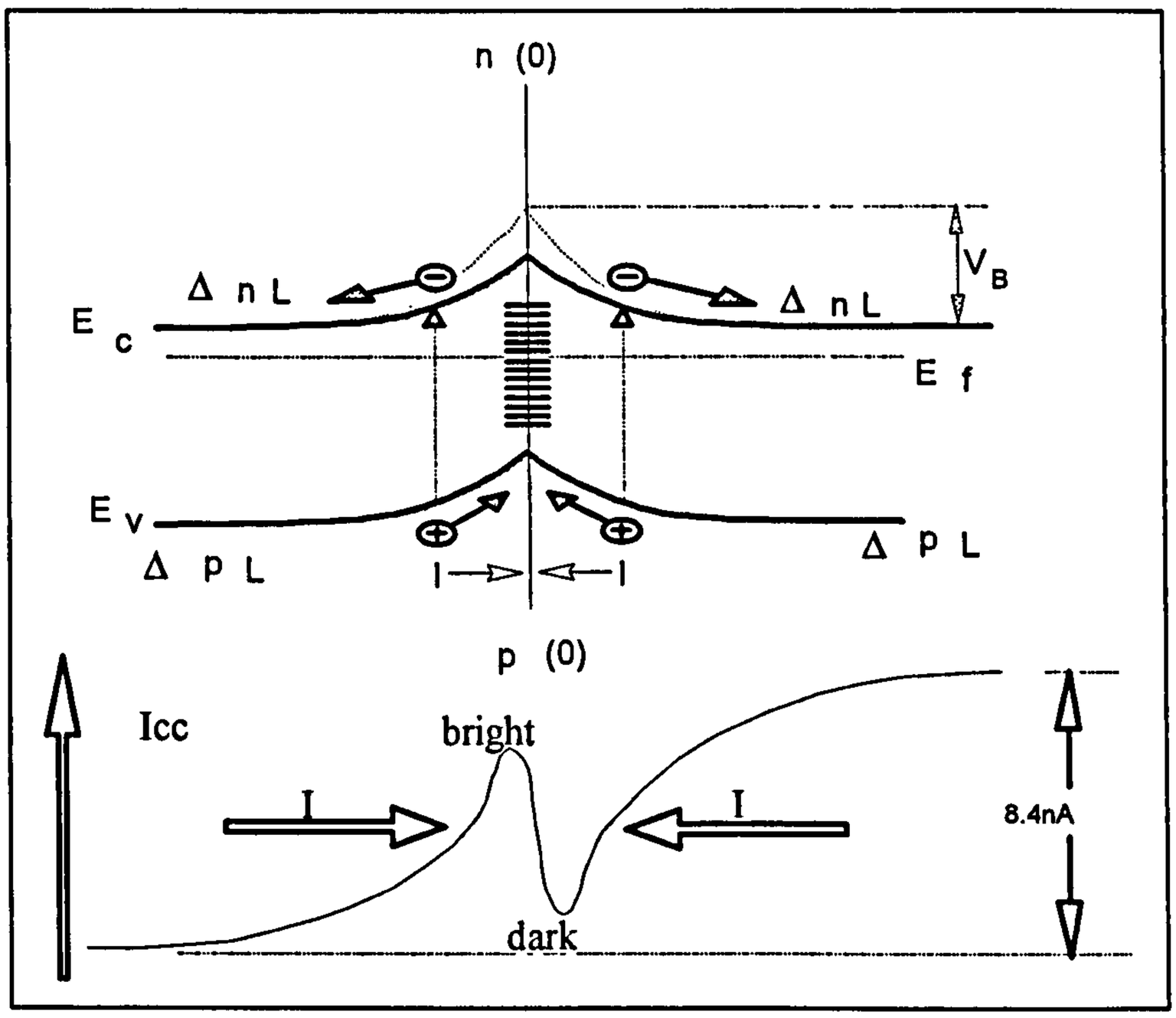


Fig. 5.2.10. Schematic illustration of carrier generation during electron bombardment of a high resistivity material such as ZnO varistor. With illumination barrier-lowering increases n(0) and thereby promotes recombination. A continuous distribution of interface states assumed.

Figs. 5.2.6 (a) to (e) are images following the SEM-EBIC analysis of ZnO ceramic sample with just the Bi_2O_3 oxide as a dopant; showing that the EBIC terraces of grain boundaries are separately decorated with white and black contrast. LSP across these GB's, as shown in Figs 5.2.6 (d) and (e) indicates separate arrays of Schottky barriers, unlike the back to back model proposed for ZnO ceramic doped with all of the five additive oxides. Varistors with these separate barriers, as modelled in Fig. 5.2.11, would

not be favourable as it may give rise to asymmetrical I:V characteristics [56] (discussed in Chapter 2, section 2.5.3.2) In any case, the bulk I:V characteristics of this sample with Bi_2O_3 as a single dopant, was measured to be about α= 1.3 (discussed in section 5.7). This would not make a useful varistor!

This method of modelling Schottky barriers has been successfully applied by **Palm** and **Alexander** [117], who developed a detailed theory and applied it to well characterised grain boundaries in silicon bi-crystals.

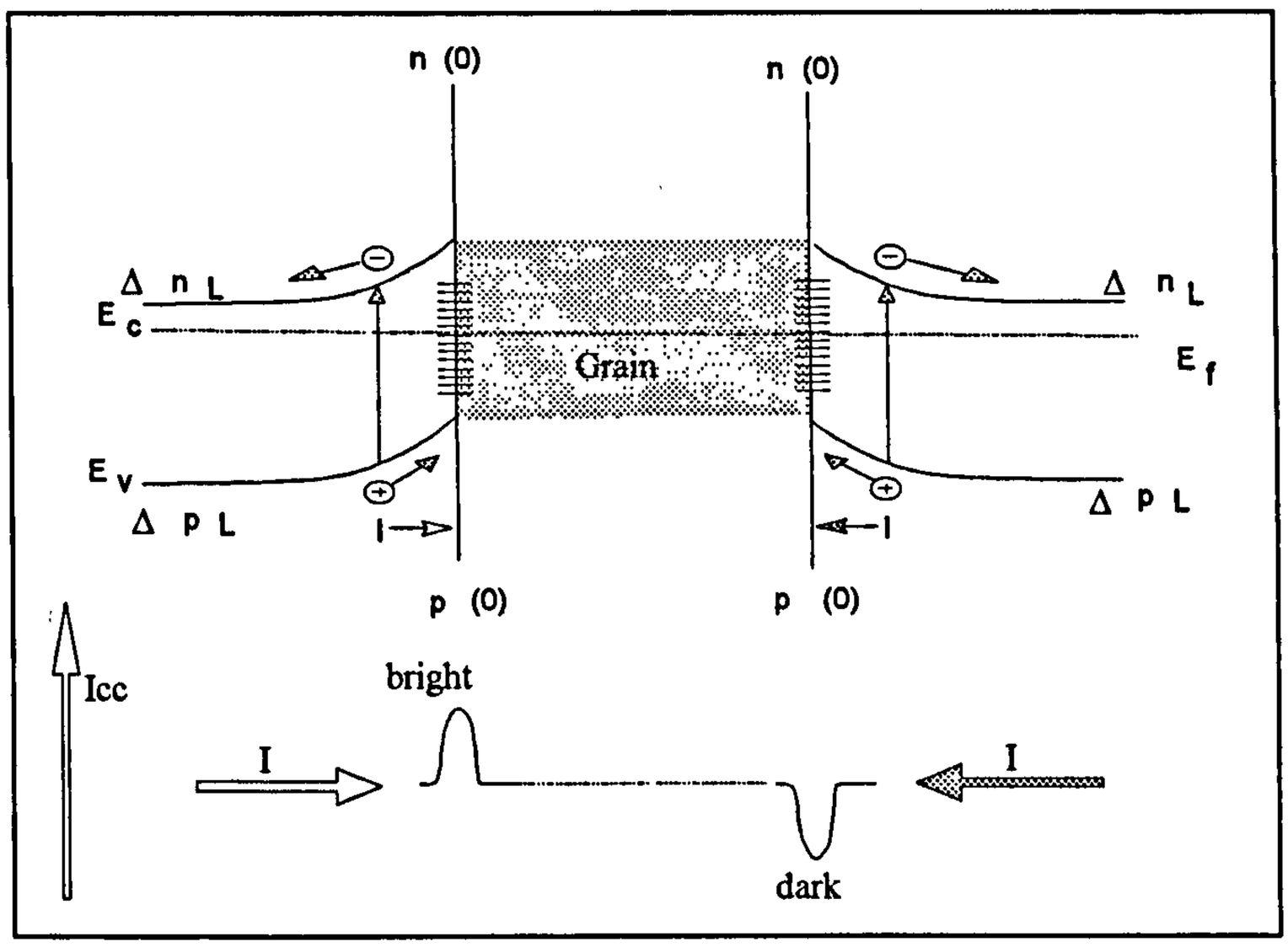


Fig. 5.2.11. Schematic illustration of carrier generation during electron bombardment of a ZnO material with Bi oxide as a single additive. 'Bright' and 'dark' signal intensities corresponds to the grain boundary contrast seen in Figs. 5.2.6 (a), (c), (d), and (e). With illumination, barrier -lowering increases n(0) and thereby promotes recombination. Continuous distribution of interface states assumed.

In this work, EBIC studies of the bi-crystal (Figs. 5.2.7) did not show any significant varistor behaviour. This may be due to the quality of an interface where some regions that are in direct contact may be short circuiting the bi-crystal. At the interface, it is important to have very small carrier generation compared to its bulk properties, in order to create a zone that is depleted of free carriers. Thus, in order to exhibit good EBIC yield, acceptor-like, negatively charged interface states are essential in order to control the resistance at the grain boundaries. I:V measurement of this bi-crystal sample yielded a non-linear coefficient (α=1.2) similar to that of a ZnO ceramic sample with a single dopant of Bi oxide (discussed in section 5.6).

SEM-EBIC analysis of $BaTiO_3$ PTCR thermistor (120°C switch on temp.) did not show any grain boundary related terraces at room temperature. Moreover, a sample of pure ZnO ceramic also failed to show any EBIC response at the grain boundaries.

5.2.5 Summary of the EBIC results

SEM-EBIC micrographs feature a kind of terrace pattern which appears to correspond to an array of electrically active grain boundaries in ZnO varistor. Regions with no significant terrace contrast may be an indication of a "bad" junction. This technique enables a direct observation of the microscopic electrical behaviour at the grain boundaries. The quality of a varistor would then depend on the ratio of these good/bad junctions in the ZnO ceramic system. The quality of these grain boundary junctions depends mainly on the procedures adopted in manufacturing these devices and in particular the additives and control over the sintering and post sintering treatments.

The main features of the SEM-EBIC studies in this work has been:

1. The acquisition of electrical terraces corresponding to the electrically active grain boundaries that are decorated by secondary phases as seen in the corresponding image of the microstructure. A clear example of this is shown in Figs. 5.2.2 (d), 5.2.4 (a), 5.2.4 (b), 5.2.5 (a) and 5.2.5 (b). This is perhaps an example of an array of electrically active grain boundaries in ZnO varistor. It is also seen that some grain boundaries do not display any significant terrace contrast and they are presumed to correspond to bad grain boundary junctions. The quality of a varistor would then depend on the ratio of these good/bad junctions in the ZnO ceramic system.

2. Under low energy beam conditions (2keV- 5keV), additional EBIC contrast of the phases at the triple points can be observed. This is shown in Figs. 5.2.2 (a), 5.2.2 (b) and 5.2.2 (c).

3. Line Scan profiling (LSP) across the grain boundary of ZnO ceramic with varistor composition, enabled a modelling of the grain boundary with Schottky barrier type of response. Hence, it is possible to observe whether or not the barriers are situated symmetrically back to back.

4. Observation of dark and bright grain boundary contrast in ZnO doped with Bi_2O_3 as a single additive. LSP across these boundaries implied a separated asymmetrical types of Schottky barriers.

5. A bi-crystal with just a Bi oxide at the interface may not be distributed uniformly in order to sustain sufficient acceptor-like, negatively charged interface states, hence the need for other additives (oxides of Sb, Mn, Co, and Cr) in the ZnO varistor system.

5.3. SEM-CL analysis of ZnO ceramic

CL analysis was used to study the band gap related processes in ZnO ceramics, arising due to native defects present as donors and acceptors in pure and and doped samples. Samples of pure, and doped ZnO ceramic and a single crystal of ZnO were analysed using the CL light collection system attached to JSM-840A SEM. The instrumentation is discussed in Chapter 3.2.4. The SEM-CL analysis was undertaken at room temperatures, using SEM, with a beam energy of 30-35 keV and a current of 78nA - 2.5 μA. Detectors used were (a) a photomultiplier of the type S20 and (b) a Ge Infra-red type.

CL analysis produces results in the form of CL images (panchromatic and monochromatic) and raw data in the form of spectra, showing various peaks intensities as a function of wave length (λ), corresponding to radiative recombination giving rise to the CL signal.

5.3.1 CL results

Fig.5.3.1 (a) shows a panchromatic image of an undoped ZnO ceramic sample, and (b) shows the corresponding image of the microstructure. A CL spectra corresponding to this analysis is shown in Fig. 5.3.3, marked as 'a'.

Fig. 5.3.2 (a) show a schematic of a monochromatic CL image, showing contrast arising, in this case, from the voids within the microstructure of the ZnO ceramic varistor sample. The corresponding CL spectra are marked as 'b', shown in Fig.5.3.3. Fig. 5.3.3. show all the CL spectra of (a) pure ZnO, polished, S20 detector, (b) ZnO + all five dopants, polished, Ge detector, (c) Single crystle of ZnO, S20 detector, (d) ZnO + all + TiO_2, polished, S20 detector, and (e) ZnO + all, sintered surface, using S20. detector.

Tables 5.3.1, 5.3.2 and 5.3.3 show the information extracted from the CL spectra acquired from the undoped and the doped samples of ZnO ceramic. The analyses were acquired at various beam parameters in order to obtain the maximum CL signal. The

calculated (RG) information depth corresponding to each CL analysis is also shown in Tables, 5.3.1, 5.3.2 and 5.3.3.

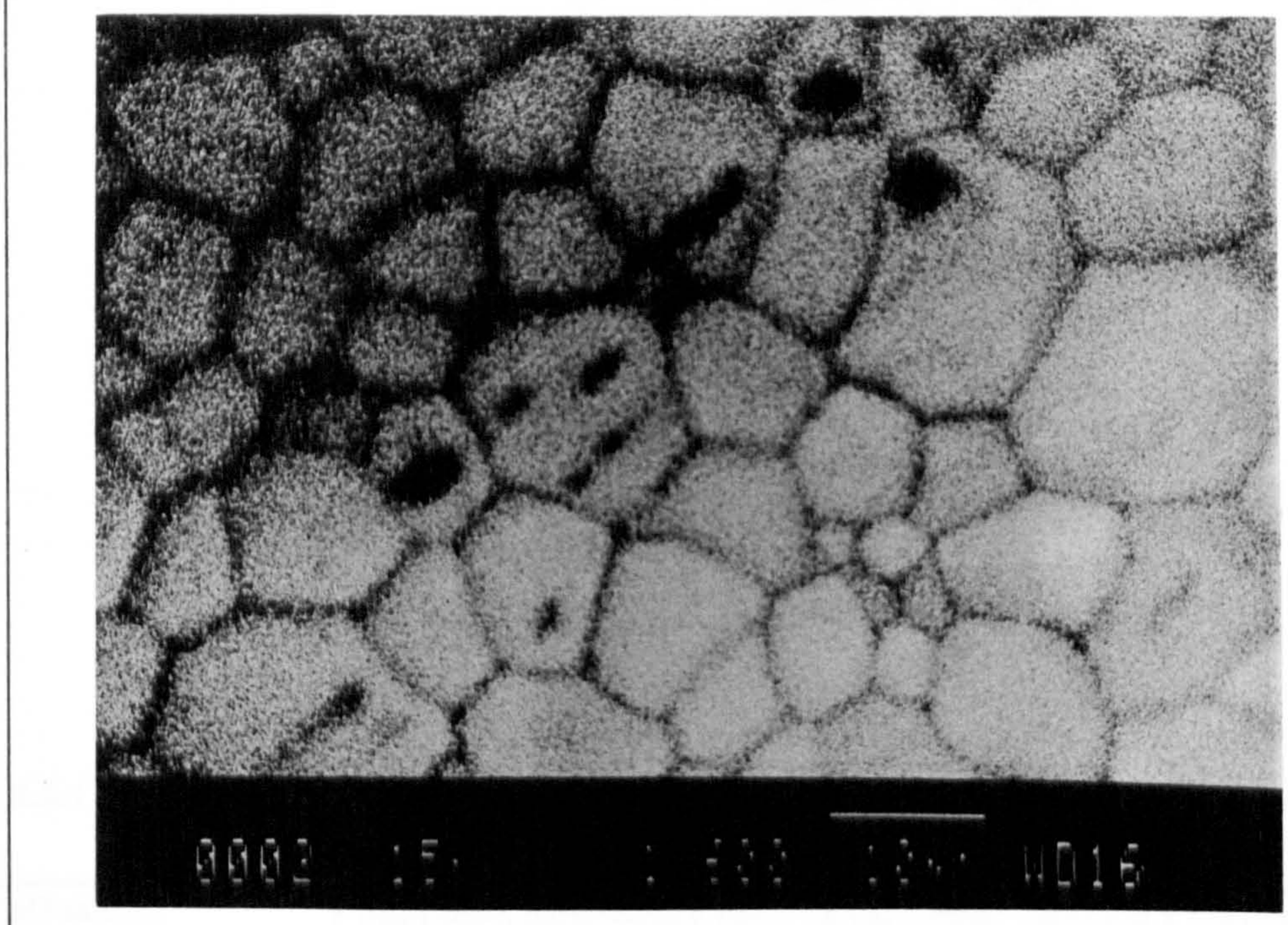


Fig.5.3.1. (a) show panchromatic image of undoped ZnO ceramic sample, and (b) show the corresponding image of the microstructure.

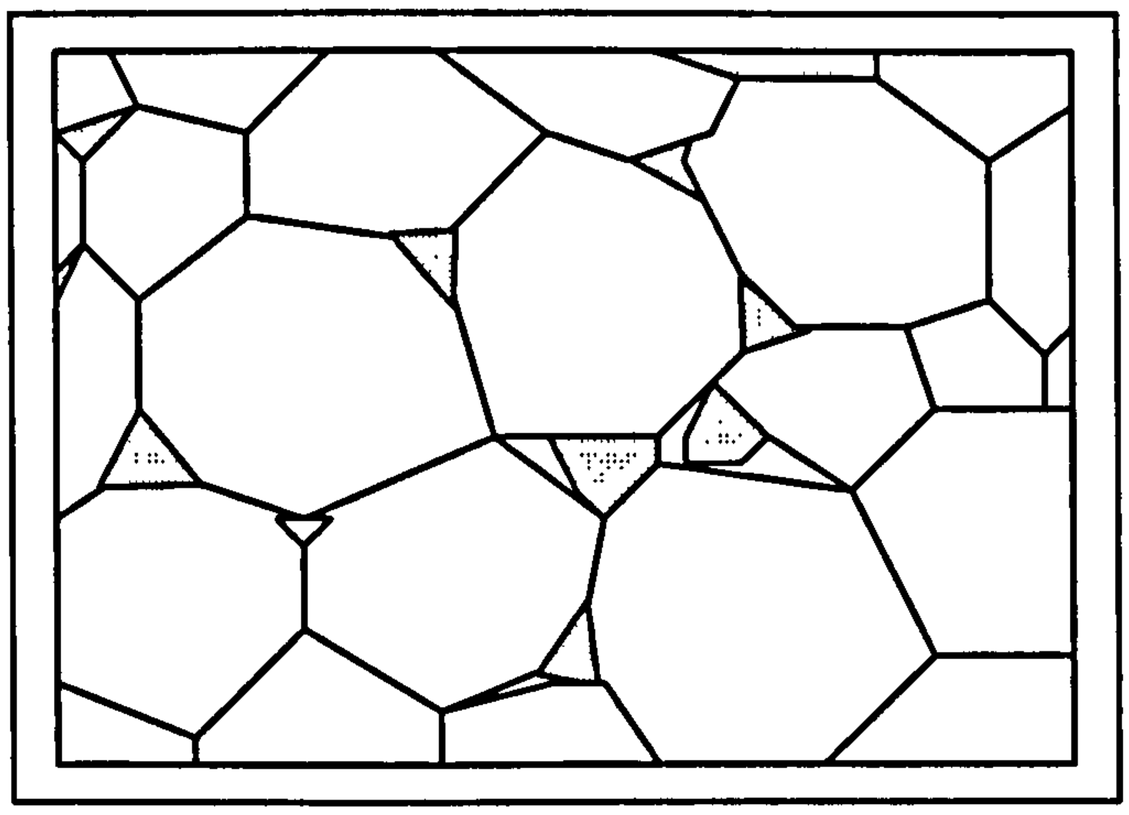


Fig. 5.3.2. Schematic image showing CL contrast (shown as shaded) arising from the regions of the ceramic microstructure of ZnO doped with all the additives (not to scale).

Table 5.3.1 CL information extracted from the CL spectra of the undoped samples of ZnO.

No	ZnO sample	SEM beam parameters	RG (μm)	CL Peak position (Å) in their order of intensities [cps]	Position in the band scheme (eV)
1	ZnO,undoped ceramic, sintered at 1250^{o}C surface as polished	15keV, 2.26μA 3700x mag. general region. PMT: S20.	0.8	3920 [15500]	3.17
2	As in 1 above	20keV, 0.97μA 10000 x mag.,grain centre. PMT: S20.	1.3	3900 [500], 7760 [110], 5260 [90]	3.18,1.60, 2.36
3	As in 1 above	15keV, 2.2μA 3700 x mag., grain centre. PMT: S20. .	0.8	5257 [3000],	2.36
4	As in 1 above	30keV, 2.43μA 2000 x mag .PMT: S20.	2.7	4000 [1800], 7920 [200]. 5300 [150]	3.1, 1.57, 2.3
5	Pure ZnO, single crystal .	35keV, 100nA, 25000 x mag. spot. PMT: Ge (IR detector).	3.6	5400 [13500], 5557 [13100],6051 [8800]	2.3, 2.23, 2.05

Table 5.3.2. CL information extracted from the CL spectra of the ZnO ceramic samples doped with Bi_2O_3,, Sb_2O_3, MnO_2, Co_3O_4, Cr_2O_3 and then sintered at 1250° - 1300°C.

	ZnO sample	SEM beam parameters	RG (μm)	CL Peak position (Å) in their order of intensities [cps]	Position in the band scheme (eV)
1	ZnO + Bi_2O_3,, Sb_2O_3, MnO_2, Co_3O_4, Cr_2O_3, sintered at 1250°C. surface as polished.	35kV, 78nA 8500x mag. Over a spot bright at 540 and 860nm. PMT Ge.	3.6	3450 [15400], 4300 [1814], 2700 [900] 2250 [500].	3.59, 2.88, 4.59, 5.5
2	As in 1 above (ZnO + All)	35kV, Ib, 78nA 2300 x mag. Over spot bright only at 540nm. PMT Ge.	3.6	3450 [16000] 2700 [1800] 4300 [900]	3.59, 4.59, 2.88
3	As in 1 above (ZnO + All)	35kV, Ib, 78nA ZnO + all, Over spot bright in all MCL images. PMT Ge.	3.6	3450 [19400], 2700 [2600],4300 [1100]	3.59, 4.59, 2.88
4	ZnO + all sintered at 1300°C.	15keV, 4.5nA, using PMT: S20, 6500 mag. PMT:S20.	0.8	4619. [227], 5216 [202], 3903 [170]	2.68, 2.38, 3.17
5	As in 4 above	15keV, 5.29nA, using PMT:S20, 5000 mag. PMT:S20.	0.8	4606 [270], 5197 [220], 3988 [210]	2.68, 2.38, 3.11
6	As in 4 above	30keV, 8.6nA, using PMT: S20, 6500 mag. PMT:S20.	2.7	6946 [600], 4648 [540],5216 [480]	1.78, 2.67, 2.38
7	As in 4 above	30keV, 3.2μA, using PMT: S20, 6500 mag. PMT:S20.	2.7	6934 [620], 4653 [560], 5243 [490]	1.78, 2.66, 2.36
8	As in 4 above	30keV, 9.7nA, using PMT: S20, 6000 mag. PMT:S20.	2.7	5237 [385], 4615 [375],	2.37, 2.68
9	As in 4 above	30keV, 3.2μA, using PMT: S20, 6500 mag. PMT:S20.	2.7	6925 [540],	1.79
10	As in 4 above	30keV, 3.2μA, using PMT: S20, 6500 mag. PMT:S20.	2.7	4650 [500], and possibly 4019 [200]	2.67, 3.08

Table 5.3.3. CL information extracted from the CL spectra of the ZnO ceramic samples doped with Bi_2O_3,, Sb_2O_3, MnO_2, Co_3O_4, Cr_2O_3 ,TiO_2 and then sintered at 1250°.

No	ZnO sample	SEM beam parameters	RG	CL Peak position (Å) in their order of intensities [cps]	Position in the band scheme (eV)
1	ZnO + all +TiO_2 sintered at 1250°C.	35keV, 1.45μA, using PMT: S20, 2000 mag. PMT:S20.	3.6	6920 [9000], 5400 [900],	1.79, 2.3
2	As in 1 above	35keV, 1.36μA, using PMT: S20, 2000 mag. PMT:S20.	3.6	6880 [8000],	1.8
3	As in 1 above	35eV, 1.39μA using PMT: S20, 2000 mag. PMT:S20.	3.6	5400 [900],	2.3

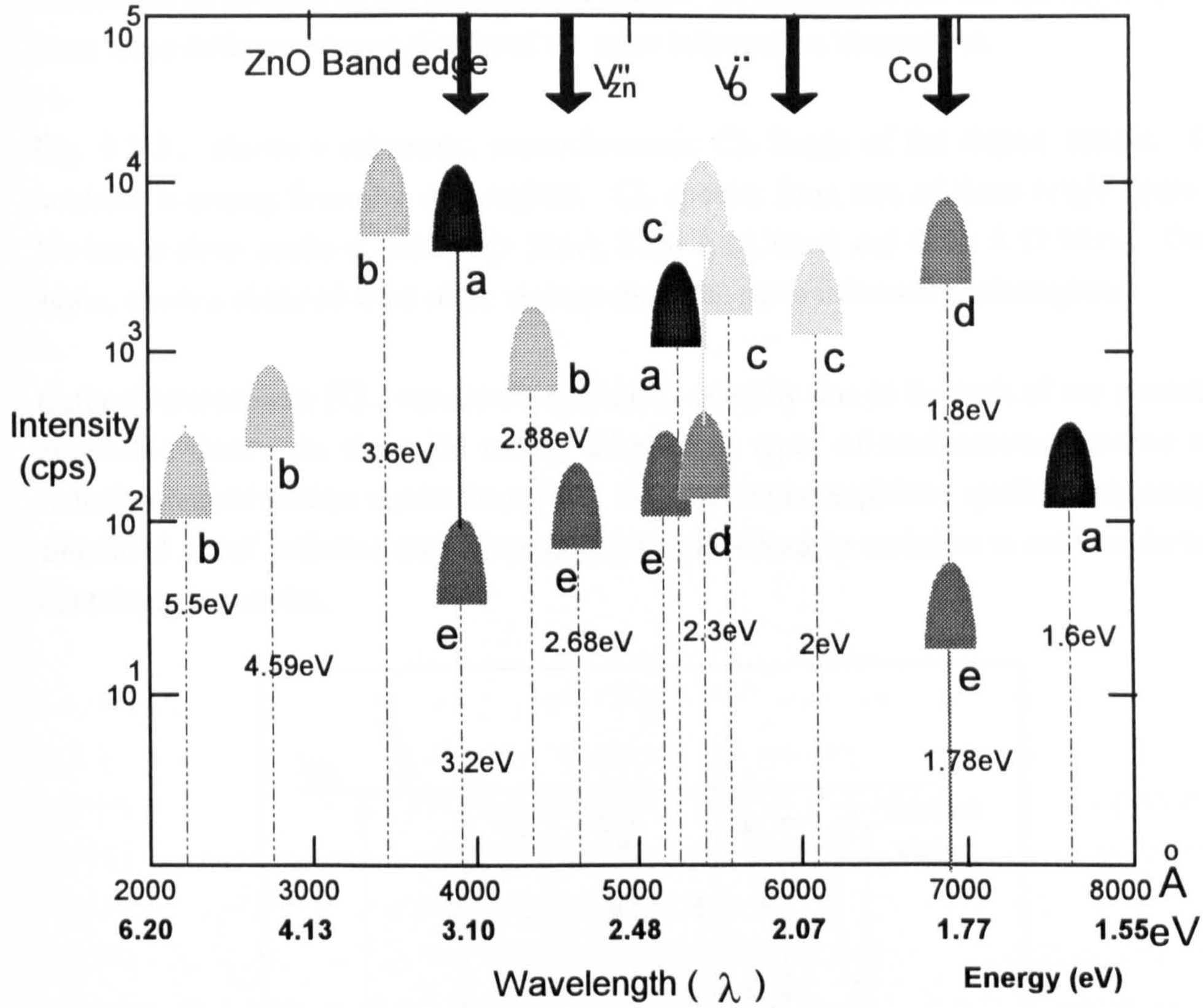


Fig. 5.3.3. The CL spectra of (a) pure ZnO, polished, used S20 detector; (b) ZnO + all five dopants, polished, used Ge detector; (c) Single crystal of ZnO, used S20 detector; (d) ZnO + all + TiO_2, polished, used S20 detector and (e), ZnO + all, Sintered surface, used S20. detector.

Fig. 5.3.3 show peak positions of all the CL spectra, acquired for different samples of doped and undoped ZnO. Spectra are labelled respectively as (a), (b), (c), (d) and (e) corresponding to pure ZnO, ZnO + all dopant additives, single crystal of ZnO, ZnO + all dopants + TiO_2 and ZnO + all dopants. These spectra show all the CL spectra spaced out with respect to their peak positions and intensities. The data of these CL spectra positioned (Å) with their relative intensities [cps] are also presented in tables 5.3.1, 5.3.2 and 5.3.3.

5.3.2. Discussion

Figs. 5.3.1 (a) and (b) show the panchromatic CL image of the undoped ZnO ceramic sample showing bright and dark contrast. This contrast is due to the depth change associated with the topographical features at the grains/grain boundaries. The CL signal at the grain boundary region is arising from the excitations at a relatively lower plane of

the sample in contrast to the grain surface region. In both cases the CL spectra acquired from these different regions displayed the same information throughout.

Fig. 5.3.2., shows a schematic, monochromatic CL image of the doped sample. CL contrast is arising from the void regions. CL spectra from one of these bright spots in the image show peaks at 3450 Å (3.59ev), 2700 Å (4.59ev) and 4300 Å (2.88ev). Once again, spectra obtained from other regions show the same information throughout.

Cathodoluminscence (CL) results are difficult to quantify due to the lack of any generally applicable theory for the wide variety of possible types of luminescence centers and radiative recombination mechanisms [70]. Results can be explained qualitatively using a simplified set of radiative transitions (Fig.5.3.4) that lead to emission in semiconductors containing impurities.

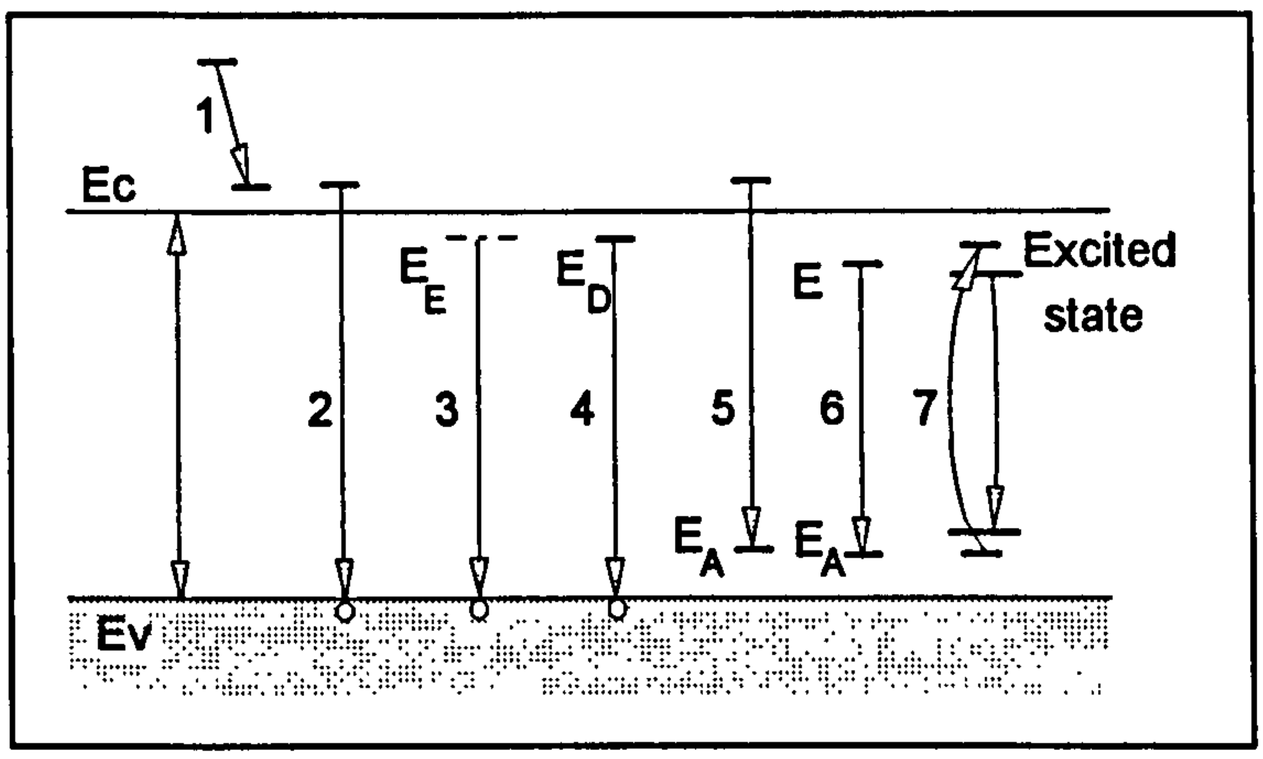


Fig. 5.3.4. Schematic diagram of radiative transitions between the conduction band (E_C) the valence band (E_V) and exciton (E_E), donor (E_D) and acceptor (E_A) levels in a semiconductor [70].

Process 1 is an intraband transition: an electron excited well above the conduction-band edge comes down and reaches thermal equilibrium with the lattice. This thermalisation process may lead to (i) phonon-assisted photon emission, or (ii) more likely, the emission of phonons only. Process 2 is an interband transition: 'intrinsic' CL; recombination of electrons from the conduction band and holes in the valence band. Process 3 is the exciton decay observable at low temperatures; both free excitons and excitons bound to an impurity may undergo such transitions. Processes 4, 5 and 6 arise from transitions which start and /or finish on localised states of impurities (e.g. donors and acceptors) in the gap; these produce 'extrinsic' CL. Transition 7 is the radiative de-excitation of a center such as a rare earth ion [70].

In this study, the CL results may be explained in terms of processes: 4, 5 and 6 (Fig.5.3.4). **Gupta** [5], **Swalin** [19], **Cordaro** [20] and **Sukkar** *et al* [28], have reported the electronic energy band diagram for ZnO ceramic, indicating possible energies associated with electronic defects (discussed in Chapter 2 section 2.2.2). Donor-like levels in the energy gap have been found experimentally [28] at ≈ 0.05, 0.2, 0.5 and 2eV below the conduction band edge of ZnO (3.3eV band gap). The first of these two levels (shallow levels: at ≈ 0.05 and 0.2 eV) have been assigned to first and second ionisation energies of a native donor ($Zn_i^{\bullet}$, $Zn_i^{\bullet\bullet}$). The donor level at ≈ 0.5eV and ≈ 2eV, below the conduction band are presumed to correspond to $V_o^{\bullet}$.and $V_o^{\bullet\bullet}$, respectively. The acceptor levels for V'_{Zn} and V''_{Zn} has been estimated to lie at ≈ 0.7- 1.1eV and ≈2.1 - 2.8 eV above the valence band edge respectively [28]. From this work it has been possible to identify and assign many of the dopant related defects to their respective position in the energy band scheme.

Looking at the CL results in this work, (Fig. 5.3.3) peak intensities at 3920Å (Tables 5.3.1 and 5.3.2) would probably correspond to the band edge ≈ 3.3eV. Peaks at 6946Å correspond to a transition arising at ≈ 1.78eV. **Mirreli** *et al* [111], (1988) studied ZnO ceramic doped exclusively with Co, and observed similar radiative transitions, centered at 7000Å (1.77eV from the conduction band) and 9500Å (1.3eV from valence band). They attribute these emissions to the transitions between the cobalt level to the conduction and valence band; thus implying that the role of the Co, is to promote a higher impact ionisation probability and increases the hole concentration at a fixed current value. Hence in the doped sample of ZnO varistor, a high recombination probability via the cobalt centres would also explain the difficulty in finding the band-to-band transition experimentally. However, in this work both doped and undoped samples of ZnO ceramic also showed some band to band transition (peaks 'a' and 'e', Fig.5.3.3). Peaks at around 2 eV were observed in the case of the single crystal sample of ZnO. This would be arising due to the oxygen vacancies ($V_o^{\bullet\bullet}$) present as donor defects in the undoped material. In the doped material these native donor defects are presumed to have been suppressed, resulting in formation of acceptor defects (V''_{Zn}).giving rise to CL transitions around 2.8 eV (peaks labelled 'e' and 'b'). Peaks arising at, 1.6 eV, 5.59eV, 4.59eV and 5.5 eV as also shown in Fig. 5.3.3, have not been reported in any previous literature. Further investigation would be needed to verify their positions, before they are to be assigned to any radiative processes.

Much difficulty was experienced in achieving a good count rate. Reduction in the count rate from one region of the sample to another has been observed by **Chernuszka** *et al* [112] (1981) who experienced the count rate at 3840Å (band edge) reduced from 100 to 40 (cps) and at 5620Å from 400 to 50 cps. This has been assigned to non radiative recombination centres produced by mechanical defects introduced during preparation.

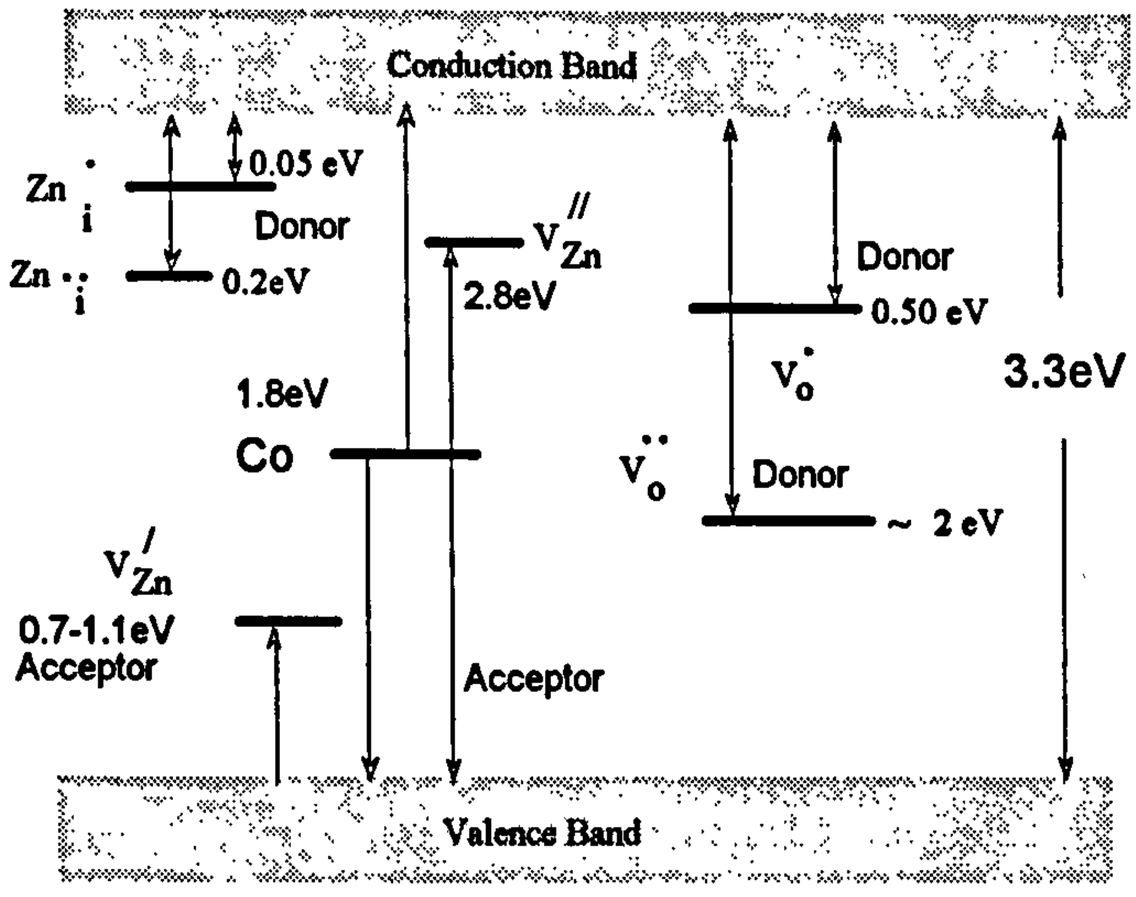


Fig. 5.3.5. Flat band diagram for ZnO indicating possible energies associated with electronic defects. Processes associated with Co (1.8eV), $V_O^{\bullet\bullet}$(2.0eV), V"zn (2.8eV) and the band edge transistions(3.3eV) were seen in this work.

5.3.3. Summary of the CL work

In this study, application of the CL technique to ZnO varistor ceramic has been somewhat speculative and quantification has been difficult. The benefit of CL lies in its sensitivity which is several orders of magnitude better than that attainable by X-ray microanalysis, in detecting impurity concentrations as low as 10^{14} cm^{-3}.

The CL results in this work showed that:

(1) A strong band edge transition around ≈ 3.3eV, was observed from undoped ZnO ceramic and from one of the doped ZnO ceramic samples.

(2) A transition at 1.8eV was observed in the doped ZnO ceramic; it could be due to Co dopant in ZnO.

(3) Transitions at ≈ 2eV were only to be observed in the undoped single crystal of ZnO and are assigned to the oxygen vacancies ($V_O^{\bullet\bullet}$) present as native donor defects. While transitions around ≈ 2.6 - 2.8eV are probably due to the acceptor defects (V"zn), and are specific to the doped ZnO ceramic.

(4) Additional CL peaks at 1.6 eV, 5.59eV, 4.59eV and 5.5 eV remain to be explored

5.4. SIMS analysis of ZnO ceramic

Analytical options such as normal depth profiling with checkerboard gating, ion imaging, and line scan were used on the SIMS instrument (Atomika 6500 ion microprobe). Experiments using these options were intended to :-

(A) Investigate the compositional variation of dopants (Bi, Sb, Co, Mn and Cr) in ZnO ceramic, using ion imaging and depth profiling.

(B) To investigate the spatial distribution of oxygen to evaluate the oxygen self diffusion coefficient (D*) and the surface exchange coefficient (k) using (*a*) Isotopic exchange / diffusion profile (IEDP) of oxygen (using ^{18}O as a tracer) in pure and doped samples of ZnO ceramic and (*b*), line scan profiling with SIMS, to study the penetration of oxygen in cross-sectioned $^{18}O/^{16}O$ exchanged samples of pure and doped ZnO ceramics.

5.4.1. Depth profiling and Ion imaging results

The samples used were ZnO ceramic doped with the oxides of Sb, Mn, Bi, Cr and Co (0.5 mol.% each). Two samples of this composition were prepared, with the only difference being their sintering condition. One sample was sintered at 1300°C and the other one at 900°C. An oxygen primary ion beam (O_2^+) of 10keV and 5nA was used. To overcome the charging problems, an electron beam of 3keV, (4 - 5 μA) was used. The ion beam energy of 10keV was selected in this analysis. The ion beam current was varied from 24nA, 5nA, 1nA to finally 0.1nA. This procedure was taken to initially, achieve an intense signal to detect the beam position and then to detect the dopants in the ZnO sample (please see basic relationship discussed in Chapter 3.3, section 3.3.1). Once the detection of all the possible dopants was established the beam current was reduced to 1nA and finally to 0.1nA in order to optimise the focusing. The beam was then left to stabilise for about 30 minutes. All the relevant experimental conditions such as the primary beam energy, current, focus and scan width., are included in Chapter 4, section 4.2.4, Table 4.2.2. The experiment was undertaken in the following stages:

(a) Initially the ZnO varistor sample (sintered at 1300°C) was analysed using the ion imaging mode, confined to a scan area of 50μm x 50μm. The images showing the distribution of the dopant elements, : Co, Cr and Mn were observed and recorded on micrographs. Figs. 5.4.1 (a) (b) and (c) show the raw SIMS data, the ion images and the corresponding checkerboard patterns.

(b) The analysis was repeated for the reference sample (900°C sintered sample with all the dopants). Fig. 5.4.2 show the raw SIMS data for the reference sample.

The ion images of the elements in the reference sample showed a homogeneous distribution of additives. Since the grain size of the ceramic reference sample is much smaller (0.7μm) when compared to the SIMS ion beam of several μm.

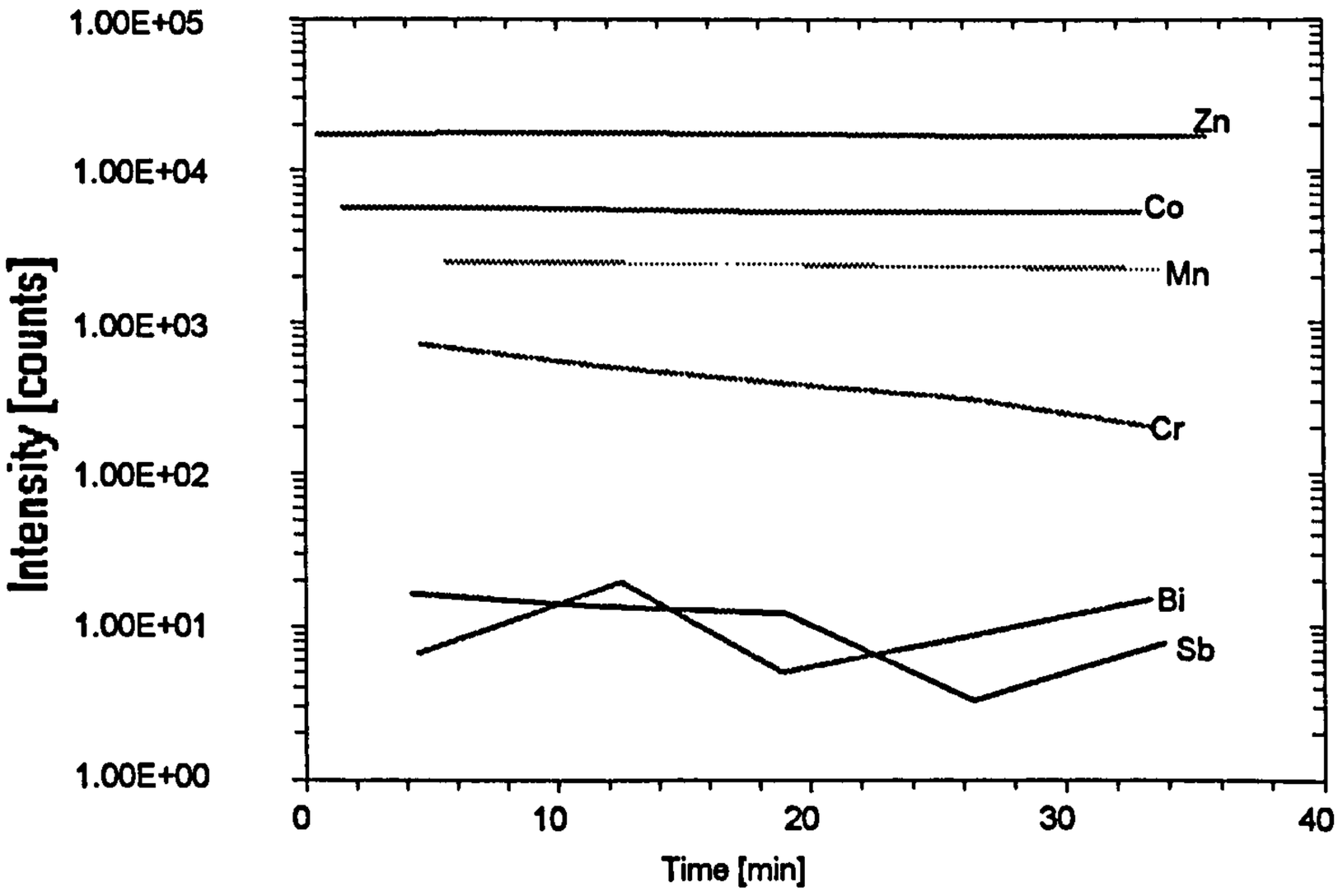


Fig. 5.4.1 (a) Raw SIMS data, showing the ion intensity vs time for ZnO varistor ceramic sample doped with the oxides of Co, Mn, Cr, Bi and Sb, all at 0.5 mol.% and then sintered at 1250^{o}C. The analysis was confined to a general area of 50μm x 50μm.

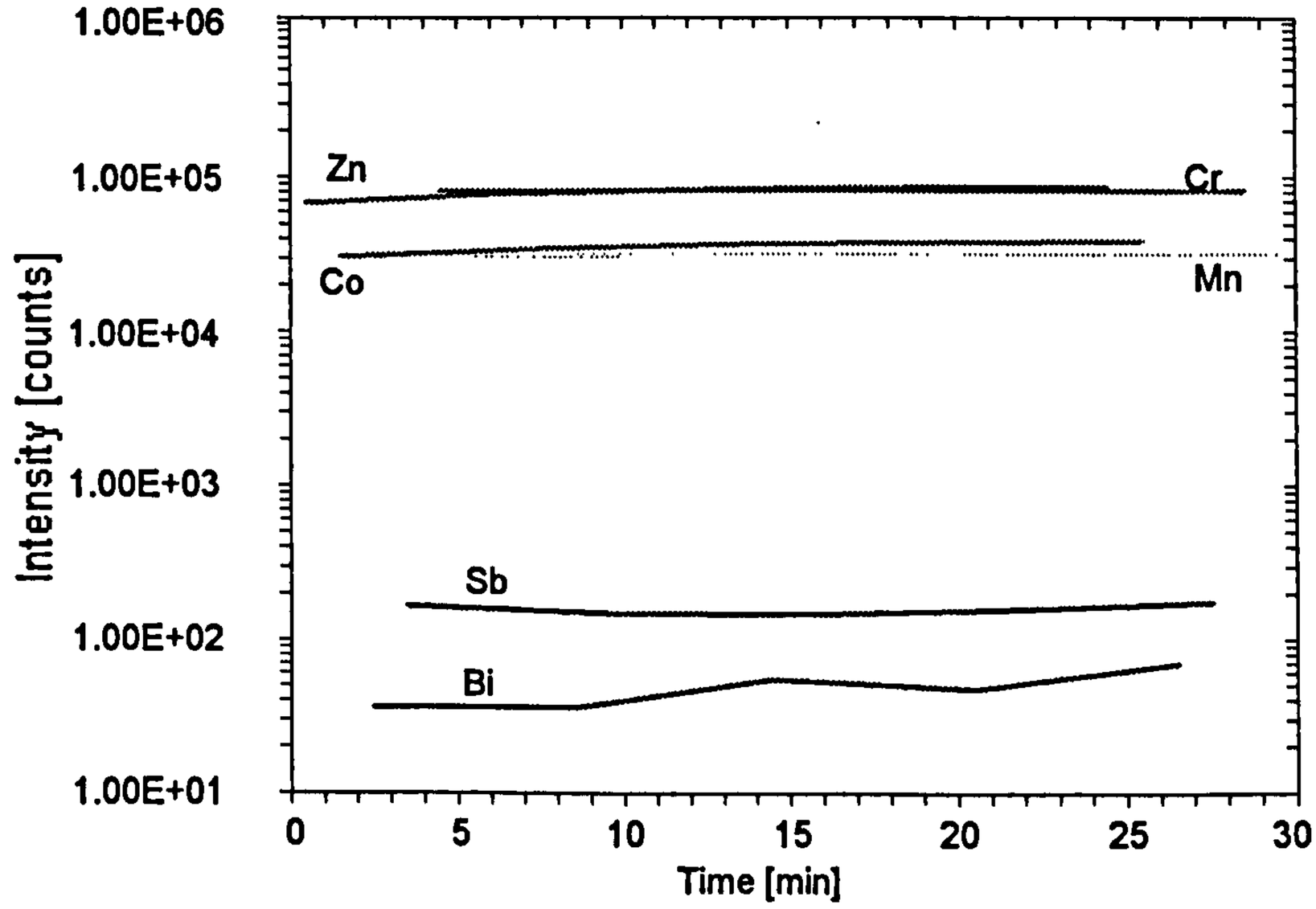


Fig. 5.4.2. Raw SIMS data, showing the ion intensity vs time for ZnO reference ceramic sample, doped with the oxides of Co, Mn, Cr, Bi and Sb, all at 0.5 mol.% and then sintered at 900^{o}C. The analysis was confined to an area of 48μm x 48μm).

(c) Analysis **(a)** was repeated on a single grain on the same sample. Here, secondary electron images were useful in identifying the grain region. Fig. 5.4.3 (a) shows the raw SIMS data of the single grain analysis, with the ion image shown in Fig. 5.4.3 (b).

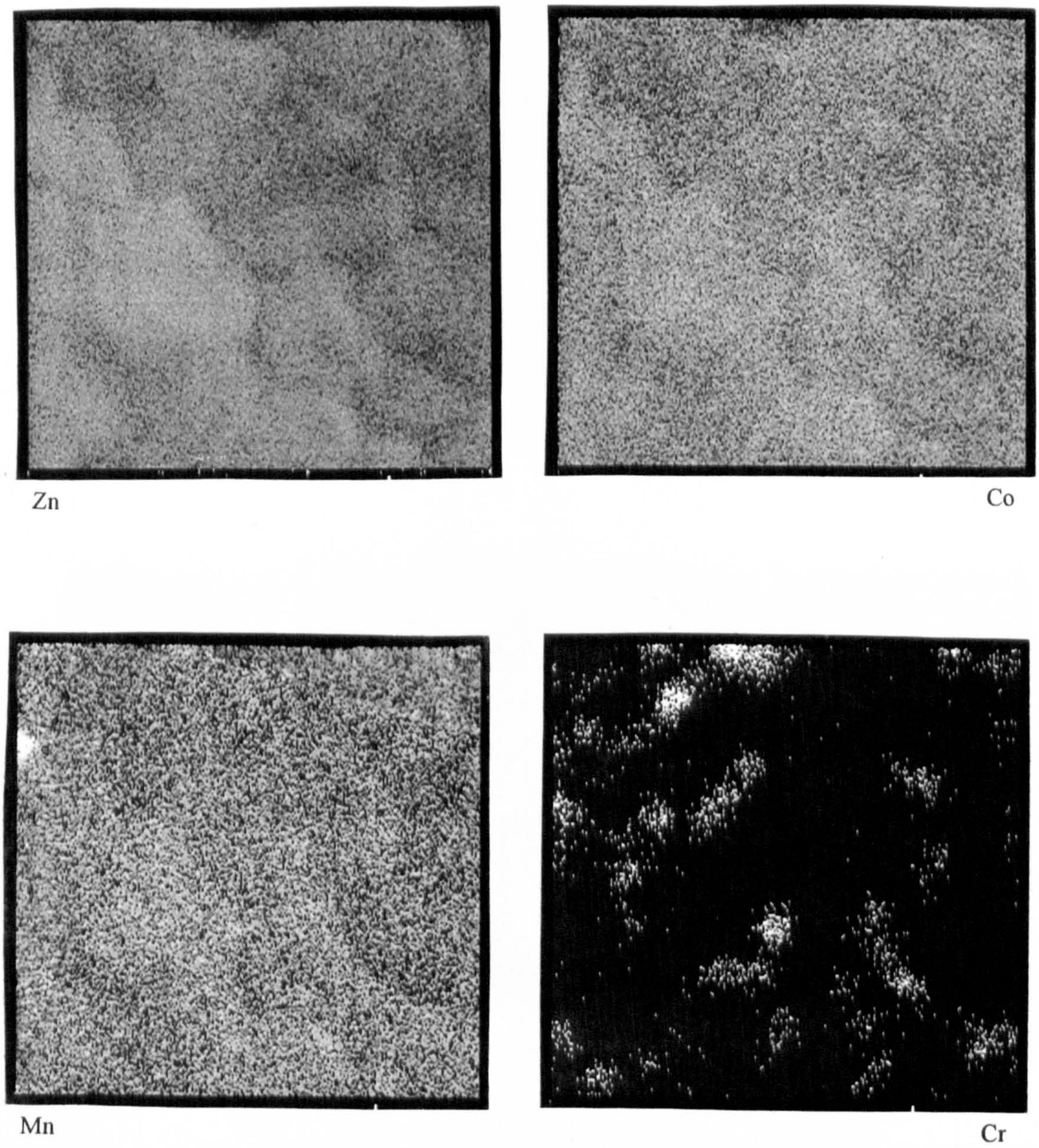


Fig.5.4.1 (b) Ion images of the segregated elements corresponding to the analysis as shown in Fig. 5.4.1 (a). A primary beam energy of 10keV was used and for improved lateral resolution, the beam current was reduced to 0.1nA. Images are: 100μm x 100μm, at the top from left, are of Zn, Co and at the bottom from left are of Mn and Cr. Due to very low signal intensities of Bi and Sb, their ion imaging of these species was not possible.

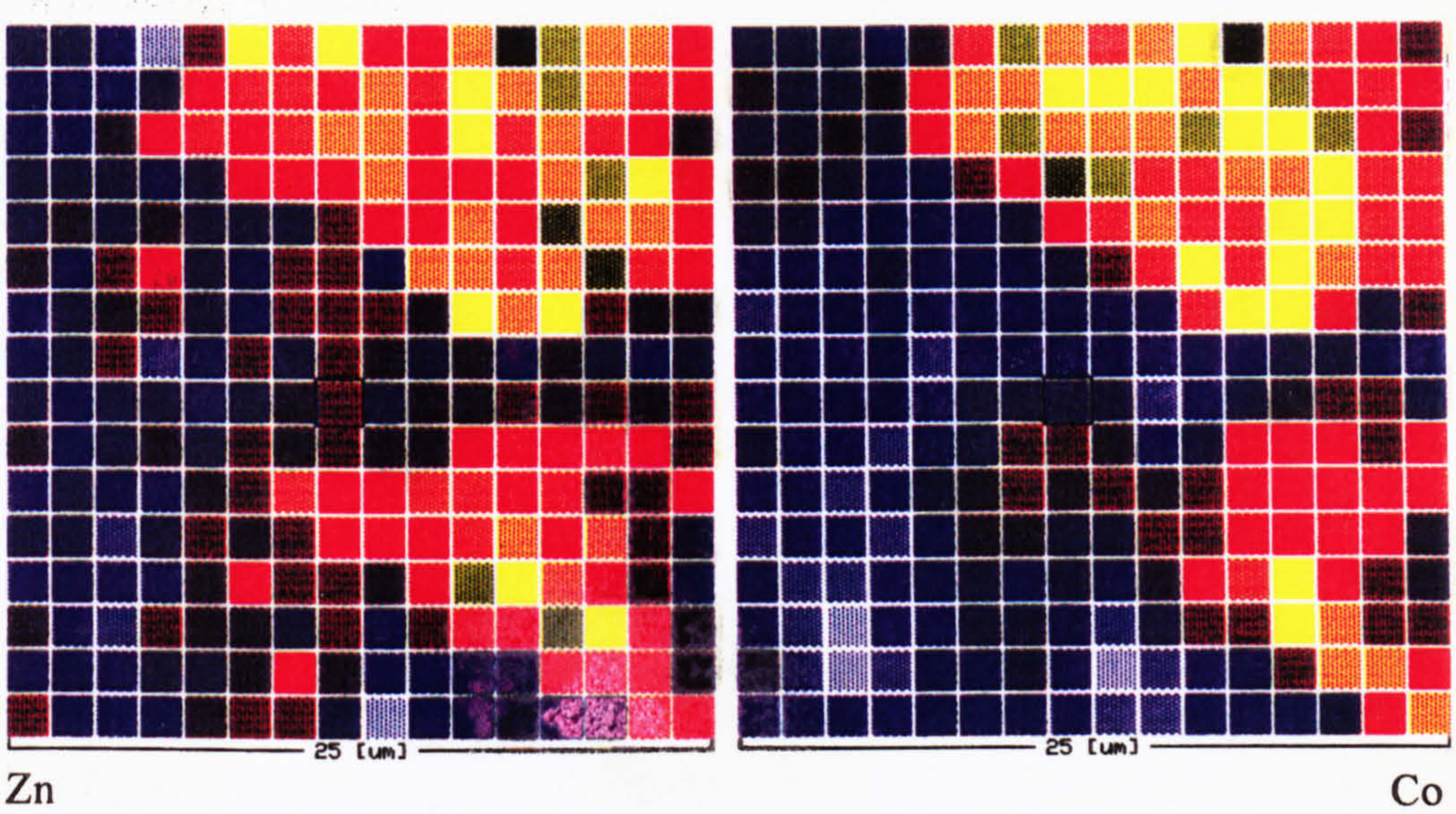


Fig. 5.4.1 (c) Checkerboard patterns taken over :25μm x 25μm gated region, corresponding to the analysis in Fig. 5.4.1 (a). Relative brightness in the colour of these images corresponds to relatively higher concentration of the particular element it represents. In the intensity scale red is high and blue is low.

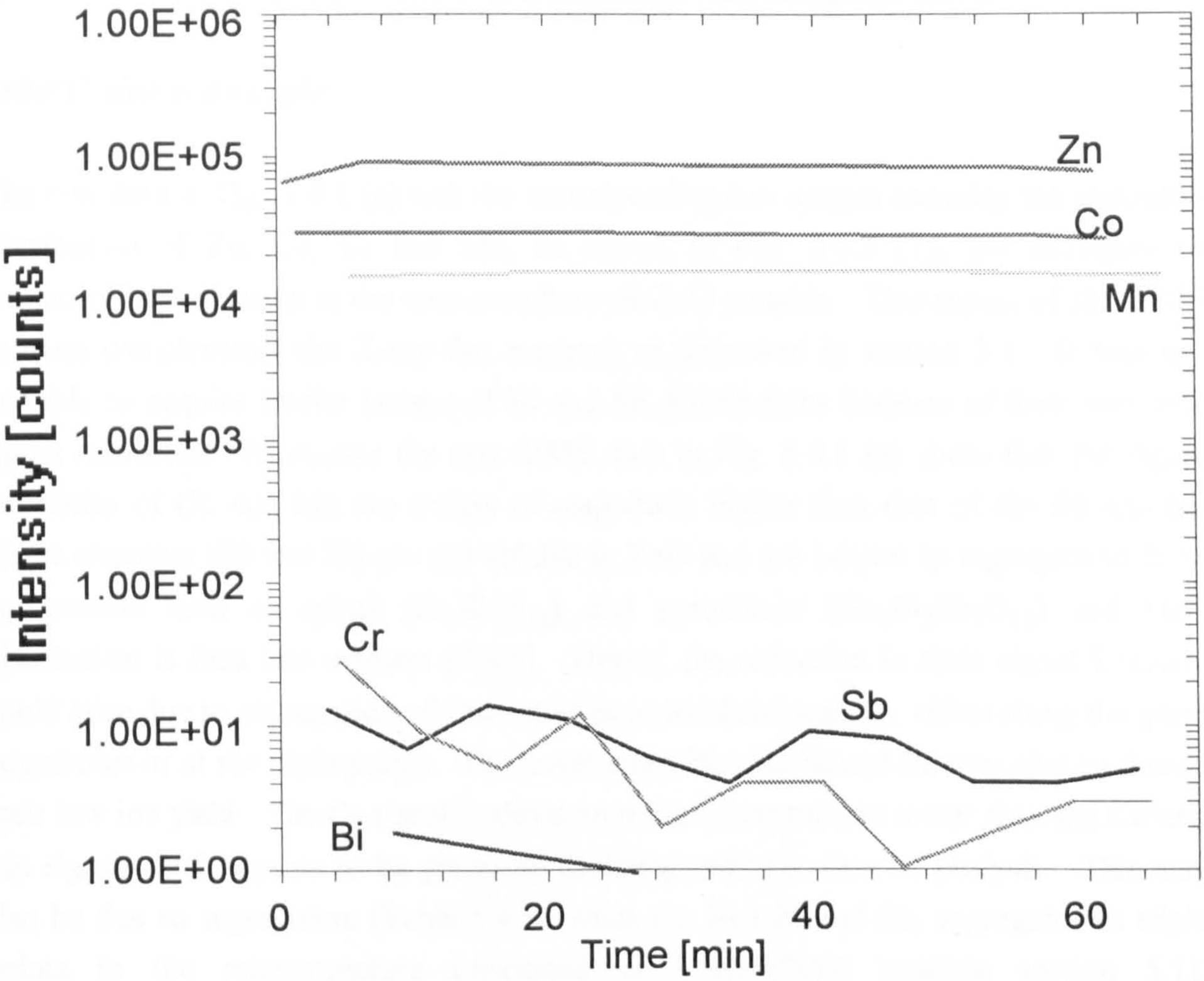


Fig. 5.4.3 (a) Raw SIMS data, showing the ion intensity vs time for ZnO varistor ceramic sample doped with the oxides of Co, Mn, Cr, Bi and Sb, all at 0.5 mol.% and then sintered at 1300^{O}C. The analysis was **confined to a single grain** region (16μm x 16μm).

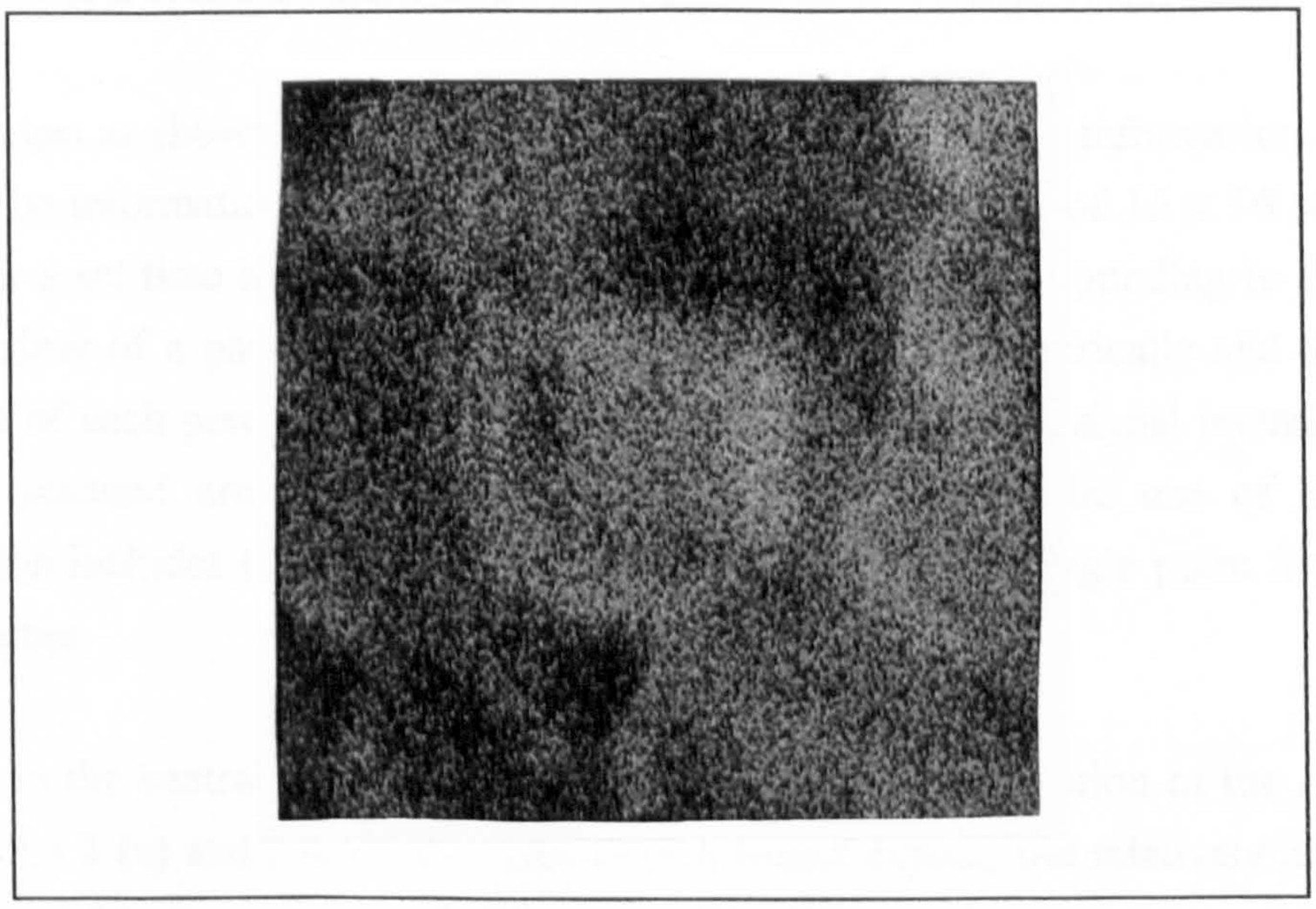


Fig. 5.4.3 (b). Secondary electron image of a grain region corresponding to the SIMS profile in Fig. 5.4.1(a). Analysis was acquired using a very fine ion beam (10keV, 0.1nA).

5.4.1.2. Discussion on the Depth profiling - Ion imaging results

1300°C sintered sample

The raw data in Fig. 5.4.1 (a) and the corresponding ion images showing the elemental distribution of Zn, Co, Cr and Mn, as shown in Fig. 5.4.1 (b), are examples of compositional variation in the microstructure of ZnO ceramic. This aspect of the SIMS analysis complements the X-ray dot mapping as discussed in section 5.1. It was not possible to acquire similar images of Bi and Sb distributions because of their very low signal intensities. Moreover the raw SIMS data in Fig. 5.4.1 (a) show that the signal intensities of Co and Mn are orders of magnitude higher than that of the Sb and Bi. These elements (Sb and Bi) are not soluble in ZnO and are known to segregate to form compounds such as spinel ($Zn_7Sb_2O_{12}$) and pyrochlore ($Zn_2Bi_3Sb_3O_{14}$) and their distribution is thus less uniform [7,8,9]. Hence, the reduction in their signal intensity could arise due to segregation of these species to localised regions, either along the grain boundaries or at the triple points. The lower intensities for Bi and Sb may also be due to their low ion yield. The Cr signal is about an order of magnitude lower than the Co and Mn signals, and appears to be gradually declining with the time of analysis. This may also be due to segregation (Table 5.4.1), since Cr, like Bi and Sb, segregates to triple points in the microstructure (discussed in SEM-EDAX analysis section 5.1). Segregation of Cr is also evident in the SIMS ion images Fig.5.4.1 (b) and checkerboard pattern. Here, although the images of Zn, Co, and Mn do not appear to be completely uniform (see for example the checkerboard patterns) the intensity does not vary as dramatically as the Cr. Also the images of Zn, Co and Mn correlate with each other. Uniform distribution of Mn and Co have also been reported by **Rossinelli** *et al.*, [81].

Checker board images as shown in Fig. 5.4.1 (c) presents complementary information to the ion images. The information is presented in a form of square arrays of 16 x 16 sub gates, collected for a set time interval (5 seconds) over each frame corresponding to the selected mass window of a particular element. The data is stored numerically and the relative brightness of each pixel on the sub gate represents the localised signal intensity arising from the scanned area of 25μm x 25μm. Advantages in the use of the checkerboard option includes the comparison of signal intensities at a single point from one sample to another.

Analysis confined to the central region of the grain confirmed the distribution of the Zn, Co, and Mn (Fig. 5.4.3 (a) and 5.4.3 (b)). Here as one would expect, the relatively high intensities of Co and Mn have remained dominant. Since the analysis at this point is confined to the single grain region, the signal intensity for the segregated species such as the Cr, Bi, and Sb, are much lower.

900°C sintered sample

Where there has been no significant segregation, as in the case of the standard sample (sintered at 900°C) as shown in Fig. 5.4.2 the signal intensity of Co, Mn and Cr are comparable, within a same order of magnitude. The ion images taken from this sample did not show any marked segregation, hence a homogeneous distribution of the additives was assumed in this case. The low signal of Bi and Sb in this sample suggests poor detection of these elements under these experimental conditions, perhaps due to low ion yield during analysis. Consequently, the ion imaging of Bi and Sb was not possible due to their low signal intensity. Due to different relative sensitivity factors RSF of each elements, direct comparison of signal intensities to their concentration is not possible. An example of this is clearly seen in Fig. 5.4.2., where ZnO at 95Mol.% has a signal intensity comparable to Cr, Co, and Mn each at 0.5Mol%. Hence, in these experimental conditions, the RSF for Cr, Co and Mn is much higher than Bi, Sb and Zn. Due to the presence of intergranular phases in ZnO varistor, for quantification purposes, the analysis was confined to a single grain on the same sample as shown in Fig. 5.4.2 and then repeated for the ref. sample as shown in Fig. 5.4.3 (a). The Checkerboard option on the SIMS was used for comparison of the data from one region to another.

First aproximation

Due to the matrix effects, from grain to grain boundary region, quantification of the dopants was only possible in the grain region. Quantitative estimates of the dopant in the ZnO grains was made by comparing the intensity ratio (dopant/Zn) of the standard sample (Rs) to that of the actual sample (Ra). For example, in one of the analysis the average Zn intensity was 84312 counts, and that of the Co was 28296 counts (ratio 0.34). Since the ratio of Co/Zn intensity in the standard (Rs) is 0.44, the concentration of Co in the grain region can be (Ra/Rs) x 100% = 76 % of the conc. in the reference sample. This gives a good first approximation, of the concentration in the standard with respect to the varistor sample. Calculated values for other dopants are shown in Table 5.4.1. Statistically this shows the presence of Co and Mn in the grain, while Bi, Sb, and Cr are not probable. This confirms the segregation of Bi, Sb and Cr in ZnO ceramic.

Table 5.4.1. signal intensity ratios and the calculated % concentration in the standard ref. to the single grain of ZnO in the varistor sample.

Additive	ZnO (900°C) Av. signal	dopant/Zn (900°C) **Ra**	ZnO (1300°C) Av. signal within 1 grain.	dopant/Zn 1300°C **Rs**	(Ra/Rs)*100%
Zn	80820		84312		
Co	35880	0.44	28296	0.34	76
Mn	31620	0.39	14911	0.18	45
Bi	49	0.0006	0.27	3.2E-6	0.5
Sb	161	0.002	7	9.1E-5	4
Cr	81340	1	6.4	7.6E-5	0.008

5.4.2. 18O/16O exchange and SIMS line-scan profiling

The isotopic exchange/diffusion profile (IEDP) technique together with line scan profiling (LSP) can be used to determine unambiguously, the oxygen diffusivity in ceramic oxides and their surface exchange coefficient [101, 102, 103,]. Some of the major advantages of SIMS for self diffusion experiments are: (a) That the detection process is mass spectrometer based, and consequently can discriminate between individual isotopes. (b) The problems of quantification as discussed in Chapter 3, section 3.3.7, no longer hold for the following reasons.

Since the two oxygen isotopes ($^{18}O/\ ^{16}O$) are stable and chemically identical, the sputter yield (S) and the ionisation yield (γ), for the sputtering of $^{18}O^-$ and $^{16}O^-$ secondary ions from any given oxide matrix can be assumed to be the same [102]. Hence, from the basic equation (3.3.5), of the SIMS process: $I_s = I_p\ S\ \gamma\ f\ C$, (where I_p is the SIMS primary ion current, S is the sputter yield, γ is the ionisation yield, f is an instrumental transmission factor and C is the concentration of the species of interest), we have:

$$^{16}I_s = I_p\ S\ \gamma\ f\ ^{16}C, \text{ and } \ ^{18}I_s = I_p\ S\ \gamma\ f\ ^{18}C,$$

As a result, the isotopic ratio R, (for ^{18}O), the quantity needed to define the self diffusion profile of oxygen is given by:

$$R = {}^{18}C/({}^{18}C + {}^{16}C) \ = \ {}^{18}I_s\ /\ ({}^{18}I_s + {}^{16}I_s). \qquad (5.4.1)$$

Thus the ^{18}O isotopic ratio is calculated directly from the secondary ion intensities without instrumental or matrix calibration.

The $^{18}O/\ ^{16}O$ isotopic exchange together with SIMS to determine diffusion profiles in both doped and undoped ZnO ceramic samples was undertaken to provide data about the surface exchange coefficient (k) and the oxygen self diffusion coefficient (D^*).

Oxygen gas / solid exchange at the surface with subsequent diffusion produces an ^{18}O penetration depth profile in the solid oxide as illustrated schematically in Fig. 5.4.4 (a). Subsequent measurement of the ^{18}O and ^{16}O concentration depth profiles by SIMS yields the ^{18}O isotopic depth profile, C, with depth, X. A regression analysis fit of the diffusion equation (5.4.2) solution to the normalised ^{18}O isotopic depth profile yields the values of D* and k for the sample at the annealing conditions [101, 103]. During $^{18}O/^{16}O$ exchange, it is assumed that the rate of exchange is proportional to the

difference between the concentrations in the gas (Cg) and the concentration in the surface (Cs)at any time (t).

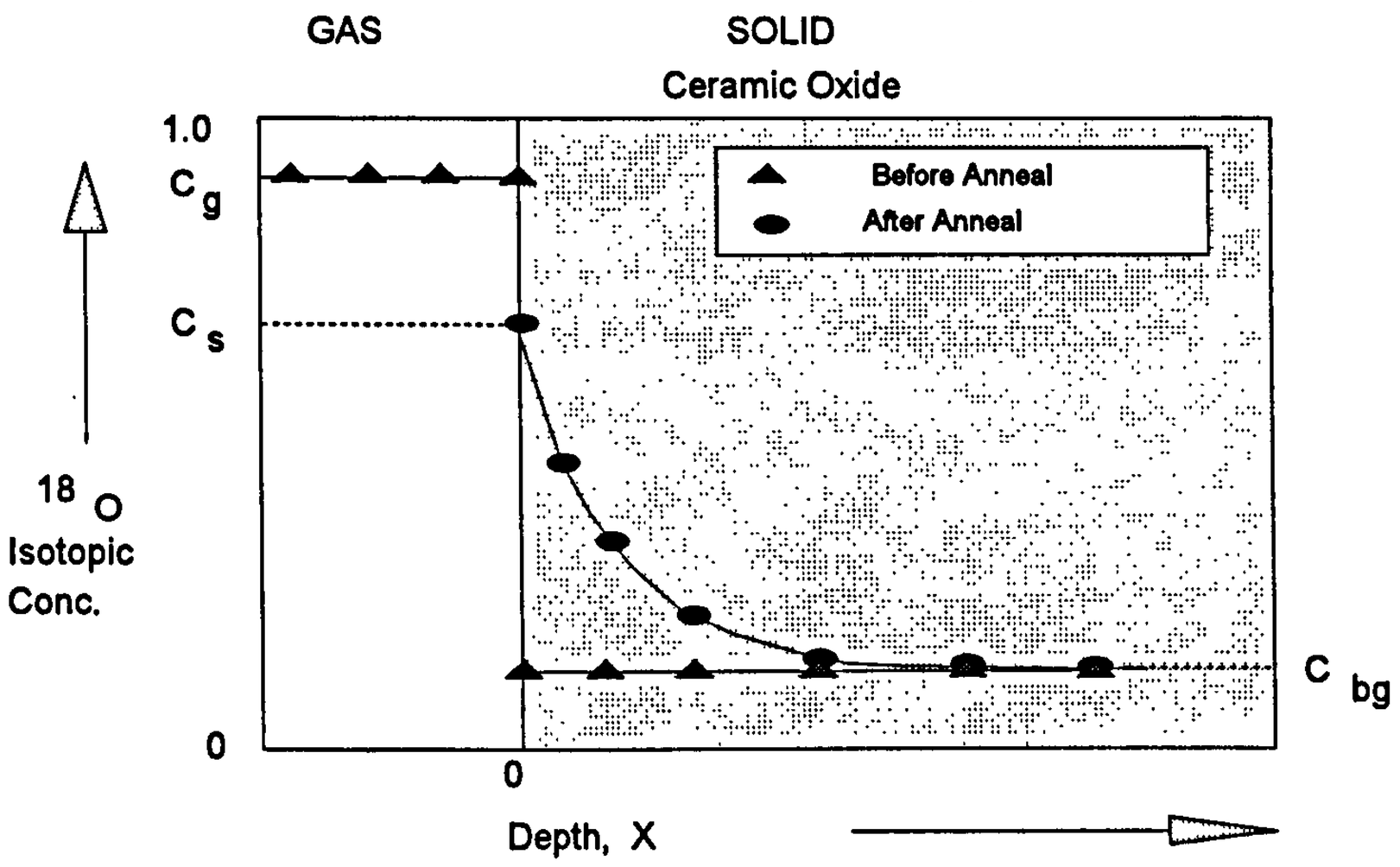


Fig.5.4.4 (a) Schematic diagram of the ^{18}O isotopic concentration depth profiles, C_x in a ceramic oxide solid, before and after anneal in an ^{18}O enriched atmosphere. The difference between Cg and Cs arises from the gas/solid exchange coefficient. C_g, C_s and C_{bg} are respectively, the ^{18}O isotopic concentrations in the anneal gas ambient, the solid surface and throughout the solid initially [101].

Kilner *et al* [103,102], has quoted that under the conditions used for the exchange anneal, the solution to the diffusion equation for large specimens in a well mixed large volume of gas is given by:

(5.4.2)

$$C'_x = \frac{C_x - C_{bg}}{C_g - C_{bg}} = \text{erfc}\left\{\frac{X}{2\sqrt{Dt}}\right\} - \exp\left(hX + h^2Dt\right)\ \text{erfc}\left\{\frac{X}{2\sqrt{Dt}} + h\sqrt{(Dt)}\right\}$$

Where

C'x, is the isotopic concentration at depth x, **Cbg**, is the natural isotopic background (0.002) concentration, **Cg** is the isotopic concentration of the gas (≈ 0.95, in this work), **t** is the diffusion time, **h** = k/D. **k** and **D** respectively are the surface exchange coefficient and the self diffusion coefficient.

Two types of solution emerge from this equation depending upon the value of $h\sqrt{(Dt)}$ [102]. For a given value of $h\sqrt{(Dt)}$, which is the approximate penetration depth (cm) of the profile, the type of solution is governed by the value of **h**. At large values of **h** the

kinetics of surface exchange are fast enough for diffusion to be the limiting process and the solution reduces to equation (5.4.3):

$$C'_x = \text{erfc}\left\{\frac{X}{2\sqrt{Dt}}\right\} \qquad (5.4.3)$$

When **h** is small the full version of equation (5.4.2) must be used and the resulting profile has the shape shown by the dashed line in Fig. 5.4.4 (b). The surface concentration of tracer is now much lower than that of the gas, because the process is limited by the rate of exchange at the surface.

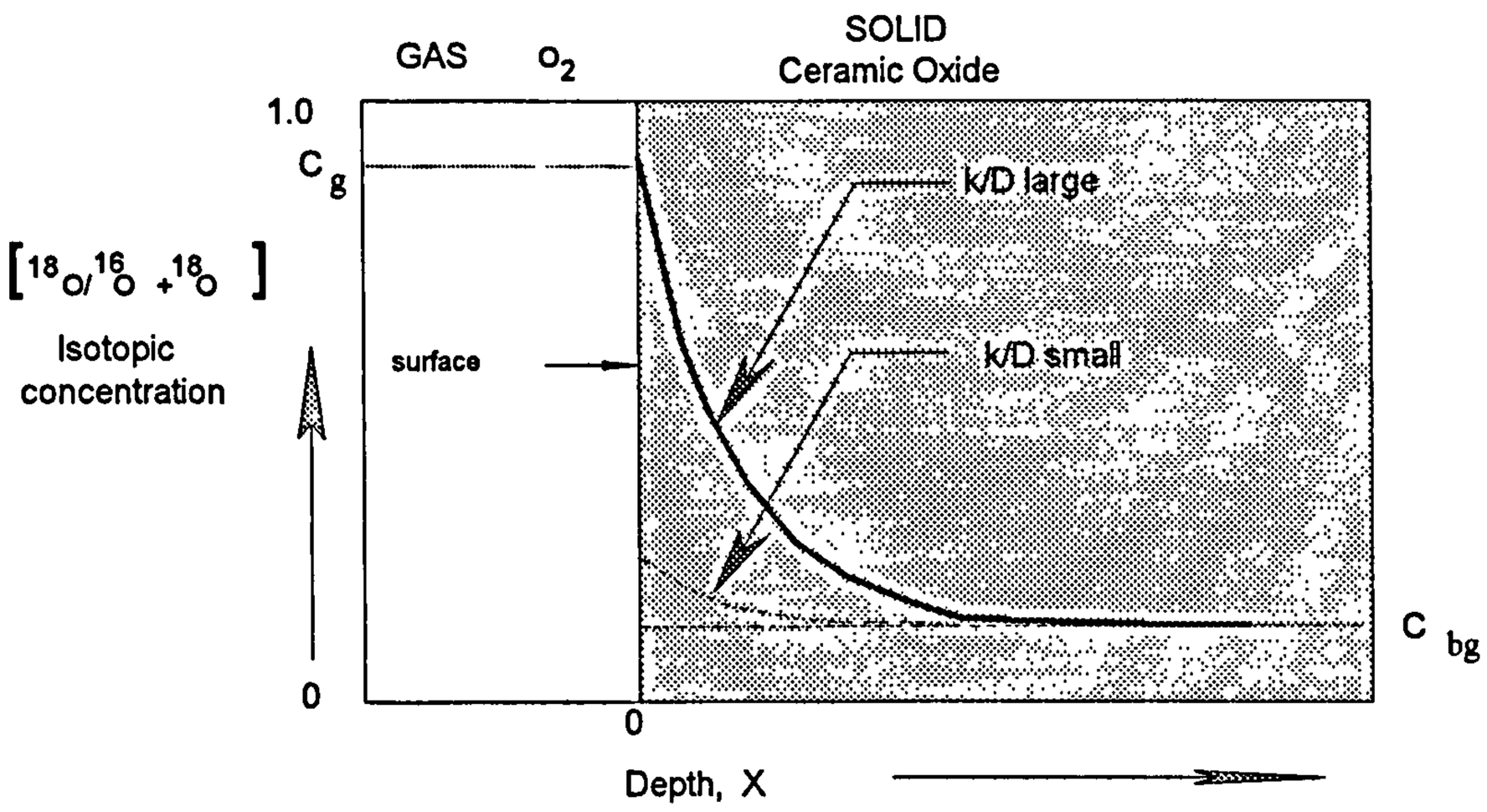


Fig.5.4.4 (b) The diagram shows the effect of fast and slow surface exchange on the isotopic profile in the solid. Note that the surface tracer conc. is equal to that of the gas [102].

Experimental results here include: (a) depth profiling of pure and doped ZnO ceramic samples (to evaluate $^{18}O/\ ^{16}O + {}^{18}O$ ratioing *vs* depth) and imaging of ^{18}O distribution in the microstructures; (b) line scan profiling of ^{18}O, across the cross-sectioned samples of pure and doped ZnO ceramics. $^{18}O/^{16}O$ exchange was undertaken at ≈ 1100°C to simulate near enough the sintering temperatures where oxygen would diffuse in to the ceramic. 10keV, Xe^+ primary beam was used throughout these isotopic exchange / diffusion profile (IEDP) experiments. During $^{18}O/\ ^{16}O$ exchange the ^{18}O gas concentration, Cg ,was 0.95. Other experimental parameters are included in Chapter 4, section 4.2.4.

5.4.2.1. $^{18}O/\ ^{16}O$ exchange SIMS depth profiling results

Fig. 5.4.5 (a) and (b), show the raw data of depth profiling of ^{18}O, ^{16}O and Zn in the pure and doped samples of ZnO ceramics respectively. The isotopic ratio Cx ($^{18}O/\ ^{16}O$

+ ^{18}O) data was normalised by, (Cx-Cbg)/(Cg-Cbg), for these pure and doped samples of ZnO ceramic and is shown in Figs. 5.4.6 (a) and (b) respectively. Fig.5.4.7 show the comparative ^{18}O depth profiles for these pure and doped samples of ZnO ceramic.

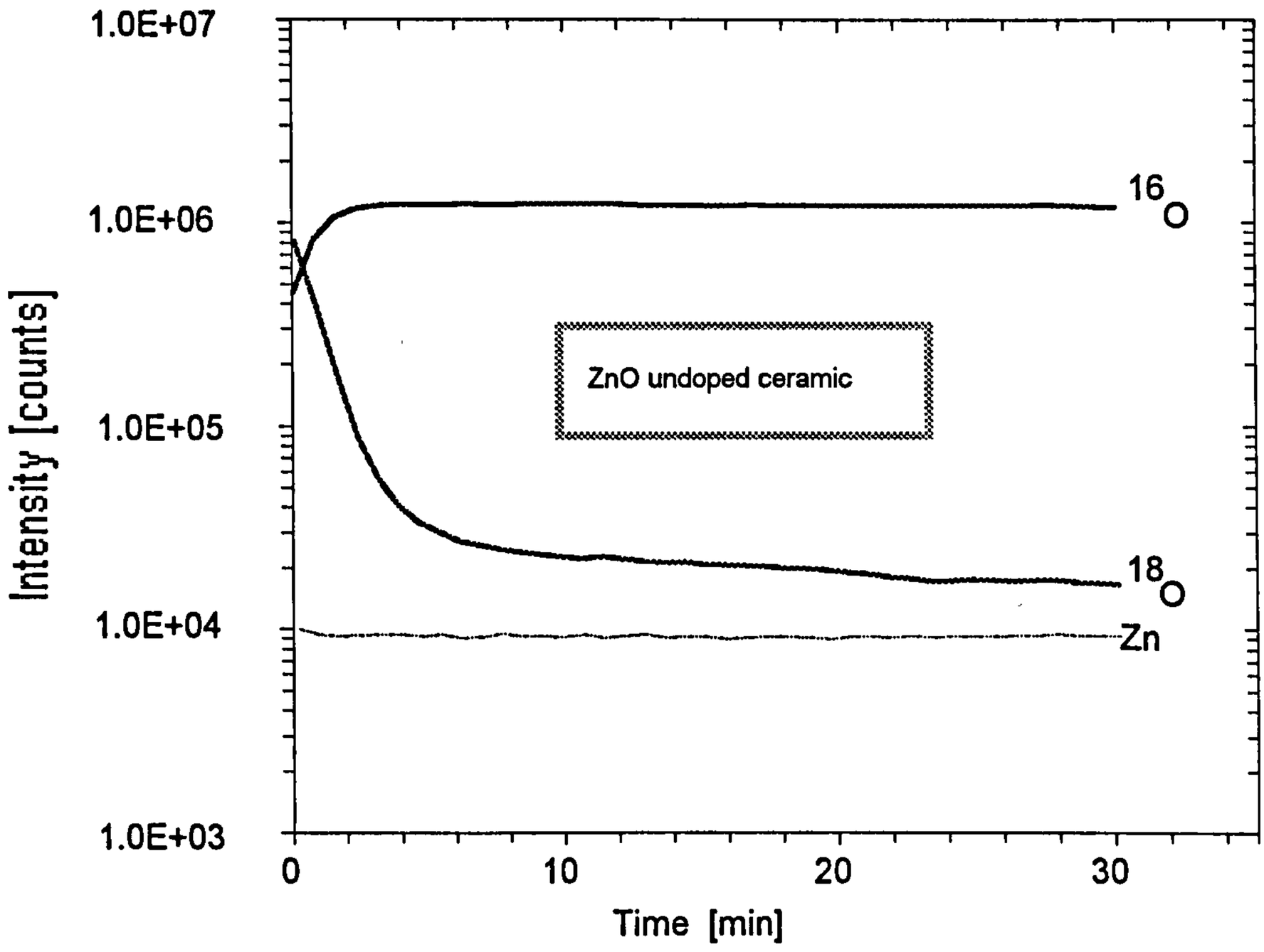


Fig. 5.4.5 (a) SIMS depth profiling of ^{18}O, ^{16}O and Zn in the pure undoped doped ZnO ceramic sample (Sint. 1250°C).

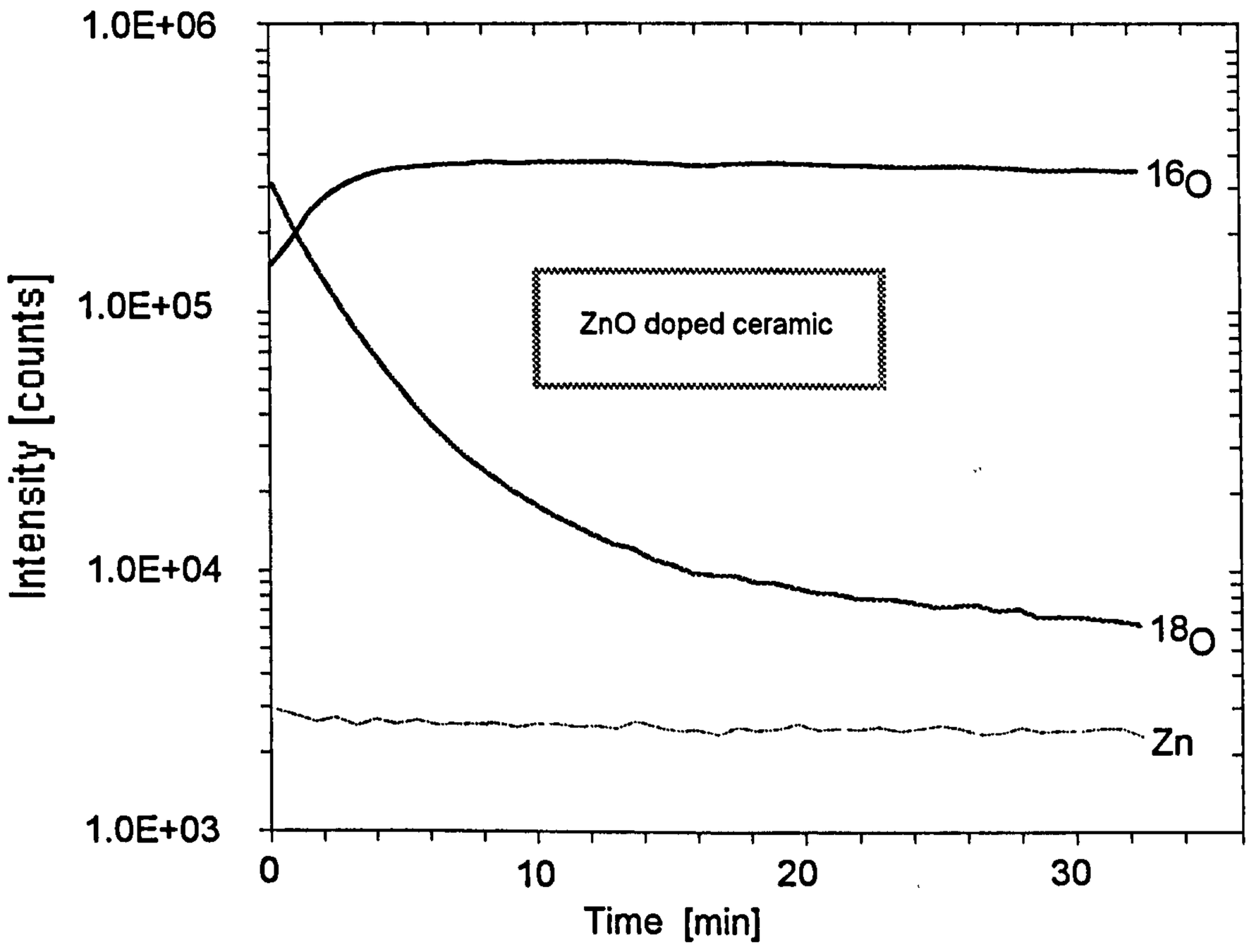


Fig. 5.4.5 (b) SIMS depth profiling of ^{18}O, ^{16}O and Zn in the doped ZnO ceramic sample (Sint. 1250°C).

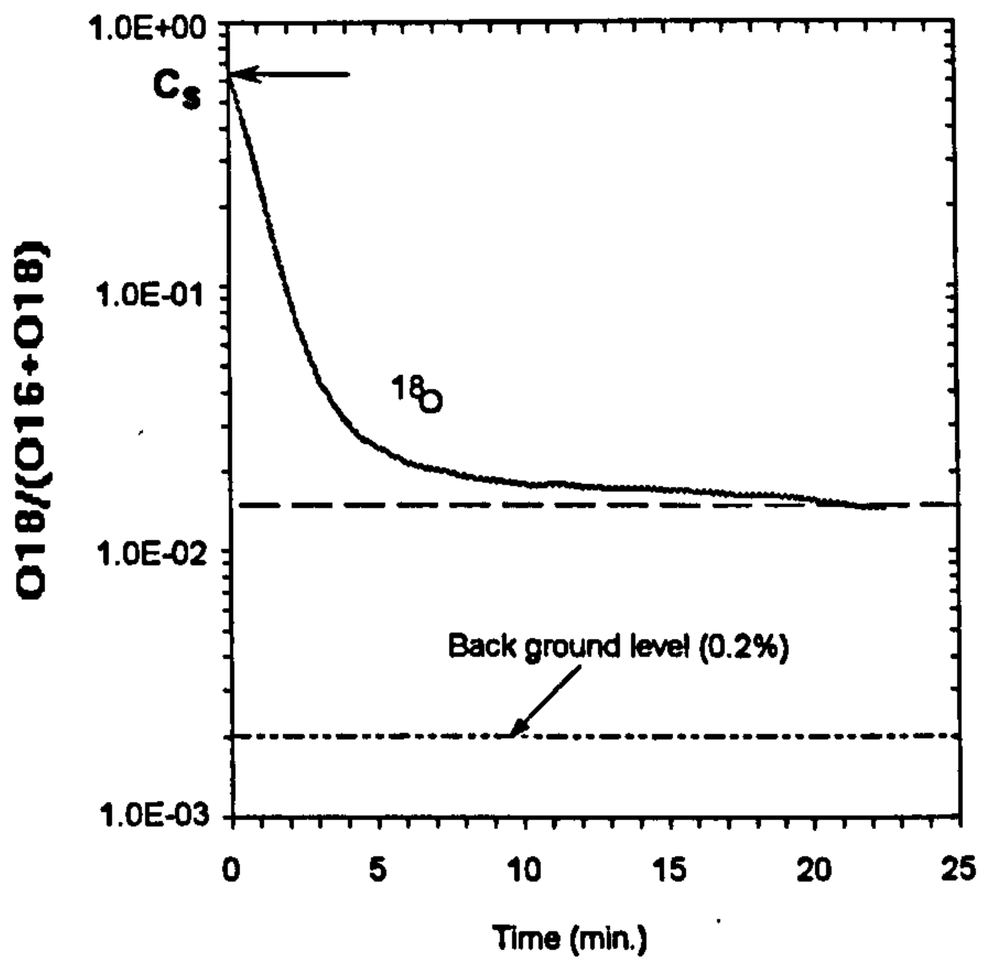


Fig. 5.4.6 (a), Raw SIMS data of isotopic ratioing for pure **undoped** ZnO ceramic sample (Sint. 1250°C).

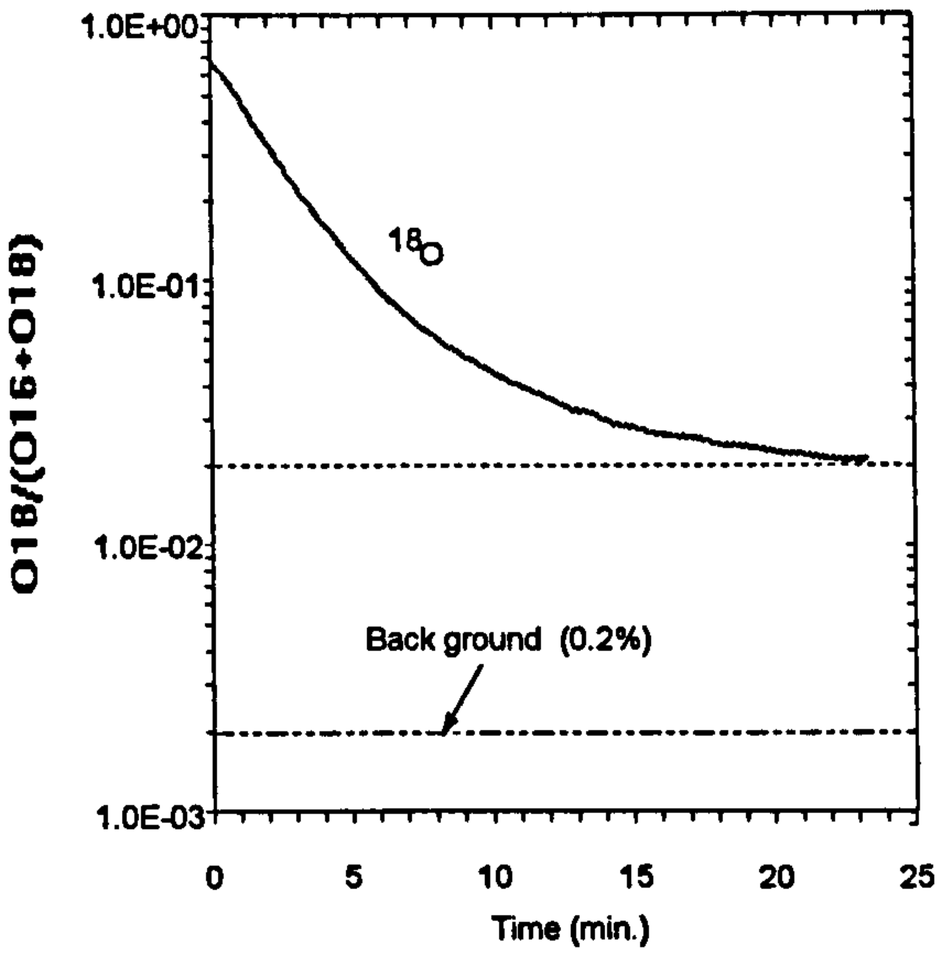


Fig. 5.4.6 (b) The raw SIMS data of isotopic ratioing for the **doped** ZnO ceramic sample (Sint. 1250°C).

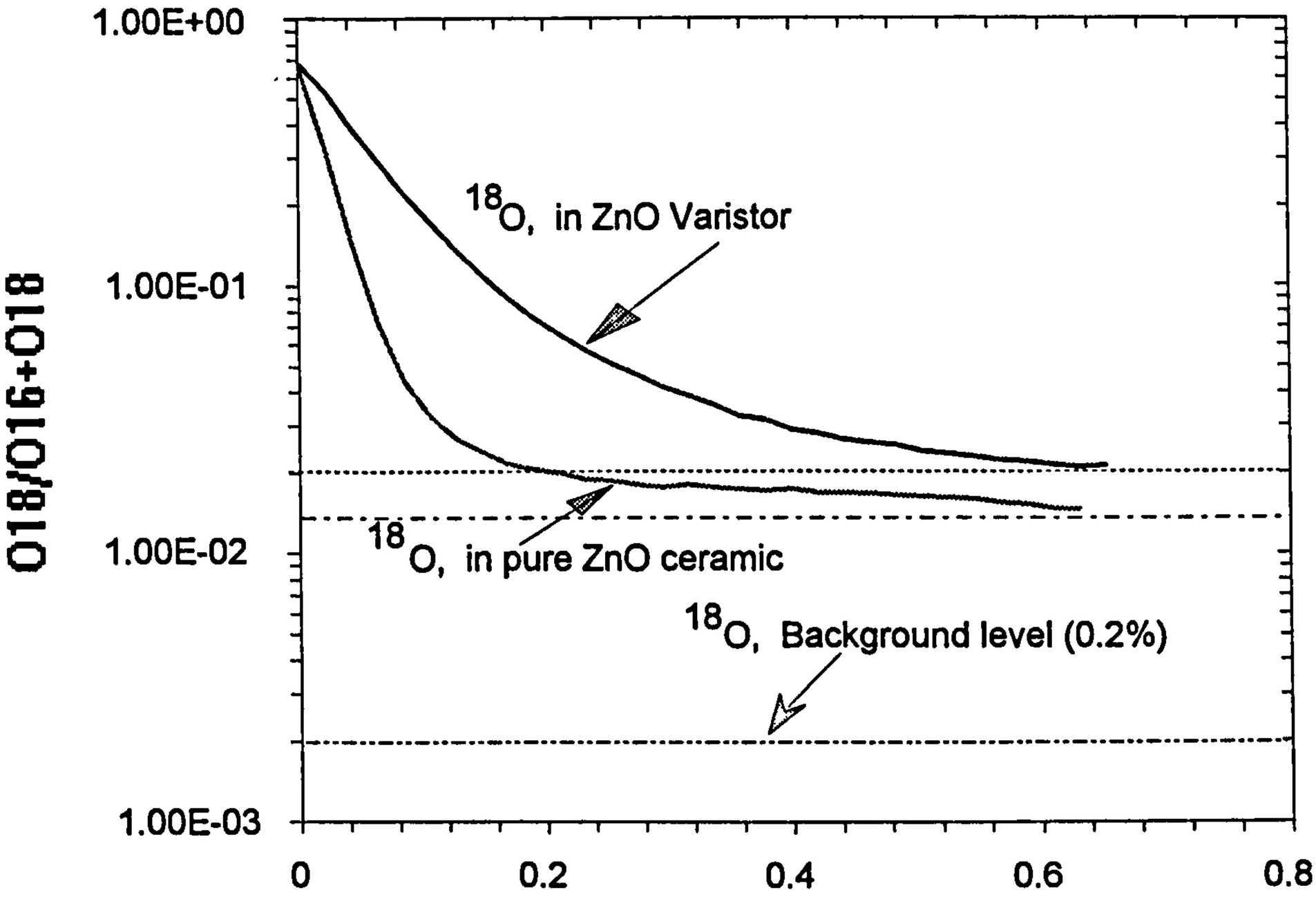


Fig. 5.4.7. The ^{18}O depth profile for pure and doped samples of Zno ceramic (Sint. 1250°C). Depth measurement was made using Taylor-Hobson, Talystep apparatus.

5.4.2.2. Discussion on $^{18}O/^{16}O$ exchange SIMS depth profiling

Samples of both pure and doped ZnO ceramic were $^{18}O/^{16}O$ exchanged for 16 hours at 1000°C. The SIMS depth profiling (raster area: 32μm x 32μm) data in Figs. 5.4.5 (a) and (b), for both undoped and the doped sample, show that the ^{18}O signal intensity at the surface is over two fold greater then the ^{16}O signal. This ^{18}O signal intensity drops down with the time of profiling until at some stage it becomes over two orders of magnitude less then the ^{16}O signal.

The isotopic ratioing $^{18}O/(^{18}O+^{16}O)$ of the data as shown in Figs. 5.4.6 (a) and (b) indicates high rate of diffusion for the doped ZnO ceramic sample as compared to the undoped ZnO ceramic. Moreover the rate of drop of ^{18}O concentration from the surface is slower for the doped ZnO ceramic, and its concentration remains higher then in the case of the undoped sample. This is clearly evident in Fig. 5.4.7. Finally at the depth of 0.8μm., ^{18}O concentration in both the undoped and the doped sample remains about an order of magnitude above the background, Cbg. of 0.002. This implies that the depth range of ^{18}O is beyond 0.8μm (discussed in section 5.4.2.3 below).

The diffusion equation solution (eqn 5.4.2) has been fitted to the experimental data. From this the bulk value for the diffusion coefficient (D*) and the surface exchange coefficient (k) for doped ZnO have been calculated to be 0.79×10^{-15} cm^2 sec^{-1} and 0.14×10^{-9} cm sec^{-1} respectively. For the undoped ZnO ceramic, respective D* and k values are: 0.13×10^{-15} cm^2 sec^{-1} and 0.58×10^{-10} cm sec^{-1}.

5.4.2.3. $^{18}O/^{16}O$ exchange SIMS line-scan profiling results

The preceding isotopic exchange / diffusion profile (IEDP) showed (Fig. 5.4.7) that within the range of the depth profiling up to 0.8μm, the $^{18}O/^{16}O$ isotopic ratio in ZnO ceramic, does not go right down to the back ground level (0.2% for ^{18}O). This would indicate fast diffusion paths prevailing throughout the grain boundaries of the ZnO ceramic. To determine the isotopic ratio deep down inside the ZnO ceramic, SIMS line scan profiling (LSP) across the cross-section of the $^{18}O/^{16}O$ exchanged samples was performed.

Figs.5.4.8 (a) and (b), show SIMS line-scan profiling for ^{18}O,^{16}O, and Zn, across the cross-section of the $^{18}O/^{16}O$ exchanged sample of undoped and doped ZnO ceramics sintered at 1250 °C. Both samples had one side of the pellet polished. Ion images of the ^{18}O distribution in the cross-sectioned samples of undoped and doped ZnO ceramic are shown in Figs.5.4.9. Fig. 5.4.10 (a) shows the corrected isotopic ratios [^{18}O / (^{18}O +

^{16}O)] across the cross-section of the doped and undoped ZnO ceramic. Close observation of this as shown in Fig. 5.4.10 (b), show that as the profiling reaches ≈ 50μm below the surface of the undoped ZnO ceramic, the ^{18}O concentration drops from **Cs** of ≈ 0.35 to **Cbg** of 0.002.

However in the case of the doped ZnO ceramic, **Cs**, drops from 0.45 to 0.01 and the diffusion tailing remains over an order of magnitude higher then the back ground value throughout the cross-section, This extended penetration of oxygen, presumably percolating along the grain boundaries is evidence of the fast diffusion path attributed to the lacy network of Bi_2O_3. This lacy network Bi_2O_3 in ZnO ceramic provides pathways for oxygen to diffuse into the ceramic and replenish oxygen at the grain boundary interface as depicted in Fig. 5.4.11. Properties of Bi_2O_3 have also been studied by **Harwig** *et al.*, [119] and are known to exhibit fast ionic conductivity.

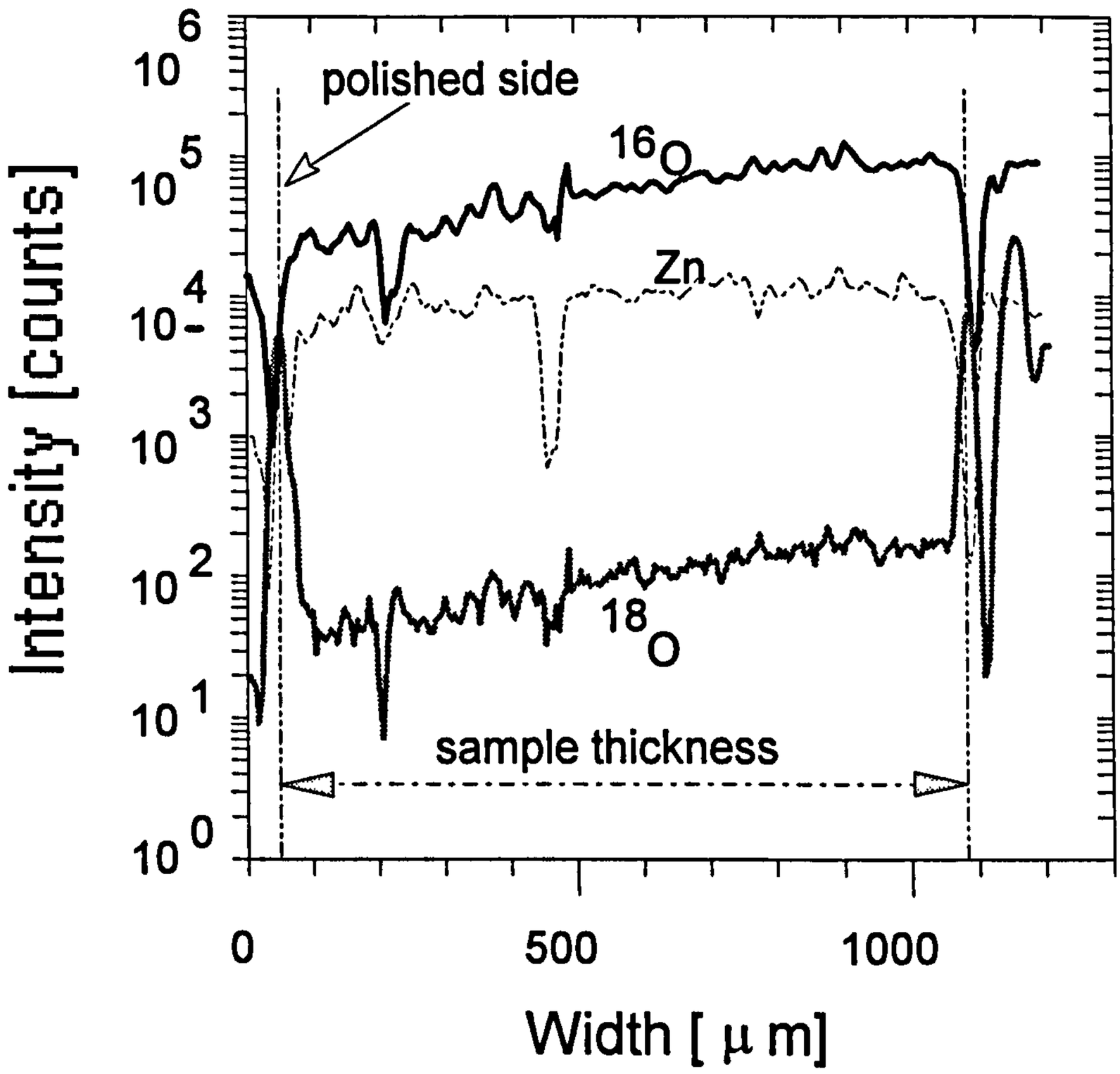


Fig.5.4.8 (a) SIMS line-scan profiling for ^{18}O,^{16}O, and Zn, across the x-section of the $^{18}O/^{16}O$ exchanged sample of **undoped** ZnO ceramic sintered at 1250 ^{o}C.

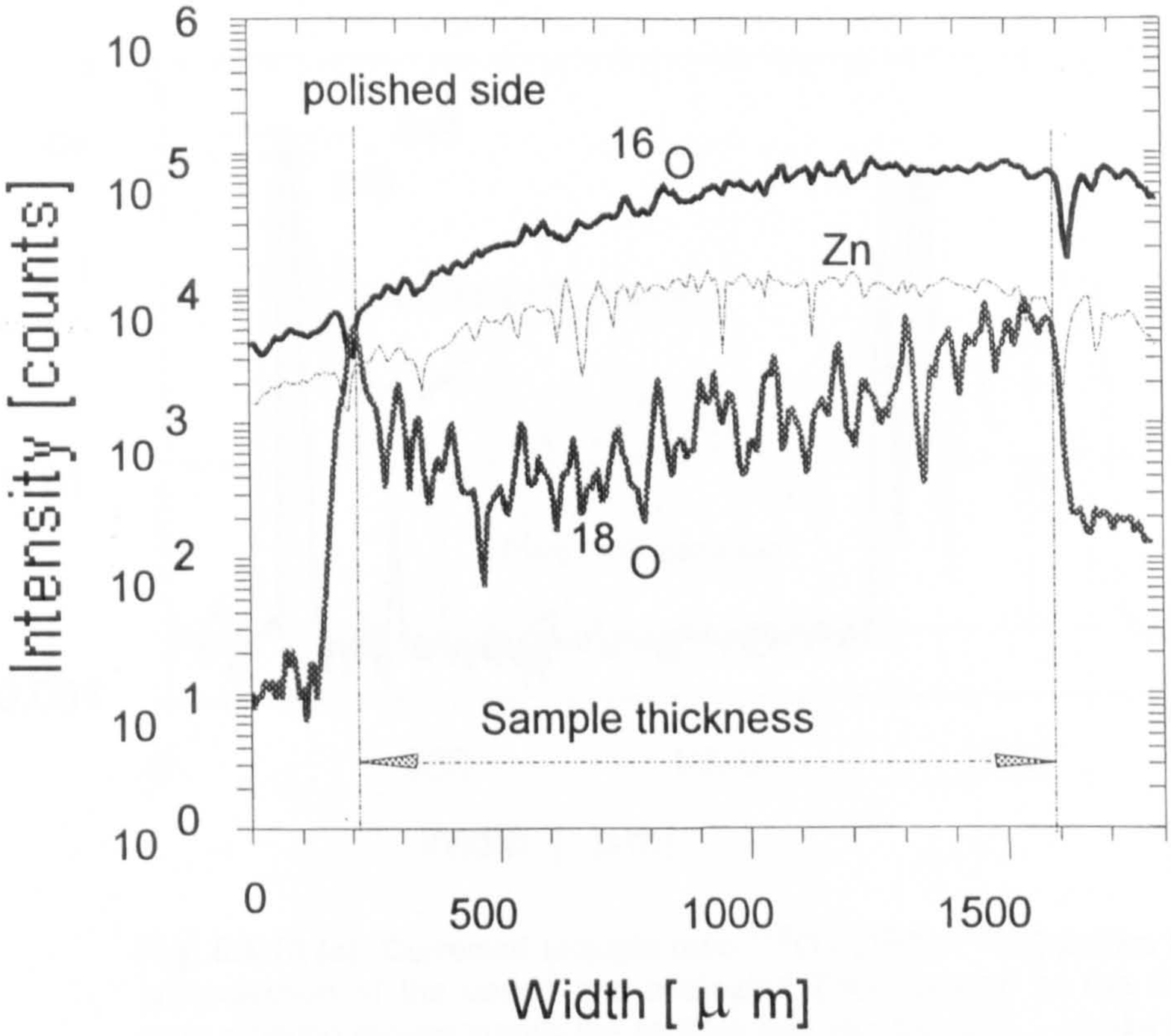


Fig. 5.4.8 (b) SIMS Line-scan profiling for ^{18}O,^{16}O, and Zn, across the x-section of the $^{18}O/^{16}O$ exchanged sample of ZnO ceramic **doped** with the oxides of Bi, Sb, Co, Mn, and Cr and then sintered at 1250 ^{o}C.

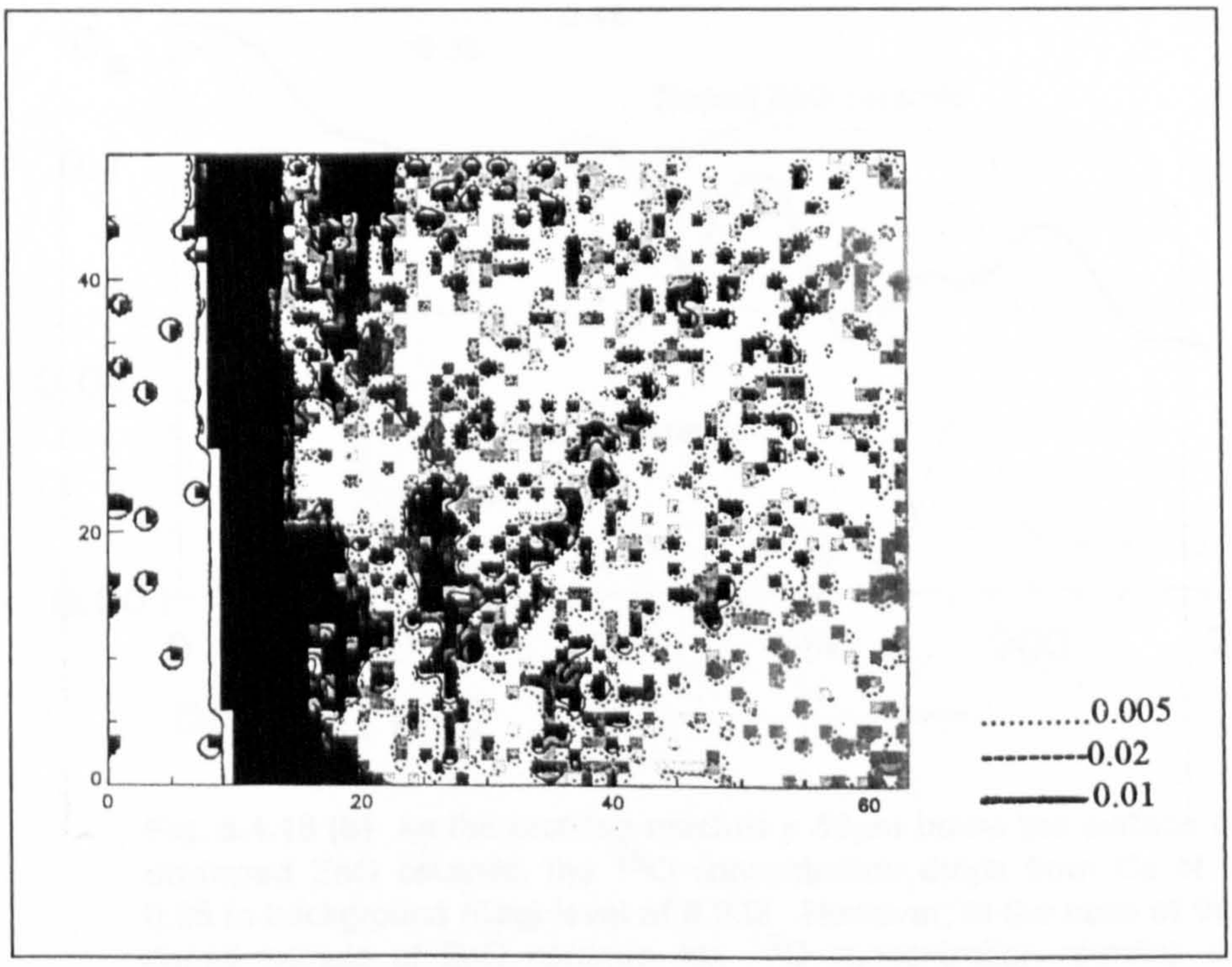


Fig.5.4.9. A map showing the spatial distribution of ^{18}O in the cross-sectioned sample of ZnO varistor. Each pixel is 3 μm, 180 x 180 μm area.

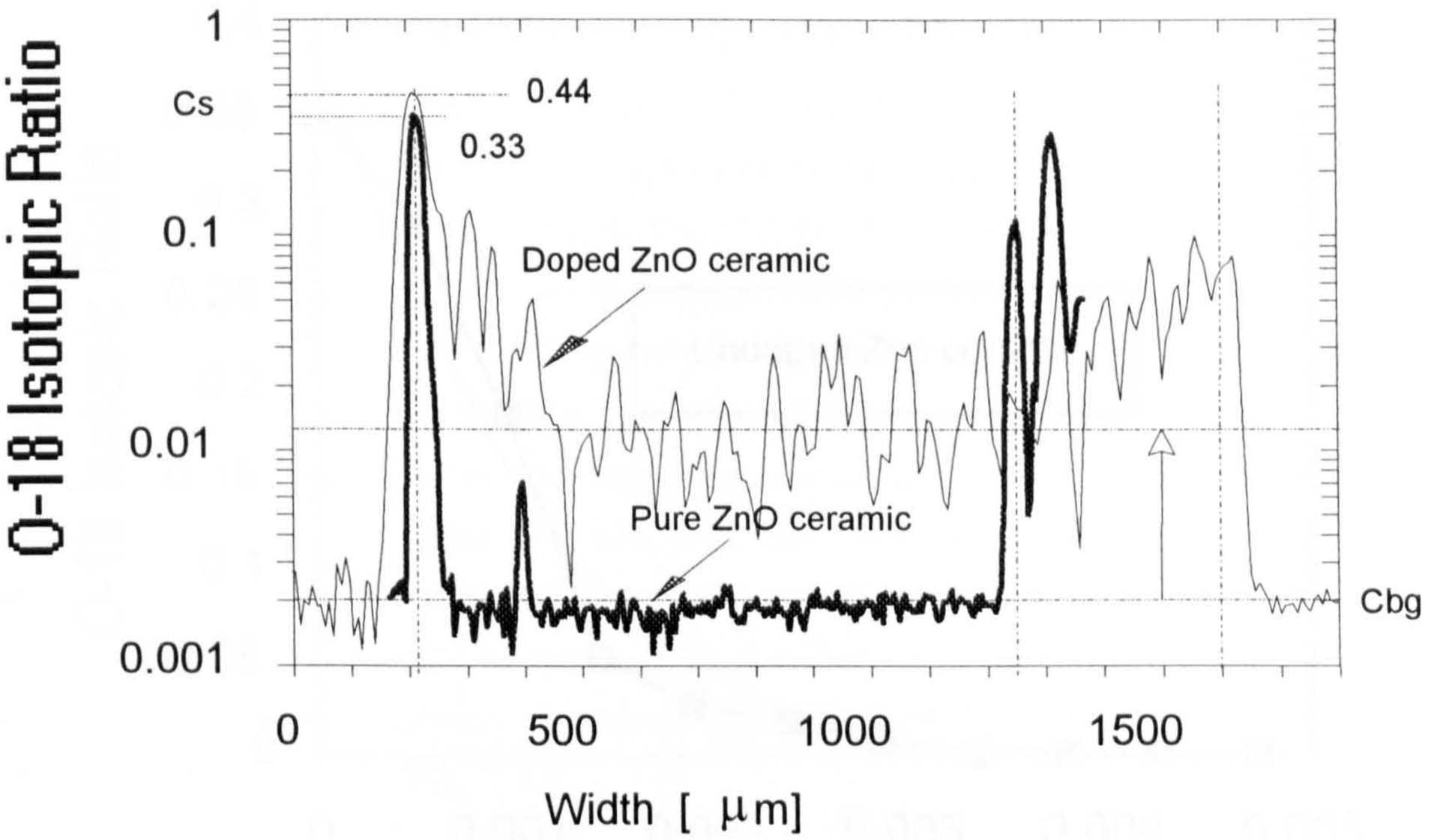


Fig. 5.4.10 (a) Corrected Isotopic ratio [^{18}O / (^{18}O +^{16}O)] across the cross-section of the doped and **undoped** ZnO ceramic as the line-scan profiling moves across the surface and into the bulk.. Unlike the doped sample, a rapid drop in the ^{18}O concentration, from Cs of 0.3 to Cbg (0.002) is observed for the undoped sample.

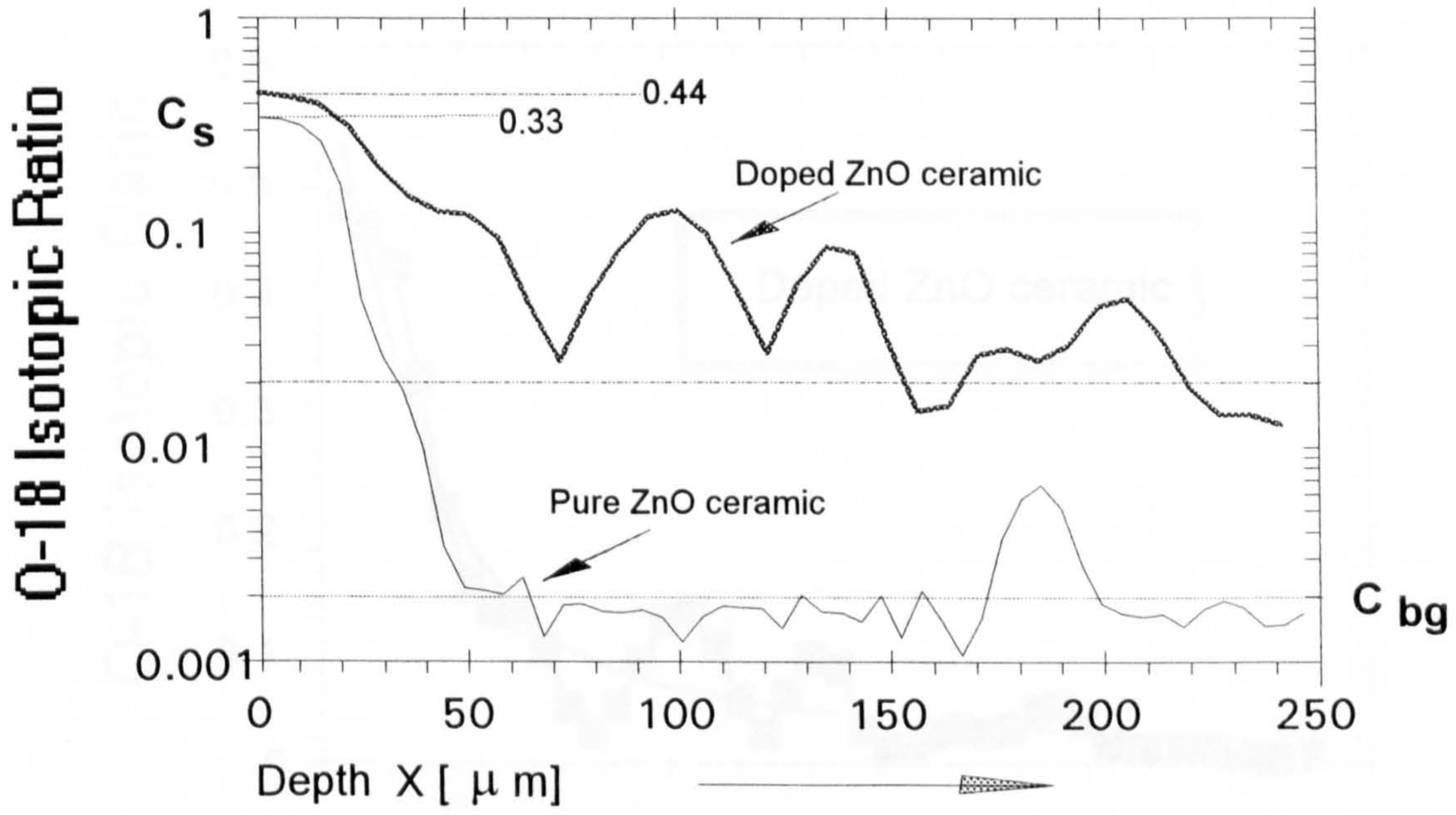


Fig. 5.4.10 (b) As the profiling reaches ≈ 50μm below the surface of **undoped** ZnO ceramic, the ^{18}O concentration drops from Cs of ≈ 0.35 to background (Cbg) level of 0.002. However, in the case of the doped sample of ZnO ceramic, the ^{18}O concentration remains an order of magnitude higher then the Cbg level, throughout the line scan.

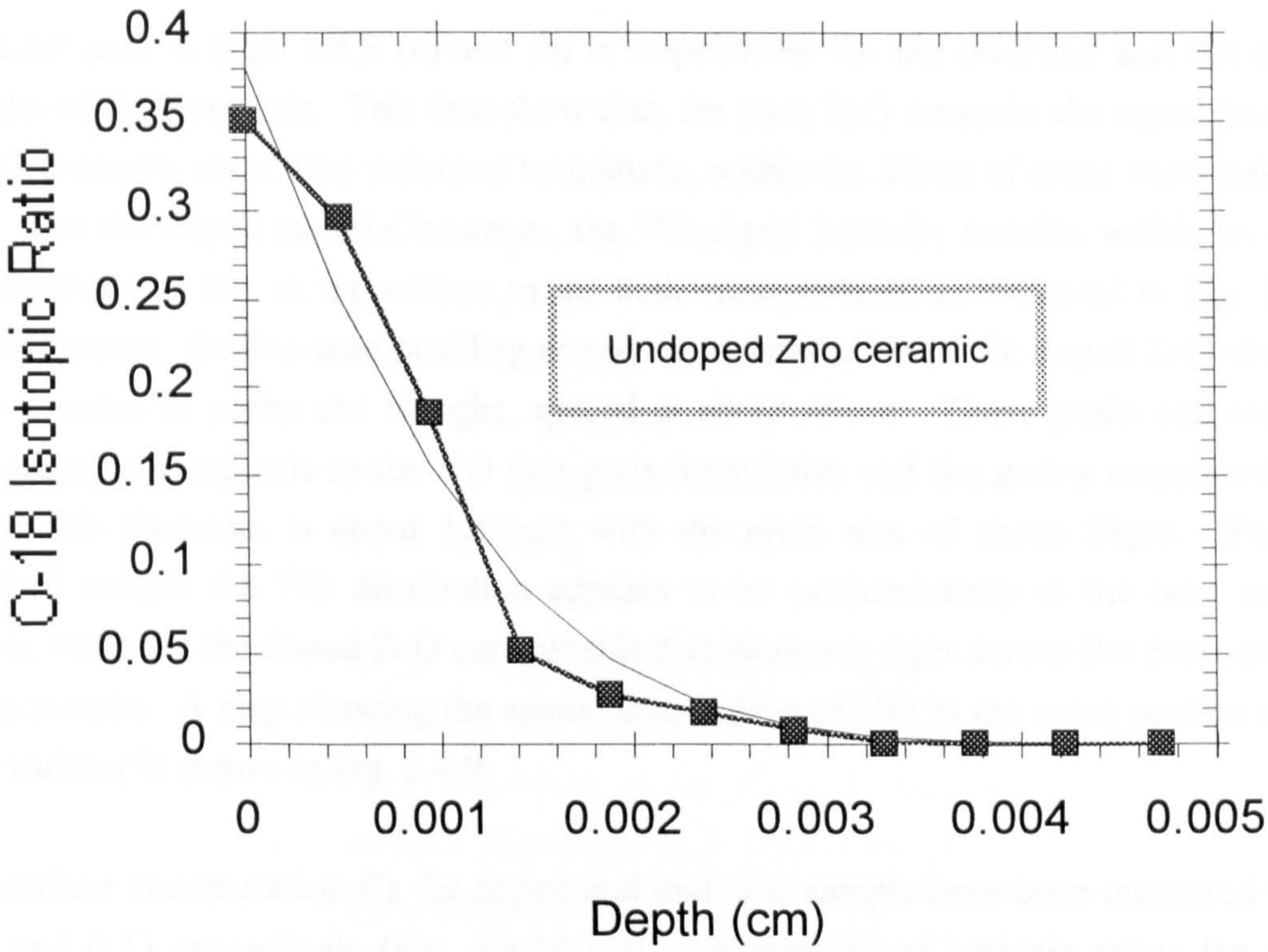


Fig.5.4.10 (c) The ^{18}O isotopic ratio line scan data and the fitted solution to the diffusion equation for the undoped ZnO ceramic. $D^*=1.19 \times 10^{-11}$ $cm^2\ s^{-1}$ and $K=5.77 \times 10^{-9}$ $cm\ s^{-1}$ (1000°C) are the fitted parameters.

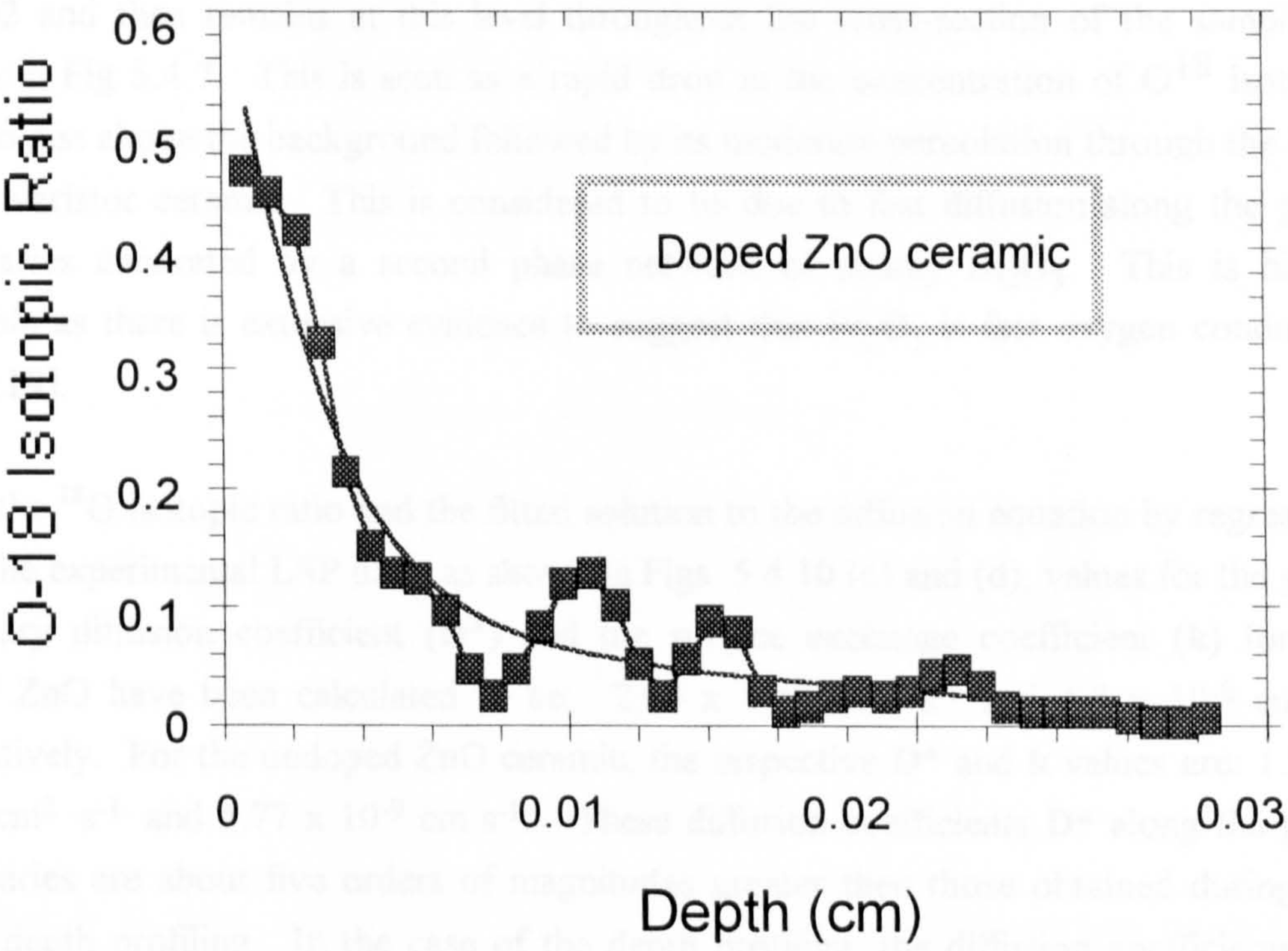


Fig.5.4.10 (d) The ^{18}O isotopic ratio line scan data and the fitted solution to the diffusion equation for the doped ZnO ceramic. $D^*=2.08 \times 10^{-10}$ $cm^2\ s^{-1}$ and $K=4.37 \times 10^{-8}$ $cm\ s^{-1}$ (1000°C) are the fitted parameters.

5.4.2.4. Discussion on $^{18}O/^{16}O$ exchange SIMS line-scan profiling

The LSP data in Figs. 5.4.8 (a) and (b) is respectively for the undoped and the doped samples of ZnO ceramic. This data show that, for pure ZnO ceramic, the signal intensity of ^{18}O drops by about two orders of magnitude, within the 20μm of cross-sectional line-scan. For the doped material however, the ^{18}O signal intensity remains within an order of magnitude of that at the surface to the bulk cross-section, as indicated in Fig. 5.4.8. (b). Moreover, the line-scan profiling across the cross-section of the doped ZnO ceramic show a series of peaks and troughs, spaced at about 40μm. These peaks and troughs presumably corresponds to the ^{18}O rich grain boundaries and the grains respectively; as the sample thickness is about 1300μm with the grain size of about 28μm. For the undoped sample the ^{18}O distribution appears to be predominantly at the near surface region, while for the doped ZnO ceramic this distribution is right across the cross-section of the sample. A map showing the spatial distribution of ^{18}O in the cross section of the ZnO varistor is shown in Fig. 5.4.9.

The surface concentration Cs for doped and undoped sample have been measured to be 0.44 and 0.33 respectively (Fig. 5.4.10 (a)). Comparison of isotopic ratios for depth profiling studies and the LSP show that the isotopic ratio ^{18}O in pure ZnO ceramic does not remain at the level, (during depth profiling) indicated in Fig.5.4.10. (b) but drops to background (0.002) as the LSP traverses about 50μm. from the edge of the sample. However for the doped ZnO ceramic the isotopic concentration initially drops from 0.44 to 0.02 and then remains at this level throughout the cross-section of the sample as shown in Fig 5.4.7. This is seen as a rapid drop in the concentration of O^{18} isotopic ratio to just above the background followed by its moderate percolation through the bulk of the varistor ceramic. This is considered to be due to fast diffusion along the grain boundaries decorated by a second phase network of mainly Bi_2O_3. This is highly probable as there is extensive evidence to suggest that Bi_2O_3 is fast oxygen conductor [113,119].

From the ^{18}O isotopic ratio and the fitted solution to the diffusion equation by regression fit to the experimental LSP data, as shown in Figs. 5.4.10 (c) and (d), values for the grain boundary diffusion coefficient **(D*)** and the surface exchange coefficient **(k)** for the doped ZnO have been calculated to be: 2.08×10^{-10} cm^2 s^{-1} and 4.3×10^{-8} cm s^{-1} respectively. For the undoped ZnO ceramic, the respective **D*** and **k** values are: 1.19×10^{-11} cm^2 s^{-1} and 5.77×10^{-9} cm s^{-1}. These diffusion coefficients **D*** along the grain boundaries are about five orders of magnitudes greater then those obtained during the initial depth profiling. In the case of the depth profiling, the diffusion coefficients are essentially that of the bulk ZnO grains, as only a few grain boundaries are sampled per unit area of the scan (32μm x 32μm). In the LSP however, the primary beam traverses

across the x-section of the sample, and encounters many grain boundaries (45 - 50) in its path. Hence, in the doped ZnO ceramic sample, the diffusion tailing remains above the back ground (0.002), suggesting fast diffusion along the diffusion paths provided by the grain boundaries. This spatial distribution of oxygen concentration at the grain boundaries of the doped ZnO ceramic is explained in terms of the proposed model as shown in Fig.5.4.11. According to this model, the oxygen transport net-work consists of lacy type of network with phases at the triple points. By virtue of this mechanism a copious supply of oxygen can be made available to replenish the grain boundaries in the bulk of the ceramic sample. Oxygen concentration at the grain boundaries is essential to exhibit varistor behaviour. The trapped charges at the grain boundary interface are attributed to the excess oxygen ions [74].

Fujitsu *et al* [113] reported in 1988, that fast oxygen transport may also occur in the porous undoped ZnO ceramic and that the undoped, but porous ZnO ceramic sample may exhibit varistor behaviour. However, in this study, a ZnO ceramic sample sintered at 800°C showed some porosity (discussed in section 5.1), but it did not exhibit any useful varistor characteristics (discussed in section 5.6).

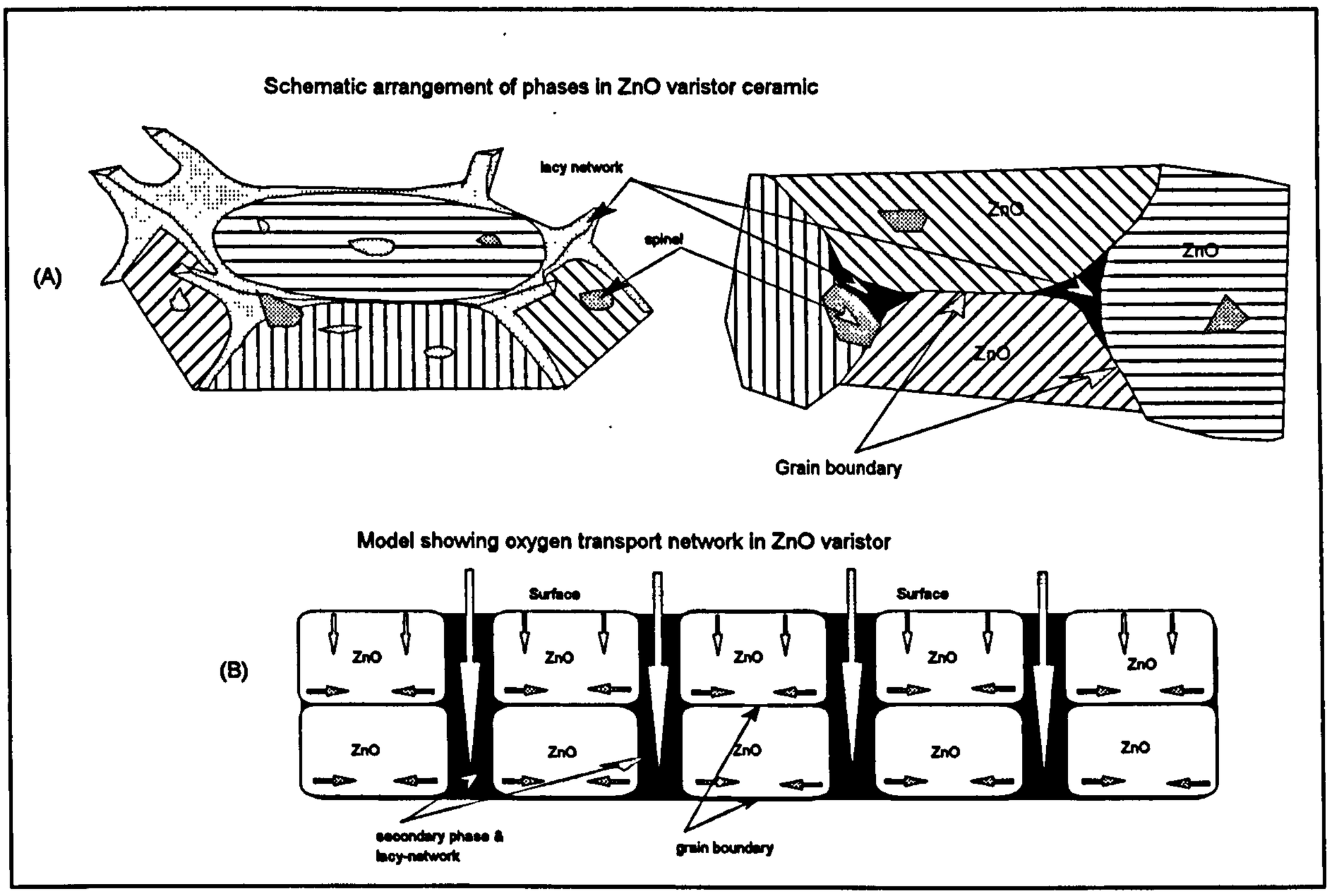


Fig. 5.4.11. A modified model (to the one presented by Fujitsu *et al.*, [113] **for the transport of oxygen in varistor.** (A) shows the schematic of different intergranular phase morphologies in doped ZnO ceramic. (B) shows that the lacy type of secondary phases acts as the major oxygen transport net-work, indicated by large arrows, while the oxygen transport through grain boundaries is indicated by smaller arrows.

5.4.3. Summary of the SIMS analysis.

(1) **Compositional imaging** by SIMS showed the distribution of dopant elements in ZnO ceramic sample. This confirms the segregation of dopant elements such as Bi, Sb and Cr in the ZnO ceramic. Comparison of the concentration of dopants within a single grain to the reference sample, confirms the uniform distribution of dopants such as Co and Mn in the ZnO ceramic. Difficulty in detecting dopant elements such as the Bi and Sb is perhaps due to very low secondary ion signal intensity as a consequence of the low sputter yields of these elements.

(2) Isotopic exchange depth profiling **(IEDP)** showed that, the ^{18}O tracer oxygen concentration remained above the back ground level, within the range of the profiling depth (1μm) in both doped and undoped ZnO ceramic sample. The diffusion equation has been fitted to the experimental data. From this, values for the oxygen self diffusion coefficient (D*) and the surface exchange coefficient (k) for doped ZnO have been calculated to be 0.79×10^{-15} cm^2 sec^{-1} and 0.14×10^{-9} cm sec^{-1} respectively. For the undoped ZnO ceramic, the respective D* and k values are: 0.13×10^{-15} cm^2 sec^{-1} and 0.58×10^{-10} cm sec^{-1}. These values are thought to represent the diffusion of oxygen into the bulk of the ZnO grains. These IEDP results compare well with the data from Robin *et al* [118] - please see Fig. 2.2.5 in chapter 2.

(3) The **$^{18}O/^{16}O$ exchange SIMS line-scan profile data confirmed:** (a) Values for the diffusion coefficient along the grain boundaries are about 5 orders of magnitudes greater then for diffusion into the bulk ZnO grains. There is evidence for fast diffusion along the grain boundaries in the doped ZnO ceramic. (b) That in the case of the undoped ZnO ceramic sample, the diffusion tailing of ^{18}O tracer oxygen concentration rapidly drops to 0.002 at the depth of ≈ 50μm from the surface. This is typically equivalent to around 2 to 3 grains. Beyond this depth there is no significant trace of ^{18}O. This lack of oxygen distribution at the grain boundaries within the bulk ceramic would probably explain why the undoped ZnO ceramic does not exhibit significant non-linear varistor characteristics (discussed in section 5.6). In the case of the doped ZnO ceramic however, the ^{18}O tracer oxygen concentration remains over an order of magnitude higher (0.02) then the background level (Cbg = 0.002).

The regression fitted solution to the above SIMS line-scan data for the doped ZnO ceramic yields the D* and k values of : 1.25×10^{-10} cm^2 sec^{-1} and 3.05×10^{-10} cm sec^{-1} respectively. For the undoped ZnO ceramic , the respective D* and k values are: 1.19×10^{-11} cm^2 sec^{-1} and 5.77×10^{-9} cm sec^{-1}.

(4) A **model** has been proposed showing the fast diffusion path to be attributed to the lacy network of Bi_2O_3 rich phases in the doped ZnO ceramic.

5.5. IS (Impedance Spectroscopy) analysis of ZnO ceramics

Aim

Impedance Spectroscopy was used to investigate the properties of ZnO ceramic samples prepared with varying number of dopant additives. It was intended to observe dopant related response, using ZnO ceramic samples synthesised with combination of dopant additives.

Samples used in these experiments include: (a) nominally undoped ZnO ceramic and a series of doped ZnO ceramic samples containing single, double and multiple additive metal oxides of the elements (Bi, Sb, Co, Mn, Cr) all at 0.5 mol.% each: For comparison purpose, some commercial ZnO varistor samples were also studied.

The complex impedances of the ceramic pellets were measured, using the equipment described in Chapter 3, section 3.4. Measurements were made (10 points per decade) over the frequency range 10^6 Hz to 1 Hz, and in the temperature range 20°C to 500°C. An applied voltage of 0.1V was used. All measurements were undertaken in air, unless stated otherwise.

Impedance measurements are made over a wide range of frequencies and the different regions of the material are characterised according to their electrical relaxation times or time constants. As the measurements proceed, the in-and out-of-phase components of the voltage across the sample are measured. Dividing these components by the magnitude of the current gives the resistive and reactive components of the impedance. The measurements are repeated as a step-wise function of frequency. Different regions of a ceramic sample are characterised by a resistance and capacitance, usually in parallel. The characteristic relaxation time or time constant, τ, of each 'parallel RC element' is given by the product of R and C (equation 5.5.1). The computed values of Z are displayed as a complex plane plot. The frequency and the real (Z') and imaginary (Z'') parts of Z are obtained from the plot.

The values for the resistance (R) can be taken from the real axis intercept and the corresponding capacitance (C) can be calculated by using the following relationship:

The time constant $\tau = R\,C$ (5.5.1)

$\omega\,C\,R = 1$ (at the apex of the semi-circle) (5.5.2)

Where ω = is the angular frequency $2\pi f$, τ is the characteristic relaxation time. From the impedance spectrum, it is usually possible to identify different RC elements and assign them to appropriate regions of the sample. This assignment is based on the magnitudes of the capacitances (Table 5.5.1) [90, 114].

Table 5.5.1 Capacitance values and their possible interpretation

Capacitance [F]	Phenomenon Responsible
10^{-12}	bulk
10^{-11} - 10^{-8}	grain boundary
10^{-7} - 10^{-5}	sample-electrode interface
10^{-4}	electrochemical reactions

So calculation of the capacitance at the apex of the semi-circle, where $\omega CR = 1$, should give an indication of the response to which it is due.

When interpreting the IS spectra it is crucial to assign the semicircular response to its respective bulk, grain-boundary or an electrode effect.

Initially, IS response of samples with evaporated aluminium electrodes were studied. Subsequently, silver pasted electrodes were used and the geometry of the samples were also varied to clearly elucidate the related response.

The resultant conductivity data for each sample, was then plotted in accordance with the Arrhenius equation (Equation (3.4-12) in Chapter 3):

$$\sigma(T) = \sigma_0 \exp(-E_a/kT)$$

T = absolute temperature

σ_0 = pre-exponential factor

E_a = activation energy (eV)

k = Boltzmann's constant (8.61735×10^{-5} eV)

Taking natural logarithms gives the linear equation:

$$\ln \sigma(T) = \ln (\sigma_o) - E_a/kT$$

Therefore, plotting $\ln \sigma (T)$ vs $1/T$ gives a straight line of slope E_a/k and intercept on the Y axis = σ_o

5.5.1 Electrical conductivity in materials

Electrical conduction occurs by the long range migration of either electrons or ions. Usually conduction by one or other type of charge carrier predominates, but in some inorganic materials both ionic and electronic conduction are appreciable in the same material. In solid materials, specific conductivity, σ. is usually of interest. This is the conductivity of a sample that has a cell constant of unity, i.e. unit cross-sectional area and unit length. Commonly used units of specific conductivity are $ohm^{-1}\ cm^{-1}$, $ohm^{-1}\ m^{-1}$, and Sm^{-1} where 1 Siemen, $S \equiv 1\ ohm^{-1}$.

For any material and charge carrier, the specific conductivity (is given by :

$$\sigma = \sum_i n_i q_i \mu_i \qquad 5.5.3$$

where n_i is the number of charge carriers of species i, q_i is their charge and μ_i their mobility. For electrons and monovalent ions, q is the charge on an electron, 1.6×10^{-19} C. Typical conductivities for a range of materials are given in Table 5.5.2 below.

Table 5.5.2 Typical values of electrical conductivity [114].

	Material	σ ($ohm^{-1}\ cm^{-1}$)
Ionic conduction	Ionic crystals	$< 10^{-18} - 10^{-4}$
	solid electrolytes	$10^{-3} - 10^{1}$
	Strong (liquid) electrolytes	$10^{-3} - 10^{1}$
Electronic Conduction	Metals	$10^{1}\ 10^{5}$
	Semiconductors	$10^{-5} - 10^{2}$
	Insulators	$<10^{-12}$

Conductivities are usually temperature dependent and for all materials, except metals, the conductivity increases with increasing temperature.

Pure ZnO ceramic is n-type semiconductor with conductivity of typically, 10^{-2} - 1, ohm cm^{-1} [18] arising from zinc interstitial (discussed in Chapter 2, section 2.2.2).

Additives such as the oxides of Bi, Sb, Mn, Co, and Cr in ZnO ceramic, modify the bulk microstructural properties and consequently influence its electrical properties. The resultant doped ZnO is thus tailored to exhibit highly insulating grain boundaries with the bulk of the grains remaining conductive.

5.5.2. Presentation of IS results.

5.5.2.1. IS of Pure ZnO ceramic

IS spectra of a pure ZnO sample is shown in Fig. 5.5.1 (a). The spectra appears to consists of a slightly depressed semicircle resulting from two overlapping semicircles. This distortion is due to two overlapping semicircles corresponding to two competing processes, possibly bulk and grain boundary in this case. Sometimes it is difficult to completely resolve these overlapping spectra with close time constant (τ).

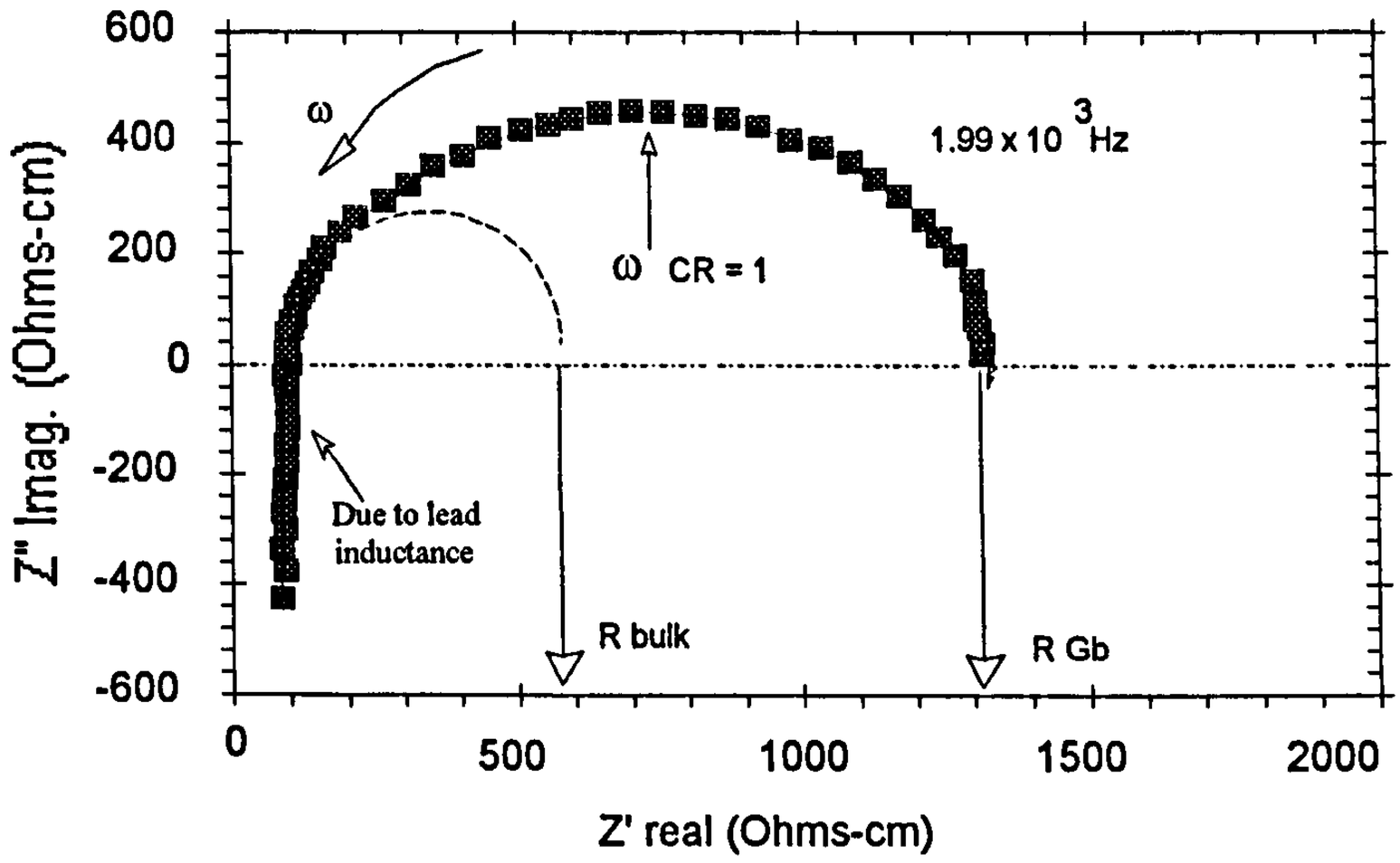


Fig. 5.5.1 (a). Impedance spectra, acquired at 335^{o}C, of a nominally undoped ZnO ceramic sample.

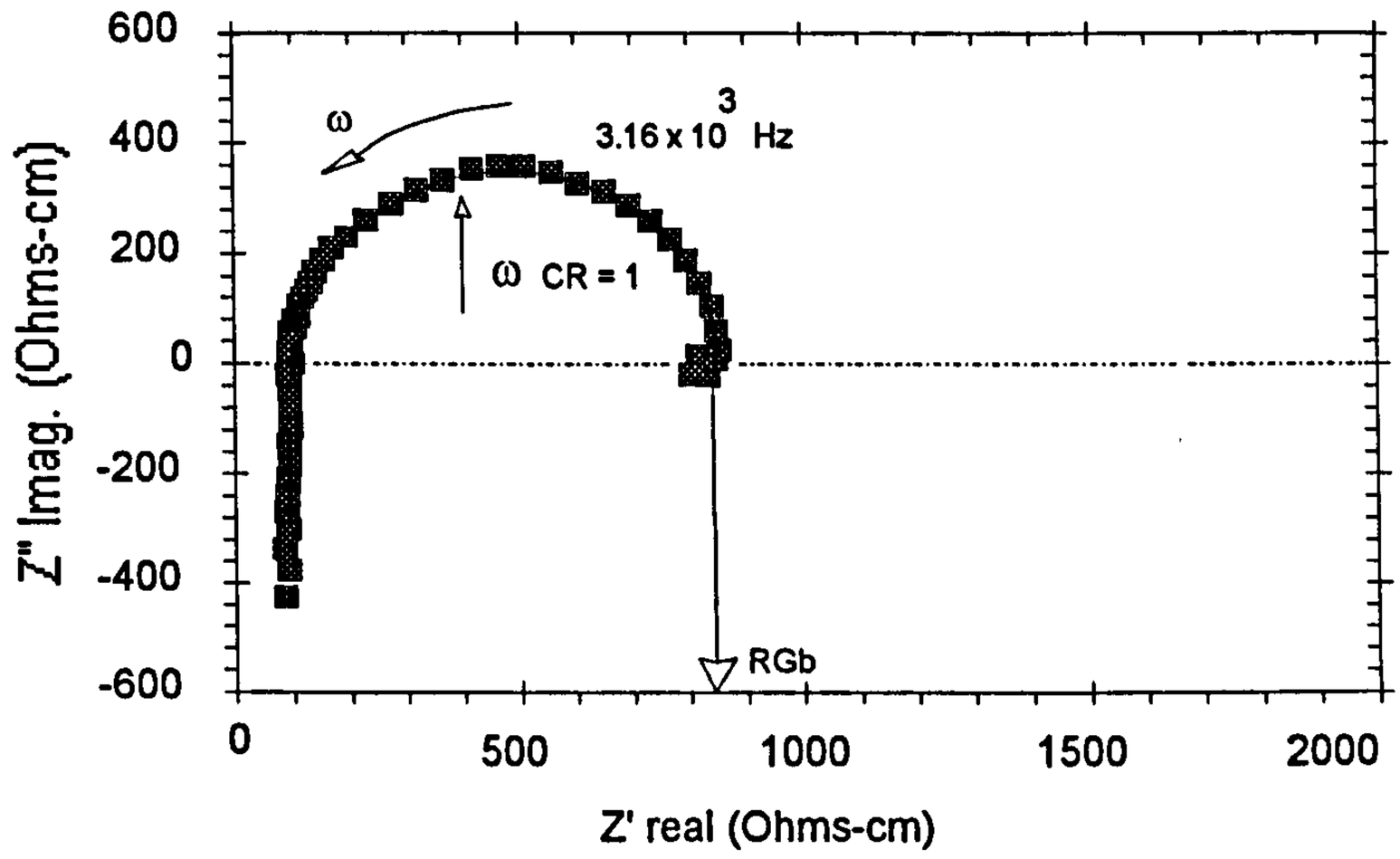


Fig. 5.5 1 (b). Impedance spectra, acquired at 435^{0}C, of a nominally undoped ZnO ceramic sample.

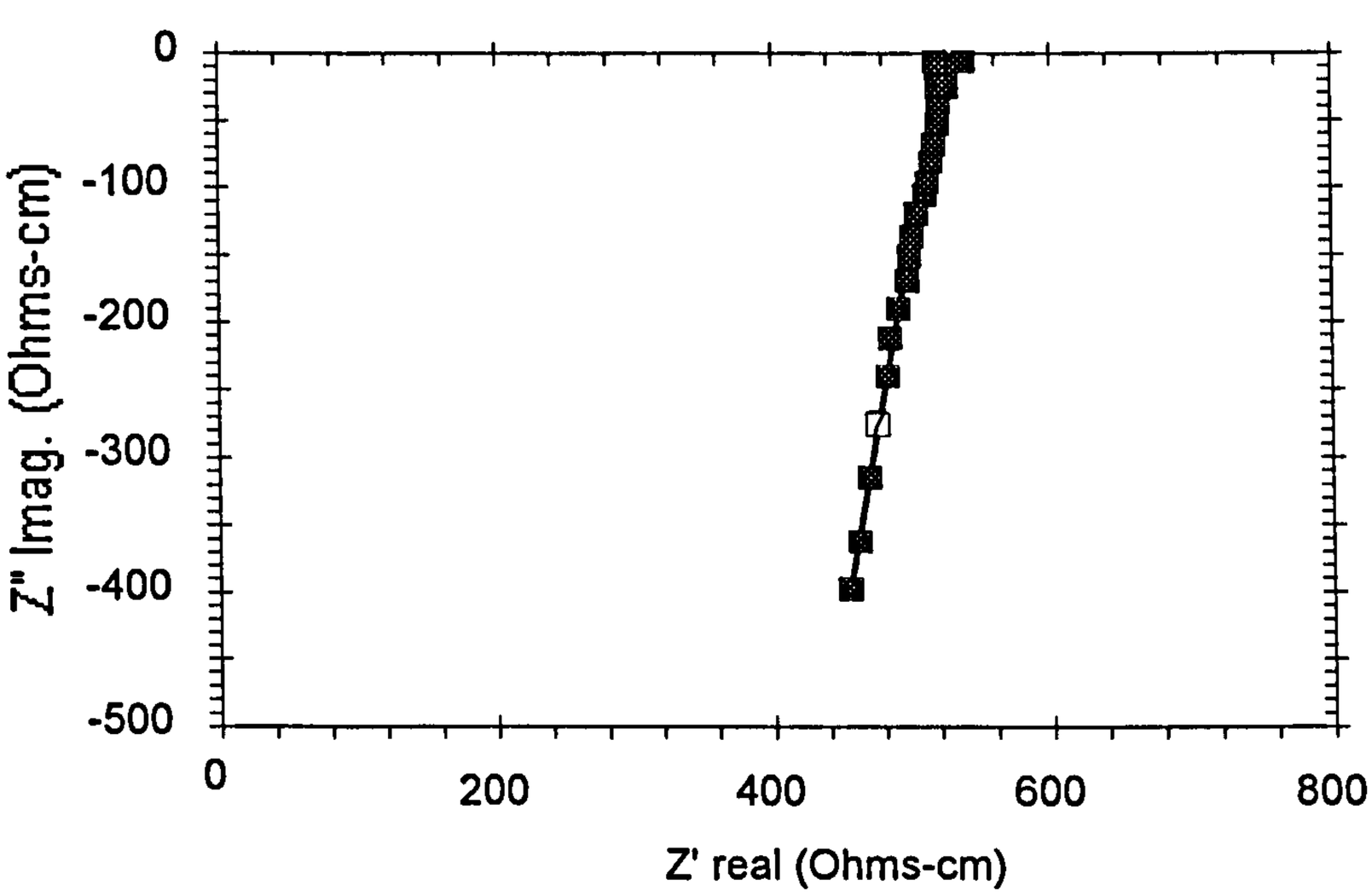


Fig. 5.5.1 (c) Impedance spectra of the undoped ZnO ceramic sample at 535^{0}C.

The value of the resistivity (Rgb) is calculated from the real axis intercept: 1.3 X 10^{3} Ω cm. The resultant value for the capacitance has been calculated to be 4.4 x 10^{-7} F. This is attributed to grain boundary effects. Some data points also appear in the negative imaginary axis. These are not related to any process in the sample, but are due to the inductance of the connecting leads. Measurements at higher temperatures (435^{0}C),

results in a noticeable decrease in resistivity with raise in temperature. There is a noticeable shift to the (Rgb) semi-circle, and the bulk response (Rb) is not seen here (Fig.5.5.1.b). Further increase in temperature (535°C) results in a purely resistive, DC response as there is no sign of any semicircle. The DC resistance of 62 Ω has been calculated (Fig.5.5.1 (c). From Arrhenius plot, as shown in Fig.5.5.4 (a), the activation energy (Ea) for the un-doped ZnO has been calculated to be 0.27 eV.

5.5.2.2. IS of ZnO varistor sample

Figure 5.5.2 (a) show the impedance spectra of a ZnO varistor sample acquired at 197°C. A semi-circle plot of this type can be modelled by a capacitor and a resistor in parallel. The calculated value of the capacitance of the order of 0.3nF/cm, in this case is associated with the grain boundary response. This has been confirmed subsequently by repeated analyses using a sample of similar composition but with different geometry. IS spectra of this sample acquired at higher temperatures are shown in Figs. 5.5.2 (b) (c), (d). In these spectra, the values of the capacitance does not change significantly, but the resistivity of this sample decreases with increase in temperature, from initially 1.28 MΩ-cm (197°C) to finally less then 100 Ω-cm (557°C). IS spectra in Fig. 5.5.2 (c) show an appearance of a second semi-circle, probably due to an electrode response, with the associated capacitance of 0.4μF/cm. Distortion of a semi-circle in Fig. 5.5.2 (e) is due to the inductance of the leads. This has affected the calculation of the grain boundary capacitance, exhibiting slightly higher value of 1.7 nF/cm in this case. An Arrhenius plot of this data (a plot of Ln(S*T) vs 1000/T) produced a straight line slope, giving a value for an activation energy of, Ea = 0.92eV, calculated by equating the gradient of the slope to equation (3.4 -12), as discussed in Chapter 3. Although capacitance is usually measured in nF, it is presented in nF/cm here, to account for changes in the physical dimensions of the sample for comparison purpose.

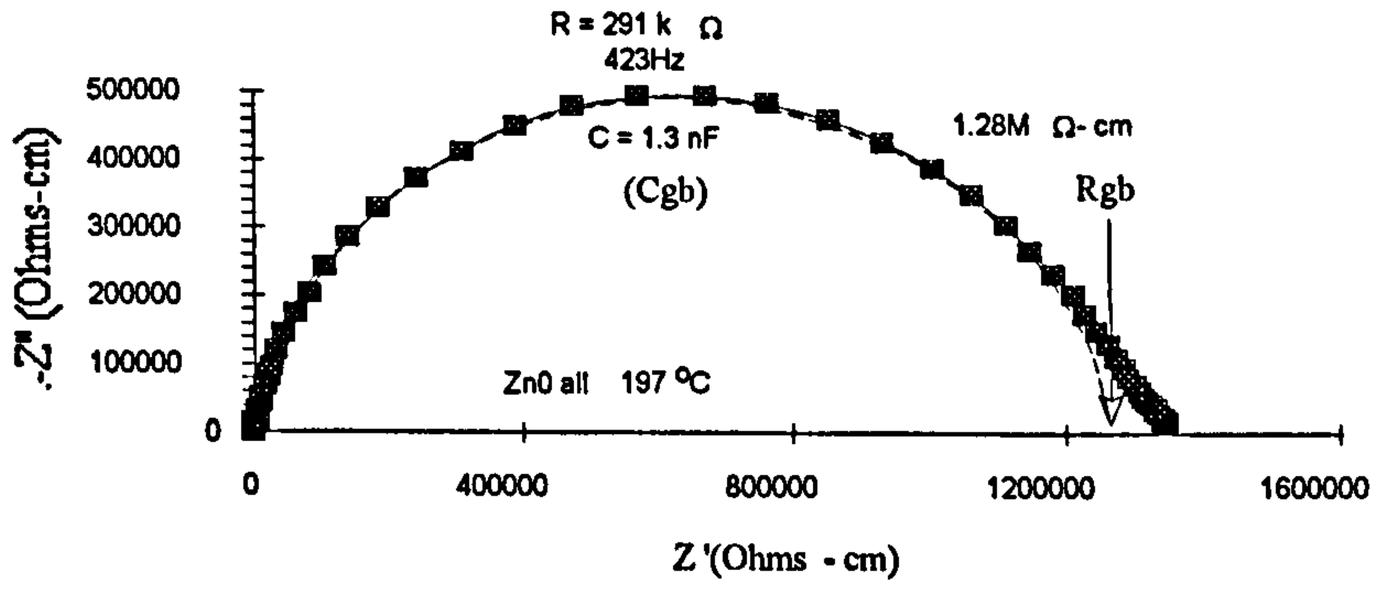


Fig. 5.5.2 (a). Impedance spectra of the ZnO ceramic (197°C) doped with additives (Bi, Sb, Mn, Co, and Cr) and then sintered at 1250°C.

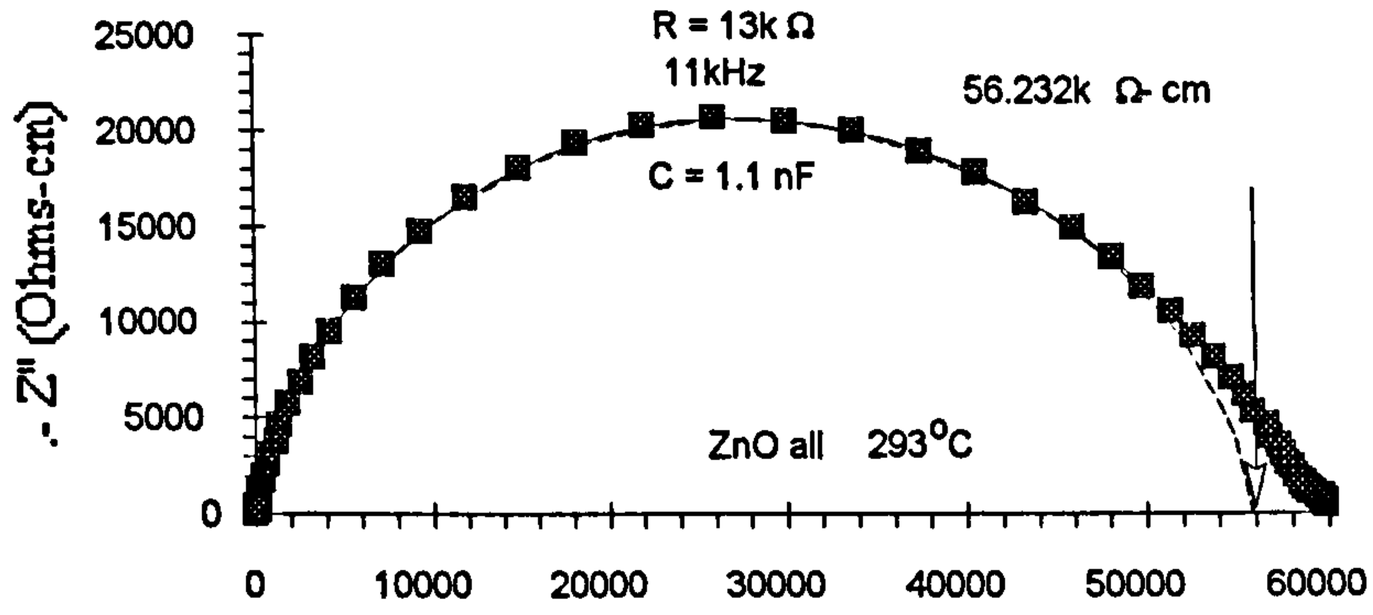


Fig. 5.5.2 (b) IS spectra of ZnO ceramic varistor at 293°C.

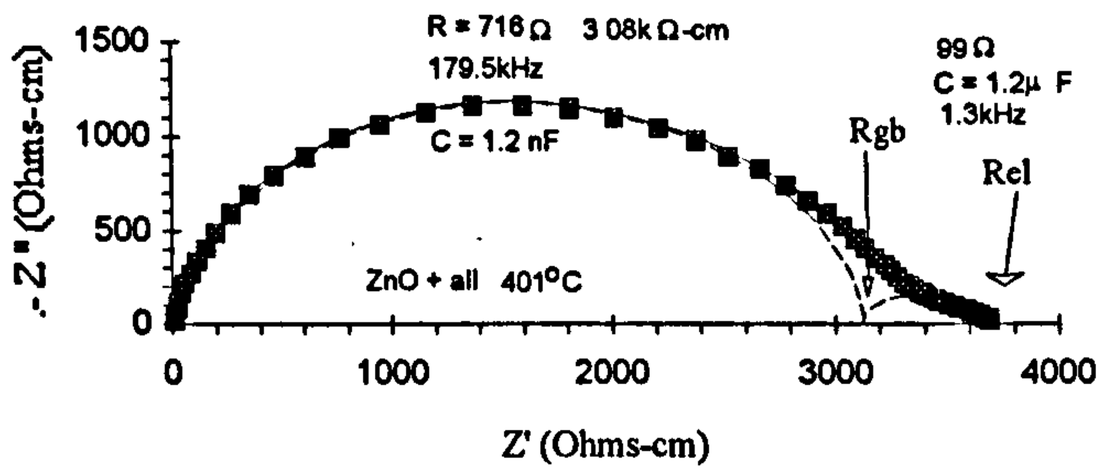


Fig. 5.5.2 (c) IS spectra of ZnO ceramic varistor at 401°C.

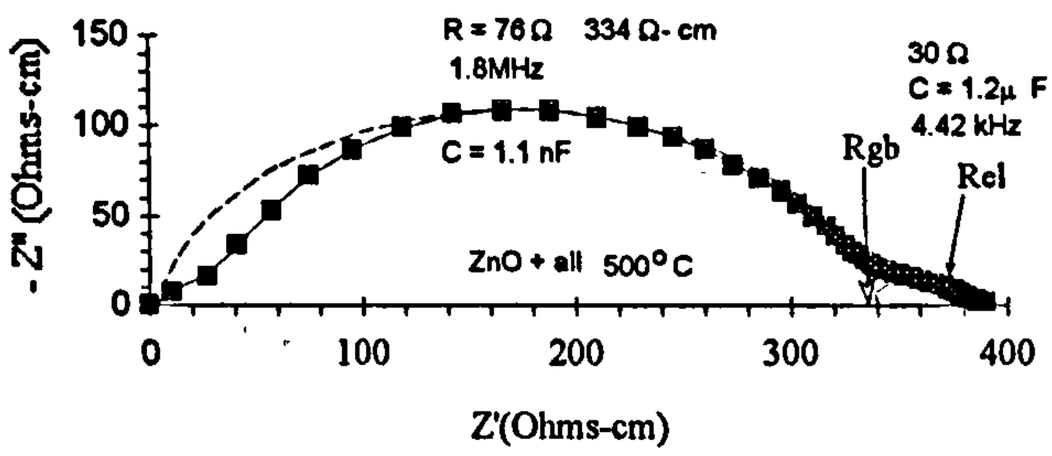


Fig. 5.5.2 (d) IS spectra of ZnO ceramic varistor at 500°C.

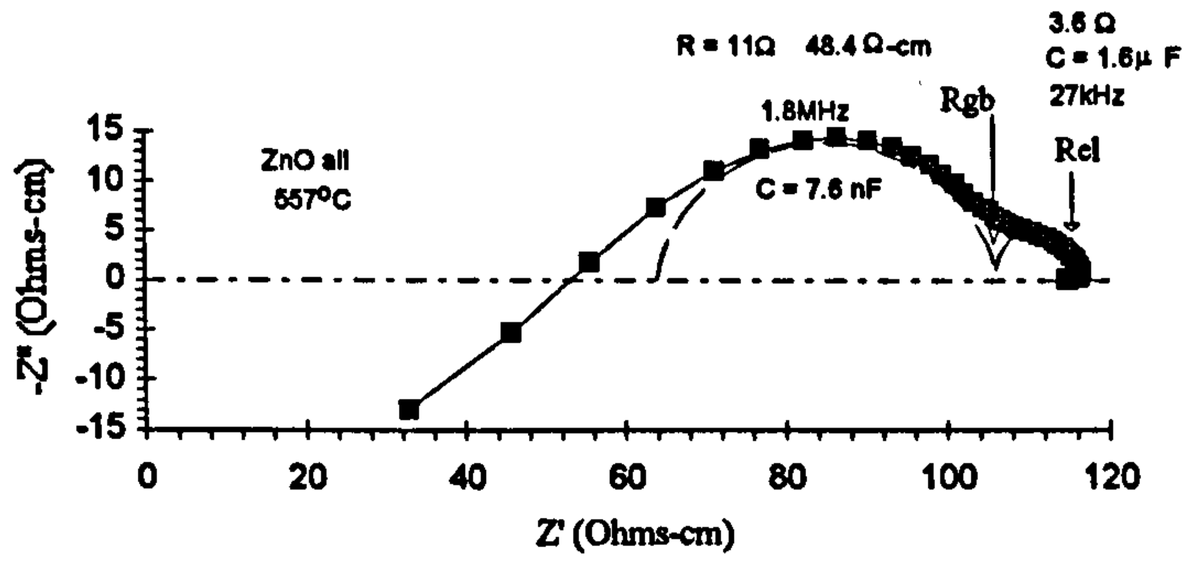


Fig. 5.5.2 (e) IS spectra of ZnO varistor sample, acquired at 557°C. Points in the negative regions exerting a downward pull on the semi-circle are due to the lead inductance effect. Consequently the grain boundary capacitance value differs from analysis taken at lower temperatures, where the lead inductance is not dominant.

IS spectra of ZnO ceramic with other compositions have been interpreted in this manner and an extraction of bulk, capacitance, resistivity, frequency, corresponding to the temperature of analysis are presented in Appendix C (**AndxTable 1 - 13**)

Conductivity as a function of temperature curves are shown in Fig.5.5.3. Measured value of the conductivity have been plotted (Figs. 5.5.4 (a), - (e)) as a reciprocal of temperature and from the gradient of such plot (Arrhenius plot), values for the activation energy, Ea has been calculated for each analysis. Capacitance is quoted in nF/cm to allow for the change in sample dimensions.

Table 5.5.3. IS data for Pure ZnO ceramic sample coated with Al electrodes.

	Samples: sintered at 1250°C, Al electrode	Temp. (°C)	ρ(Ωcm)	Freq. Hz	C (nF/cm)	Ea (eV)
1	**ZnO pure**,10.5mm Ø x 2.2mm	335	1330	2E3	60	0.27 ± 0.04
2		435	830	3E3	60	
3		535	400		0	

Table 5.5.4. IS Data for ZnO varistor synthesised in the laboratory, Al electrodes

	ZnO + all (Bi, Sb, Co, Mn, Cr) 10.6mm ∅ x 2mm .Al, Electrode	Temp (^{o}C)	ρ(Ωcm)	Freq. Hz	C	Ea (eV)
1		335	7.5E3	3.98E4	0.5nF/cm	0.97 ±0.02
2		335	8E5	<1	0.2μF/cm	
3 4		435	900 6.7E4	3.98E5 20	0.4nF/cm 0.1μF/cm	
5		535	9500	4.4E6	3.75pF/cm	
6		635	2700	8.9E6	6.6pF/cm	

Data for other measurements can be found in Appendix C

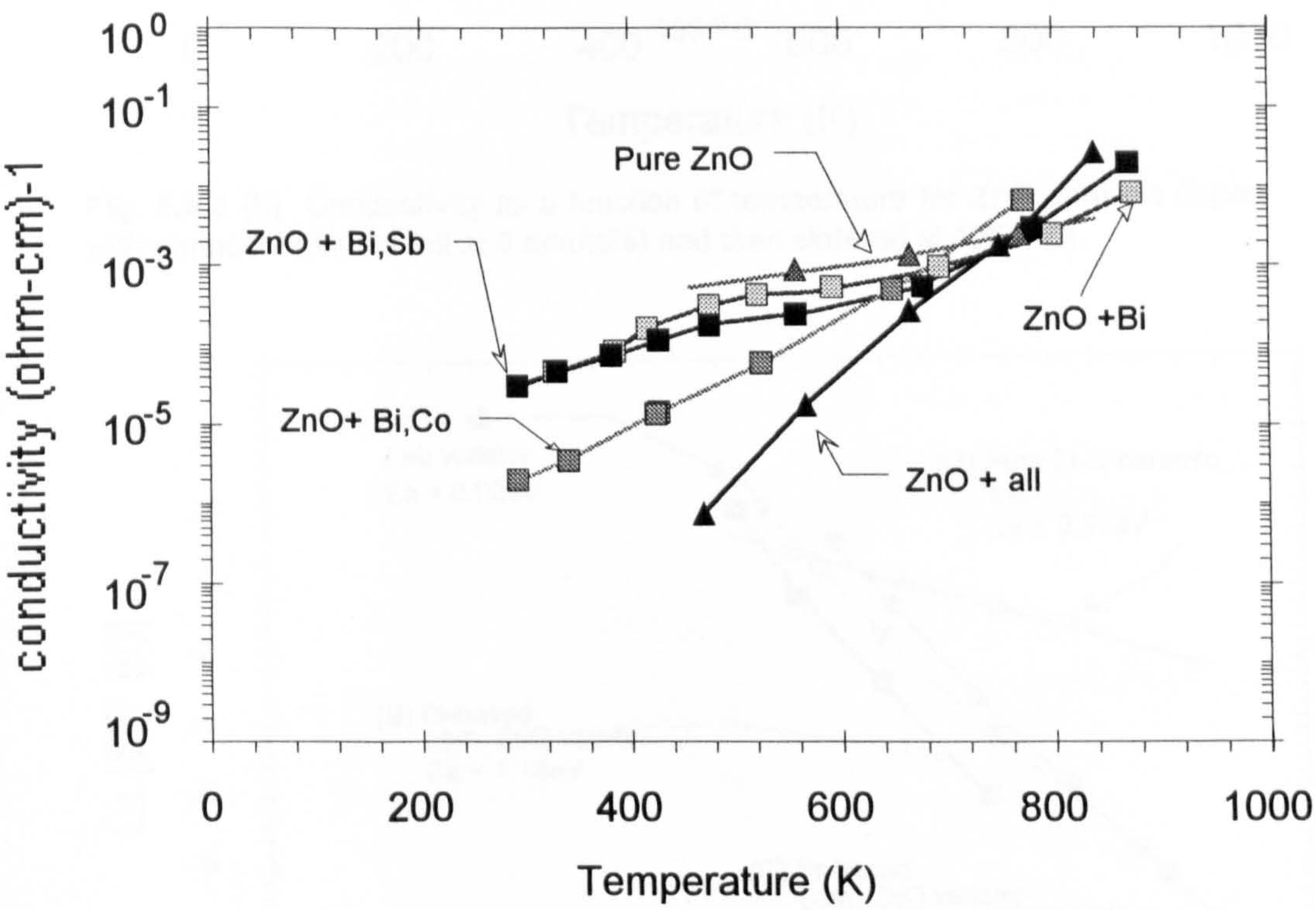


Fig. 5.5.3 (a) Conductivity as a function of temperature for ZnO ceramic doped with various additives (all at 0.5mole%) and then sintered at 1250^{o}C).

5.5.2.3. Arrhenius plots

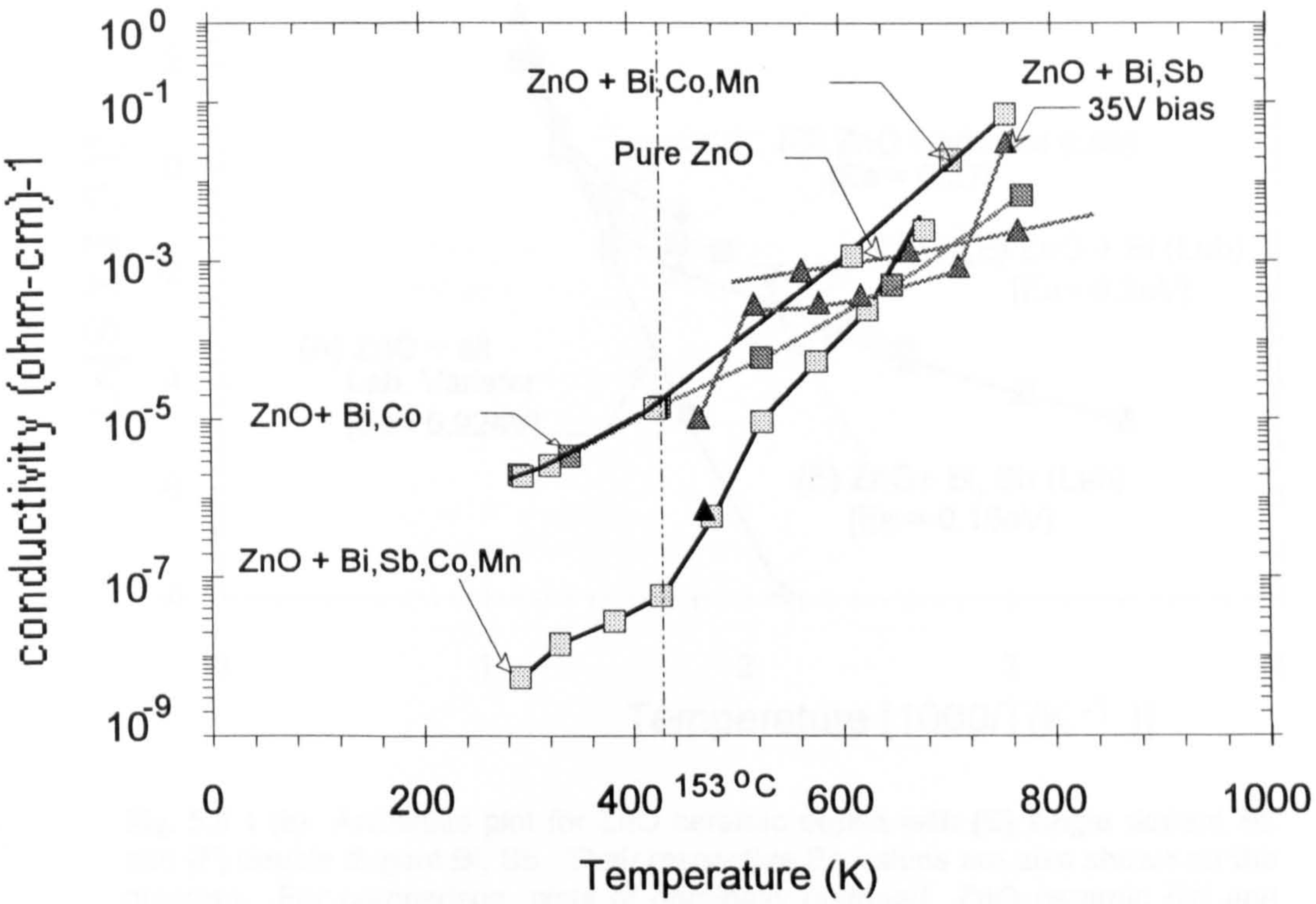


Fig. 5.5.3 (b) Conductivity as a function of temperature for ZnO ceramic doped with various additives (all at 0.5mole%) and then sintered at 1250^{o}C).

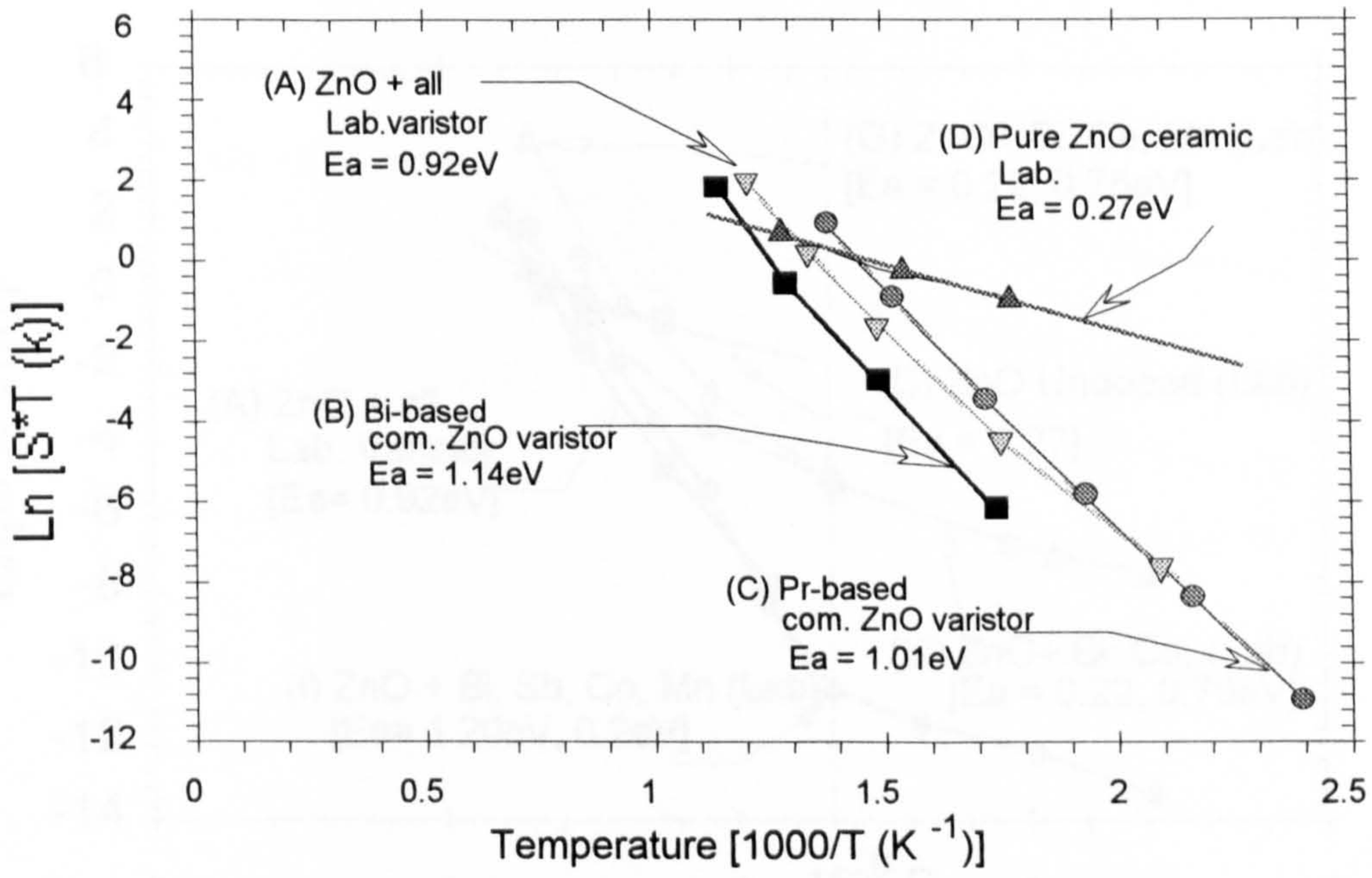


Fig.5.5.4 (a). Arrhenius plots for some ZnO ceramics. Slopes are labelled as: (A), for the synthesised ZnO ceramic , doped with Bi, Sb, Mn, Co and Cr, (B), commercial Bi based varistor, (C), a commercial Pr based varistor and (D) corresponds to the undoped ZnO ceramic.

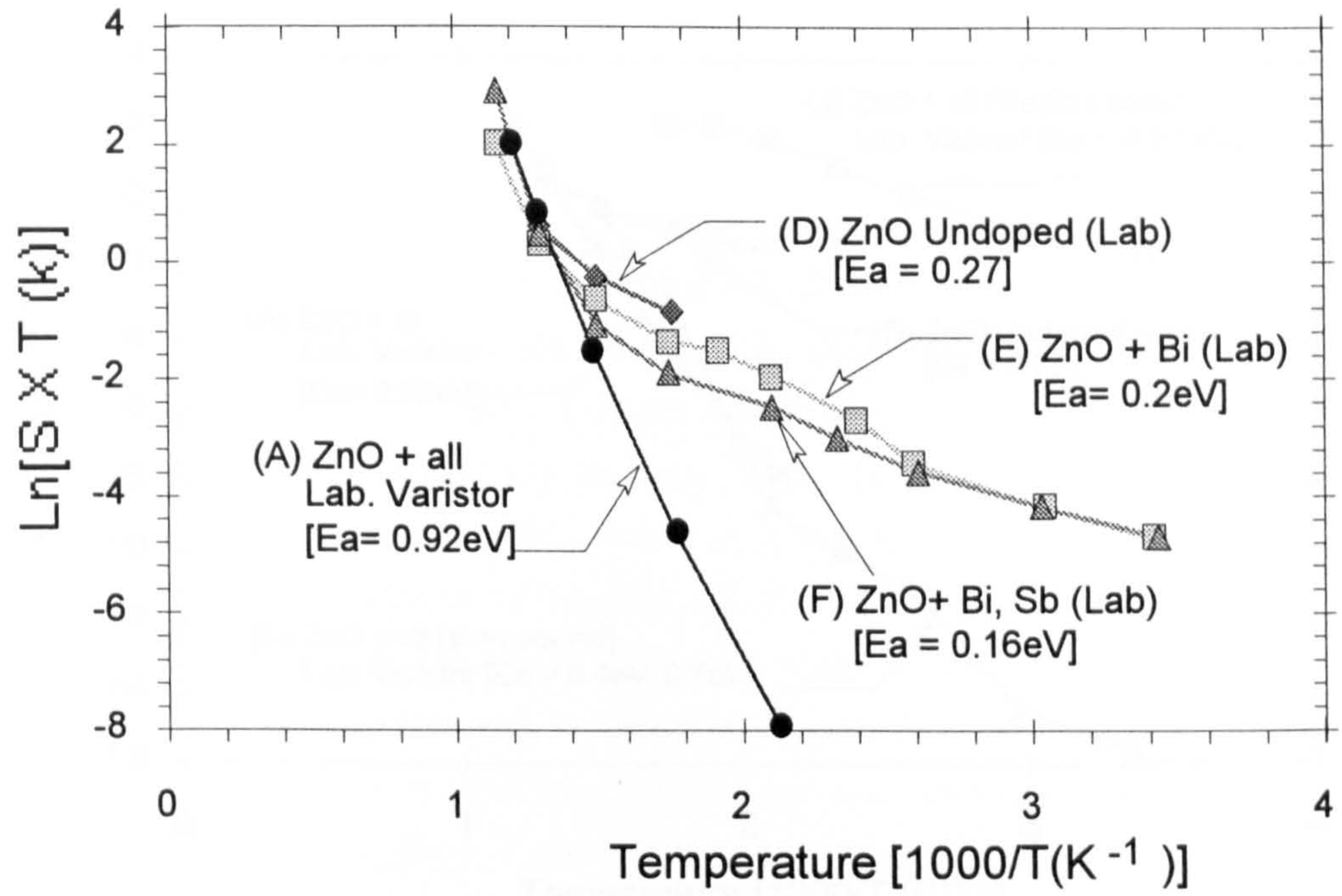


Fig. 5.5 4 (b) Arrhenius plot for ZnO ceramic doped with **(E)** single dopant Bi, and **(F)** double dopant Bi, Sb. Their respective Ea values are also shown on the diagram. For comparison, plots of nominally undoped ZnO ceramic **(D)** and the ZnO ceramic with varistor composition **(A)** are shown. Samples synthesised in the laboratory are labelled as (Lab).

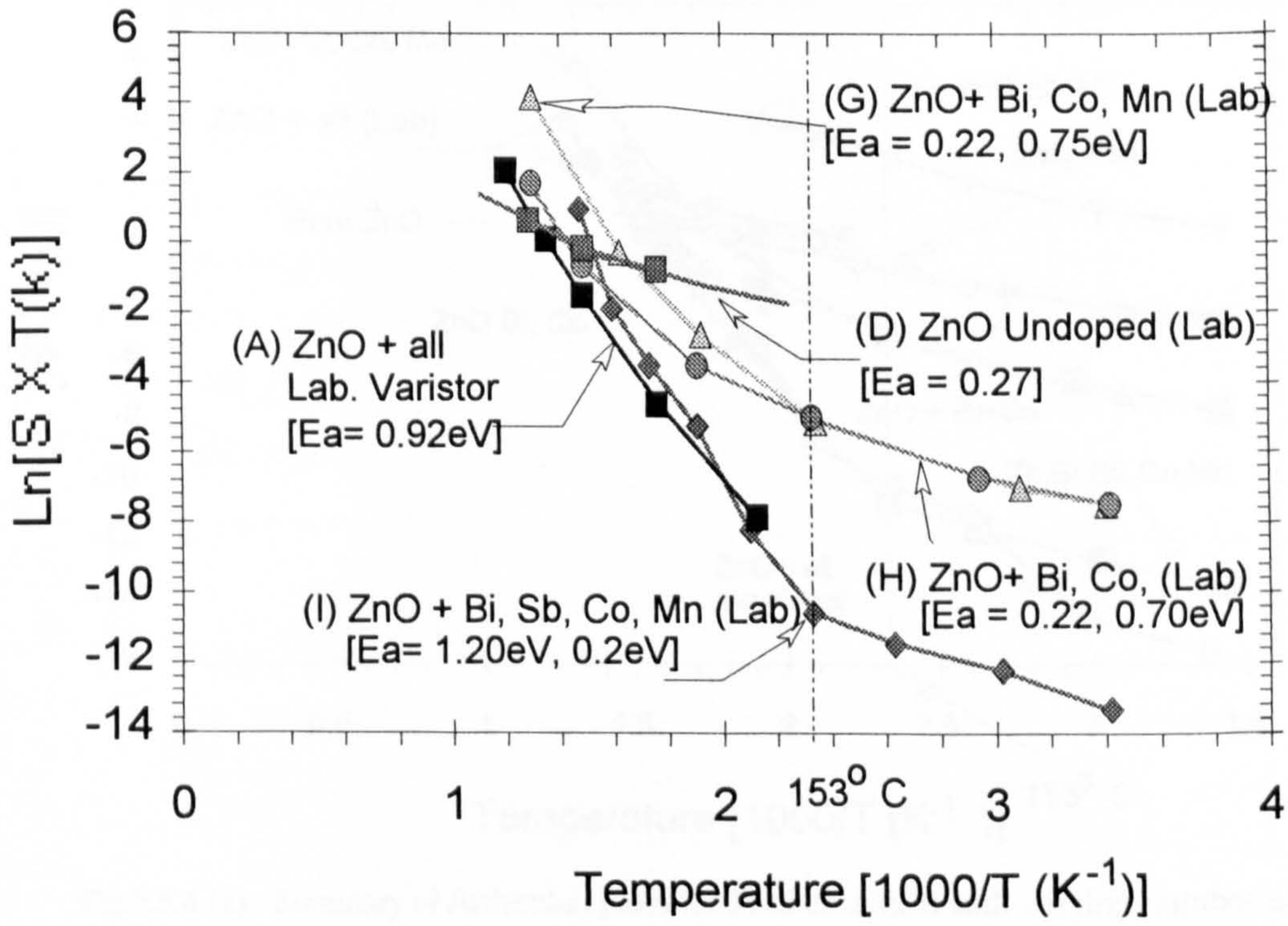


Fig. 5.5 4 (c) Arrhenius plot for ZnO ceramic doped with **(G)** Bi, Co, Mn **(H)** Bi, Co and **(I)** Bi, Sb, Co, Mn. Their respective Ea values are also shown on the diagram. For comparison, plots of nominally undoped ZnO ceramic (D) and the ZnO ceramic with varistor composition (A) are shown. Samples synthesised in the laboratory are labelled as (Lab).

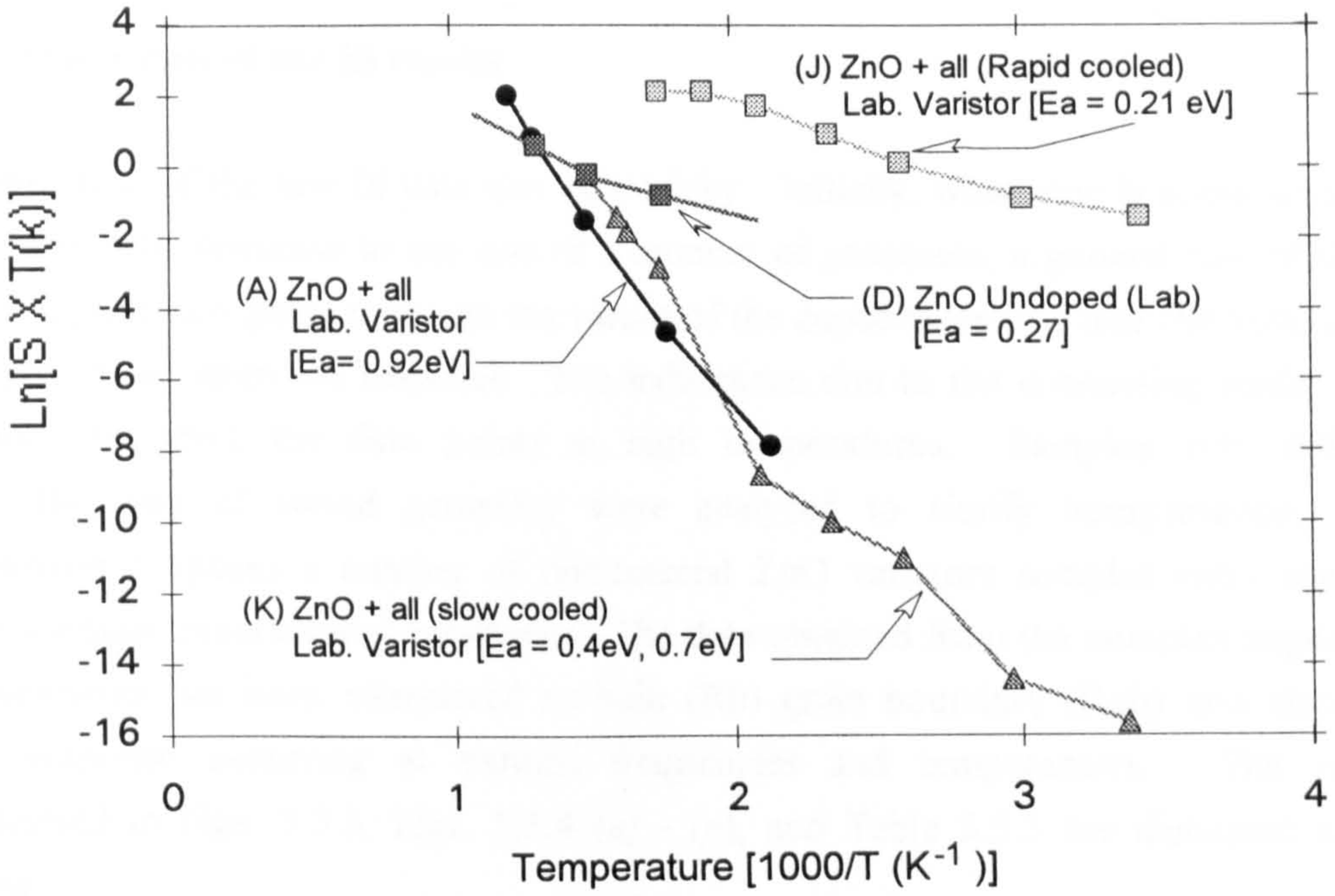


Fig. 5.5 4 (d) Arrhenius plots for ZnO ceramic doped with **(J):** Bi, Sb, Co, Mn Cr rapidly cooled, **(K):** Bi, Sb, Mn, Co, Cr slow cooled. Their respective Ea. values are shown in the diagram. For comparison, plots of nominally undoped ZnO ceramic (D) and the ZnO ceramic with varistor composition (A) are also shown. Samples synthesised in the laboratory are labelled as (Lab).

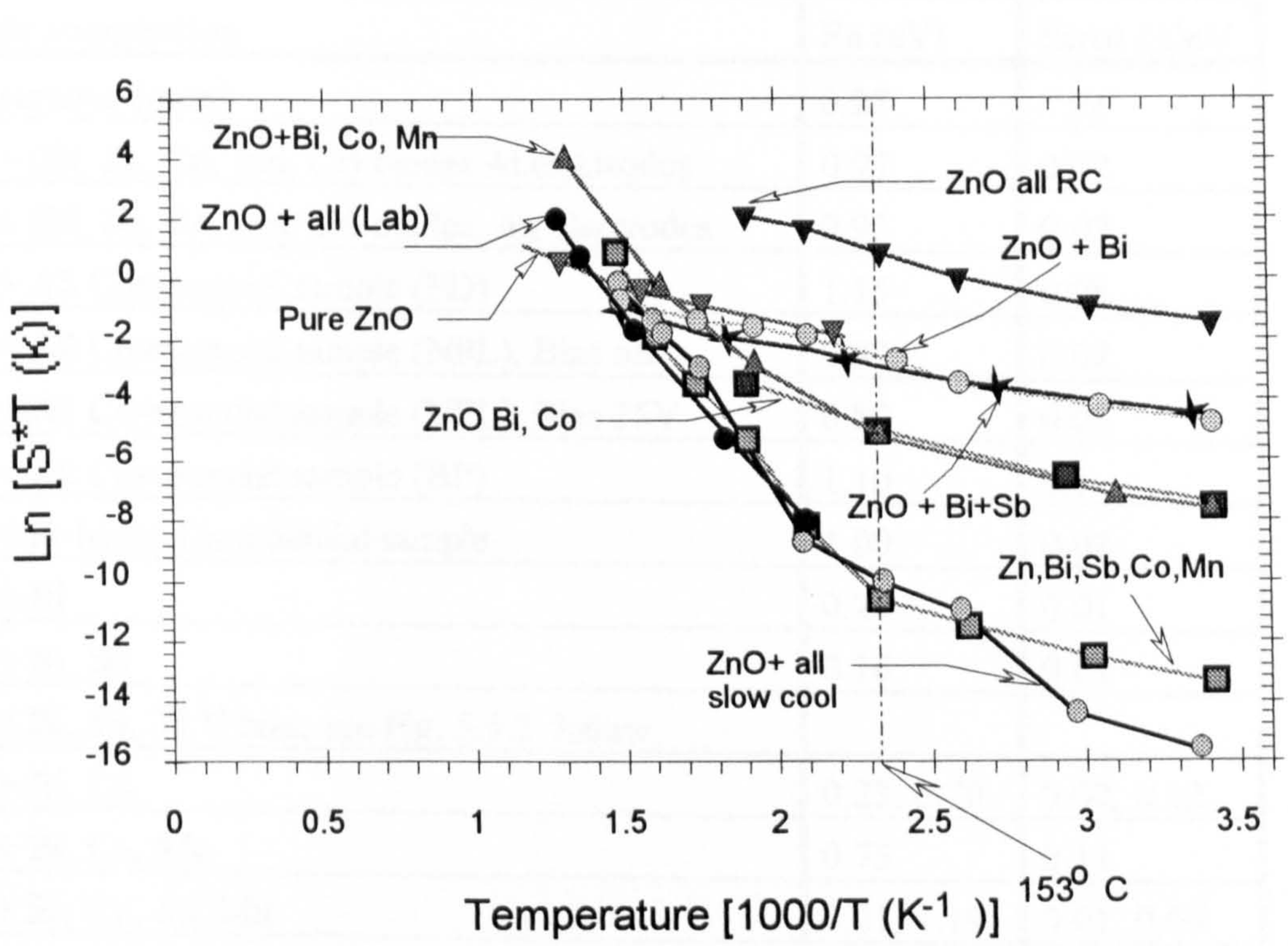


Fig.5.5.4 (e). Summary of Arrhenius plots for ZnO ceramics with varying number of additives. Synergetic effect of the combination of various additives results in types of processes giving rise to their respective Ea values. As the number of additives in to ZnO increases, the processes corresponding to Ea ≈ (0.20eV - 0.35eV) are progressively depressed, and upon complete doping, only the processes prevailing at Ea of ≈ 0.9 - 1.1 eV remains dominant.

5.5.2 Discussion of the IS results

Interpretation of the raw IS data can very tricky. Initially, when one is about to assign the semicircular response to any one of a number of processes, a general rule of thumb can be applied as a guide to assign the values of the capacitance to either the bulk, grain-boundary or an electrode response. The inductance due to the connecting leads, has a tendency to affect the data points at high temperatures. Samples with different electrodes, and of varied geometry were analysed to clarify interpretation. For comparison purposes a number of commercial ZnO varistors samples were analysed under a similar experimental conditions. The data obtained from the complex impedance measurements has been interpreted as bulk (Rb) grain boundary (Rgb) and electrode (Rel) response occurring at various frequencies and temperatures. The results summarised in Figs. 5.5.3, Figs. 5.5.4 (a) - (e), and Table 5.5.5 are discussed in this section.

Table 5.5.5. Summary of the IS data taken from the Appendix **(ApndxTable 1-13)**.

Sample composition	Ea (eV)	Error (±)eV
ZnO ceramic (pure)	0.27	0.04
ZnO + (Bi, Sb, Co, Mn, Cr) oxides Al.electrodes	0.97	0.02
ZnO + (Bi, Sb, Co, Mn, Cr) oxides, Ag electrodes	0.93	0.07
ZnO + All Commercial sample (PD)	1.15	0.05
ZnO + All Commercial sample (NPL), Bias off	0.93	0.02
ZnO + All Commercial sample (NPL), Bias 35V	0.89	0.03
ZnO + All Commercial sample (BP)	1.10	0.1
ZnO + Pr based Commercial sample	1.00	0.02
ZnO + Bi	0.20	0.01
ZnO + Bi, Sb	0.16	0.01
ZnO + Bi, Sb, 35 V bias, see Fig. 5.5.3 below		
ZnO + Bi, Co	0.23, 0.70	0.02, 0.12
ZnO + Bi, Co, Mn	0.75	0.11
ZnO + Bi, Co, Sb, Mn	0.21, 1.19	0.01, 0.09
ZnO + (Bi, Sb, Co, Mn, Cr) Rapid Cool	0.21	0.02

5.5.3.1. Electronic conduction in ZnO ceramic

The basic equation which relates the conductivity of a material, σ, to the number of mobile charge carriers in the material, *n* and their mobility μ, is

$$\sigma = n\, e\, \mu \qquad (5.5.4)$$

where e is the charge on the mobile species (electron).

If we have no grain boundary component and carriers go into a broad conduction band then μ is only weakly dependent upon T. In this case we have

$$\sigma = n_o e \mu \exp\left\{\frac{-Eaf}{kT}\right\} \qquad (5.5.5)$$

However, it has been shown by **Tilley** [115], that when we discuss the activation enthalpy for conduction for materials such as the non-stoichiometric compounds with grain boundaries it is important to consider two components in equation 5.5.4:

(a) if the carrier concentration is activated then

$$n = n_o \exp\left\{\frac{-Eaf}{kT}\right\} \qquad (5.5.6)$$

where n_o is a constant and E_{af} is formation or ionisation energy.

and (b)
$$\mu = \mu_o \exp\left\{\frac{-Ea}{kT}\right\} \qquad (5.5.7)$$

where Ea is the activation enthalpy for hopping process over gb's or any other hopping process.

Thus, we have
$$\sigma = n_o e \mu_o \exp\left\{\frac{-(Eaf + Ea)}{kT}\right\} \qquad (5.5.8)$$

Hence equation 5.5.8 is more appropriate to represent conduction processes in non-stoichiometic ZnO, associated with ionisation of Zn interstitials (requiring Eaf) to produce electronic charge carriers and activation enthalpy (Ea) for electron hopping in the bulk and over the grain boundaries. Pure ZnO ceramic is non-stoichiometic with excess cations (Zn) present at interstitial sites. Non-stoichiometry involves the introduction of electrons which are not necessarily strongly bound to particular atoms

and can therefore conduct electricity if energy is supplied to free them from the places where they may be trapped. Thermal energy is often sufficient for this purpose, and in such cases as observed here, the electronic conductivity rises with increasing temperature. The ionization energy of the cation is small (Ea = 0.27eV) and the conductivity of pure ZnO ceramic increases with temperature (Fig. 5.5.3.). **Sukkar** *et al* [28] have reported ionisation energy Ea, of singly ($Zn_i^{\cdot}$) and doubly ionised ($Zn_i^{\cdot\cdot}$) to be around 0.05eV and 0.20eV respectively. ZnO ceramic with varistor composition (ZnO + oxides of Bi, Sb, Mn, Co, and Cr) yielded a single slope with an Ea of ≈ 0.92eV. Respective Ea values of the commercial Bi-and Pr-based ZnO varistors are 1.14eV and 1.01eV. These Ea values in both pure and doped ZnO ceramic can be explained by considering the formation of the charge carriers and their transport mechanisms with respect to eqution 5.5.8. Hopping of the charge carriers both across the grain boundaries and through the bulk would be expected. Charges may cross potential barriers by (1) thermionic emission, (2) diffusional hopping, and (3) tunneling in the case of very narrow barriers. In electronic ceramics, the thermoionic emission for highly mobile electronic carriers and the diffusional hopping for less mobile carriers including ions have to be considered [61,74].

Charge transport across the grain boundary is a complex phenomenon and depends sensitively on the density of the grain boundary **(GB)** states. Due to less dense packing of atoms, grain boundaries **(Gbs)** have relatively open structure and transport of atoms or ions along the **GB** planes either by diffusion or drift is often favourable compared to the transport through the bulk lattice. The oxygen transport in ZnO varistor are fast even at temperatures regime <400K and above [74]. This **GB** diffusion of oxygen along grain boundaries is known to show a considerable impact on the leakage current at higher temperatures.

Hence, in this work activation energy of about 0.27eV are probably due to the formation and hopping of electronic charge carriers from singly and doubly ionised Zn interstitials in the pure ZnO ceramic where there is relatively small grain boundary impedance. In the fully doped ZnO ceramic, higher activation enthalpy of around 1.1 eV have been measured. This higher values probably accounts for formation and transport of charge carriers from ionised donors across active **GB**. Consequently their activation energy is much higher in this case (Table 5.5.6). ZnO ceramic synthesised with a varying combination of additives, results in two slopes in their Arrhenius plots Figs. 5.5.4 (b) - (e). Curve F in Fig. 5.5.4 (b) show that ZnO with Bi and Sb additives results in an Ea of ≈ 0.20eV. It can be said that Bi and Sb as the sole additives in ZnO ceramic do not form very resilient space charge regions and the barriers thus formed are also very sensitive to a low voltage bias (35V) as shown in Fig. 5.5.3. However, when 35V bias was applied to a sample of varistor composition the resultant effect was found to be negligible. ZnO

ceramic doped with Bi and Co results in a curved plot (curve H), possibly associated with two slopes at Ea of 0.22 and 0.70 eVs as shown in Fig. 5.5.4 (c). ZnO ceramic samples with up to four dopants (Bi, Sb, Co, Mn) clearly show Arrhenius plot with two different slopes. Their corresponding Ea values are 0.20eV and 1.20 eV.

Fig. 5.5.4 (d) show the Arrhenius plot (curve G) for ZnO ceramic samples doped with all the additives, but had undergone rapid cooling from high temperature. The resultant values for Ea is ≈ 0.21eV, exhibiting higher conductivity then any of the other preparations including the undoped ZnO ceramic. This probably explains why **Olsson** ***et al*** [48] failed to observe any varistor behaviour in samples undergoing similar preparation (discussed in Chapter 2, section 2.2).

ZnO samples doped with solely, Bi and Sb as additives does not exhibit high resistivity (Fig. 5.5.4 (b)). Although the elements Bi and Sb would segregate to grain boundaries, soluble dopants such as the Mn, Co are also necessary to enhance the donor defects in the grain core in order to stabilise the space charge region at the grain boundaries. Although Schottky barriers are formed by a single addition of Bi dopants, deep level traps associated with Mn and Co additives are necessary to pin these barriers [23, 24. 56], so that the varistor does not switch on or pass any significant leakage current (above 0.5mA/cm^2) below threshold voltage (Vth). This point is illustrated in Fig. 5.5.4 (c) where further addition of Co and Mn to the above results in much higher resistivity. Likewise Bi and Co, or Bi on its own has some effect of suppressing the conductivity at low temperatures but it is clear that ZnO ceramic requires all of the five dopant additives (Bi, Sb, Mn, CO, and Cr) to result in a proper varistor with highly resistive properties at ambient temperatures. Combination of up to 4 additives oxides (Bi, Sb, Mn, Co) show that low conductive processes are observable up to a temperature range of 153°C. Beyond this temperature the rise in conductivity is probably due to a rapid increase in charge carriers arising from the ionisation of dopants. Here, the conductivity curve of samples, irrespective of any number of additives approaches a gradient similar to a sample with all the dopants. Also at higher temperature, ionic conductivity is possible by movement of ionic species such as oxygen along the grain boundary network. However, ZnO ceramic is predominantly an electronic conductor and small ionic conductivity can be swamped by the electronic conductivity. Capacitance of all the ceramic samples remained in the nF range for grain boundaries and μF range for electrode response.

Defect ionisation energies near room temperature have been estimated [28] from data in the literature (Table 5.5.6).

Defect in ZnO material	Ionisation energy (eV)
$Zn_i^{\cdot}$ donor defect	0.05
$Zn_i^{\cdot\cdot}$ donor defect	0.20
$V_{zn}^{\cdot\cdot}$ acceptor defect	≈ 0.9 - 1.0
$V_{zn}^{'}$ acceptor defect	≥ 2
$V_O^{\cdot}$ donor defect	0.50
$V_O^{\cdot\cdot}$ donor defect	≈ 2
$[D_{Zn}]$ total donor concentration	10^{18} cm^{-3}
$D_{zn}^{\cdot}$	Singly ionised donor substitutionally incorporated on zinc sites
E_D (donor ionisation energy)	2.0

The role of additives in ZnO ceramic is to produce defect species in the ceramic in order to suppress the native donor defects ($Zn_i^{\cdot}$,$Zn_i^{\cdot\cdot}$,$V_O^{\cdot}$,and $V_O^{\cdot\cdot}$) at the grain boundary by freezing the majority of Zn interstitial in the core of the grain during cooling from high temperature sintering [28]. In the ZnO varistor system this would favourably enhance the acceptor states at the grain boundary interface and donor states in the core of the grains. In the presence of $D_{zn}^{\cdot}$, such as those found in the ZnO varistor, cooling from the fabrication temperature, results in suppression of the native donor $Zn_i^{\cdot}$,$Zn_i^{\cdot\cdot}$,$V_O^{\cdot}$,and $V_O^{\cdot\cdot}$and enhancement of the acceptor $V_{zn}^{'}$ and $V_{zn}^{\cdot\cdot}$ concentrations in the grain boundary region.

This behaviour is attributed to the thermodynamics of the system where the action of defects, either as donors or as acceptors is largely influenced by the partial pressure [28]. Incorporation of additive oxides (D_{zn}) causes atomic defects to form at the grain and the grain boundary, with donor or donor like defects dominating the depletion layer and acceptor-like defects dominating the grain boundary states. The relevant defect species in ZnO are:

$$V_{zn}^{'}\ V_{zn}^{\cdot\cdot},V_O^{\cdot},\ V_O^{\cdot\cdot},Zn_i^{\cdot},Zn_i^{\cdot\cdot},\text{and } D_{zn}^{\cdot}\text{ and } D_i^{'}$$

where $D_{zn}^{\cdot}$ and $D_i^{'}$ represent all the externally incorporated donor and acceptor atoms, respectively. It has been shown [28] that, with a substantial donor doping (Dzn ≈ 10^{18} cm^{-3}), the grain boundary becomes rich in zinc vacancy concentration [Vzn"] (an acceptor) and poor in oxygen vacancy concentration [Vö] (a donor) during cooling from high temperatures. This doping results in an excess of [Vzn"] and a deficit of [Vö] at the

grain boundary - a situation which gives rise to a barrier at the depletion layer and effectively eliminates the need for a separate interface layer at the grain boundary.

Summary of IS results

Results from this study has shown that if ZnO ceramic is doped with less then the five basic oxides (Bi, Sb, Mn, Co and Cr), it fails to suppress low Ea related processes. In this respect, the interrelated effect of various dopants to enhance grain boundary resistivity is largely influenced in the following order:

Bi <	Bi+Sb <	Bi+Co <	Bi+Co+Mn <, and	Bi+Co+Mn+Sb <	ZnO + all
ZnO + all (rapid cooled) <			ZnO + all (slow cooled)		

In ZnO of varistor composition, increase in conductivity with temperature may be due to carriers hopping across the grain boundary with relative ease. Addatives such as Co, Mn participating as donors to enhance the conductivity in the core of the ZnO grain, while, the segregated additives such as Bi, at the grain boundaries interface contributes as acceptor states by providing oxygen rich paths as discussed in section 5.5. Addatives appear to suppress the low temperature conduction. In ZnO ceramic, addition of dopant results in a decrease in conductivity at lower temperature but at higher temperatures rapid increase in conducitivy is due to donor ionisation leading to an increased number of charge carriers. ZnO ceramic of a varistor composition, including all the commercial samples, did not show any conduction corresponding to low activation energies. At higher temperatures conductivity increased and the resultant activation process is associated with Ea of about 1.0 eV. This is explained as follows:

Varistor samples with all the additives results in the occupation of the majority of the Zn vacancies at the grain boundary interface, and consequently reduction in the Zn interstitial at the grain boundaries. This can result in a high number of zn interstitials (donors) in the grain core with acceptors at the grain boundaries. A space charge depletion region is thus formed at the grain boundaries (**GBs**) resulting in increased resistance and making the **GBs** highly insulating. At high temperatures these barriers can be surmounted by the charge carriers by thermionic process. Additionally as the temperature is increased the transport of charge carriers along the grain boundary path becomes possible in ZnO with dopants. In pure ZnO ceramic such path is perhaps very narrow and significantly restricts the ionic movements along the grain boundaries. In comparision to pure ZnO ceramic, a higher degree of temperature dependent conductivity is observed in the doped ZnO ceramic of varistor composition.

5.6. I:V - Measurements of ZnO ceramic

5.6.1 Results

I:V measurements were undertaken on samples with different dopant compositions as summarised in Table 5.6.1. The break down voltage of the varistor samples are measured at $E_{0.5}$ (0.5mA/cm^2). The non-linear coefficient α has been calculated using equation (2.1.-4) discussed in Chapter 2, section 2.2.4.2.

$$\alpha = \frac{\log I_2 - \log I_1}{\log V_2 - \log V_1}$$

Using the above equation, the current ranges for the α values cited in this work, are between 0.5 and 1mA. Measurements were undertaken at ambient in the laboratory.

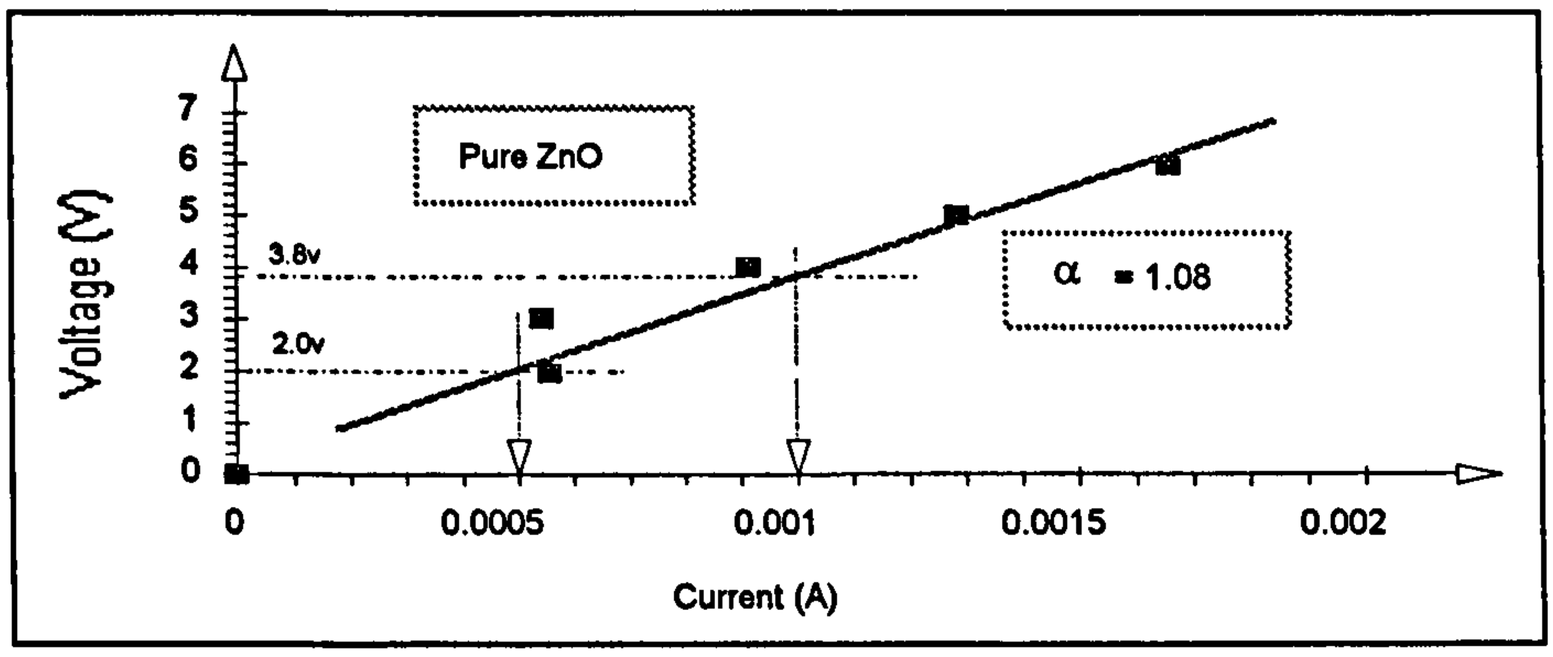
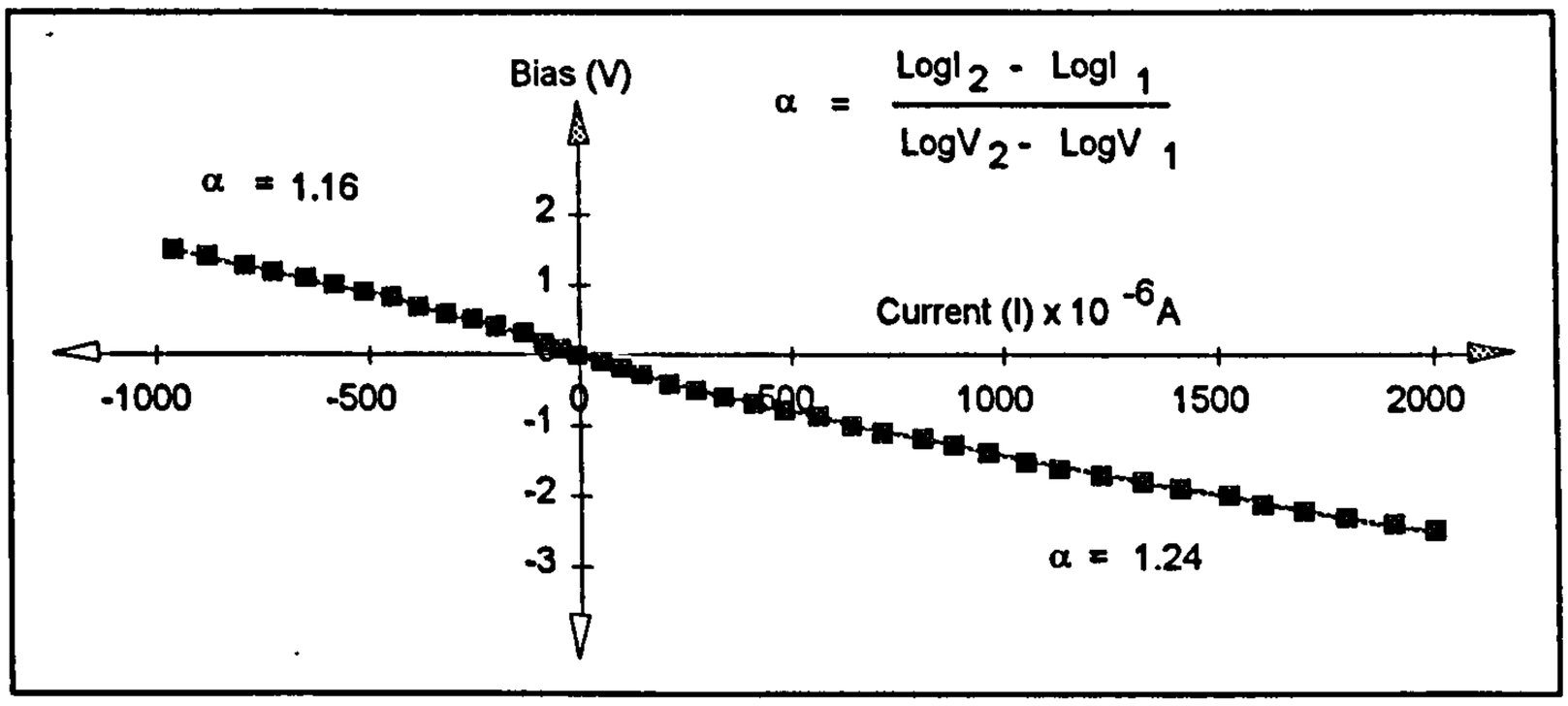


Fig. 5.6.1. I:V characteristics of pure ZnO ceramic sintered at 800^{o}C. The non-linear coefficient, $\alpha \approx$**1.08** is measured between 0.5 and 1mA. I:V measurement on the undoped ZnO ceramic sintered at 1250^{o}C was not possible here due to its very small resistance.



$$\alpha = \frac{\text{Log}I_2 - \text{Log}I_1}{\text{Log}V_2 - \text{Log}V_1}$$

Fig. 5.6.2. I:V characteristics of ZnO **bi-crystal** sample (with Bi at the interface) measured in both directions. The non-linear coefficient, $\alpha \approx$**1.2** measured between 0.5mA - 1mA. Threshold breakdown of about 1 V.

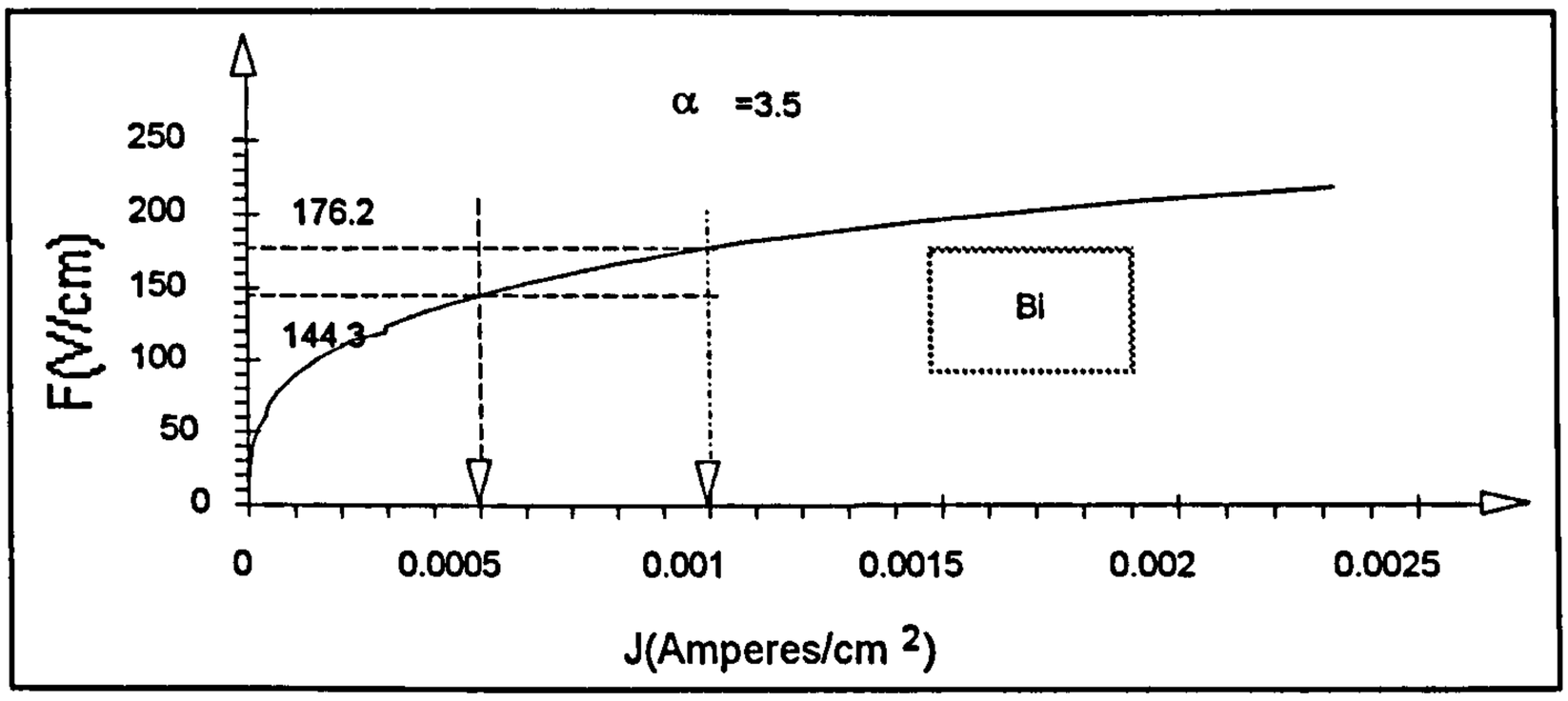


Fig 5.6.3. (a) I:V characteristics of the ZnO ceramic doped (0.5mol%) with the oxide of **Bi** sintered at 1250°C. The non-linear coefficient, **α = 3.5, sample dimensions:** 2.15mm thickness x 10.5mm dia., giving a break down voltage of about 31V.

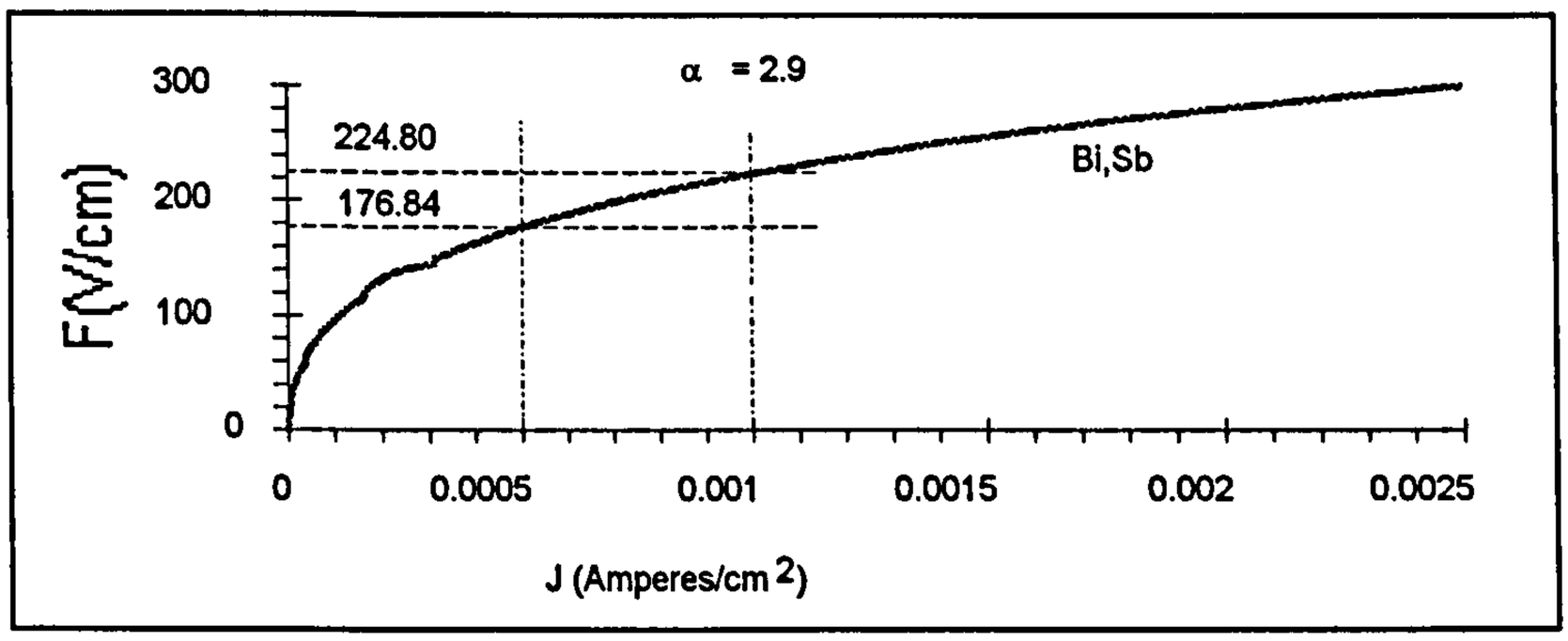


Fig 5.6.3. (b) I:V characteristics of the ZnO ceramic doped (0.5mol%) with the oxides of **Bi and Sb,** sintered at 1250°C. The sample was highly resistive and the non-linear coefficient, α = 2.9. Sample dimensions: 2.05mm thickness x 10.05mm dia., giving a Breakdown voltage of 36V.

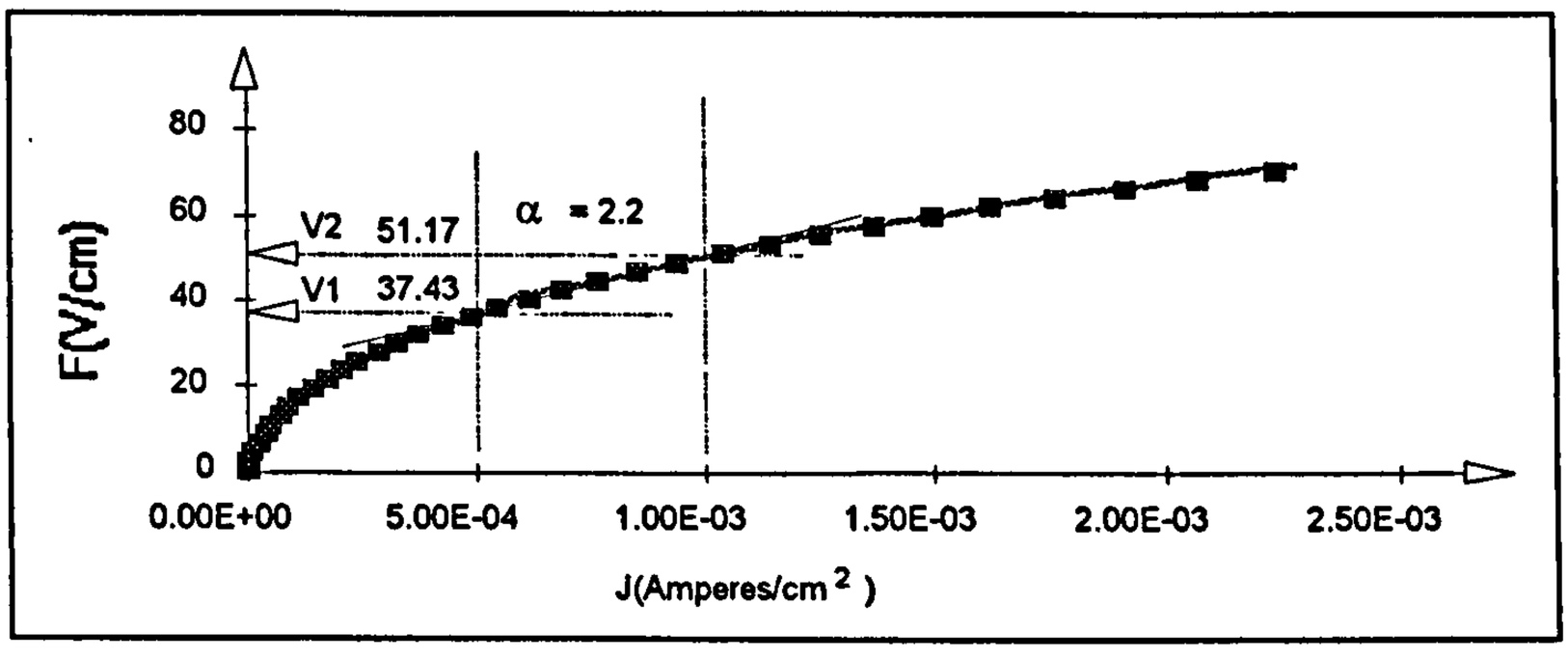


Fig 5.6.3. (c) I:V characteristics of the ZnO ceramic doped (0.5mol%) with the oxides of **Bi and Co,** sintered at 1250°C. The non-linear coefficient, **α = 2.2,** sample dimensions: 2.35mm thickness x 10.6mm dia., giving a break down voltage of about 9V.

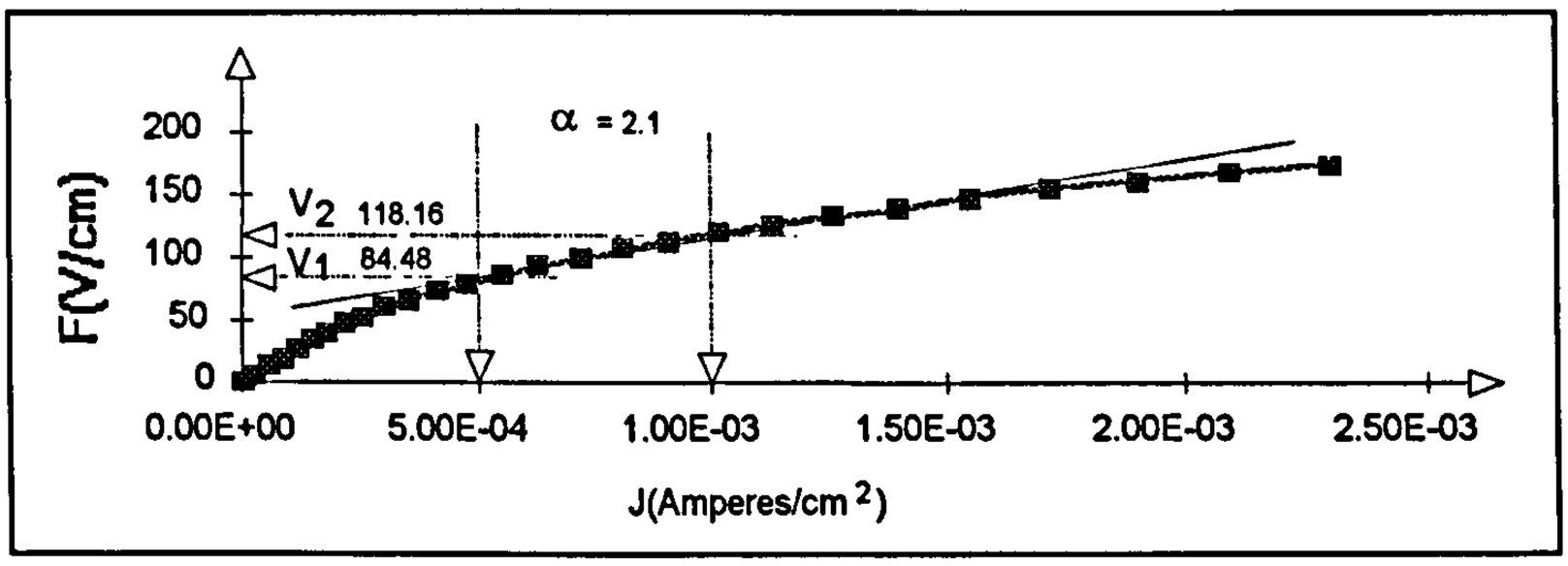


Fig 5.6.3. (d) I:V characteristics of the ZnO ceramic doped (0.5mol%) with the oxides of **Bi, Co** and **Mn** sintered at 1250°C. The non-linear coefficient, α **= 2.1,** sample dimensions: 1.5mm thickness x 10.5mm dia., giving a break down voltage of about 12 V.

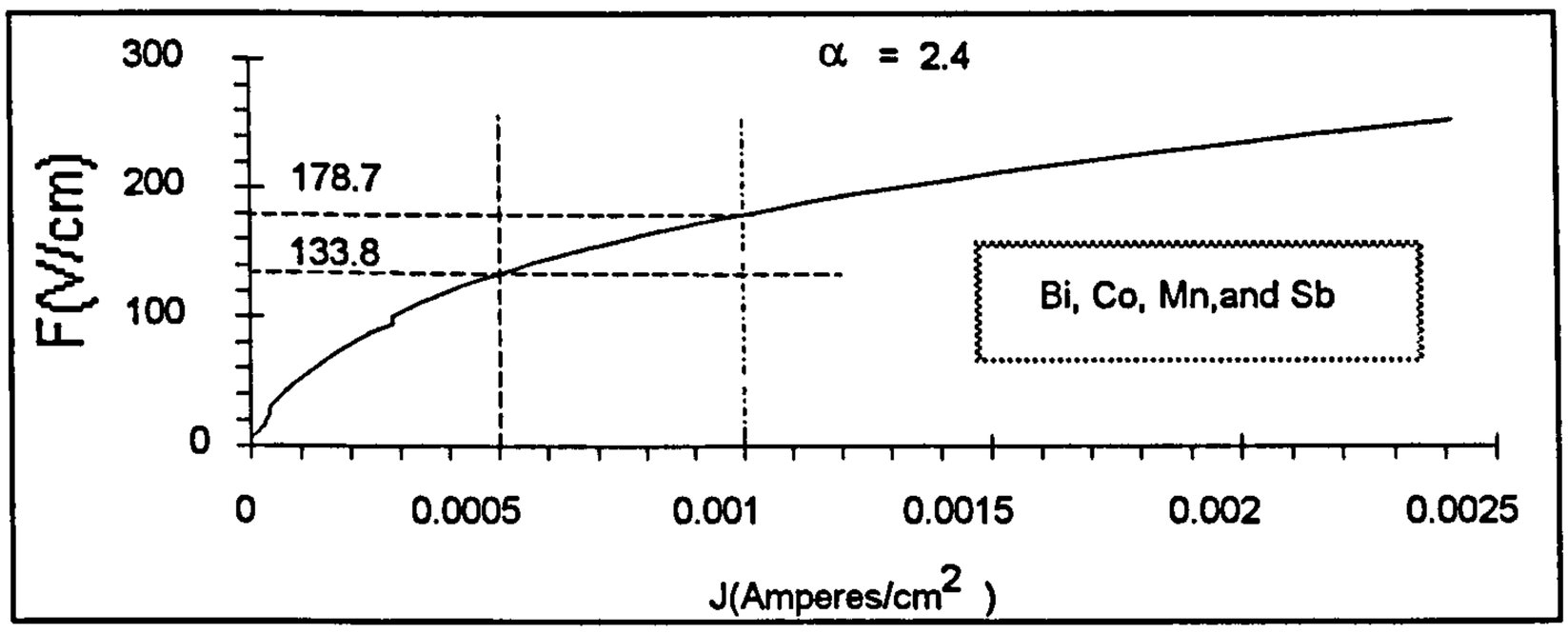


Fig 5.6.3. (e) I:V characteristics of the ZnO ceramic doped (0.5mol%) with the oxides of **Bi, Co, Mn** and Sb, sintered at 1250°C. The non-linear coefficient, α **= 2.4,** sample dimensions: 1.7mm thickness x 10.5mm dia., giving a break down voltage of about 23 V.

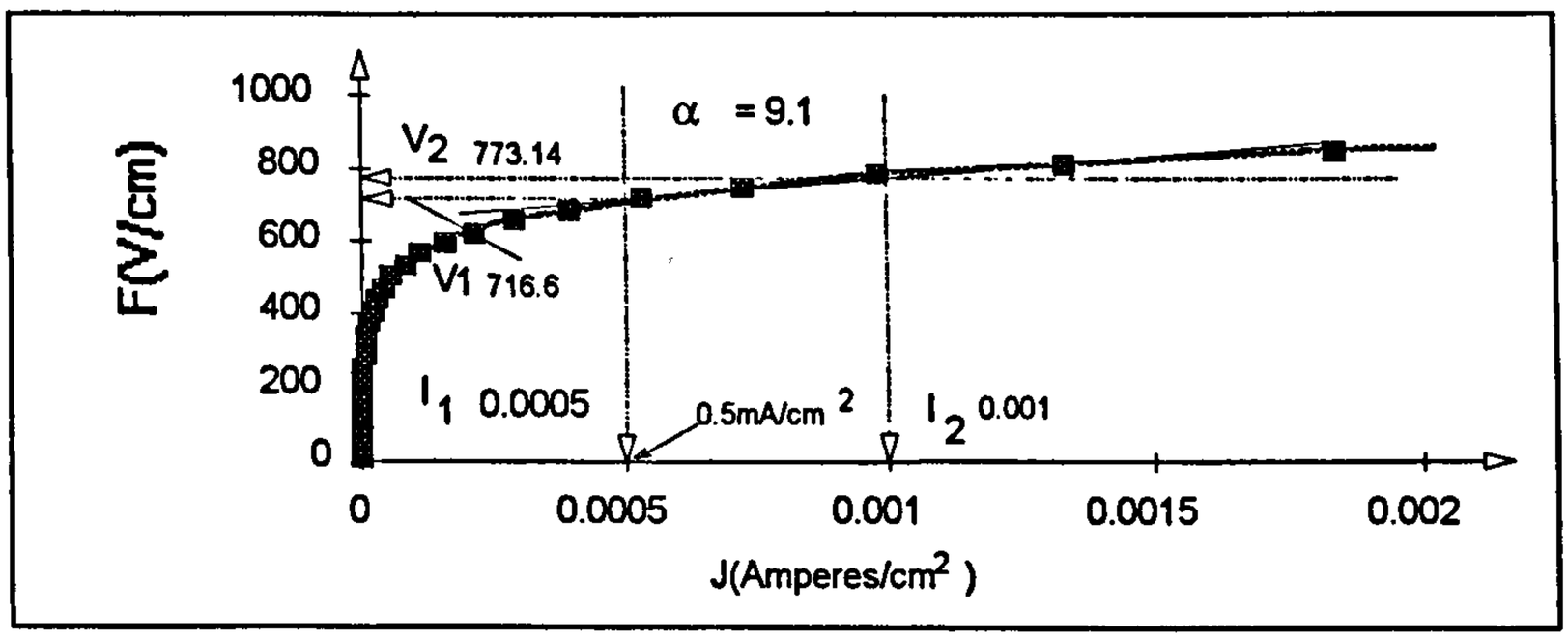


Fig 5.6.3. (f) I:V characteristics of the ZnO ceramic, doped (0.5mol%) with the oxides of Bi, Sb, Mn, Co and Cr, sample initially **rapidly cooled** from 1250°C sintering and then cured at 500°C for 3 hours. The non-linear coefficient, α = 9.1, sample dimensions: 1.6 mm thickness x 10.15 mm dia., giving a break down voltage of about 113 V.

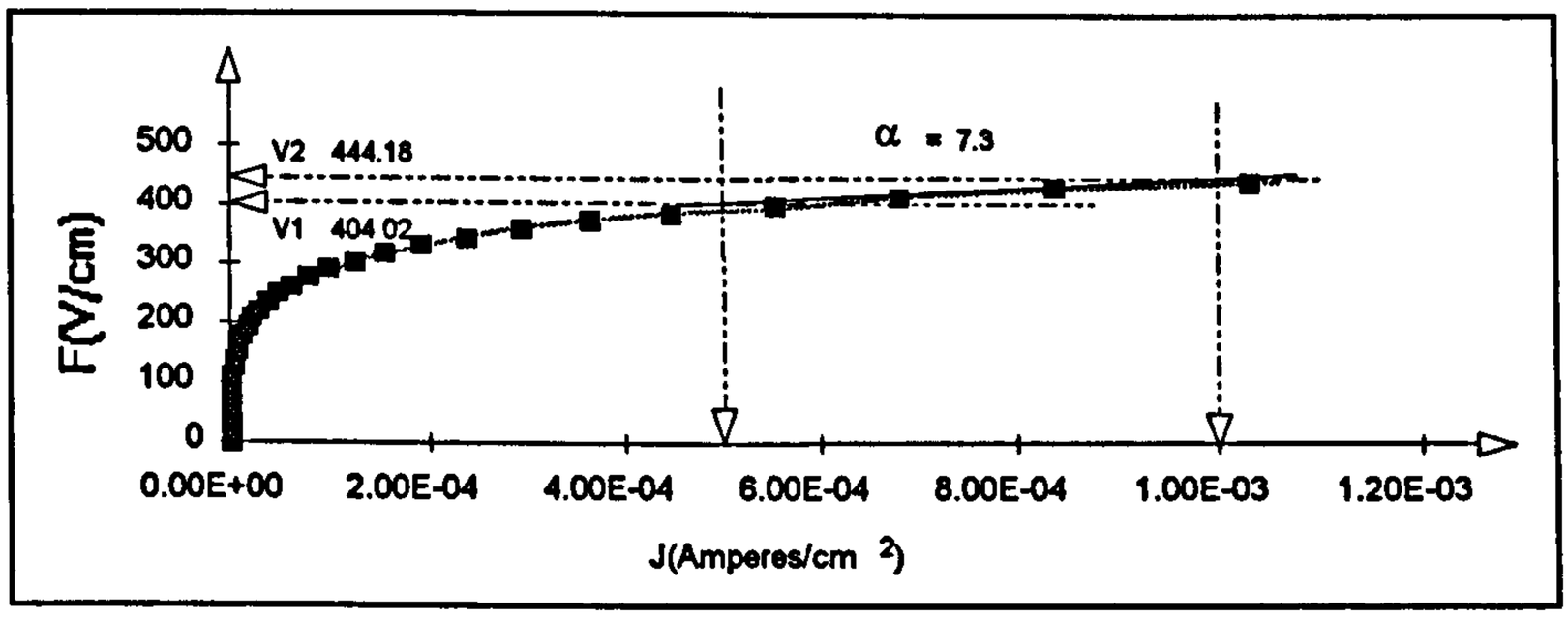


Fig 5.6.4. (a) I:V characteristics of Pr based ZnO ceramic, doped with the oxides of Pr, Co and La, sintered at 1340°C. The non-linear coefficient, α = 7.3, sample dimensions: 1.45 mm thickness x 14.97 mm dia., giving a break down voltage of about 58 V.

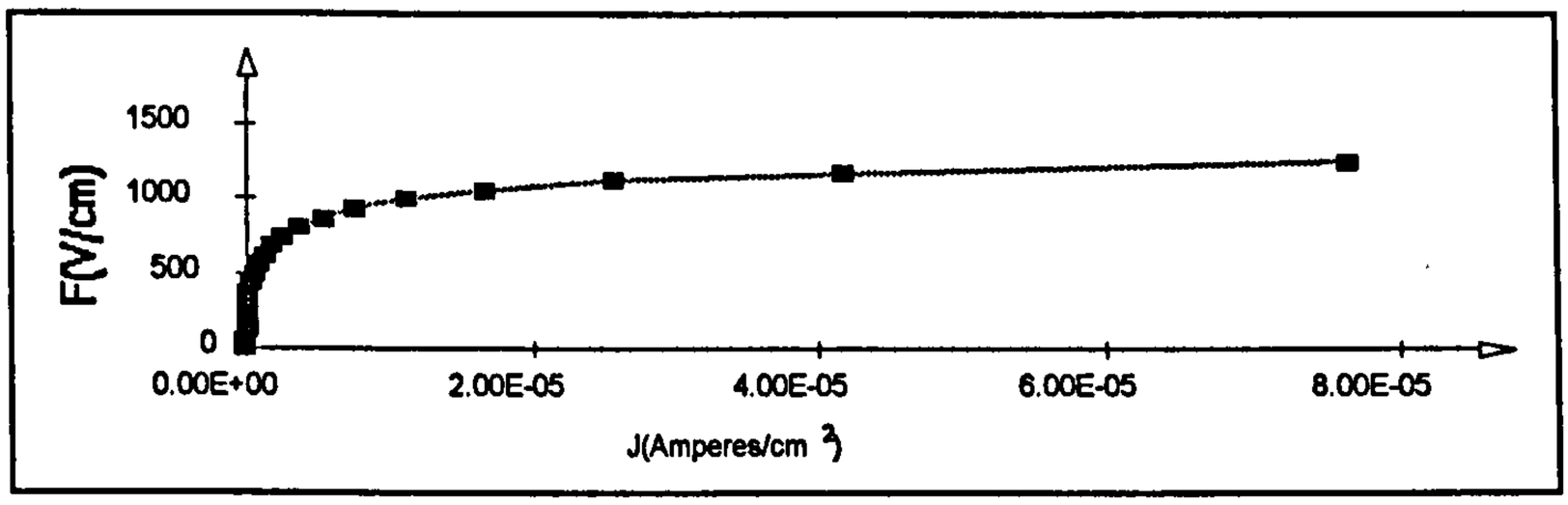


Fig 5.6.4. (b) I:V characteristics of Pr based ZnO ceramic, doped with the oxides of Pr at 0.5Mol%, Co at 1Mol% and La at 0.5Mol%, sintered at 1250°C for 30 min. The sample was highly resistive and the non-linear coefficient, α is usually measured at E0.5. In this case it is out of range but presumed to be over 50. Sample dimensions: 1.62mm thickness x 14.9 mm dia. The break down voltage is around about 200 V.

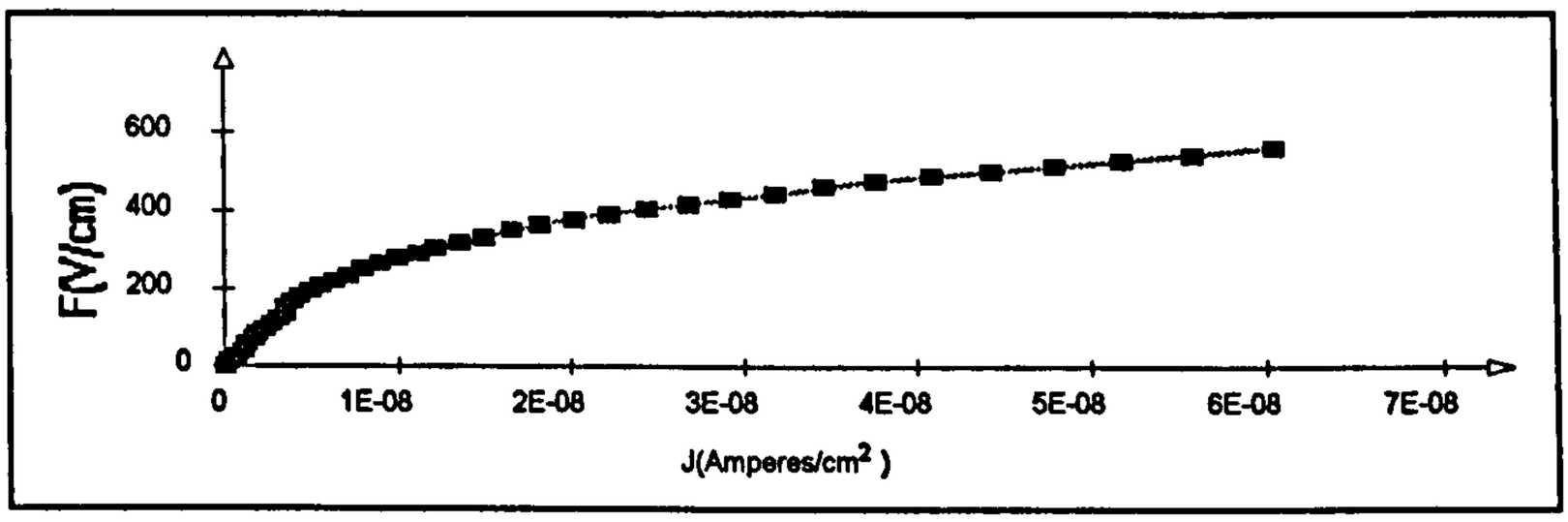


Fig 5.6.5. (a) I:V characteristics of a commercial Bi based ZnO varistor (PD, good, degraded in oil, 1 dip of 4 sec.). The sample was highly resistive and the non-linear coefficient, α usually measured at $E_{0.5}$. In this case it is out of range. Manufacturer has quoted the following values for non-linear coefficients: at 0.1 - 1mA α=67, for 1mA - 10mA, α=56, for 1mA - 100mA, α=78. Sample dimensions: 3.6mm thickness x 16.2 mm dia. The break down voltage is around about 663V.

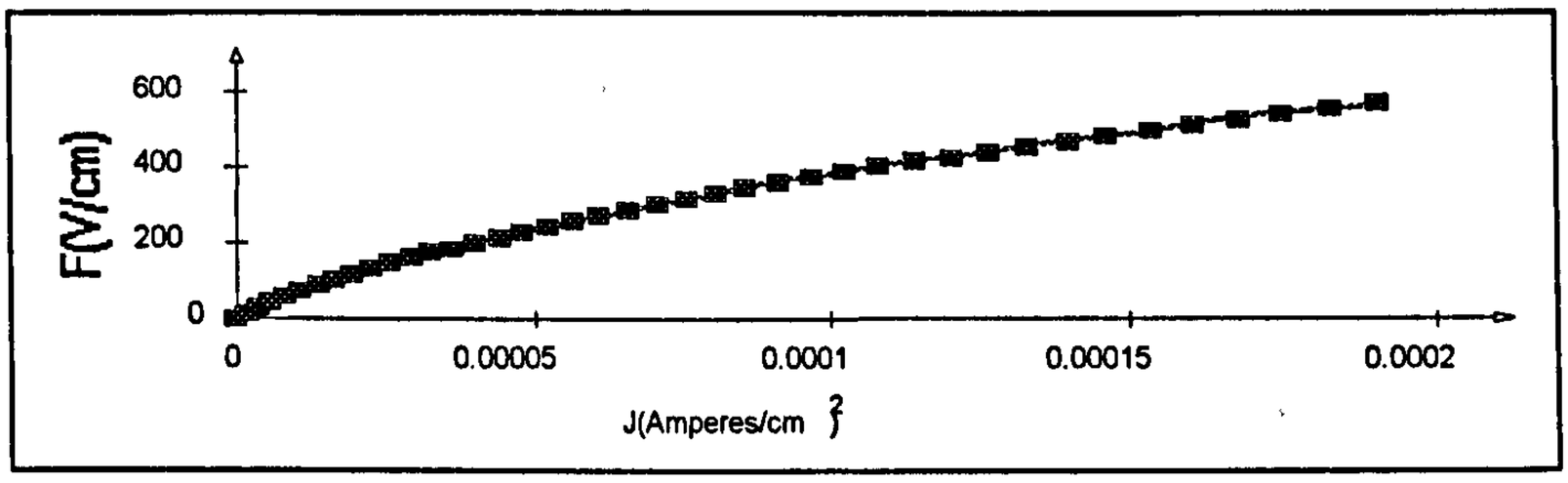


Fig 5.6.5. (b) I:V characteristics of a commercial Bi based ZnO varistor (PD, 'bad', degraded in oil, 7 dips of 30 seconds each). The sample was highly resistive and the non-linear coefficient, α is usually measured at $E_{0.5}$. In this case it is out of range. Manufacturer has quoted the following values for non-linear coefficients: at 0.1 - 1mA α=1.7, for 1mA - 10mA, α=2.7, for 1mA - 100mA, α=9.3. Sample dimensions: 3.5mm thickness x 16.2 mm dia. The break down voltage is around about 288V.

5.6.2 Discussion of I:V results

Table 5.6.1. Summary of I:V results.

Fig. No	Sample details	Vth.	α @ (0.5mA -1mA)
5.6.1	Pure ZnO sint. 800°C	/	1.08
5.6.2	ZnO bi-crystal (Bi)	1	1.2
5.6.3.(a)	ZnO + Bi	31	3.5
5.6.3.(b)	ZnO + Bi, Sb	36	2.9
5.6.3.(c)	ZnO + Bi, Co	9	2.2
5.6.3.(d)	ZnO +Bi, Co, Mn	12	2.1
5.6.3.(e)	ZnO +Bi, Sb, Co, Mn	23	2.4
5.6.3.(f)	ZnO + Bi, Sb, Mn, Co, Cr, (RC)	113	9.1
5.6.4.(a)	ZnO +Pr, Co, La (1340°C)	58	7.3
5.6.4.(b)	ZnO +Pr, Co, La (1250°C)	200	≈50
5.6.5.(a)	ZnO + all (P.D., Com.) 1 dip in oil 200°C (4 Seconds)	663	67
5.6.5.(b)	ZnO + all (P.D., Com) 7 dips in oil 200°C (30 sec.)	288	1.7

I:V characteristics of pure ZnO ceramic sintered at 800°C are shown in Fig. 5.6.1. The non-linear coefficient, $\alpha \approx 1$ confirms that pure ZnO does not have any varistor properties. Although **Fujitsu** *et al* [113] proposed the possibility of varistor behaviour in a porous ZnO ceramic, the pure ZnO sample in our work was sintered at 800°C, with

plenty of porosity (discussed here in section 5.1.3.2) but failed to show any non-linearity. A pure ZnO ceramic sample sintered at 1250°C had much reduced porosity and also showed linear I:V characteristics with very small resistance. Fig. 5.6.2., shows the I:V characteristic of a ZnO bi-crystal sample (with Bi at the interface) measured in both directions. This analysis was undertaken inside the SEM chamber. Contacts were made of gold wires, fixed with silver based vacuum compatible dag, on the either side of the single interface. Measurements were taken using similar procedures as described in Chapter 3, section 3.6, with the only difference being in the power source which in this case was a voltage generator associated with Matelect unit (discussed in Chapter 3, section 3.1.3.3.). The non-linear coefficient, $\alpha \approx 1.2$ has been measured for this sample. I:V measurement of ZnO ceramic with Bi as a single dopant show a value of the non-linear coefficient, $\alpha = 3.5$. The α value for non-linear characteristics, as shown in Fig 5.6.3. (a), is much higher when compared to the bi-crystal sample, but it is comparable to that initially measured ($\alpha = 4$) by **Matsuoka** [9].

Addition of Co with Bi appears to have a suppressing effect on the non-linearity coefficient. Fig 5.6.3. (c) show I:V characteristics of the ZnO ceramic doped with the oxides of Bi and Co, with non-linear coefficient, $\alpha = 2.2$. This is much smaller then a value of $\alpha = 13$ quoted by Matsuoka [9]. A combination of Bi and Sb yields α, of around 3, as shown in Fig 5.6.3. (b). Fig 5.6.3. (d) show I:V characteristics of the ZnO ceramic doped with the oxides of Bi, Co and Mn. The non-linear coefficient, $\alpha = 2.1$ has been measured for this sample.

Fig 5.6.3. (e) shows I:V characteristics of the ZnO ceramic doped with the oxides of Bi, Co, Mn and Sb, with a non-linear coefficient, $\alpha = 2.4$. I:V characteristics of the ZnO ceramic, doped (0.5mol%) with the oxides of Bi, Sb, Mn, Co and Cr, (sample initially rapidly cooled from 1250°C sintering and then cured at 500°C for 3 hours) yielded a 3 fold increase in the non-linearity coefficient ($\alpha = 9.1$) as shown in Fig 5.6.3. (f). According to **Olsson *et al.***, [48] This improvement in non-linearity is due to the heat treatment which presumably allows oxygen to accumulate at the ZnO interface by diffusion.

Fig. 5.6.4. (a) show an I:V characteristics of Pr based commercial ZnO ceramic varistor, doped with the oxides of Pr, Co and La, sintered at 1340°C. The non-linear coefficient, $\alpha = 7.3$, has been measured for this sample. A similar Pr based ZnO ceramic sample sintered at 1250°C exhibited much higher non-linear coefficient (out of range) shown in Fig 5.6.4. (b)

Fig 5.6.5. (a) shows the I:V characteristics of a commercial Bi based ZnO varistor. This sample was subjected to degradation in oil (a 4 second dip, in oil at ~ 250°C.) but it

remained highly resistive and the non-linear coefficient, α usually measured at $E_{0.5}$ is very high and out of range here. The manufacturer has quoted the following values for non-linear coefficients: at 0.1 - 1mA α = 67, for 1mA - 10mA, α=56, for 1mA - 100mA, α=78.

Fig 5.6.5. (b) show I:V characteristics of a commercial Bi based ZnO varistor. This sample was subjected to degradation in oil (7 dips of 30second each, in oil at ~ 250°C.). The sample was subjected to more severe degradation in oil, but still remained highly resistive and the non-linear coefficient, measurement was also out of range. The manufacturer has quoted the following values for non-linear coefficients: at 0.1 - 1mA α=1.7, for 1mA - 10mA, α=2.7, for 1mA - 100mA, α=9.3. This degradation in oil [86] can occur at moderate temperatures if the oil vapour can diffuse into the grain boundary regions and consequently adsorb chemisorbed grain-boundary oxygen in the ceramic (discussed in section 2.4.5). The effect of degradation can be seen on the gradient of the curves in these samples (Figs. 5.6.5 a and b).

Summary of I:V results

Zinc oxide varistors are characterised by the size of α values and the width of the range where the highly non-ohmic property is displayed. Usually they are measured by an ac impulse current source to avoid heat generation and thermal breakdown. (discussed in Chapter 2, section 2.1.5.3) In this work, only a dc power source was available and consequently the values measured are rather arbitrary and smaller then those quoted in the literature, for a number of reasons. During dc measurement a sample can heat up significantly and suffer degradation resulting in leakage current below Vth. This coupled with the limitation of the measuring apparatus restricted the α values in this work to be calculated from the degraded slope of the non-linear region (0.5mA - 1mA). The non-linear slope can change with time as the samples heat up and can also proceed to thermal run-away situation. During one such a measurement author experienced a thermal run-away situation and the sample practically 'blew up'. As a standard procedure, measurements in the industry are taken at 1mA - 10mA and 1mA - 100mA using an impulse current source to avoid heat generation and thermal breakdown.

Summary

5.7. Discussion of Experimental results

In this work, an improved understanding of the varistor phenomenon has been achieved in terms of the compositional variation of dopant additives and the resultant microscopic electrical behaviour. The literature survey showed some anomalies in the interpretation of the microstructural properties, particularly the distribution of dopant additives in the microstructure of ZnO ceramics and the formation of various phases. This has resulted in many different types of conduction models have been proposed to explain the functional properties of the ZnO varistor device.

Results obtained from a detailed microstructural investigation in this work combined with the observation of the microscopic electrical behaviour and oxygen diffusion studies, has helped to revise many aspects of the previous work in this area of research. For example, in varistors the trapping of charge at the grain boundaries has a decisive influence on the electrical transport properties through the formation of electrostatic potential barriers. From SEM-EBIC analysis in this work (discussed in section 5.2) a direct observation of these barriers, corresponding to electrically active grain boundaries has been achieved. The associated resistive contrast imaging (RCI) and line scan profiling (LSP) across a single grain boundary interface has revealed the microscopic electrical phenomena that are usually appreciated only intuitively. SEM-CL studies showed the band gap related information which can be useful to confirm, for example, the criterion for the hole induced model (discussed in section 2.4.4).

Although extensive SEM-EDAX analysis has been undertaken as reported in many past references (summarised in section 2.3.2.1), it was necessary to explore further the microstructure of ZnO doped ceramic samples with a combination of additives to clarify several points. For example, a 1μm intergranular layer was assumed in the early stages of research (work by **Morris** and **Wong** [25, 31]) but has been somewhat speculative. In this work it has been possible to clarify this point and to explain the reason for the initial speculation. Usually a lacy type of network is observed on a fractured surface of doped ZnO ceramic. This appears to have been mistaken for a continuous 1μm layer as initially proposed by Matsuoka [7] during his SEM-EDAX analysis. Varistor phenomena based around a pyrochlore PY network, as proposed by **Wong** [31] was another controversy highlighted here. As shown in our EDAX and XRD studies, in a good varistor, sintered at an appropriate sintering condition PY phase formation is not common. The origin of round craters due to the volatility of Bi oxide during high temperature sintering and their subsequent occupation by round spinel phase particles

has been clearly identified through SEM-EDAX and STEM-EDAX measurements of this work.

Studies showing the possible pathway for oxygen in ZnO ceramic has been confirmed through isotopic exchange diffusion profiles (IEDP) [using ^{18}O as a tracer] associated with the SIMS study of both pure and doped ZnO ceramics. Results of the self-diffusion coefficient of oxygen (discussed in section 5.4.2.2.) are comparable to data by Robin *et al.*, [118]. It has been possible to show graphically the spatial distribution of oxygen along the grain boundaries of the doped ZnO ceramic (discussed in section 5.4.2.4). SIMS line scan profiling provided information about the depth of penetration of oxygen in both the doped and undoped ZnO ceramic. The values for the self diffusion coefficient of oxygen D* (cm^2 $sec.^{-1}$) and the surface exchange coefficient k (cm $sec.^{-1}$) for ZnO ceramics have also been obtained from this work.

IS analysis of ZnO ceramic doped with various combinations of additives, showed the grain boundary response with capacitance in the nF range. Arrhenius plots of the IS data of the undoped sample produced a single straight line curve and the doped sample produced an additional steeper curve (discussed in section 5.5.3.1). The influence of dopant additives has been to suppress conductivity at low temperatures ($< \approx 153^oC$) followed by a steeper increase thereafter. To explain the charge transport in this material, the activation enthalpy for conduction is discussed in terms of two components: (a) formation or ionisation energy (Eaf) and (b) activation enthalpy for hopping process (Ea).

As a summary of the role of additives in ZnO ceramic, the following points are discussed:

1. Grain boundaries are enriched by oxygen transported through a lacy network of Bi_2O_3 which provides a fast oxygen pathway in ZnO ceramic. This lacy type of Bi_2O_3 network is proposed to act as a 'pipe line' to replenish oxygen inside the bulk of the sample, where it percolates at the smallest grain boundary interface. Bi_2O_3 is a well known oxygen ion conductor. Studies of polymorphism of bismuth oxide by **Harwig *et al.***, [119] has shown that δ-Bi_2O_3 (stable at $\approx 729^oC$) exhibits a very high ionic conductivity. Such oxygen diffusion paths in pure ZnO ceramic are not observed, and the oxygen diffusion is restricted to few grain boundaries at the surface. Undoped samples consequently do not exhibit significant varistor behaviour. Oxygen depletion is also known to reduce the insulating properties of the grain boundaries and consequently degrade the varistor. Hence, the degradation of a commercial varistor from oil vapour can be due to the reduction of oxygen at the grain boundaries. The oil begins to oxidise at moderate temperatures (120-200°C) with C=C double bonds adsorbing chemisorbed grain boundary oxygen in this case [86]. In the case of a thick intergranular layer at the

ZnO//ZnO interface, (discussed in section 2.4.3.2) resultant Schottky barriers would be separated and are likely to suffer asymmetrical deformation. A dc biasing of this type of varistor would result in asymmetrical degradation of the I:V curve [56].

2. The role of the additives such as Sb_2O_3, is initially to participate in the formation process of the ZnO ceramic microstructure, where its contribution is to act as a grain growth inhibitor by reacting with Bi_2O_3 to form clusters of PY phase, helping to distribute all the impurities. At higher temperatures Sb_2O_3 accumulates as spinel phase at the triple points and moves into voids created by the highly volatile nature of Bi oxide.

3. Previous studies proposed that additives such as Co act as donors to enhance the conductivity of ZnO grains whilst Mn stabilises the Schottky barrier. Cr stabilises the physical volume during sintering and gives dimensional stability to the sintered compact, while Ti acts as a grain growth promoter [6, 46, 49]. Moreover, then SEM-EDAX and STEM-EDAX measurements in this work indicate that Cr, Ti and Sb are all finally absorbed into the spinel phase, Co and Mn are fairly uniformly distributed while Bi oxide segregates to form a Bi_2O_3 lacy network at triple points. SEM-CL, SEM-EBIC, IS and I:V measurements from this work, confirms that all the additives play an interconnected role in enhancing the final properties of the microstructure to give optimum varistor properties.

4. Results acquired using a variety of experimental techniques, particularly the SEM-EBIC work, support models based on back-to-back Schottky barriers at the grain boundary interface in the doped ZnO ceramic. Schottky barriers at the grain boundaries can result by charge trapping at the grain boundary interface. Although this can be achieved in ZnO ceramic by incorporating Bi (to provide oxygen rich pathway) as a single dopant, the barriers thus produced would need to be 'pinned' so they do not come down at voltages below threshold. **Blatter** *et al.*, [23,24] had found Mn dopant to generate deep traps and consequently 'pin' the barrier below the threshold voltage.

Conduction models (discussed in section 2.4) are proposed to explain the I:V characteristics of the varistor in the pre-breakdown and the intermediate non-linear region. Common to most of these models are back to back Schottky barriers at the ZnO grain boundaries. Diversity in these models is due to the irregular formation of a bismuth rich intergranular phase at the grain boundaries. This irregularity depends upon the level of additives and the sintering conditions during synthesis of the varistor device. Since the discovery of the non-ohmic properties of the ZnO ceramic in 1968, many models have been proposed to explain the nonohmic conduction mechanisms. Amongst these models (summarised in section 2.5), results from this work appears to be consistent with the models by **Eda** *et al.*, [56,58], **Pike** *et al.*, [55,61], **Blatter** and **Greuter** [23,24] and

Gupta *et al.*, [37], to explain many aspects of the varistor phenomenon. From the observations of the microstructures in this work, some of the earlier models based upon a continuous intergranular layer at the grain boundaries, had to be rejected. Amongst the models presented in section 2.4, results from this work support the following models:

A model by **Eda** *et al.*, [56,58] (discussed in section 2.4.3.2), takes into account the grain boundaries with and without any heterojunctions and proposes respectively the associated separated and unseparated back-to-back Schottky barriers. This is consistant with our SEM-EBIC results arising from a ZnO ceramic sample doped with a single dopant of Bi and another sample doped with the metal oxides of all five elements (Bi, Sb, Mn, Co, and Cr). Both resistive contrast imaging (RCI) and line scan profiling (LSP) of these samples show a dopant related response, giving rise to a model based on separated and unseparated back-to-back Schottky barriers (discussed in section 5.2.4). This would explain the associated asymmetrical and symmetrical degradation of the I:V curves initially observed by **Eda** *et al.*, [56,58].

A model by **Pike** *et al.*, [56,61], later modified by **Blatter** and **Greuter** [23,24] is based on the hole-induced breakdown process. This requires band gap radiation (≈ 3.3 eV) to be emitted (discussed in section 2.4.4). Results by **Mirreli** *et al.*, [111], (1988) from their study of the effect of cobalt on the electrical characteristics of ZnO ceramic, and the SEM-CL studies of this work confirm the role of Co to promote a higher impact ionisation probability and increase the hole concentration at a fixed current value. This would explain the fast response time (a few nano seconds) of the varistor.

A defect model by **Gupta** *et al.*, [37], explains the degradation during dc measurements. This model accounts for a field induced movements of the zinc interstitials, which can migrate to the grain boundary and take up a negative trapped charge to become neutral Zn+. This would effect the stability of Schottky barriers and consequently increase the leakage current to raise (above $0.5mA/cm^2$) below a voltage threshold.

All the above models are based on the back-to-back Schottky barriers which require acceptor states at the grain boundaries and donor defects in the grain core region. This is provided respectively by means of charge traps associated with oxygen at the grain boundaries and dopant additives such as Co, and Mn in the grain core [47,53,74,86,113]. Results from this work suggest that these models would only hold true for the specific morphology of the intergranular layer at the grain boundaries, which depends on the dopant additives and sintering conditions of the ceramic samples. Finally, although results from SEM-EDAX, STEM-EDAX, IS and I:V have produced useful new information (discussed in section 1.3.1) SIMS and SEM-EBIC results are perhaps the most significant novel contributions made from this work.

Conclusions

The aim of this work has been to study the microstructural properties of ZnO ceramic varistors, and improve the understanding of the varistor phenomenon in terms of the compositional variations of dopants in the microstructure, and the resultant microscopic electrical behaviour. In this work the use of a variety of experimental techniques has provided complementary information about the microscopic properties such as the electrical behaviour, morphology and compositional variations in ZnO ceramic varistors, that no single technique can provide. Results presented in section 5.1 have been useful to compare and contrast literature on ZnO varistors. Experimental results from SEM-EBIC/CL IS and SIMS (as discussed in sections 5.2, 5.3, 5.4 and 5.5), have significantly improved the understanding of the microstructural property of the ZnO ceramic varistors. Amongst the analytical techniques used in this work, a significant novel contribution to science has been made from the interpretation of the data acquired using techniques such as the SEM-EBIC-LSP and SIMS with IEDP-LSP. Examples of the variety of information obtained using a combination of both traditional and novel analytical techniques are given below:

(1) SEM/STEM-EDAX and XRD studies of ZnO ceramics sintered at 800°C, confirmed that: The pinning effect of Sb on the grain growth is particularly noticeable on samples sintered at low temperatures (800°C). Additive Sb_2O_3 reacts with ZnO at an early stage (800°C) of the sintering process, resulting in a two-fold reduction in grain size, and the formation of mainly PY (Zn_2 Sb_3 Bi_3 O_{14}) phases in the microstructure.

At high temperatures (1250°C), additive Bi_2O_3 in ZnO ceramic reacts vigorously and produces many voids on the surface of the ZnO grains. Also at high temperatures the **PY** (Zn_2 Sb_3 Bi_3 O_{14}) phase transforms to **SP** and remains present in the ceramic microstructure as round particles at the triple points and in the voids created by the volatility of Bi_2 O_3. Bi oxide also provides liquid phase during sintering and promotes grain growth. Finally in the sintered compact Bi oxide segregates at the grain boundary interfaces to form a lacy type of network. Doping elements such as the Mn and Co are soluble in ZnO ceramic. Dopants such as Cr segregate at the triple points and are absorbed into the **SP** phases. The microstructure of the ZnO ceramic varistor shows no evidence of a 1μm intergranular layer of Bi rich species as previously reported by **Matsuoka** [9]. The microstructure of the varistor is largely decorated by **SP** phases surrounded by a Bi rich lacy network. In contrast to a report by **Wong** [25] **PY** phases are not favourable for the varistor effect.

(2) SEM-EBIC studies showed distinct electrical terraces corresponding to arrays of electrically active grain boundaries in the doped ZnO ceramic. This technique enabled a direct observation of the microscopic electrical behaviour. Some grain boundaries do not display any significant terrace contrast and are presumed to correspond to bad grain boundary junctions. The quality of a varistor would then depend on the ratio of these good/bad junctions in the ZnO ceramic system.

Line scan profiling (LSP) across a single grain boundary of a ZnO ceramic sample doped with a varistor composition enabled modelling of the grain boundary with a Schottky barrier type response. This suggests back-to-back electrical barriers at the grain boundaries. However, LSP across dark and bright grain boundary contrast in ZnO doped with Bi_2O_3 as a single additive suggests separated asymmetrical types of Schottky barriers in this case. In the case of the ZnO ceramic doped with a single dopant Bi, EBIC terraces and the corresponding line-scan response has been modelled as individual Schottky barriers separated by ZnO grains. Regions with no significant EBIC terrace contrast may be an indication of a "bad" junction. Pure ZnO ceramic did not show any EBIC terraces.

(3) From the SEM-CL results a strong band edge transition around ≈ 3.3eV was observed in undoped ZnO ceramic and in one of the doped ZnO ceramic samples. This suggests the possibility of a band to band transition in ZnO ceramic. A transition at 1.8eV in the doped ceramic with the varistor composition could be due to Co dopant in ZnO. This would enhance the probability of band to band transition as would be required during the varistor action. Transitions at ≈ 2eV were only to be observed in the undoped single crystal of ZnO and were probably due to oxygen vacancies ($V_o^{\bullet\bullet}$) present as native donor defects. Transitions around ≈ 2.6 - 2.8eV are probably due to the acceptor defects (V''_{Zn}), and are specific to the doped ZnO ceramic.

(4) The distribution of dopants in ZnO has been confirmed by SIMS studies. These results complement the analysis using SEM-EDAX. Isotopic exchange depth profiling **(IEDP)** showed that the ^{18}O tracer oxygen concentration remained above the background level within the range of the profiling depth (1μm), in both doped and undoped ZnO ceramic sample. The values for the oxygen self diffusion coefficient (D*) and the surface exchange coefficient (k) for doped ZnO have been calculated to be 0.79×10^{-15} cm^2 sec^{-1} and 0.14×10^{-9} cm sec^{-1} respectively. For the undoped ZnO ceramic, the respective D* and k values are: 0.13×10^{-15} cm^2 sec^{-1} and 0.58×10^{-10} cm sec^{-1}. These values agree well with

those of **Fujitisu** *et al.*, [113], **Robin** *et al.*, [118] and are thought to represent the diffusion of oxygen into the bulk of the ZnO grains.

(5) The $^{18}O/^{16}O$ exchange SIMS line-scan profile data confirmed that: (a) Values for the diffusion coefficient along the grain boundaries are about 5 orders of magnitude greater than the diffusion into the bulk ZnO grains. There is evidence for fast diffusion along the grain boundaries in the doped ZnO ceramic. (b) That in the case of undoped ZnO ceramic sample, the diffusion tailing of ^{18}O tracer oxygen concentration rapidly drops to 0.002 at the depth of ≈ 50μm from the surface. This is typically equivalent to around 2 to 3 grains. Beyond this depth there is no significant trace of ^{18}O. In the case of the doped ZnO ceramic however, the ^{18}O tracer oxygen concentration remains over an order of magnitude higher (0.02) than the background level (Cbg = 0.002). In a good varistor, it is necessary to have good electrically insulating electrical barriers at the grain boundaries with conductive grains. Oxygen at the grain boundaries interface is largely responsible for producing acceptor states to produce these electrical barriers, while the donor state defects in the grains (produced by ionisation of cations such as the Co and Mn) provide good conductive grains. This would probably explain why the undoped ZnO ceramic does not exhibit significant non-linear varistor characteristics.

SIMS line-scan data of the doped ZnO ceramic yields the D* and k values of : 1.25×10^{-10} cm^2 sec^{-1} and 3.05×10^{-10} cm sec^{-1} respectively. For the undoped ZnO ceramic, the respective D* and k values are: 1.19×10^{-11} cm^2 sec^{-1} and 5.77×10^{-9} cm sec^{-1}. These values are significantly larger then the ones acquired by IEDP. This can be explained by fast diffusion pathways associated with arrays of a Bi_2O_3 network in the microstructure [42,119,120].

From these microstructural investigations and studies of the compositional variations of dopant additives in ZnO ceramic, a **model** has been proposed (discussed in section 5.4.2.4), showing the fast diffusion pathways to be attributed to the lacy network of Bi_2O_3 rich phases in the doped ZnO ceramic. Studies of bismuth polymorphism by **Harwig** *et al.*, [119] have shown that Bi_2O_3 oxide may exist in several crystalline phases and that it is a very good oxygen ion conductor. At room temperature, the monoclinic α-phase is the stable form. On heating, the oxide transforms at 729°C to the fcc δ-phase which is stable up to the melting point at 824°C. These transitions in Bi_2O_3 are associated with sudden changes in the electrical conductivity [119]. The conductivity in δ-phase is very high. Hence a rapid cooling may freeze some δ-Bi_2O_3, and consequently result in a leakage of the varistor device below its threshold voltage.

(6) Results from IS study have shown that ZnO doped with fewer then the five basic oxides of Bi, Sb, Mn, Co and Cr, fails to suppress low Ea related processes which are associated with leakage current in the varistor device. In this respect, the interrelated effect of various dopants to enhance resistivity is largely influenced in the following order:

Bi, < Bi, Sb < Bi, Co < Bi, Co, Mn < Bi, Co, Mn, Sb <ZnO + all	(1)
and	
ZnO + all (rapid cooled) < ZnO + all (slow cooled)	(2)

The above sequence as derived from IS, show that by increasing the number of dopants in ZnO ceramic (as shown from left to right in row 1), a progressive improvement in varistor characteristics is achieved. Row 2 illustrates that slow-cooled samples are more likely to produce improved varistor characteristics than the rapid cooled samples with all the dopants. During the sintering process favourable distribution of a particular additive (in order to contribute to the desired varistor properties) is influenced by the presence of other groups of additives and the associated sintering conditions. Hence, in addition to the necessity of all the required additives controlled sintering conditions are also crucial to produce a good varistor device. Additives such as Co, Mn participating as donors enhance the conductivity in the core of the ZnO grain, while the segregated additives such as Bi at the grain boundary interfaces contribute as acceptor states, by providing oxygen rich pathways as discussed in section 5.5.

In ZnO ceramic, addition of dopant results in a sharp decrease in conductivity. Additives appear to suppress the low temperature conduction. ZnO ceramic of a varistor composition, including all the commercial samples, did not show any conduction corresponding to low activation energies. At higher temperatures the conductivity increased and the resultant activation process is associated with (E_{af}+E_a) of about 1.0 eV. This is explained as follows:

The effect of additives in ZnO ceramics of a varistor composition is to produce a high number of donor states in the grain core and acceptor states at the grain boundaries. The resultant space charge depletion (Schottky barriers) forms at the grain boundaries, and makes the device highly insulating. At high temperatures however, these barriers can be surmounted by the electronic charge carriers (requiring higher activation enthalpy) and the conductivity increases as the dopant donors are now ionised. The activation enthalpy for conduction is

composed of two components ($E_{af} + E_a$). (a) Formation of electronic charge carriers from ionised Zn interstitial and dopant additives (E_{af}) and (b) charge transport by hopping process (E_a). The conductivity increases with temperature due to ionisation of the dopants and increased mobility via the hopping mechanism. In the pure ZnO ceramic, such an increase in conductivity with temperature is comparatively small as it is solely attributed to electronic charge generated from the ionised Zn interstitial ($E_{af} \approx 0.27$).

(7) I:V measurements showed that pure ZnO, either as a single crystal, or in a ceramic form, does not exhibit any significant varistor behaviour; ZnO with a single doping of Bi oxide exhibits varistor behaviour with a non-linear coefficient of $\alpha \approx 3.5$. ZnO ceramic with a varistor composition showed an $\alpha \approx 9$.

A combined use of the various analytical techniques in this work has provided a better understanding of how the ZnO ceramic varistor functions. Further work, as proposed in the next section would be useful to complement results in this work.

Suggestions for future work

1. It would be very useful to be able to compare the SEM-EBIC response acquired from ZnO varistor to that of $BaTiO_3$ PTCR thermistor. This would require a hot stage inside the SEM in order to study the sample at and above its switch on point (typically around 150°C). A hot stage in the SEM would also provide an opportunity to study EBIC on the ZnO ceramic varistors as a function of temperatures. Information could be very useful to relate the particular electrical terraces and line scan profiling to the leakage currents of the varistor device below threshold voltages.

2. CL analysis using an **STEM-CL** technique could be a very useful method of studying the phases and grain boundary properties with greater precision. Although quantification in the CL technique is very difficult and results acquired can be speculative, **Holt** [70] agrees that the potential use of this technique lies in its sensitivity in detecting defects.

3. SIMS with the Ga^+ liquid metal ion source (LMIS) would provide high lateral resolution (100nm) images, due to the fine focus that can be achieved with this type of source. A combination of high sensitivity and lateral resolution would be useful to probe the grain boundary regions in ZnO ceramic. Additionally, ion implanted ZnO samples with a known concentration of impurities and depth would be useful for quantification.

4. IS analysis with biasing of the sample at and near the threshold voltage would provide further information about the transport properties of charge carriers across the grain boundaries. This technique would be useful to study the degradation of varistors.

Appendices

Appendix A: Kröger and Vink notations

Kröger and Vink theory [21], presents the type of relations existing between the concentration of the imperfections in crystalline solids. This theory is regarded as, particularly suitable for studying the intricate relations between the chemistry and the physics of compound crystals.

Basic symbols used in the Kröger and Vink notation:

Defect-----> D^{ec}_{L} ec= effective charge L= location

Defect either V - Vacancy or

Zn - Atomic symbol

Location either -lattice site labelled with chemical symbol of sublattice

for example Vzn Vo

or - interstitial space i

Effective charge

Excess charge imparted to crystal by the introduction of the defect.

Effective charge works well in ionic systems but it is not used for metals or semiconductors.

| = - ve or e^{-} ---> è

o = + ve

x = neutral

For example, in ZnO crystal if Zn^{+} is put in interstitial, one net +ve charge results. This can be represented as Zn^{o}_{i}

V^{oo}_{o} ~ means vacancy at oxygen site with charge ++

In some materials the excess or missing electrons, è or h^{o} , may not remain localized at the vacant site, the separation can be represented by the reactions

$$V^{|}Na = VNa + \grave{e}$$
$$V^{o}cl = Vcl + h^{o}$$

The superscript + and - are used to indicate real charged ions, whereas the superscripts o and | indicate effective positive and negative charges with respect to the host lattice [84].

In this theory [21] the binary nonmetallic compounds of the formula MX have been considered. Where M represents an element of a more electropositive character (cation-metal) and X an element of a more electronegative character (Anion). The theory starts by distinguishing the five primary types of atomic disorder in a pure compound MX.

(1) Interstitial sites occupied by atoms M (= Mi), together with an equal concentration of vacancies, that is sites where an M atom has been removed (Vm).

(2) Interstitial sites occupied by atoms X (=Xi), together with an equal concentration of sites where an X atom is missing (Vx).

(3) Vacant M sites (Vm), together with an equal concentration of vacant X sites (Vx).

(4) Interstitial atoms Mi together with an equal concentration of interstitial atoms Xi.

(5) Part of the atoms M occupy X positions (Mx) and an equal number of X atoms occupy M positions (Xm).

Combination of these five types are also possible. The first and second type, first mentioned by Frenkel, is generally called the *Frenkel* disorder. The third type is usually called the *Schottky-Wagner*. The fourth is thought to be very rare. The fifth type is called antistructure disorder. Further more, in each type of disorder, the two compensating imperfections may be distributed at random or may be present at adjacent sites forming association. Examples of those association which consist of a pair of imperfections are, (VmMi),(VxXi),(VmVx), and (MxXm). More intricate cases can be treated along the same lines.

Appendix B: Impedance Spectroscopy

A.C. theory is concerned with sinusoidally varying currents and voltages. Alternating voltage may be described by the relation [94],

$$E = Eo \exp(j\,\omega\,t) = Eo(\cos\omega\,t + j\sin\omega\,t) \qquad (1.2.1)$$

where Eo = signal amplitude and t = time. Similarly the current produced by such an alternating e.m.f. can be described by the expression,

$$I = Io(\cos\omega t + j\sin\omega t) \qquad (1.2.2)$$

with the real parts of the expression (1.2.1) and (1.2.2), Eo cos ω t and Io cos ω t, representing observable quantities.

For a pure resistance the current and voltage are related by Ohm's law to give,

$$I_R = E/R = (Eo/R)(\cos\omega\,t + j\sin\omega\,t) \qquad (1.2.3)$$

where I_R = the current across the resistance R.

For a purely capacitive component, C,

$$Q = CV$$

from which the current is given by,

$$\begin{aligned} I_C &= \delta Q/\delta t = \delta(CV)/\delta t \\ &= \delta/\delta t\, CEo(\cos\omega t + j\sin\omega t) \qquad (1.2.4) \\ &= CEo(-\omega\sin\omega t + j\,\omega\cos\omega t) \\ &= jC\omega Eo(-\sin\omega t/j + \cos\omega t) \\ &= jC\omega Eo(\cos\omega t + j\sin\omega t) \end{aligned}$$

Equation (1.2.3) & (1.2.4) may be written respectively as,

$$I = E/R$$

$$Ic = j\omega CE \qquad (1.2.5)$$

where Q = the charge on the capacitor plates. From equation (1.2.3) and (1.2.5) and it can be seen that the current across a pure resistance is in phase with the applied e.m.f. whilst the current across a pure capacitor leads the applied e.m.f. by a phase angle of 90^o. For an arbitrary circuit, the total impedance is related to the individual impedances of the circuit elements in the same way as the total resistance of an array of resistors. For example, in a parallel network we have,

$$Z_t^{-1} = \Sigma_j Z_j^{-1} \qquad (1.2.6)$$

where Z_t = total impedance of the parallel network. For series case we have,

$$Z_t = \Sigma_j Z_j \qquad (1.2.7)$$

Thus in the case of a parallel combination of a resistor and capacitor (or a Voigt element) the total impedance is given by,

$$Z_t = (1/R + j\,\omega C)^{-1} \qquad (1.2.8)$$

The real and imaginary components of equation (1.2.8) can be resolved into,

$$Z' = [R\,(1/R^2 + \omega^2 C^2)]^{-1} \qquad (1.2.9)$$
$$Z'' = \omega\, C\,(1/R^2 + \omega^2 C^2)^{-1} \qquad (1.2.10)$$

where Z', Z" are the real and imaginary components respectively. It has been shown [94] that a complex plane plot of Z_t will describe a semi-circle (discussed in section 3.4). At the apex of the semi-circle, it is clear that |Z'| = |Z"| and we thus have,

$$\omega_c = (RC)^{-1} \qquad (1.2.11)$$

where ω_c = the frequency at the apex of the semi-circle and is known as the time constant of the circuit.

Appendix C: IS Data for ZnO ceramic

ApndxTable 1.. IS Data for ZnO varistor synthesised in the laboratory, Ag electrodes.

	ZnO + all (Bi, Sb, Co, Mn, Cr) 10.6mm ∅ x 2mm.Ag, Electrode	19	ρ(Ωcm)	Freq. Hz	C	Ea (eV)
1		197	1277628	423	0.3nF/cm	0.92 ± 0.03
2		293	55792	11E3	0.2nF/cm	
3 4		401	3150, 435	180E3, 1.3E3	0.3nF/cm 0.3μF/cm	
5 6		500	334, 132	1.8E6, 4.4E3	0.2nF/cm 0.3μF/cm	
7 8		557	48, 16	1.8E6, 27E3	1.7nF/cm 0.4μF/cm	1.94 ±0.13
9		600	5.4	56E3	0.6μF/cm	

ApndxTable 2. IS Data for Bi based ZnO varistor (Commercial sample)

	Samples: sintered at 1250°C	Temp. (°C)	ρ(Ωcm)	Freq. Hz	C	Ea (eV)
1	PD good 8.7mm x 9.2mmx 3.4 mm	302	280416	1.8E3	0.3nF/cm	1.14 ± 0.05
2 3		400	13296, 5011	37E3,3 356	0.3nF/cm 88nF/cm	
4 5		501	1378, 240	466E3 2.8E3	0.2nF/cm 0.24μF/cm	
6 7		600	139.2, 36	2E6 57E3	0.5nF/cm 0.13μF/cm	

ApndxTable 3.. IS Data for Bi based ZnO varistor (Commercial sample).

	Samples: sintered at 1250°C	Temp. (°C)	ρ(Ωcm)	Freq. Hz	C nF/cm	Ea (eV)
1	ZnO + (BP) Commercial 7.6mm Ø, 1.3mm (cut from a large sample)	150	1.89E6	100	0.8	0.99±0.8
2		200	3.47E5	707	0.7	
3		250	4.2E4	5E3	0.7	
4		300	6.56E3	3.16E4	0.8	
5		335	3.25E5	1.78E3	0.3	
6		535	4.7E3	1.77E5	0.2	
7		635	350	1.99E6	0.2	

ApndxTable 4.. IS Data for Pr based ZnO varistor (Commercial sample).

	Samples: sintered at 1250°C	Temp. (°C)	ρ(Ωcm)	Freq. Hz	C nF/cm	Ea (eV)
1	ZnO +Pr, Co, La (1250°C) 14.4mm Ø, 1.6mm	147	20256210	20	0.4	1.00 ± 0.02
2		197	1433814	335	0.3	
3		248	167444	3.4E3	0.3	
4		302	21477	35E3	0.2	
5		399	1089	725E3	0.2	
6		453	295	2E6	0.3	
7		500	6	285E3	93	

ApndxTable 5. IS Data for ZnO ceramic doped with Bi.

	Samples: sintered at 1250°C	Temp. (°C)	ρ(Ωcm)	Freq. Hz	C (nF/cm)	Ea (eV)
1	**ZnO + Bi**, 10.5mm ∅ x 2.2mm t	20	32038.4	1.4E3	3.6	0.20 ± 0.01
2		55	21529.9	2.2E3	3.3	
3		112	11847.4	4.3E3	3	
4		144	5982.7	13E3	2	
5		202	3247	27E3	1.8	
6		247	2381	44E3	1.5	
7		300	2164	44E3	1.7	
8		398	1255	70E3	1.8	
9		600	90.0	915E3	1.8	

ApndxTable 6. IS Data for ZnO ceramic doped with Bi, Co.

	Samples: sintered at 1250°C	Temp. (°C)	ρ(Ωcm)	Freq. Hz	C (nF/cm)	Ea (eV)
1	**ZnO + Bi, Co,** 10.6mm ∅ 1.8mm	20	588315.6	52	5.2	0.35 ± 0.05
2		67	293177	132	4	
3		155	68587.8	851	2.7	
4		251	17444	3.4E3	2.7	
5		400	1318.8	56E3	2.1	
6		500	142.1	455E3	2.4	

ApndxTable 7. IS Data for ZnO ceramic doped with Bi, Sb.

	Samples: sintered at 1250°C	Temp. (°C)	ρ(Ωcm)	Freq. Hz	C (nF/cm)	Ea (eV)
1	ZnO + Bi, Sb, 10.0mm∅ 1.5mm	19	30683	13E3	0.38	0.16 ± 0.01
2		57	20891.6	22E3	0.3	
3		110	13194.7	44E3	0.3	
4		156	8744	78E3	0.3	
5		203	5916.7	112E3	0.2	
6		300	3838	142E3	0.3	
7		397	1911	226E3	0.36	
8		500	414	915E3	0.4	
9		598	49	2E6	1.6	

ApndxTable 8. IS Data for ZnO ceramic doped with Bi, Sb , Bias 35V.

	Samples: sintered at 1250°C	Temp. (°C)	ρ(Ωcm)	Freq. Hz	C (nF/cm)	Ea (eV)
1	ZnO + Bi, Sb, 10.0mm∅ 1.6mm 35V bias.	200	124000	5E3	0.25	
2		250	4550	1.41E5	0.25	
3		300	4350	1.41E5	0.26	
4		350	3460	1.58E5	0.29	
5		450	1450	2.81E5	0.4	
6		500	26	/	/	

ApndxTable 9. IS Data for ZnO ceramic doped with Bi, Co, Mn

1	ZnO +Bi, Co, Mn 10.5mm ∅ 1.5mm	21	516943	335	0.9 nF/cm	0.2 ±
2		50	375628	534	0.8	
3		153	72620	1.7E3	1.3	
4		247	7447	11E3	1.9	0.95 ±
5		343	750	89E3	2.3	
6		500	10	455E3	33.8	

ApndxTable 10. IS Data for ZnO ceramic doped with Bi, Sb, Mn, Co

	Samples: sintered at 1250°C	Temp. (°C)	ρ(Ωcm)	Freq. Hz	C (nF/cm)	Ea (eV)
1	ZnO + Bi, Sb, Mn, Co,10.1mm Ø, 1.3mm	20	1.9E8	5	0.2	1.2 ± 0.09
2		58	67636800	12	0.2	
3		108	34003200	16	0.3	
4		155	18480000	52	0.2	
5		204	1765641	674	0.1	0.21 ± 0.01
6		251	105767	13E3	0.1	
7		304	18788	70E3	0.1	
8		352	4244	285E3	0.1	
9		403	203	1E6	0.4	

ApndxTable 11. IS Data for ZnO ceramic doped with Bi, Sb, Mn, Co, Cr. Rapidly cooled.

1	ZnO + all (Bi,Sb, Mn, Co, Cr) Rapidly cooled,10.22mm Ø x 2.1mm .	20	1189.5	285E3	0.5 nF/cm	0.21± 0.02
2		58	795.6	455E3	0.5	
3		113	362.7	725E3	0.6	
4		154	175.5	915E3	1	
5		204	85.8	1E6	1.5	
6		251	66.3	1E6	2.2	
7		302	66.3	915E3	2.4	
8		349	31.2	725E3	7	
9		396	19.5	574E3	17	
10		447	15.6	574E3	16.5	
11		496	66.3	725E3	3	
12		547	124.8	915E3	1.3	
13		597	70.2	1E6	1.8	

ApndxTable 12. IS Data for ZnO ceramic commercial varistor, sample 13.3mm Ø x 1.6mm.

	Samples: Commercial ZnO varistor (NPL) sample:13.3mm Ø x 1.62mm. bias Off	Temp. (°C)	ρ(Ωcm)	Freq. Hz	C (nF/cm)	Ea (eV)
1		200	8E6	141	0.14	0.93 ± 0.02
2		250	1.4E6	891	0.13	
3		300	2.9E5	4467	0.12	
4		350	6.69E4	17783	0.13	
5		400	1.8E4	70794	0.12	
6		450	5.33E3	2.2E5	0.13	
7		500	2.1E3	5.6E5	0.13	

ApndxTable 13.. IS Data for ZnO ceramic commercial varistor

	Samples: Commercial ZnO varistor (NPL) sample:13.3mm Ø x 1.62mm thickness. 35VBs	Temp. (°C)	ρ(Ωcm)	Freq. Hz	C (nF/cm)	Ea (eV)
1		200	8.7E6	100	0.18	0.89 ± 0.03
2		250	1.4E6	631	0.18	
3		300	2.7E5	3981	0.15	
4		350	5.6E4	17783	0.16	
5		400	1.07E4	89125	0.17	
6		450	4.2E3	2.8E5	0.13	
7		500	1.8E3	6.3E5	0.14	

Appendix D: The Dihedral angle

It has been shown [84] that the dihedral angle ϕ in ceramics depends on the relationship between the interfacial and grain-boundary energies according to the relationship:

$$\text{Cos}\ (\phi/2) = 1/2\ (\gamma_{ss}/\gamma_{sL})$$

Solid liquid equilibrium condition is shown in Fig. AD1.

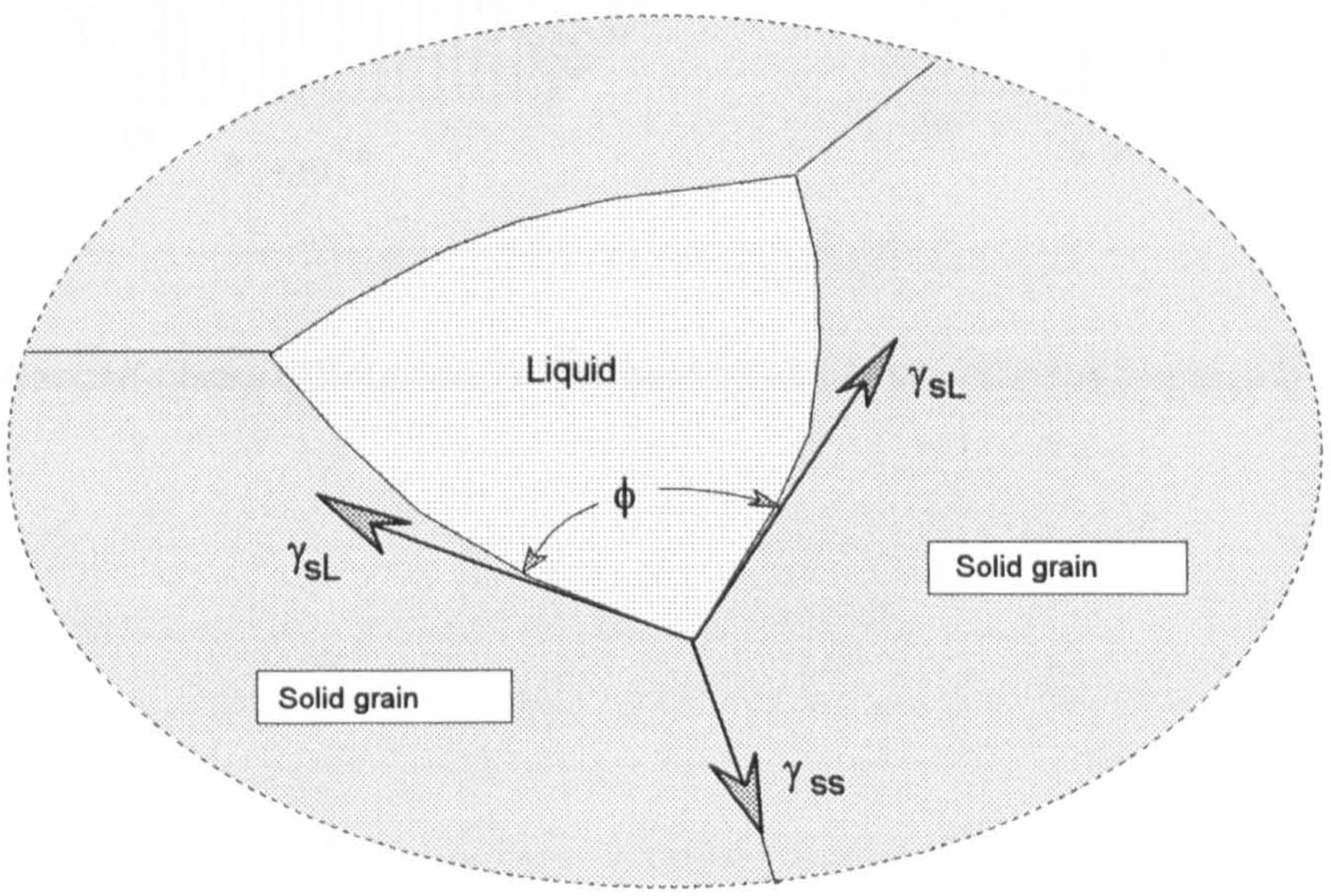


Fig.AD1. Dihedral angle for solid-solid-liquid equilibrium [84].

where γ_{ss} and γ_{sL} are the solid-liquid interfacial energy and solid-solid interfacial energy. If the interfacial energy γ_{sL} is greater than the grain-boundary energy, ϕ is greater than 120° and the second phase forms isolated pockets of material at grain intersections. If the γ_{ss}/γ_{sL} is between 1 and $\sqrt{3}$, ϕ is between 60 and 120°, and the second phase partially penetrates along the grain intersections at corner of three grains. If the ratio between γ_{ss} and γ_{sL} is greater than $\sqrt{3}$, ϕ is less than 60°, and the second phase is stable along any length of grain edge forming triangular prisms at the intersections of three grains. When γ_{ss}/γ_{sL} is equal or greater then 2, ϕ equals zero, and at equilibrium the faces of all the grains are completely separated by the second phase. Fig. AD2 illustrates these structures.

These relationships are important in processes that takes place during firing of powder compacts.

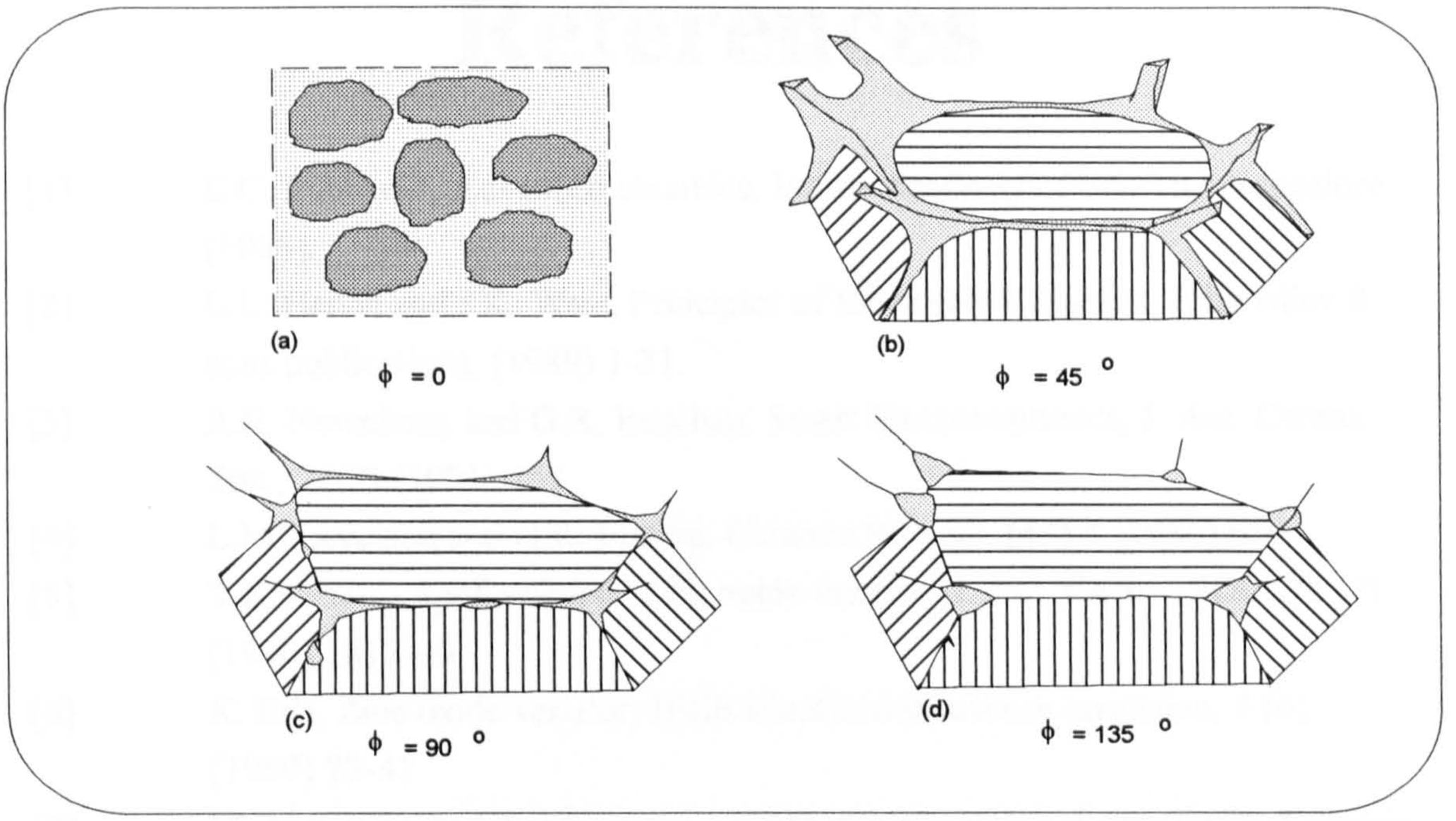


Fig. AD2. Second-phase distribution for different values of the dihedral angle [84].

References

[1] E.C. Subbarao, Advanced ceramics, Indian Academy of Sciences Bangalore (1988).

[2] L.L. Hench and J.K. West, Principles of Electronic Ceramics, John wiley & sons publications, (1989) 1-31.

[3] R.E. Newnham, and G.R. Ruschau, Smart Electroceramics, J. Am. Ceram. Soc., **74**(3) (1991) 463.

[4] L.M. Levinson and H.R. Philipp, Ceramic Bulletin, **(65)** 4 (1986) 639.

[5] T.K. Gupta, Application of Zinc oxide varistor, J. Am. Ceram. SOC.,**73** (7) (1990) 1817-40.

[6] K. Eda, Zinc oxide varistor, IEEE Electrical insulation magazine, **5** (6) (1989) 28-41.

[7] M. Matsuoka and T. Masuyama, Voltage nonlinearity of Zinc Oxide Ceramic Doped with Alkali Earth Metal oxide, Jap. J.Appl. Phys., **8** (1969) 1275-1276.

[8] M. Matsuoka, Discovery Of ZnO Varistors And Their progress For The Two Decades, Edited by L.M. Levinson, American Ceramic Society, Westerville, 1989, Proceedings of the Second International Varistor Conference held in Schenectadly, NY., Ceramic Transactions, Advances in Varistor Technology, **3** (1988) 3-9.

[9] M. Matsuoka, Non-ohmic properties of ZnO ceramics, Jap. J. Appl. Phys., **10** (6) (1971) 736-46.

[10] M.G.Gee, Electrical ceramics, Division of materials applications, National Physical Laboratory, Teddington, Middlesex, Presented in Metals and Materials, (1986) 769-775.

[11] L.M. Levinson, Advances in Varistor Technology, Ceramic Bulletin, **68** (4) (1989) 866-868.

[12] R. Einzinger, Metal oxide varistor, Am. Rev. Mat. Sci., **17** (1987) 299-321.

[13] H.C. Ling, M.F. Yan and W.W. Rhodes, Monolithic device with dual capacitor and varistor functions, J. Am. Ceram Soc., **72** (7) (1989) 1274-76.

[14] M. Sumiyoshi, Discovery of ZnO Varistor and their progress for the two decades, In Application Technology Of ZnO Varistors, Advances in Varistor Technology, Edited by L.M. Levinsom, Am. Ceram. Soc., Westerville, OH, 1989, Proceedings of the Second International Varistor Conference held in Schenectadly, NY.**3** (1988) 23-30.

[15] S.W.K. Morgan, Zinc and its Alloys and compounds, Ellis Horwood Ltd., John Wiley & Sons (1977) 218-223.

[16] A. Holderness and J.Lambert, A New Certificate Chemistry, forth edition published by Heinemann Educational Books Ltd, 48 Charles St., London W1X 8AH, (1975) 242-246.

[17] Y. Suyama, Y. Tomokiyo, T. Manabe, and E. Tanaka, Shape and structure of Zinc Oxide particles prepared by vapour phase oxidation of Zinc vapour, (Japan fine ceramic centre) J.Am. Ceram. Soc.,**71** (5) (1988) 391-95.

[18] D. Eger, Y. Goldstein and A. Many, RCA review, **36** (1975) 509-530.

[19] R. A. Swalin, Thermodynamics of Solids, John Wiley & Sons, Inc., (1964) 306-313.

[20] J.F. Cordaro, Deep Levels in Zinc Oxide Materials, Discovery of ZnO Varistor And Their progress For The Two Decades, ed by L.M. Levinsom, American Ceramic Society, Westerville, OH, 1989, Proceedings of the Second International Varistor Conference held in Schenectadly, NY.**3** (1988) 125-134.

[21] F.A KrÖger, and H.J, Vink, Relations Between The Concentrations of Imperfections In Crystalline Solids, in Solid State Physics, Academic Press, New York, **3** (1956) 307-435.

[22] W.G. Morris, Electrical properties of ZnO-Bi2O3 ceramic J.Am.Ceram. Soc., **56** (7) (1973).

[23] G.Blatter and F.Greuter, Electrical breakdown at semiconductor grain boundaries, Physical review B, **34** (12) (1986) 8555-72 .

[24] G.Blatter and F.Greuter, Carrier transport through grain boundaries in semiconductors, Physical review B, **33** (6) (1986) 3952-33.

[25] J. Wong, Microstructure and phase transformation in a highly non-Ohmic metal oxide varistor ceramic, J. Appl. Phys., **46** (4) (1975) 1653-1659.

[26] A. Paul, H.N. Acharya, Equilibrium thermodynamics of nonstoichiometry in ZnO and aluminium doping of ZnO using aluminium chloride, J. of Mat. Sci. **27** (1992) 1716-1722.

[27] S.M. Sze, Physics of Semiconductors Devices, John Wiley & Sons, 2nd edition (1981) 402 and 497.

[28] M.H. Sukkar and H.L Tuller, Defect Equilibria in ZnO Varistor Materials, Advances in Ceramics, edited by M.F. Yan and A.H. Heuer,Am. Ceram. Soc., Columbus, Ohio, 7 (1983) 71-90.

[29] J.C. Anderson, K.D.Leaver, J.M. Alexander and R.D. Rawlings, materials science, 2nd edition, Thomas Nelson and Sons Ltd., (1982) 150.

[30] E. Olsson and G.L. Dunlop, Proceedings of the 6th CIMTEC, ed., by P. Vincenzini, Elsevier, New York, (1987) 1765-1774.

[31] J. Wong and W.G.Morris, Microstructure and phases in Non-ohmic ZnO-Bi_2O_3 ceramic; Ceramic bulletin, **53** (11) (1974) 816-20.

[32] I. Masanari, Microstructure of non-ohmic ZnO ceramic, Jap. J. Appl. Phys., **17** (4) (1978) 673-77.

[33] D.R. Clark, The microstructural location of the intergranular metal oxide phase in a ZnO varistor, J.Appl. Phys., **49** (4) (1978).

[34] W.D. Kingery, J.B. Vandesande and T. Mitamura, A scanning Transmission electron microscopy investigation of grain-boundary segregation in a ZnO-Bi_2O_3 varistor, J. Am. Ceram. Soc., **62** (3-4) (1979) .221-222.

[35] I. Masanori, Effect of Heat-treatment on Crystal phases, Microstructure and Electrical properties of Nonohmic Zinc Oxide ceramics, Jap. J. Appl. Phys., **18** (8) (1979) 1439-1446.

[36] Y.M. Chiang, W.D. Kingery and Lionel M. Levinson, Compositional changes adjacent to grain boundaries during electrical degradation of a ZnO varistor, J.Appl. Phys., **53** (3) (1982).

[37] T.K. Gupta. and W.G. Carlson, A grain boundary defect model for instability / stability of a ZnO varistor, J.Mat.Sci., **20** (1985) 3487-3500.

[38] R. Einzinger, Grain Boundary Phenomena In ZnO Varistors, Mat. Res. Soc., Proc., Edited by Pike, Seager and Leamy, **5** (1982) 333-341.

[39] E. Olsson, L.K.L. Falk and G.L. Dunlop, The microstructure of a ZnO varistor material, J.Mat. Sci., **20** (1985) 4091-4098.

[40] H. Cerva and W. Russwurm, Microstructure and crystal structure of bismuth oxide phases in ZnO varistor ceramic, J.Am. Ceram. Soc., **71** (7) (1988) 522-30.

[41] S.H. Fan, H.J. Wang, S.L Wang and Y.C. Xu, Discovery Of ZnO Varistors And Their progress For The Two Decades; Edited by L.M. Levinsom, Am. Ceram. Soc., Westerville, 1989, Proceedings of the Second International Varistor Conference held in Schenectadly, NY.,Ceramic Transactions, Advances in Varistor Technology, **3** (1988) 3-9.

[42] J.P. Gambino, W.D. Kingery, G.E. Pike, L.M. Levinson and H.R. Philipp, Effect of heat treatment of the wetting behaviour of bismuth-rich intergranular phases in ZnO:Bi:Co varistors, J.Am. Ceram. Soc., **72** (4) (1989) .642-45.

[43] T. Ashokan, Nagabhushana and G.N.K. Iyengar, Improvement Of Non-Linear Characteristics Of Multicomponent ZnO-based Ceramic Containing Nb_2O_5, IEEE Transactions on Electrical Insulation, **23** (2) (1988) 279-285.

[44] T. Asokan, G.N.K. Iyenger, and G.R. Nagabhushana, Influence of Process Variables on Microstructure and V-I Characteristics of Multicomponent ZnO-Based Nonlinear Resistors, J. Am. Ceram. Soc., **70** (9) (1987) 643-650.

[45] J. Kim, T. Kimura, and T. Yamaguchi, Sintering of ZnO doped with Sb_2O_3 and Bi_2O_3, J. Am. Ceram. Soc.,**72** (8) (1989) 1390-95.

[46] E. Olsson and G.L. Dunlop, characterization of individual interfacial barriers in a Zinc oxide varistor material, J. Appl. Phys., **66** (8) (1989) 3666-75.

[47] E. Olsson and G.L. Dunlop, The effect of Bi_2O_3 content on the microstructure and electrical properties of ZnO varistor materials, J.Appl.phys., **66** (9) (1989) 4317-24.

[48] E.Olsson, G.L. Dunlop and R. Osterlund, Development of interfacial microstructure during cooling of a Zinc oxide varistor material, J. Appl. Phys., **66** (10) (1989) 5072-77.

[49] E. Olsson, G. Dunlop. and R. Osterlund, Development of Functional Microstructure during Sintering of a ZnO Varistor Material, J. Am. Ceram. Soc., **76** (1) (1993) 65-71.

[50] A. Peigney, H. Andrianjatovo, R. Legros, and A. Rousset, Influence of chemical composition on sintering of bismuth-titanium-doped zinc oxide, J.Mat.Sci. **27** (1992) 2397-2405.

[51] G.D. Mahan, L. Levinson and H.R.Philipp, GEC, N Y., Theory of conduction in ZnO varistor, J.Appl. Phys. **50** (4) (1979) 2799-2812.

[52] G.D. Mahan, Theory of ZnO Varistors, Grain Boundaries in Semiconductors, Mater. Res. Soc. Proc., ed. by Pike, Seager and Leamy, **5** (1982) 343-354.

[53] F. Greuter, G. Blatter. F. Stucki, and M. Rossinelli,"Conduction Mechanism in ZnO Varistors: An Overview"; Advances in Varistor Technology, ed. by L.M. Levinson, Am. Ceram. Soc., Proceedings of the Second International Varistor Conference held in Schenectadly, Ceramic Transactions, **3** NY. (1988) 31-53.

[54] J. Leslie, Bowen and F. J. Avella., Microstructural, electrical properties and failure prediction in low clamping voltage ZnO varistors, J.Appl. Phys., **54** (5) (1983) 2764-2772 .

[55] G.E. Pike, S.R.Kurtz and P.L.Gourley, Electroluminescence in ZnO varistors, Evidence for hole contribution to the breakdown mechanism, J.Appl. Phys., **57** (12) (1985).

[56] K. Eda, Conduction mechanism of non-Ohmic zinc oxide ceramics, J.Appl. Phys., **49** (5) (1978) 2964-72.

[57] M. Trontely, D. Kolar and V.Krasevec., The microstructure of non-ohmic ZnO ceramics, J.of microscopy, **124** (3) (1981) 285-289.

[58] K. Eda, M. Inada and M. Matsuoka, Grain growth control in ZnO varistor using seed grain, J.Appl.Phys., **54** (2) (1983) 1095-99.

[59] P.R. Ematage, The Physics of zinc oxide varistors, J. Appl.Phys.**48** (10) (1977) 4372-84.

[60] P.L. Hower and T.K. Gupta, A barrier model for ZnO varistors, J.Appl.Phys., **50** (7) (1979) 4847-55.

[61] G E. Pike, Electronic Properties of ZnO Varistors, A New Model, Mater. Res. Soc. Proc. Edited by Pike, Seager,and Leamy, **5** (1982) 369-379.

[62] L.M. Levingson and H.R.Philipp, The physics of metal oxide varistors, General Electric Corporate research N.Y. J.Applied Physics, **46** (3) (1975).

[63] Y. Suzuoki, Ohki, Mizutani and M. Ieda, Electrical Properties Of ZnO-Bi_2O_3 Thin-Film Varistors, J. Phys. D: Appl. Phys., **20** (1987).511-517.

[64] M.A. Lampert, Simplified Theory of Space-Charge-Limited Current in an Insulator with Traps, Phys. Rev., **103** (6) (1956) 1648-56.

[65] M.G. Gee and M. Stewart, Some Observations on the Structure Of Zinc Oxide Varistors, National Physical Laboratory, Teddington, Middlesex, (1990) 213-223.

[66] L.M. Levinson, H.R. Philipp, and G. D. Mahan, Evidence For Parallel Conduction Paths In ZnO Varistors, in ceramic Transactions, Advances in Varistor Technology, ed. by L.M. Levinsom, Am. Ceram. Soc., Westerville, OH, 1989, Proc. of the Second International Varistor Conference held in Schenectadly, NY., **3** (1988) 145-154.

[67] M. Tao, B. Ai, O. Dorlanne and A. Loubiere, Different "single grain junctions" within a ZnO varistor, J. Appl. Phys., **61** (4) (1987) 1562-1567.

[68] T.S. Irvine, D.C. Sinclair, and A.R. West, Electroceramics Characterisation by Impedance Spectroscopy, Adv. Mater., **2** (3) (1990) 132-138.

[69] R.G. Wilson, F.A. Steive and C.W. Magee, Secondary Ion Mass Spectrometry, A practical handbook for depth profiling and bulk impurity analysis, John Wiley & Sona (1989).

[70] D.B. Holt and D.C. Joy, SEM microcharacterisation of semiconductors Techniques of Physics, 12 Academic press limited (1989).

[71] J.R. Macdonald, Impedance Spectroscopy, John Wiley & Sons, A Wiley - Interscience publication (1987).

[72] H.J.Leamy, Charge collection scanning electron microscopy, J. Appl. Phys.**53** (6) (1982) 51-80.

[73] D.R. Clarke, High spatial resolution analysis of grain boundaries, techniques and applications, Advances in ceramics volume **1**, ed. by L. M. Levinson, Grain boundary phenomena in electronic ceramics, proceedings of a symposium Chicago, Illinois, (1980) 67-90.

[74] R. Waser, Grain Boundaries, The Functional Heart of Electronic Ceramics, Third Euro-Ceramics, **2** (1993) 23-28.

[75] R.D.K. Pindoria, D.S McPhail, B.C.H. Steele, R.J. Chater, and D.B. Holt, SEM-EBIC and SIMS studies of ZnO varistor, Third Euro-Ceramics,**1** (1993) 845-850.

[76] J.O. Levine, Theory of Varistor Electronic Properties, CRC Crit. Rev. Solid State Sci., **5** (1975) 597-608.

[77] W.G. Morris, Physical properties of the electrical barriers in varistors, J. Vac. Sci. Technol., **13** (4) (1976) 926-931.

[78] L.K.J. Vanadamme and J.C. Brugman, Conduction mechanisms in ZnO varistors, J. Appl. Phys., **51** (8) (1980) 4240-4244.

[79] J. Bernasconi, S. Strässler, B. Knecht, H. P. Klein and A. Menth, Zinc oxide based varistors, A possible mechanism, Solid State Commun., **21** (1977) 867-870.

[80] D.S. McPhail, SIMS depth profiling of semiconductors, Secondary ion mass spectrometry principles and applications, Clarenden press, Oxford, (1989), 105-148.

[81] M. Rossinelli, Blatter and F. Greuter, Grain boundary properties of ZnO varistor, Brit. Cerm. Soc., **36** Ed. by B.C.H. Steele (1986) 1-17.

[82] J.E. Bauerle, Study of solid electrolyte polarisation by a complex admittance method, J. phys. Solids, **30** (1969) 2657-2670.

[83] E.H. Rhoderick, Metal Semiconductor Contacts, Oxford University Press, Walton Street, Oxford OX2 6DP (1980).

[84] Kingery, Bowen, Uhlmann, Introduction to Ceramics, John Wiley & Sons, A Wiley - Interscience Publication, (1976), 129.

[85] H.K. Henisch, Semiconductor contacts An approach to ideas and models, International series of monographs on physics No. 70, Oxford University Press, Walton Street, Oxford, OX2 6DP, (1984).

[86] J.G. Fagan and R.W. Amarakoon, Reliability and Reproducibility of Ceramic Sensors, PTC Thermistors, American Ceramic Soc. Bulletin **72** (2) (1993) 69-76.

[87] C.A. Klein, Bandgap Dependence and Related Features of Radiation Ionization Energies in Semiconductors, J. Appl. Phys., **39** (1968) 2029-2038.

[88] W. Ehrenberg and D.J. Gibbons, Electron Bombardment Induced Conductivity and its applications, Academic Press, London, (1981).

[89] A. Smith, J.F. Baumard, P. Abelard, and M.F. Denanot, ac impedance measurements and V-I characteristics for Co-,Mn-, or Bi-doped ZnO, J. Appl. Phys., **65** (1989) 5119-125.

[90] J.D. Faktor, Ph.D., Thesis. Imperial College, University of London (1983).

[91] D.J. Gray, Ph.D., Thesis. Imperial College, University of London (1989).

[92] E.J.L. Schouler, Giroud and M. Kleitz, Application according to Bauerle of the plot of complex admittance diagrams in the electrochemistry of solids.- Conductivity of yttrium - stabilized zirconia, J. Chem. Phys., **70** (1973), 1039.

[93] Operation and service manual for 4192A LF Impedance analyser, by Hewlett and Packard, section VIII (1985) 8-1.

[94] A. Hooper, AC measurement and analysis techniques., J. Electrochem. Soc. **107**, (1960) 480.

[95] S.B. Patel, Ph.D., Thesis, Imperial College, University of London (1993) 26.

[96] H. Frenzel, J.L. Maul, H. Mertens, R. Raab, and C.H. Scholze, Proceedings of the Sixth International Conference on Secondary Ion Mass Spectrometry (SIMS VI), ed. by Benninghoven, A., Huber, A.M., Werner, H.W., John Wiley and Sons (1987) 219.

[97] K.J. Wittmaack, Appl. Phys., **50** (1) (1979) 493.

[98] S.D. Littlewood, J.K. Kilner, and S. Biswas, Proceeding of the Sixth International Conference on Secondary Ion Mass Spectrometry (SIMS VI), ed. by Benninghoven, A., Huber, A.M., Werner, H.W., John Wiley and Sons (1987) 89.

[99] D.S. McPhail, M.G. Dowsett, and E.H.C Parker, proceeding of the Fifth International Conference on Secondary Ion Mass Spectrometry (SIMS V), ed. by Benninghoven, Colton, R.J., Simons, D.S., and A.M., Werner, Springer (1985) 343.

[100] D.S. McPhail, M.G. Dowsett and E.H.C. Parker, profile distortion during secondary ion mass spectrometry analyses of resistive layers due to electrons stimulated desorption and charging, J. Appl. Phys., **60** (6) (1986) 2573.

[101] R.J. Chater, S. Carter, J.K. Kilner, B.C.H. Steele, Development of a novel SIMS technique for oxygen self-diffusion and surface exchange coefficient measurements in oxides of high diffusivity, Solid State Ionics, 53-56 (1992) 859-867,

[102] J. A. Kilner, New techniques for studying mass transport in oxides, Mat. Sci. Forum, 7 (1986), 205-222.

[103] J.A. Kilner, B.C.H. Steele and L. Ilkov, Oxygen self-diffusion studies, Solid State Ionics, **12** (1984) 89-97.

[104] J.W. Edington, Department of Metallurgy and Materials Science, University of Cambridge, England. Monographs in Practical Electron Microscopy In Material Science, Monograph 1, The operation and calibration of the electron microscope, Macmillan, Philip Technical Library, 1-33.

[105] J.W. Edington, Department of Metallurgy and Materials Science, University of Cambridge, England, Monographs in Practical Electron Microscopy In Material Science, Monograph 4, Typical Electron Microscope Investigations, Philips Technical Library, 1-75.

[106] L. L. Merrit, J. A. Dean, and F. A. Settle, Instrumental Methods of Analysis, 6th edition, Wiley Publications, (1985). 247-287.

[107] Y. Suyama, Shape and structure of Zinc Oxide Particles Prepared by Vapour-Phase Oxidation of Zinc Vapour, J. Am. Ceram. Soc., **71** (5) (1988) 391-95.

[108] D. Dey, R. C. Bradt, Grain Growth of ZnO during Bi_2O_3 Liquid-Phase Sintering., J. Am. Ceram. Soc., **75** (9) (1992) 2529-34.

[109] M. Mendelson, 'Average Grain Size in Polycrystalline Ceramics,' J. Am. Ceram. Soc., **52** (8) (1969) 443-46.

[110] A. Bernds, K. Löhnert, and E. Kubalek, SEM-EBIC Investigations Of ZnO Varistor Ceramics.,Journal De Physique, Colloque C2, supplément au no2, Tome 45, février (1984) 861-64.

[111] A. Miralles, A. Cornet, A. Herms and J.R. Morante, The influence of Cobalt on the Electrical Characteristics of ZnO Ceramics, Mat. Sci. and Eng., A109 (1989) 201-205.

[112] J.T. Czernuszka and N. Pratt, Cathodoluminescence-mode imaging of dislocation in zinc oxide, Philosophical Mag. Lett., **61** (3) (1990) 83-90.

[113] S. Fujitsu, H. Toyoda and H Yanagida, The enhanced diffusion of oxygen in ZnO varistor, Nippon-Seramikkusu-Kyokai-Gakujutsu-Ronbunshi, **96** (2) (1988), 119-123.

[114] A. R. West, Solid State Chemistry and its Applications, John Wiley & Sons Ltd., 1989, 453.

[115] R. J. D. Tilley, Defect Crystal Chemistry and its applications (1987), publishers: Blackie & Sons Ltd., Bishopbriggs, Glasgow, G 64 2 N2.

[116] J.D. Russell, D.C. Halls and C. Leach, Direct observation of grain boundary Schottky barrier behaviour in zinc oxide varistor material. (To appear in J. Mat. Sci. Lett.).

[117] J. Palm and H. Alexander, J. de phys IV, Colloq, C6, supplement to J. de Phys III 1 (1991) C6-101.

[118] R. Robin, A. R. Cooper, and A. H. Heuer, Application of a nondestructive single-spectrum proton activation technique to study oxygen diffusion in zinc oxide, J. Appl. Phys., **44** (8) (1973) 3770-3777.

[119] H. A. Harwig and A. G. Gerards, The Polymorphism of Bismuth Sesquioxide, Thermochimica Acta, **28** (1979) 121-131.

[120] J. Kim, T. Kimura and T. Yamagnchi, Effect of Bismuth oxide content on the sintering of Zinc Oxide, J. Am. Ceram. Soc., **72** (8) (1989) 1541-44.

BIBL. LORRAIN.